NDOT Research Report

Report No. 667-15-803

Analysis of Laterally-Loaded Large-Diameter Drilled Shafts

May 2018

Nevada Department of Transportation
1263 South Stewart Street
Carson City, NV 89712

Disclaimer

This work was sponsored by the Nevada Department of Transportation. The contents of this report reflect the views of the authors, who are responsible for the facts and the accuracy of the data presented herein. The contents do not necessarily reflect the official views or policies of the State of Nevada at the time of publication. This report does not constitute a standard, specification, or regulation.

TECHNICAL REPORT DOCUMENTATION PAGE

1. Report No.
667-15-803

2. Government Accession No.

3. Recipient's Catalog No.

4. Title and Subtitle
Improving Strain Wedge Model Capabilities in Analyzing Large Diameter Drilled Shafts Subjected to Lateral Loading in Cemented Soils

5. Report Date
May 31, 2018

6. Performing Organization Code

7. Author(s)
Sherif Elfass (0000-0003-3401-6513), Evan Saint-Pierre (0000-0001-7627-5279), Mohamed Ashour (0000-0001-6363-624X), Robert Watters (0000-0003-1484-1479), and Gary Norris (0000-0003-3409-8344).

8. Performing Organization Report No.

9. Performing Organization Name and Address
University of Nevada Reno
1664 N. Virginia St.
Reno, NV 89557-0258

10. Work Unit No.

11. Contract or Grant No.
P667-15-803

12. Sponsoring Agency Name and Address
Nevada Department of Transportation
1263 South Stewart Street
Carson City, NV 89712

13. Type of Report and Period Covered
Final Report

14. Sponsoring Agency Code

15. Supplementary Notes

16. Abstract

Cemented soils deposits located in Las Vegas valley have long been a challenge for engineers. These deposits can withstand considerable loads. They are, however, difficult to model or predict using typical site investigation techniques. For engineering purposes, these cemented soils, also commonly referred to as Caliche, are difficult to quantify their thickness, strength and lateral extent. This erratic and heterogeneous nature can result in inconsistent design and performance of foundations. This report presents a new material model for cemented soils in the Las Vegas region. The material model was developed using results obtained from unconfined compressive strength tests conducted on 53 cored samples, with different levels of cementation. The model, which generates the stress-strain relationship of cemented soils, recognizes three cementation levels and allows the user to account for closure of fractures if desired. Laboratory shear and primary wave velocities were measured for all samples. In addition, field shear wave velocity of the site where the samples were obtained, was assessed using Refraction Microtremor (ReMi) and Multichannel Analysis of Surface Waves (MASW) methods. Relationships between lab shear wave velocity, material unit weight, unconfined compressive strength and Young's Modulus are presented. Furthermore, a preliminary correlation between field and lab shear wave velocities is introduced. The model along with the derived relationships were implemented in Strain Wedge Model (SWM) to assess the performance of laterally loaded shafts embedded in cemented soils. Comparison between SWM prediction and field performance of laterally loaded shafts during 1996 load test program is presented.

17. Key Words
Drilled Shafts, Laterally Loaded, Cemented Soil, Caliche, Strain Wedge (SW) Model.

18. Distribution Statement
No restrictions. This document is available through the:
National Technical Information Service
Springfield, VA 22161

19. Security Classif. (of this report)
Unclassified

20. Security Classif. (of this page)
Unclassified

21. No. of Pages
279

22. Price

Form DOT F 1700.7 (8-72) Reproduction of completed page authorized

Improving Strain Wedge Model Capabilities in Analyzing Large Diameter Drilled Shafts Subjected to Lateral Loading in Cemented Soils

Prepared for

The Nevada Department of Transportation

Prepared by

Sherif Elfass, Ph.D., P.E.
Evan Saint-Pierre
Mohamed Ashour, Ph.D., P.E.
Robert Watters, Ph.D.
and
Gary Norris, Ph.D., P.E.

Department of Civil and Environmental Engineering
University of Nevada
1664 N. Virginia St.
Reno, NV 89557-0258

May 31, 2018

University of Nevada, Reno

Table of Contents

Abstract .... **ix**
Acknowledgements .... **x**
Disclaimer .... **x**

Chapter 1: Introduction **1**
1.1 Background 1
1.2 Geologic Setting for the Current Study 3
1.3 Objective and Scope of Study 3
1.4 Organization of the Report 5

Chapter 2: Background on Cemented Soils and Existing Correlations **8**
2.1 Introduction 8
2.2 Observations from Previous Studies on Cemented Soils in the Las Vegas Valley 8
    2.2.1 Rinne et al. (1996) 8
    2.2.2 Stone et al. (2001) 9
    2.2.3 Cibor (1983) 10
    2.2.4 Stone (2013) 10
2.3 Correlation of Seismic Wave Velocity to Unconfined Compressive Strength (UCS) . 11
    2.3.1 Rucker (2000) 12
    2.3.2 Rucker (2006) 13
    2.3.3 Dincer et al (2008) 14
    2.3.4 Liu et al (2014) 15
    2.3.5 Nefeslioglu (2013) 16
2.4 Size Effect of Uniaxial Compressive Strength Tests 17
    2.4.1 Tuncay et al (2009) 17

Chapter 3: Field and Laboratory Test Program 20

3.1 Introduction 20

3.2 Site Selection 20

3.3 Field Geophysics 21

3.3.1 Multi-Channel Analysis of Surface Waves (MASW)... 22

3.3.2 Refraction Microtremor (ReMi) 23

3.4 Specimen Collection 24

3.5 Specimen Preparation 24

3.5.1 Specimen Coring 25

3.5.2 Specimen Cutting and Grinding 26

3.5.3 Alternative Preparation Methods 27

3.5.4 Method 1: Confinement in Concrete 27

3.5.5 Method 2: Reconstituted Caliche 28

3.6 Ultrasonic Velocity Testing 29

3.7 Unconfined Compressive Strength Testing 32

Chapter 4: Test Results 35

4.1 Introduction 35

4.2 rimary and Shear Wave Velocities 38

4.2.1 Field Measurements 39

4.2.2 Lab Velocities 41

4.3 Correlation Between Field and Lab Shear Wave Velocities 41

4.4 Correlation of Unconfined Compressive Strength and Lab Shear Wave Velocity 42

4.5 Correlation of Elastic Modulus and Lab Shear Wave Velocity 43

4.6 Correlation of Unit Weight with Lab Shear Wave Velocity 44

Chapter 5: Material Model 46

5.1 Introduction 46

5.2 Evaluation of Axial Strain 46

5.3 Establishing Strain Offset (Δε) 48

5.4 Material Model of Cemented Soil 50

Chapter 6: Fit of Present Data to Existing Correlations 61

6.1 Introduction 61

6.2 Compressive Strength Testing 61

6.3 Lab Geophysics 61

6.4 Primary Wave Velocity versus Unconfined Compressive Strength 62

6.5 Shear Wave Velocity versus Unconfined Compressive Strength 63

6.6 Shear Wave Velocity versus Unit Weight 64

6.7 Shear Wave Velocity versus Elastic Modulus 65

6.8 Material Model 65

Chapter 7: Implementation in Strain Wedge Model (SWM) Software 67

7.1 Introduction 67

7.2 Implementation of Current Work 67

7.2.1 Implementation of Vertical Side Shear (VSS) Resistance 68

7.2.2 Incorporation of Cemented Soil Material (Caliche) in the SW Model's Lateral Resistance 74

Stress Level (SL) in Caliche Materials 74

Chapter 8: Field and Model Verification 79

8.1 Introduction 79

8.2 Suitability of Geophysical Survey Methods 79

8.2.1 Description of Site 4 79

8.2.2 Geophysical Surveys 81

8.2.3 Second Analyses 83

8.2.4 Discussion 83

8.3 Verification of the SW Model 84

8.3.1 Site 1 85

8.3.2 Site 3 89

8.3.3 Site 4 92

Chapter 9: Summary and Recommendations 96

9.1 Summary 96

9.2 Process for Designers 96

9.3 Hands-on Training 98

9.4 Limitations 98

9.5 Future Work 98

References 100

Appendix A 105

Appendix B 109

Appendix C 166

Appendix D 194

Appendix E 196

Appendix F 237

List of Figures:

Figure 1.1: Simplified figure for forces acting on large diameter shafts. 2

Figure 1.2: General lateral and axial soil-shaft model. 2

Figure 2.1: Different scenarios from model (Stone 2013). 11

Figure 2.2: Published Vp-UCS data. 12

Figure 2.3: UCS versus seismic velocities 13

Figure 2.4: UCS versus P-wave velocity (Rucker 2006). 14

Figure 2.5: UCS versus P-wave Velocity with both total sample and middle sample (Liu 2014). 16

Figure 2.6: Correlations of UCS-Vp and E-Vp (Nefeslioglu 2013). 17

Figure 2.7: Change in UCS with L/D ratio (Tuncay 2009). 18

Figure 2.8: Change in UCS with L/D with respect to loading time (Tuncay 2009). 19

Figure 3.1: Location of geophysical survey before excavation (Google Earth). 21

Figure 3.2: Location of geophysical survey after excavation (Google Earth). 21

Figure 3.3: Configuration of the geophysical survey line. 22

Figure 3.4: Geophysical survey before excavation using MASW method. 23

Figure 3.5: Block samples collected during excavation. 24

Figure 3.6: Sample of strongly and moderately/weakly cemented soil blocks. 25

Figure 3.7: Use of the drill press to core cemented soil samples. 25

Figure 3.8: Photograph of the diamond core saw used in cutting the cores. 26

Figure 3.9: Dial gauge checking for flatness tolerance. 27

Figure 3.10: Stages of constructing the sample confined in grout. 28

Figure 3.11: Process used to make a reconstituted cemented soil sample. 29

Figure 3.12: Ultrasonic testing configuration. 30

Figure 3.13: Seismic velocity plot from excel using exported data of specimen A-4-1 32

Figure 3.14: Tinius Olsen testing set-up. 33

Figure 3.15: Specimen with mounted compressometer surrounded by a set of LVDT's. 34

Figure 4.1: MASW generated Vs profile of the excavation site. 39

Figure 4.2: ReMi profile of excavation site. 40

Figure 4.3: Revised ReMi analysis of the excavated site. 40
Figure 4.4: Logging of the excavated site.. 40
Figure 4.5: Field and lab shear wave velocity relationship. 42
Figure 4.6: UCS correlation with lab shear wave velocity. 43
Figure 4.7: Elastic modulus correlation with lab shear wave velocity. 44
Figure 4.8: Correlation of lab shear wave velocity with unit weight. 45
Figure 5.1: Typical behavior of rock under axial load (Hudson, 2000). 47
Figure 5.2: LVDT and Compressometer curves from Test A-7-2....................................... 48
Figure 5.3: Typical adjusted LVDT curve. 49
Figure 5.4: Plot of stress versus shifted strain for Test B-4-4. 50
Figure 5.5: Stress Level (SL) versus strain of Test B-4-4. 51
Figure 5.6: Lambda (λ) versus SL for Test B-4-4 for SL > 0.50. 52
Figure 5.7: Evaluation of the "Best Fit" equation of λ versus.
SL from SL 0.5 to 1 for Test B-4-4. 53
Figure 5.8: SL Vs ε with "Best Fit" data points added. 54
Figure 5.9: SL vs ε curve of Figure 5.5 with Alternate and Assigned data points added...... 55
Figure 5.10: The Stress Strain curve of
Figure 5.5 with Alternate and Assigned Data Points Added. 56
Figure 5.11: λ versus SL variations for the 80% Fit and Alt K Fit equations. 57
Figure 5.12: The stress strain curve of Figure 5.5 with the 80% Fit data points added. 58
Figure 5.13: Normalized Stress Strain curves for tests in the 80% Fit category. 59
Figure 5.14: The Bounds of the normalized curves of
Figure 5.13 with the 80% Fit superposed. 59
Figure 5.15: Normalized Stress versus Normalized Strain from the 80% fit data points...... 60
Figure 6.1: Published Vp-UCS data compared with lab data. 63
Figure 6.2: Published Vs-UCS compared to lab data. 64
Figure 7.1: Vertical side shear stress distribution on the shaft cross section......................... 69
Figure 7.2: Components of soil lateral resistance of
large diameter shaft (Case of a short shaft model). 69
Figure 7.3: The development of the vertical shear
displacement component (v_d) with shaft deflection. 71

Figure 7.4: Normal and shear stress–strain relationship (σ-ε and τ-γ). 74

Figure 7.5: SWM procedure in solving the problem of laterally loaded pile/shafts in layered soils. 78

Figure 8.1: Aerial image showing location of geophysical arrays at Site 4 (Google Earth).. 80

Figure 8.2: Configuration of the geophysical survey line, L1. 81

Figure 8.3: Configuration of the geophysical survey line, L2. 81

Figure 8.4: MASW analysis of Site 4. 82

Figure 8.5: ReMi analysis of Site 4. 82

Figure 8.6: Second ReMi analysis of Site 4.. 83

Figure 8.7: Shafts' details, configuration and soil profile at Site 1. 88

Figure 8.8: Predicted shaft head response versus reported results for the 8-foot shaft at Site 1. 89

Figure 8.9: Predicted shaft head response versus reported results for the 2-foot shaft at Site 1. 89

Figure 8.10: Shafts' details, configuration and soil profile at Site 3. 91

Figure 8.11: Predicted shaft head response versus reported results for the 2-foot shaft at Site 3... 92

Figure 8.12: Shafts' details, configuration and soil profile at Site 4. 94

Figure 8.13: Predicted shaft head response versus reported results for the North shaft at Site 4. 95

List of Tables:

Table 2.1: UCS data from drilling at testing sites (Rinne et al., 1996). 9

Table 2.2: Comparison of lab velocities versus field velocities (Stone 2001). 9

Table 3.1: Comparison of calibration material with published and measured velocities. 31

Table 4.1: Strongly cemented soils (UCS > 10,000 psi). 36

Table 4.2: Moderately cemented soils (10,000 psi < UCS > 3,000 psi). 37

Table 4.3: Weakly cemented soils (UCS < 3,000 psi). 38

Table 5.1: Strain offset (Δε) by cementation level. 50

Table 5.2: Table of λ versus SL from Alternate and Assigned data points for some of the 53 LVDT tests. 56

Table 8.1: Abbreviated soil horizons at Site 4 (Rinne et al., 1996). 80

Table 8.2: Reported drilled shafts properties at Site 1. 85

Table 8.3: Reported soil input data employed in COM624P for the 8-foot shaft (Site 1). 86

Table 8.4: Reported soil input data employed in COM624P for the 2-foot shaft (Site 1). 86

Table 8.5: Soil input data employed in SWM for the 8-foot shaft (Site 1). 86

Table 8.6: Soil input data employed in SWM for the 2-foot shaft (Site 1). 87

Table 8.7: Reported soil input data employed in COM624P for the 2-foot shaft (Site 3). 90

Table 8.8: Soil input data employed in the SWM (Site 3). 90

Table 8.9: Soil input data employed in COM624P for Site 4. 93

Table 8.10: Reported soil input data employed in the SWM for Site 4. 93

Abstract

Cemented soils deposits located in Las Vegas valley have long been a challenge for engineers. These deposits can withstand considerable loads. They are, however, difficult to model or predict using typical site investigation techniques. For engineering purposes, these cemented soils, also commonly referred to as Caliche, are difficult to quantify their thickness, strength and lateral extent. This erratic and heterogeneous nature can result in inconsistent design and performance of foundations. This report presents a new material model for cemented soils in the Las Vegas region. The material model was developed using results obtained from unconfined compressive strength tests conducted on 53 cored samples, with different levels of cementation. The model, which generates the stress-strain relationship of cemented soils, recognizes three cementation levels and allows the user to account for closure of fractures if desired. Laboratory shear and primary wave velocities were measured for all samples. In addition, field shear wave velocity of the site where the samples were obtained, was assessed using Refraction Microtremor (ReMi) and Multichannel Analysis of Surface Waves (MASW) methods. Relationships between lab shear wave velocity, material unit weight, unconfined compressive strength and Young's Modulus are presented. Furthermore, a preliminary correlation between field and lab shear wave velocities is introduced. The model along with the derived relationships were implemented in Strain Wedge Model (SWM) to assess the performance of laterally loaded shafts embedded in cemented soils. Comparison between SWM prediction and field performance of laterally loaded shafts during 1996 load test program is presented.

Acknowledgements

The authors would like to recognize the Nevada Department of Transportation (NDOT) for funding this project (award number P667-15-803). They also extend their gratitude to Mike Griswold, Abbas Bafghi and Jesse Ruzicka of the Materials Division and Michael Taylor of the Bridge Division for their thoughtful insight and feedback.

Special thanks are due to Greg DeSart, Corey Newcomb, and Roger Messer for assisting with identifying an appropriate site in Las Vegas as well as coordinating the field activities. The authors are very appreciative of the support received from Dale Keller, NDOT project management office.

Disclaimer

This work was sponsored by the Nevada Department of Transportation. The contents of this report reflect the views of the authors, who are responsible for the facts and the accuracy of the data presented herein. The contents do not necessarily reflect the official views or policies of the State of Nevada at the time of publication. This report does not constitute a standard, specification, or regulation.

Chapter 1: Introduction

1.1 Background

Interest in using large-diameter drilled shafts in bridge foundations has increased over the last two decades as designers would like to take advantage of their large lateral load capacity. However, data obtained from several full-scale load tests on laterally loaded large-diameter shafts installed into stiff materials (e.g., clay and weak rock) exhibits a stiffer shaft-head response compared to the results obtained from the traditional p-y curve (Bhushan et al. 1979; Reese 1983; Brown et al. 2001; Qiu et al. 2004; Liang et al. 2007; McVay and Niraula 2009; Sorensen et al. 2009; Lesny and Hinz 2009; Kim et al. 2011). Such softer lateral response has been mainly attributed to neglecting the vertical side shear (VSS) resistance that develops on the side of large-diameter drilled shafts.

Current design approaches, which do not account for VSS result in a much larger shaft diameter for a given target top of shaft-head lateral displacement. In addition, the consequence to design when significant difference in stiffness between adjacent layers exists, such as cemented soils, needs to be evaluated. Having one computational tool that can account for all of the above-mentioned factors along with the proper integration of VSS and the appropriate soil/rock model will greatly increase designers' confidence in assessing shaft response under lateral loading. This will result in more efficient foundation design, which ultimately translates into significant cost savings.

McVay and Niraula (2009) addressed the significance of the vertical side shear's contribution to the lateral resistance of piles/drilled shafts embedded into rock, including weak rock, using a number of centrifuge model load tests. Figure 1.1 shows the different forces and moments acting on the large diameter shafts, including VSS resistance.

Soil-Shaft modeling is characterized by a nonlinear set of the p-y and t-z curves that reflect the transfer (i.e., the soil-pile interaction) of lateral and vertical loads, respectively. It should be noted that the traditional p-y and t-z curves are uncoupled and function of lateral (y) and vertical (z) shaft displacement, respectively (see Figure 1.2). However, the lateral loading and the resulting deflection of large diameter shafts are associated with both horizontal (y) and vertical displacement (v). While the horizontal displacement component (y) dominates the pattern of the large diameter shaft deflection, an accompanying small vertical displacement component (v) also develops. This increases the vertical side resistance or skin friction (τ_v) (i.e., the VSS force, V_v) on the shaft surface. The VSS that occurs under shaft rotation results in a stabilizing moment that helps to reduce the lateral pile deflection. It is especially prominent in drilled shafts which tend to have the potential to develop higher frictional resistance at the soil-shaft interface due the rough nature of cast-in-place concrete.

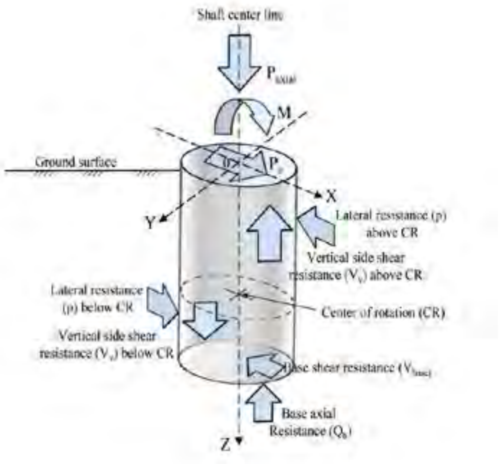
Shaft center line
P_axial
M
Ground surface
P_y
X
Y
Lateral resistance (p) above CR
Vertical side shear resistance (V_v) above CR
Lateral resistance (p) below CR
Center of rotation (CR)
Vertical side shear resistance (V_v) below CR
Base shear resistance (V_base)
Base axial Resistance (Q_b)
Z

Figure 1.1: Simplified figure for forces acting on large diameter shafts.

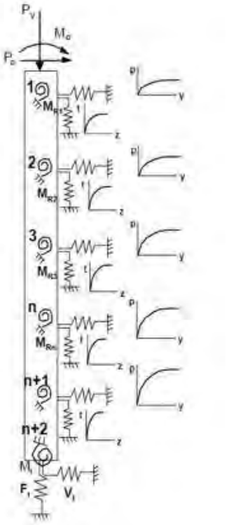
P_v
M_o
P_o
1
M_R1
2
M_R2
3
M_R3
n
M_Rn
n+1
n+2
M_t
F_t
V_t
p
y
t
z

Figure 1.2: General lateral and axial soil-shaft model.

The developing VSS resistance generates a resisting moment, M_R, (see Figure 1.2) to the lateral shaft deflection. Nevertheless, it is not recommended that the M_R, which is induced by the vertical skin friction, be a part of the p-y curve model or directly tied to lateral soil resistance per shaft unit length (p). While "p" is a function of the lateral shaft displacement, y, M_R is a function of the vertical component of the shaft deflection (v), which is influenced by the pattern of the shaft deflection and the flexural deformation of the shaft cross section.

The second, but closely related, contributing factor to the softer assessed response of drilled shafts subjected to lateral loading is the material model used in the analysis. While some soils are relatively easy to characterize and model, others present a challenge, for example cemented soils (also known as caliche), which have often been modeled as dense sand (SPT=50), stiff clay with compressive strengths as high as 400 to 820 ksf, or rock. In a recently concluded study, funded by Nevada Department of Transportation (NDOT), to calibrate the resistance factors for axially loaded drilled shafts in similar soils, it was observed that modeling cemented soils as rock in CGI-DFSAP (commercial name for Strain Wedge Model, SWM) provides the most accurate results compared to other methods of analysis for axially loaded shafts in cemented soils (Motamed et al 2015, 2017). However, the model needs to be further refined especially when assessing the strain at 50% stress level (ε_{50}).

1.2 Geologic Setting for the Current Study

The Las Vegas Valley is approximately 25-mile wide. The basin is a part of the Basin and Range province. The setting is defined by extensional faulting with north-south trending ranges. The valley deposits are mainly Tertiary and Quaternary age unconsolidated sediments derived from the surrounding mountains, which are mainly composed of igneous, sedimentary and carbonate material (Werle et al, 2007). This material has been transported into the valley by the regions' sporadic flash flooding.

Cemented soils occur throughout the valley, although somewhat erratically. Cibor (1983) believes the Springs Mountains to the west of the valley is the primary source of the cementing agents. Cemented soils are a form of evaporite deposits. They form from the evaporation of lime rich groundwater moving upwards by capillary action (Cibor, 1983).

1.3 Objective and Scope of Study

The main objective of this study was to upgrade the Strain Wedge Model to account for the vertical side shear (VSS) for laterally loaded drilled shafts as well as include a material model for cemented soils. These combined enhancements would improve SWM capabilities to predict the lateral response of drilled shafts when they are embedded within cemented soils in the Las Vegas region.

To accomplish these two main objectives, the project was divided into five tasks. The task descriptions are listed as follows:

1) **Literature Review & Data Collection**

A thorough literature review was carried out. A variety of sources were used to gather information on drilled shafts and cemented soil (caliche). These sources included journal papers, conference papers and textbooks. The origins of these papers were diverse since cemented soils are present in many parts of the world. The information sought in this review was the unconfined compressive strength (UCS) of cemented soils and predictive models using surface wave measurements. The review also focused on lateral load tests carried out on drilled shafts embedded in cemented soils.

2) **Boring, Sample Collection and Laboratory Tests**

It was essential to obtain samples of cemented soils and test them in the lab to determine their UCS. Since drilling was not in the scope, local contacts were used to gain access to sites where shallow excavations were taking place. The research group was put in contact with Kiewit Construction, the lead contractor for Project Neon. Access was granted to a site where excavation would commence, and box culverts would be installed. Geophysical surveys using Refraction Microtremor (ReMi) and multichannel analysis of surface waves (MASW) methods were carried out before excavation had started. Large block samples, representing different levels of cementation, were collected over the course of three separate trips to the site. These large samples were brought back to the University of Nevada, Reno where samples were cored using a drill press, then cut and ground. Unconfined Compressive Strength tests as well as primary and shear wave velocity tests were conducted on the prepared specimens.

3) **Material Modeling**

Fifty-eight (58) specimens of various levels of cementation were tested. Forty (40) out of the 58, were used to develop the material model. The model used the Secant Young's Modulus (E_{sec}) at strain of 50% of peak stress (ε_{50}) and the

Unconfined Compressive Strength (UCS). During testing, other inputs into the model were developed that are specific for rock-like material, e.g. a strain offset ($\Delta\varepsilon$). Strain offset accounts for the closing of fractures, void collapse and mineral compression that occurs under initial loading.

4) **Implementation in the Strain Wedge Model**

   Implementation in the SWM was completed in two steps. The first step focused on implementing the vertical side shear into the generic rock model, already available in the SWM. Preliminary verification of the implementation was carried out. Once verified, the newly developed material model for cemented soils was implemented in the SWM. The program uses one of three input parameters for the model. The input parameter can be either the lab shear wave velocity, material unit weight, or unconfined compressive strength.

5) **Verification of the Implemented Material Model**

   Data from the lateral load test program conducted at four sites in Las Vegas valley (Rinne et al., 1996) was used to verify the enhancements of the predictive model. Geophysical measurements were made at Site 4 since it was the only site that was accessible and where the tested shaft could be located. Surface measurements were taken at the site with two near perpendicular arrays intersecting at the buried drilled shaft. Data from the geophysical measurements was used to correlate with lab shear wave velocity, which is used as an input in the SWM. The results were compared to measured data from the experimental program (Rinne et al., 1996).

1.4 Organization of the Report

This report is divided into nine (9) chapters and six (6) appendices.

0 provides the background, objective, and scope of the study.

Chapter 2:discusses a review of literature regarding cemented soils and relationships amongst the elastic properties to seismic velocities. These relationships are important to the material model, since the goal of the material model is to establish relationships.

Chapter 3: examines the techniques and procedures used in various components of the research project. Both lab and field measurements are discussed in this chapter with appropriate justification based on previous work or ASTM standards.

Chapter 4: presents the results, which is the product of the lab and field-testing program. This section shows the relationships established between the lab shear wave velocity and the different properties, e.g. the unconfined compressive strength, Young's Modulus and unit weight.

Chapter 5: discusses the material model of the cemented soil from the Las Vegas region. This chapter demonstrates how the data reduction occurred and the steps used to establish the cemented soil (caliche) model to be employed in the updated Strain Wedge Model.

Chapter 6: discusses the fit of the lab results with existing correlations between material properties and laboratory wave velocities.

Chapter 7: presents the implementation of the newly developed material model in Strain Wedge (SW) analysis. It also addresses the implementation of vertical side shear in the analysis.

Chapter 8: outlines how verification of the material model was undertaken using published data from laterally loaded shaft program in cemented soils (Rinne et al., 1996).

Chapter 9: offers a summary and recommendations for future work.

Appendix A presents a table which contains measured and assessed data for all test specimens.

Appendix B shows data sheets for all test specimens. Each sheet provides information about specimen geometry, shear and pressure wave velocities, unconfined compressive strength and failure type.

Appendix C presents the stress-strain data obtained for the tested samples tested. This data was used in the generation of the material model.

Appendix D discusses the effect of L/D ratio on the unconfined compressive strength.

Appendix E provides the necessary background on Strain Wedge Model theory.

Appendix F shows the slides presented during the hands-on training offered to NDOT engineers on the findings and their implementation in Strain Wedge Model program.

Chapter 2: Background on Cemented Soils and Existing Correlations

2.1 Introduction

This chapter introduces the most relevant literature and the current state of knowledge for the topics covered in this report. It initially considers research done on drilled shafts and more generally on cemented soils from the Las Vegas region and other areas. Research correlating shear wave (S-wave) velocities to UCS are also discussed. Additionally, shape and size effects of core specimens are also examined since some specimens did not meet ASTM standards.

2.2 **Observations from Previous Studies on Cemented Soils in the Las Vegas Valley**

Cemented soils in Las Vegas have challenged designers of both shallow and deep foundations. Numerous research papers have been published on cemented soils providing insight on their behavior. A significant concern relative to cemented soils is that that their lateral extent and thickness are erratic, and their horizons are heterogeneous. Cemented soils mainly consist of sand and gravel cemented by calcium carbonate. They have been widely referred to as caliche, but have also been referenced to as Intermediate Geomaterial, or IGM (Stanton et al, 2017; Brown et al., 2010; AASHTO, 2014).

2.2.1 Rinne et al. (1996)

Kleinfelder Engineering Company conducted a large scale test program for drilled shafts in Las Vegas in 1995 as part of the I-15/US-95 upgrade. Under this test program, full scale drilled shafts were installed in four different locations, which contained layers of cemented soils. These shafts were subjected to axial and lateral loads tests. The drilled shafts tested varied in diameter from 2 feet to 11 feet. As part of the test program, drilling was undertaken at each of the four test locations. Unconfined compressive strength tests were performed on four specimens collected from Sites 1, 3, and 4. Results from these tests are shown in Table 2.1.

Table 2.1: UCS data from drilling at testing sites (Rinne et al., 1996).

Boring	Depth (ft)	Unconfined Compressive Strength (psi)
B-1	15.5	9320
B-3	54	4060
B-4	6	4840
B-4	6.5	8290

Note the change in strength from the two samples at Site 4 (B-4). There is a 40% increase in strength within six (6) inches of depth. This highlights how quickly the cementation can change, or alternatively, it represents how heterogeneous the material is.

2.2.2 Stone et al. (2001)

Rock cores were obtained from the University of Nevada, Las Vegas campus for testing to obtain the elastic properties of caliche. Previous work by Kleinfelder Associates and Western Technologies Inc. on such cores yielded UCS values of 5470 psi and 4970 psi respectively.

Stone tested the rock cores for compression and shear wave velocities using accelerometers oriented to measure both Primary (P) and Shear (S) waves. Additionally, field cross-hole measurements were taken at the test site where the cores were drilled and from the Las Vegas Springs Preserve (Table 2.2). The cross-hole geophysics were performed in 0.5-meter (1.64 ft) intervals.

Table 2.2: Comparison of lab velocities versus field velocities (Stone 2001).

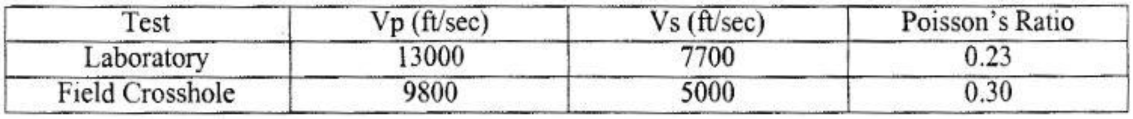

Test	Vp (ft/sec)	Vs (ft/sec)	Poisson's Ratio
Laboratory	13000	7700	0.23
Field Crosshole	9800	5000	0.30

Stone used the data to correlate with the difficulty of excavating caliche. Stone concluded that if the thickness of caliche does not exceed three (3) feet, the material is rippable based on the specification for a Caterpillar D9.

Caliche is also important to the bearing capacity of the ground beneath foundations. An analysis was carried out by the author using finite element analysis. The analysis shows that under large loads caused by structures such as hotels, these caliche horizons greatly reduce settlement due to their high stiffness and ability to distribute stress over larger areas.

2.2.3 Cibor (1983)

Cibor discusses the general setting and challenges associated with geotechnical engineering in the Las Vegas valley. The author describes caliche in the region as highly variable in its lateral extent and properties. Cibor notes that in the northern and central valley, the caliche is thicker and more abundant. While in the west and northwestern regions, the caliche is thinner and less abundant, commonly referred to as "popcorn caliche". Measured values for compressive strength of caliche range from 4,000 to 10,000 psi. In areas where the compressive strength of caliche is high, the bearing capacity failures tend to be punching failures and not general shear.

2.2.4 Stone (2013)

Stone conducted an analysis of pile foundations passing through caliche layers. The analysis was conducted using PLAXIS 2D and PLAXIS 3D. The study was done to research caliche stiffened pile foundations, which are short, high capacity drilled piles bonded to caliche in the subsurface. As a result, the drilled pile derives additional strength from the stiff caliche.

Every scenario used the same dimensions: the diameter of the pile was two (2) feet, the depth of the pile was 20 feet, and the applied load was 200 kips per pile. PLAXIS 2D was used to analyze a single pile with four (4) different subsurface conditions. Stone's analysis concluded that if the caliche has a thickness equal to the diameter of the pile, settlement is reduced by 50% regardless of the location of the caliche layer. Using PLAXIS 3D, a similar analysis was carried out with a pile group consisting of four piles. Stone's analysis shows that with the pile group, regardless of the location of the caliche horizon, settlement is reduced by 70% as the caliche's thickness is varied from one-quarter to three times the pile diameter as shown in Figure 2.1.

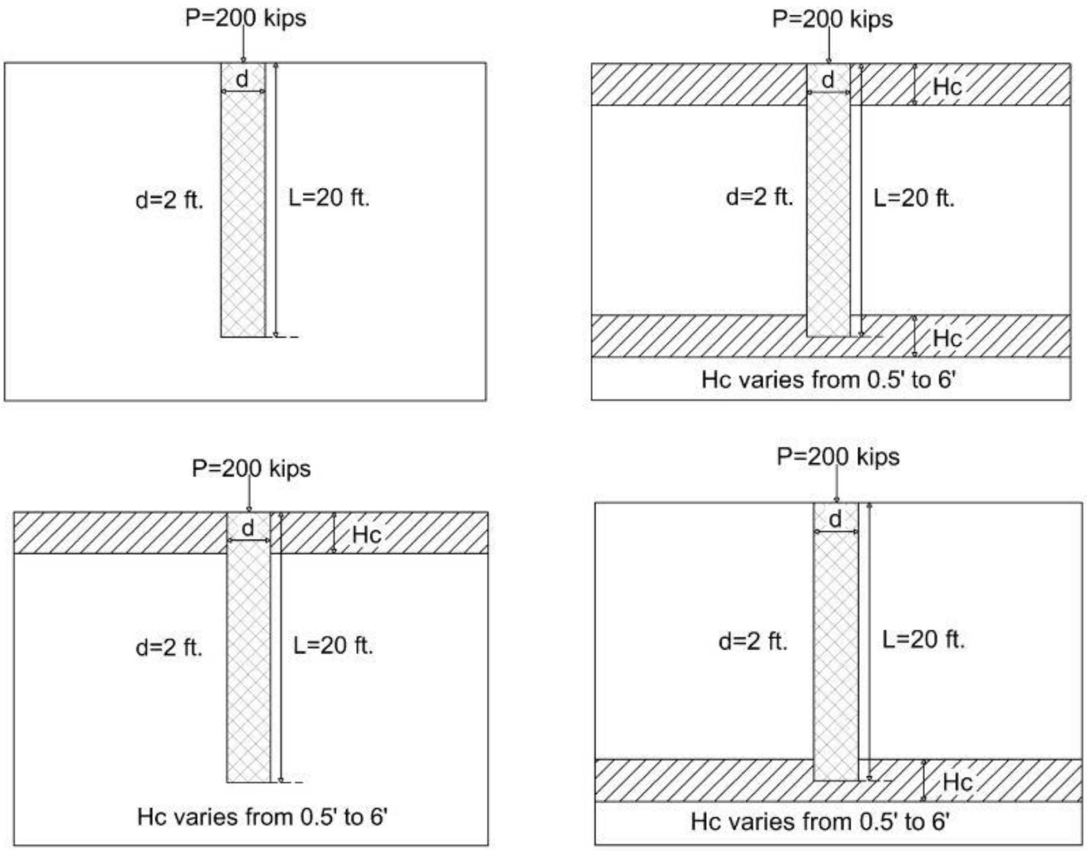
P=200 kips
d
d=2 ft.
L=20 ft.
P=200 kips
d
Hc
d=2 ft.
L=20 ft.
Hc
Hc varies from 0.5' to 6'
P=200 kips
d
Hc
d=2 ft.
L=20 ft.
Hc varies from 0.5' to 6'
P=200 kips
d
d=2 ft.
L=20 ft.
Hc
Hc varies from 0.5' to 6'

Figure 2.1: Different scenarios from model (Stone 2013).

2.3 Correlation of Seismic Wave Velocity to Unconfined Compressive Strength (UCS)

Seismic wave velocity tests are becoming increasingly popular for use in geotechnical investigations. These tests are widely used due to their simplicity, repeatability, portability and low cost (Jamshidi et al, 2014). With their increased use, research has focused on comparing seismic velocities with UCS values, which is the most sought after geotechnical property. Figure 2.2 shows Vp-UCS data relevant to cemented soils.

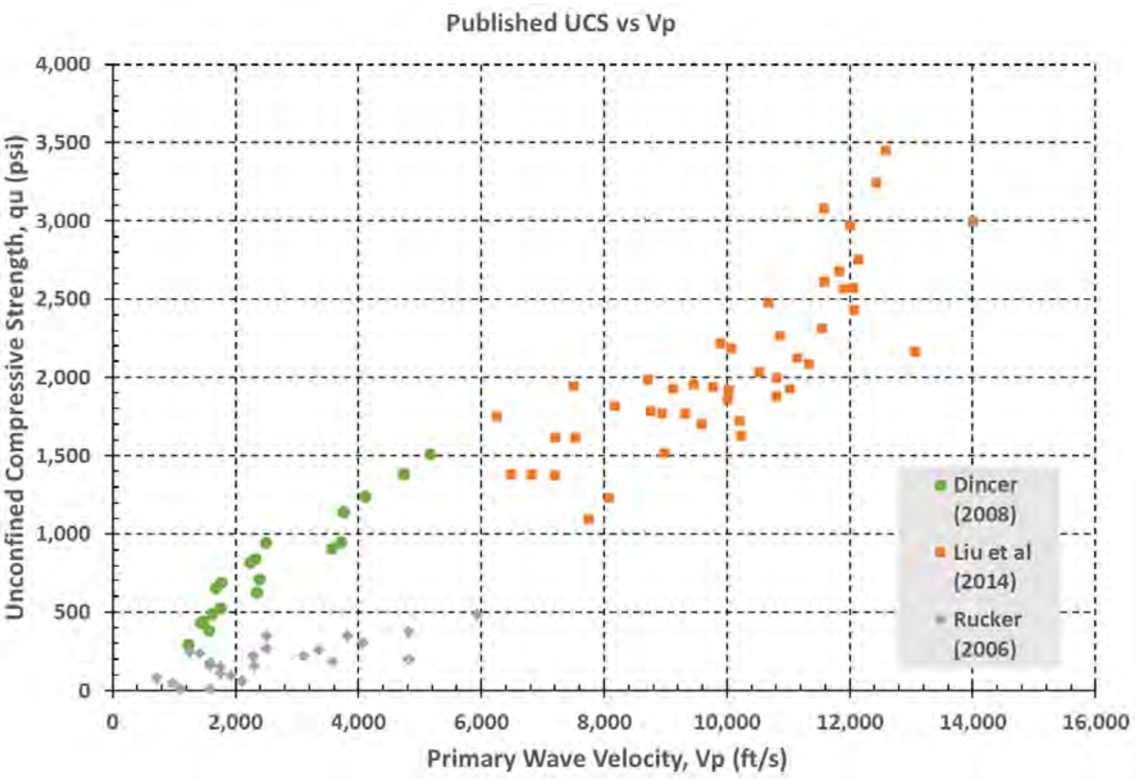

Figure 2.2: Published Vp-UCS data.

The current research project is equally interested in the relationship of shear wave velocity to Young's Modulus and Shear Modulus as it relates to stress-strain response or material stiffness, as addressed in Chapter 5:.

2.3.1 Rucker (2000)

Cemented soil core samples were obtained from a dam foundation study in Maricopa County, AZ. Prior to drilling, a seismic survey was conducted to measure P-wave velocities. UCS values were obtained from the core samples. Rucker shows a relationship between seismic velocities and minimum unconfined compressive strength which is developed through relationships of low strain to high strain modulus derived from seismic velocities and static UCS testing. These relationships are made assuming that the mass is intact, and no fractures or jointing exist. Fractures and jointing lower UCS correlations since such discontinuities reduce seismic velocity. Rucker adds other data sets to the graph to illustrate the accuracy of the strain modulus correlation. Tuff samples from near the Hoover Dam and concrete cylinders with up to one week curing time were plotted (Figure 2.3)

Rucker assumes a Poisson's ratio of 0.33, thus making the P-wave velocity twice as much as the shear wave velocity.

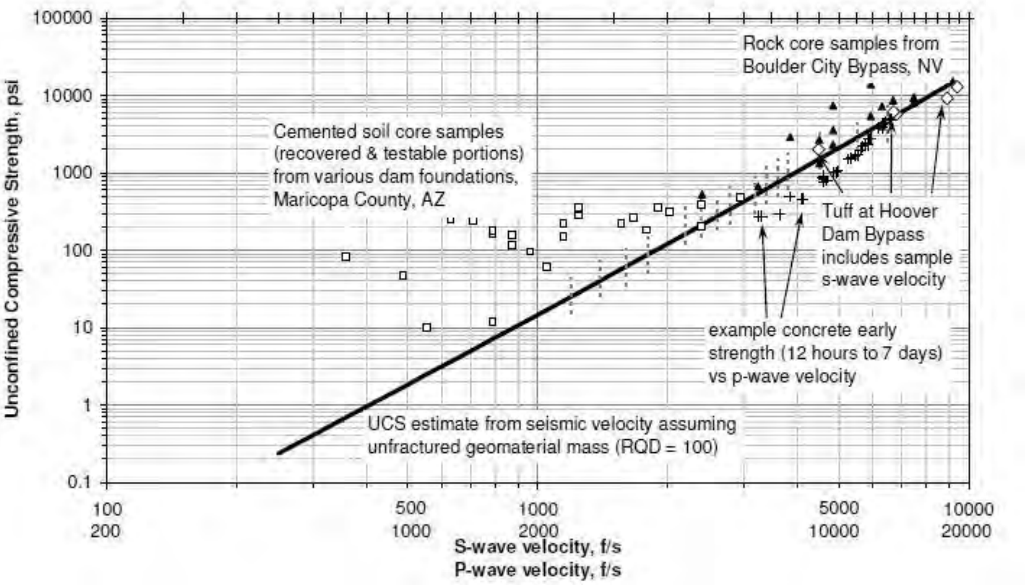

Figure 2.3: UCS versus seismic velocities.

2.3.2 Rucker (2006)

Rucker correlated P-wave velocity to UCS values to evaluate the capability of excavating cemented soil/rock. The data set came from core samples obtained from two site locations. At greater depths, the P-wave velocities are based on S-wave velocities. This is because the P-wave velocities cannot be measured accurately below the water table. This relationship can be made by assuming a Poisson's ratio as done in previous work. Similar to Rucker (2000), it is assumed that the rock mass is intact and has no existing joints or fractures, making the correlations conservative. Rucker established a conservative baseline using the 16% cementation level from the data set (Figure 2.4). Rucker uses the UCS to establish a new excavatability chart based on the Kirsten Excavation Classification System.

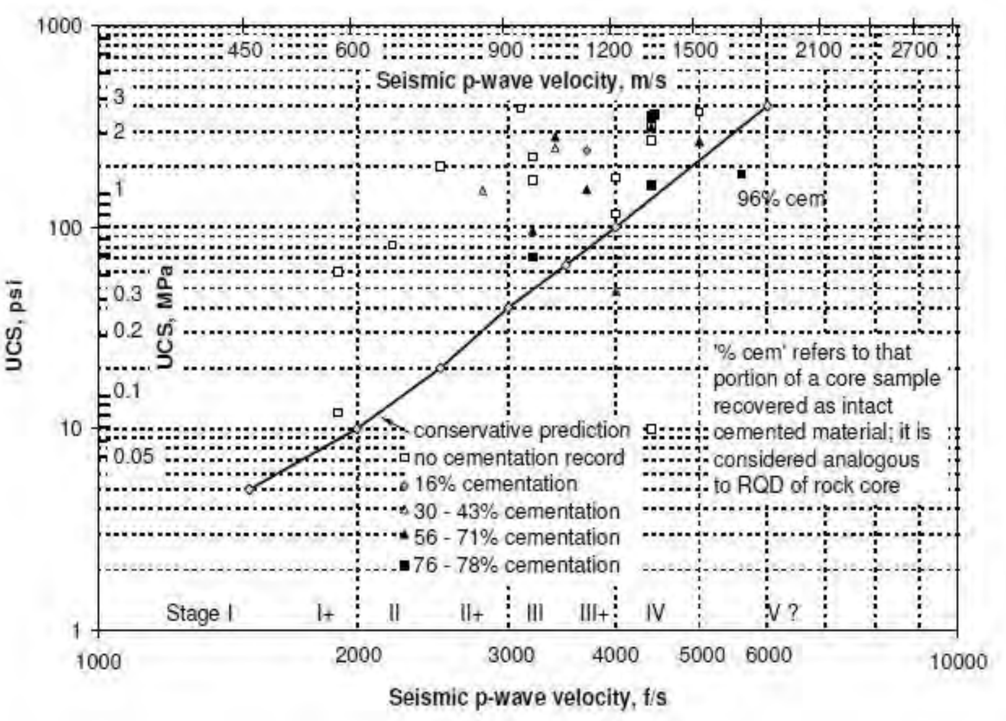

Figure 2.4: UCS versus P-wave velocity (Rucker 2006).

2.3.3 Dincer et al (2008)

Data collected on the properties of caliche were analyzed using simple regression analysis based on linear, logarithmic, power and exponential laws. Only the P-wave velocity measurements had a strong correlation with both the UCS and average Young's modulus (E_{av}), with regression coefficients (R^2) values of 0.91 and 0.87 respectively. The range of velocities were from 375 m/s (1,230 ft/s) to 1,576 m/s (5,170 ft/s). UCS was found to be a function of Vp and unit weight. The following empirical equations were derived from the data presented in the paper.

$$\text{UCS} = -6.19 + 4.418*10^{-3} * Vp + 0.427 * \gamma \qquad \text{(Eq 2.1)}$$

where,

Vp = P-wave velocity

UCS = Unconfined Compressive Strength

γ = Unit Weight

$$E_{av} = 0.944 + 5.899 * 10^{-4} * Vp - 3.17 * 10^{-2} * n \quad \text{(Eq 2.2)}$$

where, n = porosity

$$E_{av} = 2.201 + 6.244 * 10^{-4} * Vp - 4.30 * 10^{-2} * n - 1.09 * 10^{-3} * I_{d2} \quad \text{(Eq 2.3)}$$

where, I_{d2} = Slake Durability Index after second cycle

The author states that these relationships are very useful in the field of rock mechanics because seismic velocity is an important elastic property. However, he urges caution that these correlations may not apply to caliche deposits in different locations.

2.3.4 Liu et al (2014)

Liu used an extreme learning algorithm to come up with correlations to the UCS of carbonate rocks with a variety of indexes. These indexes include mineral composition, specific density, dry unit weight, total porosity, effective porosity, slake durability, P-wave velocity (Vp) and P-wave velocity horizontally through the middle of the sample (Vm). Fifty five (55) samples were tested for all of these characteristics. One sample was eliminated due to duplication. Using regression analysis, which included linear regression, multiple regression and nonlinear regression models, empirical equations were derived for each correlation. Liu determined that the UCS to Vp and Vm correlations are much stronger than the other indexes previously mentioned. These two relationships (Figure 2.5) had the highest regression coefficients of all the empirical relationships.

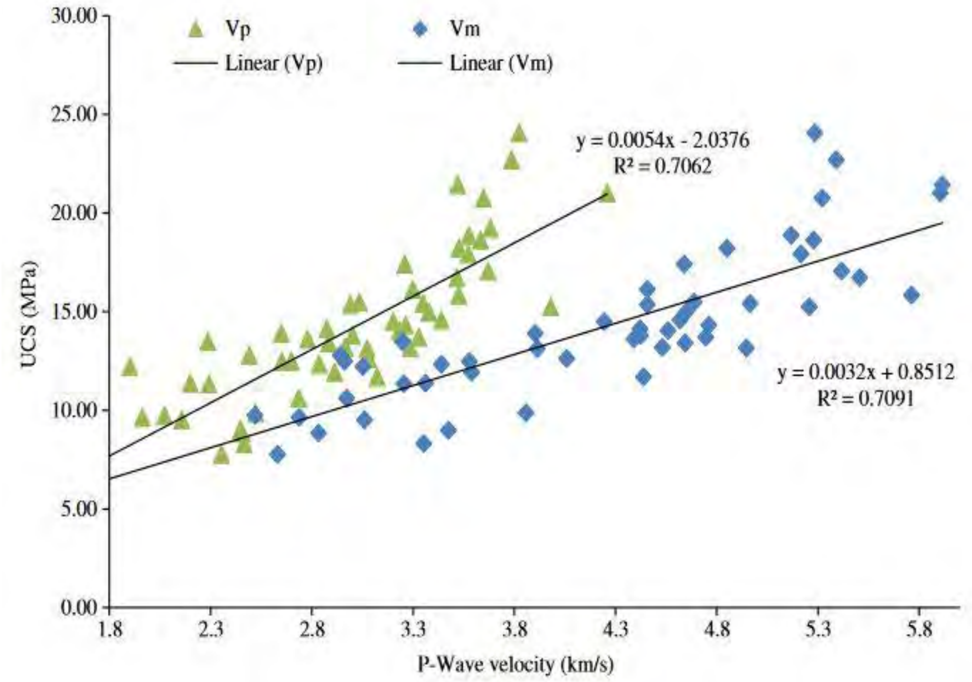

Figure 2.5: UCS versus P-wave Velocity with both total sample and middle sample (Liu 2014).

2.3.5 Nefeslioglu (2013)

The author compiled 66 core samples of weak and very weak sedimentary material to evaluate the geo-mechanical properties of what is known as "fringe" material. Nefeslioglu conducted ultrasonic velocity tests, compressive strength tests and reflectance spectroscopy to compare minerology. These correlations are between the unconfined compressive strength (UCS) and P-wave velocity, and the elastic modulus (E) and the P-wave velocity.

All 66 samples were drilled and checked for parallelism. The samples were cut to ensure the length to diameter ratio was between 2.5 and 3.0. The P-wave measurements were taken using a Pundit Plus ultrasonic device using a range of frequencies between 24 kHz to 1 MHz. Prior to measuring the seismic velocity, the samples were pre-stressed to 10 N/cm^2 and then unloaded. All samples ranged from 470 m/s (1,542 ft/s) to 1370 m/s (4,495 ft/s). Compressive strength tests yielded a range of values from 0.68 MPa (98.6 psi) to 4.06 MPa (589 psi). The calculated minimum and maximum elastic moduli ranged between 0.030 GPa (4,351 psi) and 0.309 GPa (44,817 psi).

Empirical equations were developed from the correlations of UCS-Vp and E-Vp with R values showing that they are statistically significant. The exponential model produced the highest regression analysis value of 0.815 for both correlations (Figure 2.6).

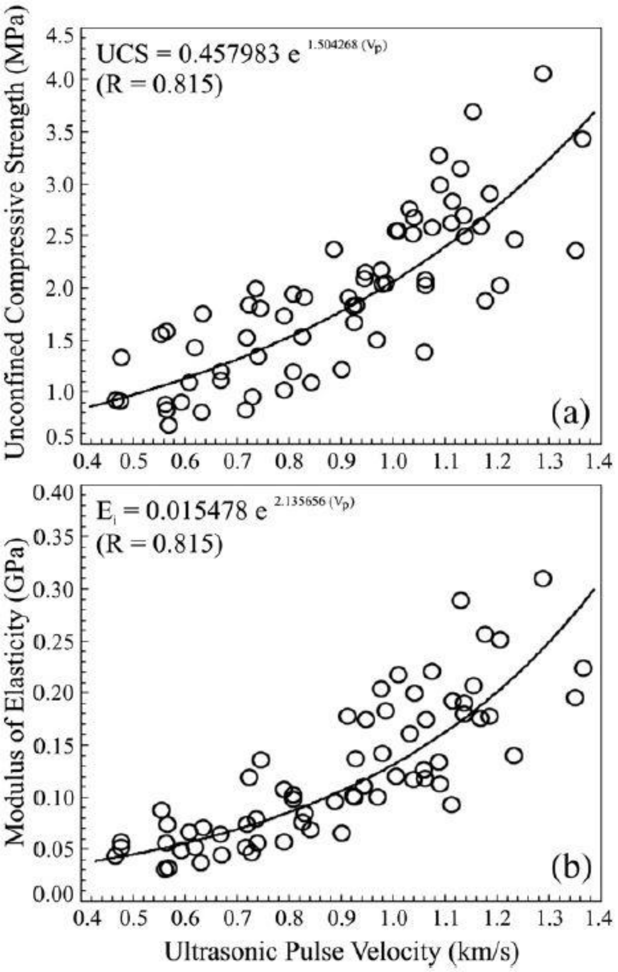

Figure 2.6: Correlations of UCS-Vp and E-Vp (Nefeslioglu 2013).

2.4 Size Effect of Uniaxial Compressive Strength Tests

2.4.1 Tuncay et al (2009)

Tuncay tested the effect of length to diameter ratio (L/D) on UCS for seven different rock types. Amongst the seven, there was sedimentary, metamorphic and igneous rock types. Each type had four specimens, all with a 47mm diameter. The four specimens had L/D ratios of 1, 1.5, 2, and 2.5. The UCS results varied, but overall, the UCS values showed little change with varying L/D ratios except for the Grey Andesite (Figure 2.7).

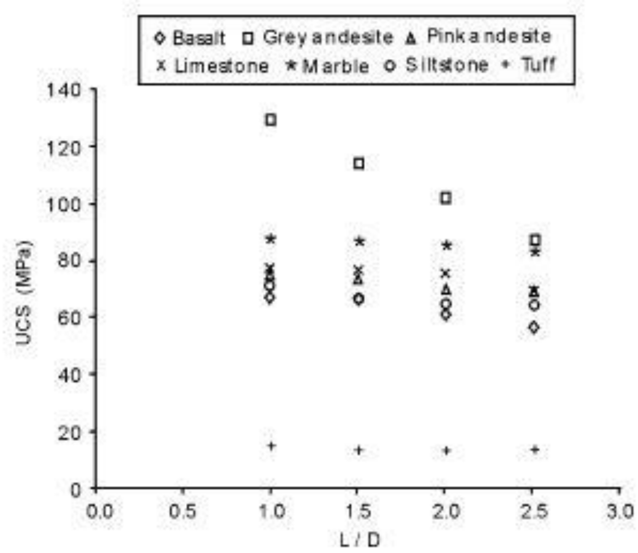

Figure 2.7: Change in UCS with L/D ratio (Tuncay 2009).

Tuncay also addressed how loading rates may affect the UCS values. ASTM 7012 states that failure should occur between 2 and 15 minutes after testing begins. Using the same rock types and same L/D ratios, Tuncay conducted UCS tests at two different loading rates. Those rates are in the range of 2-5 minutes and 8-10 minutes. All four tests from different lithologies show little to no difference in UCS values (Figure 2.8).

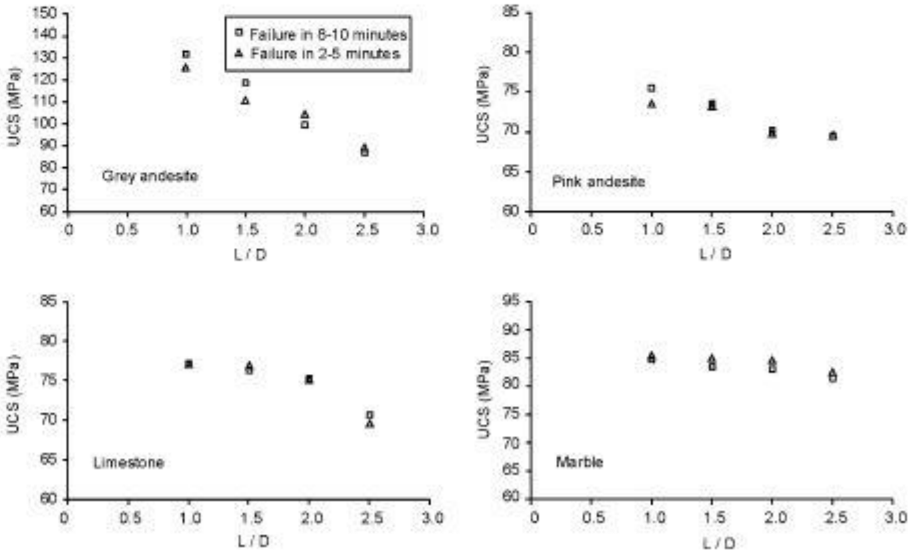

Figure 2.8: Change in UCS with L/D with respect to loading time (Tuncay 2009).

Chapter 3: Field and Laboratory Test Program

3.1 Introduction

This chapter summarizes the field measurements, collection of block samples, sample coring and preparation, and lab tests undertaken as part of the current research. Through the literature review and ASTM standards, current practices were utilized to collect the data. In absence of standards, trial and error were utilized when no literature was available on testing methods.

3.2 Site Selection

To achieve the objectives of this study, it was prudent to collect samples representing different cementation levels. Since in situ coring was not in the scope of this project, block samples from shallow excavations were obtained. Several construction projects in Las Vegas were identified and communication with the contractors was established. After evaluating several options, it was decided to coordinate with Kiewit Corporation since they were the main contractor on Project Neon, which is the largest public works project in Nevada history.

After several meetings, a site was selected and an onsite contact was identified. The selected site was near the intersection of West Charleston Blvd and South Martin Luther King Blvd (Figure 3.1). It was a site where it was planned to make a 17-ft deep excavation to install a large box culvert. The initial borings from the site showed a shallow layer of cemented soil. The site was considered an optimum choice since it was not yet excavated, had shallow layer(s) of cemented soils, block samples could be obtained from the excavation processand the project was owned by NDOT the excavation revealed different soil horizons to 17-ft depth over several hundreds of feet long.

3.3 Field Geophysics

Field geophysical measurements were conducted prior to excavation of the trench for the box culverts. A 12-channel, 4 Hz array was used in a roll-along fashion for an investigated length of 220 ft. Figure 3.1 and Figure 3.2 show the line of the geophysical survey overlying a map generated by Google Earth before and after excavation.

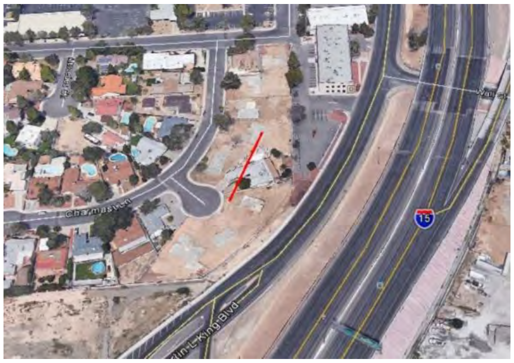

Figure 3.1: Location of geophysical survey before excavation (Google Earth).

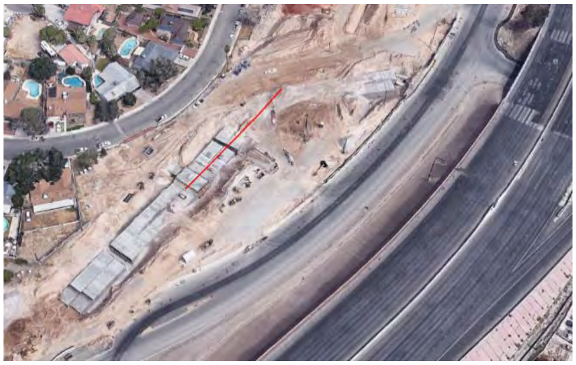

Figure 3.2: Location of geophysical survey after excavation (Google Earth).

Two geophysical measurements were acquired to suit two different methods of analysis: Multi-Channel Analysis of Surface Waves (MASW) and Refraction Microtremor (ReMi). It was simple to employ both methods in tandem on the same survey line, due to their similar setup of geophones, cable and data acquisition equipment. These two methods represent the most recently developed, non-invasive methods for determining shear wave velocity (Stephenson, 2005). Figure 3.3 shows the configuration of the geophysical survey line.

Each geophysical method requires trained individuals undertaking specific analyses to obtain shear wave velocities. Shear wave velocity is closely related to Shear Modulus (G) and, in turn, Young's Modulus (E), an important elastic constant.

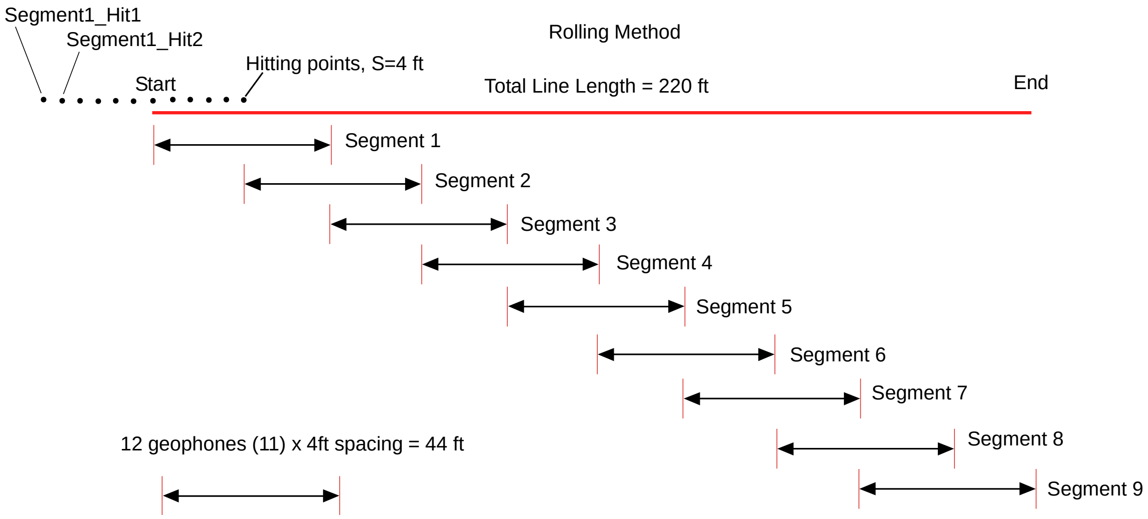
Segment1_Hit1
Segment1_Hit2
Start
Hitting points, S=4 ft
Rolling Method
Total Line Length = 220 ft
End
Segment 1
Segment 2
Segment 3
Segment 4
Segment 5
Segment 6
Segment 7
Segment 8
Segment 9
12 geophones (11) x 4ft spacing = 44 ft

Figure 3.3: Configuration of the geophysical survey line.

3.3.1 Multi-Channel Analysis of Surface Waves (MASW)

This method was developed in 1999 and is an improvement from the Spectral Analysis of Surface Waves (SASW) (Louie, 2001). It uses a conventional mode of geophysical surveying, utilizing an active seismic source, like refraction or reflection. A 12-pound sledgehammer was used for this study. The active source creates a higher frequency signal which allows for more accurate shallow measurements. However, this higher frequency signal is prone to attenuate with depth. Figure 3.4 shows the research team conducting the geophysical survey using MASW at the selected site before excavation.

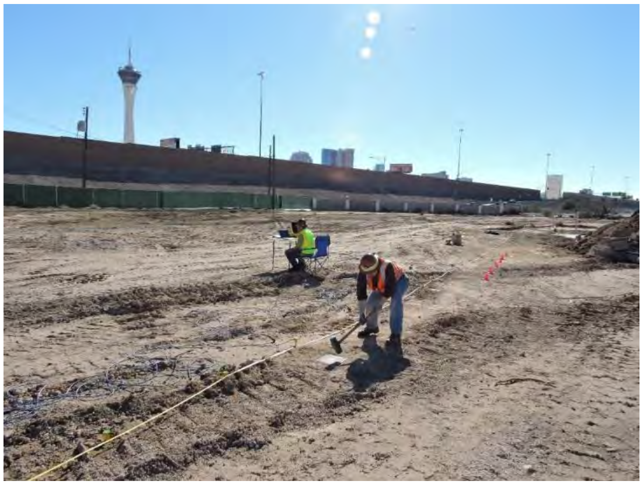

Figure 3.4: Geophysical survey before excavation using MASW method.

This method collects data in a roll-along mode, utilizing the surface waves propagating along the linear array (Park, 2007). The main advantage of MASW as stated by the developer, Choon Park, is that the MASW method is more tolerant in parameter selection than other methods because the highest ratio of signal to noise (S/N) is achieved. This is important since all geophysical methods must cope with noise contamination from other sources near the study site. Dr. Choon Park was employed to process the data and generate the results.

3.3.2 Refraction Microtremor (ReMi)

Developed in 2001 by Professor John Louie, this technique is designed to measure the shear wave velocity for geotechnical investigations. This method utilizes the same array previously described. The difference is that it uses a passive seismic source. The ambient vibrations created in an urban setting are ideal for use with ReMi.

Trained individuals are able to pick out the Rayleigh waves propagating across the array, from other types of waves and incoherent noise (Louie, 2001). This method utilizes much lower frequencies that are able to penetrate much greater depths, typically effective down to 330 feet with little attenuation.

The survey line used for the MASW method was used for the ReMi method. However, for the ReMi method, only noise, generated by the traffic, was used as the source. Also, more and longer records were recorded and used in the analysis. Dr. Satish Pullammanappallil with Optim Software, Inc. was employed to process the data and generate the results.

3.4 Specimen Collection

Large block samples were collected over the course of two weeks and three trips to the active excavation site in Las Vegas, NV shown in Figure 3.2. The samples were obtained to represent different cementation levels. All samples were logged, loaded on a truck and transported to the mining engineering laboratory at the University of Nevada, Reno. Figure 3.5 shows samples of the cemented soil blocks collected from the selected site during excavation.

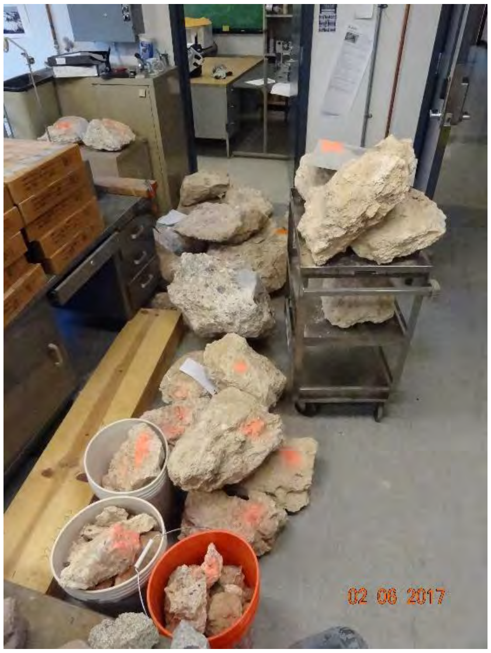

Figure 3.5: Block samples collected during excavation.

3.5 Specimen Preparation

Once the block samples arrived at the laboratory, they were divided, based on a visual assessment, into strongly and moderately/weakly cemented material. This categorization assisted in selecting the method of obtaining suitable samples from each block. Figure 3.6 is a photo of both types of blocks.

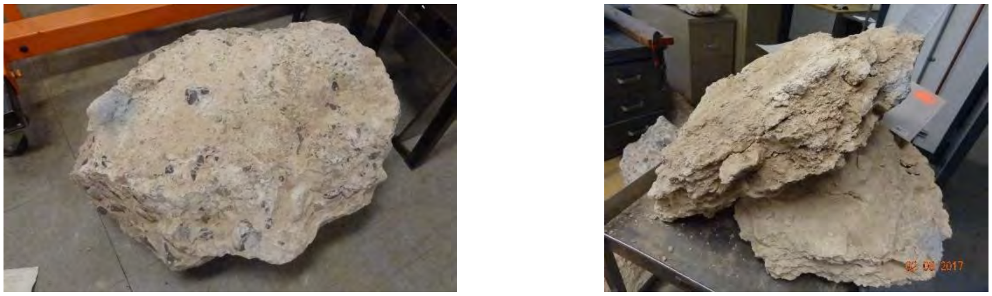

Strongly cemented soil Moderately/Weakly cemented soil

Figure 3.6: Sample of strongly and moderately/weakly cemented soil blocks.

3.5.1 Specimen Coring

Blocks representing strongly cemented soils were cored using a drill press in the Rock Preparation Lab of the Mining Engineering Department at the University of Nevada, Reno (Figure 3.7). A variety of diamond impregnated core tubes were used, ranging in diameter from 2 to 2.75 inch internal diameter (ID). These core tubes are smooth walled and connected by a water swivel to provide water pressure during drilling.

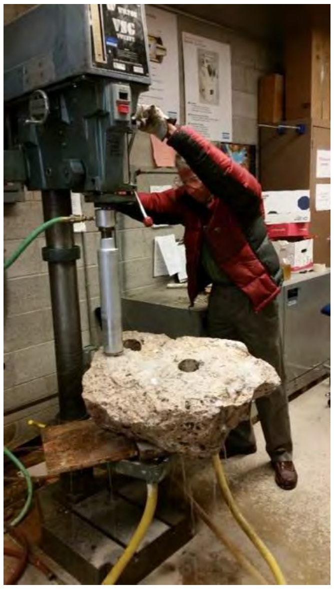

Figure 3.7: Use of the drill press to core cemented soil samples.

The same coring method was applied to moderately cemented blocks. However, these blocks experienced some damage from the jetted water produced by the drill. After trial and error adjusting the water pressure, samples were finally obtained from the moderately cemented blocks.

3.5.2 Specimen Cutting and Grinding

After coring, the specimens were cut to a length (L) approximately 2.5 times the sample diameter (2.5*D) using a diamond saw (Figure 3.8) as stated in ASTM D7012-14. Some samples failed to meet the minimum ratio of L=2*D due to either naturally occurring fracture planes, inherit weaknesses in the moderately cemented soils, or the overall depth of the block. To ensure smooth and even perpendicular ends, the core specimen was cut at 1/10-inch per minute.

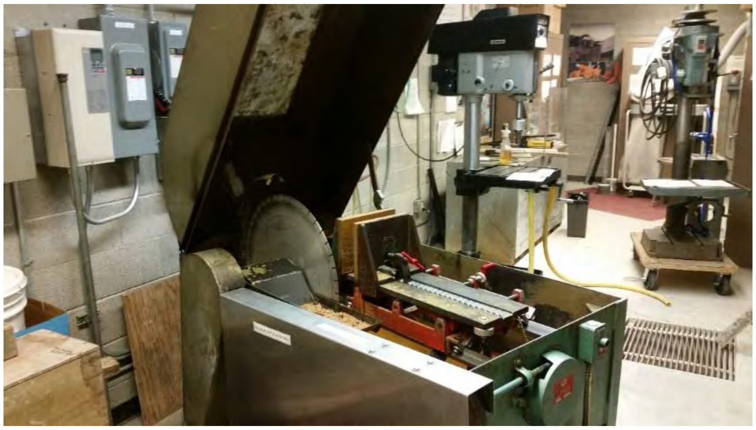

Figure 3.8: Photograph of the diamond core saw used in cutting the cores.

Once the specimens were cut, both ends were checked for flatness. Every sample went through the grinder to ensure that both ends met the ASTM 4543-08 standard for flatness tolerance of 0.001 inch displacement. To achieve this requirement, perpendicular lines were drawn on each cut side of the core. The core specimen was secured in a V-shaped steel block, with a dial gauge touching the flat surface (Figure 3.9). The sample was raised and lowered to verify flatness along both perpendicular lines.

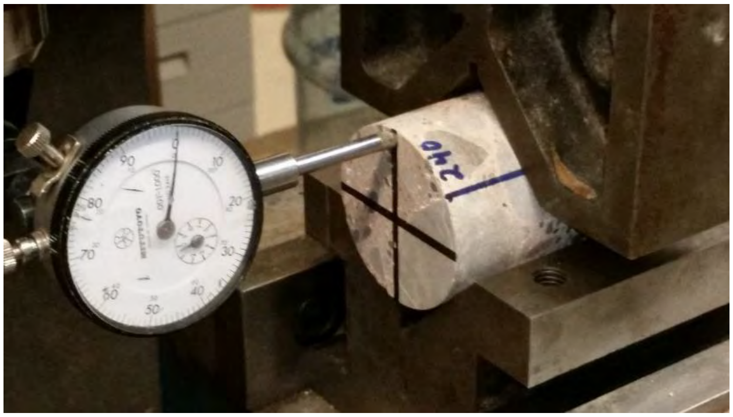

Figure 3.9: Dial gauge checking for flatness tolerance.

3.5.3 Alternative Preparation Methods

It was a challenge to obtain test specimens from the weaker material. Using a Schmidt Hammer, strength of each block was estimated prior to drilling. These strength tests, along with visual observation, determined that some of the collected cemented soil blocks would be too weak to drill. Two alternative methods were explored to obtain specimens from such materials: 1) confinement in concrete and 2) reconstituting caliche samples in 3-inch poster tubes.

3.5.4 Method 1: Confinement in Concrete

For this method, weak masses were placed in a fabricated wooden box slightly elevated above the bottom and not touching the sides of the box. Sakrete Quick Set Grout was mixed and poured into the wooden box. The confined sample was left to cure. After a suitable amount of time, the wooden box was disassembled, and the rectangular block was drilled.

Figure 3.10 presents the steps involved in the process of preparing the block and obtaining specimens from weakly cemented soils using first method. Recovery of a usable specimens still proved difficult and the method was abandoned.

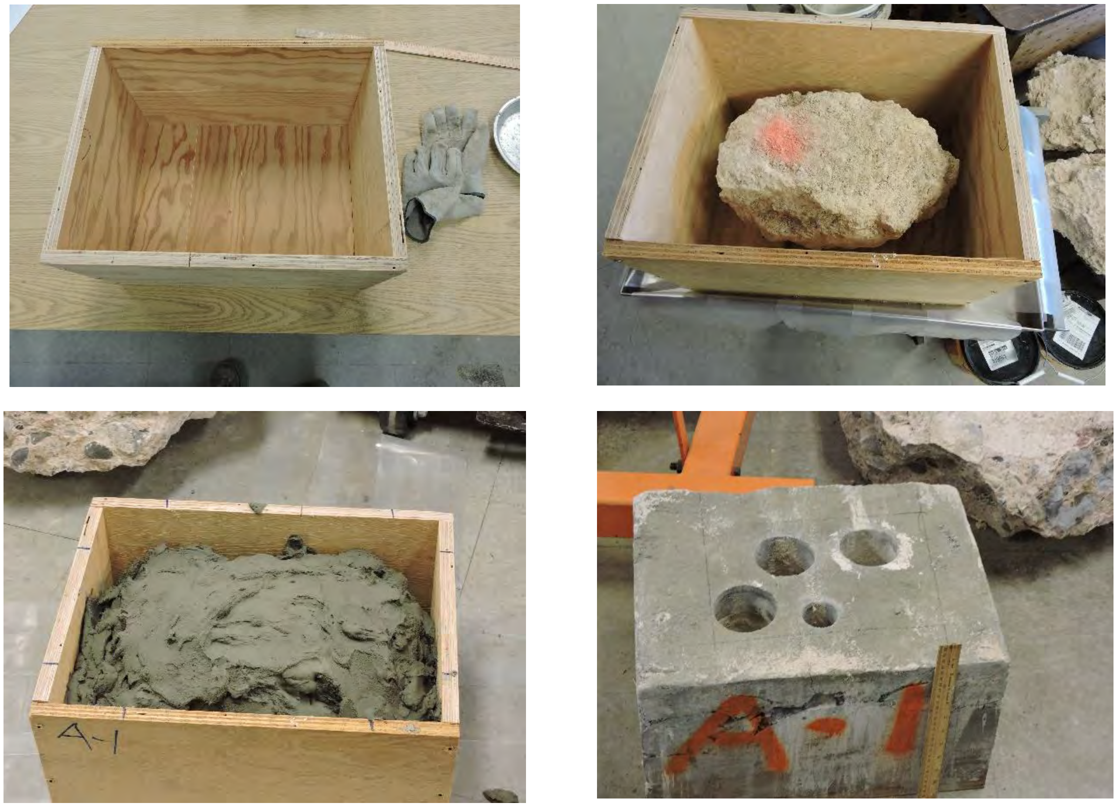

Figure 3.10: Stages of constructing the sample confined in grout.

3.5.5 Method 2: Reconstituted Caliche

For this method, weaker material was broken apart manually to a caliche soil and small aggregate pieces. The material was placed in a 5-gallon bucket. Chunks larger than 1 inch were broken or removed to ensure consolidation. By maintaining aggregate pieces, this ensured that the reconstituted sample retained its heterogeneous nature. Water was added to saturate the material, to obtain the consistency of thick mud. The saturated sample was added to 6-inch pre-cut lengths of 3-inch diameter poster tube.

Initially the specimens were air dried without mechanically consolidating the specimens. Such specimens broke easily and were not able to be successfully tested in the lab for compression and shear waves due to the numerous voids and planes of weakness. Subsequently, tests were prepared using the same procedure, however, a vibrating table was used for a short amount of time, about 10 seconds, to consolidate the specimen. Figure 3.11

shows the steps involved in preparing the specimen. These samples were air dried for over seven (7) days. The poster tube was then peeled away to reveal a testable specimen.

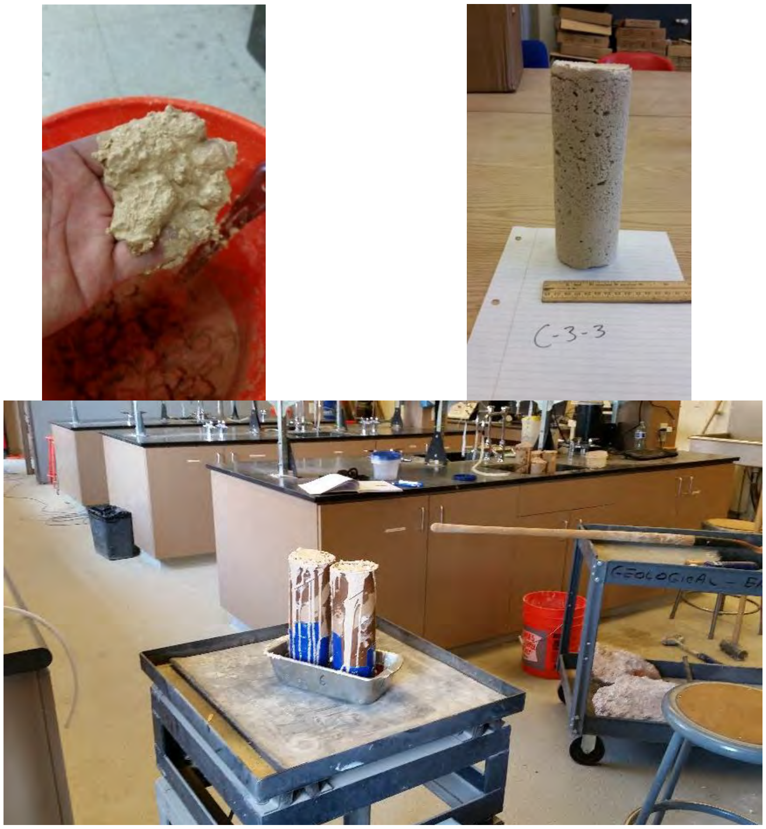

Figure 3.11: Process used to make a reconstituted cemented soil sample.

3.6 Ultrasonic Velocity Testing

Each specimen was tested for its Primary, also known as compression or pressure, (Vp) and shear (Vs) wave velocities using a Proceq Pundit PL-200 Ultrasonic Pulse Wave Transducer. A variety of transducers were used to establish velocities at different frequencies. The velocities were measured with 54, 150 and 250 kHz transducers for the Vp, and 250 kHz for the Vs. It was later determined that the lower frequency for the Vp would be the best choice since the higher frequencies are slightly distorted by voids and cavities (Ott, 2017).

Ultrasonic testing was performed in accordance with ASTM D2845-08. One parameter of the ASTM could not be met. It is stated that a limitation of the dimension of the specimen is that the aggregate should not exceed 10% of the specimen length. Given the nature of the material, this was not possible for many of the specimens.

The core specimens were mounted on an apparatus constructed from glass beaker clamps as shown in Figure 3.12. Careful consideration was made to ensure the specimen was not in contact with material that might have a higher velocity than the core specimen.

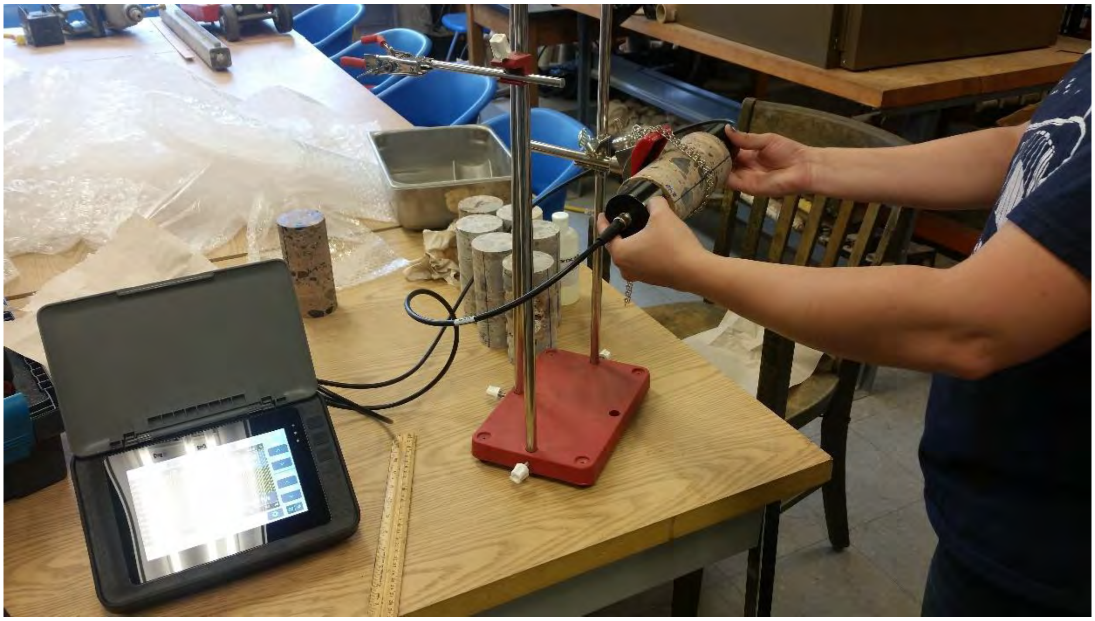

Figure 3.12: Ultrasonic testing configuration.

Each test was performed using couplant gel to ensure good contact between the transducer and the flat ends of the core specimen. Some specimens had small cavities on the core ends. By applying the gel, the cavity was filled and ensured good contact. The shear wave transducers required a much thicker special type couplant to adequately transmit the S-waves.

To ensure the accuracy of the equipment, velocity measurements were calibrated against two different materials: 1) A solid anodized aluminum cylinder; and 2) an untested concrete cylinder (of known compressive strength, f'_c). Results collected from the two different materials are reported in Table 3.1. As noted, the measured values were similar to the published values for these materials, which increased the confidence in the employed technique.

Table 3.1: Comparison of calibration material with published and measured velocities.

Material	Measured (ft/s)	Published (ft/s)
Aluminum (P-wave)	20,638	20,866 (Lee, 2009)
Aluminum (S-wave)	9,939	10,334 (Lee, 2009)
Concrete f'c (P-wave)	14,204	14,682 (Yaman et al., 2000)
Concrete f'c (S-wave)	8,254	7,929 (Birgul, 2009)

Lines were used at each end of the cored specimen to mark the center point, as shown in Figure 3.9, so the transducers could be lined up as accurately as possible. Each specimen was also marked on its lateral surface (Figure 3.12), with lines representing 120 degrees axial rotation. After the velocity was measured the first time, the specimen was rotated 120 degrees about its axis and measured again and repeated for a third measurement. Once all three measurements were taken, the direction of propagation was reversed (end for end), and the same three measurements were repeated. The average of all six measurements was assessed and reported as the value for that specimen.

The amplitudes were much higher for the 54 kHz readings than the other frequencies used. For these measurements, to maintain consistency, adjustments were made to increase or decrease the gain so that the first arrival wave peaked at 20% of the amplitude to ensure the wave forms were pronounced and unmistakable.

Using the higher frequency transducers, the wave forms became less pronounced and more difficult to read. The gain was adjusted on the console to ensure the best delineation of first arrival. However, as the gain was increased, so was the pre-arrival noise as seen in Figure 3.13. To eliminate the ambient noise and ensure a strong first arrival, the gain was increased to where the ambient noise was noticeable, then decreased two-fold (Ott, 2017).

When measuring the P-wave velocities, the equipment established the first arrival automatically. On the other hand, when measuring S-wave velocities, this selection had to be done manually. Figure 3.13 shows results obtained from one specimen as an example.

Because shear waves are linear, one of the transducers could be rotated 90 degrees which would cause the shear waves to not be visible. This would make selection somewhat easy. In a few cases, however, the transition between shear wave and primary wave was not as clear. Figure 3.13 shows that the transition between the two occurs when the primary wave does not complete a full sinusoidal waveform. It is believed that the shear wave arrives at this time.

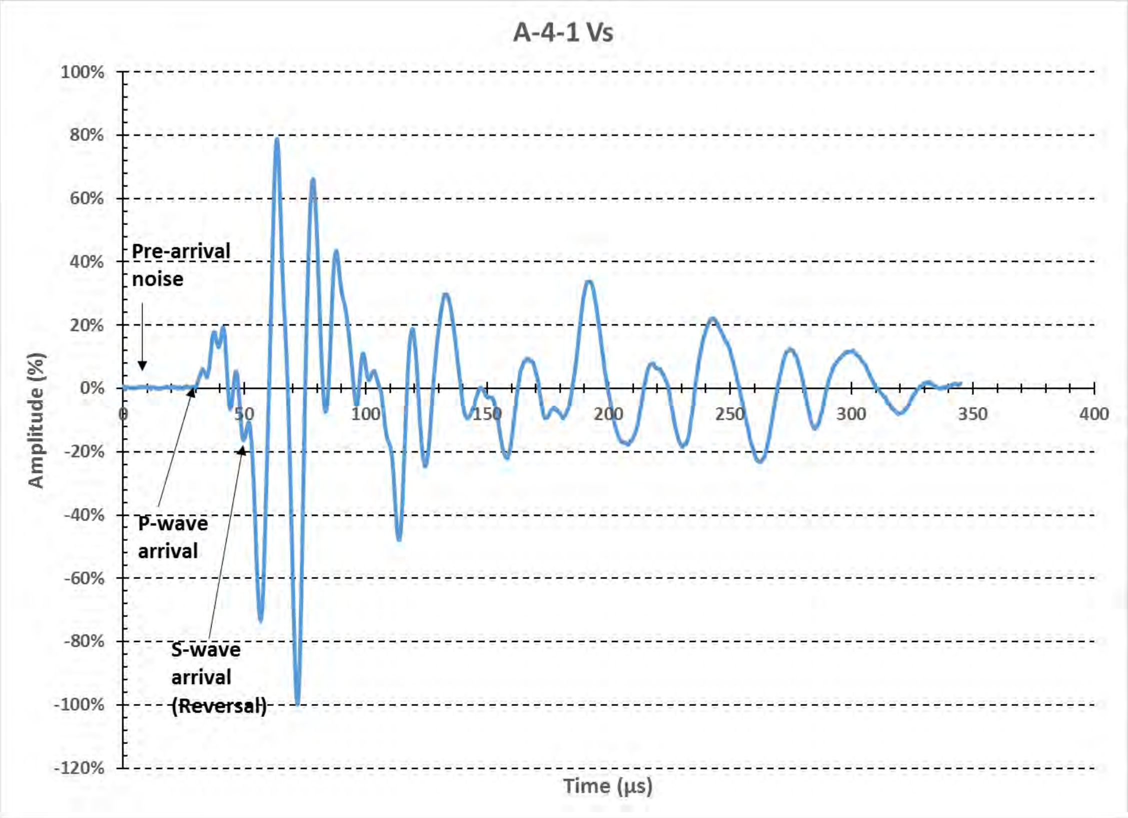

Figure 3.13: Seismic velocity plot from excel using exported data of specimen A-4-1.

3.7 Unconfined Compressive Strength Testing

Unconfined compressive strength tests were performed using a large load frame manufactured by Tinius Olsen (Figure 3.14). The hydraulic frame employs manual controls with digital output. It can be controlled in either force or displacement mode. Compressive strength tests were conducted in accordance with ASTM D7012. The strain rate was maintained as constant as possible and failure of test specimens never occurred before 2 minutes or after 15 minutes.

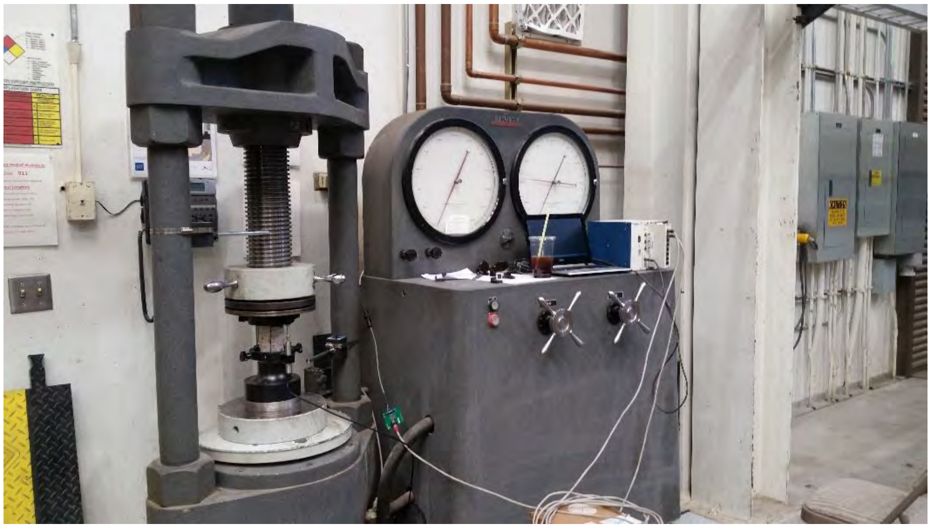

Figure 3.14: Tinius Olsen testing set-up.

A pressure gage was used to calculate the force exerted by the frame on the specimen. Several strain and displacement measuring sensors were used in the test. The types of sensors employed the Linear Variable Differential Transformer (LVDT), strain gauge, compressometer, and laser. By in large, the LVDTs proved to be the most reliable of all of the different measuring devices. The LVDT data best captured the behavior of the geomaterial by accounting for all sides of the specimen and any rotation within the apparatus. This will be discussed in greater detail in Chapter 5:.

Once the strain measuring sensors were properly mounted, the specimen was placed between two load platens. A steel blank was placed above and below the specimen to ensure the platens did not contact the axial and lateral LVDTs on the compressometer as shown in Figure 3.15. Once the hydraulics were engaged, the bottom plate advanced upwards. Specimens were loaded beyond failure to better establish and understand the failure mechanism. Appendix B shows data sheets for all test specimens. Each sheet provides information about specimen geometry, shear and pressure wave velocities, unconfined compressive strength and failure type.

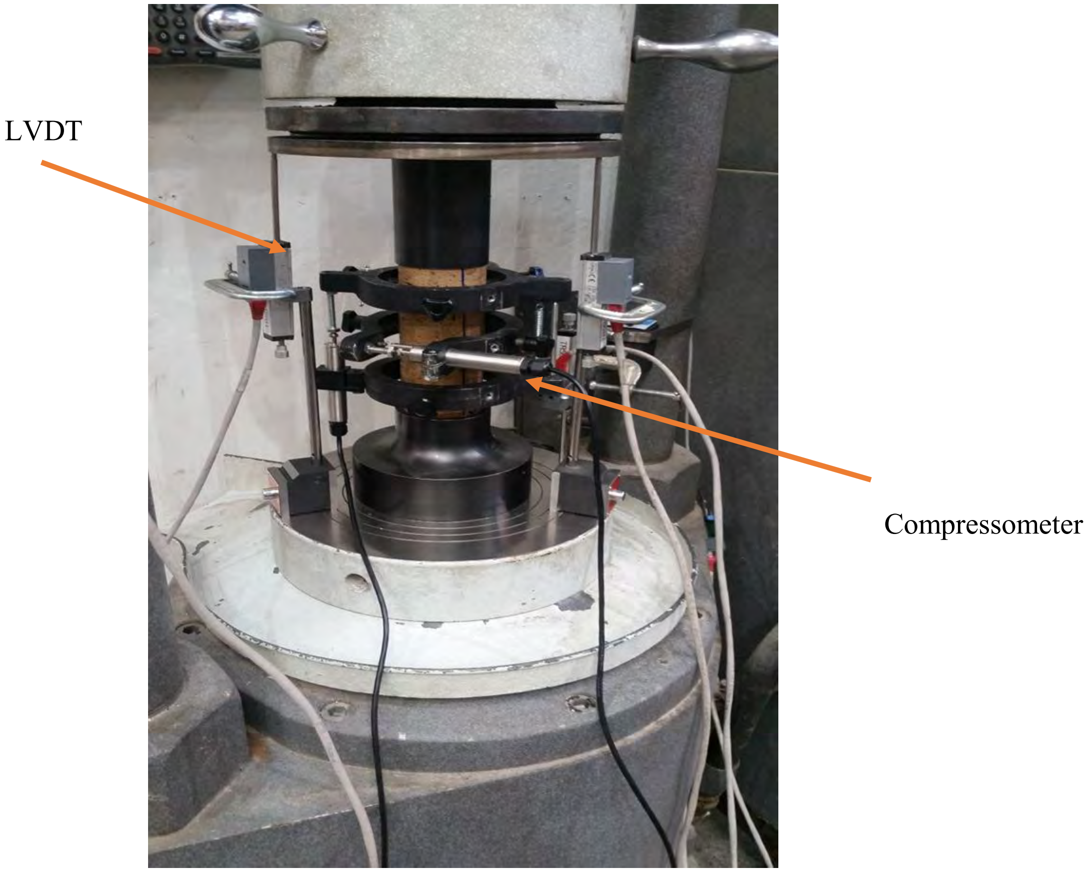
LVDT
Compressometer

Figure 3.15: Specimen with mounted compressometer surrounded by a set of LVDT's.

Chapter 4: Test Results

4.1 Introduction

The results from the lab and field tests are presented in this chapter, as well as, the derived correlations among them. Due to their variability, the materials were divided into three groups based on their measured unconfined compressive strength (UCS) values. The first group is the strongly cemented soil, which has an UCS of 10,000 psi or greater (Table 4.1). The second group is the moderately cemented soil that has an UCS values between 10,000 and 3,000 psi (Table 4.2). The third group is the weakly cemented soil that has an UCS less than 3,000 psi (Table 4.3). For this study, 53 specimens were tested for UCS, Vp and Vs. In a few re-constituted specimens, shear wave velocities were unattainable, and therefore the values were not reported. Appendix A contains a table, which contains measured and assessed data for all test specimens.

Data presented in this section was collected using the equipment mentioned in Chapter 3:. UCS tests were conducted using the Tinius Olsen load frame, where the load was assessed through measuring the hydraulic pressure in the ram, and displacement was measured using LVDTs. Meanwhile, S-wave and P-wave velocities were measured using an Ultrasonic Pulse Wave Transducer manufactured by Proceq.

The strain (ε) and the strain at 50% of the ultimate load (ε_{50}) were assessed from sample deformation recorded using LVDTs. The corresponding elastic modulus (E_{sec}) represents the slope of the secant line from the origin of the stress-strain curve to the strain at 50% of ultimate load. More details about their assessment are provided in Chapter 5:.

Poisson's Ratio (ν) was calculated using the equation from ASTM D2845 based on primary and shear wave velocities as shown in (Eq *4.1*. (eliminate italic)

$$\nu = \frac{(V_p^2 - 2*V_s^2)}{2*(V_p^2 - V_s^2)} \qquad \text{(Eq 4.1)}$$

Table 4.1: Strongly cemented soils (UCS > 10,000 psi).

No.	Specimen	UCS	Unit Weight	ε50	E_{sec}	Poissons Ratio	Vp [54kHz]	Vs [250 kHz]
		(psi)	(lb/ft^3)	(%)	(psi)		(ft/s)	(ft/s)
1	HC-1-5	20325	165.97	0.1640	6397230	0.26	19159	10967
2	HC-1-3	16284	162.95	0.1315	5685357	0.26	18164	10325
3	C-1-11	15844	166.25	0.1330	5956000	0.22	18656	11142
4	C-1-13	15365	167.18	0.1300	5910000	0.31	19274	10206
5	B-4-7	14460	156.86	0.1720	4203000	0.26	17072	9711
6	HC-1-1	14262	164.87	0.1160	5884148	0.32	18433	9577
7	HC-1-2	13937	161.19	0.1160	5529281	0.28	18187	10029
8	C-1-6	13773	162.44	0.1470	4685000	0.25	17595	10144
9	C-1-10	13618	167.98	0.1310	5198000	0.27	18965	10719
10	C-1-3	13400	163.57	0.1130	5929000	0.23	18201	10797
11	B-4-4	10791	158.96	0.1230	4387000	0.29	16624	9097
12	C-1-2	10460	161.31	0.0750	6973000	0.27	18525	10379
Std. Dev.		2457.22	3.23	0.0241	782557	0.026	770.96	576.29
Median		14099.50	163.26	0.1305	5784753	0.263	18317.00	10265.50
Average		14376.58	163.29	0.12929	5561418	0.267	18237.92	10257.75

Table 4.2: Moderately cemented soils (10,000 psi < UCS > 3,000 psi).

No.	Specimen	UCS	Unit Weight	ε50	E_{sec}	Poissons Ratio	Vp [54kHz]	Vs [250 kHz]
		(psi)	(lb/ft^3)	(%)	(psi)		(ft/s)	(ft/s)
13	B-4-6*	9070	159.58	0.0935	4850267	0.21	16968	10262
14	C-1-12	8885	163.27	0.1293	4259277	0.27	17838	9946
15	A-7-3	7756	156.71	0.1180	3286000	0.27	15859	8955
16	B-4-8	7240	156.45	0.1090	5625485	0.31	16536	8742
17	B-4-1	7016	155.55	0.0980	3580000	0.15	15677	10053
18	B-5-1	6440	147.42	0.0980	3286000	0.28	15446	8492
19	C-4-3	6228	143.26	0.2465	1263000	0.32	10393	5385
20	B-5-6*	5108	149.84	0.1462	1747400	0.26	15361	8766
21	B-5-5*	5008	145.67	0.1100	2276364	0.28	14022	7784
22	A-8-1	4660	151.55	0.1130	2062000	0.29	14788	8089
23	B-4-2*	4620	152.10	0.0530	4358491	0.21	15119	9161
24	B-5-4	4610	148.61	0.0830	2777000	0.25	14878	8572
25	C-1-14*	4574	159.33	0.0775	2345881	0.26	16919	9595
26	A-7-5	4340	151.08	0.1360	1494387	0.16	14515	9253
27	B-5-7	3847	148.72	0.1580	1217000	0.30	13679	7369
28	B-5-3	3800	145.93	0.0905	2099000	0.24	14226	8343
29	A-7-2	3540	151.73	0.0760	2329000	0.27	14589	8197
30	B-1-1*	3316	144.73	0.1720	963953	0.26	11709	6682
31	B-4-5	3250	148.91	0.0505	3218000	0.27	15091	8444
32	C-2-2*	3160	142.04	0.0670	2358209	0.15	13479	8678
Std. Dev		1803.49	5.66	0.04455	1244359	0.049	1691.54	1123.46
Median		4640.00	150.46	0.1035	2352045	0.264	14984.50	8624.75
Average		5323.40	151.12	0.11125	2769836	0.250	14854.60	8538.38

Table 4.3: Weakly cemented soils (UCS < 3,000 psi).

No.	Specimen	UCS	Unit Weight	ε50	E_{sec}	Poissons Ratio	Vp [54kHz]	Vs [250 kHz]
		(psi)	(lb/ft^3)	(%)	(psi)		(ft/s)	(ft/s)
33	B-2-2	2990	147.02	0.2400	623000	0.28	10706	5896
34	C-8-1	2960	149.95	0.1030	1437000	0.18	10749	6741
35	C-4-1	2871	140.46	0.1470	977000	0.21	10632	6420
36	B-5-2*	2802	146.63	0.0880	1592045	0.20	14226	8685
37	C-7-2	2800	128.38	0.0800	1750000	0.19	12463	7732
38	C-4-2	2670	139.05	0.1685	782000	0.22	11449	6845
39	B-4-3	2577	152.94	0.0750	1718000	0.30	14961	7968
40	B-2-1*	2168	143.70	0.1220	888525	0.21	11353	6913
41	A-2-1*	1900	123.70	0.1230	772358	0.18	9313	5813
42	C-2-3	1846	146.22	0.0420	2198000	0.18	14107	8783
43	A-7-1*	1840	147.48	0.0500	1840000	0.27	14423	8080
44	A-4-1	1666	125.61	0.1540	537776	0.20	9647	5909
45	C-7-3*	1634	133.40	0.1150	710435	0.21	8762	5309
46	C-7-1*	1582	141.57	0.0630	1255556	0.26	7967	4556
47	B-3-1	1493	138.32	0.2150	366000	0.31	10651	5570
48	C-2-4	1477	137.08	0.0420	1780000	0.24	11718	6888
49	C-8-2	1390	131.17	0.0900	774000	0.22	10208	6122
50	A-4-2	1383	121.72	0.1800	399824	0.18	8516	5331
51	A-3-1*	788	109.59	0.1300	303077	0.20	6817	4156
52	C-3-4*	34.5	94.42	0.0700	24642.9	0.03	2521	1754
53	C-3-3*	30	76.70	0.0950	15789.5	0.20	3810	2344
Std. Dev		852.79	18.59	0.0534	624949.3	0.057	3127.75	1787.74
Median		1840.00	138.32	0.1030	782000	0.205	10651.00	6122.00
Average		1852.45	132.15	0.1139	987858.4	0.213	10238.00	6086.44

4.2 Primary and Shear Wave Velocities

As discussed in Chapter 3:, a geophysical survey was conducted in the field at the site prior to its excavation to determine Vs of the different layers. Two techniques were used on the same survey line: MASW and ReMi. Data collected from both techniques were processed by independent specialist consultants to ensure confidence in the results.

Meanwhile, the ultrasonic test was utilized to determine Vp and Vs in the lab for each specimen. Lab shear wave velocity was used to establish relationships with unconfined compressive strength, elastic modulus and unit weight. A correlation between lab and field shear wave velocities was also derived.

4.2.1 Field Measurements

The analysis using MASW technique generated a shear wave velocity profile, shown in Figure 4.1, indicating a maximum velocity of approximately 1,800 ft/s at a depth of around 22 feet. The maximum depth of the excavation conducted at the site, however, was 17 feet. Thus, it is very likely that the layer where block samples representing the strongly cemented soil is delineated with yellow and has a Vs of approximately 1,400 ft/s.

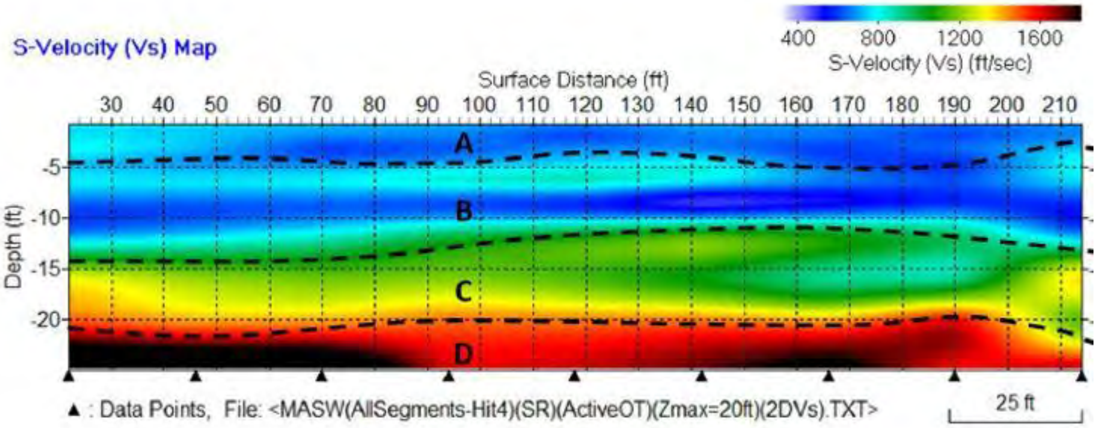

Figure 4.1: MASW generated Vs profile of the excavation site.

The analysis using ReMi technique generated a shear wave velocity profile, presented in Figure 4.2, showing an approximately 5-ft layer of hard material. The layer has a velocity of 4,000 ft/s and fluctuates in depth between 17 to 30 ft. This hard pan could represent both the strongly cemented and moderately cemented soil. Discussion with the consultant revealed that he used a pre-determined value of shear wave velocity of 4,000 ft/s for all hard, rock-like, layers. This was based on his experience with the area from a previous project. This was later contested by the research team and the data were re-analyzed. Results from the revised analysis are presented in Figure 4.3. The reanalysis shows multiple layers, which is more aligned with site logging, which is presented in Figure 4.4.

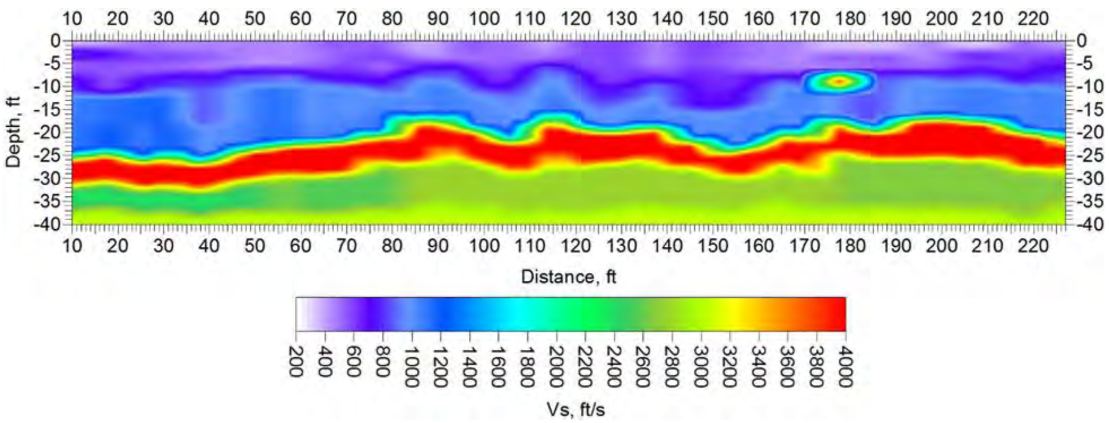

Figure 4.2: ReMi profile of excavation site.

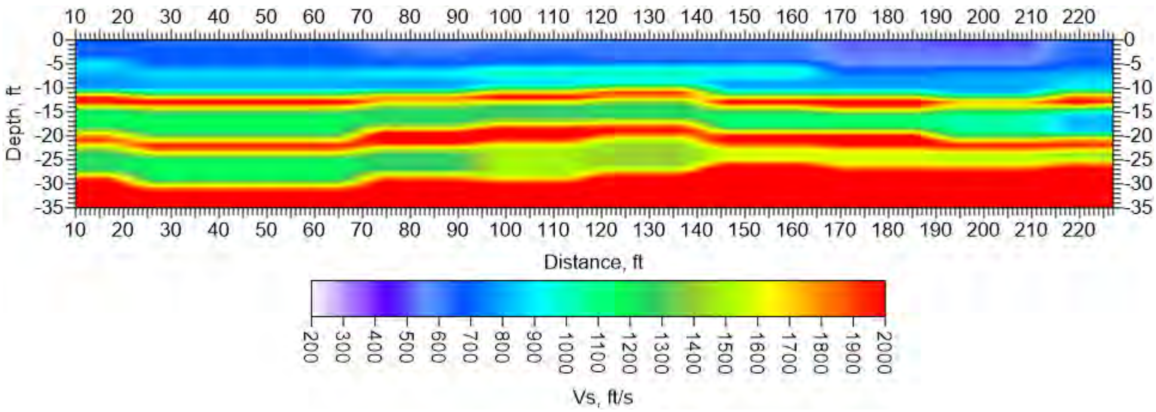

Figure 4.3: Revised ReMi analysis of the excavated site.

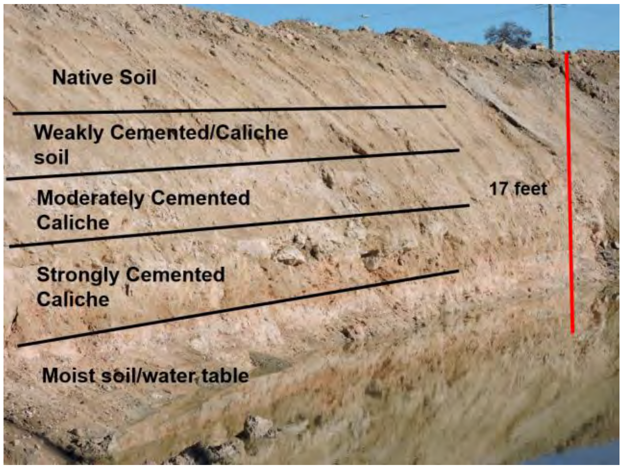
Native Soil
Weakly Cemented/Caliche soil
Moderately Cemented Caliche
Strongly Cemented Caliche
Moist soil/water table
17 feet

Figure 4.4: Logging of the excavated site.

4.2.2 Lab Velocities

The lab measured primary (Vp) and shear (Vs) velocities can be found in Tables Table 4.1, Table 4.2 and Table 4.3. As expected, seismic velocities tend to increase with cementation level and UCS values. Although some outliers exist, where a drop-in velocity, in some specimens, is noted when there is an increase in UCS. This can be attributed to several factors, including aggregate size and/or distribution, or the mineralogy of the specimen, both of which are out of the scope of this study. The ratio of Vp : Vs (not shown in tables) did not fluctuate much. Its range was from 1.6-1.8. The stronger samples tended to have a higher ratio, while the average dropped for the weaker samples. While, this information was not statistically relevant, it was used to check for inconsistencies and anomalous data.

4.3 Correlation Between Field and Lab Shear Wave Velocities

Based on the field and lab geophysics, a correlation factor was developed. This correlation factor is to be used when the designer wishes to compute the lab shear wave velocity in order to use the established Vs_l correlations presented in Chapter 4:. This relationship between the lab and field geophysics was found to be (Figure 4.5):

$$Vs_{(lab)} = Vs_{(field)} * 5.129 \qquad \text{for ReMi analysis}$$

$$Vs_{(lab)} = Vs_{(field)} * 6.411 \qquad \text{for MASW analysis}$$

These correlations were developed by taking the average shear wave velocity from the strongly cemented soil grouping, equal to 10,258 ft/s, and dividing by the peak shear wave velocity from the Revised ReMi analysis of the excavated site (Figure 4.3) of 2,000 ft/s and 1600 ft/s from the MASW analysis (Figure 4.1).

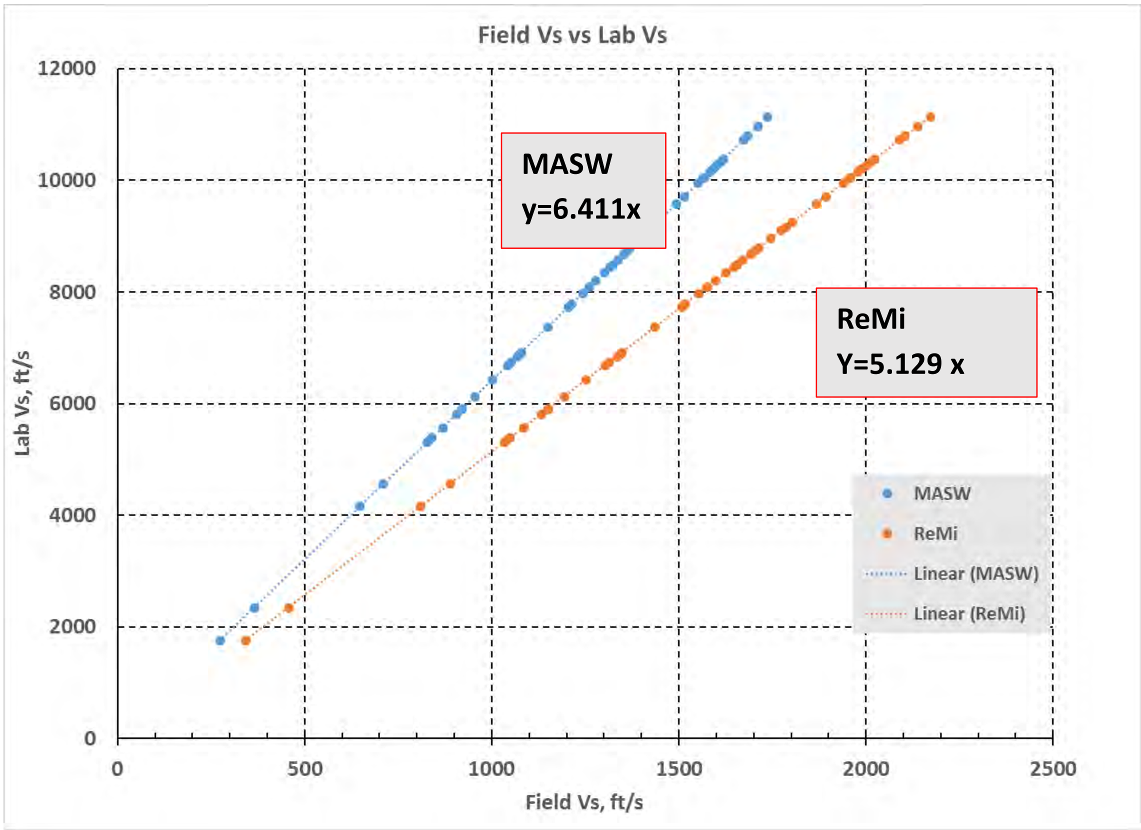

Figure 4.5: Field and lab shear wave velocity relationship.

4.4 Correlation of Unconfined Compressive Strength and Lab Shear Wave Velocity

To achieve one of the objectives of this project, a correlation between unconfined compressive strength and shear wave velocity was explored. The UCS is a typically reported parameter for rocks and is commonly used in many rock mass classification systems. Furthermore, UCS is used in geotechnical design, more specifically for foundations.

Unconfined compressive strength was correlated with the lab assessed shear wave velocity (Vsl) and the results are presented in Figure 4.6. Data from 57 specimens were used in establishing this correlation. The highest UCS value in the data is 20,325 psi while the lowest is 30 psi. A power model trend line yields a coefficient of determination (R^2) value of 0.748.

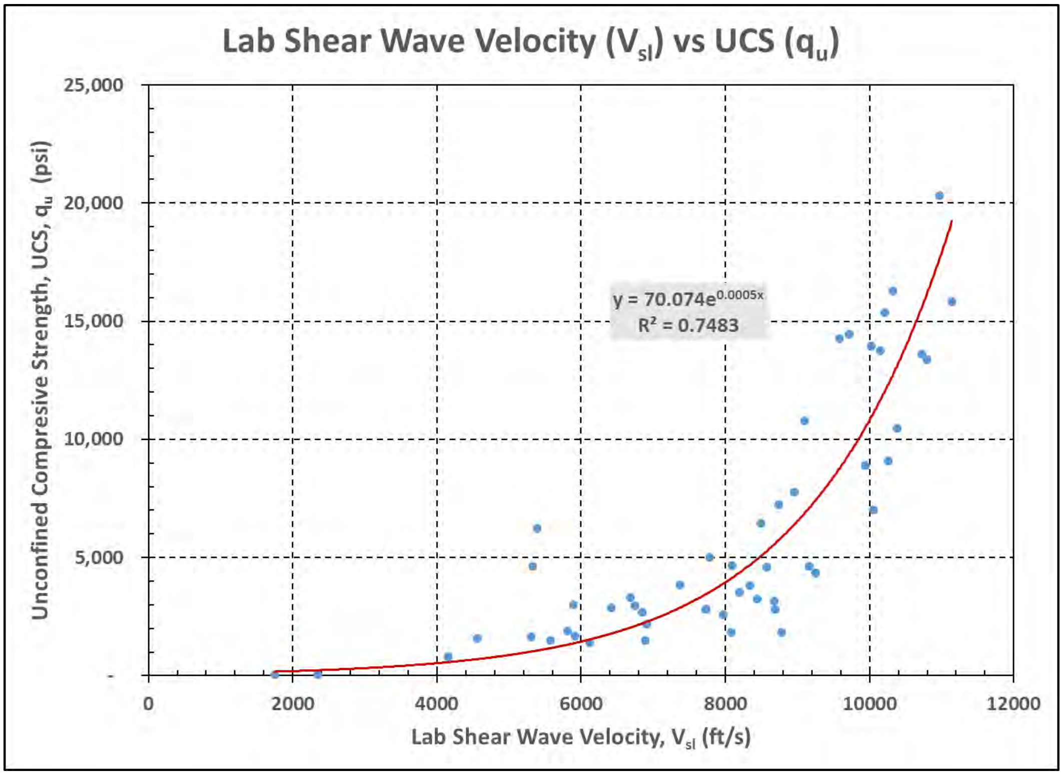

Figure 4.6: UCS correlation with lab shear wave velocity.

4.5 Correlation of Elastic Modulus and Lab Shear Wave Velocity

The relationship between elastic modulus and lab shear wave velocity was also examined. The elastic or Young's modulus (E) is a measurement of the stiffness of the material, a secant slope (E_{sec}), commonly assessed at a specific level of strain. Figure 4.7 shows the relationship between the elastic modulus at a strain level of 50% (E_{50}) and the lab shear wave velocity (Vsl). For this correlation, data from 53 specimens were used, since some of the compressive strength tests did not employ LVDTs to assess the strain. A best fit power model trend line yielded an R^2 value of 0.906. Data from the 53 specimens showing the stress-strain plots from which the elastic modulus slopes were assessed is presented in Appendix C.

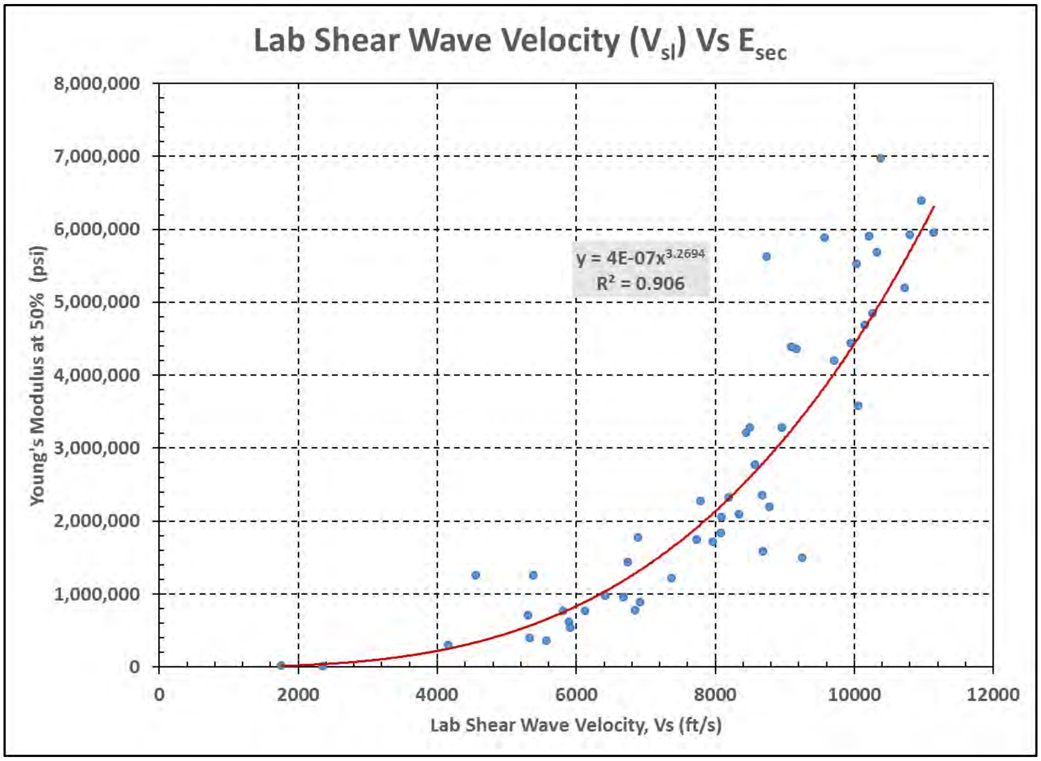

Figure 4.7: Elastic modulus correlation with lab shear wave velocity.

4.6 Correlation of Unit Weight with Lab Shear Wave Velocity

Material unit weight is a parameter that can, sometimes, be assessed in the field without significant effort. A correlation of material unit weight and lab shear wave velocity would be beneficial, and thus, was investigated. Figure 4.8 presents the correlation between lab shear wave velocity and unit weight. Data from 57 samples were used in developing this correlation yielding an R^2 value of 0.818 for an exponential trend line model.

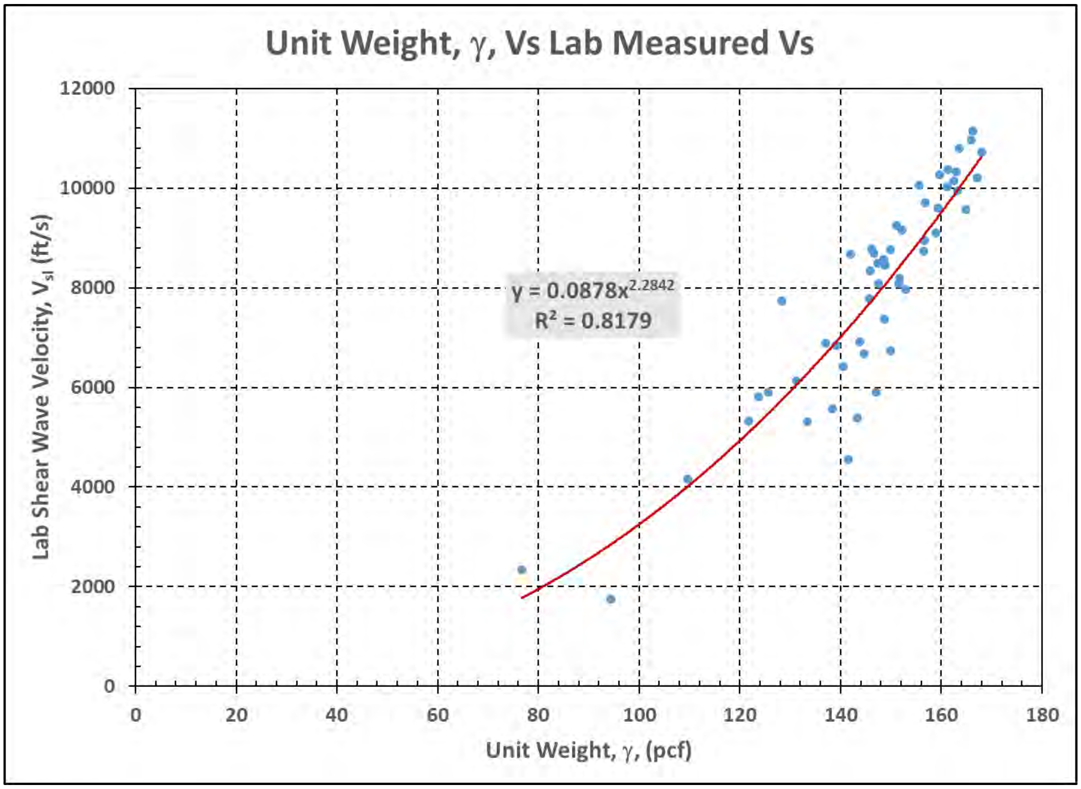

Figure 4.8: Correlation of lab shear wave velocity with unit weight.

Chapter 5: Material Model

5.1 Introduction

This chapter presents the methodology employed to model the stress-strain relationship for cemented soils using unconfined compression tests of samples taken from the excavation site discussed in Chapter 3:.

5.2 Evaluation of Axial Strain

Vertical sample deformation, used to assess axial strain, was measured using different sensors (LVDTs, compressometer, strain gage and laser). The advantage of the using a compressometer, that it measures the axial deformation within the central portion of the specimen (away from its ends). However, such measurement is captured between two yokes secured on one side with a hinge mechanism, while free to move at the other end, where the one LVDT measuring vertical deformation is attached (see Figure 3.15). Consequently, the compressometer's LVDT readings should be corrected as described in ASTM C469-14. The correction factor is based on compressometer dimensions and for the model that was used in these tests, the factor was calculated to be 0.505. (The advantage the compressometer provides is the complementary, horizontally aligned LVDTs, that measure radial displacement, which can be used in conjunction with the vertical displacement to establish a Poisson's ratio as it changes during loading.)

Another complementary method used to measure axial deformation employed three LVDTs placed at 120 degrees around the specimen. The base of each LVDT was secured to the bottom platen while the tip was in contact with the upper platen. This allowed the axial deformation recordings in three vertical planes, which can, then, be averaged to reflect overall specimen response. A laser sensor was also used to measure the axial deformation. However, its readings, by contrast, exhibited a wide variation (wide band of readings) with increasing deformation. Strain gages were only used in a few tests. Their utilization was terminated early on because the data did not capture the behavior of the entire specimen.

While the compressometer curves were “cleaner” (i.e. more linear to 50% strain) and, therefore, easier to work with, the undulations in the LVDT curve are indicative of adjustments the sample is undergoing on various natural internal fractures in the specimen, and thus more realistic. The upward curvature of the lower portion of the LVDT curve (Figure 5.1) can be attributed to initial closure of fractures, void closure and mineral compression (Goodman, 1989). This behavior was not necessarily recorded by the compressometer. Since the compressometer is not an equipment typically used in testing rock samples (it has only recently been employed in testing concrete samples), and the judged lack of capture of sample behavior (the single, central vertical plane of recorded deformation and the record’s absence of ongoing adjustments on internal fractures under load), the LVDT deformation data was used to establish the strain. Hence, 53 of the total 58 tests were conducted with LVDT readings.

Figure 5.2 provides a comparison of the LVDT derived stress-strain curve versus the uncorrected and the corrected compressometer curves of Test A-7-2. Note that the compressometer curve and its corrected version offer a smoother response compared to that of the averaged LVDT curve. It yields a well-defined origin, while the LVDT curve needs to be shifted horizontally (Figure 5.2) and an offset value of strain recorded relative to the newly established origin, which will be discussed in 5.3

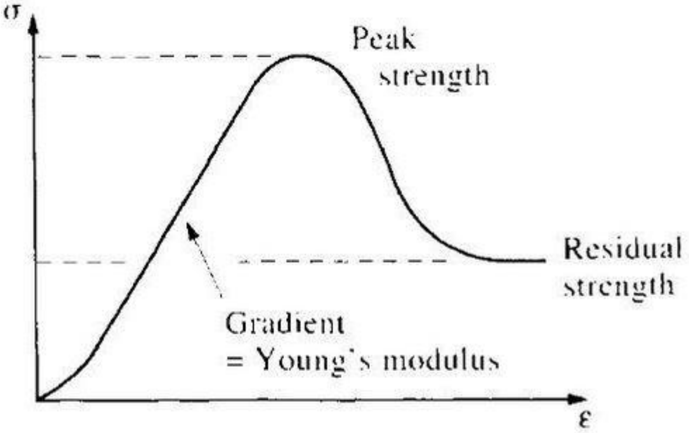

Figure 5.1: Typical behavior of rock under axial load (Hudson, 2000).

The dashed red line in Figure 5.2 needs to be moved over to match the LVDT curve at approximately 1600 psi.

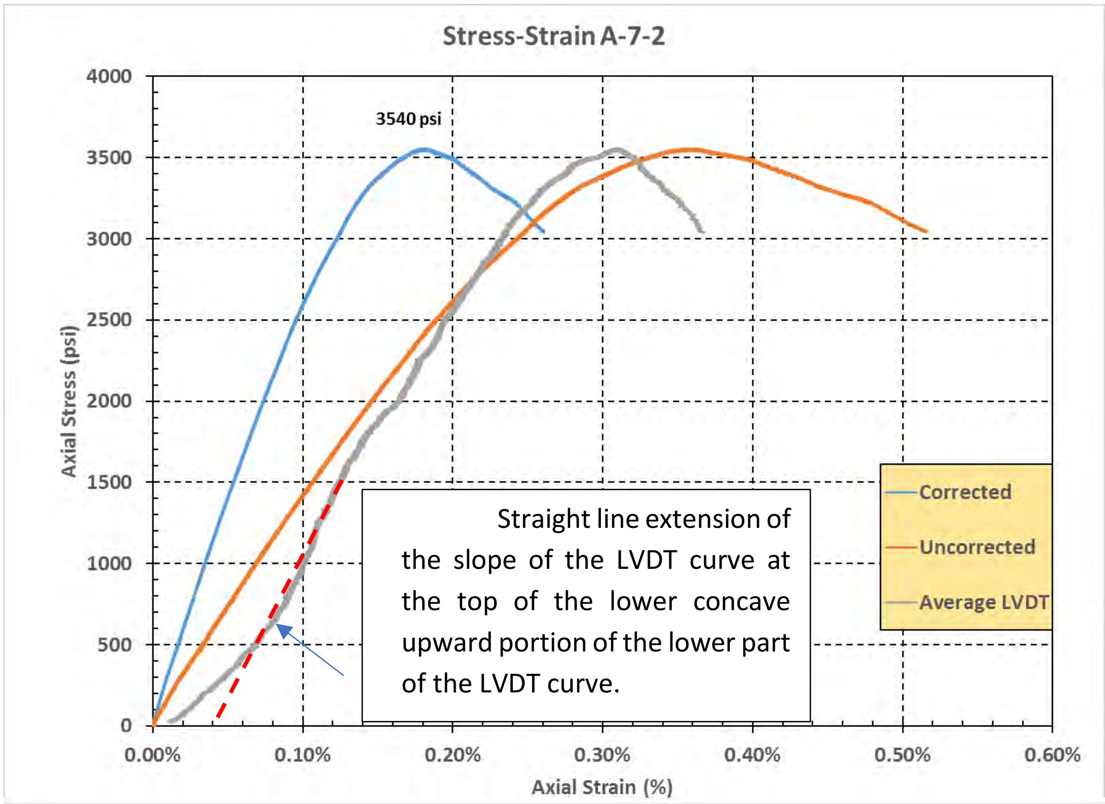

Figure 5.2: LVDT and Compressometer curves from Test A-7-2.

5.3 Establishing Strain Offset (Δε)

A line (whose characteristics are described in Figure 5.2) of each LVDT test, when extended to intersect the horizontal axis represents the origin of the elastic portion of the stress strain response. The value of strain at the line's intersection with the horizontal axis, when subtracted from the values of strain of the test, shifts the entire plot and lines up the elastic region of the curve to this new origin (Figure 5.3). Most LVDT curves showed error or noise at very low stress. To eliminate this, the part of the curve with stress less than 1% of UCS was disregarded from all tests. Thus, a Δε value attributed to fracture closure or void collapse was measured from the adjusted origin, to where the 1% UCS line intercepts the bottom of the curve (Figure 5.3). To establish a systematic characterization of strain offset, the Δε values were averaged within each cementation grouping (previously discussed in the Chapter 4: and presented in Table 4.1) and presented in Table 5.1.

Table 5.1As indicated, the stronger material exhibited the behavior of highly competent material with very little curvature at the start. In some cases the weaker material exhibited very large gradual curvature, showing that there is significant void and fracture closure.

The secant slope (E_{sec}) from the adjusted origin to the stress at 50% of the strength (UCS) was established for all test curves. Such E_{sec} values are the elastic modulus (or E_{50}) values from Figure 5.4. While not taken to be the same as the E_{50} line, it is almost identical to it, exhibiting the linearity of the elastic portion of the stress-strain plots.

The results of this analysis were positive. The stronger material exhibited the behavior of highly competent material with very little curvature at the start. In some cases, the weaker material exhibited very large gradual curvature, indicating that there is significant void and fracture closure.

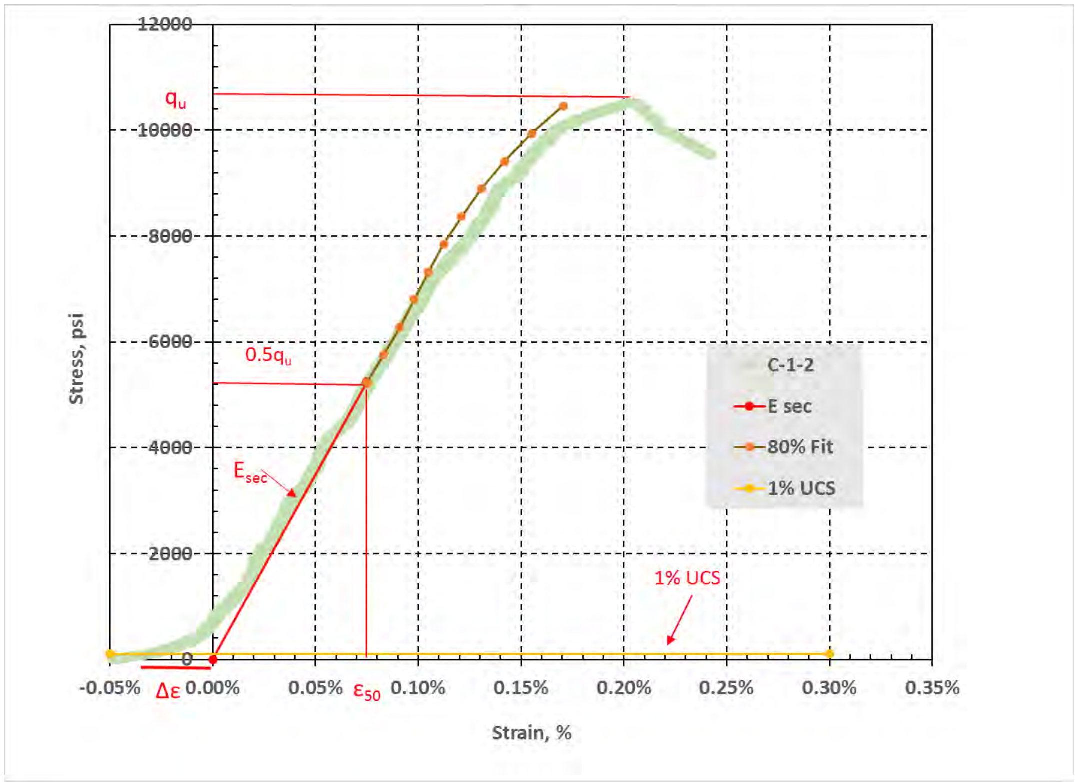

Figure 5.3: Typical adjusted LVDT curve.

Table 5.1: Strain offset (Δε) by cementation level.

Type	**UCS, q_u (psi)**	**Δε (%)**
Strongly Cemented	$q_u > 10{,}000$	0.015
Moderately Cemented	$10.000 > q_u > 3{,}000$	0.035
Weakly Cemented	$q_u < 3{,}000$	0.056

5.4 Material Model of Cemented Soil

Once every stress-strain plot was shifted, each plot resembled the form shown in Figure 5.4. The y-axis of each curve was then normalized to represent stress level (SL) instead of stress. The value of the axial stress divided by the peak stress. q_u (= 10791 psi for sample B-4-4) yields its stress level ($SL=\frac{\sigma_d}{q_u}$) value.

Figure 5.5 is the corresponding plot of SL versus strain. It is relative to this SL versus strain curve for which an equation is sought.

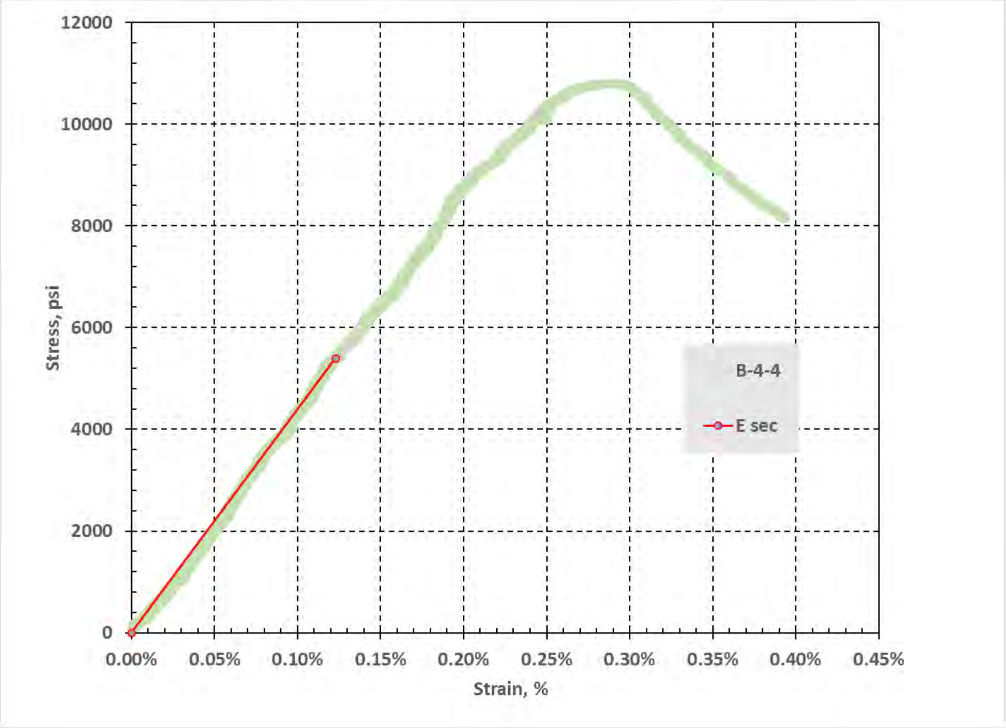

Figure 5.4: Plot of stress versus shifted strain for Test B-4-4.

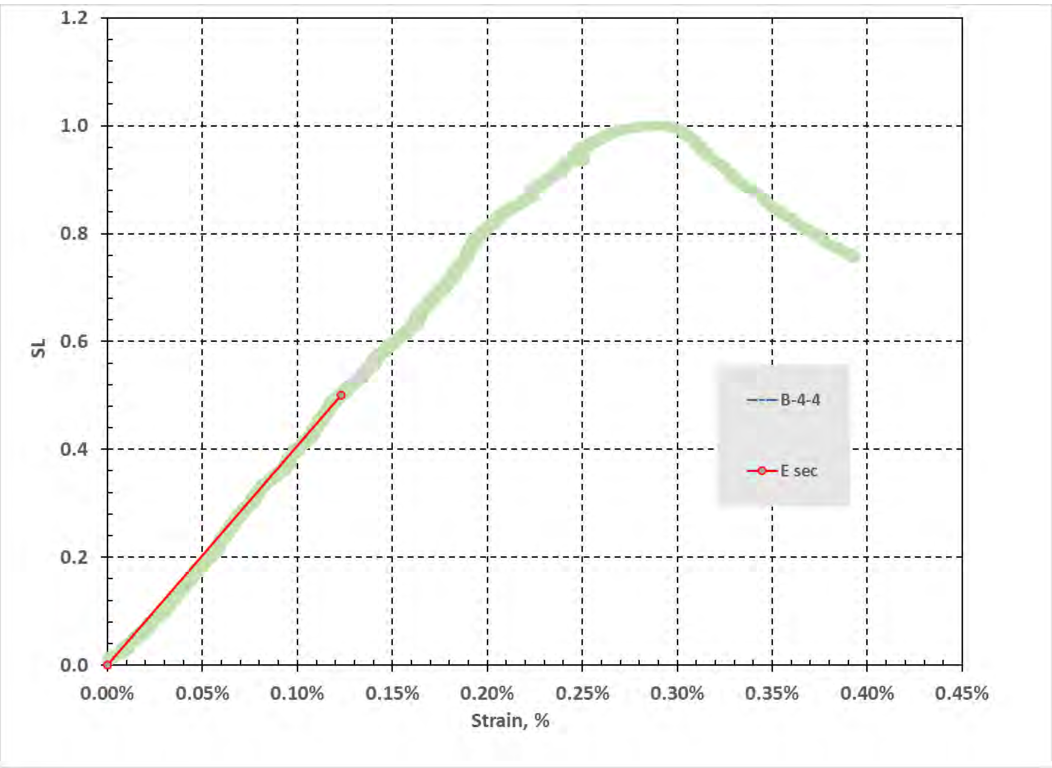

Figure 5.5: Stress Level (SL) versus strain of Test B-4-4.

The SL values are then used to model the strain for any given point on the curve using the equation

$$\varepsilon = \mathrm{SL}^{*}\frac{q_u}{E_{sec}},$$

or simply

$$\varepsilon = 2^{*}\mathrm{SL}^{*}\varepsilon_{50} \qquad \text{(Eq. 5.1a)}$$

corresponding to linear elastic behavior for SL ≤ 0.50. Above the SL of 0.50, the equation

$$\varepsilon = \mathrm{SL}^{*}e^{3.707\mathrm{SL}}{}^{*}\varepsilon_{50} / \lambda \qquad \text{(Eq. 5.1b)}$$

for soil from Ashour and Norris (1999) will be employed. However, the equation for λ for cohesive and cohesionless soils,

$$\lambda = -7.121\ \mathrm{SL}^2 + 7.0592\ \mathrm{SL} + 1.4403 \quad \text{for SL} \geq 0.50 \qquad \text{(Eq. 5.2)}$$

as given by Norris (2017) is modified here to reflect the response of the cemented samples tested.

To establish the variation in λ for SL > 0.5 for cemented soils, Equation 5.2 was rearranged to give Equation 5.3

$$\lambda = SL\, e^{3.707SL} \varepsilon_{50} / \varepsilon \qquad \text{(Eq. 5.3)}$$

Backfigured values of λ based on values of SL and ε (the shifted LVDT curve) were assessed and plotted versus SL. Figure 5.6 is a λ versus SL plot so obtained.

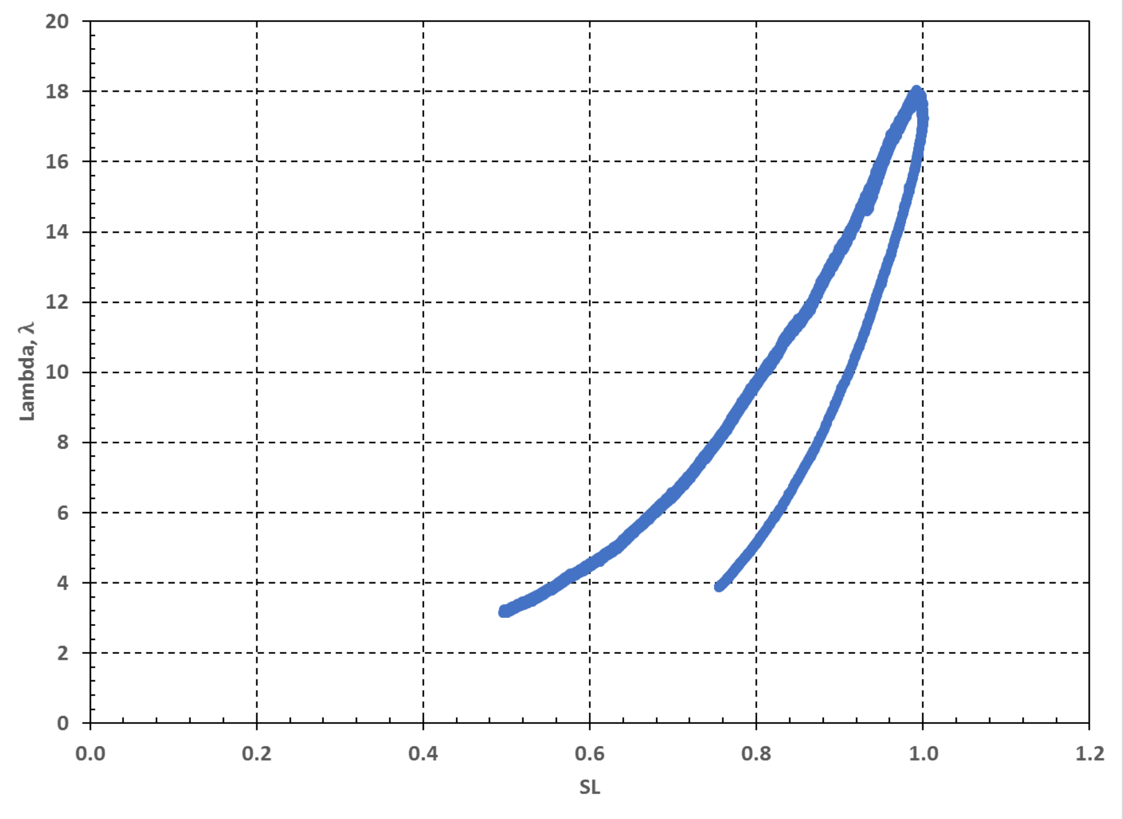

Figure 5.6: Lambda (λ) versus SL for Test B-4-4 for SL > 0.50.

Figure 5.6 includes the variation in λ beyond the peak (at q_u) of the stress strain curve. Once the variation between SL = 0.5 and 1 is isolated, a best fit 2nd order polynomial is fitted to the data and the equation recorded (Figure 5.7).

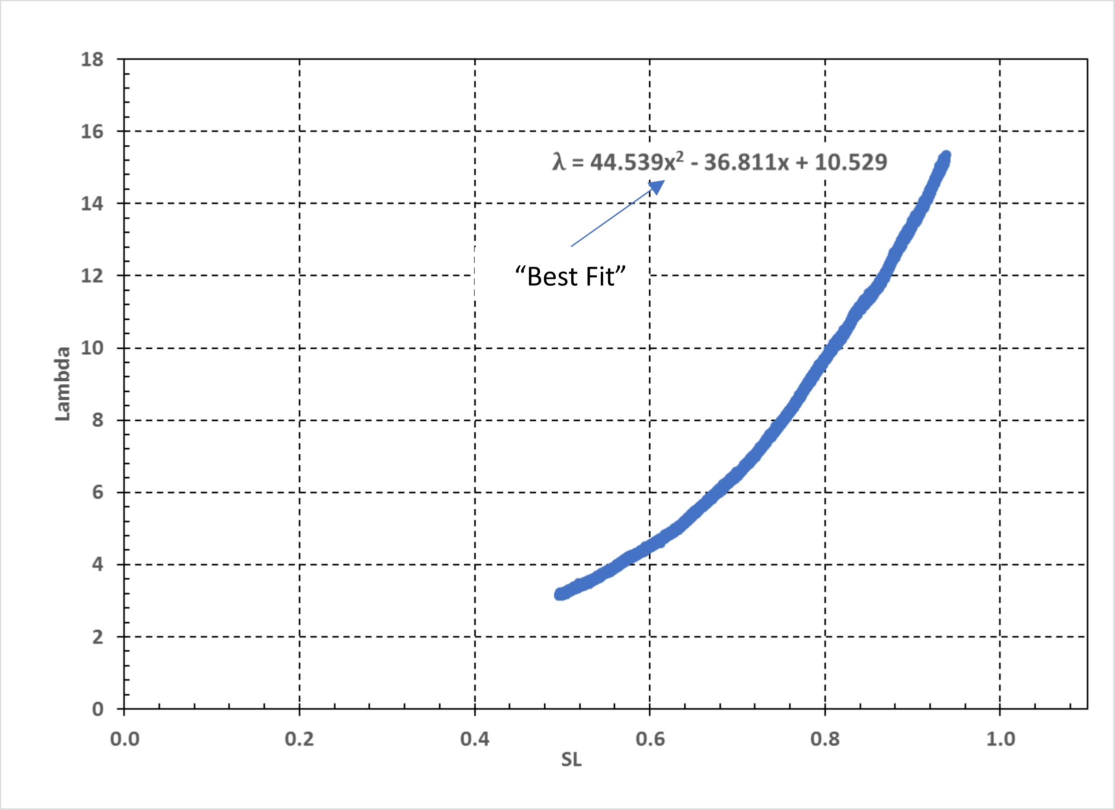

Figure 5.7: Evaluation of the "Best Fit" equation of λ versus. SL from SL 0.5 to 1 for Test B-4-4.

Using only SL values of 0.5, 0.55….0.95, 1, values of λ are computed based on Eq. 3. The "Best Fit strain" in Figure 5.7 contains strain (ε) values based on the equation (where x is SL and y is λ). Best Fit (ε, SL) pairs are then added to the SL vs ε plot as shown in Figure 5.8.

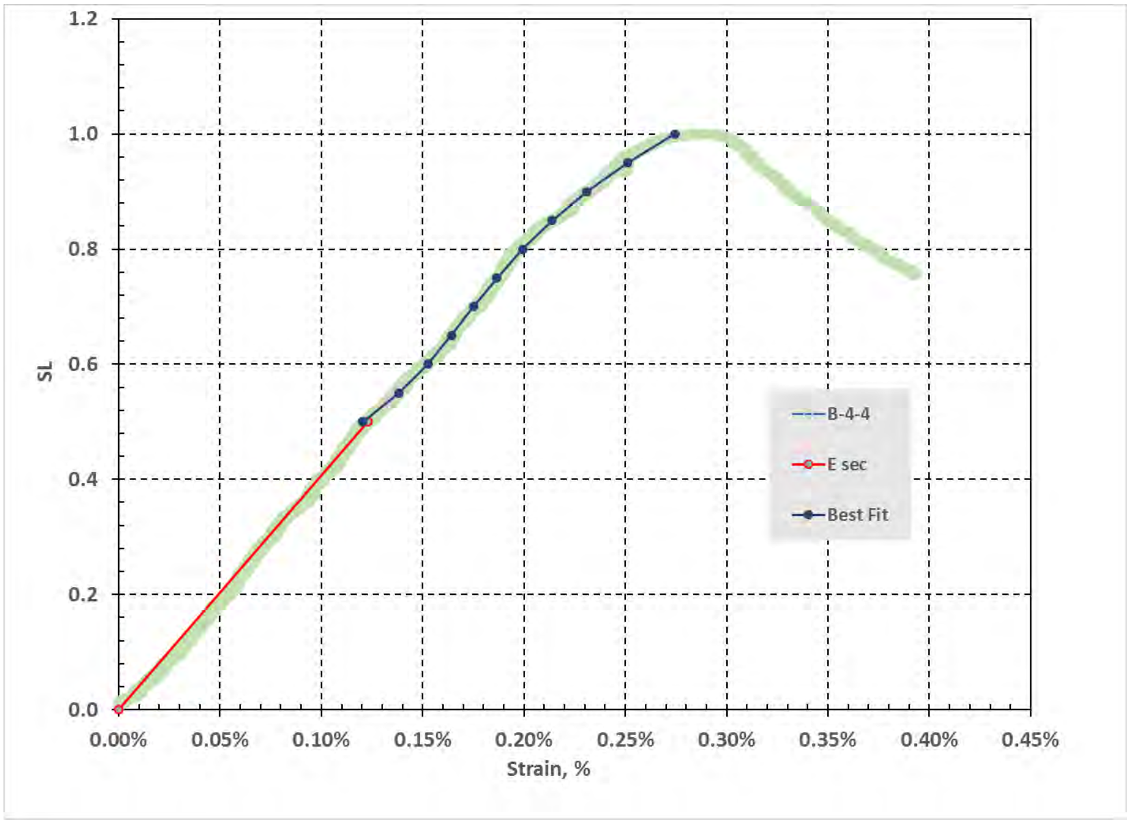

Figure 5.8: SL Vs ε with "Best Fit" data points added.

Unfortunately, the "Best Fit" curve does not match the top of the E_{sec} line which requires a λ value of 3.191059 at SL = 0.50. Furthermore, the curve is somewhat concave from SL 0.50 to 0.70. An attempt to improve upon the "Best Fit" variation, not described here, yielded an Alternate λ equation. While there is some difference, there was still need for further improvement which led to manually assigning values at certain SL's. Such assigned values of ε are those in the TableXX highlighted in yellow. A plot of the "Alternate & Assigned" data points is shown in Figure 5.9.

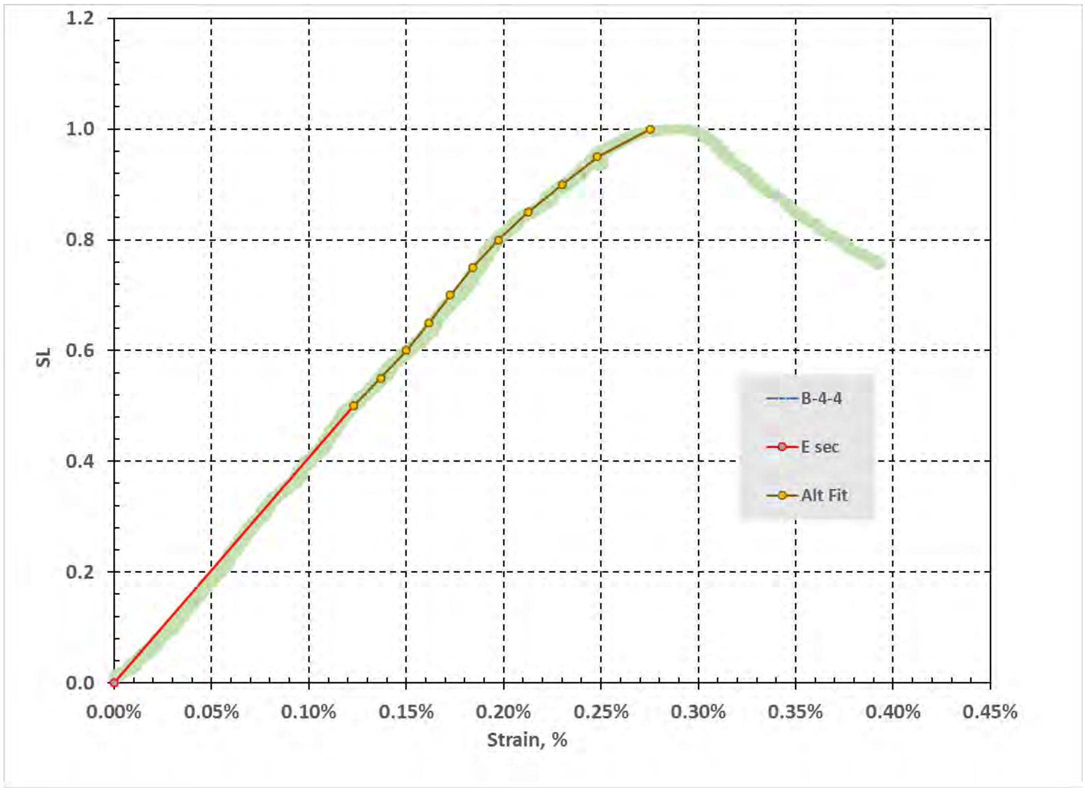

Figure 5.9: SL vs ε curve of Figure 5.5 with Alternate and Assigned data points added.

Figure 5.9 is Figure 5.5 with the "Alternate and Assigned" data points added. Note that the concave curvature from SL 0.50 to 0.70 has been eliminated and a match at SL = 0.50 with E_{sec} achieved. Figure 5.10 is a similar plot of Figure 5.4 with Alternate and Assigned data points added.

A partial list of the λ versus SL variation collected from all 53 tests is shown in the Table 5.2. Note that there are two categories of test fits, the "80% fit" (because the stress strain curves are nearly linear up to a stress level of 80%) and an "Alt k Fit". There are forty 80% Fit curves and eleven Alt k Fit curves and two curves that do not fall in either category (No Fit). Such Lambda variations by category were averaged to provide the 80% and Alt k Fit equations of Lambda (λ) versus stress level (SL) as shown in Figure 5.11. One of the two No Fit tests, B-5-2, is also shown along with the Lambda variation for soil as expressed in Equation 5.2.

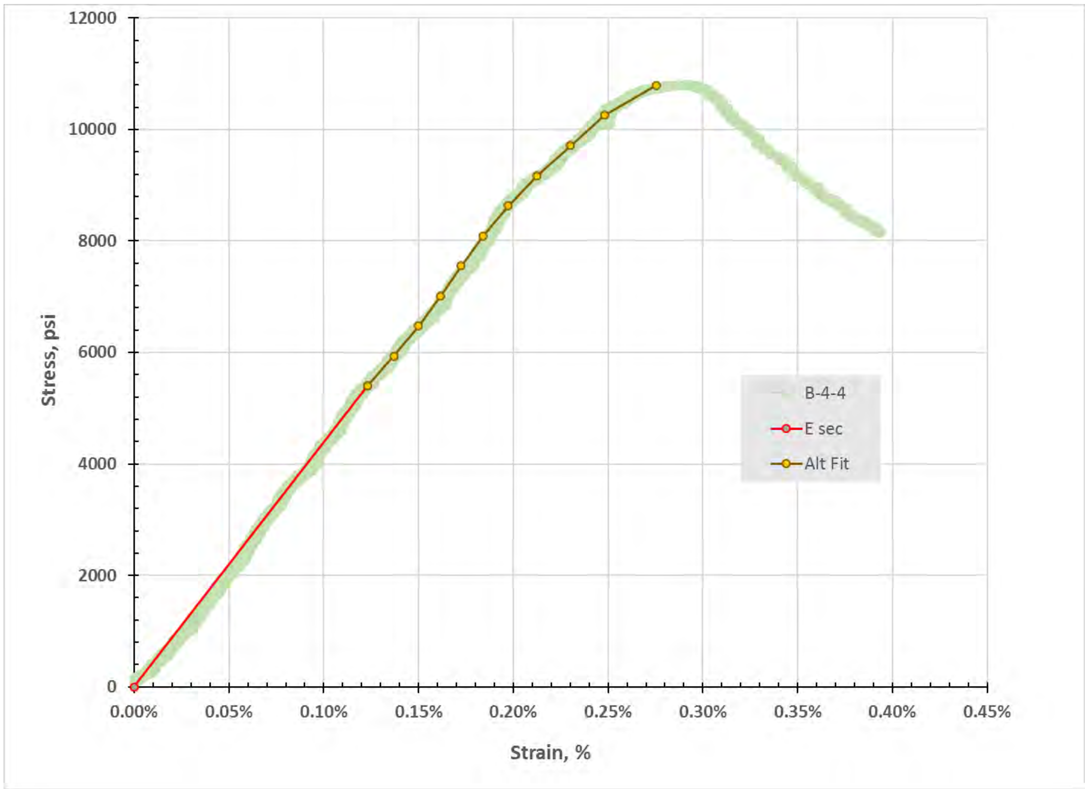

Figure 5.10: The Stress Strain curve of Figure 5.5 with Alternate and Assigned Data Points Added.

Table 5.2: Table of λ versus SL from Alternate and Assigned data points for some of the 53 LVDT tests.

Test	HC-1-5	HC-1-3	C-1-11	C-1-13	B-4-7	HC-1-1	HC-1-2	C-1-6*	C-1-10	C-1-3	B-4-4*
SL		Lambda vs SL			Lambda vs SL						
0.5	3.191	3.193	3.203	3.223	3.200	3.221	3.196	3.225	3.197	3.219	3.191
0.55	3.849	3.754	3.849	3.841	3.785	3.890	3.770	3.810	3.898	3.730	3.793
0.6	4.595	4.531	4.611	4.594	4.544	4.697	4.438	4.634	4.719	4.353	4.549
0.65	5.570	5.436	5.594	5.430	5.433	5.632	5.311	5.555	5.700	5.207	5.503
0.7	6.776	6.566	6.685	6.559	6.535	6.734	6.365	6.691	6.901	6.170	6.686
0.75	8.229	7.911	8.079	7.884	7.934	8.125	7.629	8.154	8.337	7.447	8.079
0.8	9.946	9.496	9.682	9.301	9.537	9.721	9.082	9.795	10.019	8.939	9.682
0.85	11.884	11.466	11.495	11.030	11.421	11.522	10.723	11.674	11.986	10.646	11.494
0.9	14.163	13.551	13.517	13.035	13.516	13.528	12.553	14.004	14.381	12.569	13.516
0.95	17.037	15.861	15.954	15.145	16.168	15.739	14.571	16.524	17.189	14.707	15.944
1	20.304	18.397	18.876	17.451	18.316	18.155	16.778	18.982	19.431	17.061	18.191

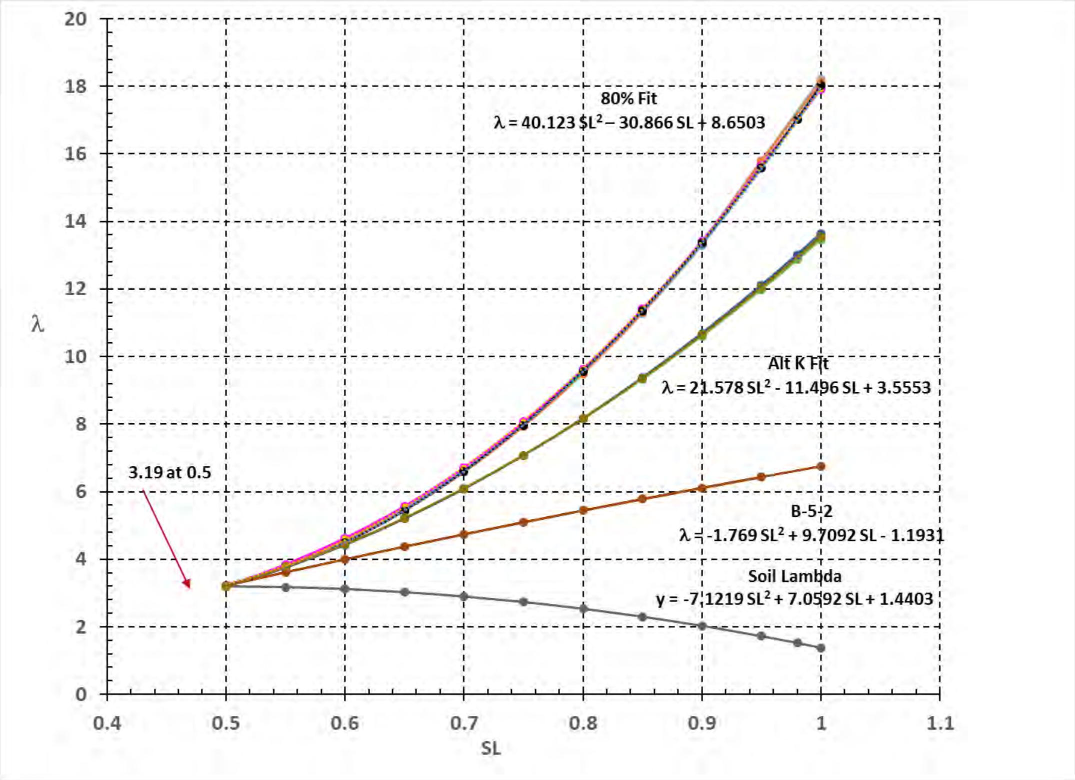

Figure 5.11: λ versus SL variations for the 80% Fit and Alt K Fit equations.

It is the 80% Fit equation that has been adopted for use in the Strain Wedge Model program. The program provides the option of using an offset strain (Δε) preceding the stress strain variation given in Equation 5.1 using the 80% λ variation.

The 80% Fit equation (determined from an average of (SL, λ) data from tests of greater than 6 ksi) works reasonably well in matching the curves of all but one test of 6 ksi strength and above, and several of lesser strength. Figure 5.12 shows its fit relative to the SL versus strain curve of test B-4-4. It compares quite reasonably with Figure 5.10 showing Alternate and Assigned data points specific to Test B-4-4.

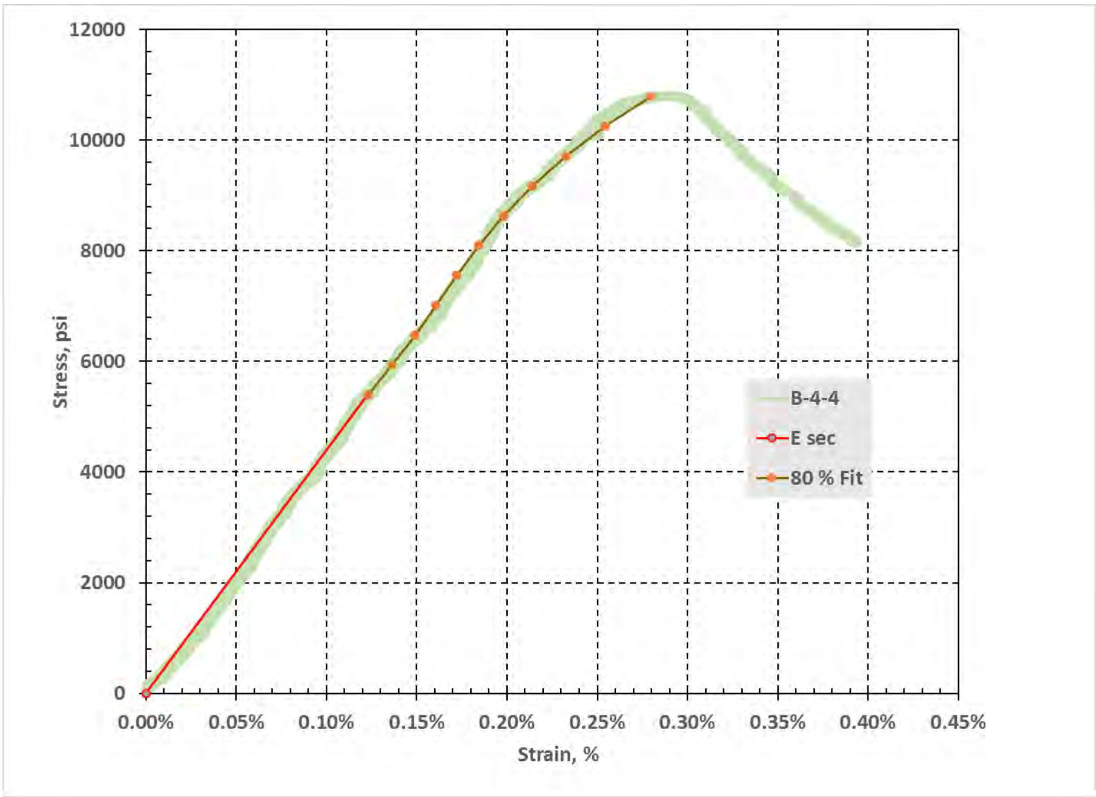

Figure 5.12: The stress strain curve of Figure 5.5 with the 80% Fit data points added.

Figure 5.13 is a plot of all the normalized stress strain test curves from the 80% Fit category. By normalized, it is meant that not only is the stress divided by q_u to give SL, but the stain ε is normalized by its 50% value, i.e. ε_{50}. The 80% Fit curve has been superposed on the collection. While it is hard to judge the 80% Fit from such a figure, Figure 5.14 is a plot of just the bounds of the Figure 5.13 curves with the 80% Fit curve added.

Figure 5.15 is a plot of the normalized Alternate and Assigned data points for all 80% Fit tests with the 80% Fit curve superposed.

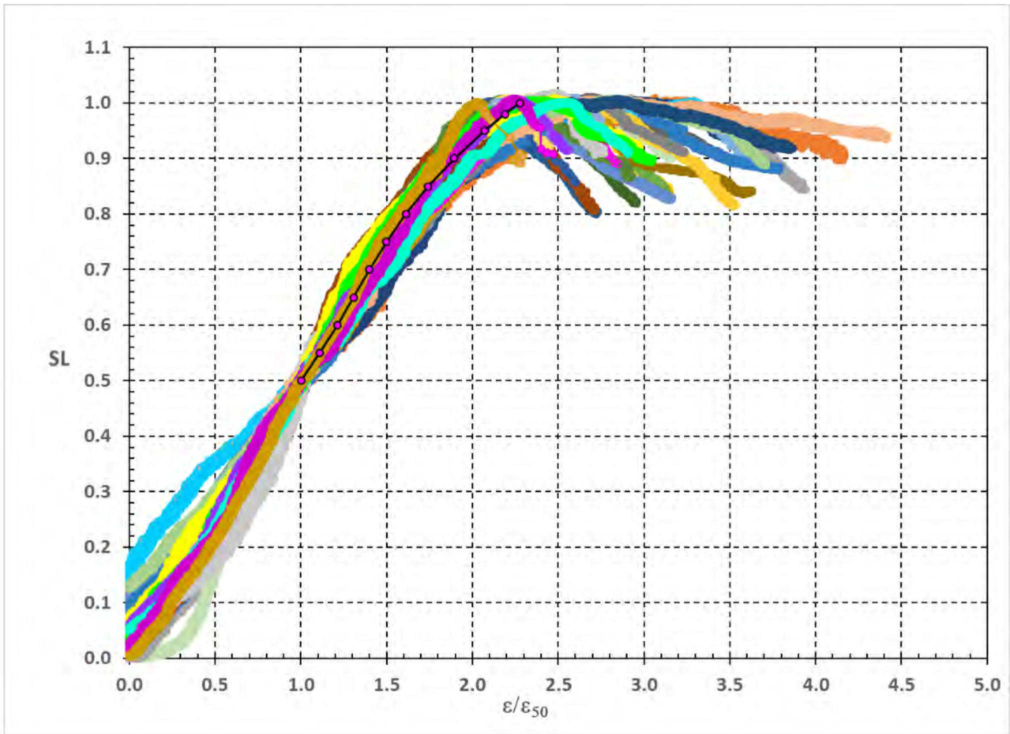

Figure 5.13: Normalized Stress Strain curves for tests in the 80% Fit category.

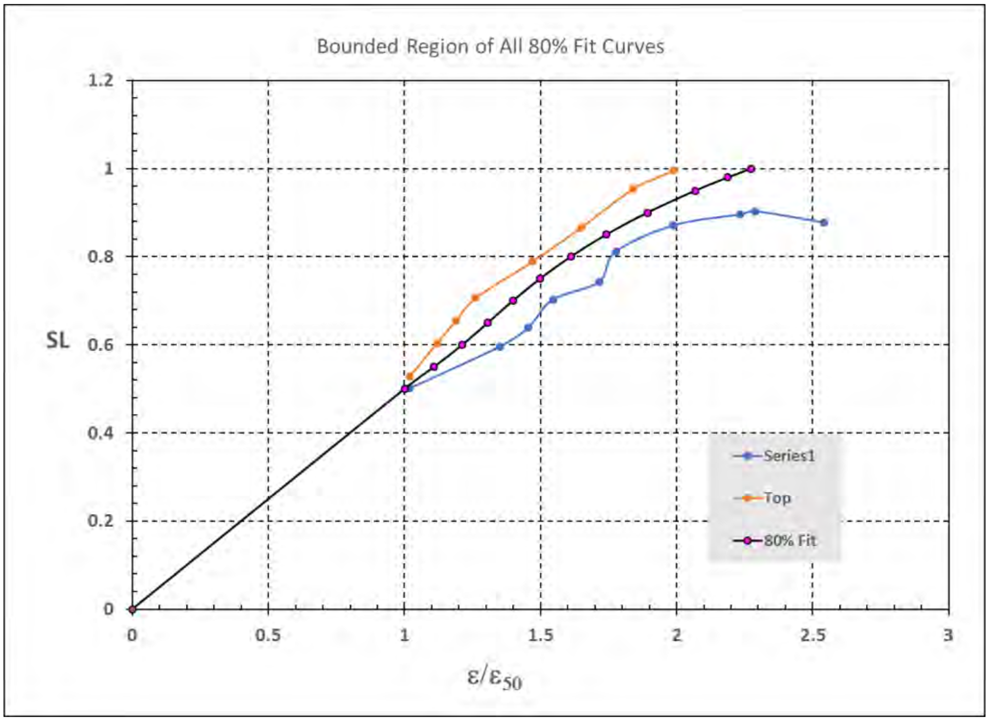

Figure 5.14: The Bounds of the normalized curves of Figure 5.13 with the 80% Fit superposed.

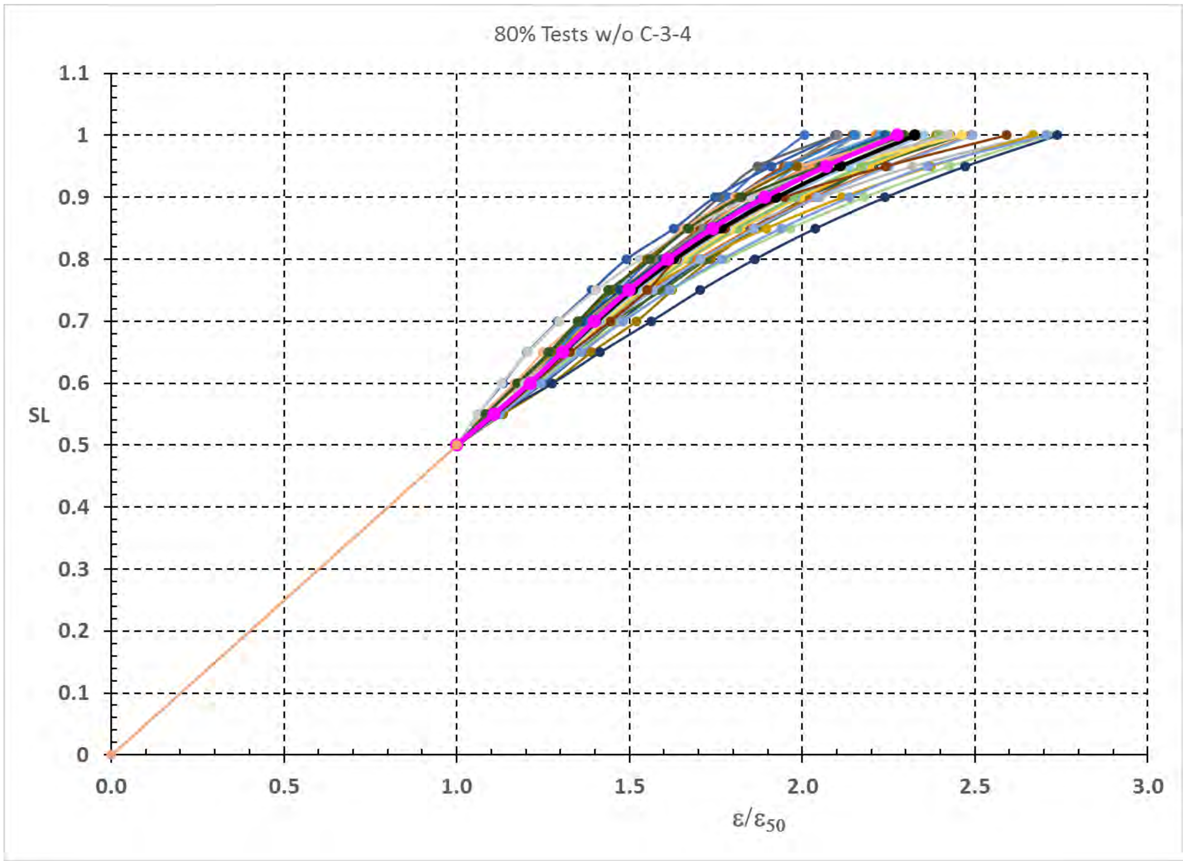

Figure 5.15: Normalized Stress versus Normalized Strain from the 80% fit data points.

5.5 Use of Material Model in Strain Wedge

The material model discussed in this chapter was utilized to improve upon an existing program called Strain Wedge Model. The Strain Wedge Model (SWM) is an approach that has been developed to predict the response of a flexible pile under lateral loading (Norris 1986 and Ashour et al. 1998). The SW model was initially established to analyze a free-head pile embedded in one type of uniform soil (sand or clay). However, the SW model has been improved and modified through additional research to accommodate a laterally loaded pile embedded in multiple soil layers, now to include cemented soils. The addition of the cemented soil data allows for the inclusion of vertical side shear (VSS) to be accounted for when designing drilled shafts in cemented soils. The cemented soils, should it spread laterally with sufficient extent, will ultimately decrease the deflection that would otherwise not be modelled. This will result in monetary savings on the final design.

Chapter 6: Fit of Present Data to Existing Correlations

6.1 Introduction

The lab results presented in Chapter 4: will be discussed herein. The discussion will focus on the results obtained from the laboratory testing program and how the data correlates with published data on cemented soils.

6.2 Compressive Strength Testing

The Unconfined Compressive Strength data showed values far exceeding those of engineered material, e.g. concrete, which is often compared to cemented soil. This could be because of the aggregate or other characteristics of the cemented soil. One component of the data was interesting and illustrates the possible influence of the aggregate. The data series "HC" in Table 4.1 ranked amongst the highest strengths of all the specimens. These specimens were drilled perpendicular to deposition to check for anisotropy. This data may suggest that the alignment of the aggregate may increase strength of the material.

It should be noted that not many of the specimens met the dimensional requirement of ASTM 7012. ASTM 7012 suggests that the length to diameter ratio be between 2-2.5. Due to inherit weaknesses in the materials, especially with the moderately cemented material, a paucity of specimens was recovered from lab drilling that met this requirement. Testing proceeded using these specimens and literature shows that the change in strength with decreased L/D ratio is minimal (Tuncay et al., 2009). Appendix D discusses the effect of L/D ratio on unconfined compressive strength.

6.3 Lab Geophysics

The range of lab velocities measured was large. P-wave velocities ranged from 2,521 ft/s to 19,274 ft/s and S-wave velocities from 1,754 ft/s to 11,142 ft/s (Table 4.1 to Table 4.3). The correlation to the field geophysical survey velocities to the tested lab sample velocities from the same location was poor. The peak shear wave velocities from the MASW and ReMi surveys were 1,800 ft/s and 2000/4,000 ft/s, respectively. Non-invasive geophysical techniques tend to yield lower velocities, mostly due to effects of scale (Werle et al, 2007). The larger scale measurements tend to average the velocities of each zone, while the laboratory measurements are made on a much smaller scale which accounts for the fractures, aggregate and degree of cementation. Even with the laboratory measurements accounting for the voids, fractures and variation of cementation, the lab velocities were still much higher than the field measurements.

It should be noted that many of the specimens were unable to meet the dimensional specification of ASTM 2845 for wave velocity measurement. ASTM 2845 states that the diameter of the aggregate should not exceed 10% of the specimen length. Given the composition of the cemented soil, especially the strongly cemented material, this proved to be impossible.

6.4 Primary Wave Velocity versus Unconfined Compressive Strength

While the focus of this research was on shear wave velocity, much more data was available comparing P-wave velocity to UCS. In Figure 8.1, a positive correlation is shown between measured lab velocities and published data. The data sets presented in Figure 8.1 are from various areas and represent different geo-materials. The Rucker (2006) data are for cemented soil from Maricopa County, Arizona. The Liu et al (2014) data are for carbonate rocks, which is what the cemented soil in Las Vegas closely resembles. The Dincer (2008) data are from cemented soil samples from southeastern Turkey.

In Figure 8.1, the measured lab P-wave data is plotted with a power model trend line. The published data fits well on the trend line, especially Rucker (2006) and Liu et al (2014).

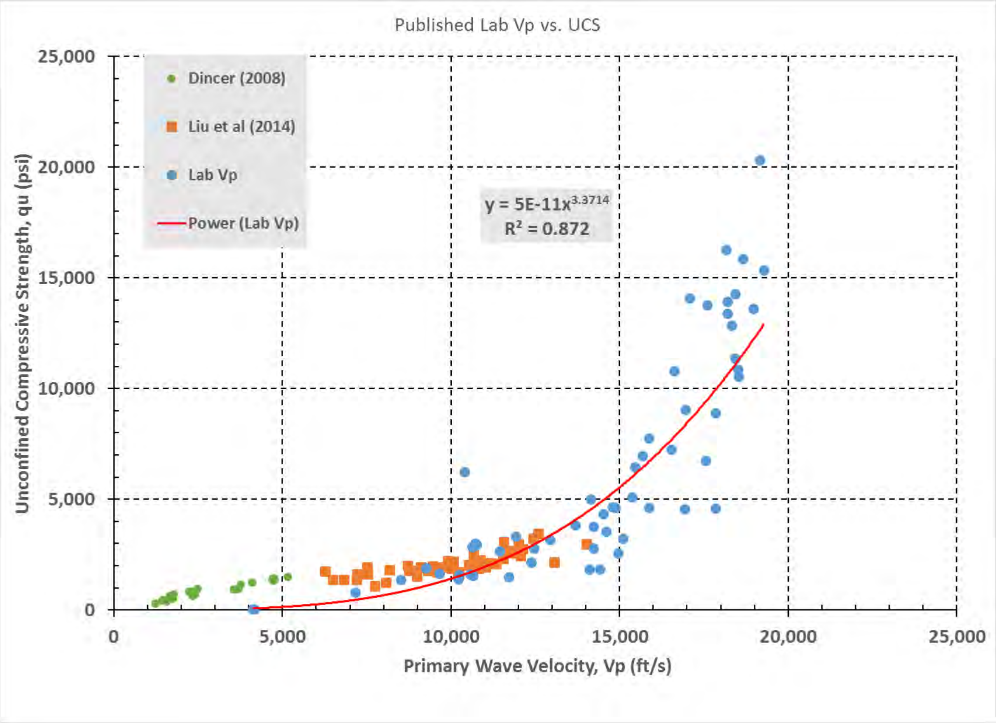

Figure 6.1: Published Vp-UCS data compared with lab data.

6.5 Shear Wave Velocity versus Unconfined Compressive Strength

Figure 8.2 shows the comparison of published Vs-UCS data with measured Vs-UCS data collected from this project. This project's power model trendline fits well with Rucker (2008). The Rucker (2008) shear wave velocities were calculated based on recorded P-wave velocities from a seismic refraction study. Assuming a Poisson's ration of 0.33, Vs = 0.5*Vp. The Rucker (2000) UCS data were estimated using previously established relationships. The published data is much smaller than the measured data from this research. This is most likely because the correlations are made from field velocities while this research uses lab correlations.

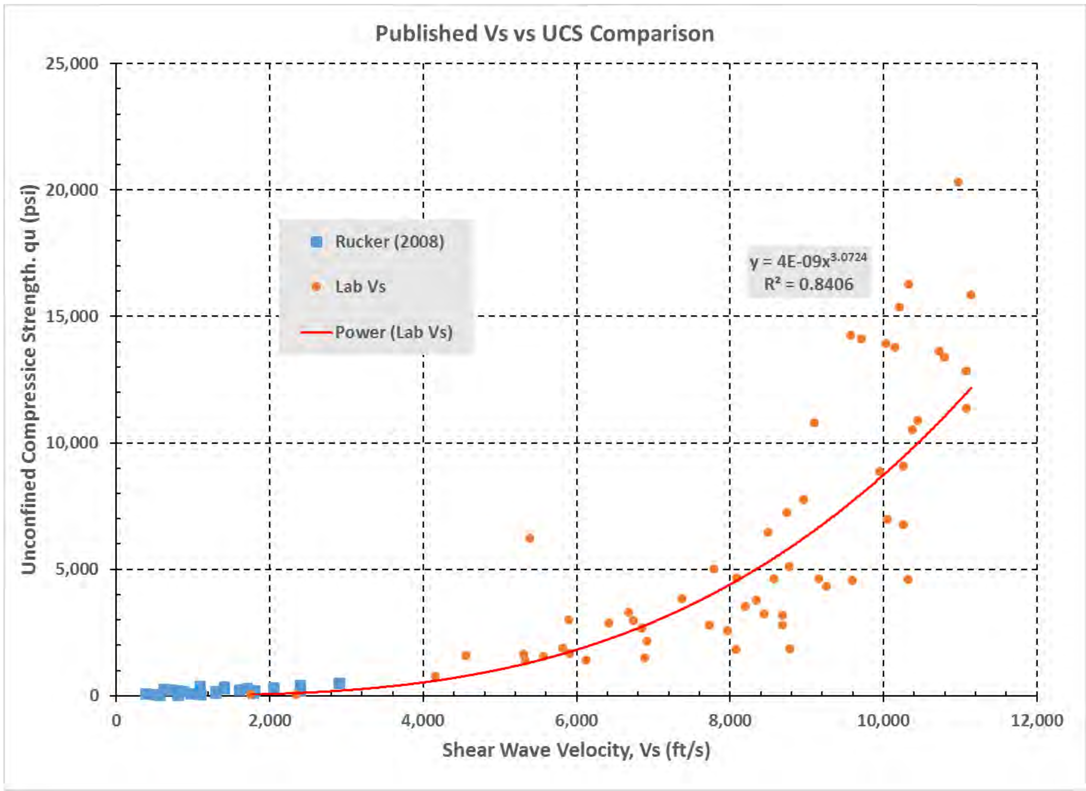

Figure 6.2: Published Vs-UCS compared to lab data.

As expected, the UCS increases with the increased shear wave velocity. However, due to the cemented soil's nature, this relationship is not perfect. As seen in Table 4.1 to 4.3, some specimens with higher Vs can show lower UCS values than other specimens of similar Vs values. This demonstrates the heterogeneous nature of the cemented soil and that other factors could be influencing these values that this study did not consider.

6.6 Shear Wave Velocity versus Unit Weight

Figure 4.5 showed a correlation between increasing unit weight and increasing shear wave velocity, although, Tables 4.1 to 4.3 show that this trend is erratic. This is likely because of the numerous aggregate pieces in the cemented soil causing large variability in the weight to volume relationship. Since the aggregate was mainly limestone, it should be of similar density to the carbonate rich cemented soil. However, some of the aggregate was igneous in origin, and some pieces even had nicely banded sedimentary aggregate. These pieces would most likely be lighter than the cemented soil matrix.

Other causes for the heterogeneous nature of this relationship is that some specimens were noted to have numerous voids, even extending well into the specimen. In addition, as stated previously, it was harder to obtain a testable sample of the moderate and weakly cemented material. During drilling, some fragments dislodged from the sides. This was difficult to account for when measuring volume.

6.7 Shear Wave Velocity versus Elastic Modulus

The relationship of shear wave velocity to Elastic Modulus is the most statistically significant correlation of the whole study. As shown in Figure 4.4, the R^2 value for this correlation is 0.89, by far the highest of any of the correlations. This finding was also the case for Nefeslioglu (2013). In this study, using sedimentary rock, the shear wave velocity-UCS correlation had a coefficient of correlation (R) of 0.92. In Table 4.1, the highest value for E was reported as 6,973,000 psi, which is greater than the reported values of 3,000,000 to 5,000,000 psi of concrete.

Tables 4.1 to 4.3 show significant standard deviation for all three groupings of cemented soil. These high deviation values highlight just how heterogeneous the material is. To emphasize this point, in Table 4.1, specimen B-4-7 has an UCS of 14,460 psi while specimen C-1-2 has an UCS of 10,460 psi. However, C-1-2 has an E of 6,973,000 psi while B-4-7 has an E of 4,203,000 psi. The stronger sample is less stiff than the weaker sample. This illustrates that there is another component influencing the strength of this material.

6.8 Material Model

This material model is the result of an extensive lab testing program of a very diverse specimen group. The generated model is capable of calculating the stress-strain relationship of the material with a few inputs based on the relationships previously discussed. These relationships provide the UCS, E_{sec}, and ε_{50}, which enables the material model to generate the strain at any stress level above 50% of UCS.

The material model developed will allow engineers to better design foundations for structures in which cemented soils appear in the subsurface. Because of the range in levels of cementation in the tested material, the model is a viable method with which to account for the varying levels of cementation, and thus strength and stiffness often encountered during subsurface site investigation.

This model has many positive attributes, mainly the ability to model a highly unpredictable geo-material. There is a possibility that this model's λ variation (Figure 5.11) could be adjusted to account for a variety of materials. In its current form, however, the model is specifically applicable to cemented soils in the Las Vegas area and other cemented soils with similar mineralogical structure to those in this study. It is suggested that this material model is not assumed to be applicable to all cemented soil deposits.

Chapter 7: Implementation in Strain Wedge Model (SWM) Software

7.1 Introduction

The strain wedge model (SWM) is an approach that has been developed to predict the response of a flexible pile under lateral loading (Norris 1986, Ashour et al. 1996 and Ashour et al. 1998). The main concept associated with the strain wedge model is that traditional one-dimensional Beam on Elastic Foundation (BEF) pile response parameters can be characterized in terms of envisioned three-dimensional soil-pile interaction behavior. The SWM was initially established to analyze a free-head pile embedded in one type of uniform soil (sand or clay). However, the SWM has been improved and modified through additional research to accommodate a laterally loaded pile embedded in multiple soil layers (sand and clay) and rock. The SW model has been further modified to include the effect of pile head conditions on soil-pile behavior. The main objective behind the development of the SWM is to solve the BEF problem of a laterally loaded pile based on the envisioned soil-pile interaction and its dependence on both soil and pile properties.

7.2 Implementation of Current Work

Implementation in SWM was conducted in two steps: taking account of vertical side shear (VSS) resistance into shaft response followed by implementation of the newly developed cemented soil material model. While the focus of the following sections is the implementation of these enhancements in SWM, Appendix E provides the necessary background about the SWM and the theory behind its analysis.

7.2.1 Implementation of Vertical Side Shear (VSS) Resistance

7.2.1.1 Resisting Moment (M_R) caused by Vertical Side Shear Resistance (VSS)

As seen in Figure 7.1, the vertical side shear stress distribution around the shaft cross section is assumed to follow a cosine function. It is assumed that there is no contact (active pressure) on the backside of the shaft due to the lateral deflection. The peak (q) of side shear stress develops at angle θ = 0 and decreases to zero at angle θ = +/-90º. The total vertical side shear force (V_v) induced along a unit length of the shaft is expressed as

$$V_v = 2\int_0^{\pi/2} q\, r \cos\theta \, d\theta \quad = \quad 2q\,(r\sin\theta)_0^{\pi/2} \quad = \quad D q \qquad \text{(Eq 7.1)}$$

and the induced moment ($M_{x\text{-}x}$) per unit length of the shaft is given as

$$\begin{aligned} M_{x-x} &= 2\int_0^{\pi/2} (q\, r\cos\theta \, d\theta)\,(r\cos\theta) \quad = \quad 2qr^2 \int_0^{\pi/2} \cos^2\theta \, d\theta \\ &= 2qr^2 \int_0^{\pi/2} \frac{1}{2}\,(\cos 2\theta + 1)\, d\theta \\ &= qr^2 \int_0^{\pi/2} (\cos 2\theta + 1)\, d\theta \\ &= qr^2 \left(\frac{1}{2}\,(\sin 2\theta + \theta\right)_0^{\pi/2} \quad = \frac{q\,D^2\,\pi}{8} \end{aligned} \qquad \text{(Eq 7.2)}$$

Note that $M_{x\text{-}x}$ represents the term M_R in the fourth-order ordinary differential equation of beam on elastic foundation (Equation 7.3), which the SWM solves.

$$EI\left(\frac{d^4 y}{d^4 x}\right) + E_s(x)\, y + P_x\left(\frac{d^2 y}{d^2 x}\right) + \left(\frac{d^2 M_R}{d^2 x}\right) = 0 \qquad \text{(Eq 7.3)}$$

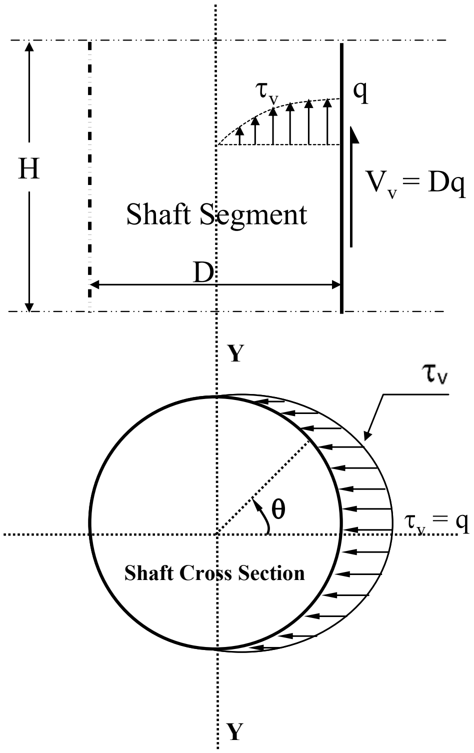
H
D
τ_v
q
$V_v = Dq$
Shaft Segment
Y
τ_v
θ
$\tau_v = q$
Shaft Cross Section
Y

Figure 7.1: Vertical side shear stress distribution on the shaft cross section.

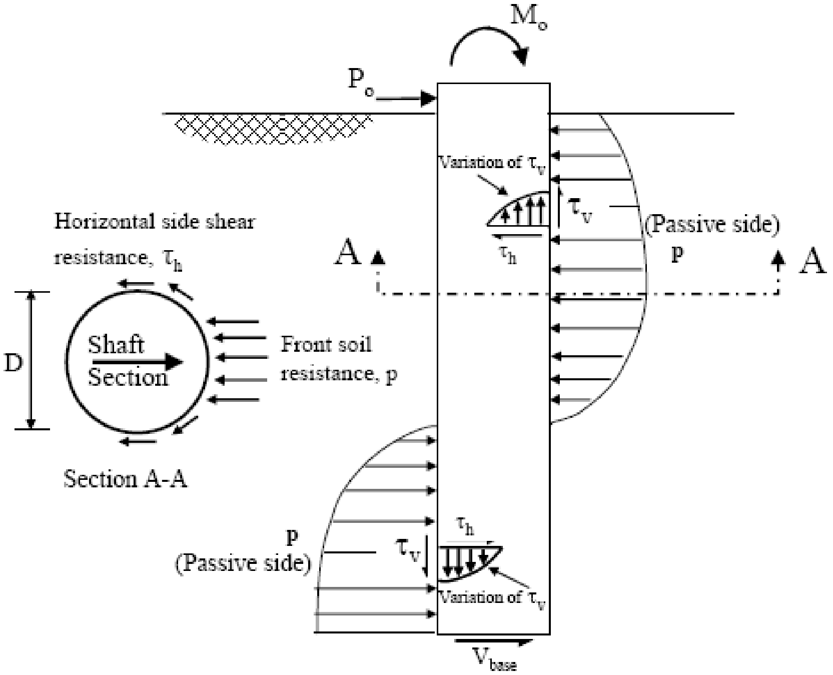
M_o
P_o
Variation of τ_v
τ_v
τ_h
(Passive side)
p
A
A
Horizontal side shear resistance, τ_h
D
Shaft Section
Front soil resistance, p
Section A-A
p
(Passive side)
τ_v
τ_h
Variation of τ_v
V_{base}

Figure 7.2: Components of soil lateral resistance of large diameter shaft (Case of a short shaft model).

7.2.1.2 Vertical Displacement of Shaft Sections Under Lateral Deflection

Figure 7.3 portrays the change in elevation of a point on the shaft surface (i.e., the cross section) due to shaft rotation and bending deformation. The vertical displacement component (v) of shaft segment i is governed by the rotation of the shaft (i.e., v_d) and the bending deformation (i.e., v_b) of that particular segment. Therefore,

$$v_i = (v_d + v_b)_i \quad \text{(Eq 7.4)}$$

In this situation, v is mainly dominated by the shaft vertical displacement component (v_d) that decreases as it approaches the pivot point (i.e., the zero deflection point), as is shown in Figure 7.3 and expressed as

$$(v_d)_i = y_i \alpha_i \quad \text{(Eq 7.5)}$$

where i is the number of the shaft segment and α is the rotation angle of shaft segment i. However, the bending deformation of the shaft segment could add a much smaller value of vertical displacement (v_b) to the total amount of vertical displacement (v) on the passive side of the shaft. In addition, v_b induced by the flexural deformation (i.e., the cross section curvature, η) diminishes approaching the location of the neutral axis of the section (Figure 7.3).

$$(v_b)_i = L_1 \eta \quad \text{(Eq 7.6)}$$

It should be mentioned that the term *z* represents the vertical shaft displacement under "axial load" which is directly related to the *t-z* curve. Therefore, the term *v* is used to differentiate between the shaft vertical displacement (*z*) caused by the axial load and the shaft vertical displacement component (*v*) generated by shaft deflection under lateral load. Practically, the shaft surface could be subjected to two components of vertical displacement (*z* and *v*) when axial and lateral loads are applied at the pile/shaft head, which is a common case.

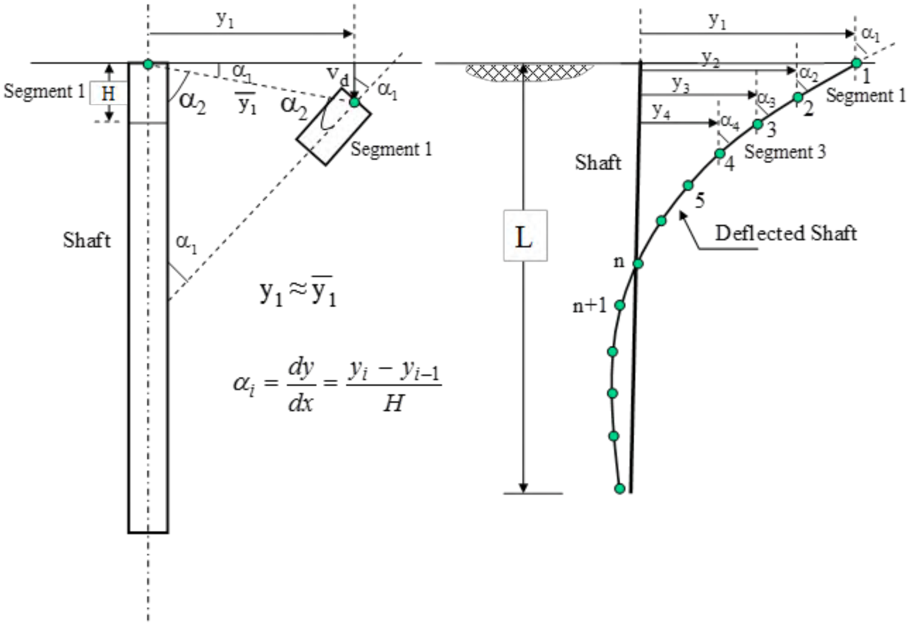

y1
α1
vd
α1
Segment 1
H
α2
ȳ1
α2
Segment 1
Shaft
α1
$y_1 \approx \overline{y}_1$
$\alpha_i = \frac{dy}{dx} = \frac{y_i - y_{i-1}}{H}$
y1
α1
y2
α2
1
y3
α3
Segment 1
2
y4
α4
3
Segment 3
Shaft
4
5
L
Deflected Shaft
n
n+1

Figure 7.3: The development of the vertical shear displacement component (v_d) with shaft deflection.

7.2.1.3 Vertical Side Shear (τv) in Stiff Clay and Cemented Soils (aka caliche)

The vertical side shear stress (τ_v) develops at the soil-pile interface as a result of the vertical displacement *v*. τ_v (i.e. q in Figure 7.1) is assessed as a function of q_u and ε_{50} of clay, intermediate geo-materials and cemented soils. For a given vertical displacement *v*, the mobilized shear stress (τ_v) at the shaft-soil interface can be expressed as a function of the ultimate shear strength (τ_{ult}) via the shear stress level $SL_t = \frac{\tau_v}{\tau_{ult}}$ which is characterized by the Ramberg-Osgood model (Richart 1975), i.e.

$$\frac{v}{v_r} = \frac{\gamma}{\gamma_r} = \frac{\tau_v}{\tau_{ult}}\left[1 + \beta\left(\frac{\tau_v}{\tau_{ult}}\right)^{R-1}\right] = SL_t\ \left[1 + \beta\left(SL_t\right)^{R-1}\right] \qquad \text{(Eq 7.7)}$$

where *v* is the vertical displacement of the shaft segment. γ and τ_v are the average shear strain and stress in the soil adjacent to the shaft segment generated by the soil-shaft displacement *v*. The reference strain (γ_r) is determined as

$$\gamma_r = \frac{S_u}{G_i} = \frac{\tau_{ult}}{G_i} \qquad \text{(Eq 7.8)}$$

G_i is the initial shear modulus at a very low stress/strain, and v_r is the shaft segment movement associated with γ_r (Figure 7.4).β and *R-1* are the fitting parameters of the Ramberg-Osgood model. At $\tau/\tau_{ult} = SL_t = 1$, β can be expressed as

$$\beta = \frac{\gamma_f}{\gamma_r} - 1 \qquad \text{(Eq 7.9)}$$

At $\tau/\tau_{ult} = 0.5$ and $\gamma = \gamma_{50}$, *R-1* is obtained as follows:

$$R - 1 = \frac{\log\left(\dfrac{2\dfrac{\gamma_{50}}{\gamma_r} - 1}{\beta}\right)}{\log\ (0.5)} = \frac{\log\left(\dfrac{2\dfrac{\gamma_{50}}{\gamma_r} - 1}{\dfrac{\gamma_f}{\gamma_r} - 1}\right)}{\log\ (0.5)} \qquad \text{(Eq 7.10)}$$

To determine β and *R-1*, the normal stress-strain relationship for clay (σ - ε) presented by Ashour et al. (2010), based on ε_{50} and S_u, is employed to find γ_r, γ_{50}, and γ_f of Figure 7.23. For a given shaft, one finds that

$$\frac{v_{50}}{v_f} = \frac{\gamma_{50}}{\gamma_f} \qquad \text{(Eq 7.11)}$$

where v_{50} and γ_{50} are the pile/shaft vertical displacement and associated shear strain in soil at $SL_t = 0.5$ (i.e. $\tau_v = 0.5\,\tau_{ult}$), respectively. v_f and γ_f are the shaft displacement and associated shear strain at failure where $SL_t = 1.0$ (i.e. $\tau = \tau_{ult}$). Therefore, the variation in the soil shear strain (γ) occurs in concert with the variation in shaft vertical displacement. The shear strain at failure (γ_f) is determined in terms of the normal strain at failure (ε_f) as given in Eq. 7.12. ε_f is evaluated at $SL = 1$ or at normal strength, σ_{df}, where $\sigma_{df} = q_u = 2\,S_u$. Accordingly,

$$\gamma_f = \frac{\varepsilon_f}{(1+\nu)} = \frac{\varepsilon_f}{1.5} \qquad \text{(at failure)} \qquad \text{(Eq 7.12)}$$

At $SL_t = 0.5$

$$\gamma_{50} \quad = \quad \frac{0.5\, S_u}{G_{50}} \qquad \text{(Eq 7.13)}$$

The initial shear modulus (G_i) at a very low SL_t and the shear modulus at $SL_t = 0.5$ (i.e. G_{50}) can be determined via their direct relationship with the normal stress-strain relationship and Poisson's ratio (ν). While $\nu = 0.5$ for clay under undrained conditions, ν varies linearly with SL, i.e.

$$\nu = 0.1 + 0.4\, SL_t \qquad \text{(Eq 7.14)}$$

for weak rock and caliche. Hence,

$$G_i = \frac{E_i}{2\,(1+\nu)} \quad = \; E_i\,/\,2.2 \qquad \text{(Eq 7.15)}$$

and

$$G_{50} = \frac{E_{50}}{2\,(1+\nu)} \quad = \; E_{50}\,/\,2.6 \qquad \text{(Eq 7.16)}$$

where E_i and E_{50} of caliche are equal to $4*10^{-7}V_{sl}^{3.27}$ and S_u/ε_{50}, respectively. E_i is the initial Young's modulus of clay at a very small value of the normal strain (ε) or *SL*. Evans and Duncan (1982) provide ε_{50} for clay after Reese. Ashour and Helal (2014) provide the detailed calculations of the Ramberg–Osgood (*R–O*) model fitting parameters β and *R-1* which are equal to 18.14 and 2.92, respectively, for caliche.

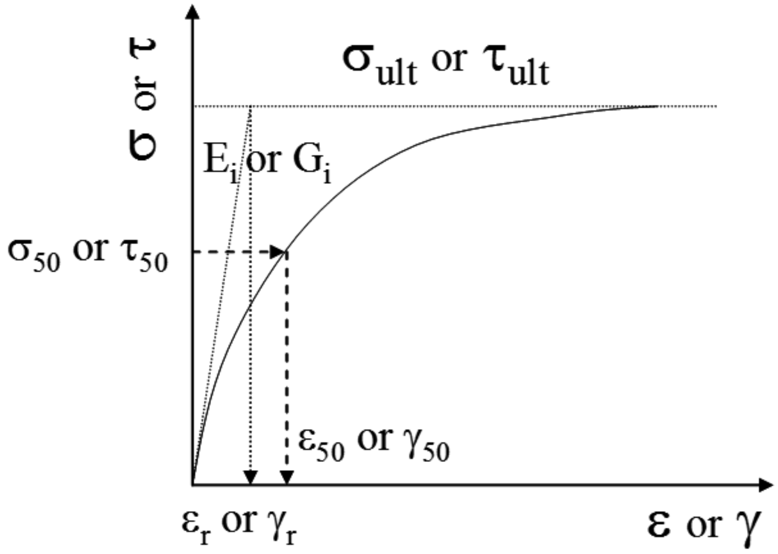

Figure 7.4: Normal and shear stress–strain relationship (σ-ε and τ-γ).

7.2.2 Incorporation of Cemented Soil Material (Caliche) in the SW Model's Lateral Resistance

The incorporation of any soil or geomaterials in the SW model is based on the ability to develop a constitutive (i.e. stress-strain) relationship for that material. The development of a constitutive relationship of a cemented/cohesive geomaterials, such as the caliche material, would be a great challenge without performing specific field and experimental tests to assess basic properties of the caliche materials which are needed to establish the desired constitutive model. The experimental data collected and formulated in the earlier chapters provides a good and reliable source of data to develop the following constitutive model (i.e. stress-strain or SL-ε) for the caliche materials and to generate correlations among the unconfined compressive strength, shear weave velocity and normal strain (ε).

Stress Level (SL) in Caliche Materials

Stage I (SL ≤ 0.55)

Based on experimental data, the relationship between stress level and strain in caliche materials in the first stage is assessed using the following equation,

$\varepsilon_m = 2 SL \varepsilon_{50}$ for SL < 0.55

Stage II (SL> 0.55)

In this second stage of loading which extends from 55 percent to 100percent stress level, the following equations apply.

$$\varepsilon_m = SL\ e^{(3.707\ SL)}\ \varepsilon_{50}/\lambda \qquad \text{(Eq 7.17)}$$

Where,

$$\lambda = 40.123\ SL^2 - 30.866\ SL + 8.6503 \qquad \text{(Eq 7.18)}$$

Based on the following correlations obtained in Chapter 3: Chapter 4:, and Chapter 5:, ε_{50} and q_u of the caliche materials will be determined in the SW model. It should be noted that there are two sets of correlations which rely on either the shear wave velocity (Vs) or the material unit weight (γ) as input data to calculate ε_{50} and qu.

V_{sl}=0.0878 $\gamma^{2.2842}$; V_{sl} in ft/sec for γ in lb/ft^3 (Eq 7.19)

q_u=70.074 $e^{0.0005\ V_{sl}}$ q_u in psi for V_{sl} in ft/sec (Eq 7.20)

E_{50}=4∗$10^{-7} V_{sl}^{3.27}$ E_{50} in psi for V_{sl} in ft/sec (Eq 7.21)

where

$$\varepsilon_{50} = (0.5\ q_u)/E_{50} \qquad \text{(Eq 7.22)}$$

$$SL = \Delta\sigma_h / \Delta\sigma_{hf} \qquad \text{(Eq 7.23)}$$

$\Delta\sigma_{hf} = 2\ S_u = q_u$ the unconfined compressive strength (UCS) (Eq 7.24)

$$SL = \Delta\sigma_h / \Delta\sigma_{hf} = (\tan\ \bar{\varphi}_m)/(\tan\ \bar{\varphi}) \qquad \text{(Eq 7.25)}$$

The material model presented above, which represents the stress-strain relationship of the caliche materials, is implemented in the SW model technique to determine the associating Young's modulus (E) and the modulus of subgrade reaction (Es) for each soil-pile segments (i) at every step of lateral loading as shown in the following flow chart.

$$(E)_i = \frac{SL\,(\Delta\sigma_{hf})_i}{\varepsilon_m} \qquad \text{(Eq 7.26)}$$

To take account of possible initial fracture closure, the actual or full strain is given as

$$\varepsilon_{\text{actual}} = \varepsilon_{\text{m}} + \Delta\varepsilon \qquad \text{(Eq 7.27)}$$

where the closure strain, $\Delta\varepsilon$, when considered ($\Delta\varepsilon>0$) varies with UCS as given below

Type	UCS, q_u (psi)	$\Delta\varepsilon$ (%)
Strongly Cemented	$q_u > 10{,}000$	0.015
Moderately Cemented	$10{,}000 > q_u > 3{,}000$	0.035
Weakly Cemented	$3{,}000 > q_u$	0.056

***Caliche is treated as soil (clay) when q_u becomes below 25,000 psf

The stress-strain model of the caliche material (i.e. constitutive model) presented above along with the effect of the vertical side shear force (VSS) are integrated into the SW model to assess a profile for the modulus of subgrade reaction along the shaft as an element in the following fourth-order ordinary equation of the Beam on Elastic Foundation (BEF).

$$EI\left(\frac{d^4 y}{d^4 x}\right) + E_s(x)\, y + P_x\left(\frac{d^2 y}{d^2 x}\right) + \left(\frac{d^2 M_R}{d^2 x}\right) = 0$$

where M_R is the resisting bending moment per unit length induced along the shaft length (x) due to the vertical side shear (VSS) (Figure 7.1). To appreciate the SW model's enhancement of BEF analysis, one should first consider the governing analytical formulations related to the passive wedge in front of the shaft, the soil's stress-strain and the vertical side shear (t-z curve) formulations, and the related soil-pile/shaft interaction.

Since the SW model also deals with sand, clay and silt soils, and weathered rock in addition to the caliche materials presented in this report, Appendix E displays the basic equations of the SW model technique as applied in an iterative fashion to capture the correct profile of the modulus of subgrade reaction (Es) of multi-soil layers along the pile/shaft which are determined from the SW model equations and then employed in a BEF model to satisfy the soil-pile equilibrium under the current increment of pile-head lateral/moment loads (Po and Mo) and restraint conditions. The iterative process at any pile-head load increment of (Po and Mo) is achieved once both the depth of zero-deflection point on the pile $(X_o)_{SWM}$ and the pile-head deflection $(Y_o)_{SWM}$ are equal to $(X_o)_{BEF}$ and $(Y_o)_{BEF}$ obtained from the BEF analysis under the same values of Po and Mo. The flowchart (Figure 7.5) provides a summary of the SW model procedure in solving the problem of laterally loaded pile/shafts in layered soils including caliche materials.

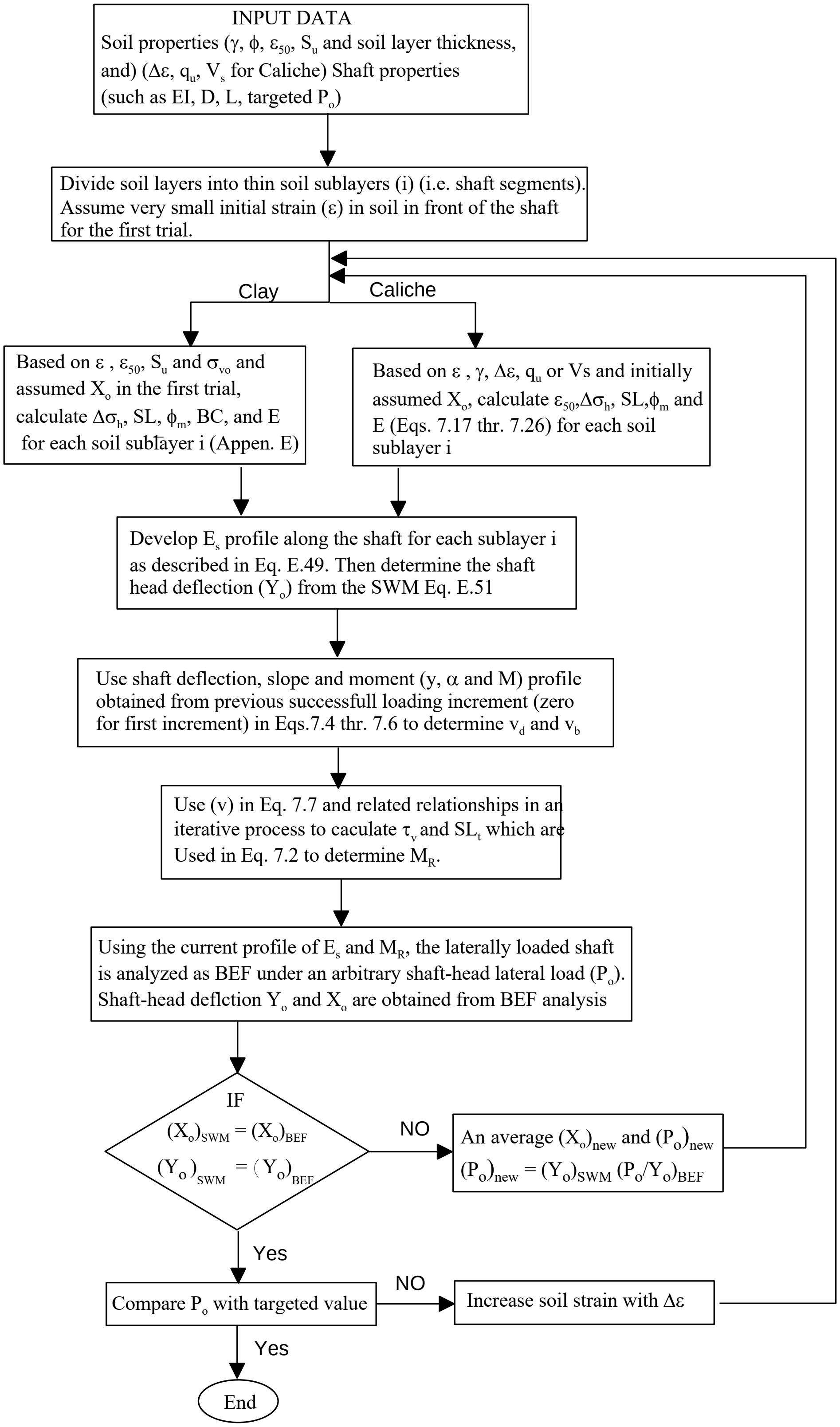
INPUT DATA
Soil properties (γ, ϕ, ε_{50}, S_u and soil layer thickness, and) ($\Delta\varepsilon$, q_u, V_s for Caliche) Shaft properties (such as EI, D, L, targeted P_o)
Divide soil layers into thin soil sublayers (i) (i.e. shaft segments). Assume very small initial strain (ε) in soil in front of the shaft for the first trial.
Clay
Caliche
Based on ε , ε_{50}, S_u and σ_{vo} and assumed X_o in the first trial, calculate $\Delta\sigma_h$, SL, ϕ_m, BC, and E for each soil sublayer i (Appen. E)
Based on ε , γ, $\Delta\varepsilon$, q_u or Vs and initially assumed X_o, calculate ε_{50},$\Delta\sigma_h$, SL,ϕ_m and E (Eqs. 7.17 thr. 7.26) for each soil sublayer i
Develop E_s profile along the shaft for each sublayer i as described in Eq. E.49. Then determine the shaft head deflection (Y_o) from the SWM Eq. E.51
Use shaft deflection, slope and moment (y, α and M) profile obtained from previous successfull loading increment (zero for first increment) in Eqs.7.4 thr. 7.6 to determine v_d and v_b
Use (v) in Eq. 7.7 and related relationships in an iterative process to caculate τ_v and SL_t which are Used in Eq. 7.2 to determine M_R.
Using the current profile of E_s and M_R, the laterally loaded shaft is analyzed as BEF under an arbitrary shaft-head lateral load (P_o). Shaft-head deflction Y_o and X_o are obtained from BEF analysis
IF
$(X_o)_{SWM} = (X_o)_{BEF}$
$(Y_o)_{SWM} = (Y_o)_{BEF}$
NO
An average $(X_o)_{new}$ and $(P_o)_{new}$
$(P_o)_{new} = (Y_o)_{SWM}\ (P_o/Y_o)_{BEF}$
Yes
Compare P_o with targeted value
NO
Increase soil strain with $\Delta\varepsilon$
Yes
End

Figure 7.5: SWM procedure in solving the problem of laterally loaded pile/shafts in layered soils.

Chapter 8: Field and Model Verification

8.1 Introduction

This section discusses the suitability of geophysical methods in identifying the existence, depth and thickness of cemented soils as well as its shear wave velocity. It also discusses the verification of the implemented material model in Strain Wedge Model (SWM) program. For this task, the research team consulted the Kleinfelder report (Rinne et al., 1996) to locate the sites where drilled shafts where laterally load-tested in partially cemented soils. The objective was to revisit each site, locate the test shaft(s) at the site, and conduct a geophysical investigation at the reported location. While three Sites (1, 3 and 4) were identified, only one site, Site 4, was judged to be useable. Site 4 from the Kleinfelder study satisfied the following criteria: 1) The drilled shaft was located; 2) Access to the site was possible; and 3) The site had not been buried or covered with decorative rock. Thus, the team conducted a site-specific geophysical survey at Site 4. At the time, data from all four sites were used in the verification of the cemented soil model implemented in SWM.

8.2 Suitability of Geophysical Survey Methods

8.2.1 Description of Site 4

Site 4 was located just off the I-15 freeway at the corner of West Washington Ave and A Street (Figure 8.1). The geophysical survey that was conducted consisted of two geophysical arrays, one trending North-South (line 1) and the other East-West (line 2) and as shown in Figure 8.1. Use of Site 4 was advantageous to the current study because according to Rinne et al. (1996), the cemented soil horizon occurs at relatively shallow depth of 6 feet (Table 8.1).

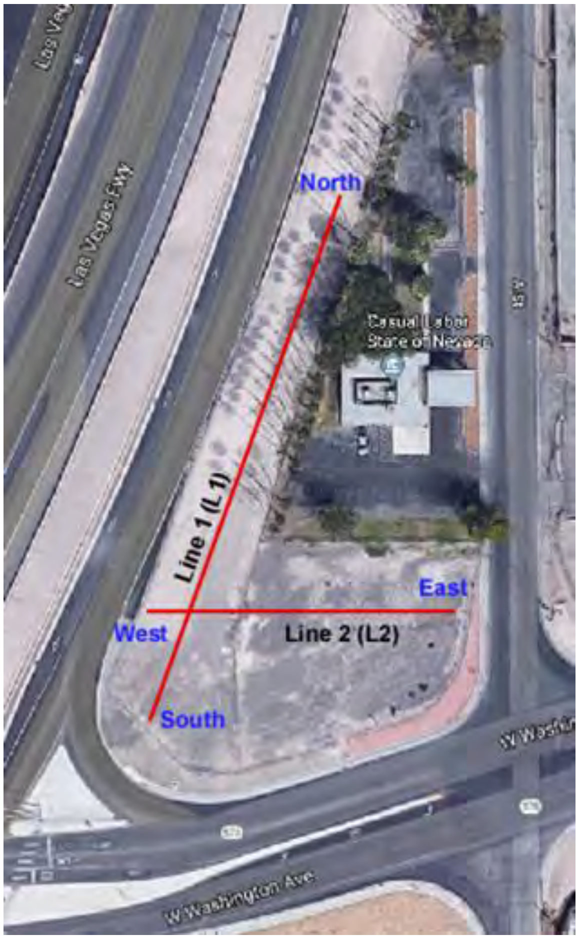
Las Vegas Fwy
North
Casual Labor State of Nevada
Line 1 (L1)
East
West
Line 2 (L2)
South
W Washington Ave

Figure 8.1: Aerial image showing location of geophysical arrays at Site 4 (Google Earth).

Table 8.1: Abbreviated soil horizons at Site 4 (Rinne et al., 1996).

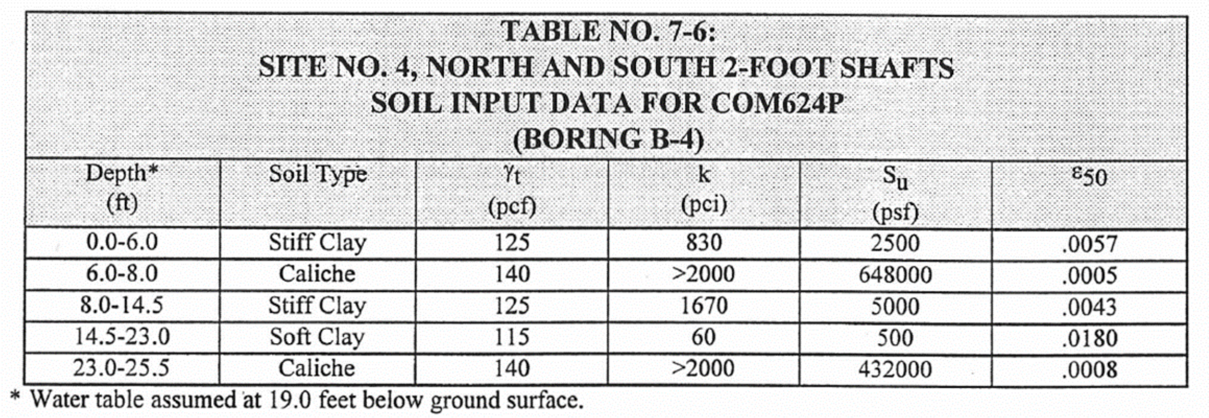

TABLE NO. 7-6:
SITE NO. 4, NORTH AND SOUTH 2-FOOT SHAFTS
SOIL INPUT DATA FOR COM624P
(BORING B-4)

Depth* (ft)	Soil Type	γ_t (pcf)	k (pci)	S_u (psf)	ε_{50}
0.0-6.0	Stiff Clay	125	830	2500	.0057
6.0-8.0	Caliche	140	>2000	648000	.0005
8.0-14.5	Stiff Clay	125	1670	5000	.0043
14.5-23.0	Soft Clay	115	60	500	.0180
23.0-25.5	Caliche	140	>2000	432000	.0008

* Water table assumed at 19.0 feet below ground surface.

8.2.2 Geophysical Surveys

The same non-invasive geophysical methods utilized at the excavation site at West Charleston and Martin Luther King Blvd were used at Site 4. Line 1 was 188 feet in length, while line 2 was 140 feet in total length. A heavy sledge hammer was used to strike a steel plate placed at ground surface at specific locations, denoted as striking locations, to create a seismic source for MASW analysis. Striking locations and geophones were placed at 4-ft intervals. Both MASW and ReMi methods were used on line 1, while MASW only was used for line 2. Figure 8.2 and Figure 8.3 show the configuration for line 1 and line 2, respectively.

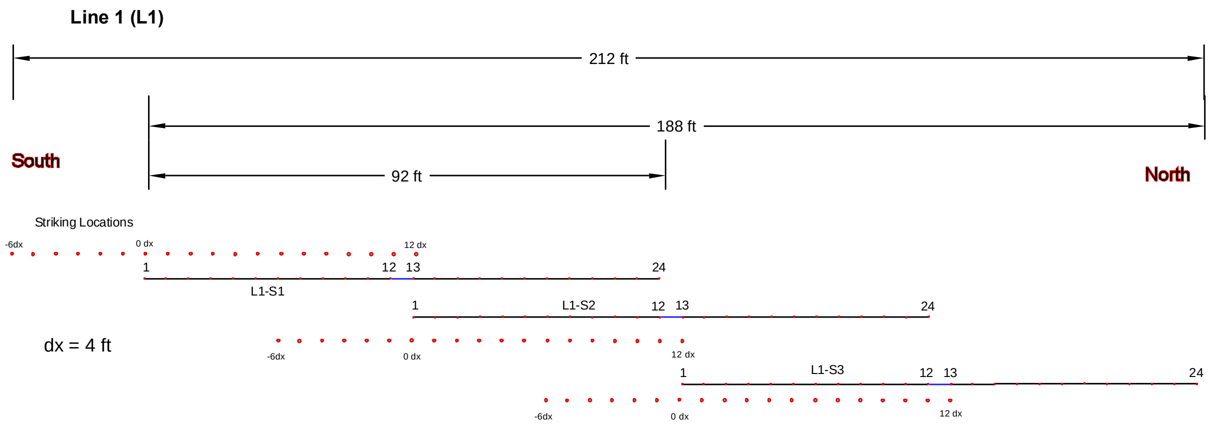

Line 1 (L1)
212 ft
188 ft
92 ft
South
North
Striking Locations
-6dx
0 dx
12 dx
1
12
13
24
L1-S1
L1-S2
L1-S3
dx = 4 ft

Figure 8.2: Configuration of the geophysical survey line, L1.

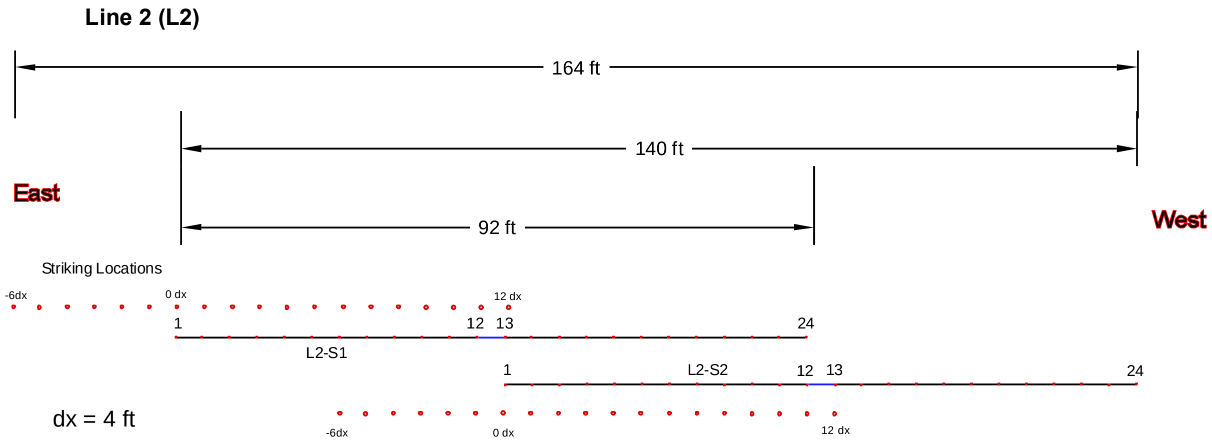

Line 2 (L2)
164 ft
140 ft
92 ft
East
West
Striking Locations
-6dx
0 dx
12 dx
1
12
13
24
L2-S1
L2-S2
dx = 4 ft

Figure 8.3: Configuration of the geophysical survey line, L2.

The MASW analysis is shown in Figure 8.4 and the ReMi analysis is shown in Figure 8.5. The MASW shows a peak shear wave velocity of 1800 ft/s, but the light blue band at around 6 feet is where the cemented soil is. This gives the cemented soil layer a Vs of 1000 ft/s, compared to the 1600 ft/s from Figure 4.1.

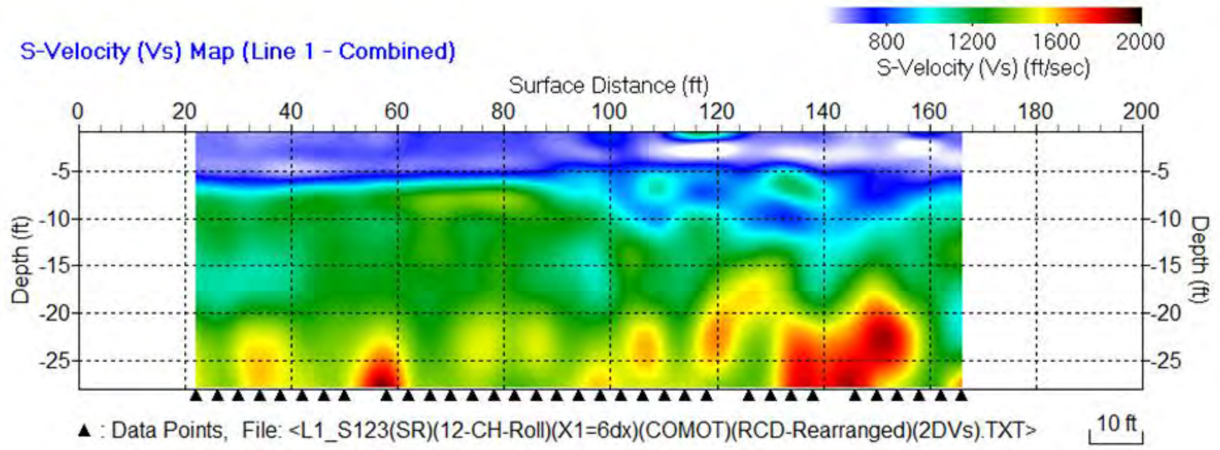

Figure 8.4: MASW analysis of Site 4.

The ReMi analysis shown in Figure 8.5 is much more coherent and accurately shows the cemented soil layer at 6-8 feet. As with the original ReMi analysis at the excavation site (Figure 4.1), the peak velocity is 4000 ft/s for the cemented horizons. The analysis does fail to acknowledge a second cemented soil horizon at 23 feet (Table 8.1).

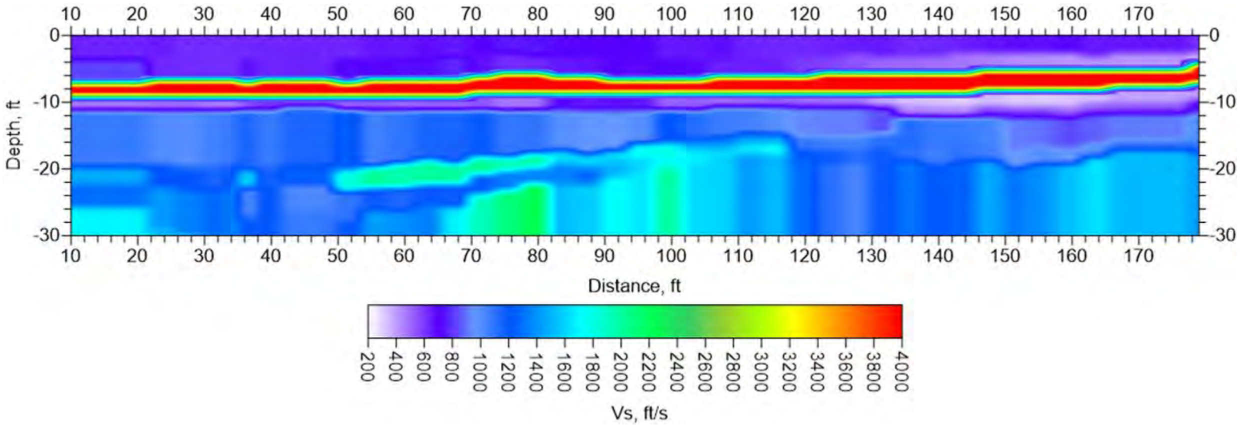

Figure 8.5: ReMi analysis of Site 4.

These two separate analyses were repeated due to inaccuracies or implicit bias. The MASW method either failed to measure velocities of the cemented soil or recorded a decrease in velocity for a material that is in some cases stronger than concrete. The ReMi analysis has bias within the analysis because the interpreter knew of the location of the two ReMi studies and assigned a pre-determined velocity to the cemented soil horizons.

8.2.3 Second Analyses

The same individuals were asked to interpret the same data records but consider the data as if they had no previous knowledge of the site or previously assigned velocities. The second ReMi analysis (Figure 8.6) accurately depicts the site's subsurface profile. This is in part because the individual conducting the analysis received the subsurface profile but did not consider the 4000 ft/s velocity for the cemented soil horizons. The analysis shows a significant decrease in velocity from 4000 ft/s to 2000 ft/s as the peak shear wave velocity.

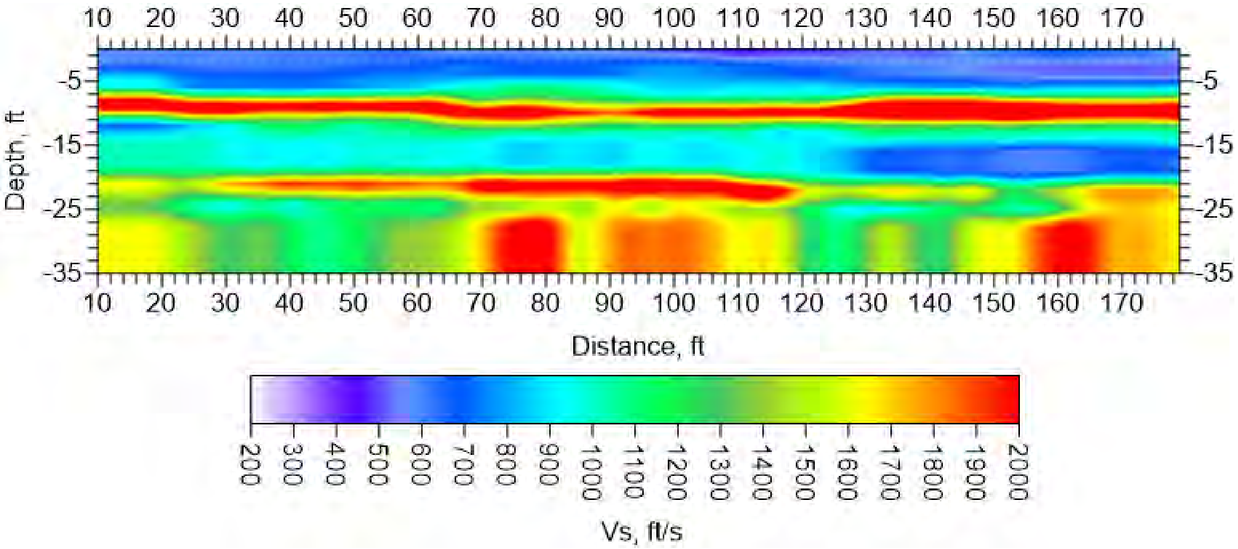

Figure 8.6: Second ReMi analysis of Site 4.

8.2.4 Discussion

It was expected that the MASW would yield the best results. Because the MASW uses an active, higher frequency source, this method should prove to be more accurate at shallow depths. ReMi uses a lower frequency, passive source that would be able to give a broader analysis to depths of up to 100 meters (Louie, 2001) due to low attenuation.

The MASW was unable to clearly identify the cemented soil horizons and provided very low velocities for material that had reported unconfined compressive strength values according to Rinne et al., 1996 and as illustrated in Table 8.1. The ReMi analysis had a certain degree of bias in the previous interpretations. In the second analysis, the peak shear wave velocity was reduced by 50%.

The verification of the field geophysics for the material model is inconclusive. Neither could corroborate one another or the initial geophysical study at the excavation near Martin Luther King Blvd. The material model was not able to be verified since samples could not be obtained at Site 4. In the future, if samples can be collected and tested, in conjunction with field geophysics, the material model can be validated properly, thus making the SWM more accurate.

8.3 Verification of the SW Model

Zafir and Vanderpool (1998) conducted a full-scale load test program on 2- and 4-ft diameter reinforced concrete drilled shafts at four sites in Las Vegas, Nevada. The main objective of the study was to inspect the overly-conservative design values usually used for the design of drilled shafts subject to lateral loading in partially to fully cemented caliche soil. Zafir and Vanderpool (1998) used the COM624P computer program to analyze the lateral behavior of the isolated drilled shafts using the initial and reduced values for the shaft flexural stiffness (EI). The reduced EI (i.e. cracked section) reflects the degradation in EI due to the developing cracks in the shaft cross section with increasing lateral loads. The reported soil properties at the four test sites were based on laboratory and field tests. It was reported that regardless of the soil gradation classification, the subsurface soils at the four test sites behaved as cohesive soils due to their partial cementation. Furthermore, the soils shear strength values were found to be higher than the values obtained through correlations with the SPT-N values. This led Zafir and Vanderpool (1998) to adjust the shear strength values implemented in the COM624P computer program until a reasonable agreement with the field test data was achieved, which certainly affects the reliability of the data input. It's noteworthy that the only drilled shaft tested in the lateral direction at Site 2 was subjected to cyclic lateral load. Therefore, it's not of interest to us in this report.

The shafts' properties employed by Zafir and Vanderpool (1998) for the use in COM624P computer program are presented in Table 8.2. A brief description of the predicted and reported load tests' results at Sites 1, 3 and 4 follows.

Table 8.2: Reported drilled shafts properties at Site 1.

Site No.	Shaft	f'_C (psi)	E_C (*10^6 psi)	E_S (*10^6 psi)	A_C (in^2)	A_S (in^2)	AE (*10^6 lbs)	I (*10^4 in^4)	EI (*10^{11} lbs-in^2)
Site 1	8-ft	6300	4.573	29	7473	71	36.24	452.77	217.5
	2-ft	7000	4.811	29	523	8	2.75	2.2432	1.161
Site 3	2-ft	7000	4.811	29	523	8	2.75	2.2432	1.161
Site 4	North	6300	4.564	29	523	8	2.619	2.2432	1.161
	South	6800	4.742	29	523	8	2.712	2.2432	1.146

c = concrete   s = steel

8.3.1 Site 1

Zafir and Vanderpool (1998) tested two drilled shafts and a shaft group at this site. The two drilled shafts of interest were 8-foot and 2-foot in diameter and 32-feet and 35-feet in length, respectively. Axial load tests were performed on the two shafts prior to being tested in the lateral direction. The shafts' details, configuration and soil profile are shown as reported in Figure 8.7. The pile properties reported by Zafir and Vanderpool (1998) are presented in Table 8.2 and the geotechnical parameters used in COM624P for the 8-foot diameter and the 2-foot diameter shafts are presented in Table 8.3 and Table 8.4, respectively. The soil properties employed in the SWM are presented in Table 8.5 and Table 8.6 for the 8-ft diameter and the 2-ft diameter shafts, respectively. Figure 8.78 shows the SWM predicted results and the reported results for the 8-foot diameter shaft. It is noted that the shaft head measured response lies between the predicted and COM624P uncracked calculation at low load levels, closer to the later. However, with increasing load COM624P uncracked calculations deviate from the observed response and better agreement is noted between the observed data and the SWM results. The SWM predicted results and the reported results for the 2-foot diameter shaft are show in Figure 8.9. Good agreement occurs between the SWM results and the measured field date for loads up to 80 tons. However, for loads more than 80 tons the SWM results and COM624P uncracked calculations start to predict stiffer shaft head response. The observed response is bounded by the SWM results and COM624P cracked results. There is overall good agreement between the SWM results and the observed shaft head responses for the 8-foot and the 2-foot diameter shafts (Figure 8.8 and Figure 8.9). Of note, the caliche properties used in the SWM analysis are obtained based the caliche material model developed in the current study (Chapter 7:). The unit weight of the caliche material presented in Table 8.5 was utilized to determine the associated compressive strength and ε_{50}.

Table 8.3: Reported soil input data employed in COM624P for the 8-foot shaft (Site 1).

Depth (ft)	Soil type	γ_t (pcf)	K (pci)	S_u (psf)	ε_{50}
0.0-5.0	Stiff Clay	120	550	1600	0.007
5.0-9.0	Stiff Clay	125	1000	3000	0.005
9.0-13.5	Stiff Clay	120	680	2000	0.0063
13.5-21.0	Caliche	140	>2000	690000	0.001
21.0-35.0	Stiff Clay	125	1160	3500	0.0048
35.0-38.0	Caliche	140	>2000	576000	0.001

Table 8.4: Reported soil input data employed in COM624P for the 2-foot shaft (Site 1).

Depth (ft)	Soil type	γ_t (pcf)	K (pci)	S_u (psf)	ε_{50}
0.0-10.0	Stiff Clay	125	1000	3000	0.005
10.0-14.0	Stiff Clay	120	600	1300	0.0066
14.0-18.5	Caliche	140	>2000	566000	0.001
18.5-35.0	Stiff Clay	125	2000	6000	0.004
35.0-38.0	Caliche	140	>2000	560000	0.005

Table 8.5: Soil input data employed in SWM for the 8-foot shaft (Site 1).

Depth (ft)	Soil type	γ_t (pcf)	S_u (psf)	ε_{50}**
0.0-5.0	Clay	120	1600	0.0
5.0-9.0	Clay	125	3000	0.0
9.0-13.5	Clay	120	2000	0.0
13.5-21.0	Caliche	140	167864*	0.00077
21.0-35.0	Clay	125	3500	0.0
35.0-38.0	Caliche	140	167864*	0.00077

*q_u (i.e. $2S_u$) of caliche is determined in the SWM program based on γ as presented in Chapter 7:

**Enter zero for ε_{50} of clay to use the SWM program default (correlation by Evans and Duncan, 1982)

**ε_{50} of caliche is determined in the SWM program based the correlations presented in Chapter 7:

Table 8.6: Soil input data employed in SWM for the 2-foot shaft (Site 1).

Depth (ft)	Soil type	γ_t (pcf)	S_u (psf)	ε_{50}**
0.0-10.0	Clay	125	3000	0.0
10.0-14.0	Clay	120	1300	0.0
14.0-18.5	Caliche	140	167864*	0.00077
18.5-35.0	Clay	125	6000	0.0
35.0-38.0	Caliche	140	167864*	0.00077

*q_u (i.e. 2Su) of caliche is determined in the SWM program based on γ as presented in Chapter 7:

**Enter zero for ε_{50} of clay to use the SWM program default (correlation by Evans and Duncan, 1982)

**ε_{50} of caliche is determined in the SWM program based the correlations presented in Chapter 7:

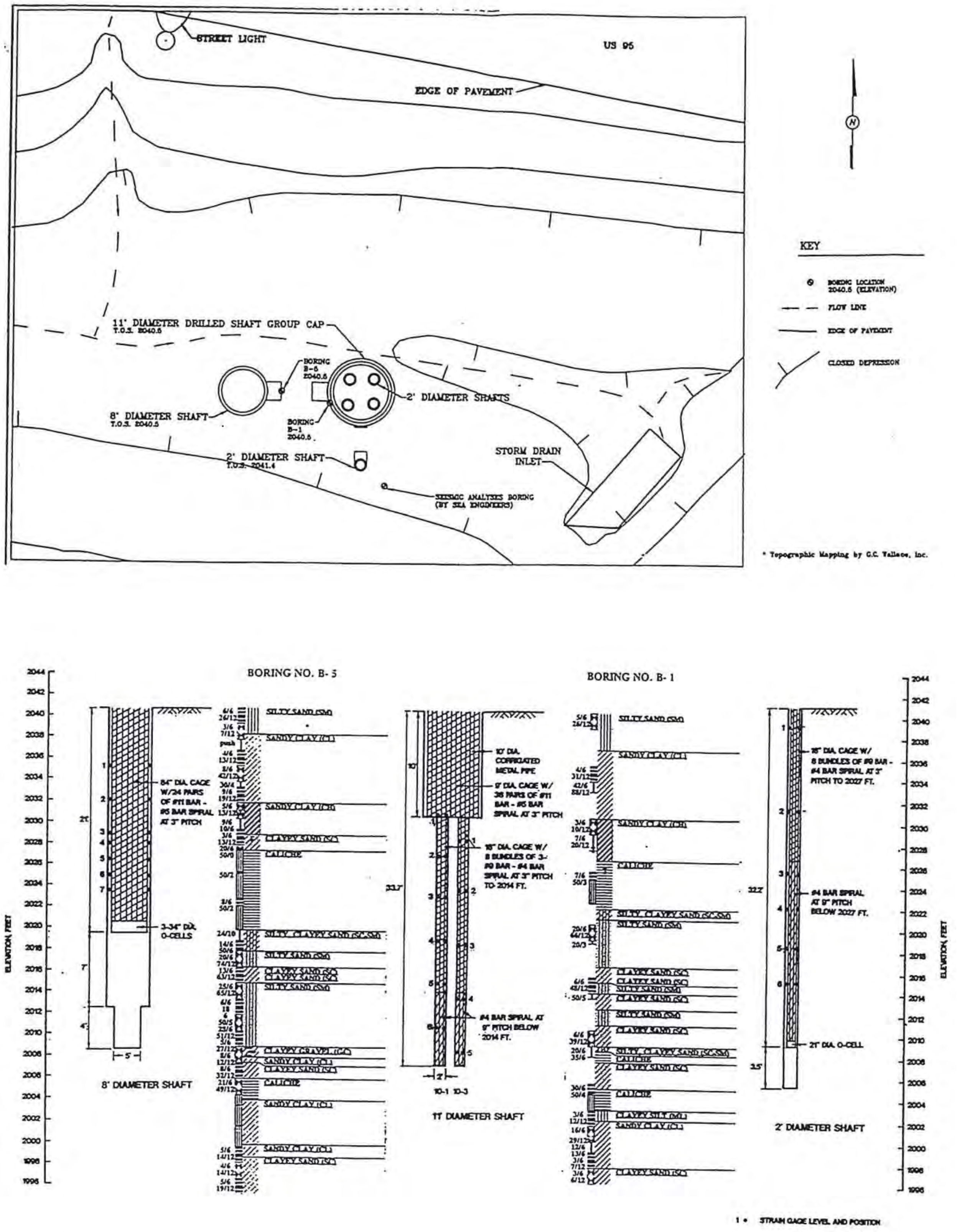
STREET LIGHT
US 95
EDGE OF PAVEMENT
N
KEY
BORING LOCATION 2040.5 (ELEVATION)
FLOW LINE
EDGE OF PAVEMENT
CLOSED DEPRESSION
11' DIAMETER DRILLED SHAFT GROUP CAP
T.O.S. 2040.5
BORING B-5 2040.5
2' DIAMETER SHAFTS
8' DIAMETER SHAFT
T.O.S. 2040.5
BORING B-1 2040.5
2' DIAMETER SHAFT
T.O.S. 2041.4
STORM DRAIN INLET
SEISMIC ANALYSES BORING (BY SEA ENGINEERS)
* Topographic Mapping by G.C. Wallace, Inc.
BORING NO. B-5
BORING NO. B-1
ELEVATION, FEET
2044
2042
2040
2038
2036
2034
2032
2030
2028
2026
2024
2022
2020
2018
2016
2014
2012
2010
2008
2006
2004
2002
2000
1998
1996
84" DIA. CAGE W/24 PAIRS OF #11 BAR - #5 BAR SPIRAL AT 3" PITCH
3-34" DIA. O-CELLS
21'
7'
4'
5'
8' DIAMETER SHAFT
SILTY SAND (SM)
SANDY CLAY (CL)
SANDY CLAY (CH)
CLAYEY SAND (SC)
CALICHE
SILTY, CLAYEY SAND (SC-SM)
CLAYEY GRAVEL (GC)
CLAYEY SILT (ML)
10'
33.7'
10' DIA. CORRUGATED METAL PIPE
9' DIA. CAGE W/ 36 PAIRS OF #11 BAR - #5 BAR SPIRAL AT 3" PITCH
18" DIA. CAGE W/ 8 BUNDLES OF 3-#9 BAR - #4 BAR SPIRAL AT 3" PITCH TO 2014 FT.
#4 BAR SPIRAL AT 9" PITCH BELOW 2014 FT.
2'
10-1 10-3
11' DIAMETER SHAFT
18" DIA. CAGE W/ 8 BUNDLES OF #9 BAR - #4 BAR SPIRAL AT 3" PITCH TO 2027 FT.
#4 BAR SPIRAL AT 9" PITCH BELOW 2027 FT.
21" DIA. O-CELL
32.2'
3.5'
2' DIAMETER SHAFT
1 • STRAIN GAGE LEVEL AND POSITION

Figure 8.7: Shafts' details, configuration and soil profile at Site 1.

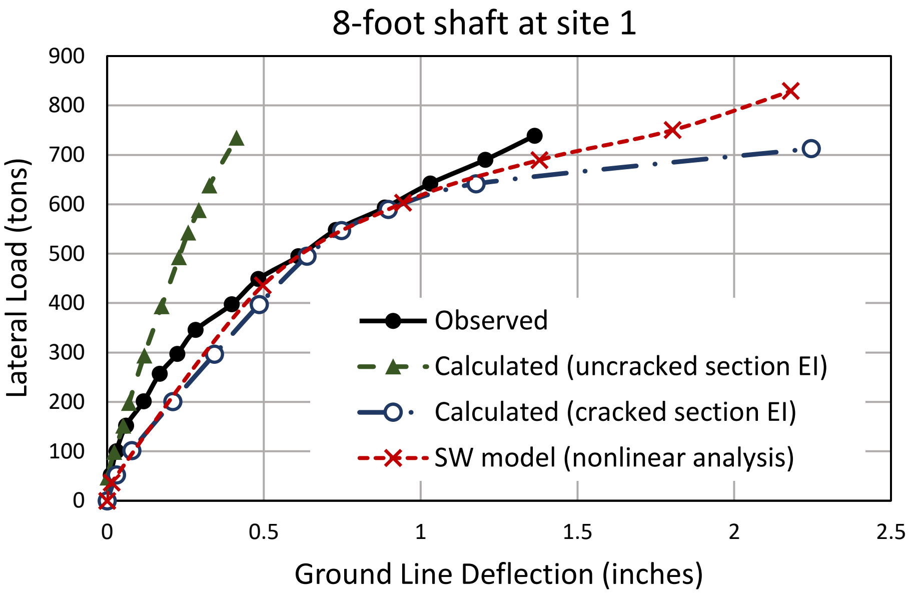

Figure 8.8: Predicted shaft head response versus reported results for the 8-foot shaft at Site 1.

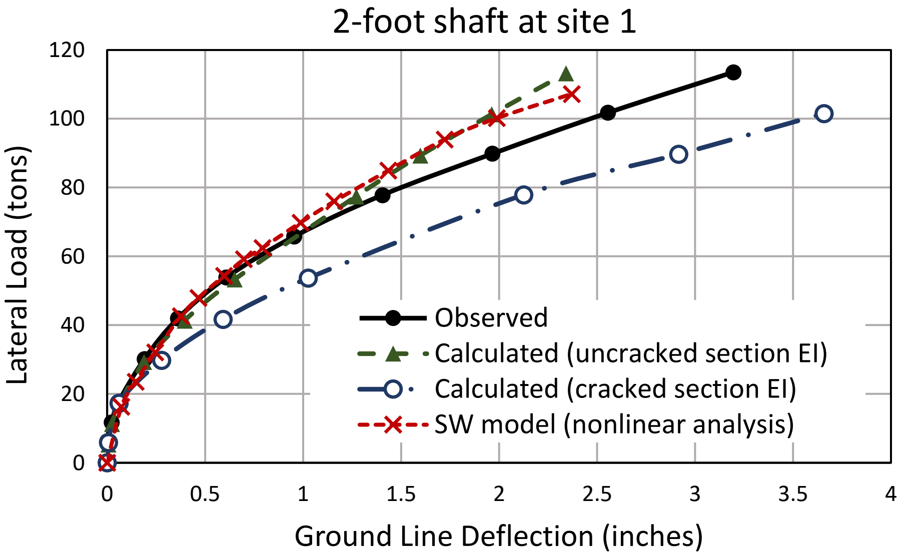

Figure 8.9: Predicted shaft head response versus reported results for the 2-foot shaft at Site 1.

8.3.2 Site 3

A 2-foot diameter 43-foot long shaft was tested in the axial direction and then in the lateral direction at Site 3. The subsurface soil condition and the shaft details are shown as reported in Figure 8.10. The pile and soil properties employed by Zafir and Vanderpool (1998) in the COM624P computer program are presented in Table 8.2 and Table 8.7, respectively. Soil properties reported by Zafir and Vanderpool (1998) and other interpreted parameters for the use in the SWM are presented in Table 8.8. A comparison between the SWM results and the reported results for the 2-foot diameter shaft at Site 3 is shown in Figure 8.11. The observed response is slightly stiffer than the SWM predicted results and the COM624P cracked and uncracked results. It is noted that the uncracked COM624P results yield a shaft head response that is considerably softer than the measured response at higher deflection.

Table 8.7: Reported soil input data employed in COM624P for the 2-foot shaft (Site 3).

Depth (ft)	Soil type	γ_t (pcf)	K (pci)	S_u (psf)	ε_{50}
0.0-4.0	Stiff Clay	125	1230	3700	0.0048
4.0-9.0	Stiff Clay	120	750	2200	0.006
9.0-20.0	Stiff Clay	125	1100	3200	0.0049
20.0-22.0	Stiff Clay	125	1600	4500	0.0045
22.0-43.0	Stiff Clay	125	1670	5000	0.0043
43.0-45.5	Caliche	140	>2000	432000	0.0008

Table 8.8: Soil input data employed in the SWM (Site 3).

Depth (ft)	Soil type	γ_t (pcf)	S_u (psf)	ε_{50}**
0.0-4.0	Clay	125	3700	0
4.0-9.0	Clay	120	2200	0
9.0-20.0	Clay	125	3200	0
20.0-22.0	Clay	125	4500	0
22.0-43.0	Clay	125	5000	0

**Enter zero for ε_{50} of clay to use the SWM program default (correlation by Evans and Duncan, 1982)

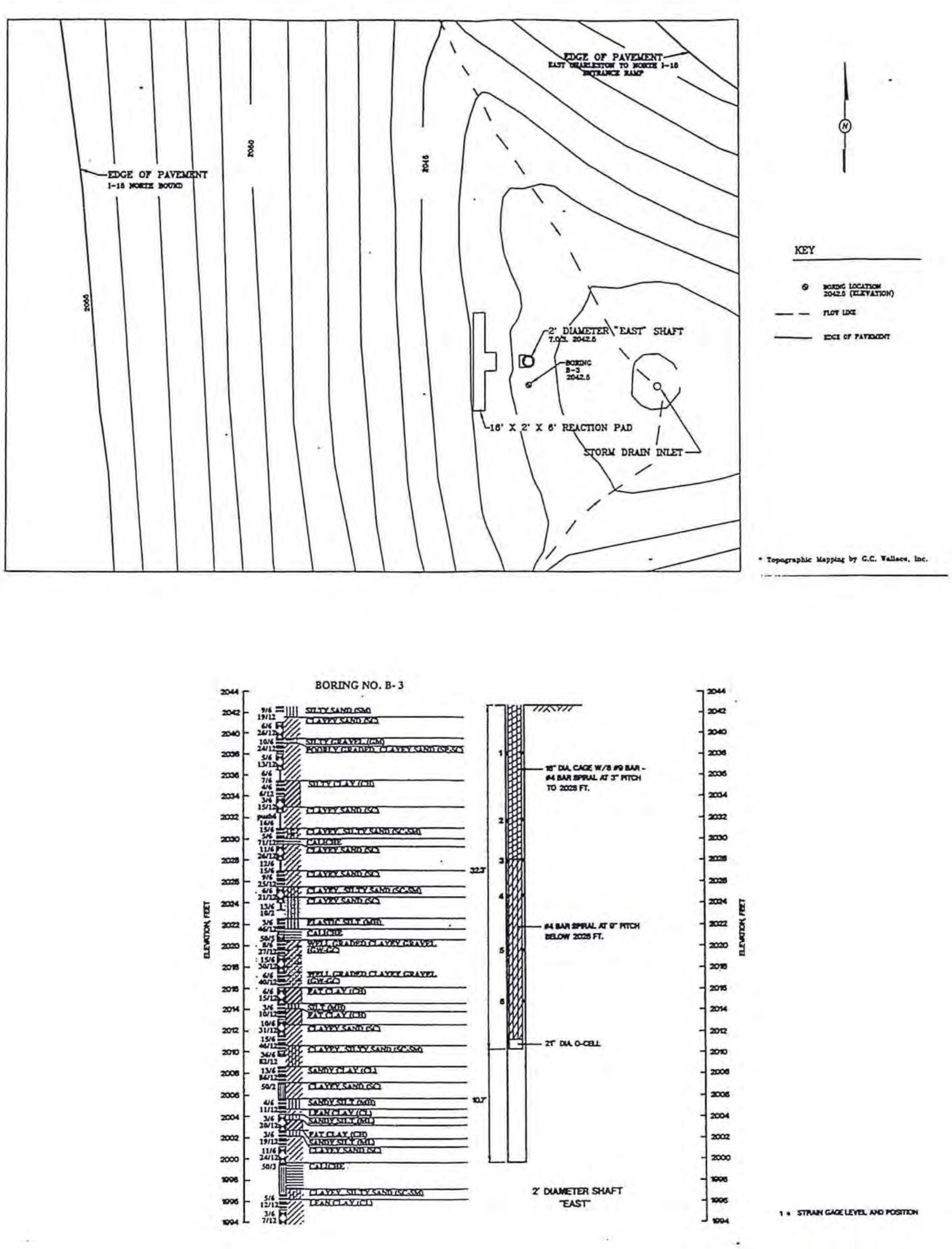
EDGE OF PAVEMENT
EAST CHARLESTON TO NORTH I-15 ENTRANCE RAMP
EDGE OF PAVEMENT
I-15 NORTH BOUND
2055
2050
2045
N
KEY
BORING LOCATION 2042.5 (ELEVATION)
FLOW LINE
EDGE OF PAVEMENT
2' DIAMETER "EAST" SHAFT
T.O.S. 2042.5
BORING B-3 2042.5
16' X 2' X 6' REACTION PAD
STORM DRAIN INLET
* Topographic Mapping by G.C. Wallace, Inc.
BORING NO. B-3
ELEVATION, FEET
SILTY SAND (SM)
CLAYEY SAND (SC)
SILTY GRAVEL (GM)
POORLY GRADED CLAYEY SAND (SP-SC)
SILTY CLAY (CH)
CLAYEY SAND (SC)
CLAYEY SILTY SAND (SC-SM)
CALICHE
CLAYEY SAND (SC)
CLAYEY SAND (SC)
CLAYEY SILTY SAND (SC-SM)
CLAYEY SAND (SC)
PLASTIC SILT (MH)
CALICHE
WELL GRADED CLAYEY GRAVEL (GW-GC)
WELL GRADED CLAYEY GRAVEL (GW-GC)
FAT CLAY (CH)
SILT (MH)
FAT CLAY (CH)
CLAYEY SAND (SC)
CLAYEY SILTY SAND (SC-SM)
SANDY CLAY (CL)
CLAYEY SAND (SC)
SANDY SILT (MH)
LEAN CLAY (CL)
SANDY SILT (ML)
FAT CLAY (CH)
SANDY SILT (ML)
CLAYEY SAND (SC)
CALICHE
CLAYEY SILTY SAND (SC-SM)
LEAN CLAY (CL)
32.3'
10.7'
18" DIA. CAGE W/8 #9 BAR - #4 BAR SPIRAL AT 3" PITCH TO 2025 FT.
#4 BAR SPIRAL AT 9" PITCH BELOW 2025 FT.
21" DIA. O-CELL
2' DIAMETER SHAFT "EAST"
1 • STRAIN GAGE LEVEL AND POSITION
1
2
3
4
5
6
2044
2042
2040
2038
2036
2034
2032
2030
2028
2026
2024
2022
2020
2018
2016
2014
2012
2010
2008
2006
2004
2002
2000
1998
1996
1994

Figure 8.10: Shafts' details, configuration and soil profile at Site 3.

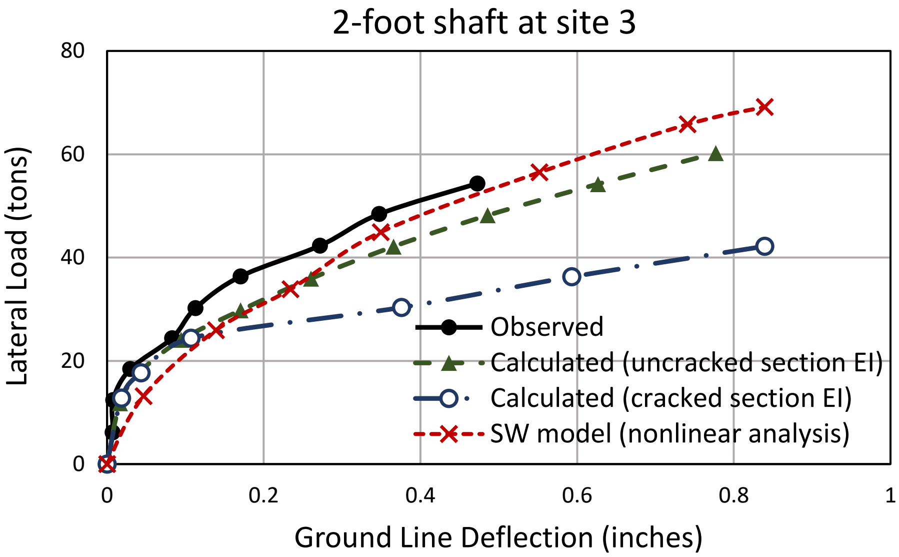

Figure 8.11: Predicted shaft head response versus reported results for the 2-foot shaft at Site 3.

8.3.3 Site 4

Two lateral load tests were conducted at Site 4 on two 2-foot diameter 24-foot long shafts (i.e., North haft and South shaft). However, the North shaft was loaded axially prior to being loaded in the lateral direction. Figure 8.12 shows the soil profile and the details of the shafts' tested at Site 4. Table 8.2 and Table 8.9 show the shafts' and soil properties employed by Zafir and Vanderpool (1998) in the COM624P computer program. Table 8.10 shows the reported and interpreted soil properties used in the SWM. The reported response of the North and the South shafts is almost identical. Therefore, only the results of the North shaft are presented in this report. Good agreement between the SWM results and the observed results is noted in Figure 8.13. The shaft response in the SWM analysis ceased with the predicted development of a plastic hinge (i.e. plastic moment). Reported field observations indicated that that shaft experienced a sudden shear failure in the upper part of the shaft at large level of deflections. In fact, the test shaft developed a plastic hinge and continued to defect under lateral load with sustained resistance due to the presence of the shallow caliche deposit before the development of shear failure in the upper portion of the shaft.

Similar to the tests at Site 1, the caliche properties used in the SWM analysis are obtained based on the caliche material model developed in the current study (Chapter 7:). The unit weight of the caliche material presented in Table 8.10 was utilized to determine the associated compressive strength and ε_{50}.

Table 8.9: Soil input data employed in COM624P for Site 4.

Depth (ft)	Soil type	γ_t (pcf)	K (pci)	S_u (psf)	ε_{50}
0.0-6.0	Stiff Clay	125	830	2500	0.0057
6.0-8.0	Caliche	140	>2000	648000	0.0005
8.0-13.5	Stiff Clay	125	1670	5000	0.0043
13.5.0-23.0	Soft Clay	115	60	500	0.018
23.0-25.5	Caliche	140	>2000	432000	0.0008

Table 8.10: Reported soil input data employed in the SWM for Site 4.

Depth (ft)	Soil type	γ_t (pcf)	S_u (psf)	ε_{50}**
0.0-6.0	Clay	125	2500	0.0
6.0-8.0	Caliche	140	167864*	0.00077
8.0-13.5	Clay	125	5000	0.0
13.5.0-23.0	Clay	115	6000	0.0
23.0-25.5	Caliche	140	167864*	0.00077

*q_u (i.e. 2Su) of caliche is determined in the SWM program based on γ as presented in Chapter 7:

**Enter zero for ε_{50} of clay to use the SWM program default (correlation by Evans and Duncan, 1982)

**ε_{50} of caliche is determined in the SWM program based the correlations presented in Chapter 7:

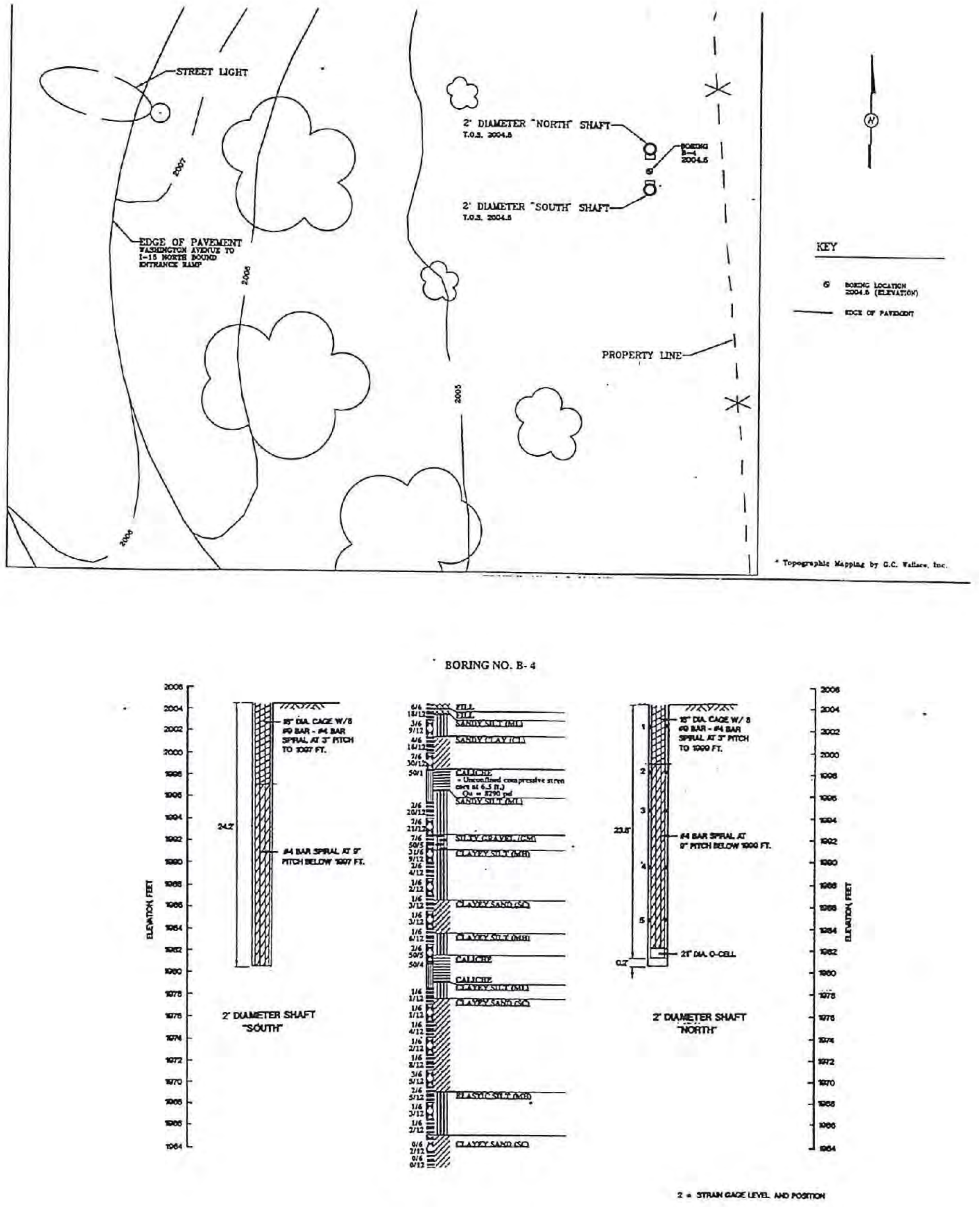
STREET LIGHT
2' DIAMETER "NORTH" SHAFT
T.O.S. 2004.5
BORING B-4 2004.5
2' DIAMETER "SOUTH" SHAFT
T.O.S. 2004.5
EDGE OF PAVEMENT
WASHINGTON AVENUE TO I-15 NORTH BOUND ENTRANCE RAMP
2007
2006
2005
2006
PROPERTY LINE
N
KEY
BORING LOCATION 2004.5 (ELEVATION)
EDGE OF PAVEMENT
* Topographic Mapping by G.C. Wallace, Inc.
BORING NO. B- 4
ELEVATION, FEET
2006
2004
2002
2000
1998
1996
1994
1992
1990
1988
1986
1984
1982
1980
1978
1976
1974
1972
1970
1968
1966
1964
18" DIA. CAGE W/8 #9 BAR - #4 BAR SPIRAL AT 3" PITCH TO 1997 FT.
#4 BAR SPIRAL AT 9" PITCH BELOW 1997 FT.
24.2'
2' DIAMETER SHAFT "SOUTH"
6/6
18/12
3/6
9/12
4/6
16/12
7/6
30/12
50/1
2/6
20/12
7/6
21/12
7/6
50/5
31/6
9/12
2/6
4/12
1/6
2/12
1/6
3/12
1/6
3/12
1/6
6/12
2/6
50/5
50/4
1/6
3/12
1/6
1/12
1/6
4/12
1/6
2/12
1/6
8/12
3/6
5/12
2/6
5/12
1/6
3/12
1/6
2/12
0/6
2/12
0/6
0/12
FILL
FILL
SANDY SILT (ML)
SANDY CLAY (CL)
CALICHE
= Unconfined compressive stren core at 6.5 ft.)
Qu = 8290 psf
SANDY SILT (ML)
SILTY GRAVEL (GM)
CLAYEY SILT (MH)
CLAYEY SAND (SC)
CLAYEY SILT (MH)
CALICHE
CALICHE
CLAYEY SILT (ML)
CLAYEY SAND (SC)
ELASTIC SILT (MH)
CLAYEY SAND (SC)
18" DIA. CAGE W/ 8 #9 BAR - #4 BAR SPIRAL AT 3" PITCH TO 1999 FT.
#4 BAR SPIRAL AT 9" PITCH BELOW 1999 FT.
21" DIA. O-CELL
1
2
3
4
5
23.5'
0.2'
2' DIAMETER SHAFT "NORTH"
2 = STRAIN GAGE LEVEL AND POSITION

Figure 8.12: Shafts' details, configuration and soil profile at Site 4.

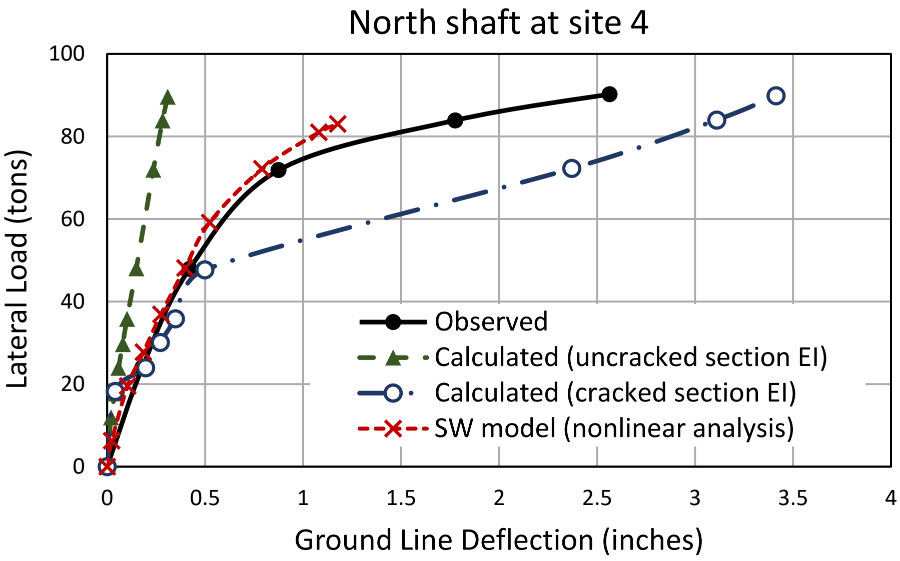

Figure 8.13: Predicted shaft head response versus reported results for the North shaft at Site 4.

Chapter 9: Summary and Recommendations

9.1 Summary

Cemented soils in the Las Vegas area are problematic for engineers. These calcareous rock formations in the subsurface are challenging to model with current data and site investigation techniques. Because of these materials' erratic lateral extent and varying strengths and depths, engineers tend to significantly overdesign foundations for the numerous freeways and increasing number of mega-hotels.

The material model discussed in this report shows a new and viable method for modelling the stress-strain behavior of this unpredictable geomaterial. Utilizing current, non-invasive field geophysical methods, in conjunction with lab ultrasonic velocity measurements, preliminary relationships were introduced between shear wave velocity and unit weight, Young's modulus and unconfined compressive strength. These relationships make the model easier to use and ensure that the various levels of cementation encountered in the Las Vegas valley are accounted for in the material model.

This new material model, along with the incorporation of vertical side shear to laterally loaded drilled shafts, greatly improves strain wedge modelling capabilities. These additions allow for more accurate simulations for lateral shaft response when embedded within a cemented soil horizon. This improved model will result in better foundation design, which would ultimately mean increased cost savings.

9.2 Process for Designers

The implementation of the new model in SWM allows designers to assess the performance of laterally loaded drilled shafts embedded in cemented soils with higher certainty than before. Since the material model depends on correct assessment of the unconfined compressive strength of the cemented soils, the implementation considers three confidence levels when assessing such property.

The three confidence levels are:

1. **Low confidence:** UCS based on field shear wave velocity

    Step 1: Measure field shear wave velocity (using MASW or ReMi)
    Step 2: Assess lab shear wave velocity (Figure 4.5) as input to the SWM
    Step 3: Assess Unconfined Compressive Strength (Figure 4.6)
    Step 4: Assess Elastic Modulus, E_{50} (Figure 4.7)
    Step 5: Compute ε_{50} (strain at 50% ultimate stress)
    Step 6: Calculate modeled strain, ε_m
    Step 7: Assess $\Delta\varepsilon$ (user discretion)
    Step 8: Compute ε_{actual}

    Steps 3 through 8 are computed internally in the SWM

2. **Moderate confidence:** UCS based on material unit weight

    Step 1: Obtain bulk samples and assess unit weight
    Step 2: Assess lab shear wave velocity (Figure 4.8) as input to the SWM
    Step 3: Assess Unconfined Compressive Strength (Figure 4.6)
    Step 4: Assess Elastic Modulus, E_{50} (Figure 4.7)
    Step 5: Compute ε_{50} (strain at 50% ultimate stress)
    Step 6: Calculate modeled strain, ε_m
    Step 7: Assess $\Delta\varepsilon$ (user discretion)
    Step 8: Compute ε_{actual}

    Steps 3 through 8 are computed internally in the SWM

3. **High confidence:** UCS based on actual lab tests

    Step 1: Obtain samples and assess UCS as input to the SWM
    Step 2: Assess Elastic Modulus, E_{50} (Figure 4.7)
    Step 3: Compute ε_{50} (strain at 50% ultimate stress)
    Step 4: Calculate modeled strain, ε_m
    Step 5: Assess $\Delta\varepsilon$ (user discretion)
    Step 6: Compute ε_{actual}

    Steps 2 through 6 are computed internally in the SWM

9.3 Hands-on Training

The research team conducted a hands-on training of NDOT engineers and designers on May 10, 2018 presenting the findings of this project, communicating the enhancements to the SWM, and demonstrating to attendees the SWM new capabilities. The training was held on University of Nevada, Reno campus and lasted for one day. Appendix F presents the handout from the training.

9.4 Limitations

The limitations of this research are that it creates a material model to be used in the Las Vegas region. However, the samples collected are from one location in the area and may not represent the region as a whole. In addition, the material model would need further verification that could be undertaken as the data set is expanded.

Another limitation lies in the correlation between field and lab shear wave velocities. As mentioned, all samples were taken from one site and the field measurements were taken from the same site. Further investigation is needed to refine this correlation.

9.5 Future Work

Surprisingly, in a region with so much growth, the available data on cemented soils is limited. This research greatly increased that data set to include new correlations that were previously not made or poorly understood. However, all the data from this research is from one single location. To build a material model for the area that is to be more accurate and comprehensive, the data set would need to incorporate samples from a greater variety of locations and depths. This is important because the cemented soil in the area is so diverse and may exhibit different characteristics depending on its location in the valley.

In addition, future work should be done on the influence of the aggregate. As previously discussed, some of the strongest specimens were drilled horizontal to deposition. This could indicate that the orientation may influence strength of the material. Most fracture patterns were columnar. These patterns, described in ASTM C469, are irregular and oriented in the axial direction. Very few specimens exhibited shear failure. This may also indicate that the failure mechanism is dictated by the embedded aggregate, and that the aggregate is stronger than the calcareous matrix.

Lastly, one challenge of this project was the correlation of the lab and field geophysical measurements. Although the two scales of measurement are very different, perhaps a relationship does exist. Future work should focus on obtaining more precise and accurate field geophysical measurements to improve the ease of use for the material model by directly correlating the engineering properties to field geophysical measurements.

References

AASHTO. (2014). “AASHTO LRFD Bridge Design Specifications.” Washington D.C.

Ashour, M., and Helal, A. (2014) “Contribution of Vertical Skin Friction to the Lateral Resistance of Large Diameter Shafts” Journal of Bridge Engineering, ASCE, Vol. 19, No. 2, pp. 289–302.

Ashour, M., Norris, G. M., Al-Hamdan, A., and Elfass, S. (2010). “Mobilized Side and Tip Resistances of Piles in Clay.” Journal of Computers and Geotechnics, ELSEVIER, Vol. 37, No. 8, pp. 858-866

Ashour, M. and Norris, G. (2000). “Modeling Lateral Soil-Pile Response Based on Soil-Pile Interaction.” Journal of Geotechnical and Geoenvironmental Engineering, ASCE, Vol. 126, No. 5, pp. 420-428.

Ashour, M., Norris, G., and Pilling, P. (1998). “Lateral Loading of a Pile in Layered Soil Using the Strain Wedge Model.” Journal of Geotechnical and Geoenvironmental Engineering, ASCE, Vol. 124, No. 4, pp. 303-315.

Ashour, M., Pilling, P., Norris, G., and Perez, H.. (1996). “Development of Strain Wedge Model Program for Pile Group Interference and Pile Cap Contribution Effects.” CCEER, Report No. 96-4, Civil Engrg Dept., University of Nevada, Reno.

ASTM Standard, (2010). C469/C469M,(2010). Standard test method for static modulus of elasticity and Piosson’s ratio of concrete in compression.

ASTM Standard, D2845-08 (2008) Standard test method for laboratory determination of pulse velocities and ultrasonic elastic constants of rock. ASTM International, West Conshohocken.

ASTM Standard, (2008). D4543. Standard Practices for Preparing Rock Core as Cylindrical Test Specimens and Verifying Conformance to Dimensional and Shape Tolerances. *Annual Book of ASTM Standards, American Society for Testing and Materials, West Conshohocken, PA*.

ASTM Standard D7012-14. (2014). Standard test methods for compressive strength and elastic moduli of intact rock core specimens under varying states of stress and temperatures. *Annual Book of ASTM Standards*, *4*(9).

Birgül, R. (2009). Hilbert transformation of waveforms to determine shear wave velocity in concrete. *Cement and concrete research*, *39*(8), 696-700.

Briaud, J. L., Smith, T., and Mayer, B. (1984). “Laterally Loaded Piles and the Pressuremeter: Comparison of Existing Methods.” Laterally Loaded Deep Foundations, ASTM, STP 835, pp. 97-111.

Brown, D. A., Turner, J. P., & Castelli, R. J. (2010). *Drilled shafts: Construction procedures and LRFD design methods*. US Department of Transportation, Federal Highway Administration.

Cibor, J. M. (1983, October). Geotechnical considerations of Las Vegas valley. In *Geological environmental and soil properties* (pp. 351-373). ASCE.

Coyle, H. M. and Reese, L. C. (1966). “Load Transfer for Axially Loaded Piles in Clay.” Journal of Soil Mechanics and Foundations Division, ASCE, Vol. 92, NO. SM2.

Design Manual 7.1 (DM 7.1) (1986). “Soil Mechanics.” Naval Facilities Engg. Command, 200 Stovall str., Alexandria, Virginia 22332-2300.

Design Manual 7.2 (DM 7.2) (1986). “Foundations and Earth Structures.” Naval Facilities Eng. Command, 200 Stovall str., Alexandria, Virginia 22332-2300.

Dinçer, İ., Acar, A., & Ural, S. (2008). Estimation of strength and deformation properties of Quaternary caliche deposits. *Bulletin of Engineering Geology and the Environment*, *67*(3), 353-366.

Evans, Jr. L. T., and Duncan, G. M. (1982). "Simplified Analysis of Laterally Loaded Piles. University of California Berkeley, Rept. No. UCB/GT/82-04; 1982.

Goodman, R. E. (1989). *Introduction to rock mechanics* (Vol. 2). New York: Wiley.

Gowda, P. (1991). “Laterally Loaded Pile Analysis for Layered Soil Based on the Strain Wedge Model.” M. S. Thesis, University of Nevada, Reno.

Hudson, J. A., & Harrison, J. P. (2000). *Engineering rock mechanics: an introduction to the principles*. Elsevier.

Hughes, J. M. O., Goldsmith, P. R., and Fendall H.D.W. 1978. “The Behavior of Piles to Lateral Loads.” Civil Engg. Dept., Univ. of Auckland, Auckland, New Zealand, Report No. 178.

Jamshidi, A., Nikudel, M. R., Khamehchiyan, M., & Sahamieh, R. Z. (2016). The effect of specimen diameter size on uniaxial compressive strength, P-wave velocity and the correlation between them. *Geomechanics and Geoengineering*, *11*(1), 13-19.

Karakouzian, M., Afsharhasani, R., & Kluzniak, B. Elastic Analysis of Drilled Shaft Foundations in Soil Profiles with Intermediate Caliche Layers. In *IFCEE 2015* (pp. 922-928).

Korkmaz, N., & Ceryan, N. (2011). Example for the Prediction of the Umconfined Compressive Strength of Weathered Rocks Using the Weathering Indices Based on P-Wave Velocity. *International Multidisciplinary Scientific GeoConference: SGEM: Surveying Geology & mining Ecology Management*, *1*, 347.

Liu, Z., Shao, J., Xu, W., & Wu, Q. (2015). Indirect estimation of unconfined compressive strength of carbonate rocks using extreme learning machine. *Acta Geotechnica*, *10*(5), 651-663.

Louie, J. N. (2001). Faster, better: shear-wave velocity to 100 meters depth from refraction microtremor arrays. *Bulletin of the Seismological Society of America*, *91*(2), 347-364.

Mackiewicz, S. M., & Lehman-Svoboda, J. (2012). Measured versus predicted side resistance of drilled shafts in a heterogeneous soil profile. In *GeoCongress 2012: State of the Art and Practice in Geotechnical Engineering* (pp. 2412-2421).

Matlock, H. and Reese, L. C. (1961). "Generalized Solution for Laterally Loaded Piles." Journal of Soil Mechanics and Foundations Division, ASCE, Vol. 86, No. SM5, pp. 673-694.

Motamed, R., Elfass, S., & Stanton, K. (2016). *LRFD Resistance Factor Calibration for Axially Loaded Drilled Shafts in the Las Vegas Valley* (No. Report No. 515-13-803).

NAVFAC (1982). "Foundations and Earth Retaining Structures Design manual." Dept. of navy, DM 7.2, Alexandria, VA.

Nefeslioglu, H. A. (2013). Evaluation of geo-mechanical properties of very weak and weak rock materials by using non-destructive techniques: Ultrasonic pulse velocity measurements and reflectance spectroscopy. *Engineering Geology*, *160*, 8-20.

Norris, G. M. (1977). "The Drained Shear Strength of Uniform Quartz Sand as Related to Particle Size and Natural Variation in Particle Shape and Surface Roughness." Ph.D. Thesis, University of California , Berkeley, 523 pp.

Norris, G. M. (1986). "Theoretically Based BEF Laterally Loaded Pile Analysis." Third International Conference on Numerical Methods in Offshore Piling, Nantes, France, pp. 361-386.

Ott, Tom. Personal Communication. 2017

Park, C. B., Miller, R. D., Xia, J., & Ivanov, J. (2007). Multichannel analysis of surface waves (MASW)—active and passive methods. *The Leading Edge*, *26*(1), 60-64.

Reese, L. C. (1958). "Discussion of Soil Modulus for Laterally Loaded Piles." by Bramlette McClelland and John A. Focht, Jr., Transactions, ASCE, Vol. 123, pp. 1071.

Reese, L. C. (1977). "Laterally Loaded Piles: Program Documentation." Journal of Geotechnical Engineering, ASCE, Vol. 103, No. GT4, pp. 287-305.

Reese, L. C. (1983). "Behavior of Piles and Pile Groups Under Lateral Load." Report to the U.S. Department of Transportation, Federal Highway Administration, Office of Research, Development, and Technology, Washington, D.C.

Richart, E. F. (1975). “Some Effects of dynamic Soil Properties on Soil-Structure Interaction.” J. of Geotech. Engg. Division,. ASCE, Vol. 101, GT12, pp. 1197-1240

Rinne, E., Thompson, J., & Vanderpool, W. (1996). I-15/US 95 load test program, Las Vegas, Nevada. *Rep. No. 31-215903-07A*.

Rowe, P. W. (1956). “The Single Pile Subject to Horizontal Force.” Geotechnique, Vol. 6.

Rucker, M. L. (2008). Estimating in situ geo-material mass density, modulus and unconfined compressive strength from field seismic velocity measurements. In *Highway Geophysics—Nondestructive Evaluation Conference, Charlotte, NC, December* (pp. 1-4).

Rucker, M. L., & Fergason, K. C. (2006). Characterizing unsaturated cemented soil profiles for strength, excavatability and erodability using surface seismic methods. In *Unsaturated Soils 2006* (pp. 589-600).

Skempton, A. W. (1951). “The Bearing capacity of Clays.” Proceedings, Bldg, Research Congress, Inst. Og Civil Engineering, London, Eng., 1951, Vol. I.

Skempton, A. W. (1954). “The Pore Pressure Coefficients A and B.” Geotechnique, 4, pp. 148.

Stone, R. C., Luke, B., Jacobson, E., & Werle, J. (2001, March). An overview of engineering with cemented soils in Las Vegas. In *Luke B. Jacobson E. Werle J., eds., Proceedings: 36 th Annual Symposium on Engineering Geology and Geotechnical Engineering* (pp. 135-144).

Stone, R., Karakouzian, M., Afsharhasani, R. “The Stiffening Effect of A Caliche Layer on Pile Foundations.” (pp 513-518)

Terzaghi, K. (1955). “Evaluation of Coefficients of Subgrade Reaction.” Geotechnique, Vol. 5, No. 4, pp. 297-326.

Tecle, M., Giorgis, A., Luke, B., Elfass, S., Norris, G., & Watters, R. (2003). Comparison of seismic downhole to crosshole measurements in a complex-layered system. In *Proc., 38th Ann. Symp. Eng. Geology and Geotechnical Eng* (pp. 217-232).

Tomlinson, M. J. (1957). “The Adhesion of Piles Driven in Clay Soils.” Proceedings of Fourth International Conf. on Soil mechanics and Foundation Engrg, Vol. II, London, pp. 66-71.

Tuncay, E., & Hasancebi, N. (2009). The effect of length to diameter ratio of test specimens on the uniaxial compressive strength of rock. *Bulletin of engineering geology and the environment*, *68*(4), 491.

Werle, J. L., & Luke, B. (2007). Engineering with heavily cemented soils in Las Vegas, Nevada. In *Problematic soils and rocks and in situ characterization* (pp. 1-9).

Wu, T. H. (1966). Soil Mechanics, Boston, Allyn and Bacon Inc., pp. 169.

Yaman, I. O., Inci, G., Yesiller, N., & Aktan, H. M. (2001). Ultrasonic pulse velocity in concrete using direct and indirect transmission. ACI Materials Journal, 98(6), 450.

Zafir, Z. and Vanderpool, W. (1998). "Lateral Response of Large Diameter Drilled Shafts: I-15/US 95 Load Test Program." 33rd Engineering Geology and Geotechnical Engineering Symposium, March 25-27, Reno, Nevada, pp. 161-176.

Appendix A:

Table Showing Measured and Assessed Data for All Test Specimens

#	Sample	Length	Diameter	L/D	Mass	Volume	Unit Weight	Moisture Content	UCS	Elastic Modulus	Vp [54kHz]	Vp [150KHz]	Vp [250KHz]	Vs [250kHz]
		ft	ft		pounds	ft^3	lb/ft^3	%	psi	psi	ft/s	ft/s	ft/s	ft/s
1	C-1-1	0.591	0.229	2.58	3.89	0.0243	159.86	0.30%	6668					
2	C-2-1	0.479	0.229	2.09	2.77	0.0197	140.61	2.60%	1270					
3	A-1-1	0.583	0.25	2.33	2.69	0.0286	94.21	0.06%	37					
4	C-1-2	0.502	0.229	2.19	3.33	0.0070	161.31	0.12%	10540	7007978	18525	18101	18091	10379
5	C-1-3	0.497	0.229	2.17	3.35	0.0205	163.57	0.18%	13401	6022471	18201	18113	18403	10797
6	C-1-4	0.497	0.228	2.18	3.29	0.0202	162.74	0.54%	12850		18324	18091	18049	11078
7	C-1-5	0.499	0.229	2.18	3.34	0.0205	162.53	0.52%	11366		18420	18142	18044	11083
8	C-1-6	0.494	0.229	2.16	3.30	0.0203	162.44	0.20%	13773	5225358	17595	16994	16782	10144
9	C-1-7	0.505	0.229	2.21	3.34	0.0208	160.62	0.81%	4601		17837	17933	17890	10315
10	C-1-8	0.479	0.228	2.10	3.21	0.0196	164.02	0.55%	6757.5		17560	17813	17560	10261
11	C-1-9	0.494	0.227	2.17	3.29	0.0200	164.12	0.45%	10876		18508	18508	18382	10443
12	C-1-10	0.36	0.177	2.03	1.49	0.0089	167.98	0.11%	13618	5245358	18965	19080	18915	10719
13	C-1-11	0.365	0.177	2.06	1.49	0.0090	166.25	0.13%	15844	5996064	18656	18719	18501	11142
14	C-1-12	0.365	0.177	2.06	1.47	0.0090	163.27	0.15%	8885	4259277	17838	17969	18069	9946
15	C-1-13	0.365	0.177	2.06	1.50	0.0090	167.18	0.10%	15365	5250854	19274	19292	19273	10206
16	C-1-14	0.411	0.229	1.79	2.69	0.0169	159.33	0.35%	4574	2345881	16919	16563	16332	9595
17	HC-1-1	0.407	0.173	2.35	1.58	0.0096	164.87	0.10%	14262	5884148	18433	18772	19082	9577
18	HC-1-2	0.416	0.173	2.40	1.58	0.0098	161.19	0.10%	13937	5529281	18187	18075	18302	10029
19	HC-1-3	0.421	0.173	2.43	1.61	0.0099	162.95	0.13%	16284	5685357	18164	18332	18279	10325
20	HC-1-4	0.321	0.173	1.86	1.25	0.0075	166.04				0	0	0	0
21	HC-1-5	0.409	0.173	2.36	1.59	0.0096	165.97	0.08%	20325	6397230	19159	19871	20001	10967
22	A-7-1	0.453	0.228	1.99	2.73	0.0185	147.48	0.31%	1833	841169	14404	14481	14423	8080
23	A-7-2	0.451	0.228	1.98	2.80	0.0185	151.73	0.26%	3540	1521402	14589	14822	14604	8197
24	A-7-3	0.342	0.227	1.50	2.18	0.0139	156.71	0.08%	7763	3560550	15859	15798	15618	8955
25	A-7-5	0.343	0.175	1.96	1.25	0.0083	151.08	0.12%	4340	1587998	14515	14599	14290	9253
26	A-8-1	0.362	0.227	1.59	2.22	0.0147	151.55	0.06%	4662	2403092	14788	14579	14363	8089
27	C-2-2	0.489	0.229	2.14	2.85	0.0201	142.04	0.52%	3177	1792325	12933	13910	13479	8678
28	C-2-3	0.362	0.229	1.58	2.18	0.0149	146.22	0.71%	1846	1590282	14107	14787	14688	8783
29	C-2-4	0.297	0.229	1.30	1.68	0.0122	137.08	1.22%	1504	1780724	11718	11547	11411	6888
30	A-2-1	0.276	0.229	1.21	1.41	0.0114	123.7	1.50%	1901	647359	9258	9324	9313	5813
31	A-3-1	0.286	0.229	1.25	1.29	0.0118	109.59	1.60%	788	243978	7147	6877	6817	4156
32	A-4-1	0.297	0.229	1.30	1.53	0.0122	125.61	1.20%	1666	537776	9647	9159	8988	5909

#	Sample	Length	Diameter	L/D	Mass	Volume	Unit Weight	Moisture Content	UCS	Elastic Modulus	Vp [54kHz]	Vp [150KHz]	Vp [250KHz]	Vs [250kHz]
		ft	ft		pounds	ft^3	lb/ft^3	%	psi	psi	ft/s	ft/s	ft/s	ft/s
33	A-4-2	0.281	0.229	1.23	1.41	0.0116	121.72	1.50%	1383	399824	8516	8609	8843	5331
34	B-1-1	0.270	0.230	1.17	1.62	0.0112	144.73	0.39%	3316	939803	11920	11943	11709	6682
35	B-2-1	0.358	0.227	1.58	2.08	0.0145	143.70	0.70%	2168	826220	12367	11963	11353	6913
36	B-2-2	0.354	0.228	1.55	2.12	0.0144	147.02	0.39%	2998	629726	10706	10082	9096	5896
37	C-4-2	0.360	0.229	1.58	2.05	0.0148	139.05	0.38%	2669	792538	11449	11042	10775	6845
38	B-3-1	0.408	0.228	1.79	2.30	0.0166	138.32	0.77%	1572	371245	10651	6348	6577	5570
39	C-4-1	0.295	0.228	1.30	1.69	0.0120	140.46	0.34%	2871	923899	10632	10198	9625	6420
40	C-4-3	0.314	0.227	1.38	1.82	0.0127	143.26	0.45%	6228	1297662	10393	9415	9613	5385
41	C-7-1	0.501	0.227	2.20	2.88	0.0203	141.57	0.77%	1582	985915	10236	8321	7967	4556
42	C-7-2	0.346	0.228	1.52	1.80	0.0141	128.38	0.13%	2799	1768832	12463	12431	11824	7732
43	C-7-3	0.346	0.228	1.52	1.87	0.0140	133.40	0.19%	1634	7070604	10572	9992	8762	5309
44	C-8-1	0.299	0.227	1.32	1.82	0.0121	149.95	0.28%	2960	1533519	10749	10573	10432	6741
45	C-8-2	0.420	0.227	1.85	2.22	0.0170	131.17	0.77%	1394	741410	10208	10249	10231	6122
46	B-4-1	0.394	0.228	1.73	2.50	0.0160	155.55	0.47%	6982	3290292	15677	15563	15503	10053
47	B-4-2	0.351	0.228	1.54	2.17	0.0143	152.10	0.20%	4639	3233203	15862	15659	15119	9161
48	B-4-3	0.375	0.228	1.64	2.33	0.0153	152.94	0.32%	2577	1560266	14961	14678	11493	7968
49	B-4-4	0.471	0.228	2.07	3.05	0.0192	158.96	0.24%	10791	4410201	16624	16488	15606	9097
50	B-4-5	0.421	0.228	1.85	2.55	0.0171	148.91	0.29%	3249	2999446	15091	14808	14595	8444
51	B-4-6	0.438	0.228	1.92	2.85	0.0179	159.58	0.22%	9070	4836817	16944	16934	16968	10262
52	B-4-7	0.342	0.228	1.50	2.18	0.0139	156.86	0.19%	14100	3947147	17072	16604	16366	9711
53	B-4-8	0.379	0.228	1.66	2.42	0.0155	156.45	0.21%	7240	5625485	16536	16038	13483	8742
54	B-5-1	0.338	0.228	1.48	2.03	0.0138	147.42	0.29%	6468	2765284	15446	15101	14625	8492
55	B-5-2	0.423	0.228	1.86	2.52	0.0172	146.63	4.37%	2801	1385452	14226	13824	10992	8685
56	B-5-3	0.521	0.228	2.29	3.10	0.0212	145.93	0.50%	3776	1828217	14226	14056	13926	8343
57	B-5-4	0.390	0.228	1.71	2.36	0.0159	148.61	0.49%	4631	2154490	14878	14491	13357	8572
58	B-5-5	0.473	0.228	2.08	2.80	0.0193	145.67	0.51%	5008	1980229	14143	13899	14022	7784
59	B-5-6	0.299	0.228	1.31	1.82	0.0122	149.84	0.41%	5108	1747400	15361	15168	14742	8766
60	B-5-7	0.331	0.228	1.46	2.01	0.0135	148.72	0.50%	3847	1023362	13679	13294	11699	7369
61	C-3-1	0.656	0.250	2.62	2.82	0.0322	87.73				4227	3095	3138	1627
62	C-3-2	0.760	0.250	3.04		0.0373	0.00							

#	Sample	Length	Diameter	L/D	Mass	Volume	Unit Weight	Moisture Content	UCS	Elastic Modulus	Vp [54kHz]	Vp [150KHz]	Vp [250KHz]	Vs [250kHz]
		ft	ft		pounds	ft^3	lb/ft^3	%	psi	psi	ft/s	ft/s	ft/s	ft/s
63	C-3-3	0.760	0.250	3.04	2.86	0.0373	76.70	0.00%	38	15525	4126	3793	3810	2344
64	C-3-4	0.656	0.250	2.62	3.04	0.0322	94.42	0.00%	45	21107	4157	2695	2457	1754
65	C-3-5	0.719	0.250	2.88	3.18	0.0353	90.06				3903	3275	2878	1966
66	C-3-6	0.890	0.250	3.56	4.30	0.0437	98.38				4252	2904	2381	2044
67	C-3-7	0.864	0.250	3.46	3.31	0.0424	78.13							
68	A-5-1	0.625	0.250	2.50	2.59	0.0307	84.41							
69	A-5-2	0.625	0.250	2.50	2.70	0.0307	88.07							
70	A-5-3	0.625	0.250	2.50	2.76	0.0307	90.09							
71	C-4-1	0.625	0.250	2.50	2.63	0.0307	85.74							
72	A-6-1	0.563	0.245	2.30	2.69	0.0264	101.94				3342			1278
73	A-6-2	0.625	0.242	2.58	3.00	0.0287	104.42				2627			1304
74	A-6-3	0.604	0.247	2.44	2.98	0.0290	102.80				2284			1151
75	A-6-4	0.583	0.247	2.36	2.82	0.0279	100.80				2317			1273
Aluminium		0.583	0.233		4.21	0.0249	168.91				20638			9939
Concrete		0.661	0.333		8.28	0.0577	143.60				14204			8254

Appendix B

Data Sheets for All Test Specimens

Sample #	Investigator	Date
A-2-1	**Saint-Pierre**	**1/16/2018**

Failure Mechanism: Based on ASTM C39

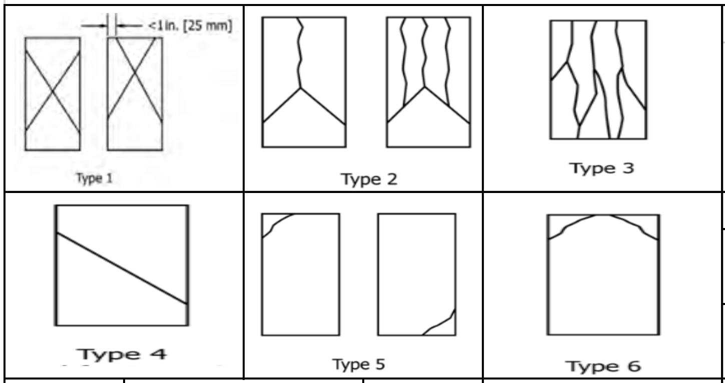

Type of Failure(s): type 3

Diameter rock vs. diameter core: 0.45

L > 2.5*D ? No

E (psi)	596746	$\varepsilon_{50(\%)}$	0.199	Diameter (ft)	0.23
Vs (ft/s)	5813	ν	0.18	Length (ft)	0.28
Vp(ft/s)	9528	γ (lb/ft^3)	123.7	UCS (psi)	1900.00

Measured largest Aggregate:	Position of Large Aggregate	Percent Aggregate	Percent matrix
1.25 inches	bottom surface	3%	97%

Notes

Weakly cemented matrix. Noticeable difference between the top and bottom halves. Lower half has many voids and irreguarities from drilling while the upper half does not. Most fracturing occurred in the lower half. Scattered fin dolomite gravels. Several large chunks of what appear to be more cemented matrix. In this instance, they were counted as gravels seeing as how the level of cementation was so different.

Initial Sample

Pictures:

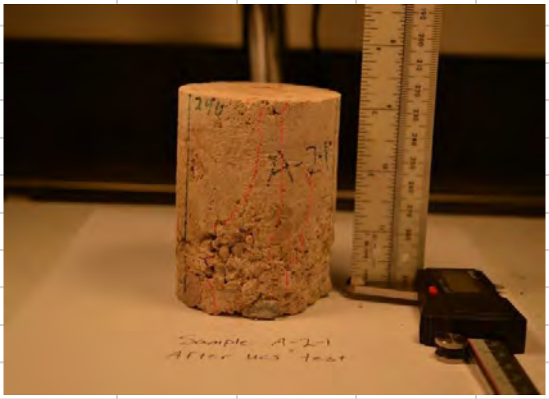

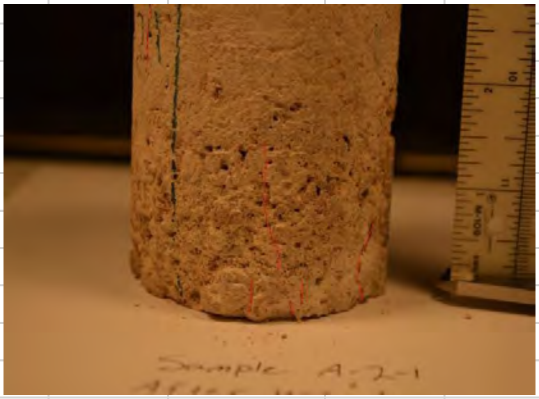

Sample #	Investigator	Date
A-3-1	Saint-Pierre	1/16/2018

Failure Mechanism: Based on ASTM C39

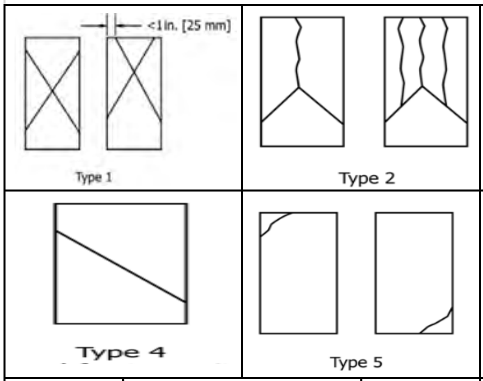

<1 in. [25 mm]
Type 1
Type 2
Type 3
Type 4
Type 5
Type 6

Type of Failure(s):	Type 3
Diameter rock vs. diameter	0.12
L > 2.5*D ?	No

E (psi)	276632	ε_{50} (%)	0.048149	Diameter (ft	0.23
Vs (ft/s)	4156	ɥ	0.2	Length (ft)	0.29
Vp (ft/s)	7147	ɣ (lb/ft^3)	109.59	UCS (psi)	788.00

Measured largest Aggregate:	Position of Large Aggregate	Percent Aggregate	Percent matrix
0.32 inches	bottom surface	1%	99%

Notes	Initial Sample
Sample had large pre-existing voids from drilling. Smaller pinhole voids throughout sample. Specimen was not tested to total failure so failure mechanism is not clear. Verticl fractures indicate columnar failure. Few scattered fine gravels. Noticeable clusters of matrix with increased cementation.	

Pictures:

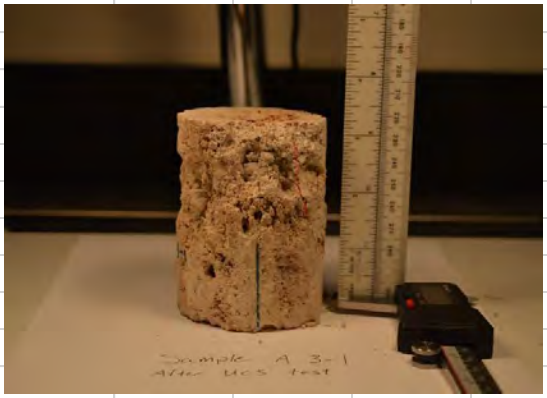

Sample A 3-1
After UCS test

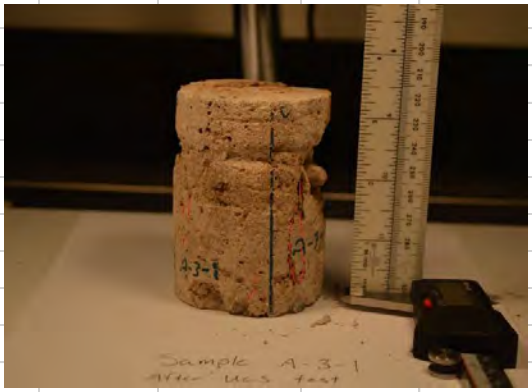

Sample A-3-1
After UCS test

Sample #	Investigator	Date
A-4-1	Saint-Pierre	1/16/2018

Failure Mechanism: Based on ASTM C39

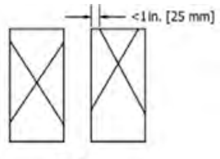 Type 1	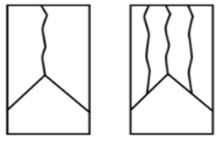 Type 2	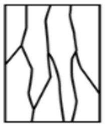 Type 3	Type of Failure(s): type 3, type 5
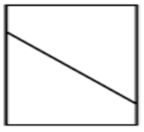 Type 4	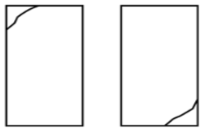 Type 5	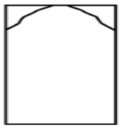 Type 6	Diameter rock vs. diameter core 0.16 L > 2.5*D ? No

E (psi)	556199	ε_{50} (%)	0.1549	Diameter (ft	0.23
Vs (ft/s)	5909	ɥ	0.2	Length (ft)	0.30
Vp (ft/s)	9647	ɣ (lb/ft^3)	125.6	UCS (psi)	1666

Measured largest Aggregate:	Position of Large Aggregate	Percent Aggregate	Percent matrix
0.44 inch	near upper surface	1%	99%

Notes	Initial Sample
Sample is fairly soft and had many pre-existing voids before testing. Voids seem to not alter path of fractures. Several side failures visible. Probably due to pre-existing weakness or fractures within sample. Few aggregates visibel but are fine to medium. Cemented matrix aggregate noticeable on both top and bottom surfaces.	

Pictures:

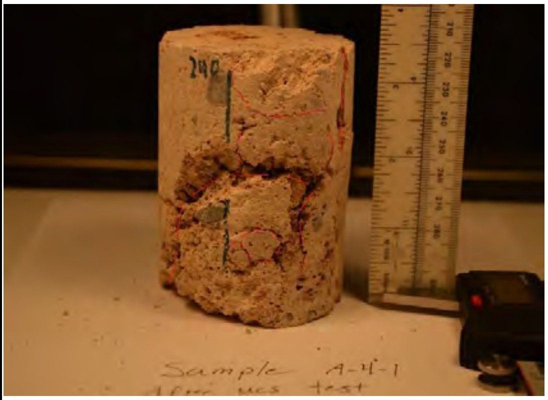

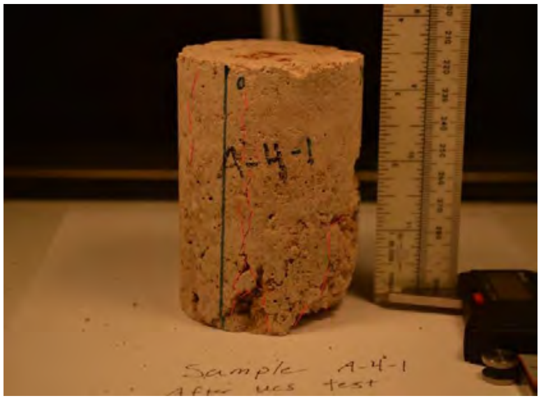

Sample #	Investigator	Date
A-4-2	Saint-Pierre	1/16/2018

Failure Mechanism: Based on ASTM C39

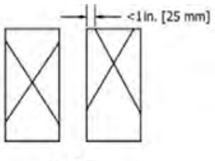 Type 1	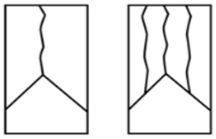 Type 2	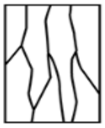 Type 3	Type of Failure(s): Type 3, Type 5
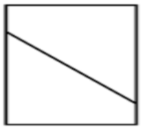 Type 4	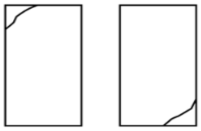 Type 5	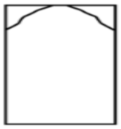 Type 6	Diameter rock vs. diameter core 0.06 L > 2.5*D ? No

E (psi)	395450	ε_{50} (%)	0.3828	Diameter (ft	0.23
Vs (ft/s)	5331	ɥ	0.18	Length (ft)	0.28
Vp (ft/s)	8516	ɣ (lb/ft^3)	121.718	UCS (psi)	1383

Measured largest Aggregate:	Position of Large Aggregate	Percent Aggregate	Percent matrix
0.17 inch	bottom surface	1%	99%

Notes

Samle is full of voids visible on the specimen surface. Vertical fractures travel through a void concentration and is difficult to follow failure. One fracture almost develops as shear but is confined to one side, so is similar toa side fracture. On both upper and lower surfaces, fine aggregate looking concentration visible. They are more cemented matrix. Very few aggregates throughout sample.

Initial Sample

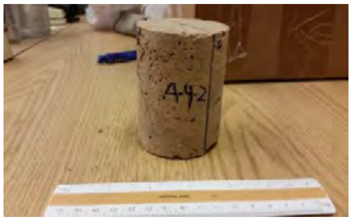

Pictures:

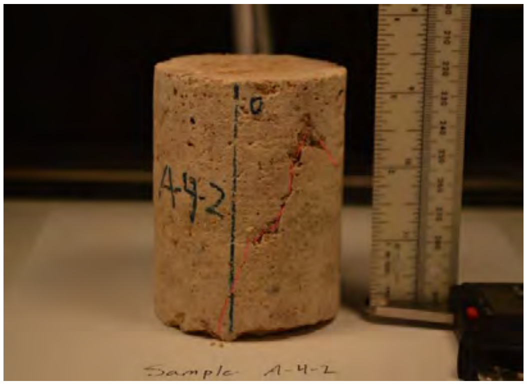

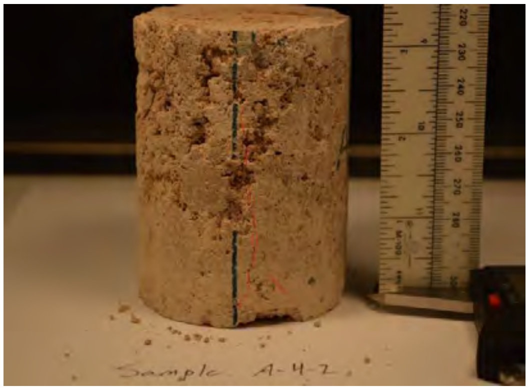

Sample #	Investigator	Date	
A-7-1	Saint-Pierre	1/11/2018	
Failure Mechanism: Based on ASTM C39			
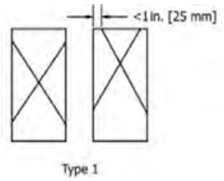 Type 1	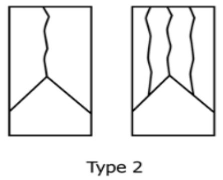Type 2	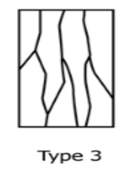Type 3	Type of Failure(s): Type 3
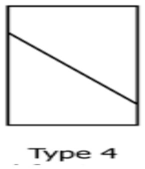Type 4	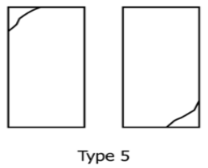Type 5	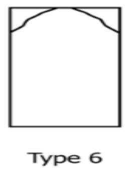Type 6	Diameter rock vs. diameter 1.98 L > 2.5*D no

E (psi)	886950	ε_{50} (%)	0.05	Diameter	0.23
Vs (ft/s)	8080	ɥ	0.27	Length	0.45
Vp (ft/s)	14404	ɣ (lb/ft^3)	147.479	UCS	1840.00

Measured largest Aggregate:	Position of Large Aggregate	Percent Aggregate	Percent matrix
1.23 inches	bottom surface	25%	75%

Notes	Initial Sample
Large pre-existing voids from drilling. Because of this, fracturing is not continuous and disapears into the sample. Aggregate is a mix of fine to large gravels. Matrix reacts violently to 5% HCl. Top of sample has many more fine aggregate while bottom is a mix with more larger gravels. Fracturing does no pass through any gravels due to the weak matrix. No lateral movement in fractures when intersecting voids.	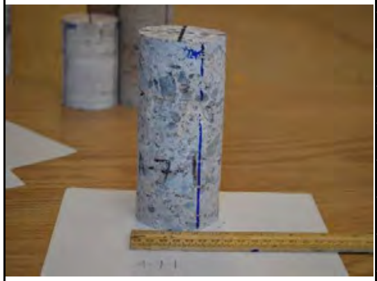

Pictures:

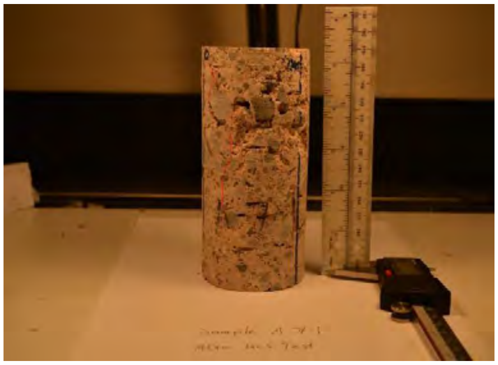

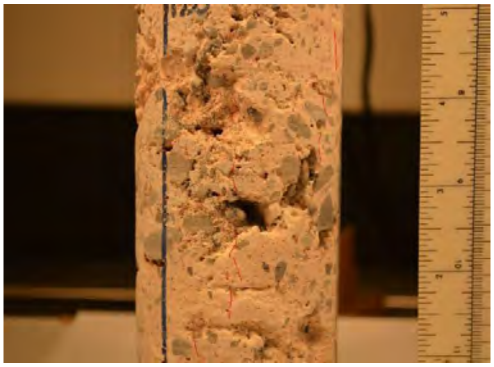

Sample #	Investigator	Date
A-7-2	Saint-Pierre	1/11/2018
Failure Mechanism: Based on ASTM C39		

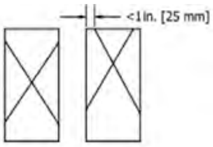 Type 1	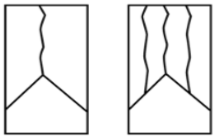 Type 2	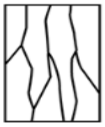 Type 3	Type of Failure(s): Type 3
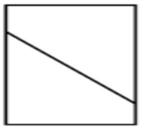 Type 4	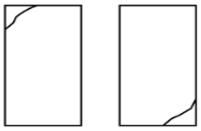 Type 5	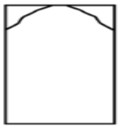 Type 6	Diameter rock vs. diameter core 1.97
			L > 2.5*D ? yes

E (psi)	1584114	ε_{50} (%)	0.07527	Diameter (ft)	0.23
Vs (ft/s)	8197	ųMu	0.27	Length (ft)	0.45
Vp (ft/s)	14589	ɣ (lb/ft^3)	151.72	UCS (psi)	3540.00

Measured largest Aggregate:	Position of Large Aggregate	Percent Aggregate	Percent matrix
1.15 inches	top surface	30%	70%

Notes	Initial Sample
Fine to medium gravels throughout sample. Bottom of sample has smaller gravels while the top has small and medium indicating the top is stratigraphically downward. Many natural voids throughout section. Matrix is weaker than aggreagte. Almost no aggregate is bisected by fracturing. Many fractures are not continuous.	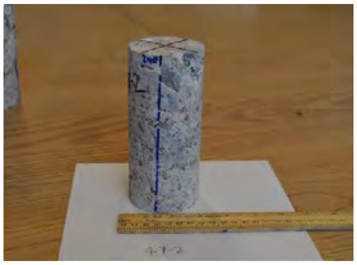

Pictures:

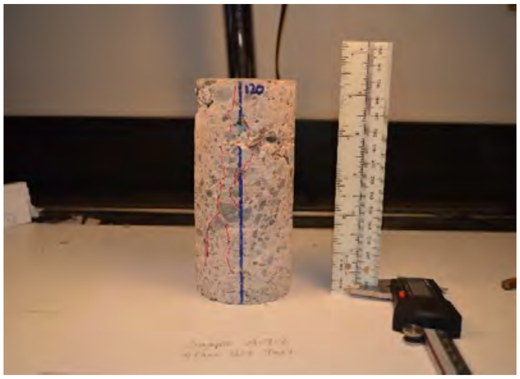

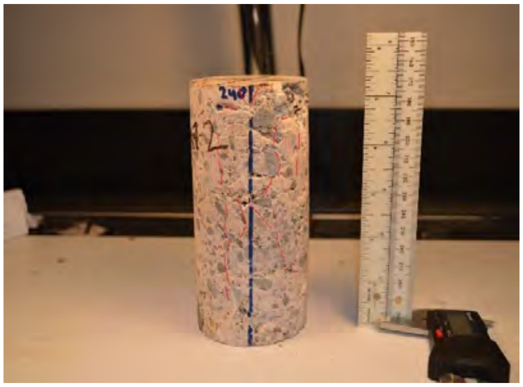

Sample #	Investigator	Date
A-7-3	Saint-Pierre	1/6/2018

Failure Mechanism: Based on ASTM C39

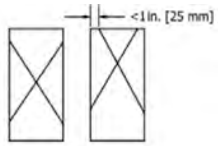 Type 1	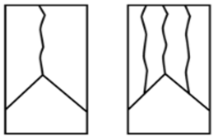 Type 2	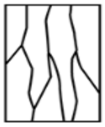 Type 3	Type of Failure(s): Type 3, Type 4
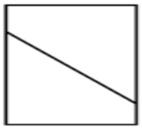 Type 4	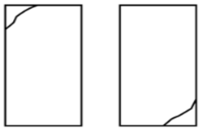 Type 5	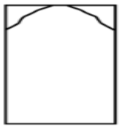 Type 6	Diameter rock vs. diameter 1.50 L > 2.5*D ? No

E (psi)	3057113	ε_{50} (%)	0.1175	Diameter (ft	0.23
Vs (ft/s)	8955	ɥ	0.27	Length (ft)	0.34
Vp (ft/s)	15859	γ (lb/ft^3)	156.7	UCS (psi)	7467.64

Measured largest Aggregate:	Position of Large Aggregate	Percent Aggregate	Percent matrix
.94 inches	near top of sample	10%	90%

Notes	Initial Sample
Aggregate is sub-angular to rounded. Mostly Dolomite. Small pinhole cavaties throughout specimen. Noticeable voids around aggregate. Aggregate is mostly fine, with a few larger gravels. Fracturing shows cracking both around and through gravels. Fracturing only shows on one end or the sample.	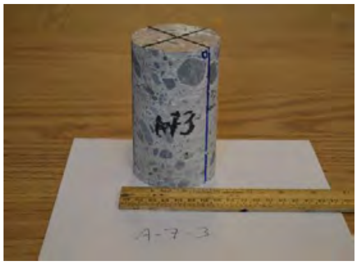

Pictures:

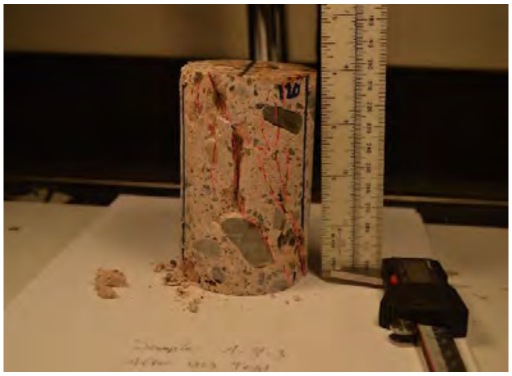

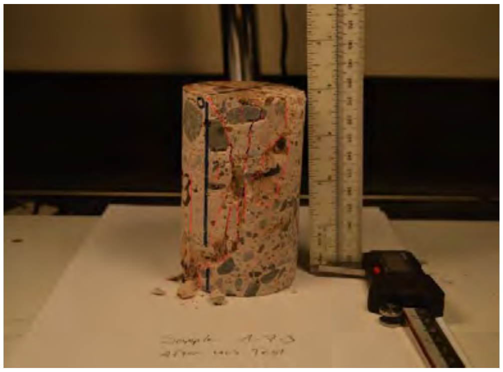

Sample #	Investigator	Date
A-7-5	Saint-Pierre	1/16/2018

Failure Mechanism: Based on ASTM C39

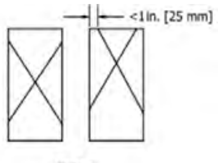 Type 1	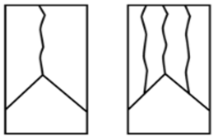 Type 2	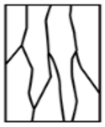 Type 3	Type of Failure(s): type 3
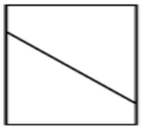 Type 4	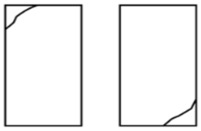 Type 5	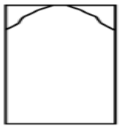 Type 6	Diameter rock vs. diameter core 0.37 L > 2.5*D ? no

E (psi)	18118378	ε_{50} (%)	0.4116	Diameter (ft)	0.18
Vs (ft/s)	9253	ɥ		Length (ft)	0.34
Vp (ft/s)	14515	ɣ (lb/ft^3)	151.07	UCS (psi)	4340.00

Measured largest Aggregate:	Position of Large Aggregate	Percent Aggregate	Percent matrix
0.78 inch	middle	25%	75%

Notes

Many fine to medium gravels with scattered large gravels. Fractures prefer to go around larger gravels while bisecting smaller gravels. Some pre-existing voids that appear deep. Others created by failure.

Initial Sample

Pictures:

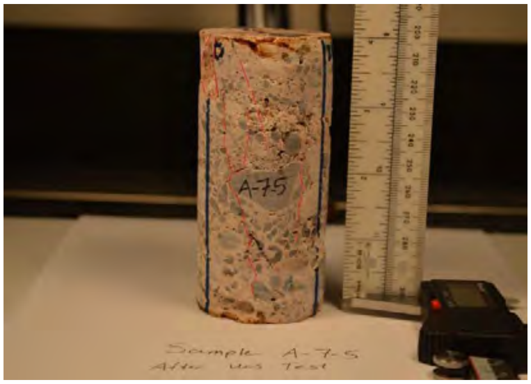

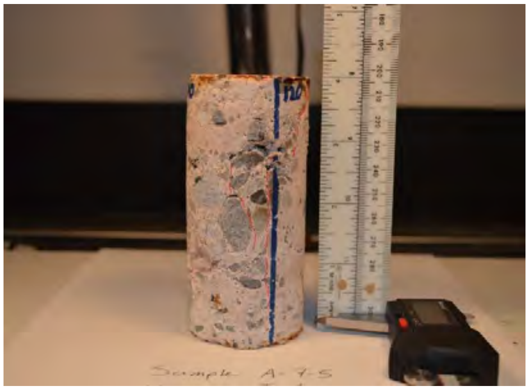

Sample #	Investigator	Date
A-8-1	Saint-Pierre	1/6/2018

Failure Mechanism: Based on ASTM C39

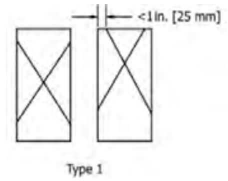

Type 1

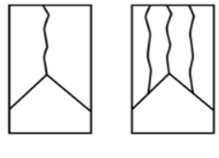

Type 2

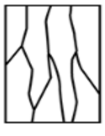

Type 3

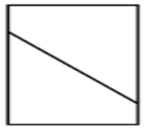

Type 4

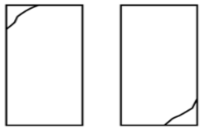

Type 5

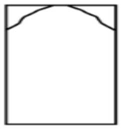

Type 6

Type of Failure(s): Type 3-Columnar

Diameter rock vs. diameter core: 0.18

L > 2.5*D ? No

E (psi)	2469783	ε_{50} (%)	0.2419	Diameter (ft)	0.23
Vs (ft/s)	8089	ɥ	0.29	Length (ft)	0.36
Vp (ft/s)	14788	ɣ (lb/ft^3)	151.55	UCS (psi)	4662.00

Measured largest Aggregate:	Position of Large Aggregate	Percent Aggregate	Percent matrix
.5 inches	bottom	15%	85%

Notes

Aggregate is mostly rounded. Mostly fine and some are elongated. Most fractures appear to travel around aggregate. Possibly because most of the gravels are circular and rounded. One inch elongated void at bottom of sample which altered course of one failure plane. Some other failure planes appear to travel from void to void Fine gravels become less frequent moving downward with sample. Few gravels which become larger. For the elongated gravels, fractures go through the aggregate and not aroound. Some areas of sample with fresh fractures show white clacium carbonate that reacts violently with 5% HCl

Initial Sample

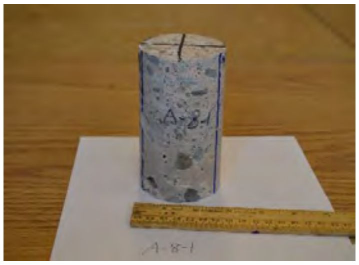

Pictures:

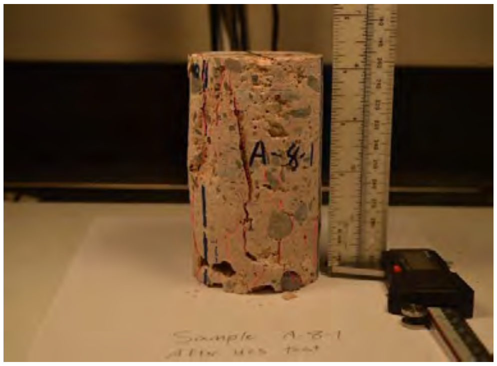

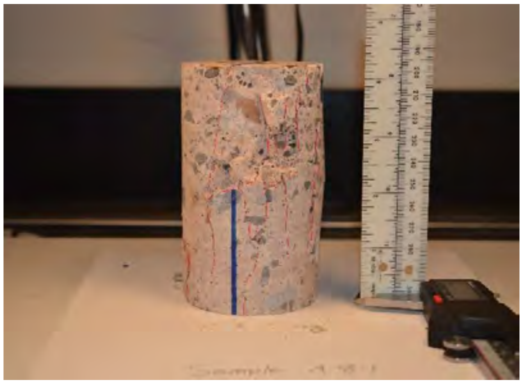

Sample #	Investigator	Date
B-1-1	Saint-Pierre	1/16/2018

Failure Mechanism: Based on ASTM C39

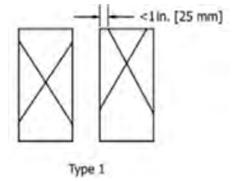 Type 1	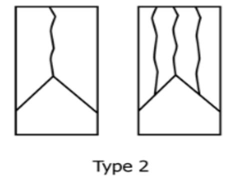 Type 2	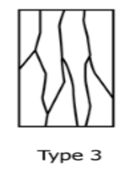 Type 3	Type of Failure(s): type 3
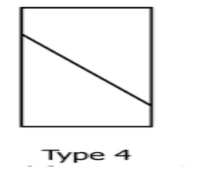 Type 4	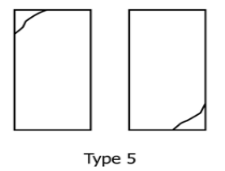 Type 5	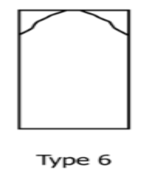 Type 6	Diameter rock vs. diameter core 0.06 L > 2.5*D ? No

E (psi)	1039170	ε_{50} (%)	0.1549	Diameter (ft)	0.23
Vs (ft/s)	6682	ɥ	0.26	Length (ft)	0.27
Vp (ft/s)	11920	ɣ (lb/ft^3	144.72	UCS (psi)	3316.00

Measured largest Aggregate:	Position of Large Aggregate	Percent Aggregate	Percent matrix
0.16 inch	bottom surface	1%	99%

Notes	Initial Sample
Fairly uniform matrix. Small linear voids surrounding sample. Few fine gravels throughout specimen. Vertical fractures step laterally with voids. Some gray colors on sample from concrete mix.	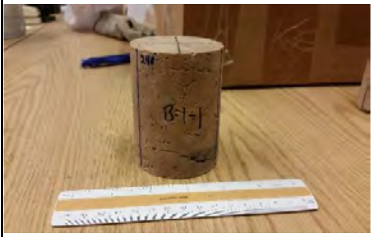

Pictures:

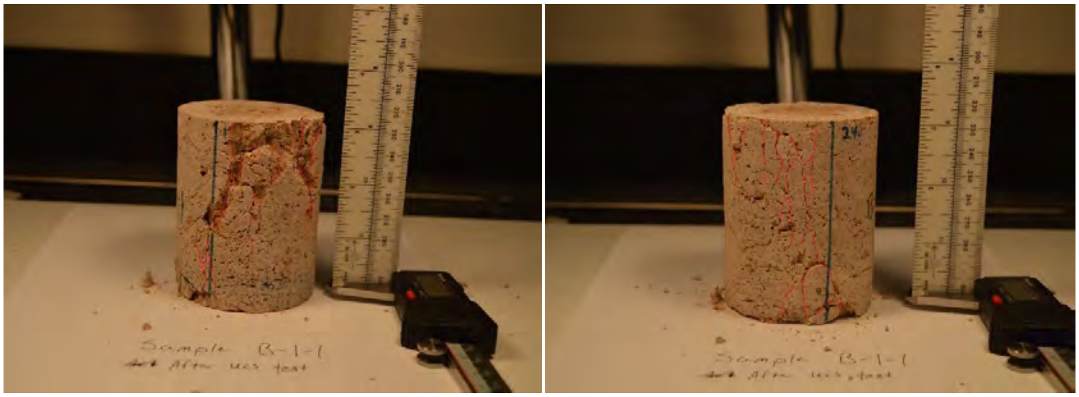

Sample #	Investigator	Date
B-2-1	Saint-Pierre	1/7/2018

Failure Mechanism: Based on ASTM C39

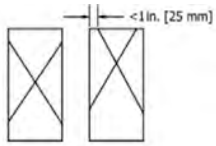 Type 1	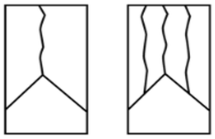 Type 2	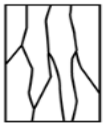 Type 3	Type of Failure(s): Type 3
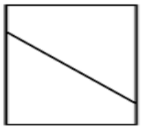 Type 4	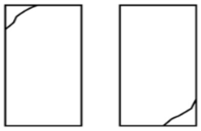 Type 5	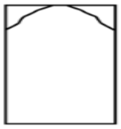 Type 6	Diameter rock vs. diameter core 0.21 L > 2.5*D ? No

E (psi)	762660	ε_{50} (%)	0.1302	Diameter (ft)	0.23
Vs (ft/s)	6913	ų	0.21	Length (ft)	0.36
Vp (ft/s)	12367	ɣ (lb/ft^3)	143.7	UCS (psi)	2168

Measured largest Aggregate:	Position of Large Aggregate	Percent Aggregate	Percent matrix
.56 inches	top of sample	2%	98%

Notes	Initial Sample
Specimen is mostly a weaker, brown matrix. Reacts slightly to 5% HCl. No fractures go through the rounded gravel. Probably because gravel is so much stronger than matrix. On upper plane of sample, significant failure that goes around dolomite gravel. Short and discontinuous lineations with small pinhole voids. No prefered orientation. SOme areas where matrix is darker and more smooth, probably increased cementation.	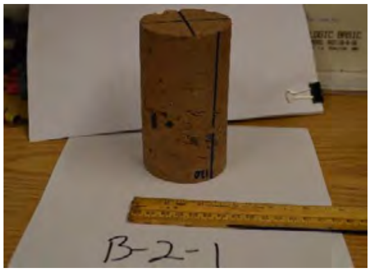

Pictures:

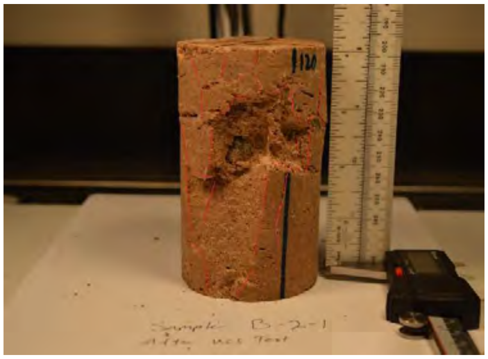

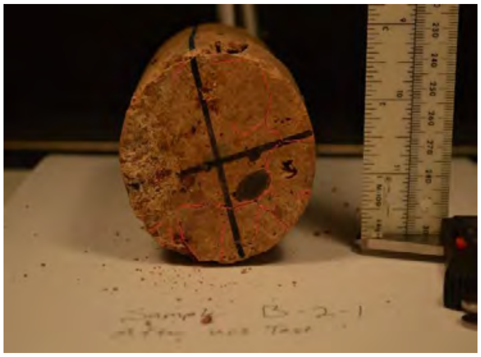

Sample #	Investigator	Date
B-2-2	Saint-Pierre	1/12/2018

Failure Mechanism: Based on ASTM C39

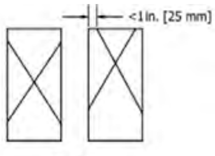 Type 1	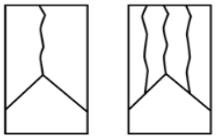 Type 2	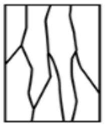 Type 3	Type of Failure(s): Type 3
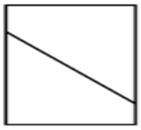 Type 4	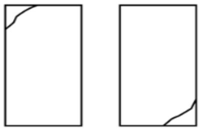 Type 5	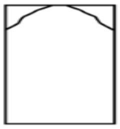 Type 6	Diameter rock vs. diameter core 0.16 L > 2.5*D ? No

E (psi)	677245	ε_{50} (%)	0.1829	Diameter (ft)	0.23
Vs (ft/s)	5896	ɥ	0.28	Length (ft)	0.35
Vp (ft/s)	10706	ɣ (lb/ft^3	147.01	UCS (psi)	2990

Measured largest Aggregate:	Position of Large Aggregate	Percent Aggregate	Percent matrix
0.45 inch	top surface	1%	99%

Notes	Initial Sample
Sample has very few aggreagte. Large pre-existing plane of weakness within sample. Most of failure occurred latterally along this plane. Some columnar cracking within sample. Large amounts of fracturing occurred on upper surface. Some on bottom surface. Most of upper half of sample is not intact.	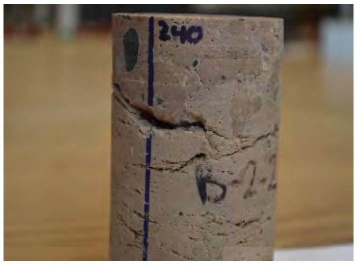

Pictures:

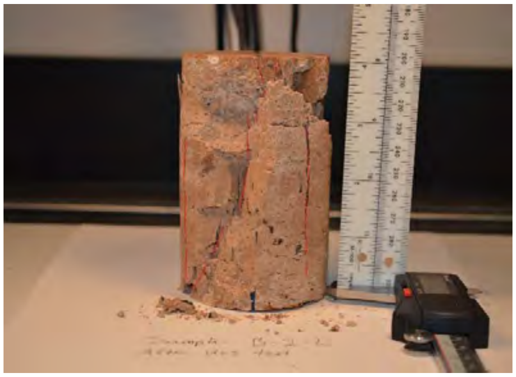

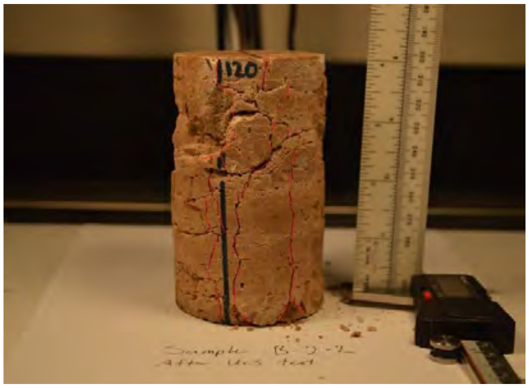

Sample #	Investigator	Date
B-3-1	Saint-Pierre	1/12/2018

Failure Mechanism: Based on ASTM C39

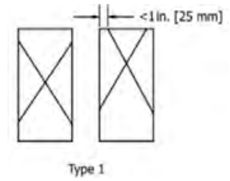

Type 1

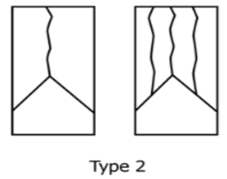

Type 2

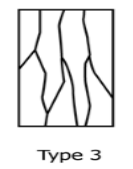

Type 3

Type of Failure(s):

Type 3, Type 4

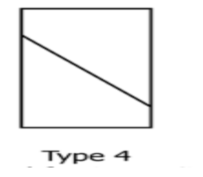

Type 4

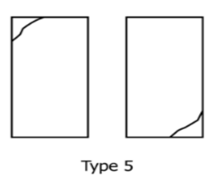

Type 5

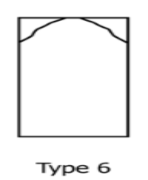

Type 6

Diameter rock vs. diameter

0.04

L > 2.5*D ? No

E (psi)	345017	ε_{50} (%)	0.2298	Diameter (f	0.23
Vs (ft/s)	5570	ɥ	0.31	Length (ft)	0.41
Vp (ft/s)	10651	γ (lb/ft^3	138.32	UCS (psi)	1493

Measured largest Aggregate:	Position of Large Aggregate	Percent Aggregate	Percent matrix
0.1 inch	near bottom surface	1%	99%

Notes

Specimen has a main horizontal failure plane. From this plane, several prominent vertical fractures occur and a shear plane travel through. The upper most area of the specimen broke off into many small pieces. Very few aggregate in the sample. Small pinhole voids surround the sample. Some lateral movement in fractures caused by voids.

Initial Sample

Pictures:

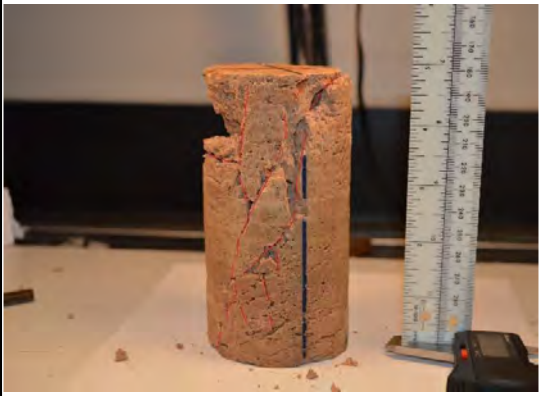

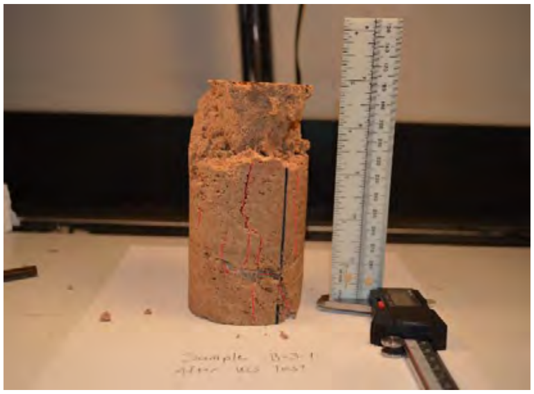

Sample #	Investigator	Date
B-4-1	Saint-Pierre	1/8/2018

Failure Mechanism: Based on ASTM C39

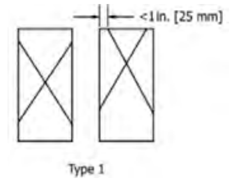 Type 1	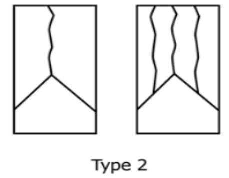 Type 2	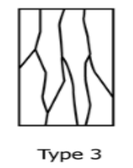 Type 3	Type of Failure(s): Type 3
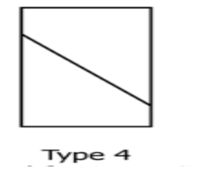 Type 4	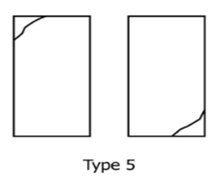 Type 5	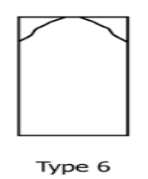 Type 6	Diameter rock vs. diameter 0.07 L > 2.5*D ? No

E (psi)	3268738	ε_{50} (%)	0.0959	Diameter (f	0.23
Vs (ft/s)	10053	ɥ	0.15	Length (ft)	0.39
Vp (ft/s)	15677	γ (lb/ft^3)	155.54	UCS (psi)	7016

Measured largest Aggregate:	Position of Large Aggregate	Percent Aggregate	Percent matrix
0.18 inch	top surface	1%	99%

Notes	Initial Sample
Sample is isotropic. Very little aggregate in sample. Fewer voids on surface, but tend to be a little larger. Three calcium carbonate planes of weakness visible from missing fragment. Fractures tend to move laterally with linear voids. The few visible pieces of aggregate are rounded to sub-rounded.	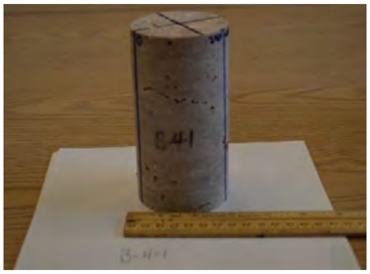

Pictures:

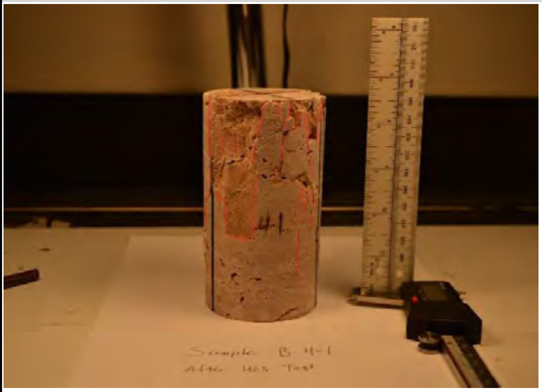

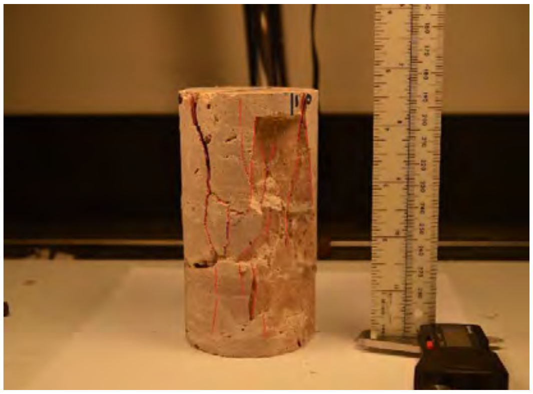

Sample #	Investigator	Date
B-4-2	Saint-Pierre	1/9/2018

Failure Mechanism: Based on ASTM C39

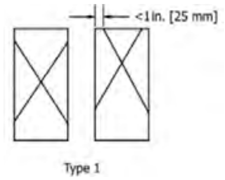

Type 1

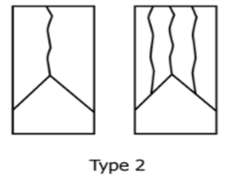
Type 2

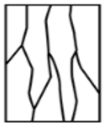
Type 3

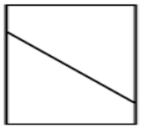
Type 4

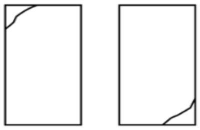
Type 5

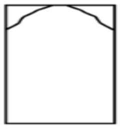
Type 6

Type of Failure(s):	Type 3
Diameter rock vs. diameter core	0.10
L > 2.5*D ?	No

E	4358491	ε_{50}	0.053	Diameter (ft)	0.23
Vs	9161	ν	0.21	Length (ft)	0.35
Vp	15119	γ (lb/ft^3)	152.1	UCS	4620.00

Measured largest Aggregate:	Position of Large Aggregate	Percent Aggregate	Percent matrix
0.3 inch	Near bottom surface	2%	98%

Notes

Scattered fine rounded gravels. Top of specimen shows clusters of more cemented matrix. Linear plane of weakness near top of specimen with voids. Fractures seem to be propagating from this plane. Upper surface of core has significant fracture through it. Columnar fracturing sidesteps when encountering voids.

Initial Sample

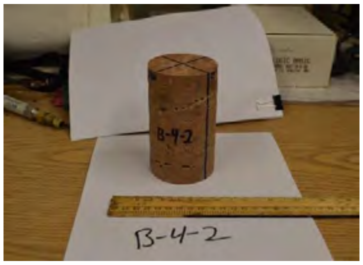

Pictures:

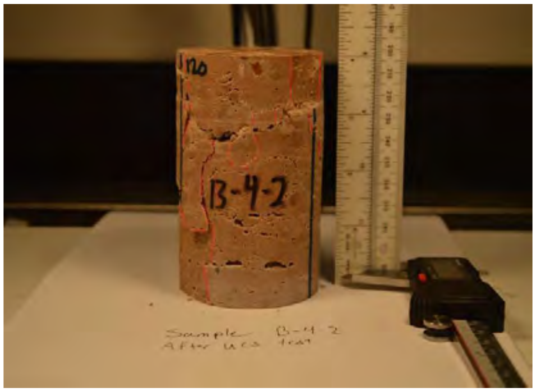

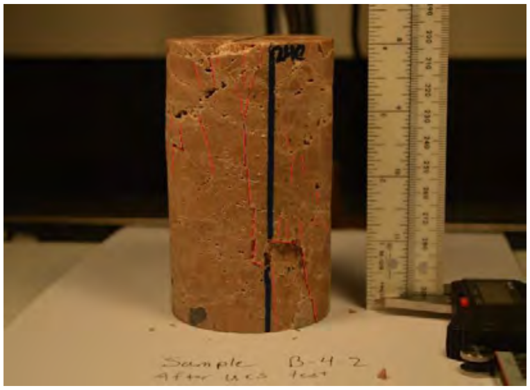

Sample #	Investigator	Date
B-4-3	Saint-Pierre	1/9/2018

Failure Mechanism: Based on ASTM C39

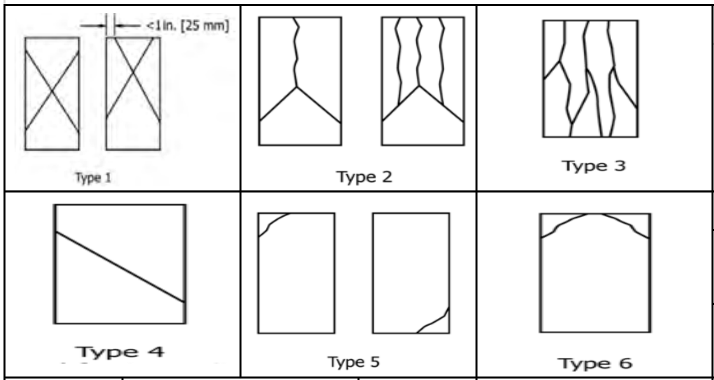

Type of Failure(s): Type 3 Type 5 Type 6

Diameter rock vs. diameter core: 0.10

L > 2.5*D ? No

E (psi)	1419541	ε_{50} (%)	0.07662	Diameter (ft)	0.23
Vs (ft/s)	7968	ɥ	0.3	Length (ft)	0.38
Vp (ft/s)	14961	ɣ (lb/ft^3	152.93	UCS (psi)	2577

Measured largest Aggregate:	Position of Large Aggregate	Percent Aggregate	Percent matrix
0.27	middle	2%	98%

Notes

Sample seems fairly homogeneous, with few gravel size aggregate. Side fractures on bottom of sample in combination with columnar failure. Many small lineations with voids. Fracturing tends to favor within these lineations. Some visible carbonate within fractures and voids.

Initial Sample

Pictures:

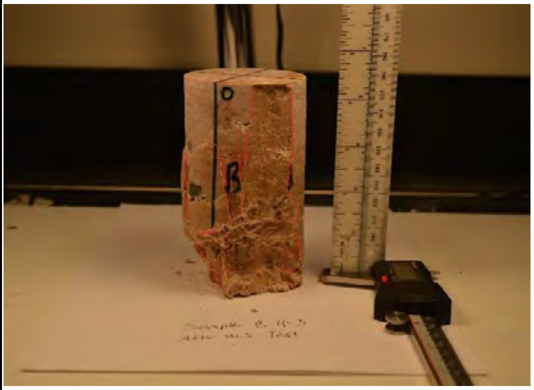
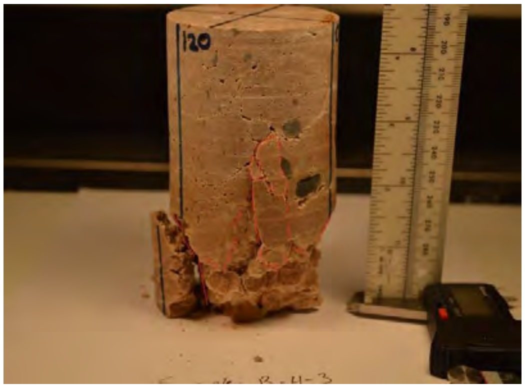

Sample #	Investigator	Date
B-4-4	Saint-Pierre	1/3/2018

Failure Mechanism: Based on ASTM C39

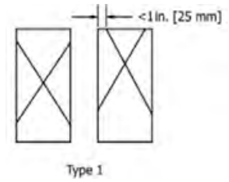 Type 1	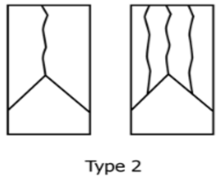 Type 2	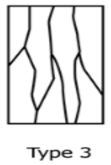 Type 3	Type of Failure(s): Type 3-Columnar Failure
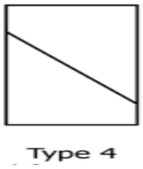 Type 4	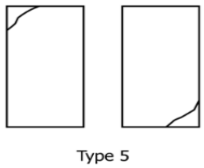 Type 5	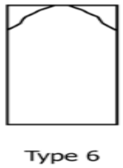 Type 6	Diameter rock vs. diameter 0.08 L > 2.5*D ? Yes

E (psi)	4470000	ε_{50} (%)	0.1136	Diameter (f	0.23
Vs (ft/s)	9097	ɥ	0.29	Length (ft)	0.47
Vp (ft/s)	16624	γ (lb/ft^3)	158.96	UCS (psi)	10791.00

Measured largest Aggregate:	Position of Large Aggregate	Percent Aggregate	Percent matrix	
.23 inch	Small and Infrequent	2%	98%	

Notes

Round to Sub-angular dark gray aggregate. Mostly dolomite. Small horizontal lineations with small voids. The fractured horizontal lineations show a white powdery substance, most likely calcium carbonate. These planes appear to be zones of weakness into the sample. Fracturing is mostly vertical with some side-stepping along small voids.

Initial Sample

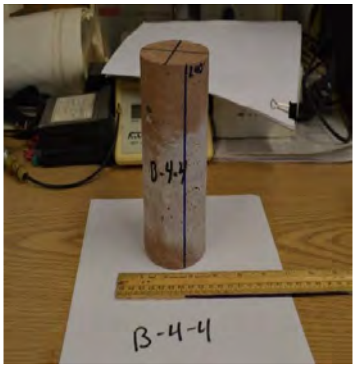

Pictures:

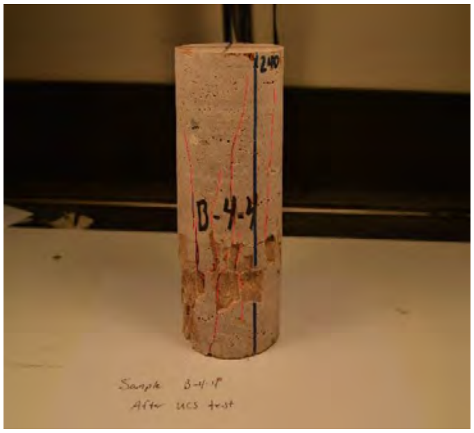

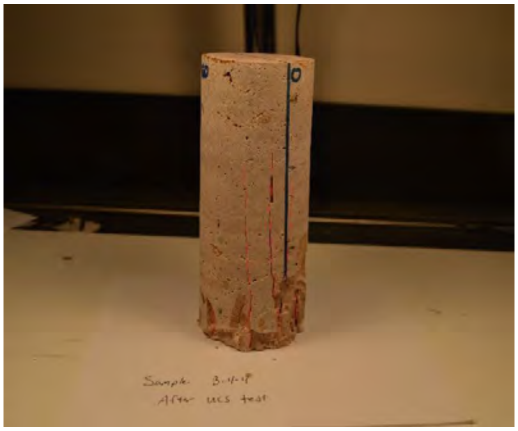

Sample #	Investigator	Date
B-4-5	Saint-Pierre	1/9/2018

Failure Mechanism: Based on ASTM C39

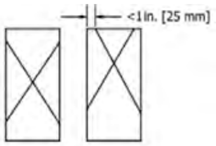 Type 1	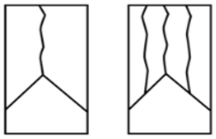 Type 2	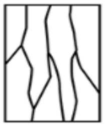 Type 3	Type of Failure(s): Type 3 - columnar
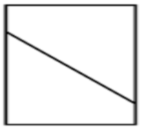 Type 4	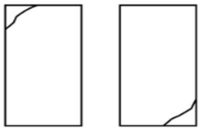 Type 5	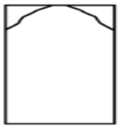 Type 6	Diameter rock vs. diameter 0.37 L > 2.5*D ? No

E (psi)	3000289	ε_{50} (%)	0.0404	Diameter (f	0.23
Vs (ft/s)	8444	ɥ	0.27	Length (ft)	0.42
Vp (ft/s)	15091	γ (lb/ft^3)	148.91	UCS (psi)	3249

Measured largest Aggregate:	Position of Large Aggregate	Percent Aggregate	Percent matrix
1.0 inch	middle	3%	97%

Notes	Initial Sample
One large gravel that is sub-rounded. Littered with fine gravel. Matrix appears to be fairly homogenous. A few large linear voids appear to make a pre-existing plane of weakness. Some white carbonate visible within. Fractures tend to sidestep laterally with smaller voids. Fractures going through large gravel piece and not around.	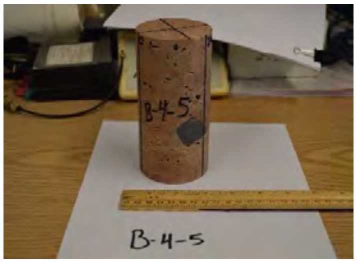

Pictures:

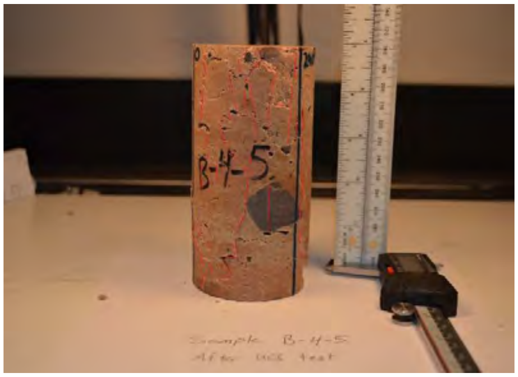

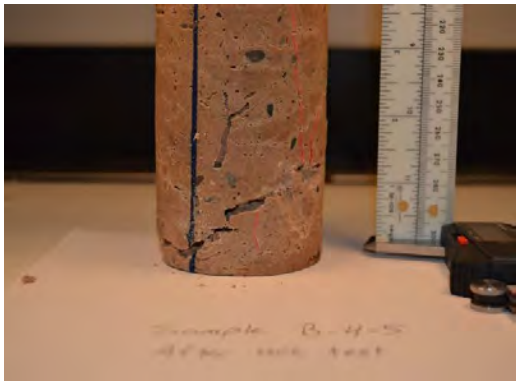

Sample #	Investigator	Date
B-4-6	Saint-Pierre	1/8/2018

Failure Mechanism: Based on ASTM C39

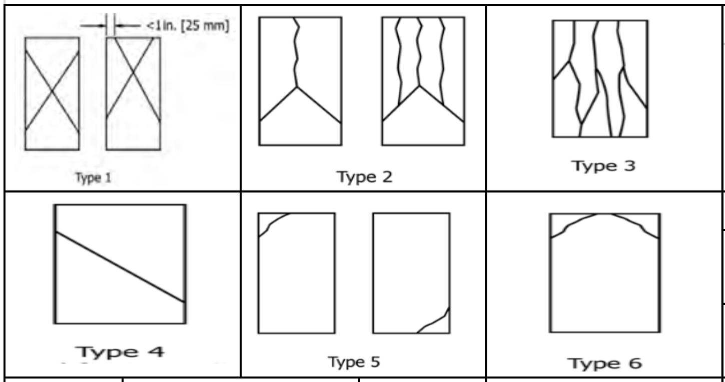
<1in. [25 mm]
Type 1
Type 2
Type 3
Type 4
Type 5
Type 6

Type of Failure(s):

Type 3 Columnar

Diameter rock vs. diameter core

0.15

L > 2.5*D ? yes

E (psi)	4576398	ε_{50} (%)	0.0852	Diameter (ft)	0.23
Vs (ft/s)	10262	ų	0.21	Length (ft)	0.44
Vp (ft/s)	16944	ɣ (lb/ft^3)	159.58	UCS (psi)	9070

Measured largest Aggregate:	Position of Large Aggregate	Percent Aggregate	Percent matrix
0.40 inches	middle	1%	99%

Notes

Sample is very isotropic. Small coarse material that is rounded. Visible white calcium carbonate plane of weakness in middle of sample. Plane is fairly horizontal and large amount of fracturing along the plane. Sample overall has many small pinhole voids. No pertern besides the one horizontal plane. Failure planes daylighted at upper surface of specimen but not the lower.

Initial Sample

Pictures:

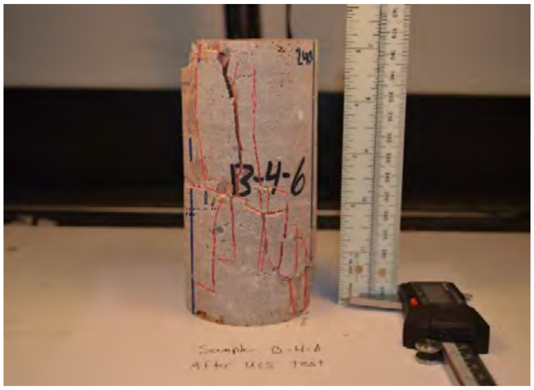
B-4-6
Sample B-4-6
After UCS test

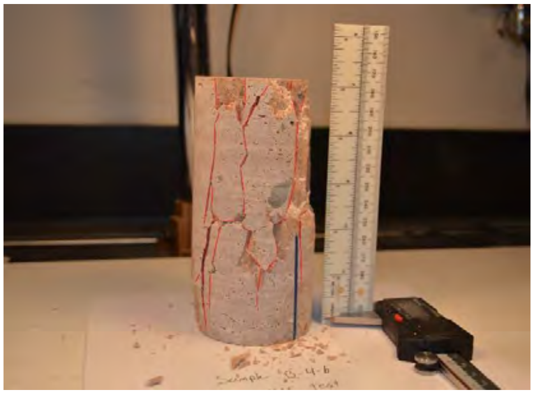
Sample B-4-6
test

Sample #	Investigator	Date
B-4-7	Saint-Pierre	1/9/2018

Failure Mechanism: Based on ASTM C39

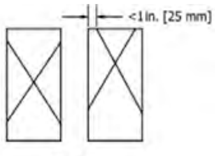 Type 1	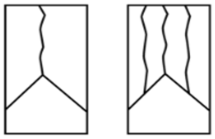 Type 2	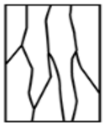 Type 3	Type of Failure(s): Type 3, Type 4
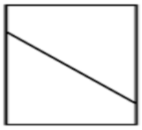 Type 4	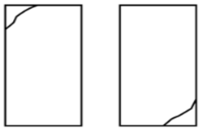 Type 5	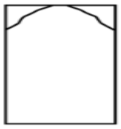 Type 6	Diameter rock vs. diameter core 0.09 L > 2.5*D ? No

E (psi)	4102460	ε_{50} (%)	0.1636	Diameter (ft	0.23
Vs (ft/s)	9711	ɥ	0.26	Length (ft)	0.34
Vp (ft/s)	17072	ɣ (lb/ft^3)	156.86	UCS (psi)	14460.00

Measured largest Aggregate:	Position of Large Aggregate	Percent Aggregate	Percent matrix	
0.25 inch	near top surface	1%	99%	

Notes	Initial Sample
Fairly homogenous specimen. Sample shows shear failure is a semi stair step pattern. Lateral bands of voids throughout specimen. Fairly brittle.	

Pictures:

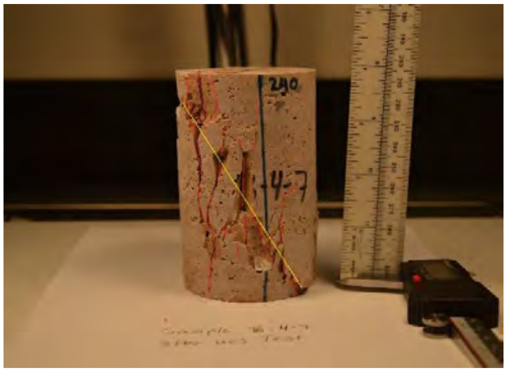

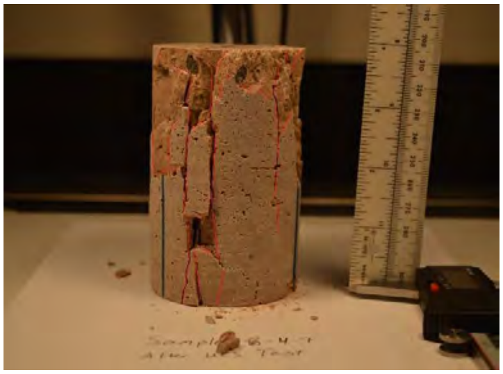

Sample #	Investigator	Date
B-4-8	Saint-Pierre	1/8/2018

Failure Mechanism: Based on ASTM C39

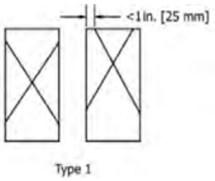 Type 1	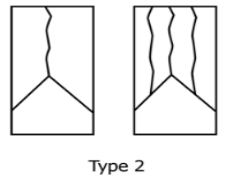 Type 2	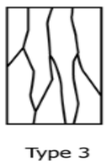 Type 3	Type of Failure(s): Type 3 Columnar
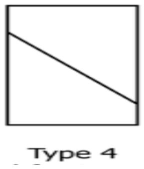 Type 4	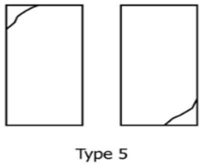 Type 5	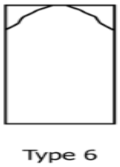 Type 6	Diameter rock vs. diameter core 0.20 L > 2.5*D ? No

E (psi)	3823813	ε_{50} (%)	0.11	Diameter (ft)	0.23
Vs (ft/s)	8742	ɥ	0.21	Length (ft)	0.38
Vp (ft/s)	16536	ɣ (lb/ft^3)	156.45	UCS (psi)	7240

Measured largest Aggregate:	Position of Large Aggregate	Percent Aggregate	Percent matrix
0.56 inches	top cut	5%	95%

Notes	Initial Sample
Fine to medium rounded gravels. Fractures travel through plane of weakness in the middle of the sample. White calcium carbonate visible in plane. Visible bulging near the middle of the sample, from plane of weakness. Sample is fairly isotropic. Slightly more aggreagte on top of sample than bottom. Some areas with larger cavaties, some with linear trends.	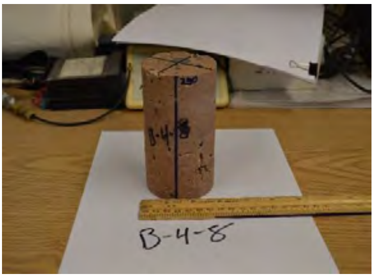

Pictures:

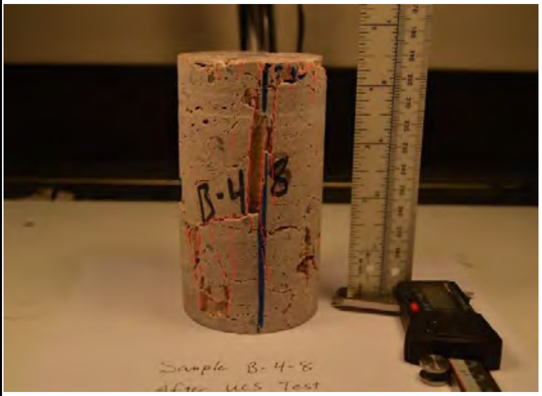

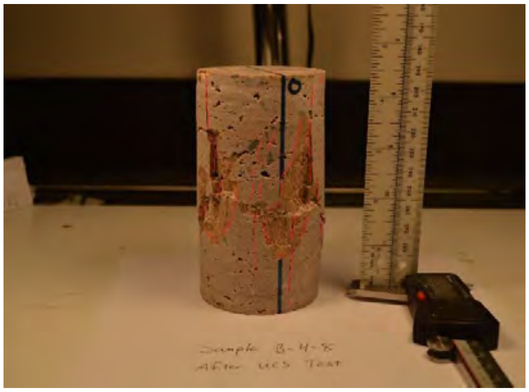

Sample #	Investigator	Date
B-5-1	Saint-Pierre	1/9/2018

Failure Mechanism: Based on ASTM C39

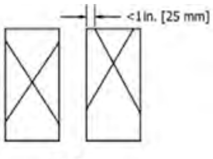

Type 1

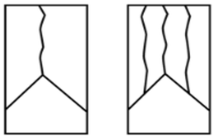
Type 2

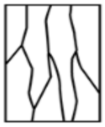
Type 3

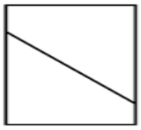
Type 4

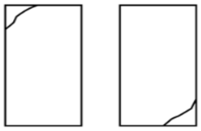
Type 5

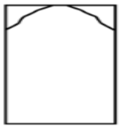
Type 6

Type of Failure(s):

Type 3 Columnar

Diameter rock vs. diameter core

0.07

L > 2.5*D ? No

E (psi)	2116282	ε_{50} (%)	0.1169	Diameter (ft)	0.23
Vs (ft/s)	8492	ɥ	0.28	Length (ft)	0.34
Vp (ft/s)	15446	ɣ (lb/ft^3)	147.42	UCS (psi)	6440.00

Measured largest Aggregate:	Position of Large Aggregate	Percent Aggregate	Percent matrix
0.2 inches	middle within fractur	2%	98%

Notes

Sample is light brown and failry isotropic. Few lineations with small voids. In the middle of specimen, closer to the top, a noticeable planar weakness with white calcium carbonate is exposed by fractures. Small pinhole cavaties throughout the specimen.

Initial Sample

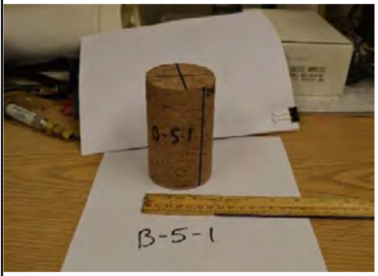

Pictures:

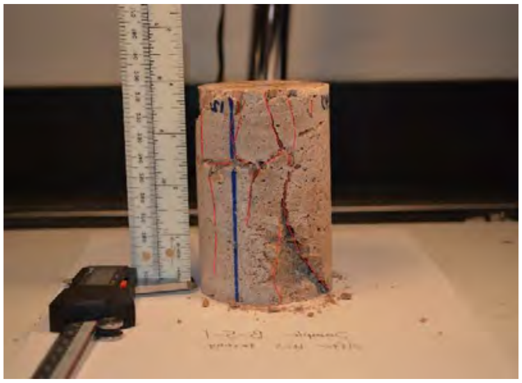

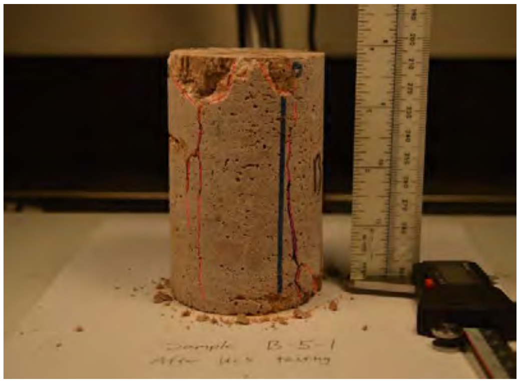

Sample #	Investigator	Date
B-5-2	Saint-Pierre	1/7/2018

Failure Mechanism: Based on ASTM C39

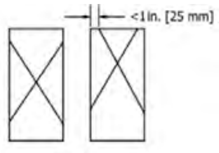

Type 1

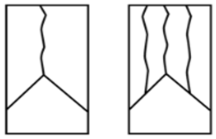

Type 2

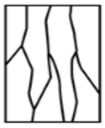

Type 3

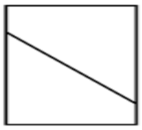

Type 4

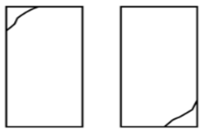

Type 5

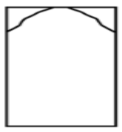

Type 6

Type of Failure(s):	Type 3
Diameter rock vs. diameter	0.14
L > 2.5*D ?	no

E (psi)	1295210	ε_{50} (%)	0.0876	Diameter (ft	0.23
Vs (ft/s)	8685	ɥ	0.2	Length (ft)	0.42
Vp (ft/s)	14226	ɣ (lb/ft^3)	146.62	UCS (psi)	2801.00

Measured largest Aggregate:	Position of Large Aggregate	Percent Aggregate	Percent matrix
.37 inches	middle	2%	98%

Notes

Matrix is light to dark brown. Specimen is littered with dark brown, more cemented sections with rounded edges similar to aggregate. Large dark grey blotch at top of sample. This does not appear to be aggregate. It is softer than weak matrix. Edges are too wavy to be aggreagte. Most likley clay cluster. Fracturing is inconsistant and tends to travel aroud the gravels and harder matrix areas. Many small pinhole voids surrounding the sample. They tend to cluster in areas.

Initial Sample

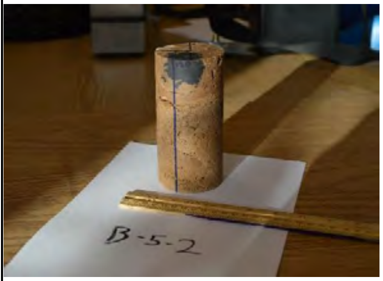

Pictures:

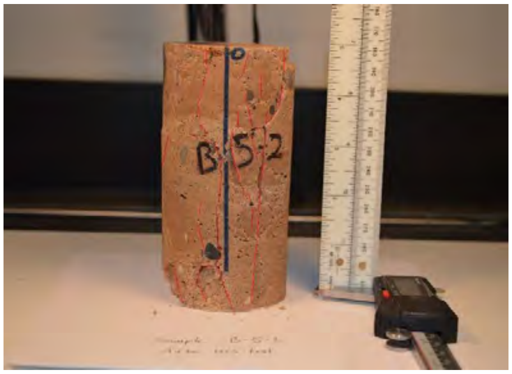

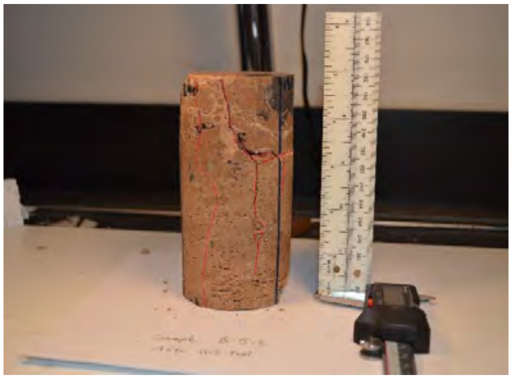

Sample #	Investigator	Date
B-5-3	Saint-Pierre	1/8/2018

Failure Mechanism: Based on ASTM C39

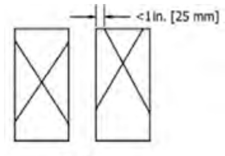 Type 1	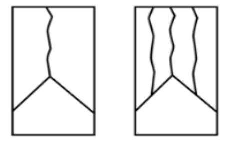 Type 2	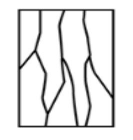 Type 3	Type of Failure(s): Type 3
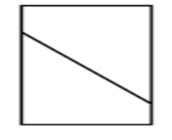 Type 4	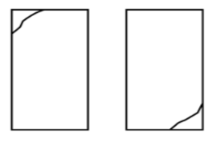 Type 5	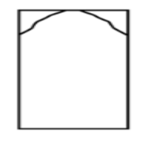 Type 6	Diameter rock vs. diameter core 0.33 L > 2.5*D ? Yes

E (psi)	1965542	ε_{50} (%)	0.1042	Diameter (ft)	0.23
Vs (ft/s)	8343	ɥ	0.24	Length (ft)	0.52
Vp (ft/s)	14226	ɣ (lb/ft^3)	145.93	UCS (psi)	3800.00

Measured largest Aggregate:	Position of Large Aggregate	Percent Aggregate	Percent matrix
0.9 inches	near top surface	3%	97%

Notes	Initial Sample
Matrix is light to dark brown. Aggregate is fine to gravel size. Rounded to sub-rounded. Many darker brown sections of the specimen showing increased levels of cementation. Fracturing seems to not continue halfway up the specimen. The upper half of the specimen has most of the aggregate and all the gravel and more cemented matrix. This indicates that the bottom of the sample is despositionally upwards. Visible lineations with small voids and some cavaties are around the specimen. Fracturing tends to travel towards the voids and sidestep with the voids. Visible bulging in the lower half of the sample where the matrix is weaker.	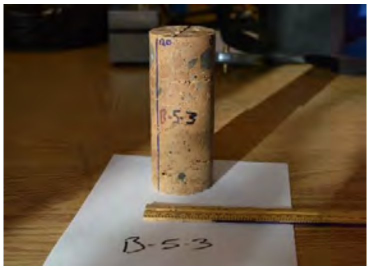

Pictures:

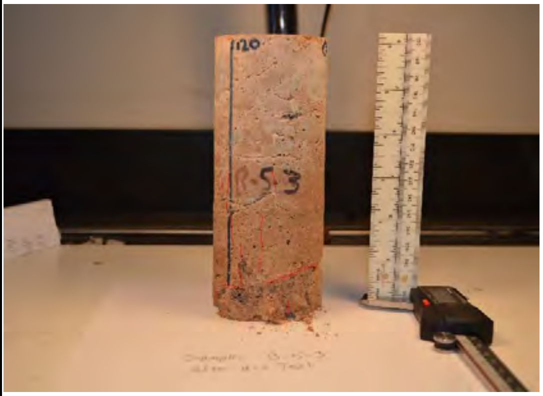

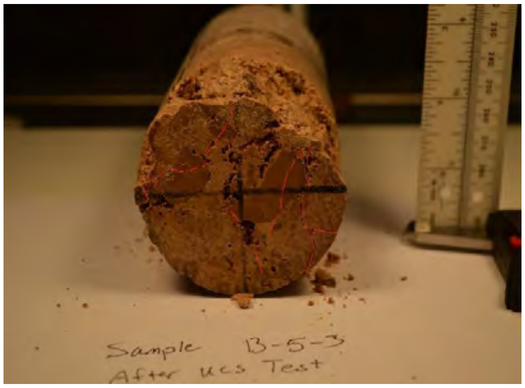

Sample #	Investigator	Date
B-5-4	Saint-Pierre	1/8/2018

Failure Mechanism: Based on ASTM C39

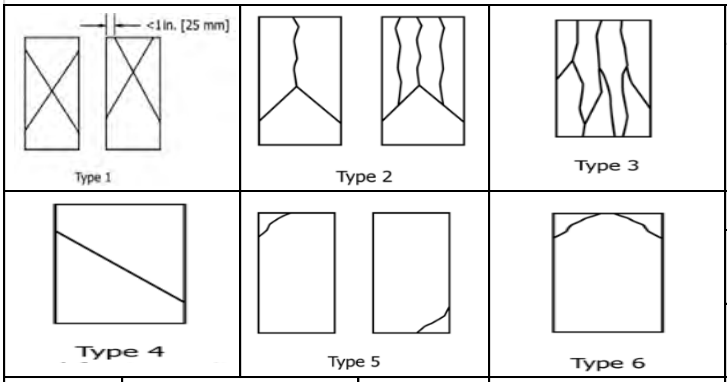

<1in. [25 mm]
Type 1
Type 2
Type 3
Type 4
Type 5
Type 6

Type of Failure(s):	Type 3 Columnar
Diameter rock vs. diameter core	0.27
L > 2.5*D ?	No

E (psi)	2233947	ε_{50} (%)	0.0783	Diameter (ft)	0.23
Vs (ft/s)	8572	ɥ	0.25	Length (ft)	0.39
Vp (ft/s)	14878	ɣ (lb/ft^3)	148.61	UCS (psi)	4610

Measured largest Aggregate:	Position of Large Aggregate	Percent Aggregate	Percent matrix
.75 inch	lower middle of sample	2%	98%

Notes

Light brown matrix with many small pinhole voids on the surface of the specimen and persist into the sample. Fine gravel is rounded to sub-rounded. Sample seems fairly isotropic. Natural failure plane near top of sample with visible calcium carbonate.

Initial Sample

Pictures:

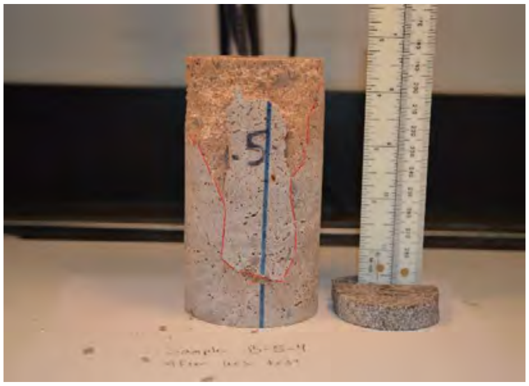

Sample B-5-4 After UCS test

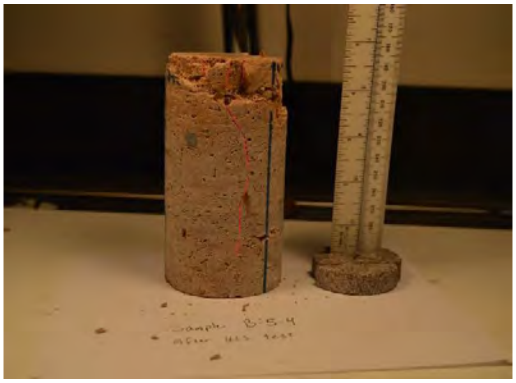

Sample B-5-4 After UCS test

Sample #	Investigator	Date
B-5-5	Saint-Pierre	1/10/2018

Failure Mechanism: Based on ASTM C39

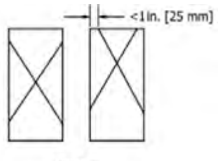 Type 1	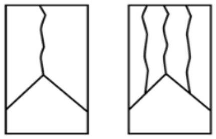 Type 2	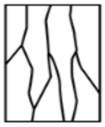 Type 3	Type of Failure(s): Type 3
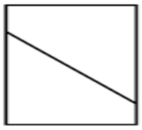 Type 4	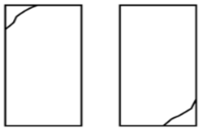 Type 5	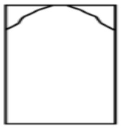 Type 6	Diameter rock vs. diameter core 0.15 L > 2.5*D ? yes

E (psi)	1978086	ε_{50} (%)	0.0838	Diameter (ft)	0.23
Vs (ft/s)	7784	ɥ	0.28	Length (ft)	0.47
Vp (ft/s)	14143	ɣ (lb/ft^3)	145.66	UCS (psi)	5008

Measured largest Aggregate:	Position of Large Aggregate	Percent Aggregate	Percent matrix
0.4 inch	middle	2%	98%

Notes	Initial Sample
Sampe is ight to dark brown. Numerous dark brown clusters represent regions of higher cementation. Fracturing both goes through and around these clusters like aggreagate. Small pinhole voids throughout specimen. Fractures tend to not change course with voids.	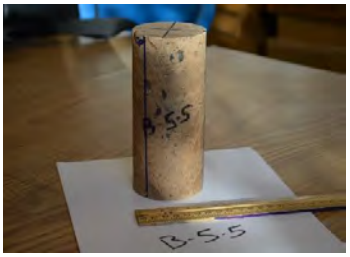

Pictures:

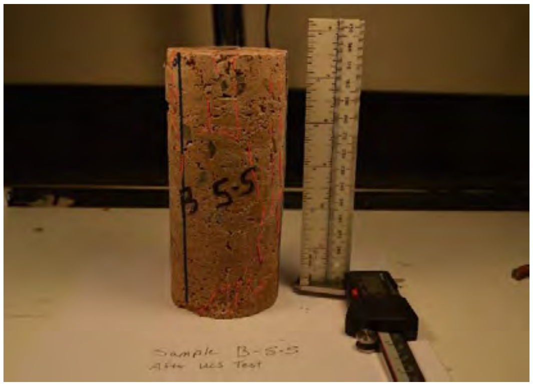

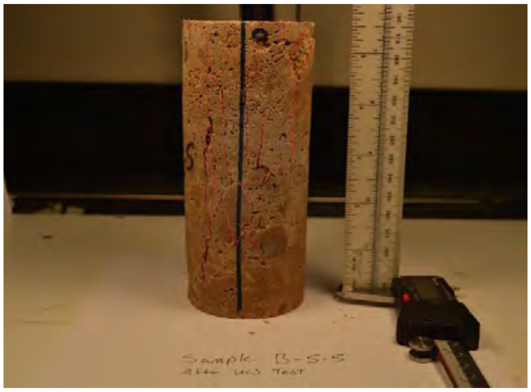

Sample #	Investigator	Date
B-5-6	Saint-Pierre	1/15/2018

Failure Mechanism: Based on ASTM C39

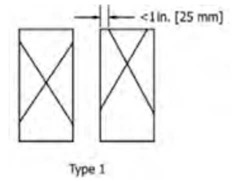 <1in. [25 mm] Type 1	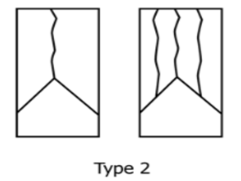	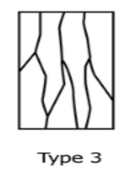	Type of Failure(s): Type 3
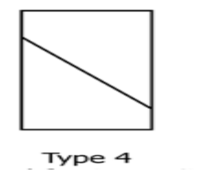	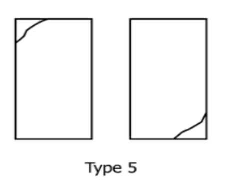	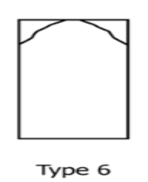	Diameter rock vs. diameter core 0.16 L > 2.5*D ? No

E (psi)	2156517	ε_{50} (%)	0.109	Diameter (ft)	0.23
Vs (ft/s)	8766	ɥ	0.26	Length (ft)	0.30
Vp (ft/s)	15361	ɣ (lb/ft^3)	149.84	UCS (psi)	5108

Measured largest Aggregate:	Position of Large Aggregate	Percent Aggregate	Percent matrix
0.44 inch	middle	1%	99%

Notes	Initial Sample
Small aggreagte scattered throughout. Some clusters of more cemented matrix that look like aggregate but are slightly darker. Most of failure occurred on bottom of sample with large fragments missing. Vertical fractures travel through small voids throughout sample with some fractures side stepping laterally.	

Pictures:

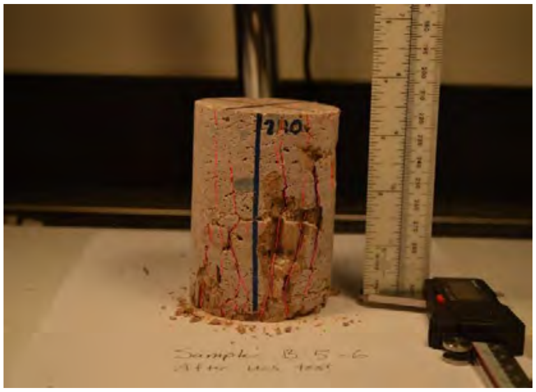
Sample B-5-6
After UCS test

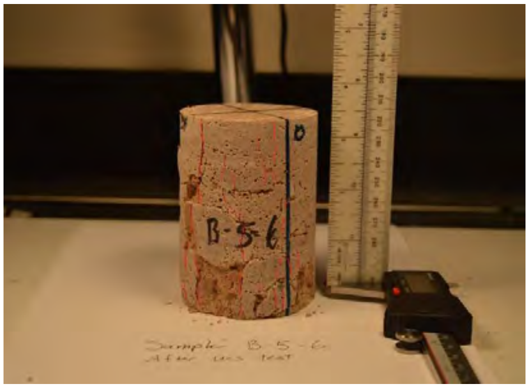
B-5-6
Sample B-5-6
After UCS test

Sample #	Investigator	Date
B-5-7	Saint-Pierre	1/11/2018

Failure Mechanism: Based on ASTM C39

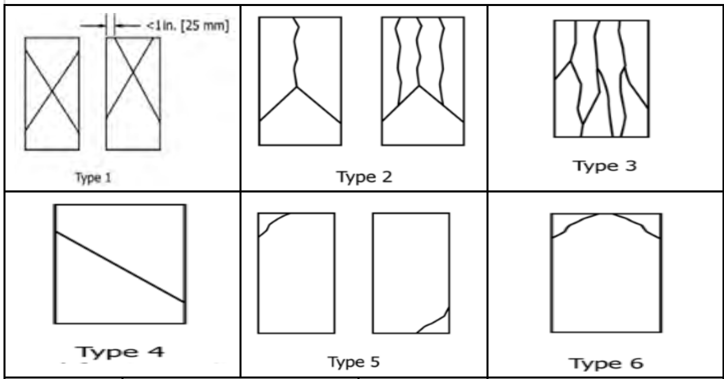
<1in. [25 mm]
Type 1
Type 2
Type 3
Type 4
Type 5
Type 6

Type of Failure(s):	Type 3
Diameter rock vs. diameter core	0.30
L > 2.5*D ?	No

E (psi)	1106575	ε_{50} (%)	0.1308	Diameter (ft)	0.23
Vs (ft/s)	7369	ɥ	0.3	Length (ft)	0.33
Vp (ft/s)	13679	ɣ (lb/ft^3)	148.71	UCS (psi)	3847

Measured largest Aggregate:	Position of Large Aggregate	Percent Aggregate	Percent matrix
0.83	bottom surface	5%	95%

Notes

Upper third of specimen is weaker matrix than the rest. Large part of upper area broke off of specimen. Upper part of specimen has many small chunks of higher cemented matrix, looks like fine aggregate. Some parts of specimen show linear voids in no particular orientation. Most fracturing does not make it all the way to the bottom of the more cemented matrix.

Initial Sample

Pictures:

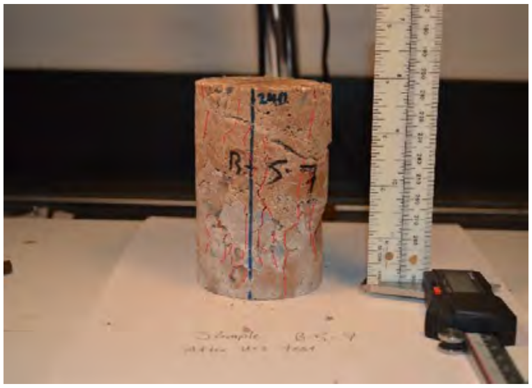
B-5-7
Sample B-5-7
After UCS test

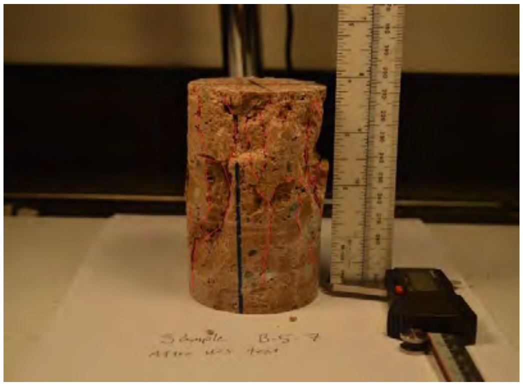
Sample B-5-7
After UCS test

Sample #	Investigator	Date
C-1-2	Saint-Pierre	1/6/2018

Failure Mechanism: Based on ASTM C39

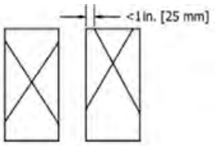

Type 1

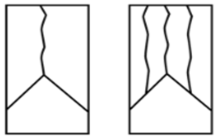

Type 2

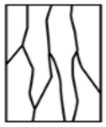

Type 3

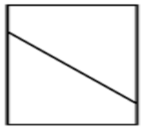

Type 4

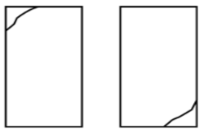

Type 5

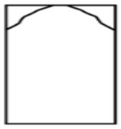

Type 6

Type of Failure(s):

Type 3-columnar

Type 2-poorly defined. Cone appears but is cracking around aggregate

Diameter rock vs. diameter core	0.84
L > 2.5*D ?	yes

E (psi)	6325083	ε_{50} (%)	0.0765	Diameter (ft)	0.23
Vs (ft/s)	10379	ɥ	0.27	Length (ft)	0.50
Vp (ft/s)	18525	ɣ (lb/ft^3)	161.31	UCS (psi)	10540.00

Measured largest Aggregate:	Position of Large Aggregate	Percent Aggregate	Percent matrix
> 2.31 inch	near bottom of sample	25%	75%

Notes

Aggregate is angular to rounded. Composed of dolomite, limestone, sandstone and possibly quartzite. Sample shows aggregate grading from fine to cobbles indicating upwards direction. Largest cobbles are near the bottom but do not contact the bottom surface. Predominate fracturing around largest cobbles, with cracking extedning through cobbles as well. The most well formed fracture contacts large cobble. It has white calcium carbonate on surface and is semi-horizontal. Visible cavity on bottom side of second largest cobble with fracture extending around the cobble. Small voids surrounding aggregate. Small horizontal lineations with small

Initial Sample

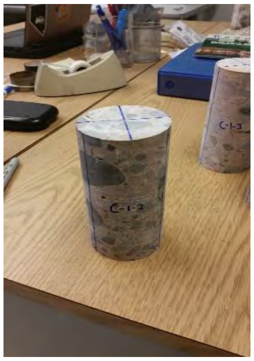

Pictures:

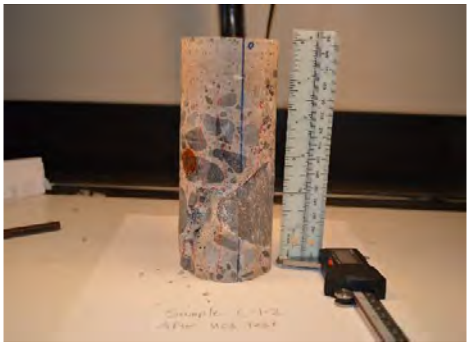

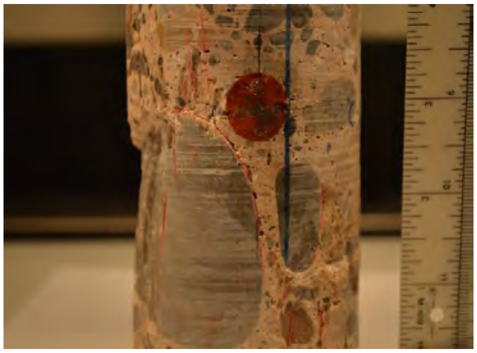

Sample #	Investigator	Date
C-1-3	Saint-Pierre	1/6/2018

Failure Mechanism: Based on ASTM C39

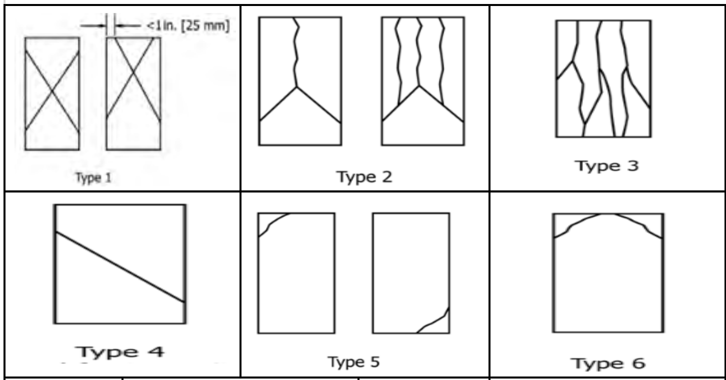

Type of Failure(s): Type 3-Columnar Failure

Diameter rock vs. diameter core: 0.58

L > 2.5*D ? yes

E (psi)	5533554	ε_{50} (%)	0.1122	Diameter (ft)	0.23
Vs (ft/s)	10797	ɥ	0.23	Length (ft)	0.50
Vp ft/s)	18201	ɣ (lb/ft^3)	163.57	UCS (psi)	13401

Measured largest Aggregate:	Position of Large Aggregate	Percent Aggregate	Percent matrix
1.6 inches	in middle	30%	70%

Notes

Fracturing is mostly axial. Small side steps with aggregate and small voids. Fracturing goes around aggregate and through. Does not appear to matter what sort of rock type. Dolomite, limestone and sandstone is visible. Small cavitites surrounding some of the calcite matrix appear to be darker and more cemented, however shows no effect on failure cracks. Failure planes go through both outer areas of the core specimen.

Initial Sample

Pictures:

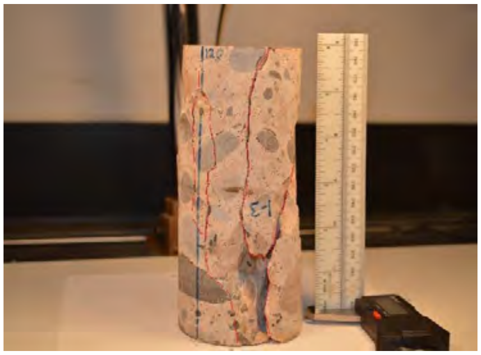

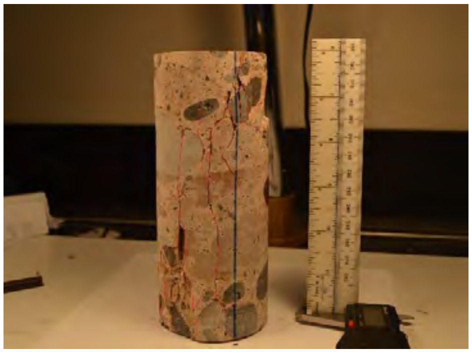

Sample #	Investigator	Date
C-1-4	Saint-Pierre	1/9/2018

Failure Mechanism: Based on ASTM C39

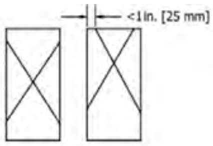

Type 1

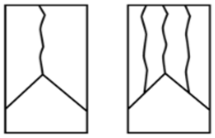

Type 2

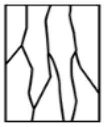

Type 3

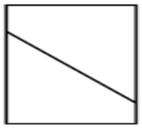

Type 4

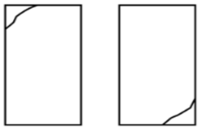

Type 5

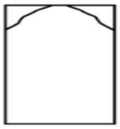

Type 6

Type of Failure(s):

Type 3, Type 4

Diameter rock vs. diameter core

0.67

L > 2.5*D ? yes

E (psi)	N/A	ε_{50} (%)	N/A	Diameter (ft)	0.23
Vs (ft/s)	11078	ɥ	0.212	Length (ft)	0.497
Vp (ft/s)	18324	ɣ (lb/ft^3)	162.74	UCS	12850.00

Measured largest Aggregate:	Position of Large Aggregate	Percent Aggregate	Percent matrix
1.85 inches	bottom of sample	30%	70%

Notes	Initial Sample
Highy cemented sample with disticnt gradational pattern from the top down. Top of specimen has fine gravel and gets increasingly larger towards the bottom. Shear failure through the coarse gravel area. Terminates jjust when it hits the fine gravels. About a quarter of ssample frfactured off. Fractures seem to go through gravel and not around.	

Pictures:

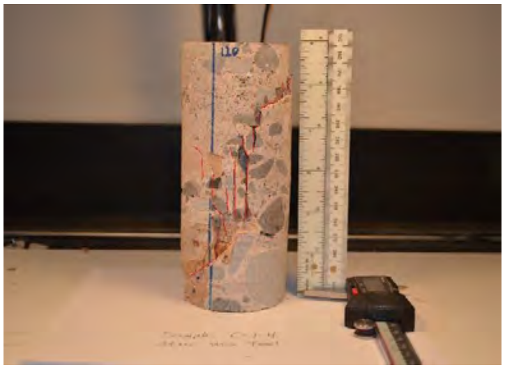

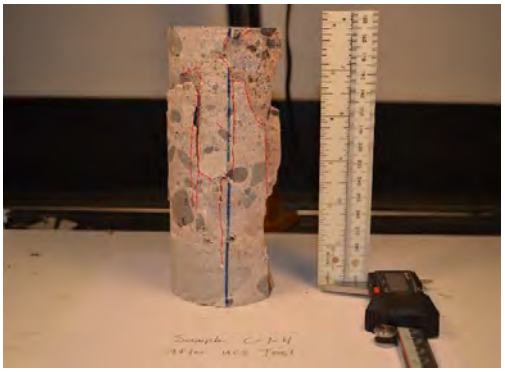

Sample #	Investigator	Date
C-1-5	Saint-Pierre	1/6/2018

Failure Mechanism: Based on ASTM C39

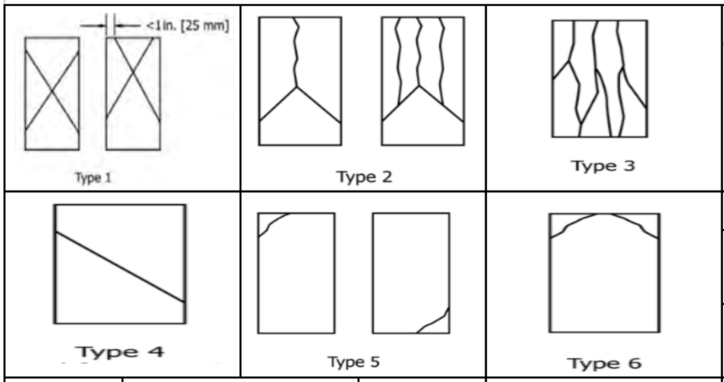

Type of Failure(s):

Type 3-Columnar Sample almost shows shear but failure extends end to end

Diameter rock vs. diameter core

0.57

L > 2.5*D ?	Yes

E (psi)	3357410	$\varepsilon_{50\,(\%)}$	0.1463	Diameter (ft)	0.23
Vs (ft/s)	11083	ɥ	0.216	Length (ft)	0.50
Vp (ft/s)	18420	ɣ (lb/ft^3)	162.529	UCS (psi)	11201

Measured largest Aggregate:	Position of Large Aggregate	Percent Aggregate	Percent matrix	
1.56 inches	bottom of sample	30%	70%	

Notes

Aggregate is mostly Dolomite. Rounded to sub rounded. Gravels are more elongated in this specimen. Causing more fractures to go though gravels and not around. Some zones of darker matrix appear like aggreagte but appear to be more cemented matrix. Some naturally occuring zones of weakness show white calcium carbonate the reacts violently to 5% HCl. Voids surrounding gravels appear to be predominatly on the downside of the gravels, so voids created by deposition. Large failure plane which could almost be shear plane extends from end of specimen to other end.

Initial Sample

Pictures:

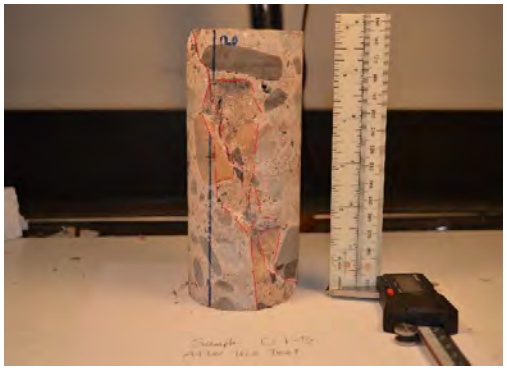

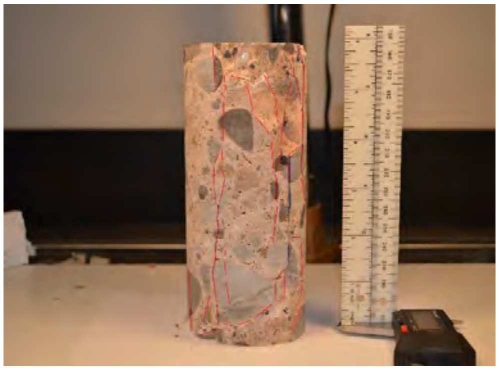

Sample #	Investigator	Date
C-1-6	Saint-Pierre	1/11/2018

Failure Mechanism: Based on ASTM C39

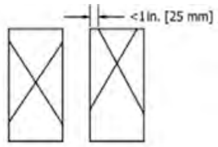 Type 1	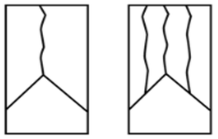 Type 2	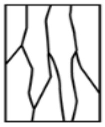 Type 3	Type of Failure(s): Type 3
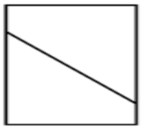 Type 4	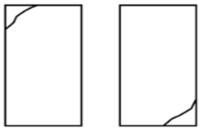 Type 5	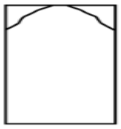 Type 6	Diameter rock vs. diameter core 0.82 L > 2.5*D ? yes

E (psi)	4914590	ε_{50} (%)	0.127	Diameter (ft)	0.23
Vs (ft/s)	10144	ų	0.251	Length (ft)	0.49
Vp (ft/s)	17595	γ (lb/ft^3)	162.44	UCS (psi)	13773

Measured largest Aggregate:	Position of Large Aggregate	Percent Aggregate	Percent matrix
2.25 inches	top surface	20%	80%

Notes	Initial Sample
Top of sample has cobble of weak banded sandstone. Other Aggregate ranges from fine to medium gravel. Most of one half of sample broke off due to numerous fractures. Angular fracture but not shear. Fracture goes through sandstone on upper surface easily.	

Pictures:

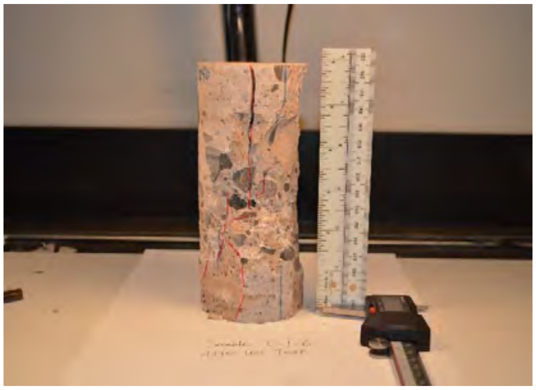

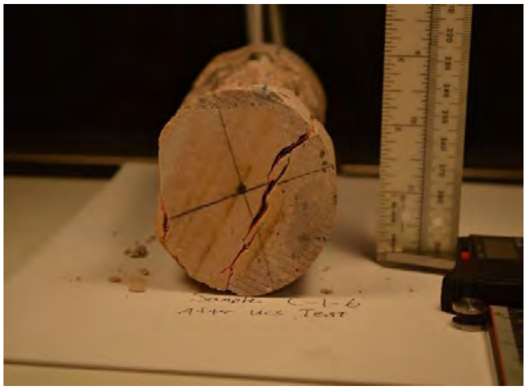

Sample #	Investigator	Date
C-1-7	Saint-Pierre	1/11/2018

Failure Mechanism: Based on ASTM C39

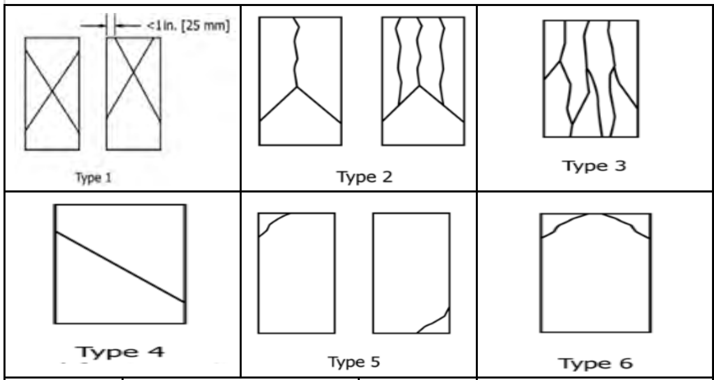

Type of Failure(s):	Type 3
Diameter rock vs. diameter	0.84
L > 2.5*D ?	yes

E (psi)	1786028	ε_{50} (%)	0.1242	Diameter (f	0.23
Vs (ft/s)	10315	ɥ	0.249	Length (ft)	0.51
Vp (ft/s)	17837	ɣ (lb/ft^3)	160.61	UCS (psi)	4601

Measured largest Aggregate:	Position of Large Aggregate	Percent Aggregate	Percent matrix
2.3 inches	middle	35%	65%

Notes

Sample broke apart completely. Reconstructed for pictures. Some larger cobbles. The largest aggregate fractured through the shortest area and the rest broke off completely from the matrix. Fracturing seems to both go through the aggregate and around. Both ends of the sample are mostly intact with the greatest amount of stress being in the middle of the specimen.

Initial Sample

Pictures:

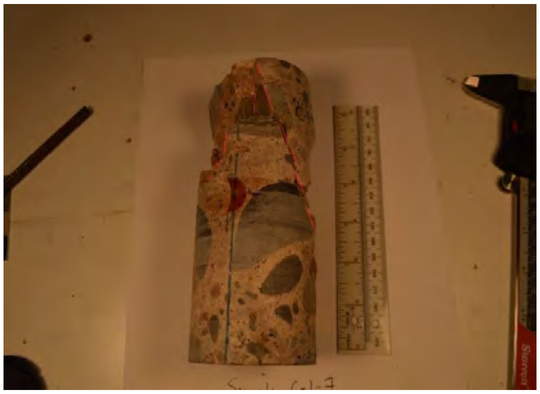

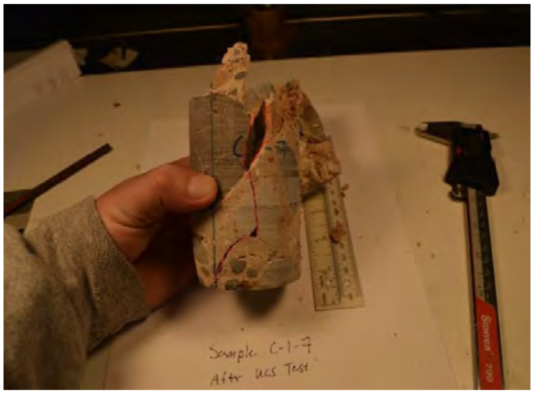

Sample #	Investigator	Date
C-1-8	Saint-Pierre	1/10/2018

Failure Mechanism: Based on ASTM C39

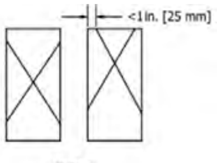 Type 1	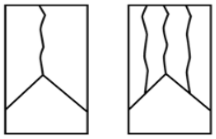 Type 2	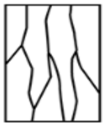 Type 3	Type of Failure(s): Type 3
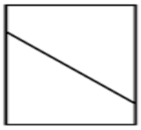 Type 4	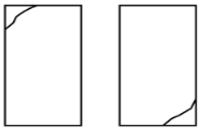 Type 5	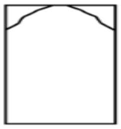 Type 6	Diameter rock vs. diameter core 0.76 L > 2.5*D ? yes

E (psi)	2369740	ε_{50} (%)	0.1186	Diameter (ft)	0.23
Vs (ft/s)	10261	ɥ	0.241	Length (ft)	0.48
Vp (ft/s)	17560	ɣ (lb/ft^3)	164.02	UCS (psi)	6757

Measured largest Aggregate:	Position of Large Aggregate	Percent Aggregate	Percent matrix
2.08 inches	top of sample	35%	65%

Notes	Initial Sample
Fine to medium sized gravel mixed in with small cobbles. Strongly cemented matrix. Fractures both going through and around aggregate. One entire large gravel popped out cleanly due to become loosened by fracturing. Top of sample is mostly small to medium gravel with one cobble. Bottom is mostly small cobbles with few gravels.	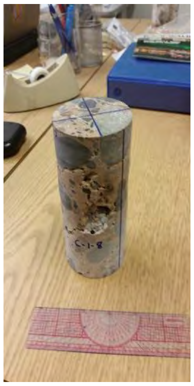

Pictures:

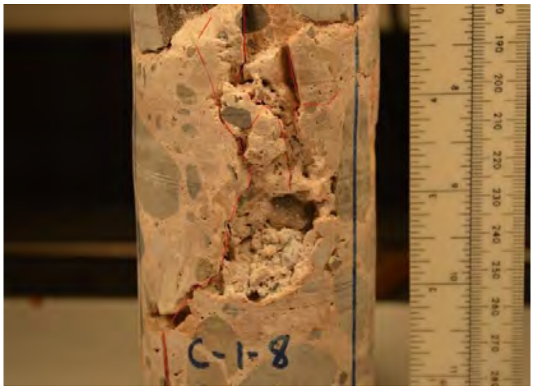

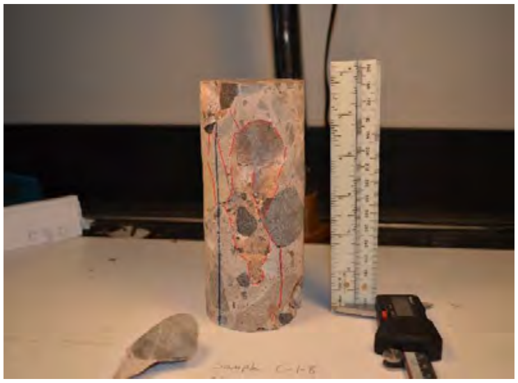

Sample #	Investigator	Date
C-1-9	Saint-Pierre	1/10/2018

Failure Mechanism: Based on ASTM C39

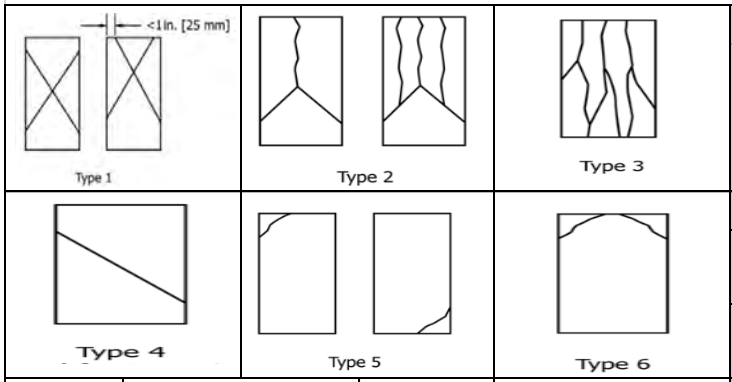

Type of Failure(s):	Type 3, Type 4
Diameter rock vs. diameter core	0.73
L > 2.5*D ?	yes

E (psi)	3567024	ε_{50} (%)	0.138	Diameter (ft)	0.23
Vs (ft/s)	10443	ч	0.266	Length (ft)	0.49
Vp (ft/s)	18508	ɣ (lb/ft^3)	164.12	UCS (psi)	10875.00

Measured largest Aggregate:	Position of Large Aggregate	Percent Aggregate	Percent matrix
2.01 inches	middle	35%	56%

Notes

Specimen is full of aggregate, large cobble on bottom of sample. Fine to large gravels with one smaller cobble mixed in. Shear plane travels through the smallest area of largest cobble then around it. Preferred path would have been through it. Both sawed ends show similar size aggregate with larger gravels in the middle. The matrix seems failry homogenous. The sample has a noticeable diversity of aggregate with dolomite, limestone, volcanics, quartzite and hydrothermally altered rock. Fractures going through some of the smaller aggregates, preferred path is through the clasts and not around.

Initial Sample

Pictures:

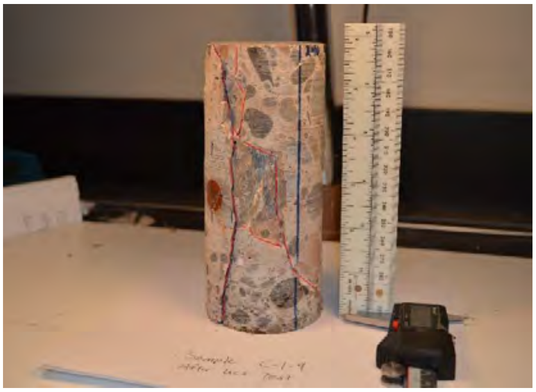

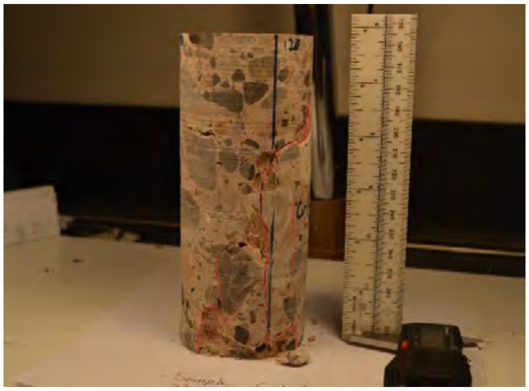

Sample #	Investigator	Date
C-1-10	Saint-Pierre	1/16/2018

Failure Mechanism: Based on ASTM C39

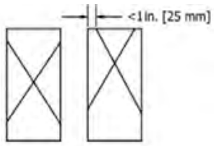 Type 1	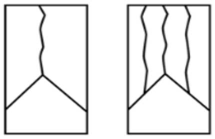 Type 2	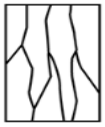 Type 3	Type of Failure(s): Type 3
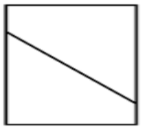 Type 4	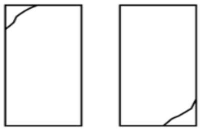 Type 5	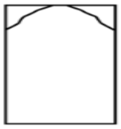 Type 6	Diameter rock vs. diameter core 0.82 L > 2.5*D ? yes

E (psi)	5585382	ε_{50} (%)	0.1498	Diameter (ft)	0.18
Vs (ft/s)	10719	ɥ	0.265	Length (ft)	0.36
Vp (ft/s)	18965	ɣ (lb/ft^3)	167.98	UCS (psi)	13618

Measured largest Aggregate:	Position of Large Aggregate	Percent Aggregate	Percent matrix
1.75	near upper surface	25%	75%

Notes	Initial Sample
Fracturing both goes through and around aggregate. One large gravel brok off entirely leaving a circular impressionin the sample. Pre-existing failure plane in middel of sample with pillow like carbonate. Highly reactive to 5% HCl. Most fractures terminated at pre-existing failure plane.	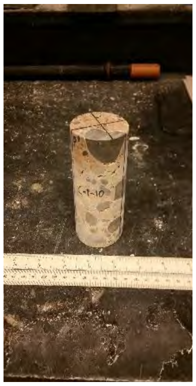

Pictures:

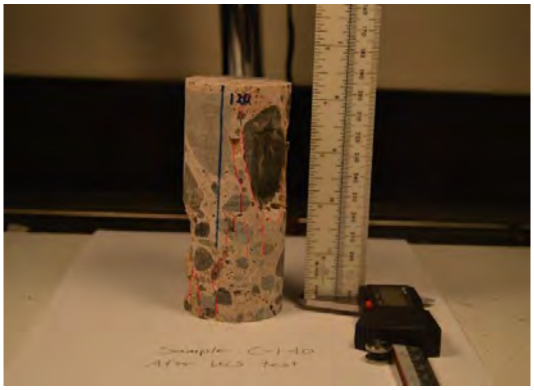

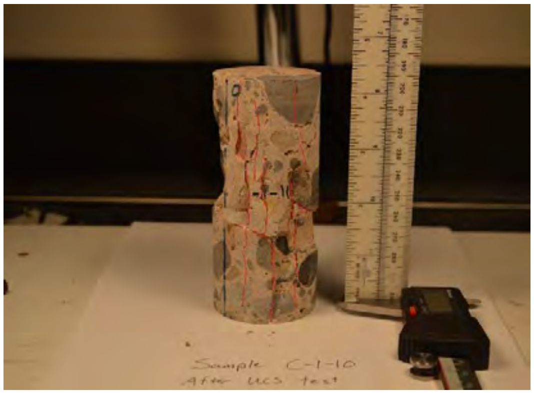

Sample #	Investigator	Date
C-1-11	Saint-Pierre	1/15/2018

Failure Mechanism: Based on ASTM C39

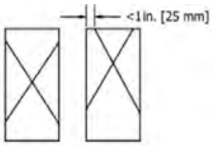 Type 1	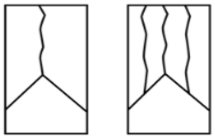 Type 2	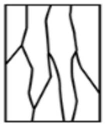 Type 3	Type of Failure(s): type 3
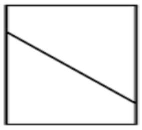 Type 4	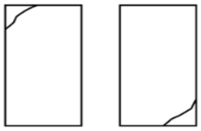 Type 5	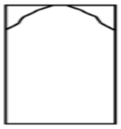 Type 6	Diameter rock vs. diameter core 0.75 L > 2.5*D ? yes

E (psi)	6415048	ε_{50} (%)	0.1621	Diameter (ft)	0.18
Vs (ft/s)	11142	ɥ	0.223	Length (ft)	0.37
Vp (ft/s)	18656	γ (lb/ft^3)	166.25	UCS (psi)	15844

Measured largest Aggregate:	Position of Large Aggregate	Percent Aggregate	Percent matrix
1.6 inches	near bottom surface	20%	80%

Notes	Initial Sample
Sample fractured inot several large pieces. It was reconstructed for post failure photographs. Upper surface of sample has much smaller gravels than bottom showing that it is stratigraphically upwards. Despite the numerous fractures, no shear developed. Fracturing both goes around and through the many larger gravels. Small voids scattered around sample. Fresh fracture surfaces show carbonate on faces.	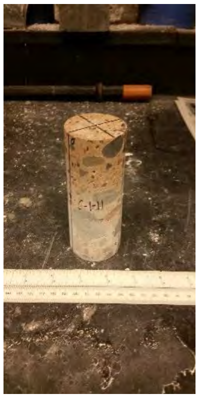

Pictures:

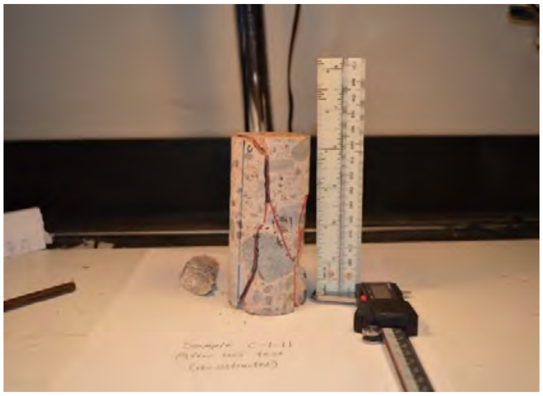

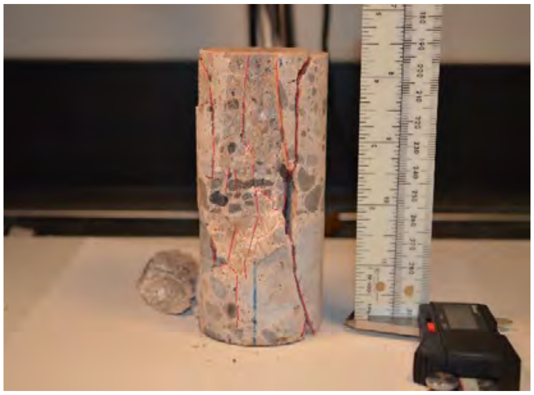

Sample #	Investigator	Date
C-1-12	Saint-Pierre	1/15/2018

Failure Mechanism: Based on ASTM C39

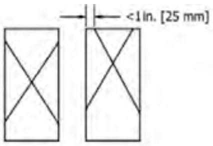 Type 1	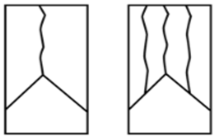 Type 2	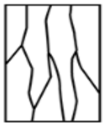 Type 3	Type of Failure(s): Type 3
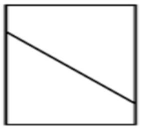 Type 4	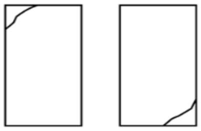 Type 5	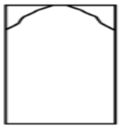 Type 6	Diameter rock vs. diameter core 0.67 L > 2.5*D ? yes

E (psi)	4402522	ε_{50} (%)	0.1292	Diameter (ft)	0.18
Vs (ft/s)	9946	ɥ	0.274	Length (ft)	0.37
Vp (ft/s)	17838	ɣ (lb/ft^3)	163.27	UCS (psi)	8885.00

Measured largest Aggregate:	Position of Large Aggregate	Percent Aggregate	Percent matrix
1.42 inches	middle	20%	80%

Notes	Initial Sample
Largest aggregate is a banded sandstone. Fracturing through larger gravels in abundant. Most elongate gravels lay horizontal with deposition. Fracturing travels around the more rounded gravels. Sevaral regions of sample have deep voids. Noticeable white film of carbonate line the void and reacts violently with 5% HCl. Fracture goes into the largest void and then dissapears into sample.	

Pictures:

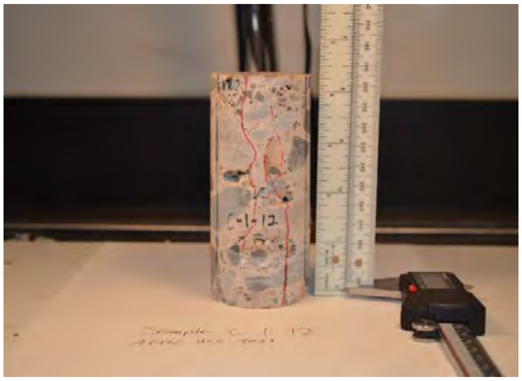

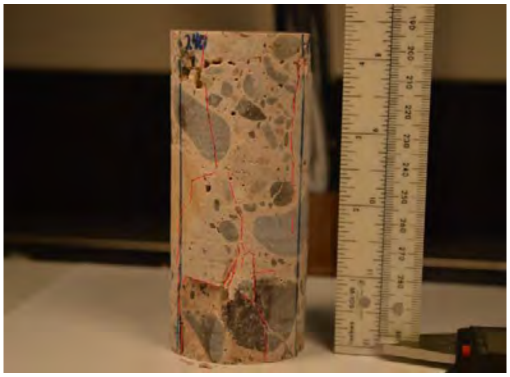

Sample #	Investigator	Date
C-1-13	Saint-Pierre	1/15/2018

Failure Mechanism: Based on ASTM C39

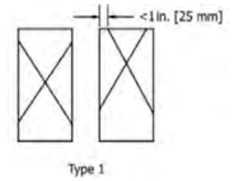 Type 1	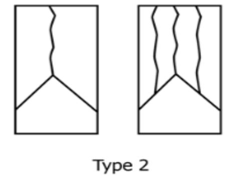 Type 2	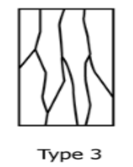 Type 3	Type of Failure(s): type 3
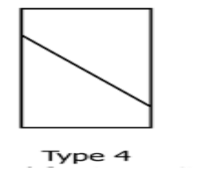 Type 4	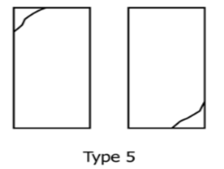 Type 5	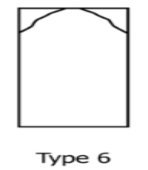 Type 6	Diameter rock vs. diameter core 0.99 L > 2.5*D ? yes

E (psi)	5859688	ε_{50} (%)	0.1463	Diameter (ft)	0.18
Vs (ft/s)	10206	ɥ	0.305	Length (ft)	0.37
Vp (ft/s)	19274	ɣ (lb/ft^3)	167.17	UCS (psi)	15365.00

Measured largest Aggregate:	Position of Large Aggregate	Percent Aggregate	Percent matrix
> 2.1 inches	bottom surface	40%	60%

Notes	Initial Sample
Sample had to be reconstructed for post failure photographs. Large aggregate on the bottom and fine gravels on upper surface indicating depostion. Large cobbles on bottom surface caused catastrophic failure during testing. Failures created shards from within the cobble. Fracturing both travels through and around aggregate.	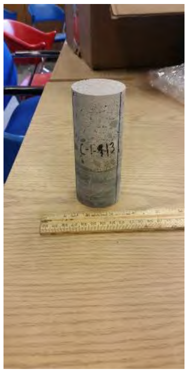

Pictures:

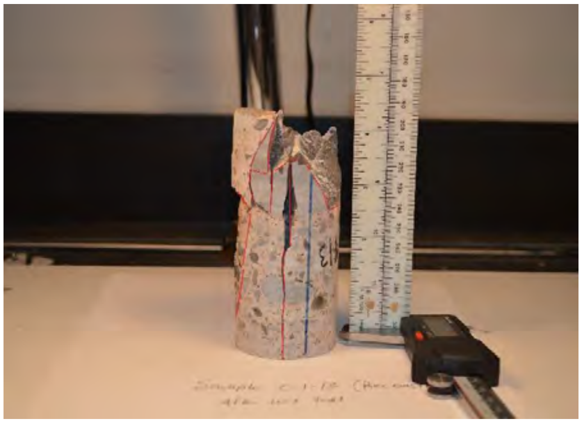

Sample #	Investigator	Date
C-1-14	Saint-Pierre	1/11/2018

Failure Mechanism: Based on ASTM C39

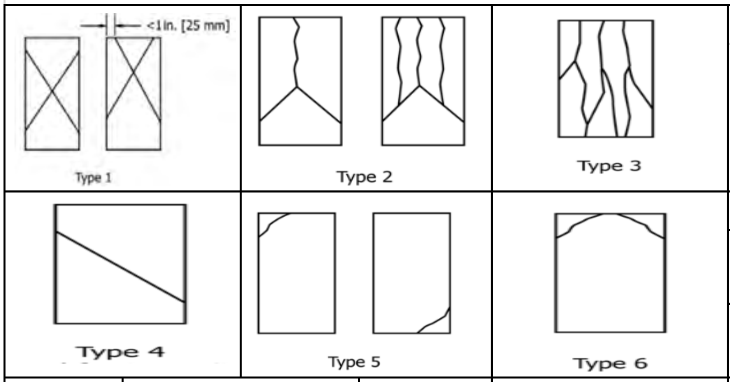

<1 in. [25 mm]
Type 1
Type 2
Type 3
Type 4
Type 5
Type 6

Type of Failure(s):	Type 3
Diameter rock vs. diameter core	0.40
L > 2.5*D ?	No

E (psi)	2725863	ε_{50} (%)	0.0586	Diameter (ft)	0.23
Vs (ft/s)	9595	ɥ	0.263	Length (ft)	0.41
Vp (ft/s)	16919	ɣ (lb/ft^3)	159.32	UCS (psi)	4574.00

Measured largest Aggregate:	Position of Large Aggregate	Percent Aggregate	Percent matrix
1.10 inches	Near top surface	20%	80%

Notes

Sub angular to rounded aggregate. Uniform matrix. Bottom of specimen looks like stratigraphic up by location of linear voids around aggreagte and size of aggregate at bottom surface. Fracturing for the most part goes through aggregate. Showing matrix is stronger than aggregate. One piece of large gravel is fractured around but is most likely popping out.

Initial Sample

C-1-14
150
C-1-14

Pictures:

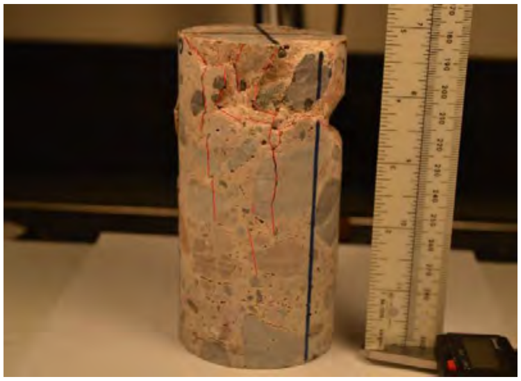

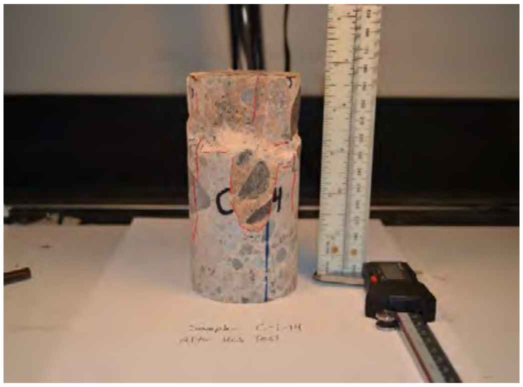

C-1-14
Sample C-1-14
After UCS Test

Sample #	Investigator	Date
C-2-2	Saint-Pierre	1/10/2018

Failure Mechanism: Based on ASTM C39

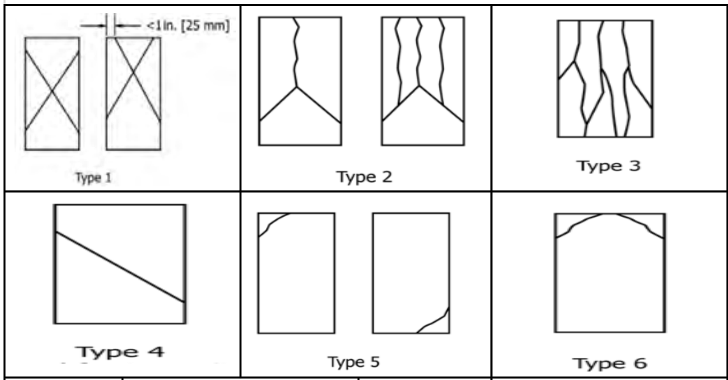

<1 in. [25 mm]
Type 1
Type 2
Type 3
Type 4
Type 5
Type 6

Type of Failure(s):	Type 3
Diameter rock vs. diameter core	0.11
L > 2.5*D ?	yes

E (psi)	2013066	ε_{50} (%)	0.0686	Diameter (ft)	0.23
Vs (ft/s)	8678	ɥ	0.091	Length (ft)	0.49
Vp (ft/s)	12933	ɣ (lb/ft^3)	142.03	UCS (psi)	3177

Measured largest Aggregate:	Position of Large Aggregate	Percent Aggregate	Percent matrix
0.3 inch	top surface	1%	99%

Notes

Fine to medium rounded gravel sparse in specimen. Bottom of sample has large linear voids from drilling. Bottom of sample is most likley upwards depsotion due to matrix being weaker. Fracturing is not visible through larger voids, but probably continues. Fracturing tends to maove laterally with voids.

Initial Sample

Pictures:

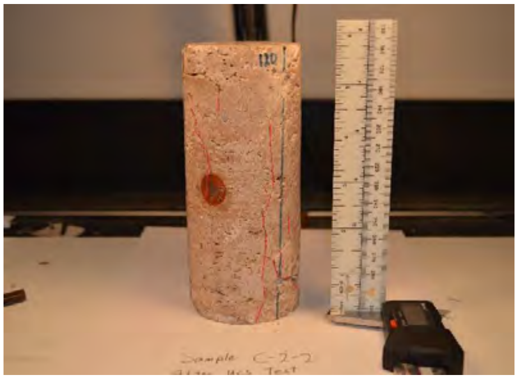

Sample C-2-2
After UCS Test

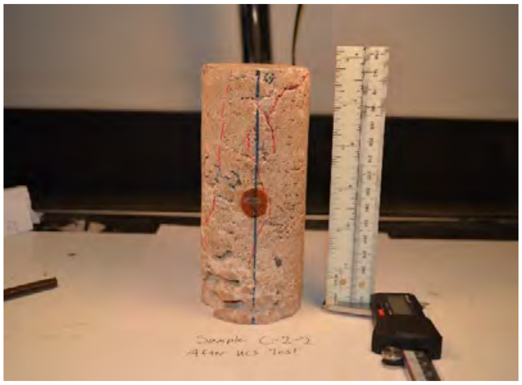

Sample C-2-2
After UCS Test

Sample #	Investigator	Date
C-2-3	Saint-Pierre	1/7/2018

Failure Mechanism: Based on ASTM C39

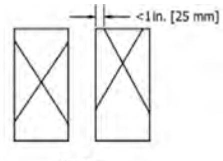 Type 1	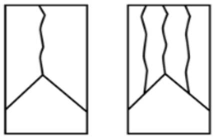 Type 2	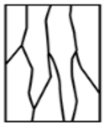 Type 3	Type of Failure(s): Type 3
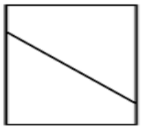 Type 4	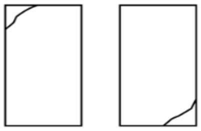 Type 5	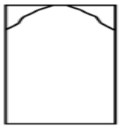 Type 6	Diameter rock vs. diameter core 0.15 L > 2.5*D ? No

E (psi)	1451616	ε_{50} (%)	0.1794	Diameter (ft)	0.23
Vs (ft/s)	8783	η	0.184	Length (ft)	0.36
Vp (ft/s)	14107	γ (lb/ft^3)	146.22	UCS (psi)	1846.00

Measured largest Aggregate:	Position of Large Aggregate	Percent Aggregate	Percent matrix
0.4 inch	middle	1%	99%

Notes	Initial Sample
Matrix is light brown and feels like harder matrix. Sample has many horizontal lineations that appear to be clay seams that were washed out during drilling. Gravels are small and rounded. Fracturing tends to travel around the gravels, which are harder than the matrix. Fracturing seems to side step with the lineations, showing that they are zones of weakness. bottom side of sample has majjor cracking in it, which connect all major failures.	

Pictures:

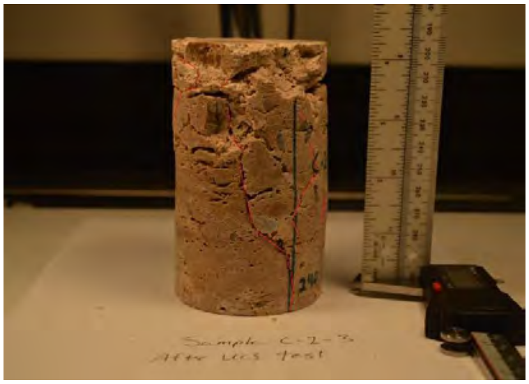

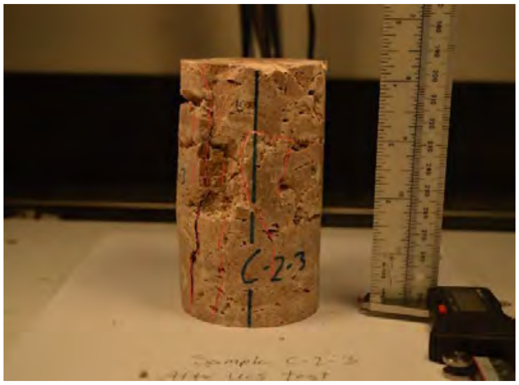

Sample #	Investigator	Date
C-2-4	Saint-Pierre	1/11/2018

Failure Mechanism: Based on ASTM C39

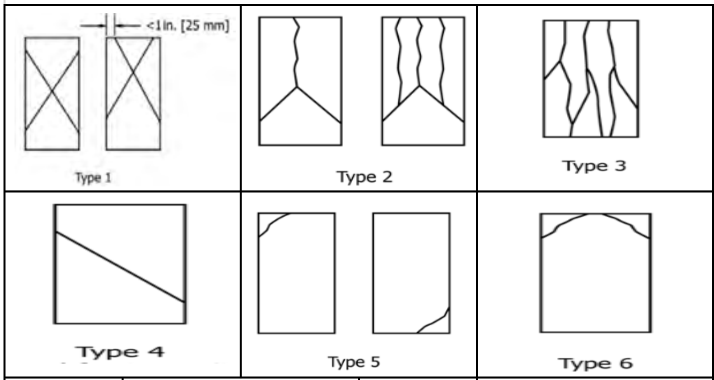

Type of Failure(s): Type 3, Type 4

Diameter rock vs. diameter: 0.11

L > 2.5*D ? No

E (psi)	763489	ε_{50} (%)	0.0697	Diameter (f	0.23
Vs (ft/s)	6888	ɥ	0.236	Length (ft)	0.30
Vp (ft/s)	11411	ɣ (lb/ft^3)	137.08	UCS (ft)	1504.00

Measured largest Aggregate:	Position of Large Aggregate	Percent Aggregate	Percent matrix
0.3 inch	top surface	1%	99%

Notes

Many larger voids both linear and circular. Cause by drilling and fracturing. Fracturing shows lateral movement with voids. Shear failure stair steps the whole way up sample. Fracturing exposes weak and powdery material within sample.

Initial Sample

Pictures:

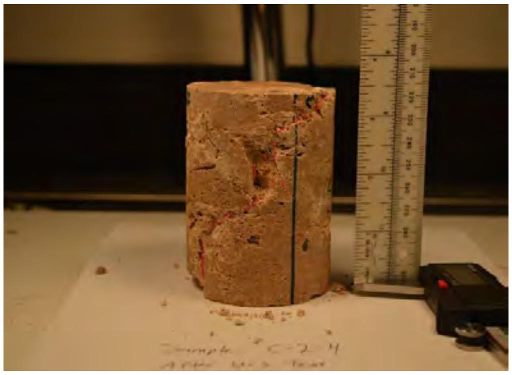

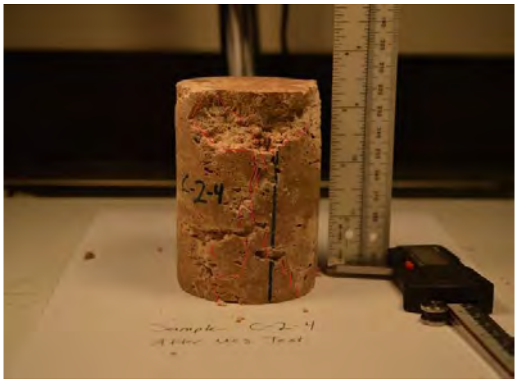

Sample #	Investigator	Date
C-4-1	Saint-Pierre	1/12/2018

Failure Mechanism: Based on ASTM C39

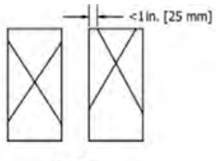 Type 1	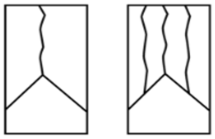 Type 2	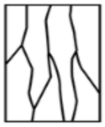 Type 3	Type of Failure(s): Type 3, Type 4
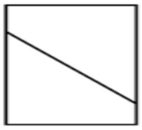 Type 4	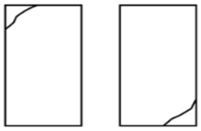 Type 5	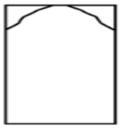 Type 6	Diameter rock vs. diameter 0.04 L > 2.5*D ? No

E (psi)	837263	ε_{50} (%)	0.1761	Diameter (f	0.23
Vs (ft/s)	6420	ɥ	0.213	Length (ft)	0.30
Vp (ft/s)	10632	ɣ (lb/ft^3	140.45	UCS (psi)	2871

Measured largest Aggregate:	Position of Large Aggregate	Percent Aggregate	Percent matrix
0.1 inch	near top surface exposed by fracture	1%	99%

Notes

Almost no visible aggregate. Noticeable bulging along main lateral fracture. Fairly well defined shear plane. It is not linear but more parabolic. Shear failure is not expressed on the opposite side, more columnar and massive.

Initial Sample

Pictures:

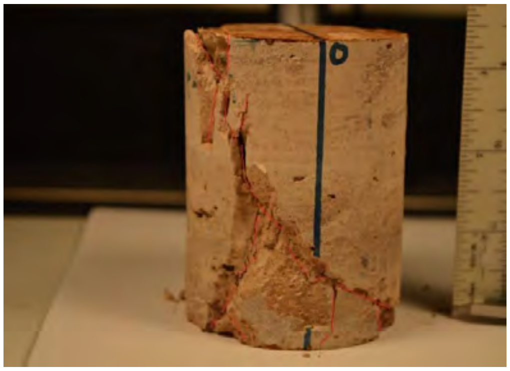

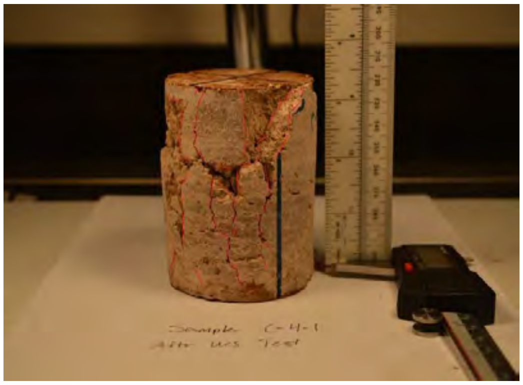

Sample #	Investigator	Date
C-4-2	Saint-Pierre	1/10/2018

Failure Mechanism: Based on ASTM C39

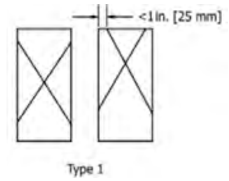 <1 in. [25 mm] Type 1	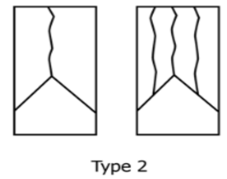	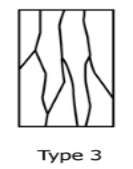	Type of Failure(s): Type 3, Type 4
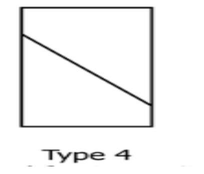	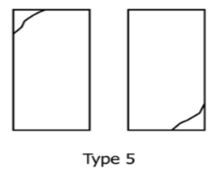	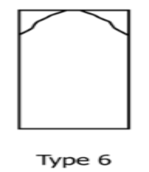	Diameter rock vs. diameter 0.07 L > 2.5*D ? No

E (psi)	633797	ε_{50} (%)	0.1557	Diameter (f	0.23
Vs (ft/s)	6845	ɥ	0.222	Length (ft)	0.36
Vp (ft/s)	11449	ɣ (lb/ft^3	139.04	UCS (psi)	2669

Measured largest Aggregate:	Position of Large Aggregate	Percent Aggregate	Percent matrix	
0.18 inches	middle	1%	99%	

Notes	Initial Sample
Few fine gravels scattered throughout specimen. Matrix is hereorgenous showing a varying level of cementation throughout. Sample does have a shear plane but it is not planar and travels through both the less cemented and more cemented material.	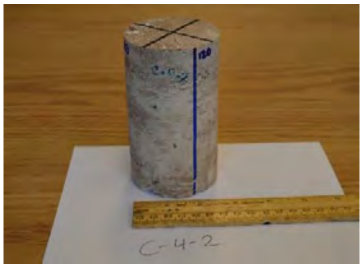

Pictures:

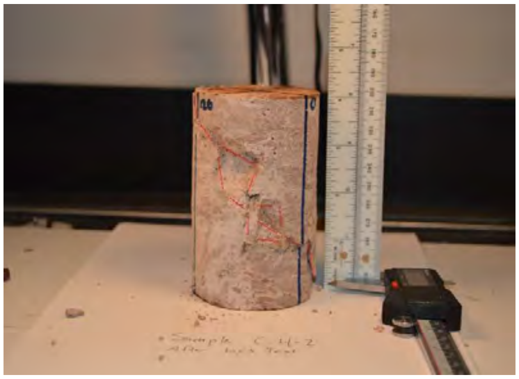
Sample C-4-2
After UCS Test

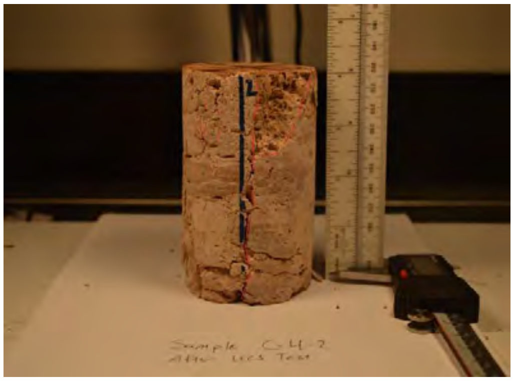
Sample C-4-2
After UCS Test

Sample #	Investigator	Date
C-4-3	Saint-Pierre	1/12/2018

Failure Mechanism: Based on ASTM C39

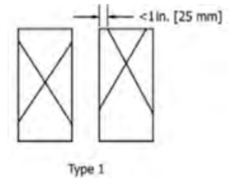

Type 1

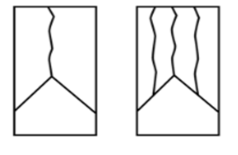

Type 2

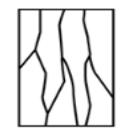

Type 3

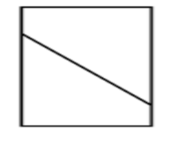

Type 4

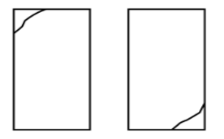

Type 5

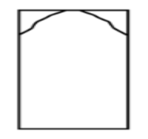

Type 6

Type of Failure(s): Type 3, Type 4

Diameter rock vs. diameter core: 0.09

L > 2.5*D ? No

E (psi)	1185436	ε_{50} (%)	0.209	Diameter (ft)	0.23
Vs (ft/s)	5385	ɥ	0.316	Length (ft)	0.31
Vp (ft/s)	10393	ɣ (lb/ft^3)	143.266	UCS (psi)	6228

Measured largest Aggregate:	Position of Large Aggregate	Percent Aggregate	Percent matrix
0.24 inch	near upper surface	1%	99%

Notes

Somewhat uniform matrix. Few scattered small aggregate. Undulating shear failure formed on one side, almost the other. Vertical cracking thoughout. Both top and bottom surfaces are intact.

Initial Sample

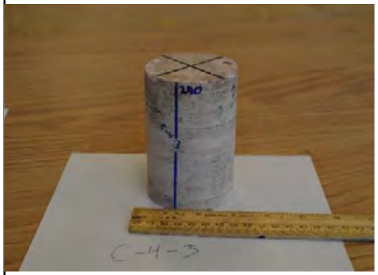

Pictures:

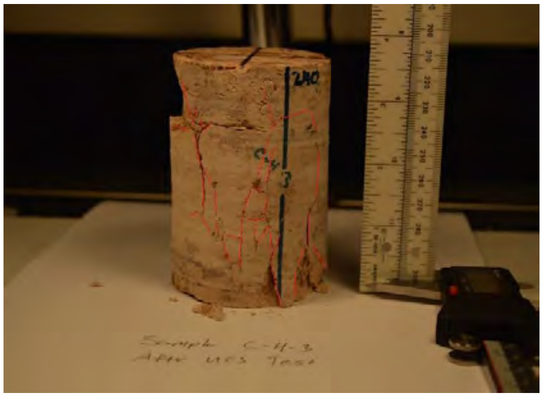

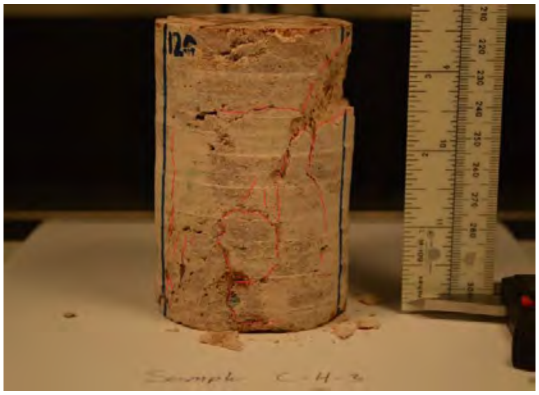

Sample #	Investigator	Date
C-7-1	Saint-Pierre	1/11/2018

Failure Mechanism: Based on ASTM C39

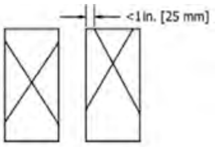

Type 1

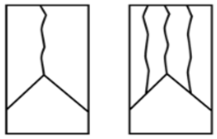

Type 2

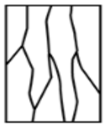

Type 3

Type of Failure(s):	Type 3
Diameter rock vs. diameter core	0.18
L > 2.5*D ?	yes

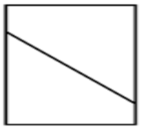

Type 4

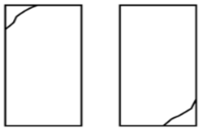

Type 5

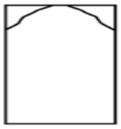

Type 6

E (psi)	869382	ε_{50} (%)	0.0542	Diameter (ft)	0.23
Vs (ft/s)	4556	ɥ	0.376	Length (ft)	0.50
Vp (ft/s)	10236	ɣ (lb/ft^3)	141.56	UCS (psi)	1582

Measured largest Aggregate:	Position of Large Aggregate	Percent Aggregate	Percent matrix
0.48 inch	middle	15%	85%

Notes

Sample has a clear divide between the top and the bottom. The top apeears to be harder, more compitent matrix with less aggregate. The bottom has most of the aggregate and is certainly weaker and has more voids. On the bottom surface, there is a large more cemented chunk of matrix that looks like aggregate. Fracturing is minimal. Sample failed but fracturing did not widel develop. Most of the small fractures are in the weaker half of the sample.

Initial Sample

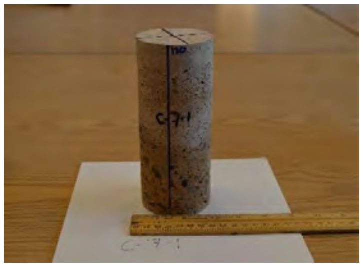

Pictures:

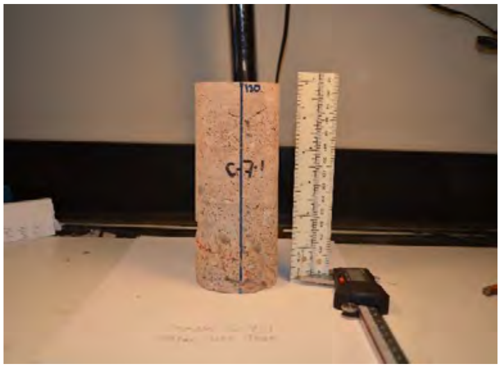

Sample #	Investigator	Date
C-7-2	Saint-Pierre	1/10/2018

Failure Mechanism: Based on ASTM C39

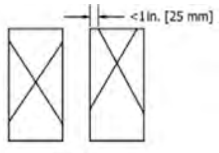 Type 1	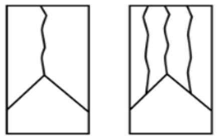 Type 2	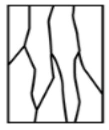 Type 3	Type of Failure(s): side failure
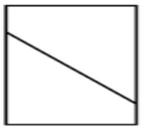 Type 4	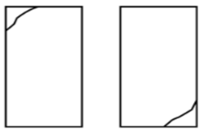 Type 5	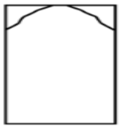 Type 6	Diameter rock vs. diameter core 0.11 L > 2.5*D ? No

E (psi)	1311784	ε_{50} (%)	0.1041	Diameter (ft)	0.23
Vs (ft/s)	7732	ɥ	0.187	Length (ft)	0.35
Vp (ft/s)	12463	ɣ (lb/ft^3)	128.37	UCS (psi)	2799

Measured largest Aggregate:	Position of Large Aggregate	Percent Aggregate	Percent matrix
0.31 inch	middle	7%	93%

Notes	Initial Sample
Failure is failry non descript. Most of one side blew out with almost no fractures penetrating through sample. Possible that sample was uneven and one side held most of the stress. Upper half of sample appears to be less cemented and underwent more deformation. Upper half of sample has many more smaller voids exposed by fracturing.	

Pictures:

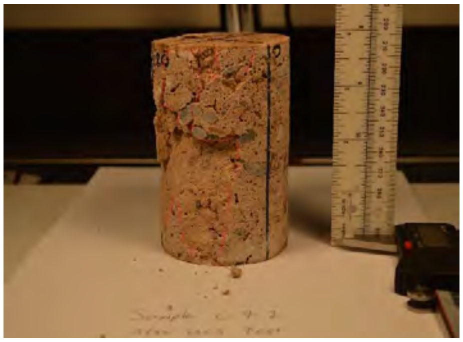

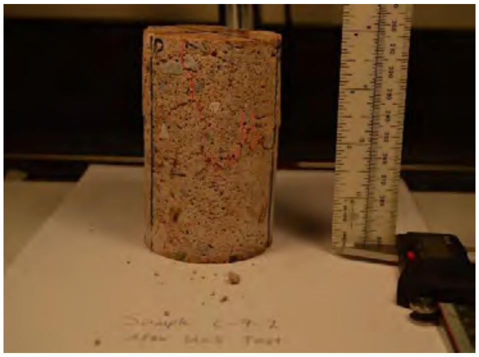

Sample #	Investigator	Date
C-7-3	Saint-Pierre	1/16/2018

Failure Mechanism: Based on ASTM C39

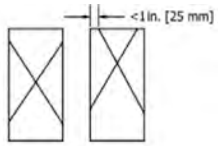 Type 1	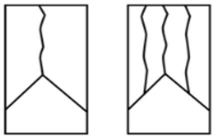 Type 2	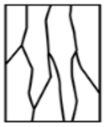 Type 3	Type of Failure(s): Type 3, Type 4
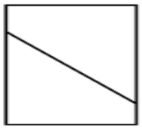 Type 4	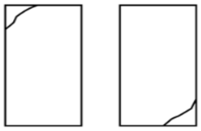 Type 5	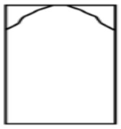 Type 6	Diameter rock vs. diameter core 0.41 L > 2.5*D ? No

E (psi)	345009	ε_{50} (%)	0.0674	Diameter (ft)	0.23
Vs (ft/s)	5309	ɥ	0.331	Length (ft)	0.35
Vp (ft/s)	10572	ɣ (lb/ft^3)	133.4	UCS (psi)	1634

Measured largest Aggregate:	Position of Large Aggregate	Percent Aggregate	Percent matrix
1.12 inches	bottom surface	5%	95%

Notes	Initial Sample
Sample had many pre-existing voids and planes of weakness before test. Upper half of sample broke off and into several pieces. Shear plane is poor but noticeable in photographs that were reconstructed after test. Vertical fractures prefer path through voids. Scattered fine to medium gravels throughout specimen. Many voids visible on both top and bottom surfaces. Predominant failure in middle of sample has noticeable carbonate on surface.	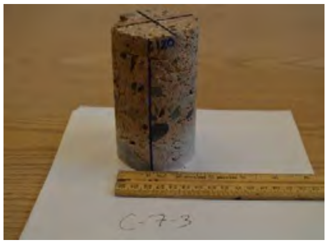

Pictures:

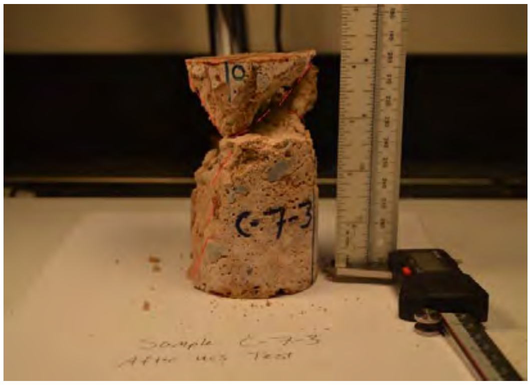

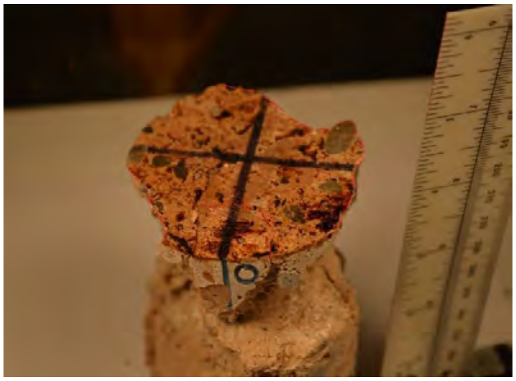

Sample #	Investigator	Date
C-8-1	Saint-Pierre	1/7/2018

Failure Mechanism: Based on ASTM C39

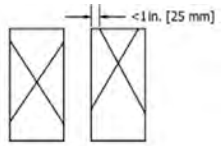 Type 1	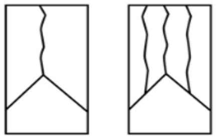 Type 2	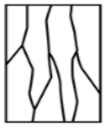 Type 3	Type of Failure(s): Type 3 Type 4 Shear
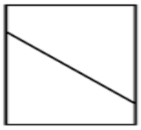 Type 4	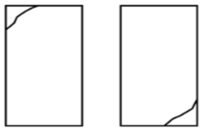 Type 5	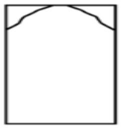 Type 6	Diameter rock vs. diameter core 0.12 L > 2.5*D ? No

E (psi)	1378619	ε_{50} (%)	0.103	Diameter (ft)	0.23
Vs (ft/s)	6741	ɥ	0.176	Length (ft)	0.30
Vp (ft/s)	10749	ɣ (lb/ft^3)	149.95	UCS (psi)	2960

Measured largest Aggregate:	Position of Large Aggregate	Percent Aggregate	Percent matrix	
.33 inch	middle	2%	98%	

Notes	Initial Sample
Mostly brownish matrix with few rounded gravels. Sample almost shows shear failure but fracture ends in upper side of sample. Both ends of sample have very few gravels. Faractures tend to travel around gravels due to weaker matrix. One large enlongated area of matrix is darker and appears to be more compitent. Fracture travels both around and through the more cemented matrix. Shear failure stair steps up the sample following zones of weakness.	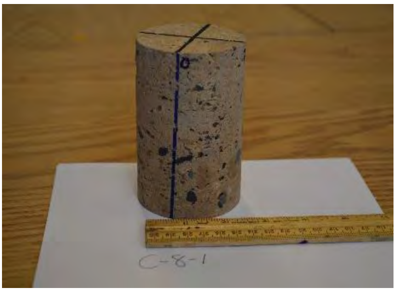

Pictures:

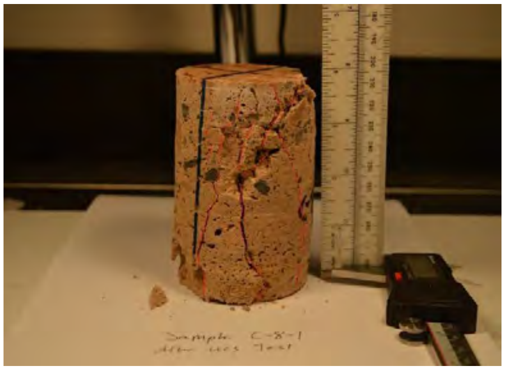

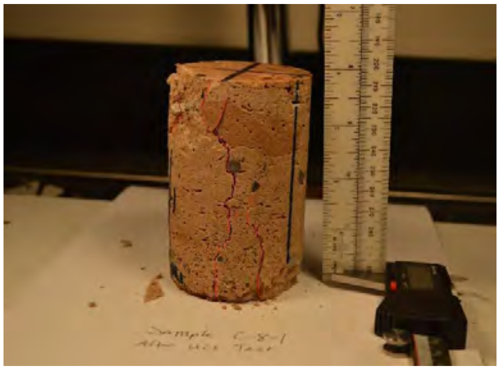

Sample #	Investigator	Date
C-8-2	Saint-Pierre	1/11/2018

Failure Mechanism: Based on ASTM C39

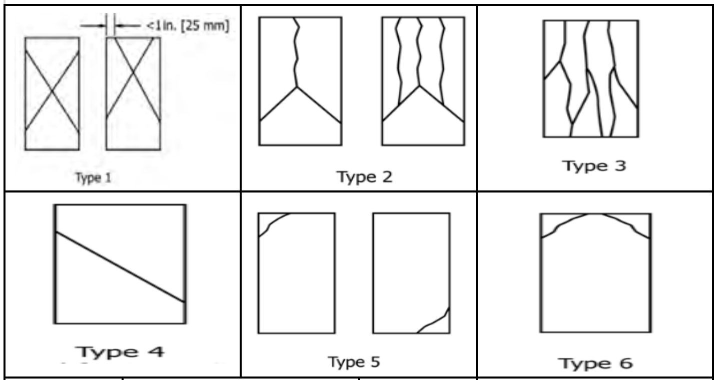

Type of Failure(s):	Type 4
Diameter rock vs. diameter	0.17
L > 2.5*D ?	no

E (psi)	842921	ε_{50} (%)	0.089	Diameter (f	0.23
Vs (ft/s)	6122	ɥ	0.219	Length (ft)	0.42
Vp (ft/s)	10208	γ (lb/ft^3	131.16	UCS (psi)	1390

Measured largest Aggregate:	Position of Large Aggregate	Percent Aggregate	Percent matrix
0.45 inch	top surface	1%	99%

Notes

Sample is fairly uniform with a weak matrix and small voids all around the perimeter. Small to medium gravel scarce throughout sample. Noticeable shear that wraps aroun entire sample. Continuous but changes dips. No fracturing occurred on either end of sample.

Initial Sample

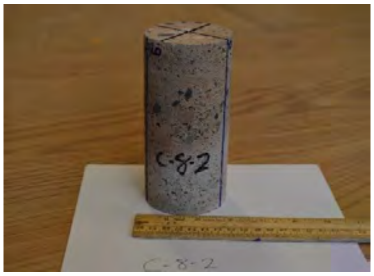

Pictures:

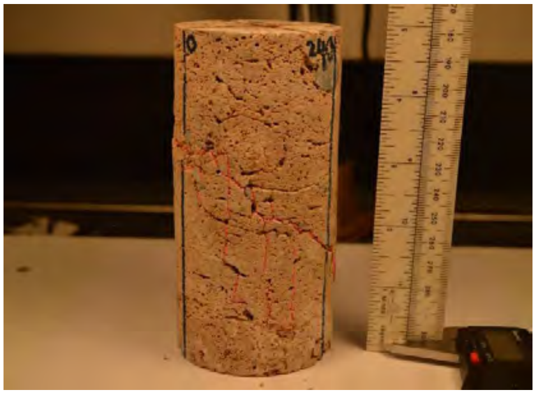

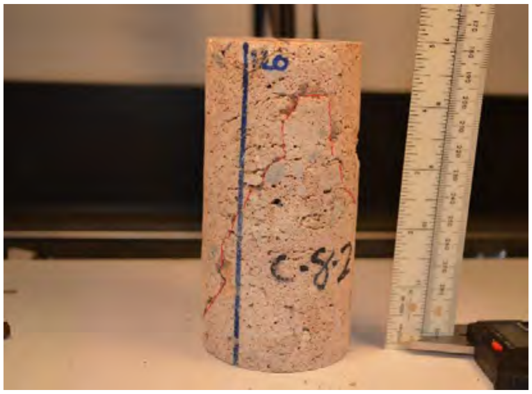

Sample #	Investigator	Date
HC-1-1	Saint-Pierre	1/15/2018

Failure Mechanism: Based on ASTM C39

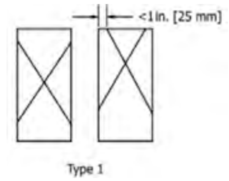
<1in. [25 mm]
Type 1

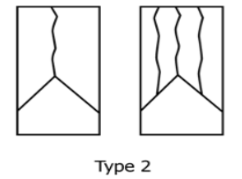

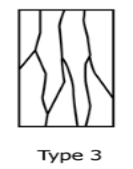

Type of Failure(s):

Type 3

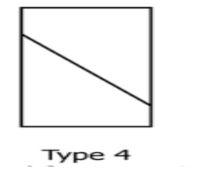

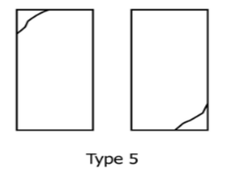

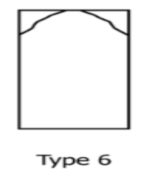

Diameter rock vs. diameter core	0.67
L > 2.5*D ?	yes

E (psi)	5925469	ε_{50} (%)	0.1661	Diameter (ft)	0.17
Vs (ft/s)	9577	ɥ	0.315	Length (ft)	0.41
Vp (ft/s)	18433	ɣ (lb/ft^3)	164.87	UCS (psi)	14262

Measured largest Aggregate:	Position of Large Aggregate	Percent Aggregate	Percent matrix
1.4 inches	bottom surface	25%	75%

Notes	Initial Sample
Sample mostly consists of matrix and fine gravels. Medium to large gravels scattered throughout. Some of the larger aggreagte seem to be dictating direction of fracture. One large failure plane seems to follow aggregate, then turns vertical. Fracturing travels through the smaller gravels. Large section of sample brok off due to fracture. About a third of upper surface is gone.	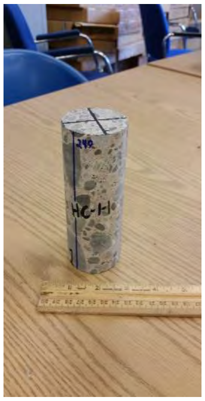

Pictures:

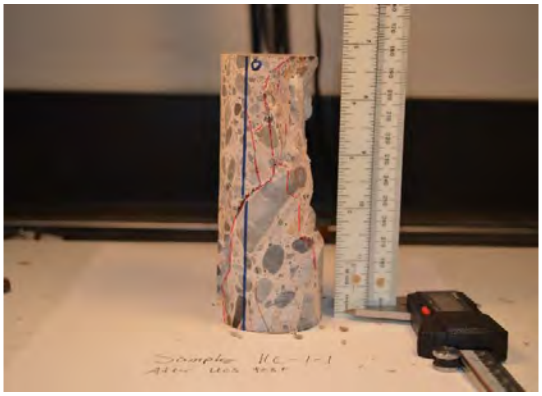
Sample HC-1-1
After UCS test

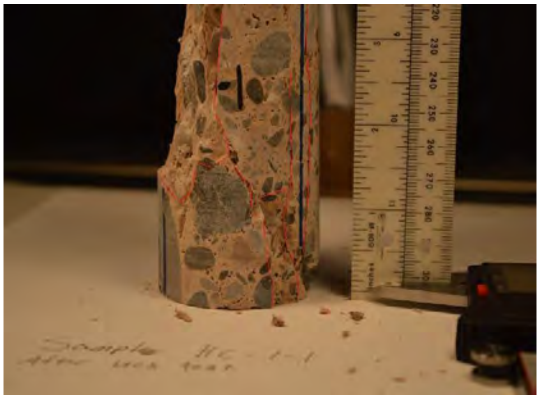
Sample HC-1-1
After UCS test

Sample #	Investigator	Date
HC-1-2	Saint-Pierre	1/15/2018

Failure Mechanism: Based on ASTM C39

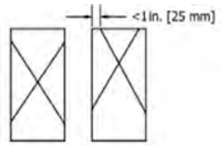 Type 1	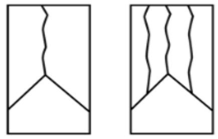 Type 2	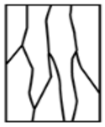 Type 3	Type of Failure(s): Type 3
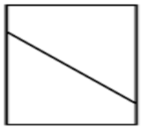 Type 4	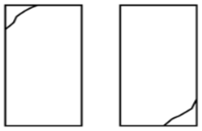 Type 5	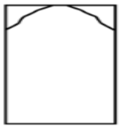 Type 6	Diameter rock vs. diameter core 0.51 L > 2.5*D ? yes

E (psi)	5538651	ε_{50} (%)	0.4973	Diameter (ft)	0.17
Vs (ft/s)	10029	ʮ	0.28	Length (ft)	0.42
Vp (ft/s)	18187	ɣ (lb/ft^3)	161.19	UCS (psi)	13937

Measured largest Aggregate:	Position of Large Aggregate	Percent Aggregate	Percent matrix
1.08 inches	near top surface	20%	80%

Notes	Initial Sample
Sample fractured into shards. About a quarter of sample broke off. Sample contain fine to large gravels, mostly rounded. Fracturing mostly travels through aggregate but in few cases it travels around. In the few cases fracturing travels around aggreagte, the elongate aggregate is oriented upwards.	

Pictures:

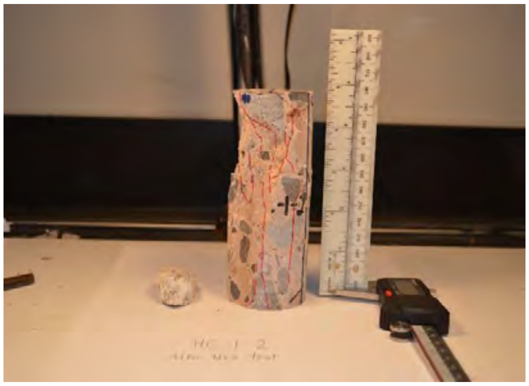

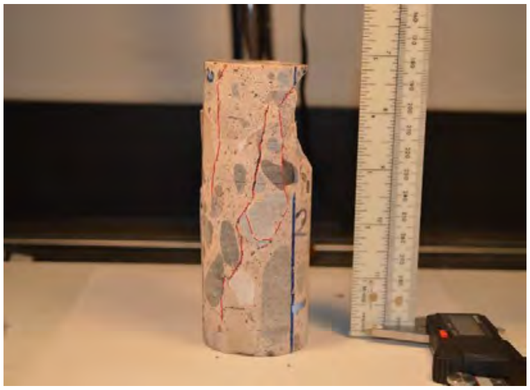

Sample #	Investigator	Date
HC-1-3	Saint-Pierre	1/16/2017

Failure Mechanism: Based on ASTM C39

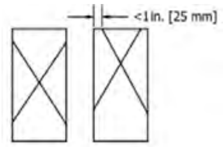 Type 1	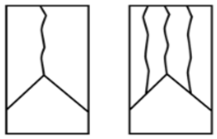 Type 2	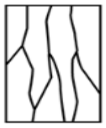 Type 3	Type of Failure(s): type 3
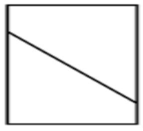 Type 4	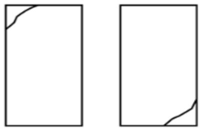 Type 5	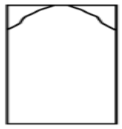 Type 6	Diameter rock vs. diameter core 0.73 L > 2.5*D ? yes

E (psi)	5660946	ε_{50} (%)	0.2682	Diameter (ft)	0.17
Vs (ft/s)	10325	ɥ	0.26	Length (ft)	0.42
Vp (ft/s)	18164	ɣ (lb/ft^3)	162.95	UCS (psi)	16284

Measured largest Aggregate:	Position of Large Aggregate	Percent Aggregate	Percent matrix	
1.52 inches	middle	25%	75%	

Notes	Initial Sample
Sample is composed of mostly matrix and large gravels with scattered fine gravel throughout. Fractures creating shards within sample. Fractures seem more likely to travel through aggregate than around, possibly because matrix is stronger. Some clusters of darker, more cemented matrix that look like aggregate.	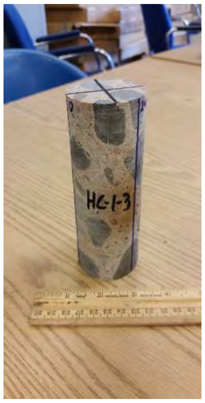

Pictures:

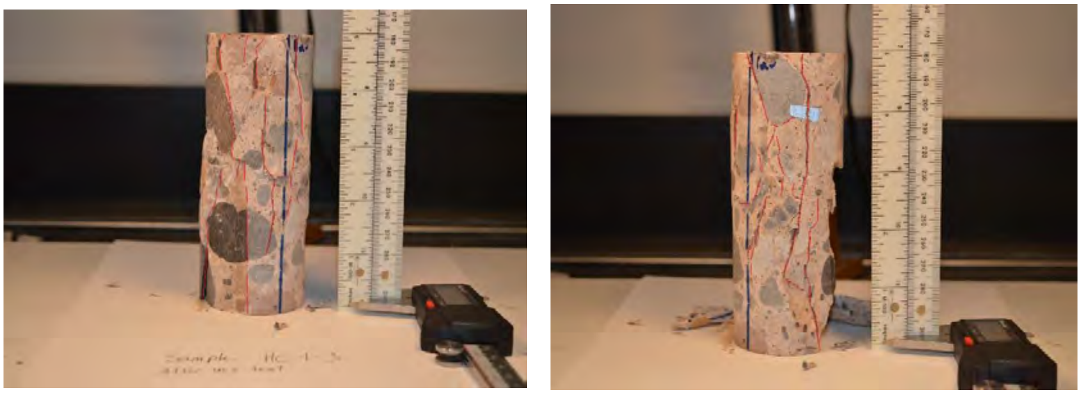

Sample #	Investigator	Date
HC-1-5	Saint-Pierre	1/16/2018

Failure Mechanism: Based on ASTM C39

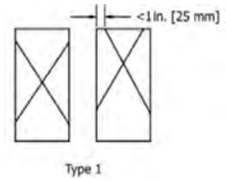 Type 1	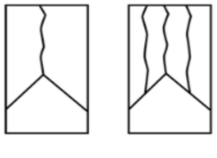 Type 2	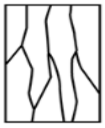 Type 3	Type of Failure(s): type 3
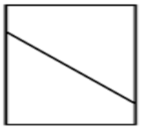 Type 4	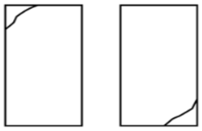 Type 5	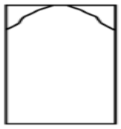 Type 6	Diameter rock vs. diameter core 0.70 L > 2.5*D ? yes

E (psi)	6897028	ε_{50} (%)	0.3158	Diameter (ft)	0.17
Vs (ft/s)	10967	ɥ	0.26	Length (ft)	0.41
Vp (ft/s)	19159	γ (lb/ft^3)	165.96	UCS (psi)	20325

Measured largest Aggregate:	Position of Large Aggregate	Percent Aggregate	Percent matrix
1.45 inches	middle within sample	20%	80%

Notes	Initial Sample
During testing sample broke into several smaller fragments. Based off failure pattern, failure mechanism appears to be columnar. Few fractures appear to travel around aggregate indicating that matrix is as hard as aggreagte and the casue of the catastrophic failure.	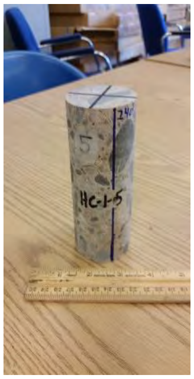

Pictures:

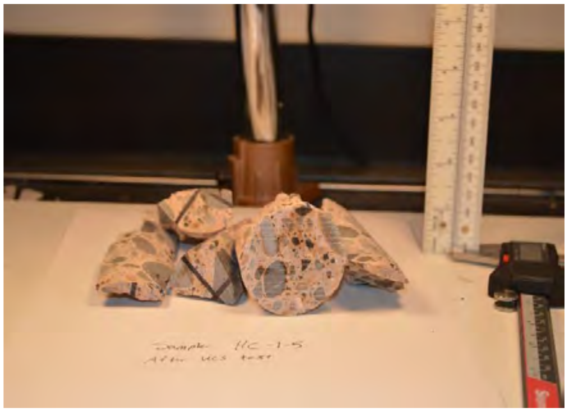

Appendix C

Stress-Strain Curves of all 53 Tests with Material Models

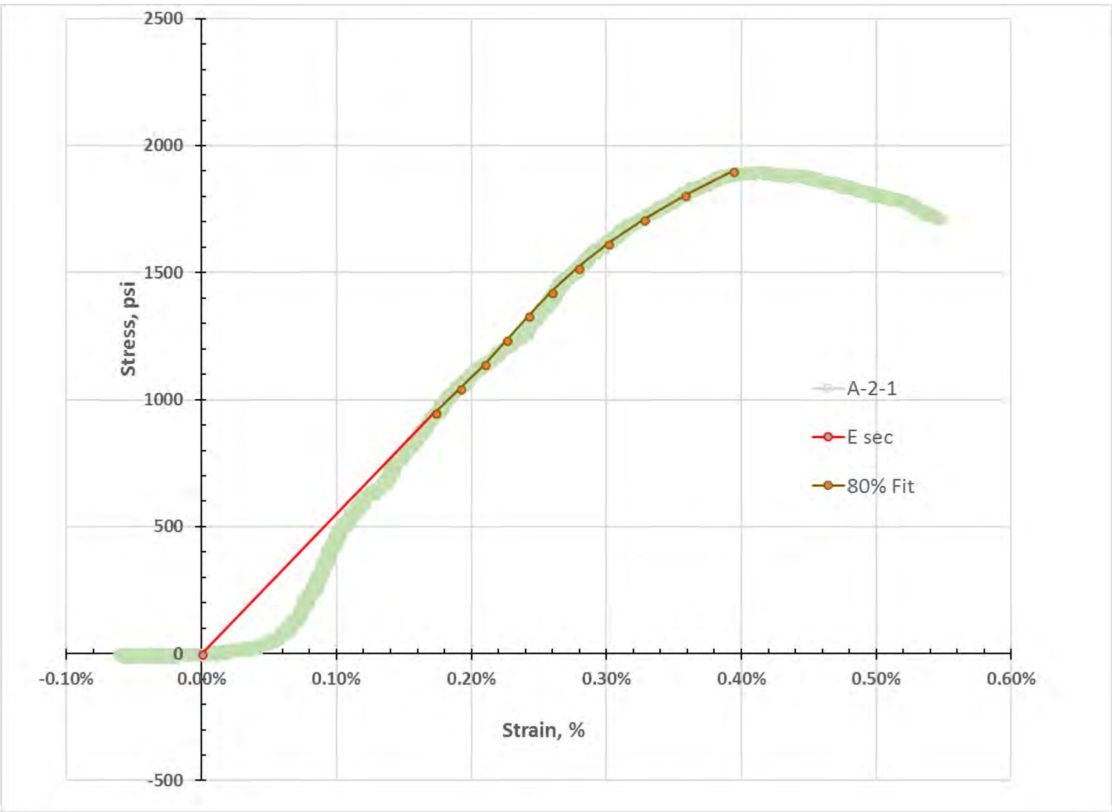
2500
2000
1500
1000
500
0
-500
Stress, psi
-0.10%
0.00%
0.10%
0.20%
0.30%
0.40%
0.50%
0.60%
Strain, %
A-2-1
E sec
80% Fit

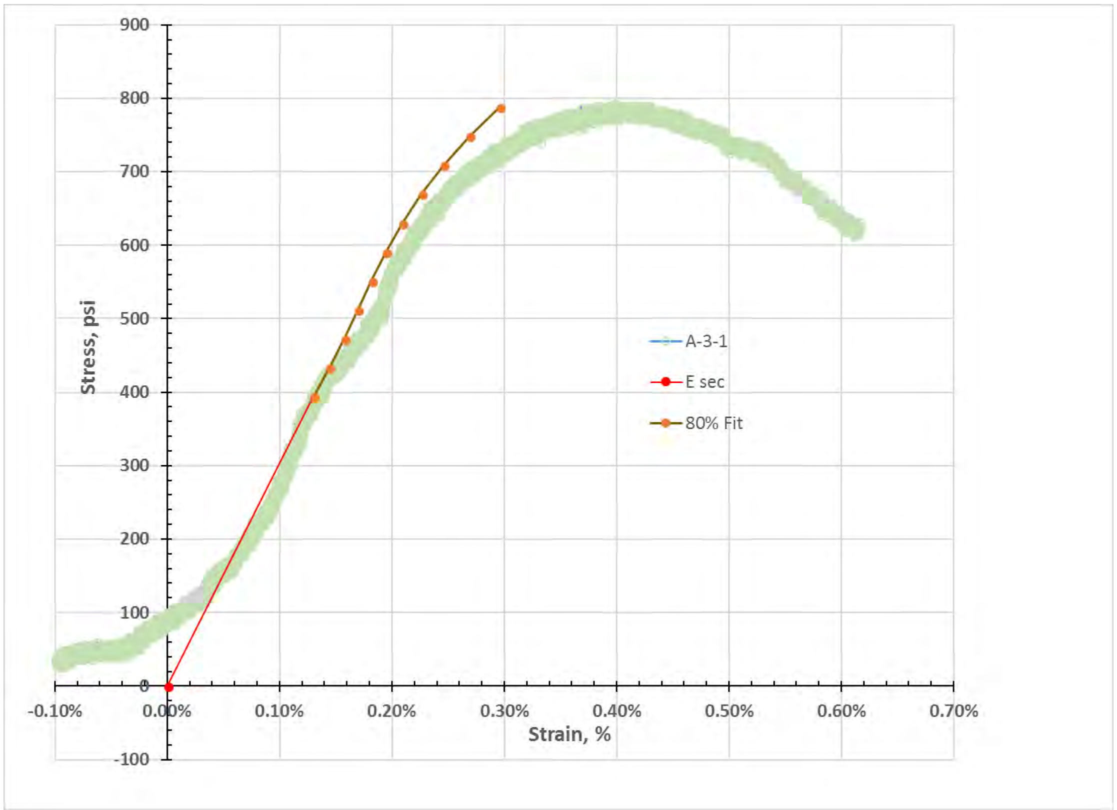
900
800
700
600
500
400
300
200
100
0
-100
Stress, psi
-0.10%
0.00%
0.10%
0.20%
0.30%
0.40%
0.50%
0.60%
0.70%
Strain, %
A-3-1
E sec
80% Fit

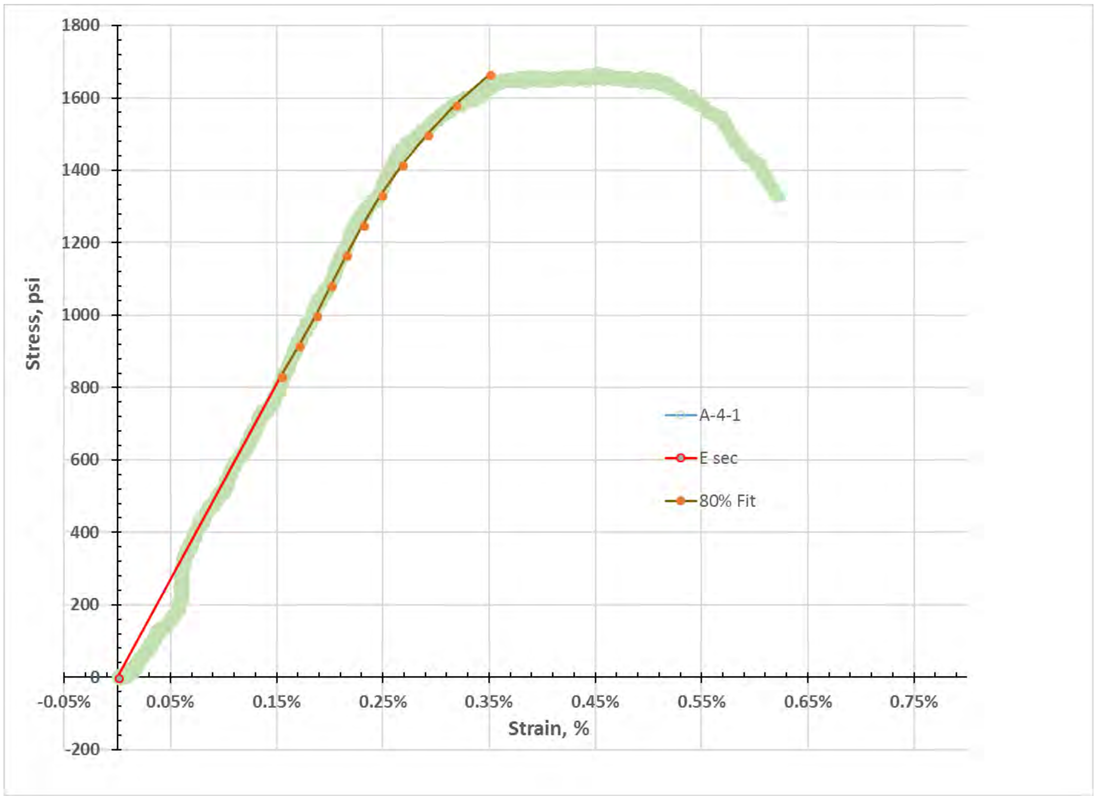

Stress, psi
1800
1600
1400
1200
1000
800
600
400
200
0
-200
-0.05%
0.05%
0.15%
0.25%
0.35%
0.45%
0.55%
0.65%
0.75%
Strain, %
A-4-1
E sec
80% Fit

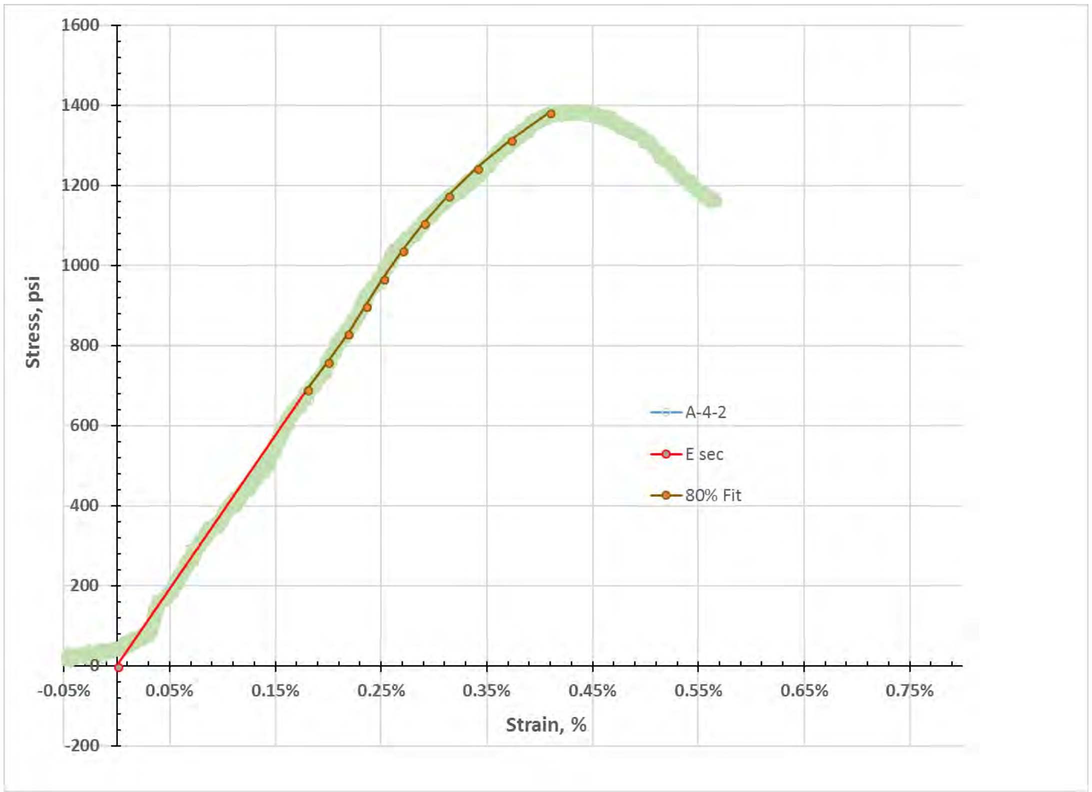

Stress, psi
1600
1400
1200
1000
800
600
400
200
0
-200
-0.05%
0.05%
0.15%
0.25%
0.35%
0.45%
0.55%
0.65%
0.75%
Strain, %
A-4-2
E sec
80% Fit

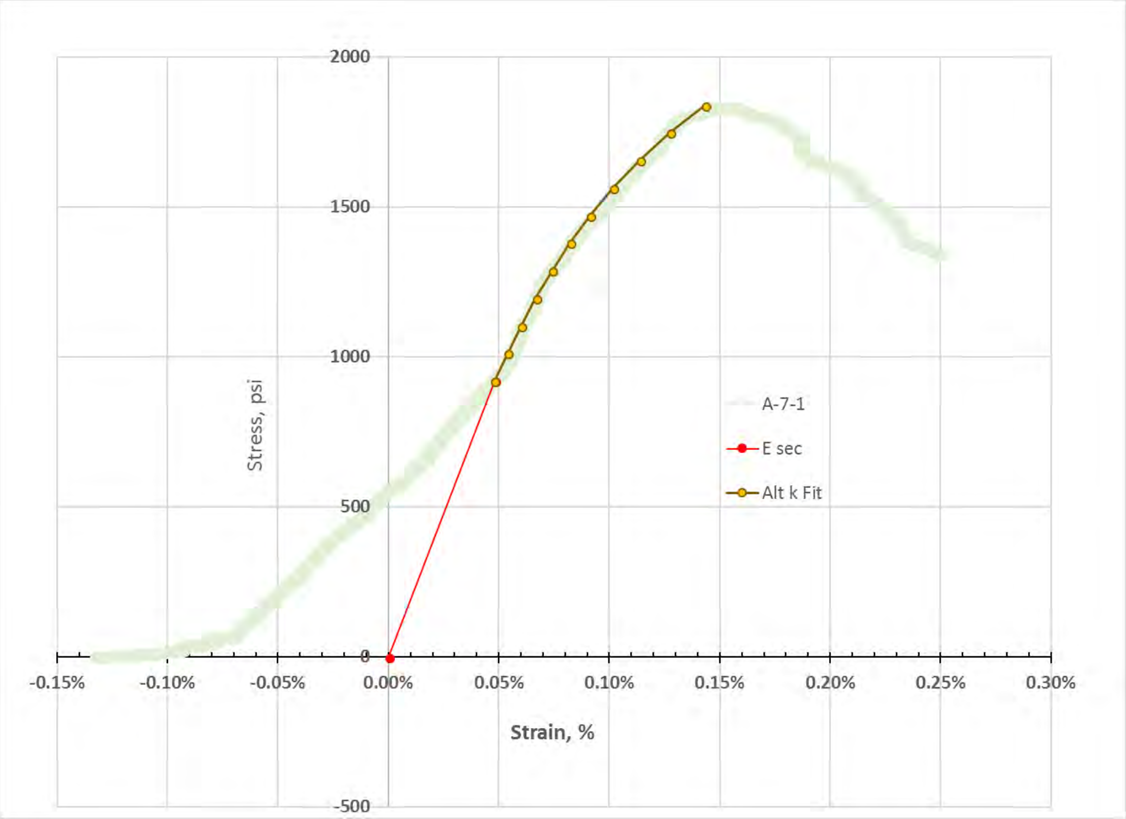
2000
1500
1000
500
0
-500
Stress, psi
-0.15%
-0.10%
-0.05%
0.00%
0.05%
0.10%
0.15%
0.20%
0.25%
0.30%
Strain, %
A-7-1
E sec
Alt k Fit

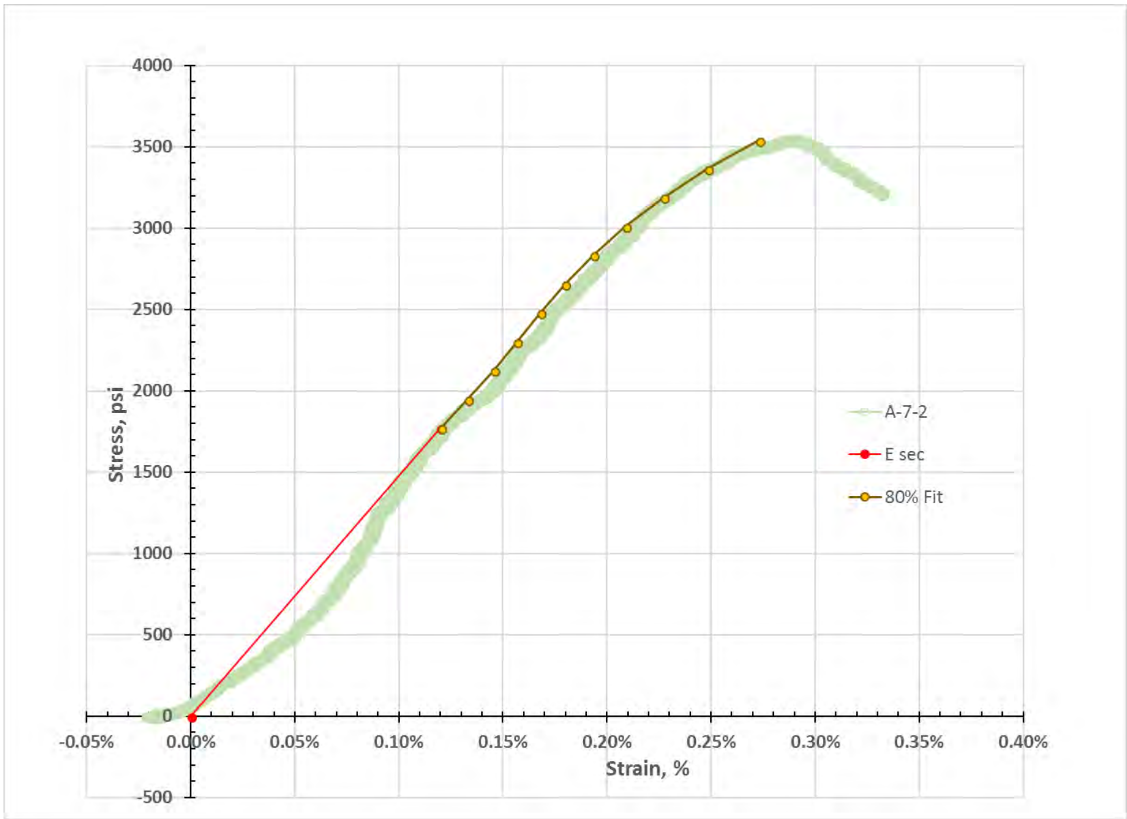
4000
3500
3000
2500
2000
1500
1000
500
0
-500
Stress, psi
-0.05%
0.00%
0.05%
0.10%
0.15%
0.20%
0.25%
0.30%
0.35%
0.40%
Strain, %
A-7-2
E sec
80% Fit

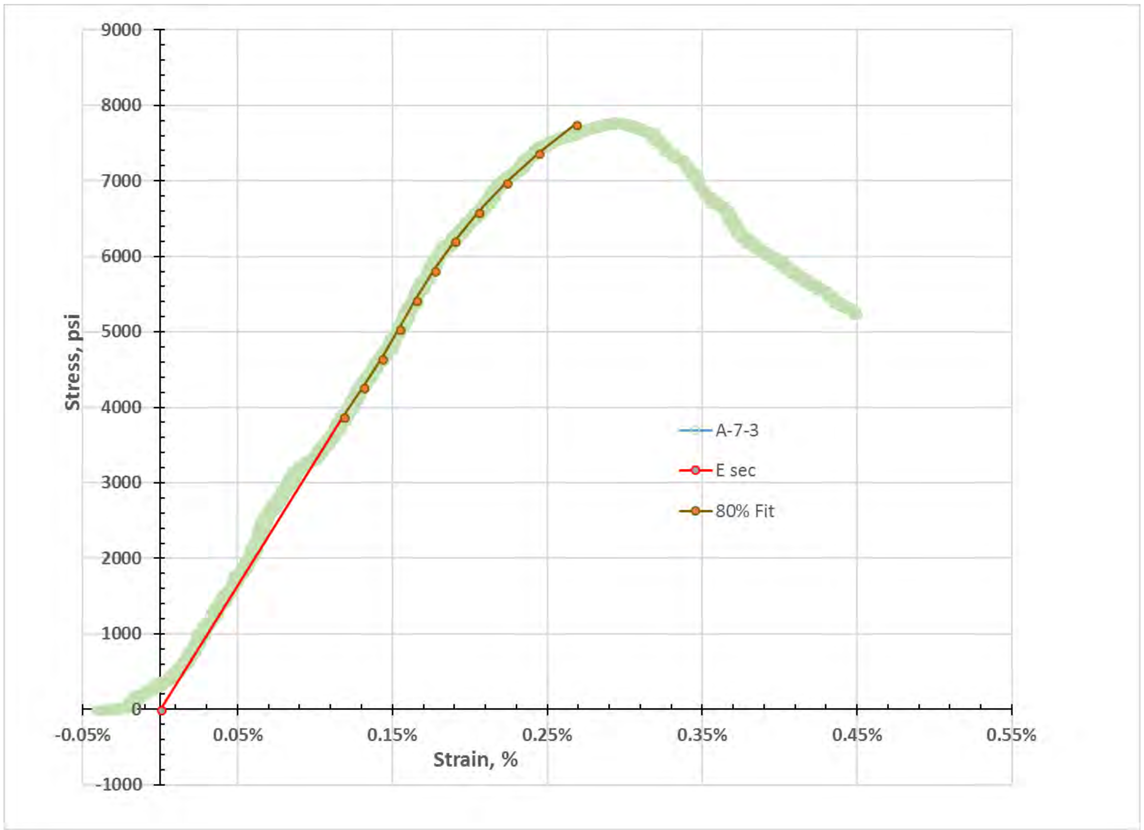
9000
8000
7000
6000
5000
4000
3000
2000
1000
0
-1000
Stress, psi
-0.05%
0.05%
0.15%
0.25%
0.35%
0.45%
0.55%
Strain, %
A-7-3
E sec
80% Fit

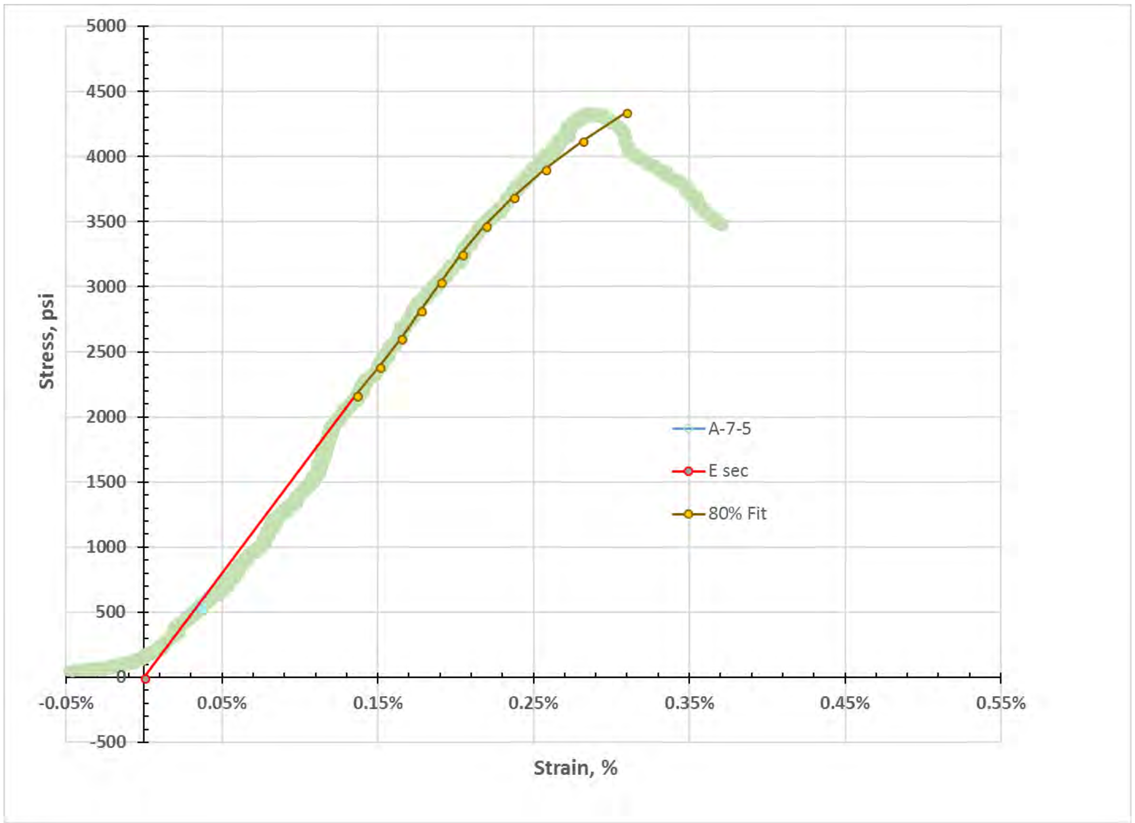
5000
4500
4000
3500
3000
2500
2000
1500
1000
500
0
-500
Stress, psi
-0.05%
0.05%
0.15%
0.25%
0.35%
0.45%
0.55%
Strain, %
A-7-5
E sec
80% Fit

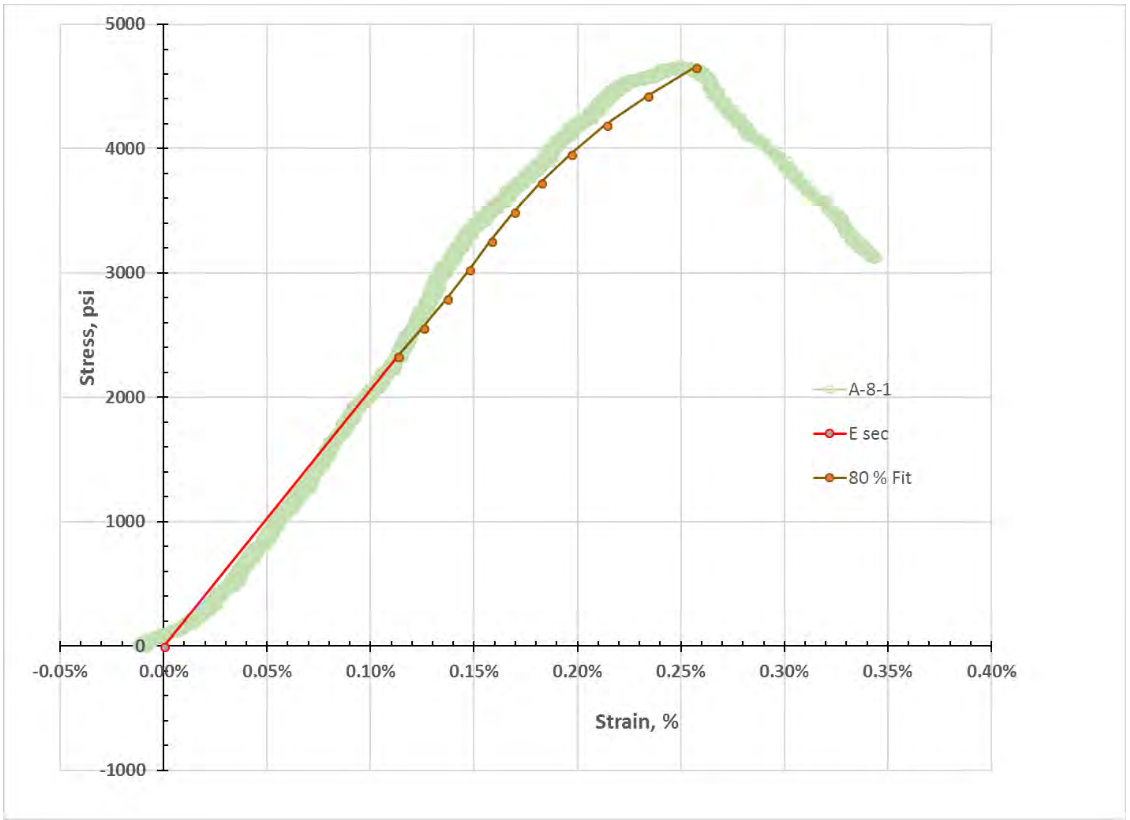

5000
4000
3000
2000
1000
0
-1000
Stress, psi
-0.05%
0.00%
0.05%
0.10%
0.15%
0.20%
0.25%
0.30%
0.35%
0.40%
Strain, %
A-8-1
E sec
80 % Fit

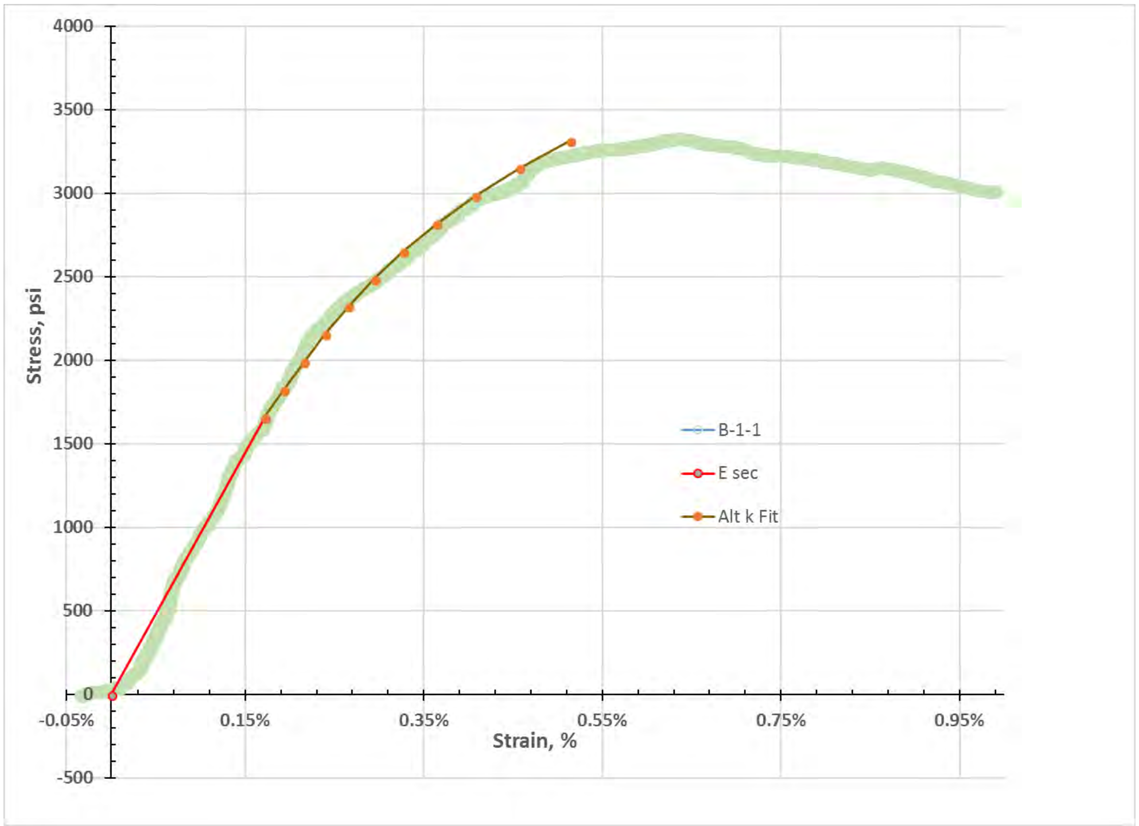

4000
3500
3000
2500
2000
1500
1000
500
0
-500
Stress, psi
-0.05%
0.15%
0.35%
0.55%
0.75%
0.95%
Strain, %
B-1-1
E sec
Alt k Fit

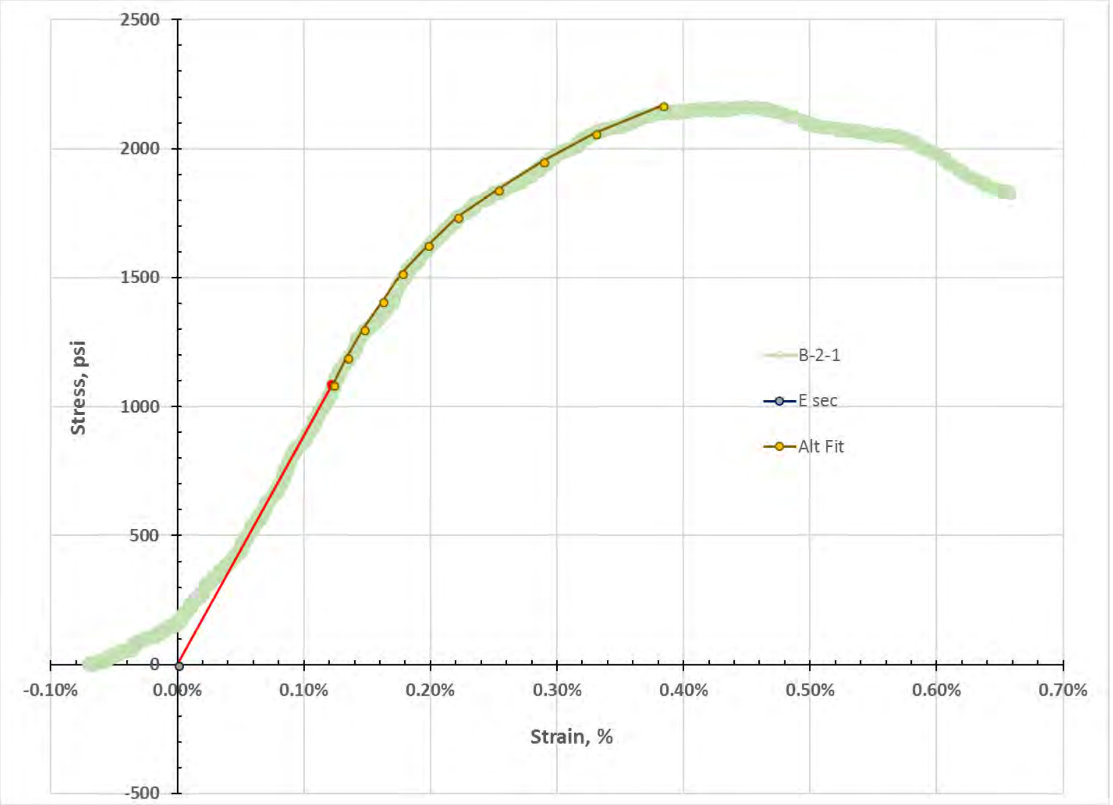
2500
2000
1500
1000
500
0
-500
Stress, psi
-0.10%
0.00%
0.10%
0.20%
0.30%
0.40%
0.50%
0.60%
0.70%
Strain, %
B-2-1
E sec
Alt Fit

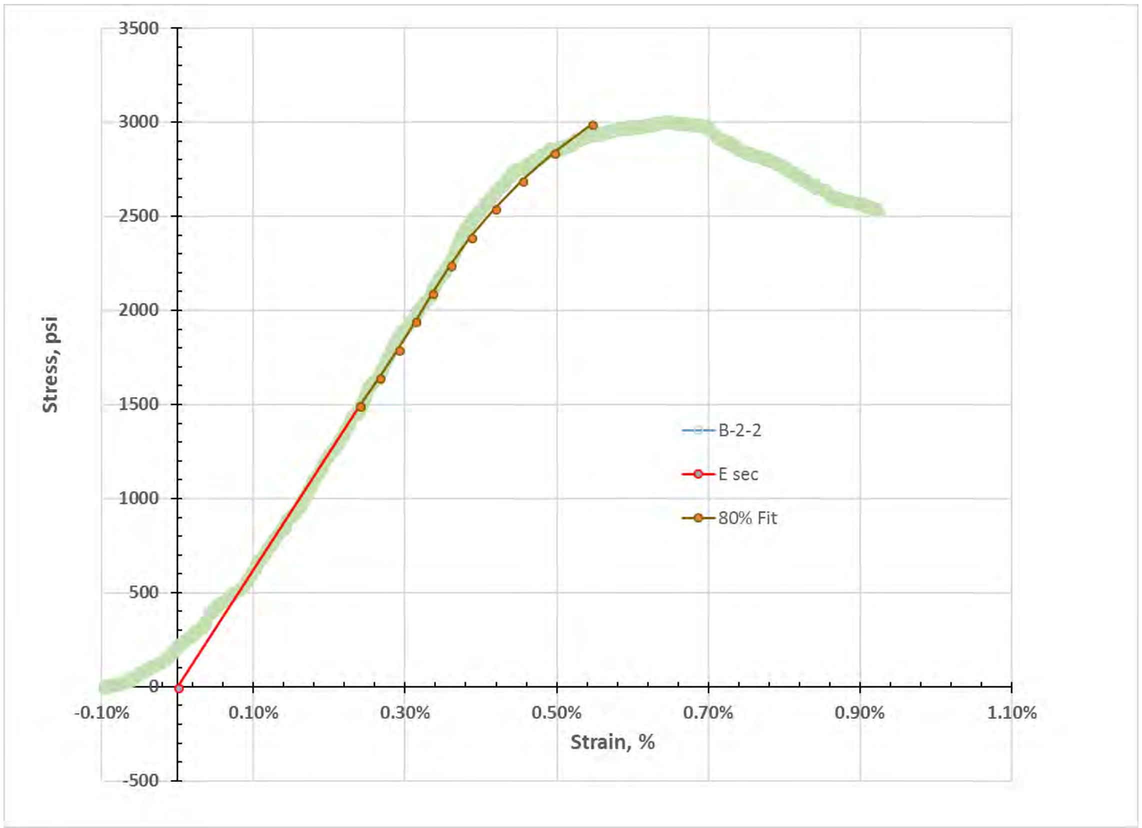
3500
3000
2500
2000
1500
1000
500
0
-500
Stress, psi
-0.10%
0.10%
0.30%
0.50%
0.70%
0.90%
1.10%
Strain, %
B-2-2
E sec
80% Fit

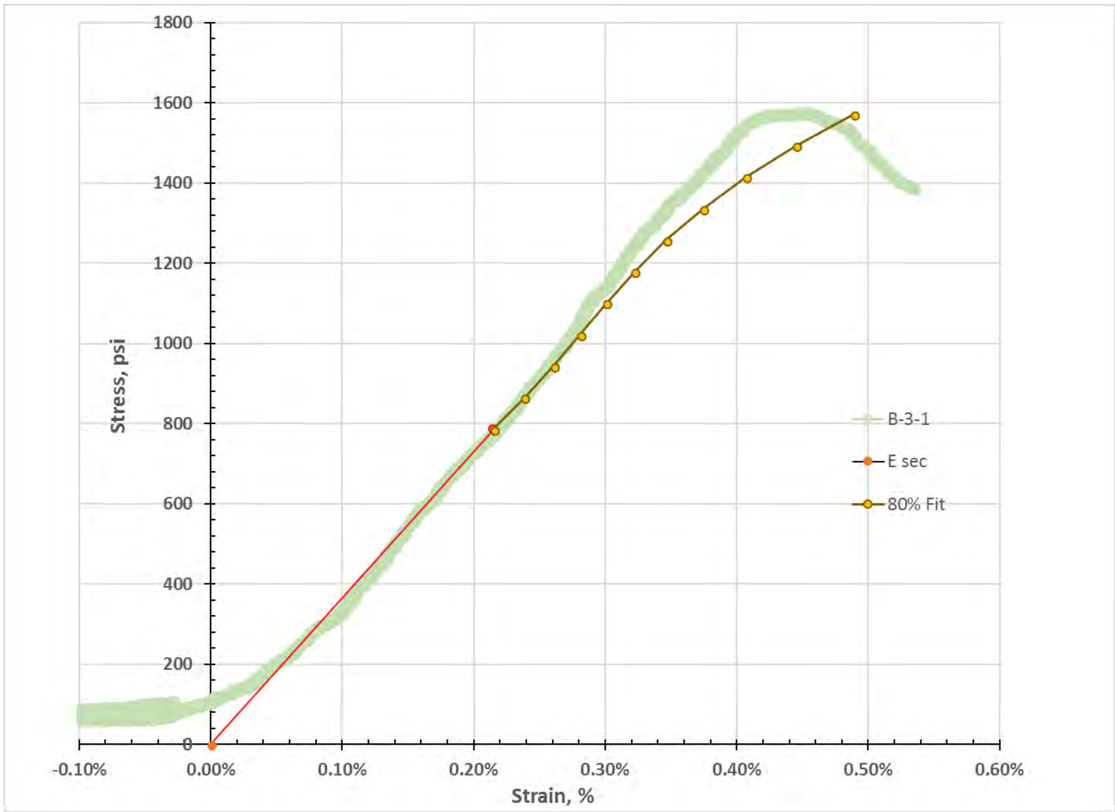
1800
1600
1400
1200
1000
800
600
400
200
0
Stress, psi
-0.10%
0.00%
0.10%
0.20%
0.30%
0.40%
0.50%
0.60%
Strain, %
B-3-1
E sec
80% Fit

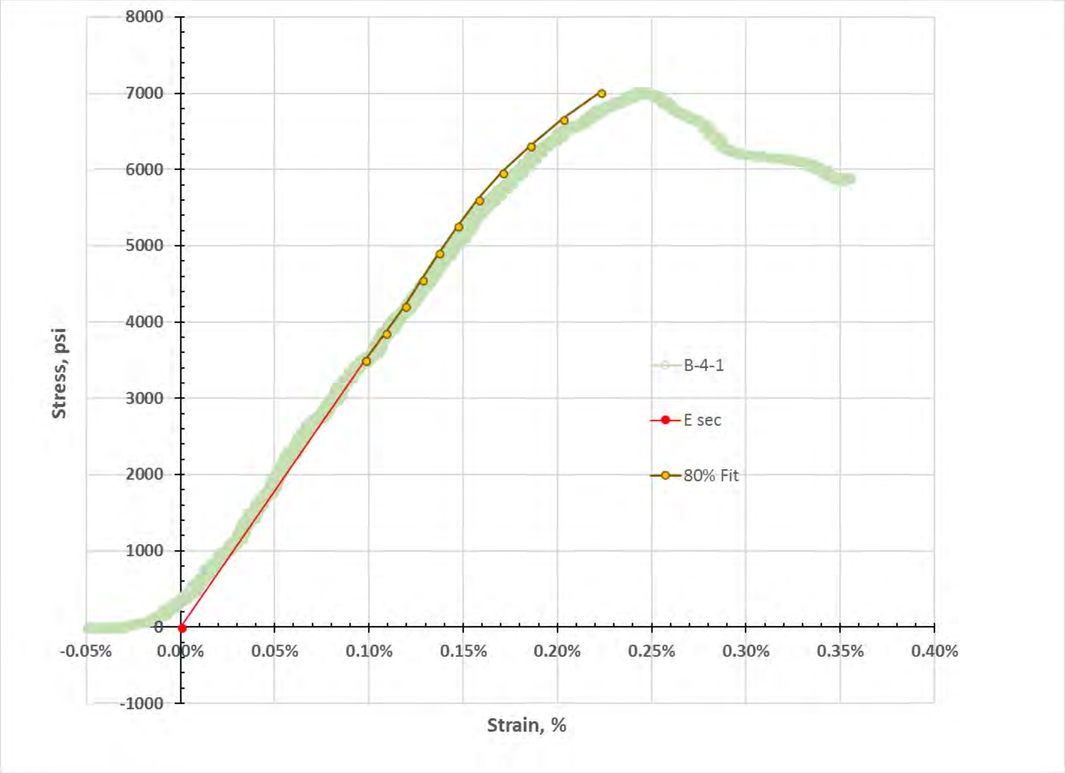
8000
7000
6000
5000
4000
3000
2000
1000
0
-1000
Stress, psi
-0.05%
0.00%
0.05%
0.10%
0.15%
0.20%
0.25%
0.30%
0.35%
0.40%
Strain, %
B-4-1
E sec
80% Fit

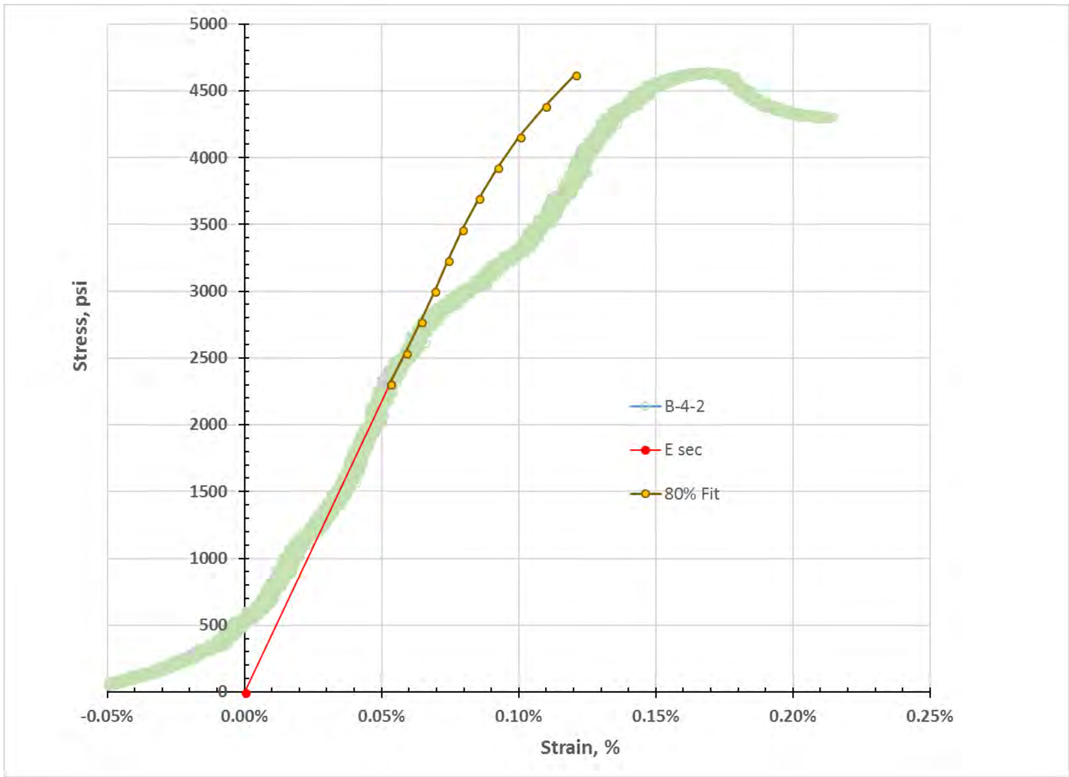
5000
4500
4000
3500
3000
2500
2000
1500
1000
500
0
Stress, psi
-0.05%
0.00%
0.05%
0.10%
0.15%
0.20%
0.25%
Strain, %
B-4-2
E sec
80% Fit

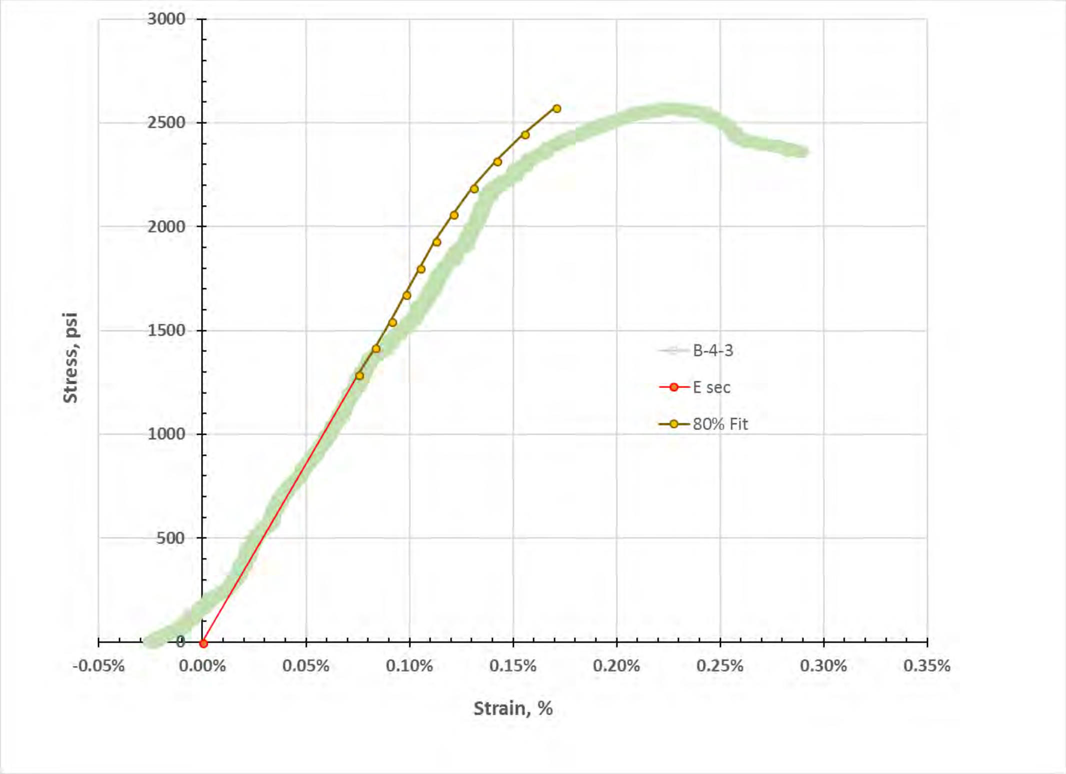
3000
2500
2000
1500
1000
500
0
Stress, psi
-0.05%
0.00%
0.05%
0.10%
0.15%
0.20%
0.25%
0.30%
0.35%
Strain, %
B-4-3
E sec
80% Fit

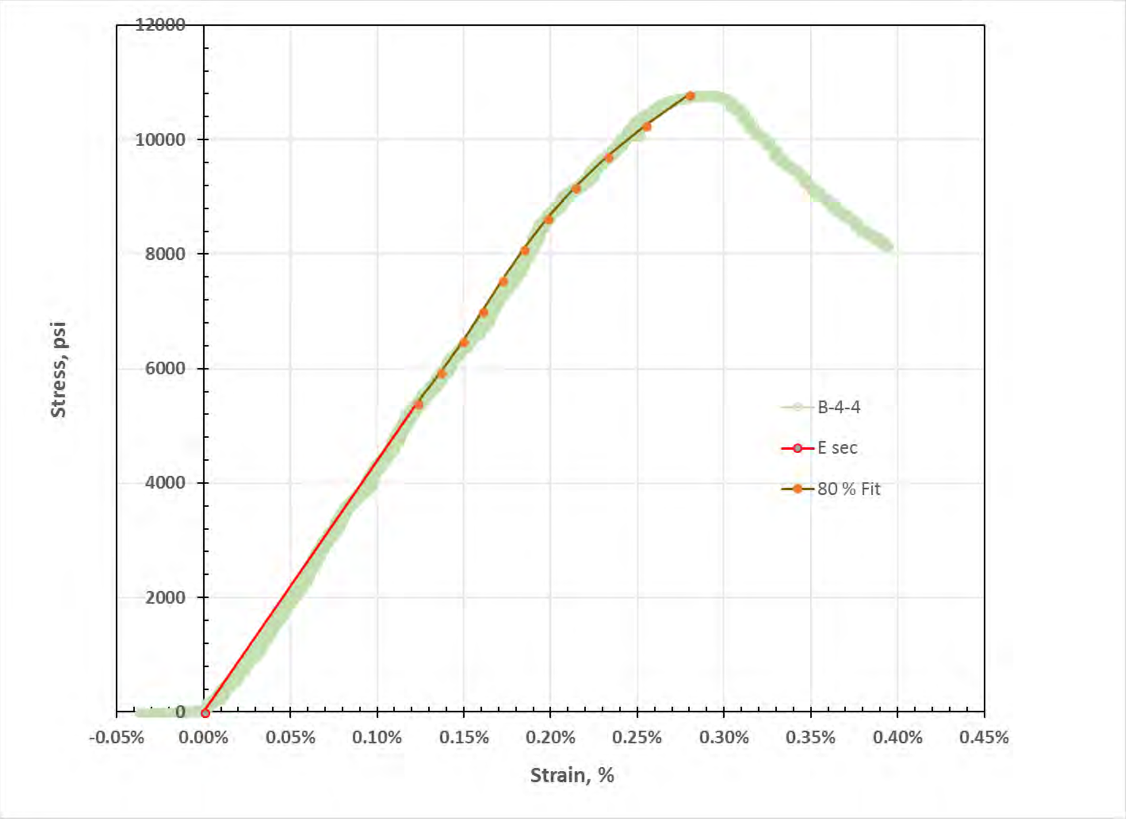
Stress, psi
Strain, %
12000
10000
8000
6000
4000
2000
0
-0.05%
0.00%
0.05%
0.10%
0.15%
0.20%
0.25%
0.30%
0.35%
0.40%
0.45%
B-4-4
E sec
80 % Fit

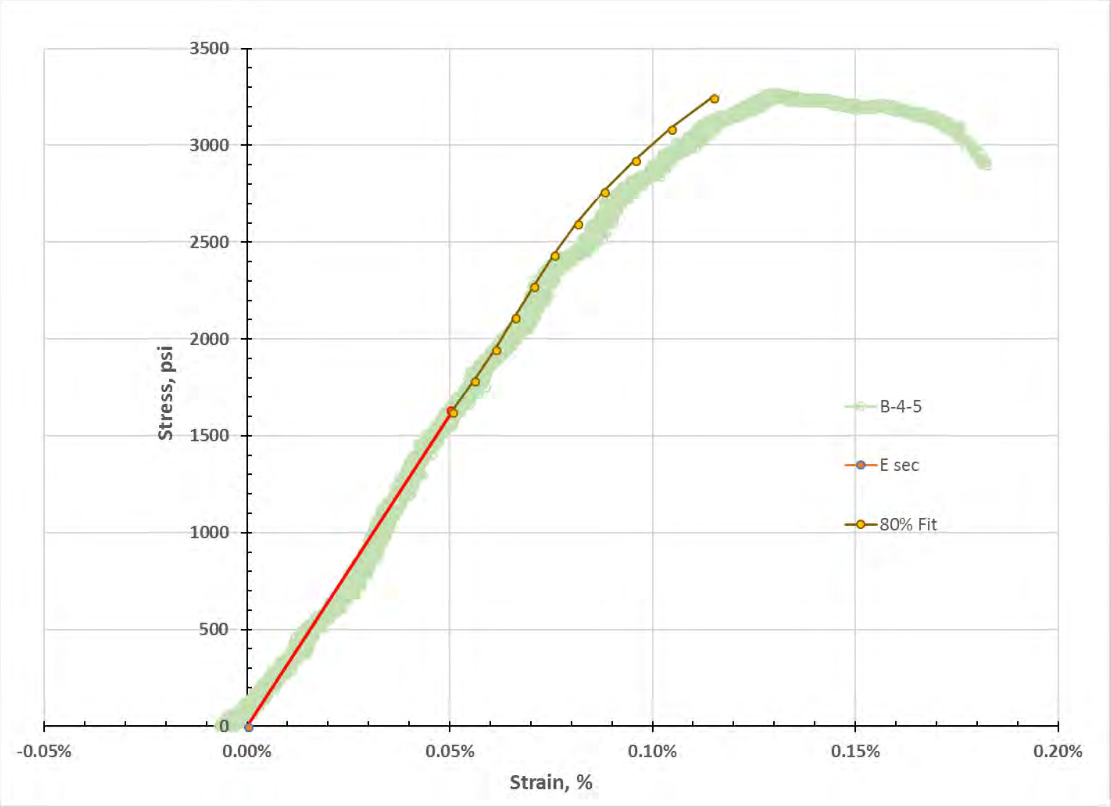
Stress, psi
Strain, %
3500
3000
2500
2000
1500
1000
500
0
-0.05%
0.00%
0.05%
0.10%
0.15%
0.20%
B-4-5
E sec
80% Fit

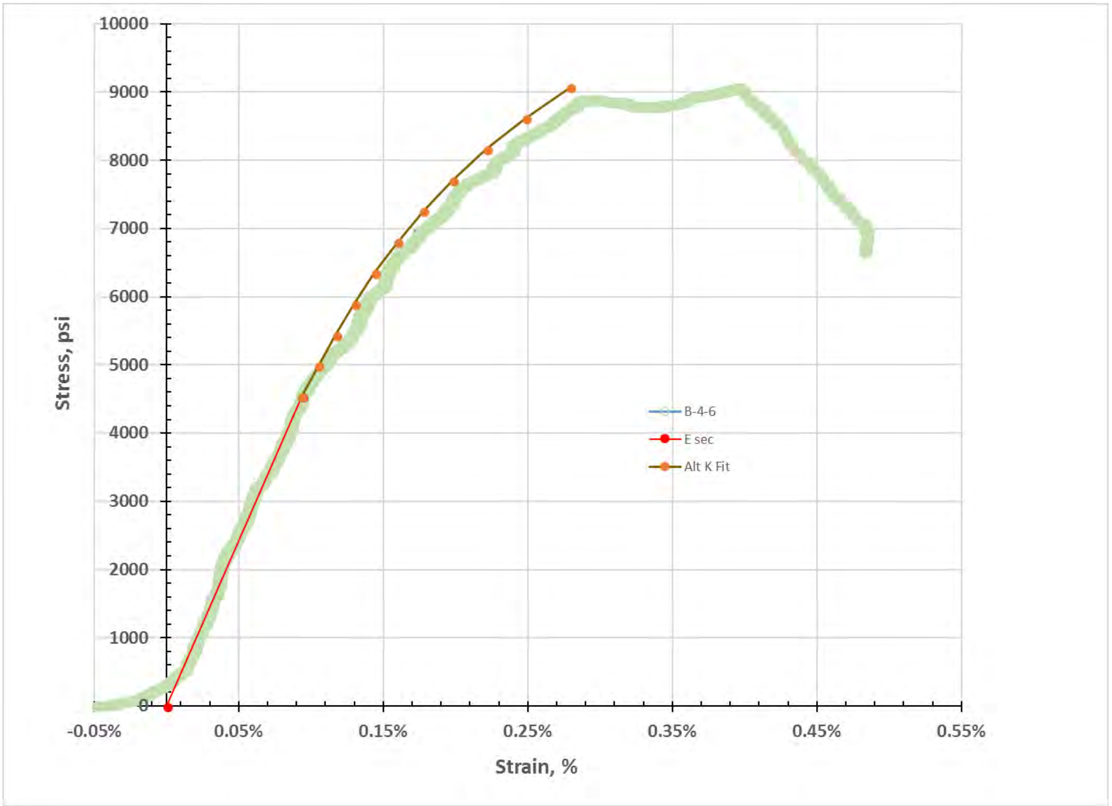

10000
9000
8000
7000
6000
5000
4000
3000
2000
1000
0
Stress, psi
-0.05%
0.05%
0.15%
0.25%
0.35%
0.45%
0.55%
Strain, %
B-4-6
E sec
Alt K Fit

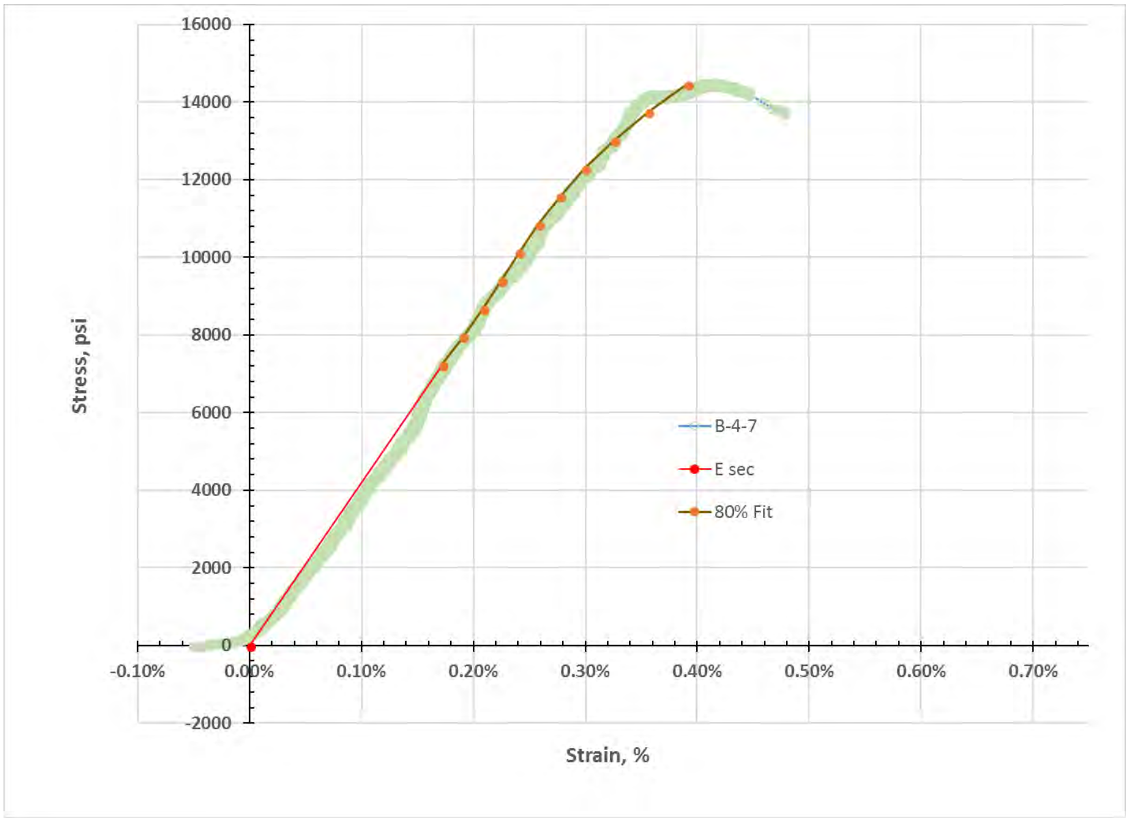

16000
14000
12000
10000
8000
6000
4000
2000
0
-2000
Stress, psi
-0.10%
0.00%
0.10%
0.20%
0.30%
0.40%
0.50%
0.60%
0.70%
Strain, %
B-4-7
E sec
80% Fit

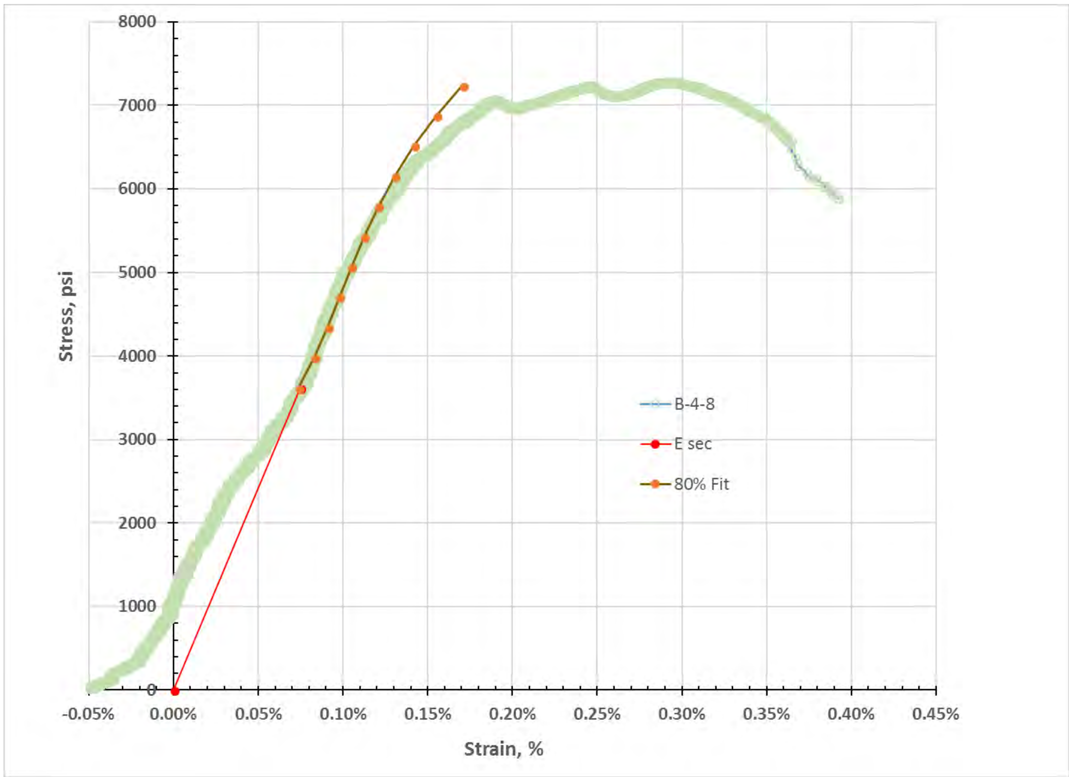
8000
7000
6000
5000
4000
3000
2000
1000
0
Stress, psi
-0.05%
0.00%
0.05%
0.10%
0.15%
0.20%
0.25%
0.30%
0.35%
0.40%
0.45%
Strain, %
B-4-8
E sec
80% Fit

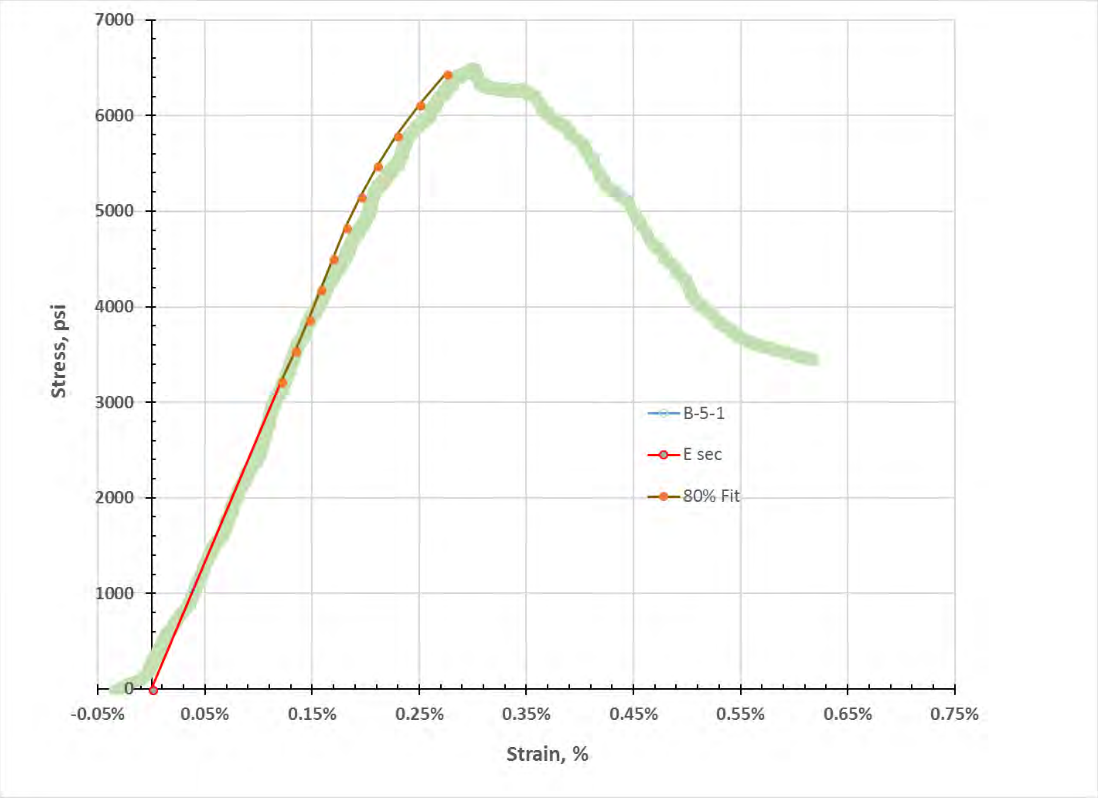
7000
6000
5000
4000
3000
2000
1000
0
Stress, psi
-0.05%
0.05%
0.15%
0.25%
0.35%
0.45%
0.55%
0.65%
0.75%
Strain, %
B-5-1
E sec
80% Fit

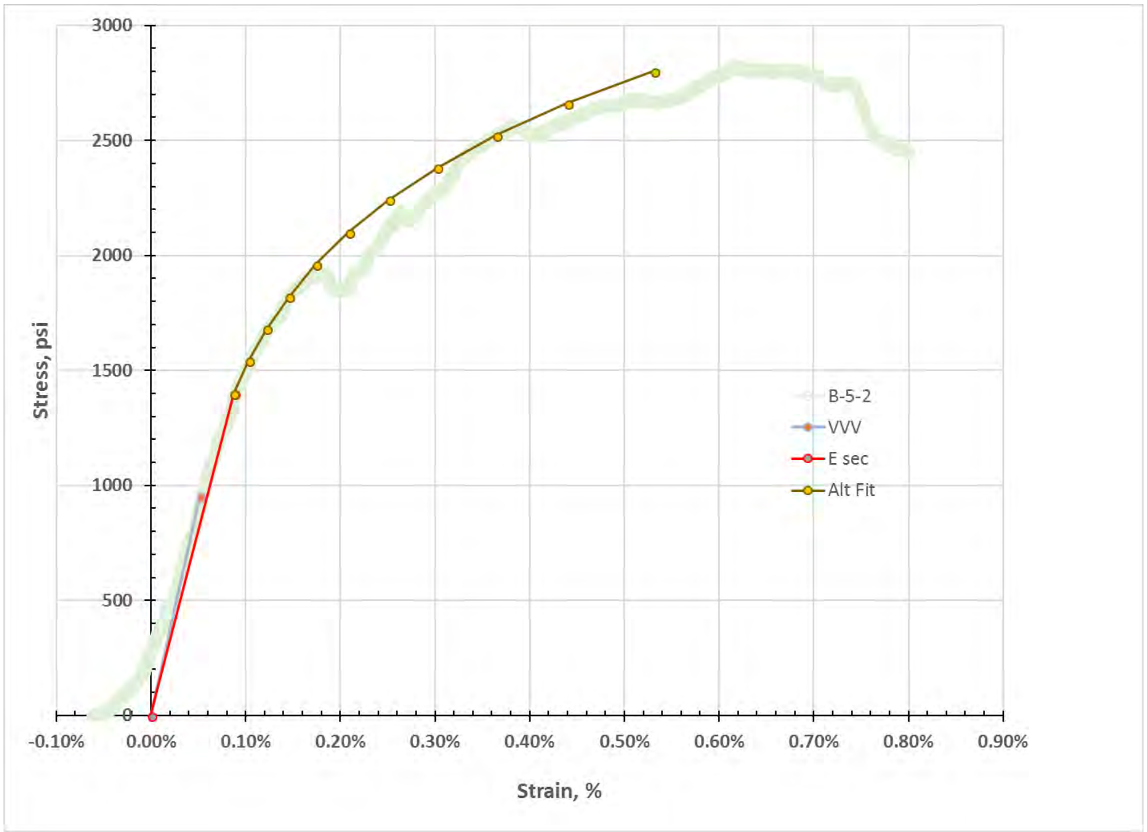
3000
2500
2000
1500
1000
500
0
Stress, psi
-0.10%
0.00%
0.10%
0.20%
0.30%
0.40%
0.50%
0.60%
0.70%
0.80%
0.90%
Strain, %
B-5-2
VVV
E sec
Alt Fit

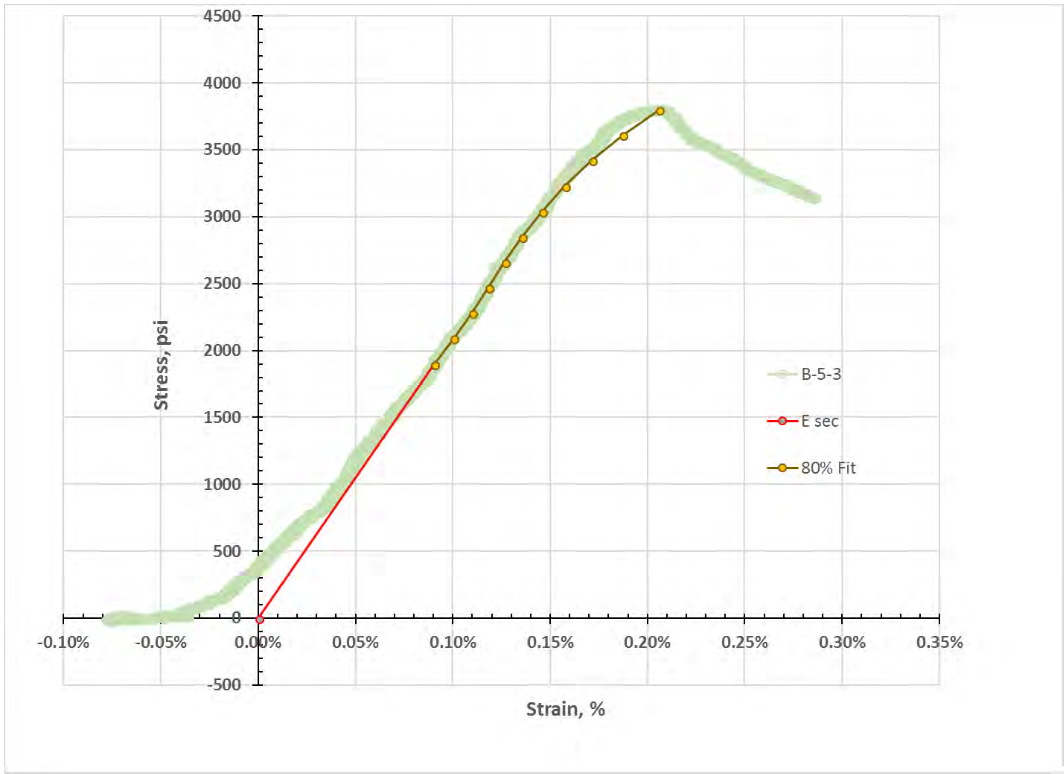
4500
4000
3500
3000
2500
2000
1500
1000
500
0
-500
Stress, psi
-0.10%
-0.05%
0.00%
0.05%
0.10%
0.15%
0.20%
0.25%
0.30%
0.35%
Strain, %
B-5-3
E sec
80% Fit

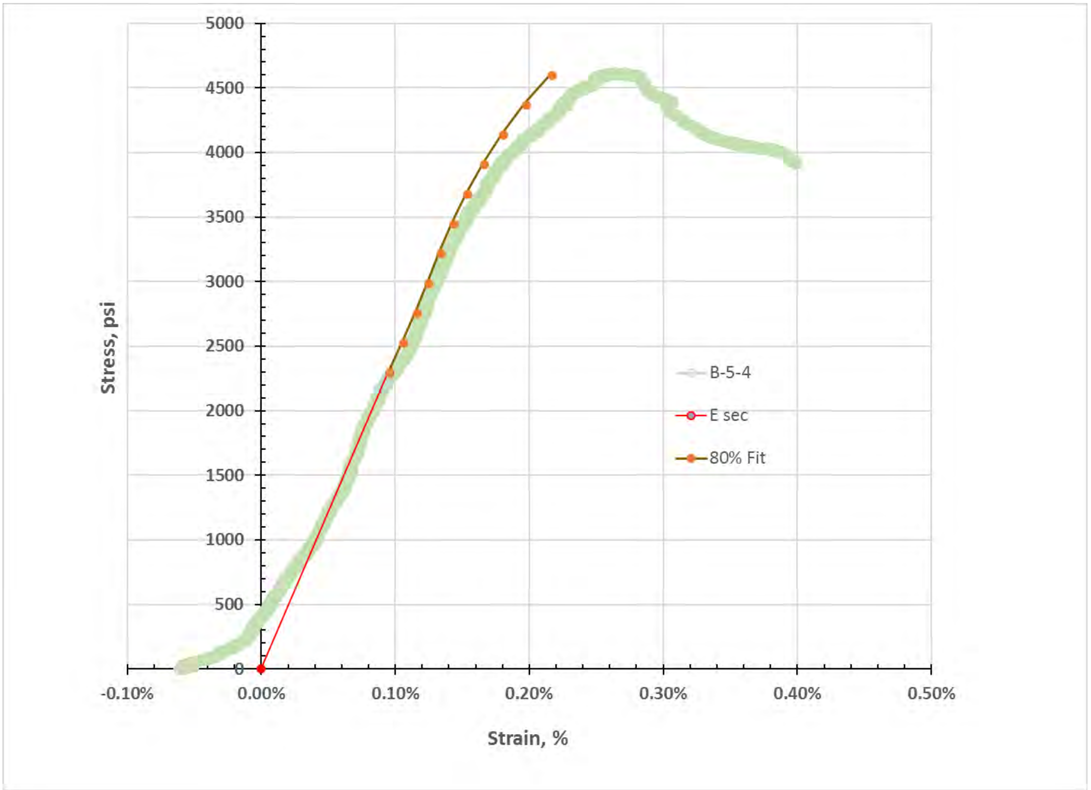
5000
4500
4000
3500
3000
2500
2000
1500
1000
500
0
Stress, psi
-0.10%
0.00%
0.10%
0.20%
0.30%
0.40%
0.50%
Strain, %
B-5-4
E sec
80% Fit

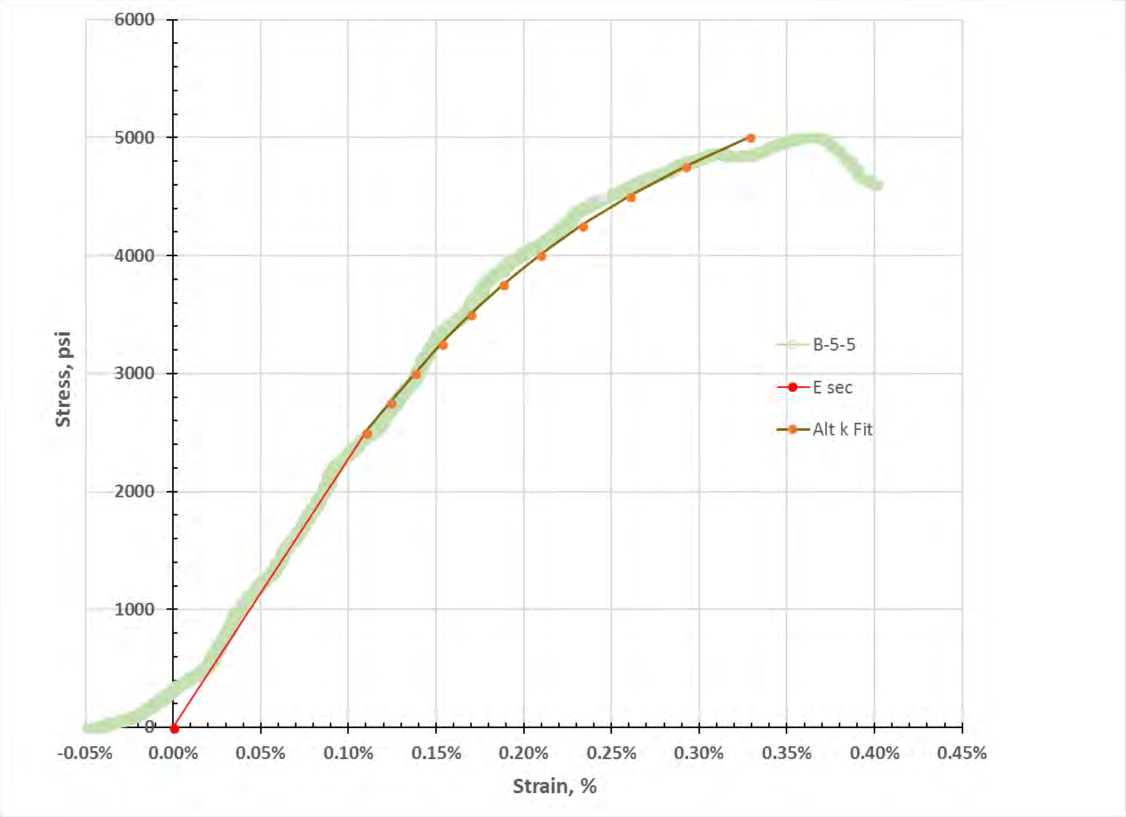
6000
5000
4000
3000
2000
1000
0
Stress, psi
-0.05%
0.00%
0.05%
0.10%
0.15%
0.20%
0.25%
0.30%
0.35%
0.40%
0.45%
Strain, %
B-5-5
E sec
Alt k Fit

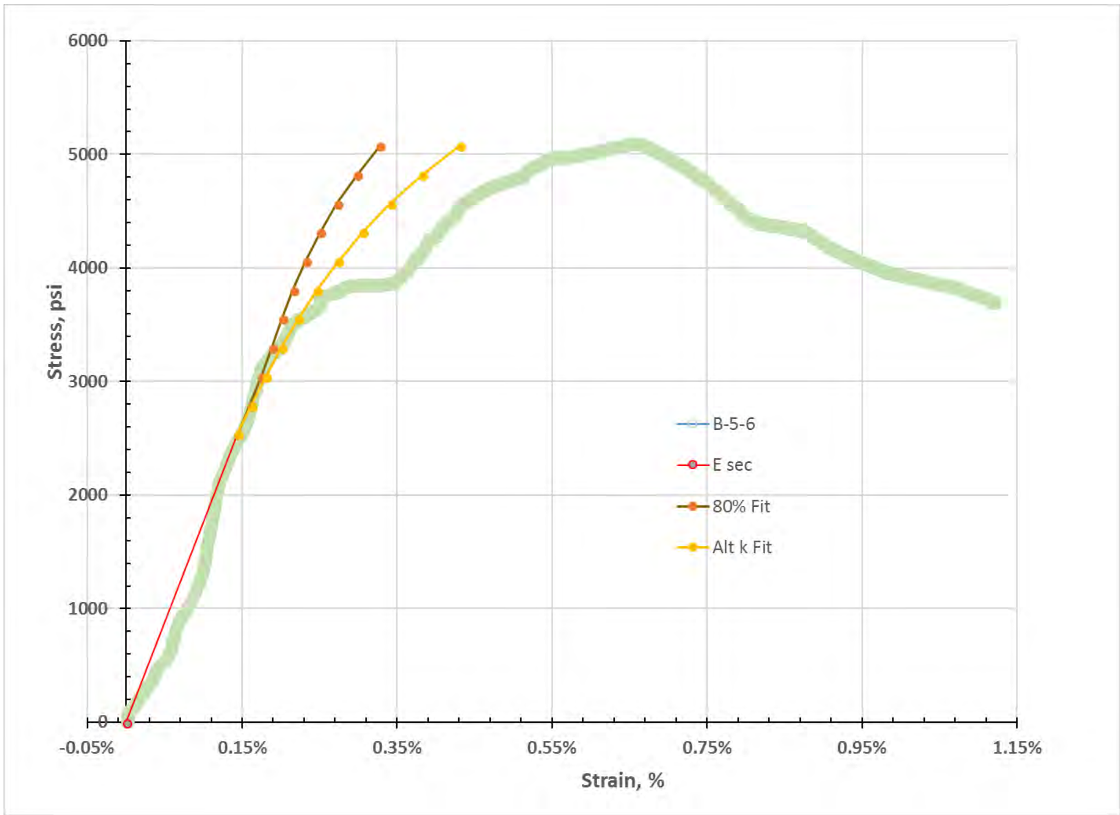
6000
5000
4000
3000
2000
1000
0
Stress, psi
-0.05%
0.15%
0.35%
0.55%
0.75%
0.95%
1.15%
Strain, %
B-5-6
E sec
80% Fit
Alt k Fit

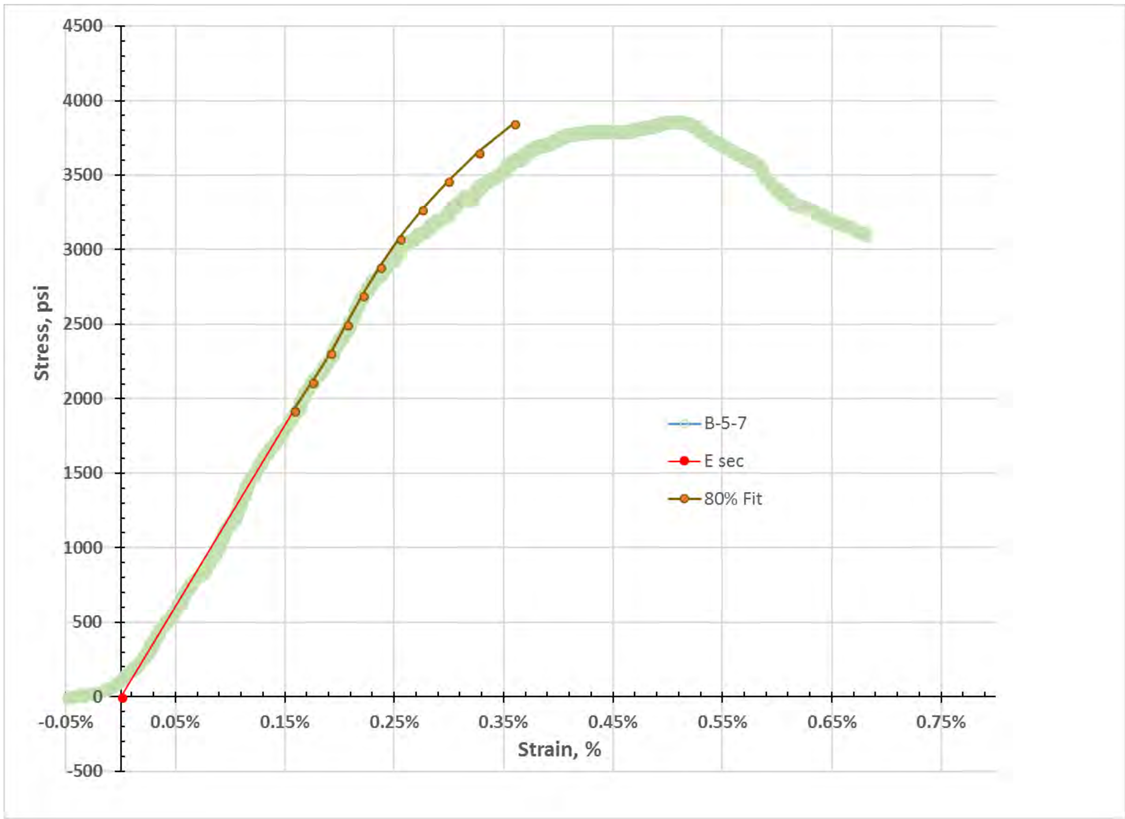
4500
4000
3500
3000
2500
2000
1500
1000
500
0
-500
Stress, psi
-0.05%
0.05%
0.15%
0.25%
0.35%
0.45%
0.55%
0.65%
0.75%
Strain, %
B-5-7
E sec
80% Fit

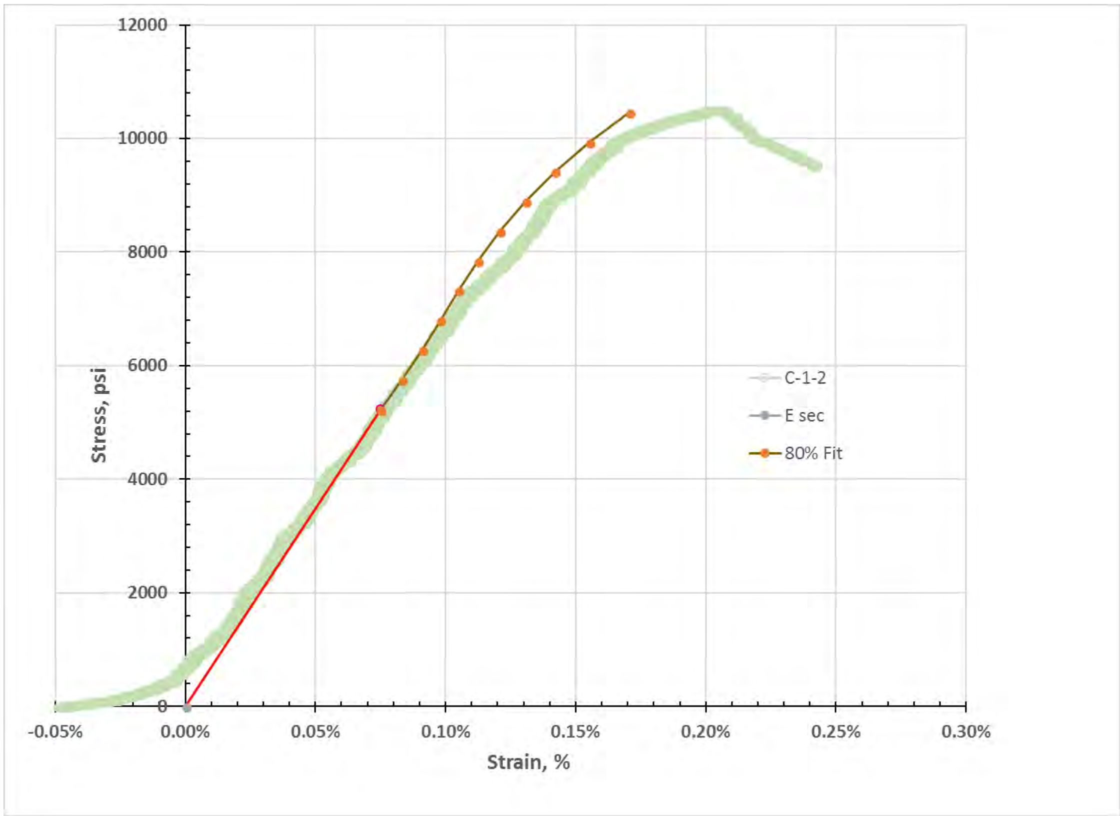
12000
10000
8000
6000
4000
2000
0
Stress, psi
-0.05%
0.00%
0.05%
0.10%
0.15%
0.20%
0.25%
0.30%
Strain, %
C-1-2
E sec
80% Fit

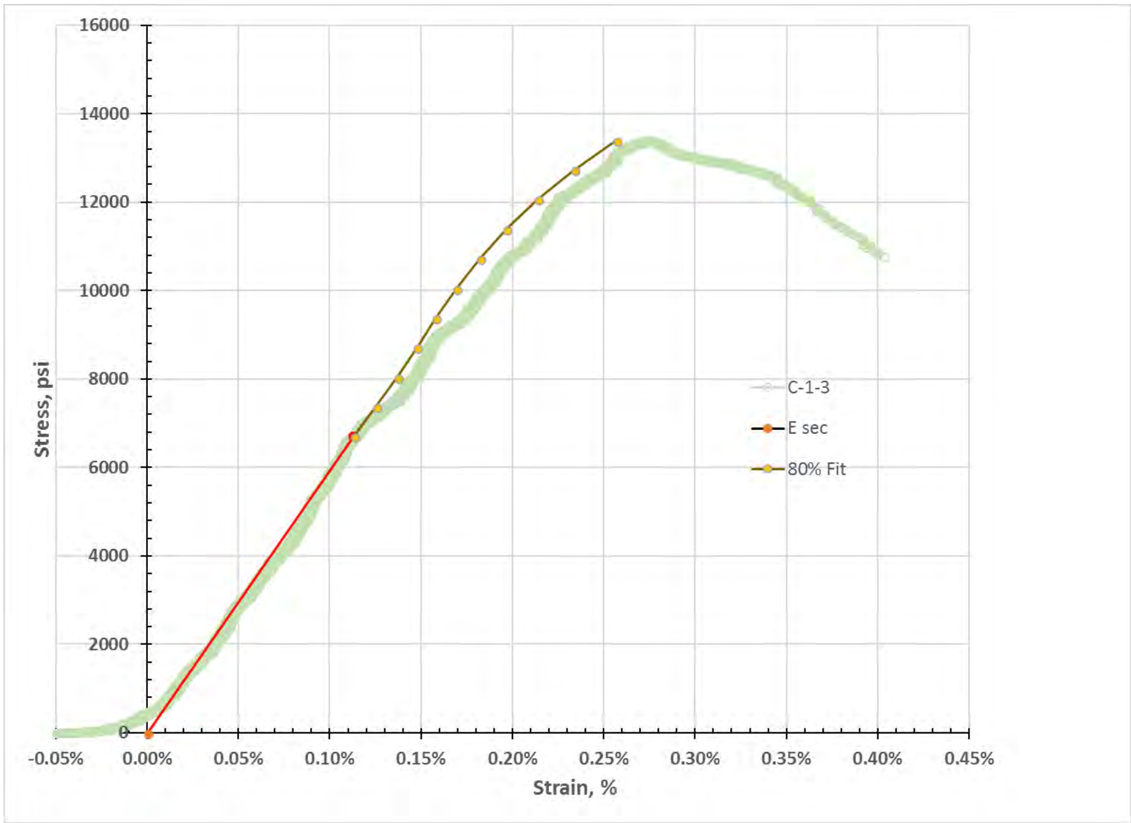
16000
14000
12000
10000
8000
6000
4000
2000
0
Stress, psi
-0.05%
0.00%
0.05%
0.10%
0.15%
0.20%
0.25%
0.30%
0.35%
0.40%
0.45%
Strain, %
C-1-3
E sec
80% Fit

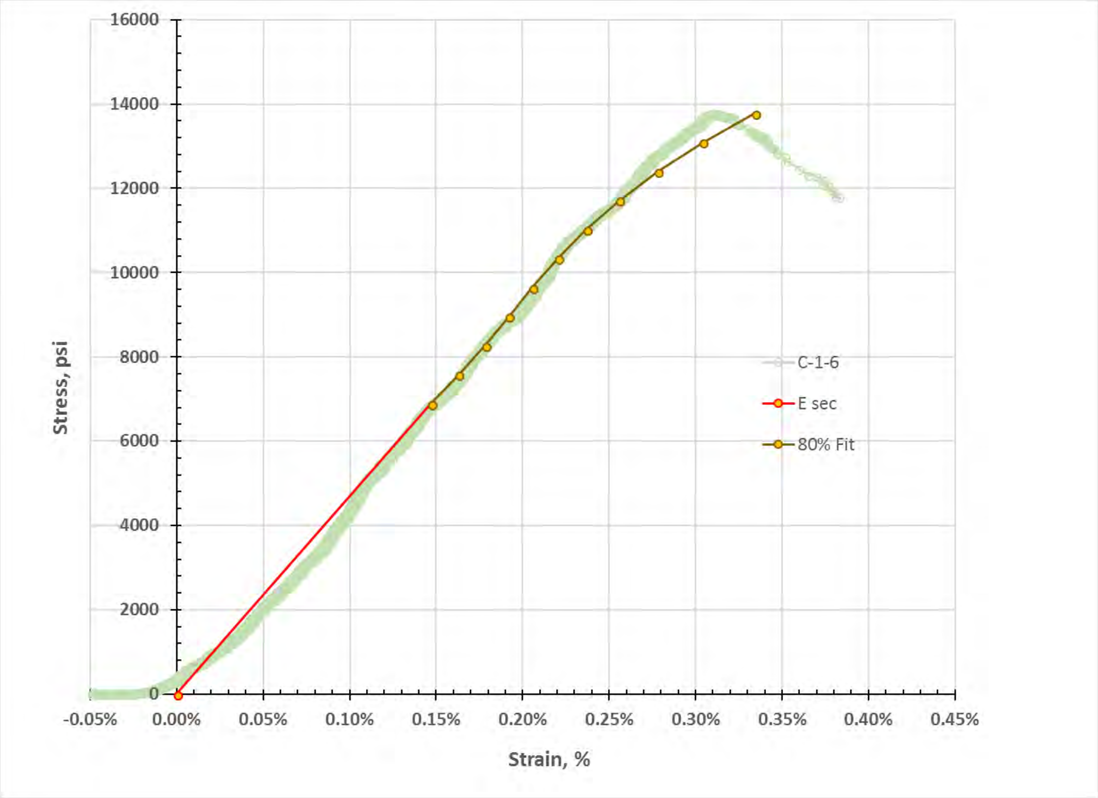
Stress, psi
16000
14000
12000
10000
8000
6000
4000
2000
0
-0.05%
0.00%
0.05%
0.10%
0.15%
0.20%
0.25%
0.30%
0.35%
0.40%
0.45%
Strain, %
C-1-6
E sec
80% Fit

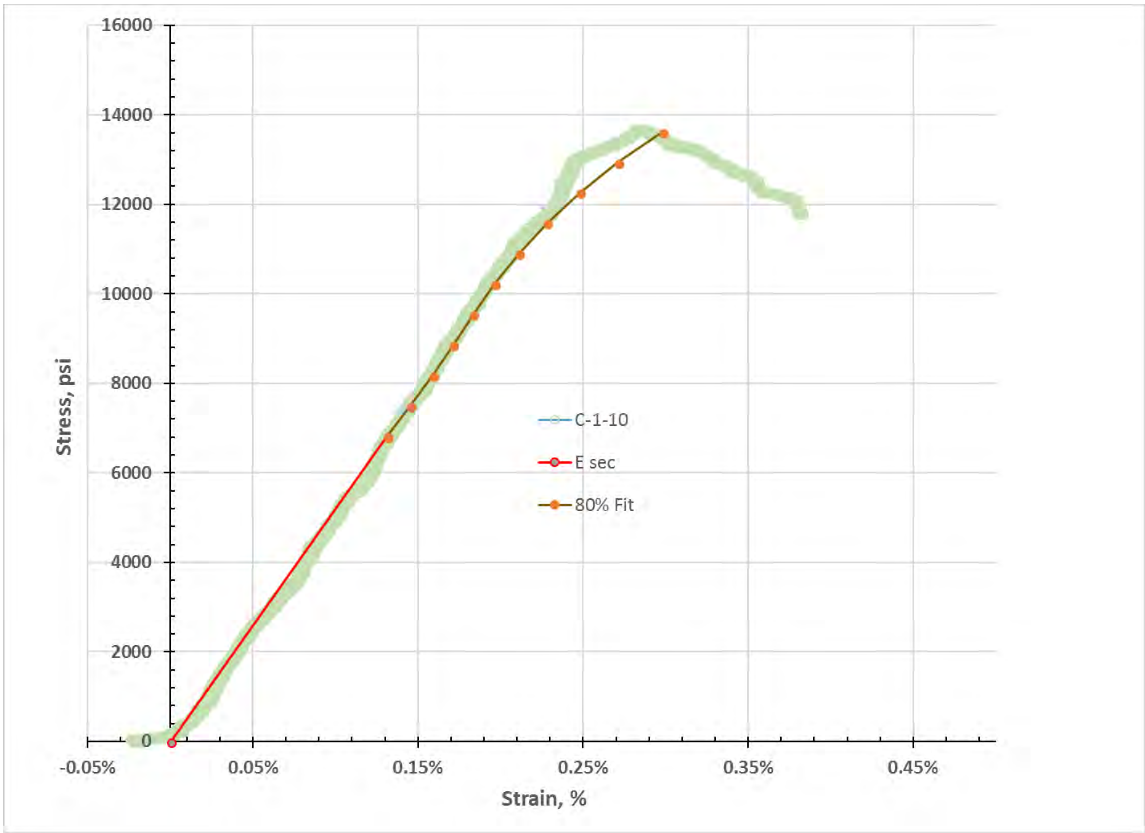
Stress, psi
16000
14000
12000
10000
8000
6000
4000
2000
0
-0.05%
0.05%
0.15%
0.25%
0.35%
0.45%
Strain, %
C-1-10
E sec
80% Fit

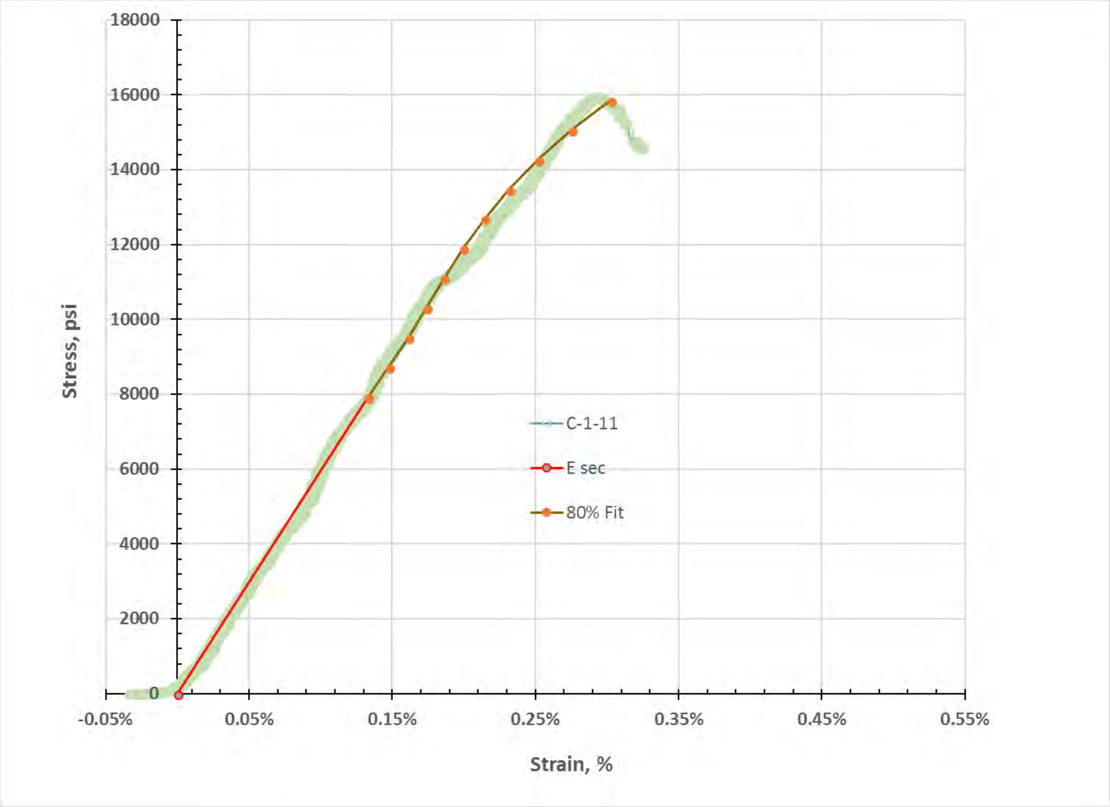

Stress, psi
Strain, %
18000
16000
14000
12000
10000
8000
6000
4000
2000
0
-0.05%
0.05%
0.15%
0.25%
0.35%
0.45%
0.55%
C-1-11
E sec
80% Fit

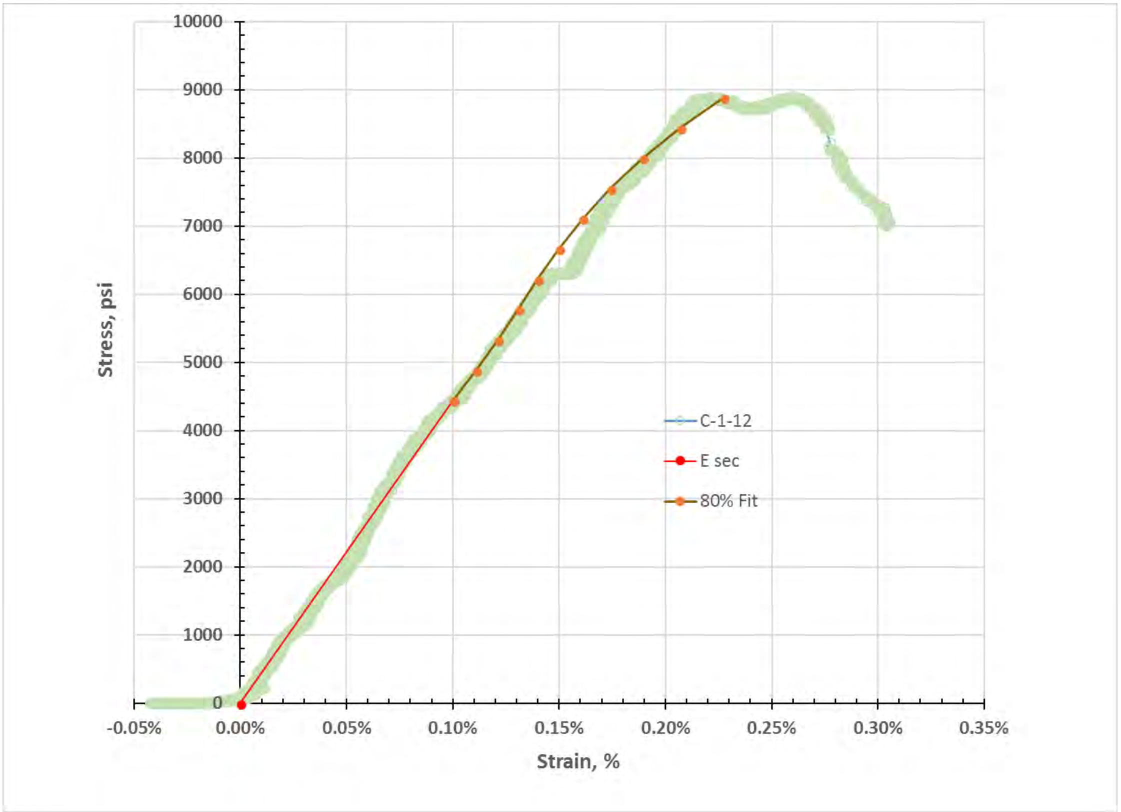

Stress, psi
Strain, %
10000
9000
8000
7000
6000
5000
4000
3000
2000
1000
0
-0.05%
0.00%
0.05%
0.10%
0.15%
0.20%
0.25%
0.30%
0.35%
C-1-12
E sec
80% Fit

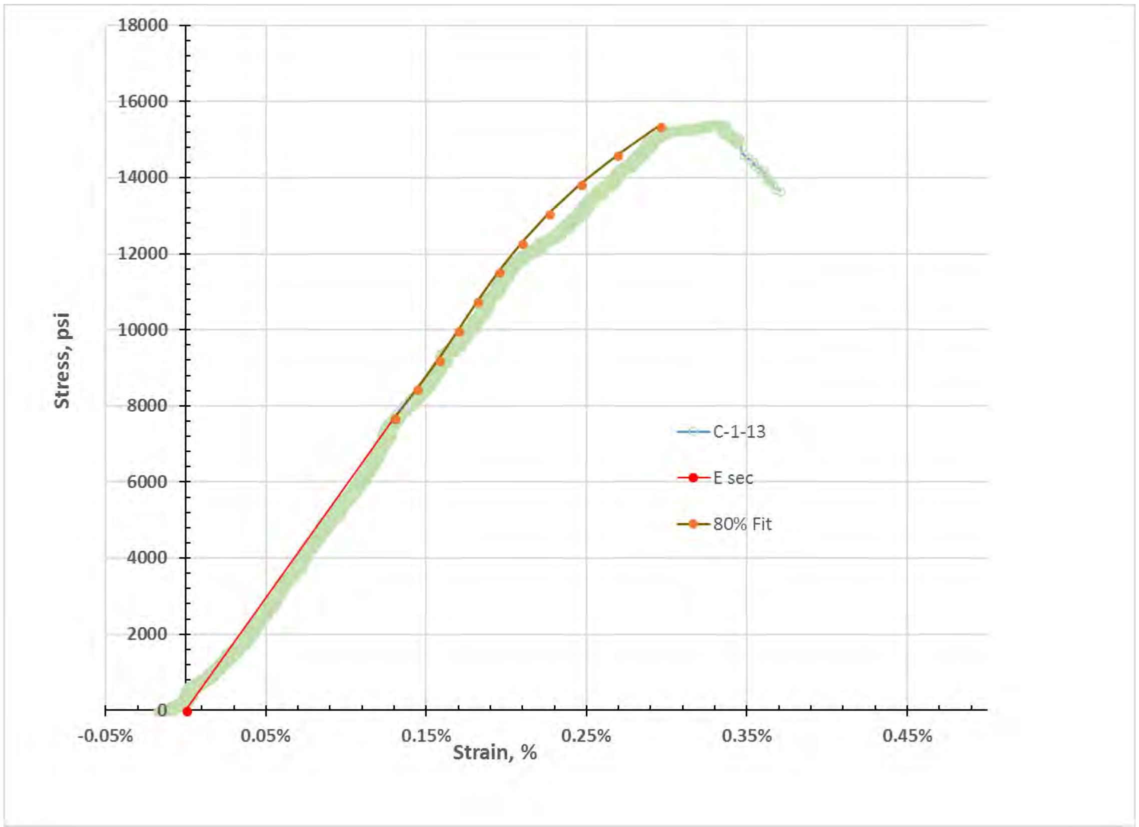

Stress, psi
18000
16000
14000
12000
10000
8000
6000
4000
2000
0
-0.05%
0.05%
0.15%
0.25%
0.35%
0.45%
Strain, %
C-1-13
E sec
80% Fit

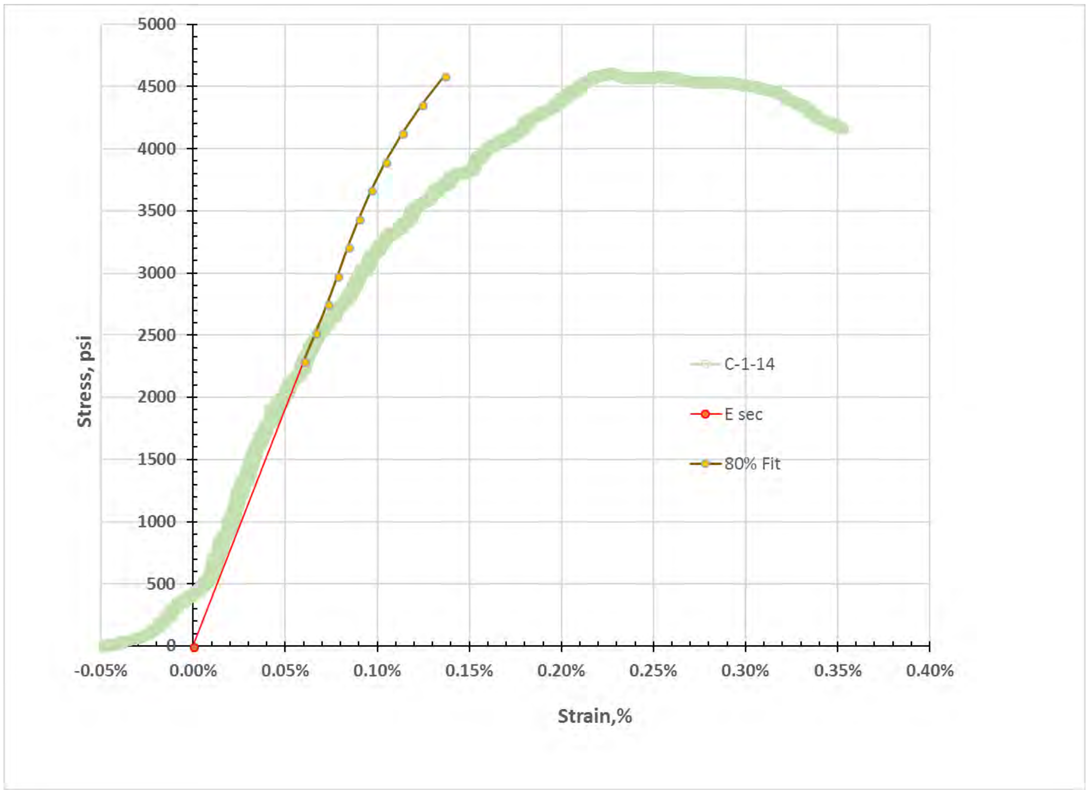

Stress, psi
5000
4500
4000
3500
3000
2500
2000
1500
1000
500
0
-0.05%
0.00%
0.05%
0.10%
0.15%
0.20%
0.25%
0.30%
0.35%
0.40%
Strain,%
C-1-14
E sec
80% Fit

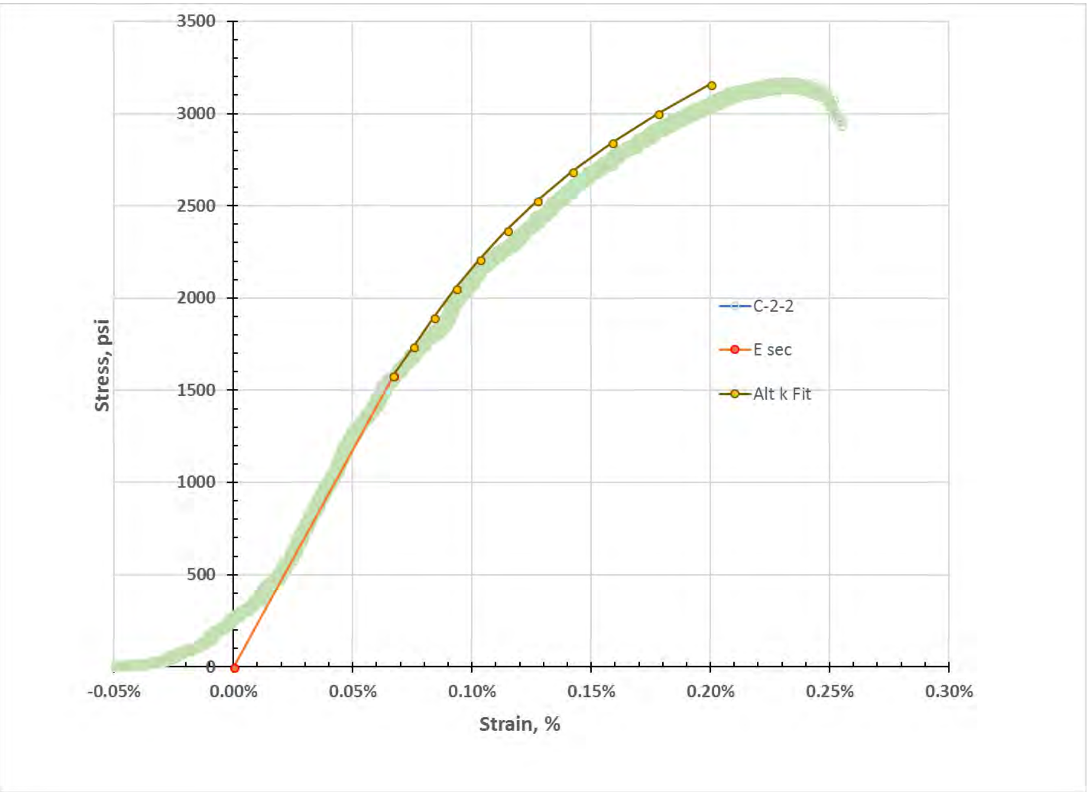
3500
3000
2500
2000
1500
1000
500
0
Stress, psi
-0.05%
0.00%
0.05%
0.10%
0.15%
0.20%
0.25%
0.30%
Strain, %
C-2-2
E sec
Alt k Fit

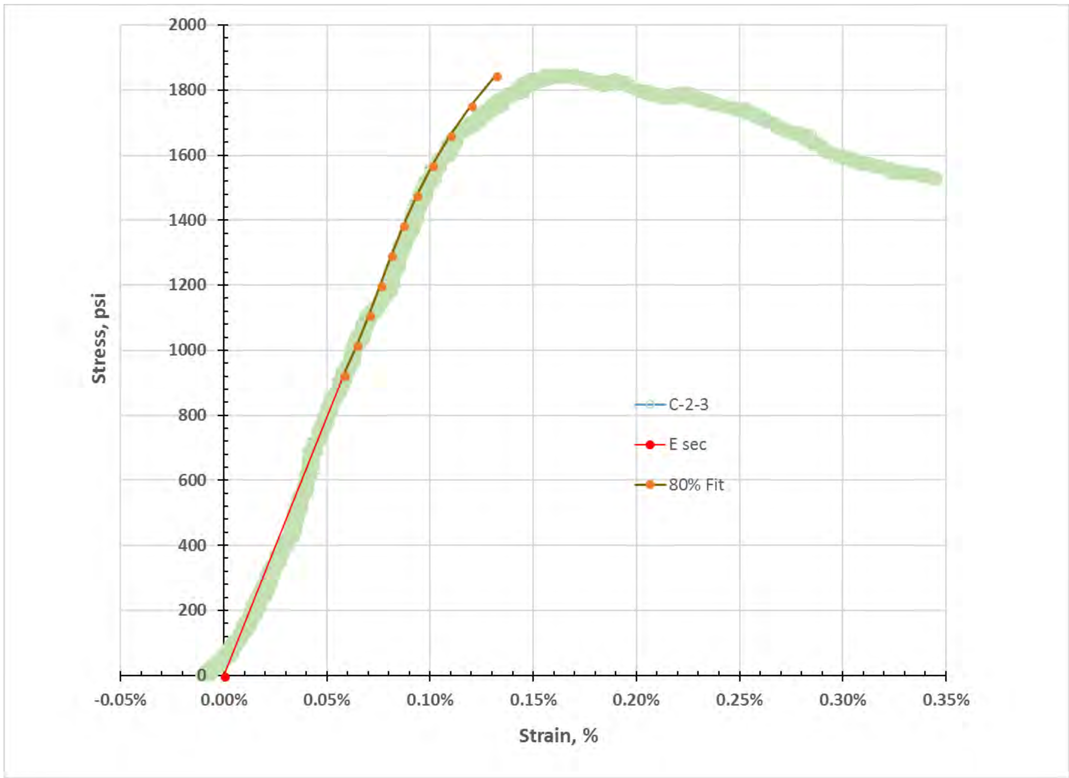
2000
1800
1600
1400
1200
1000
800
600
400
200
0
Stress, psi
-0.05%
0.00%
0.05%
0.10%
0.15%
0.20%
0.25%
0.30%
0.35%
Strain, %
C-2-3
E sec
80% Fit

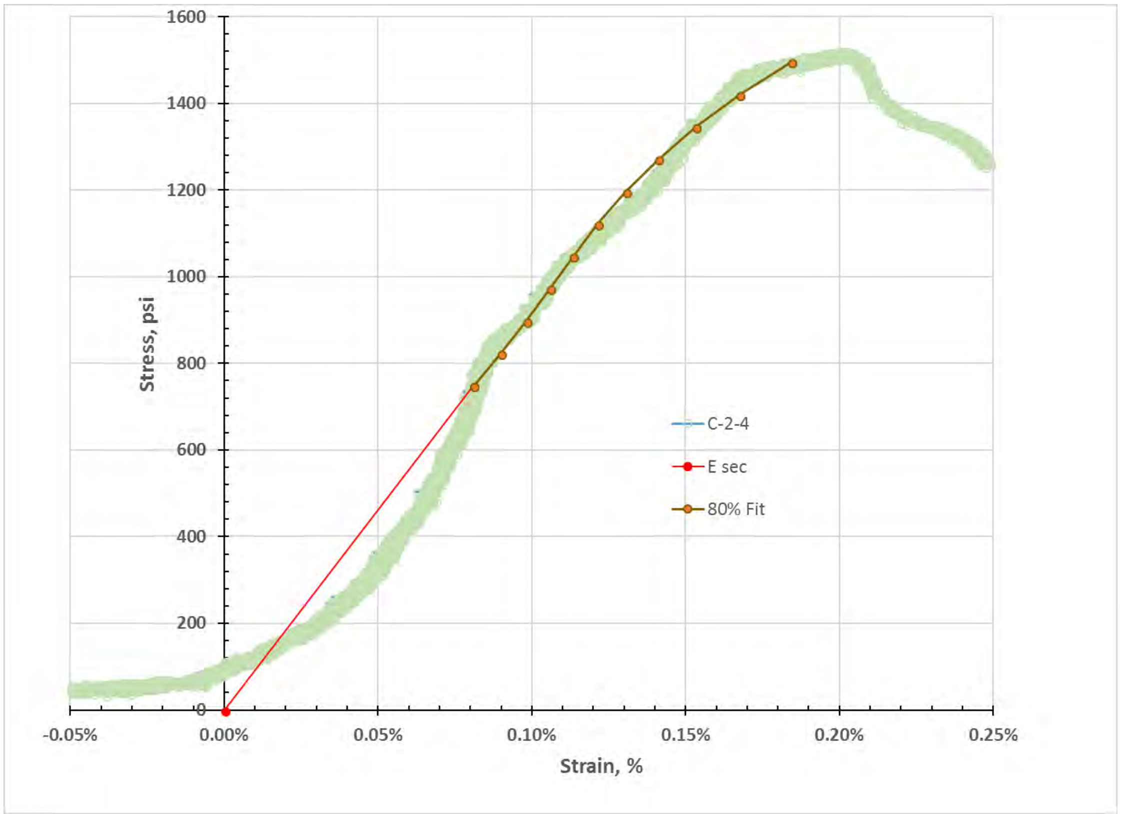
Stress, psi
1600
1400
1200
1000
800
600
400
200
0
-0.05%
0.00%
0.05%
0.10%
0.15%
0.20%
0.25%
Strain, %
C-2-4
E sec
80% Fit

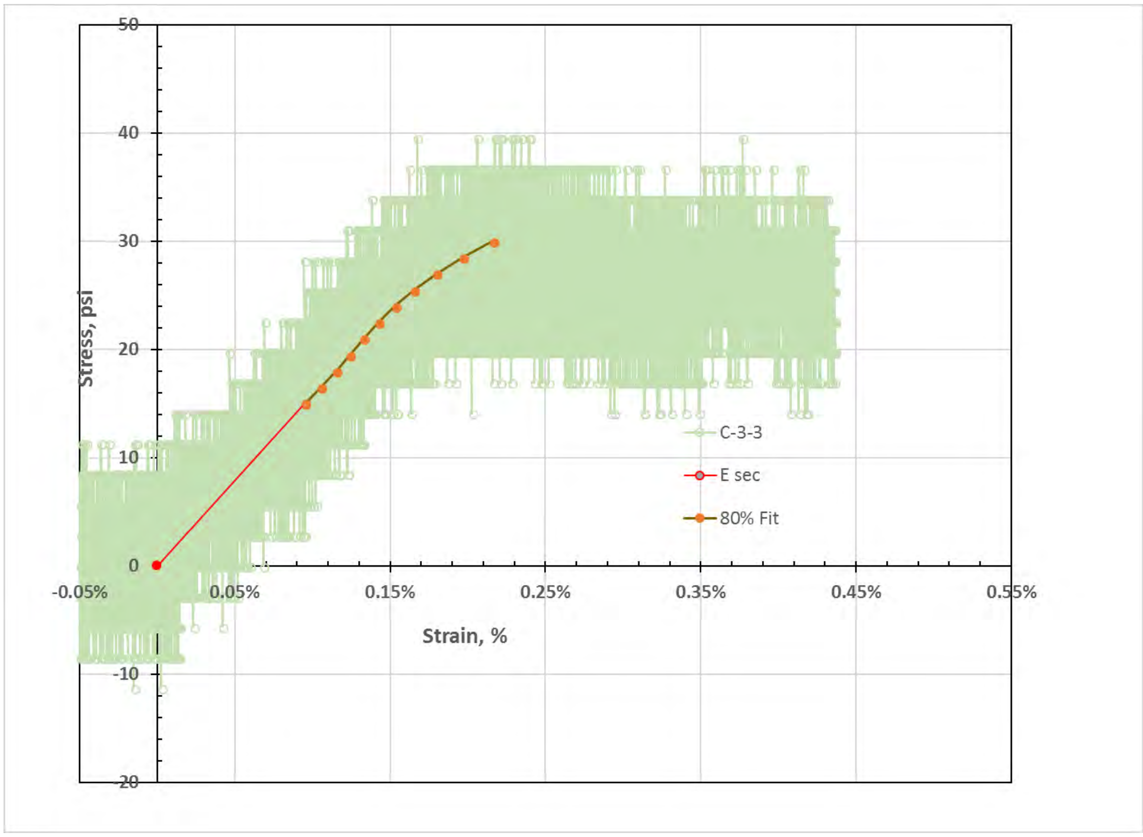
Stress, psi
50
40
30
20
10
0
-10
-20
-0.05%
0.05%
0.15%
0.25%
0.35%
0.45%
0.55%
Strain, %
C-3-3
E sec
80% Fit

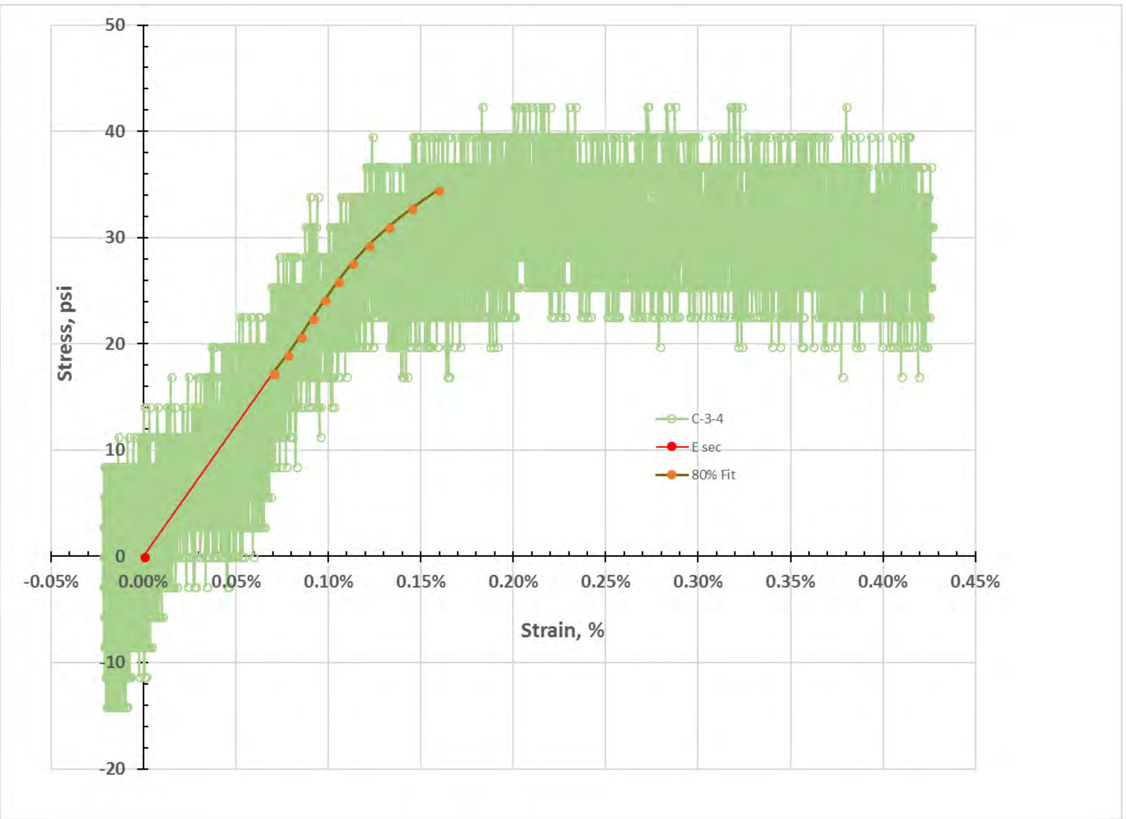

Stress, psi
Strain, %
50
40
30
20
10
0
-10
-20
-0.05%
0.00%
0.05%
0.10%
0.15%
0.20%
0.25%
0.30%
0.35%
0.40%
0.45%
C-3-4
E sec
80% Fit

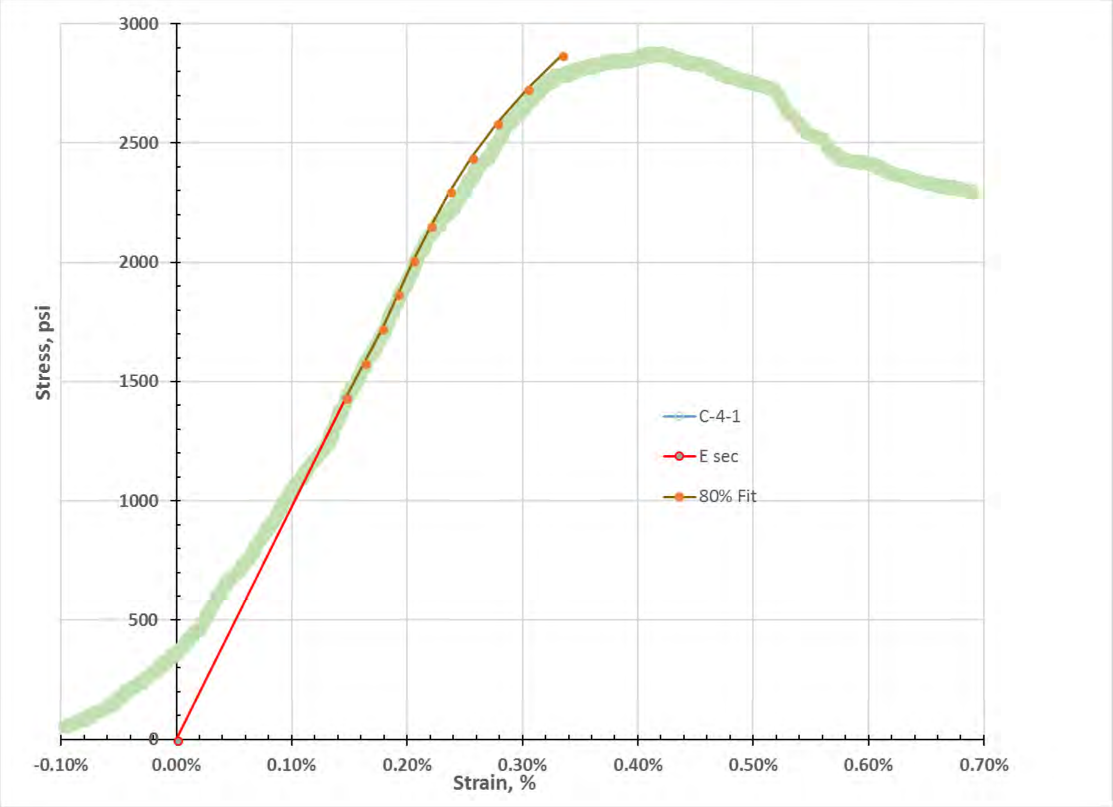

Stress, psi
Strain, %
3000
2500
2000
1500
1000
500
0
-0.10%
0.00%
0.10%
0.20%
0.30%
0.40%
0.50%
0.60%
0.70%
C-4-1
E sec
80% Fit

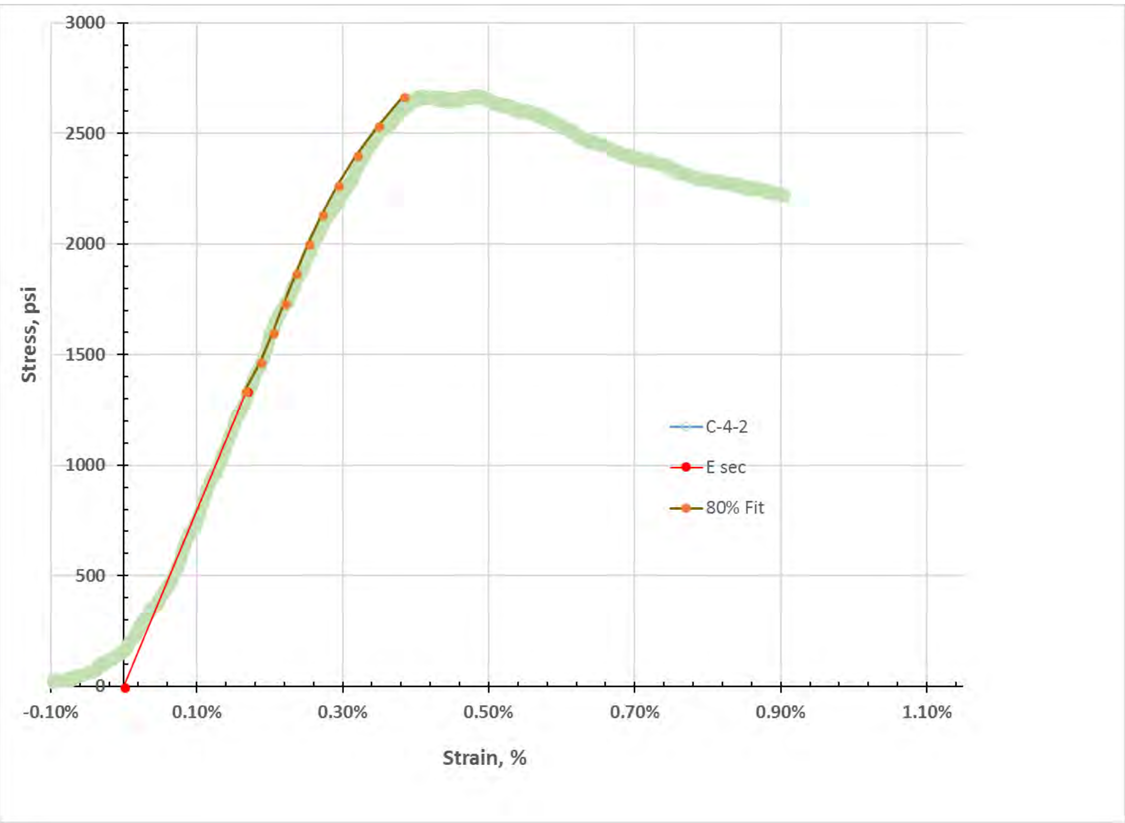

Stress, psi
3000
2500
2000
1500
1000
500
0
-0.10%
0.10%
0.30%
0.50%
0.70%
0.90%
1.10%
Strain, %
C-4-2
E sec
80% Fit

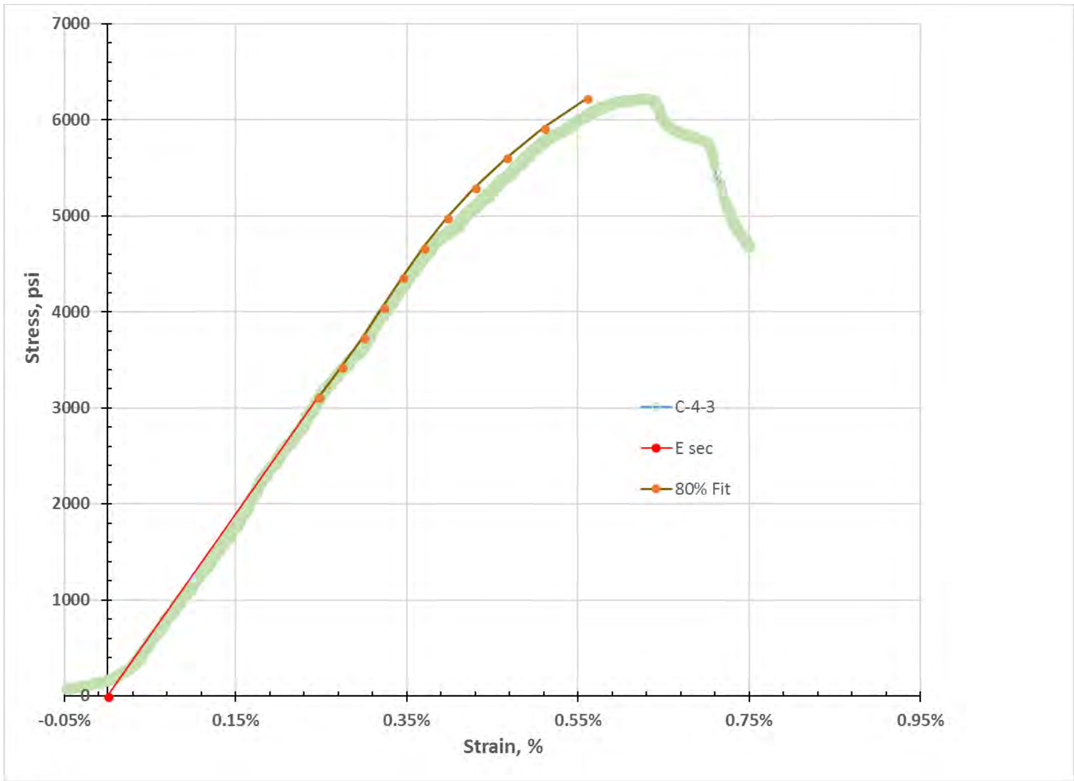

Stress, psi
7000
6000
5000
4000
3000
2000
1000
0
-0.05%
0.15%
0.35%
0.55%
0.75%
0.95%
Strain, %
C-4-3
E sec
80% Fit

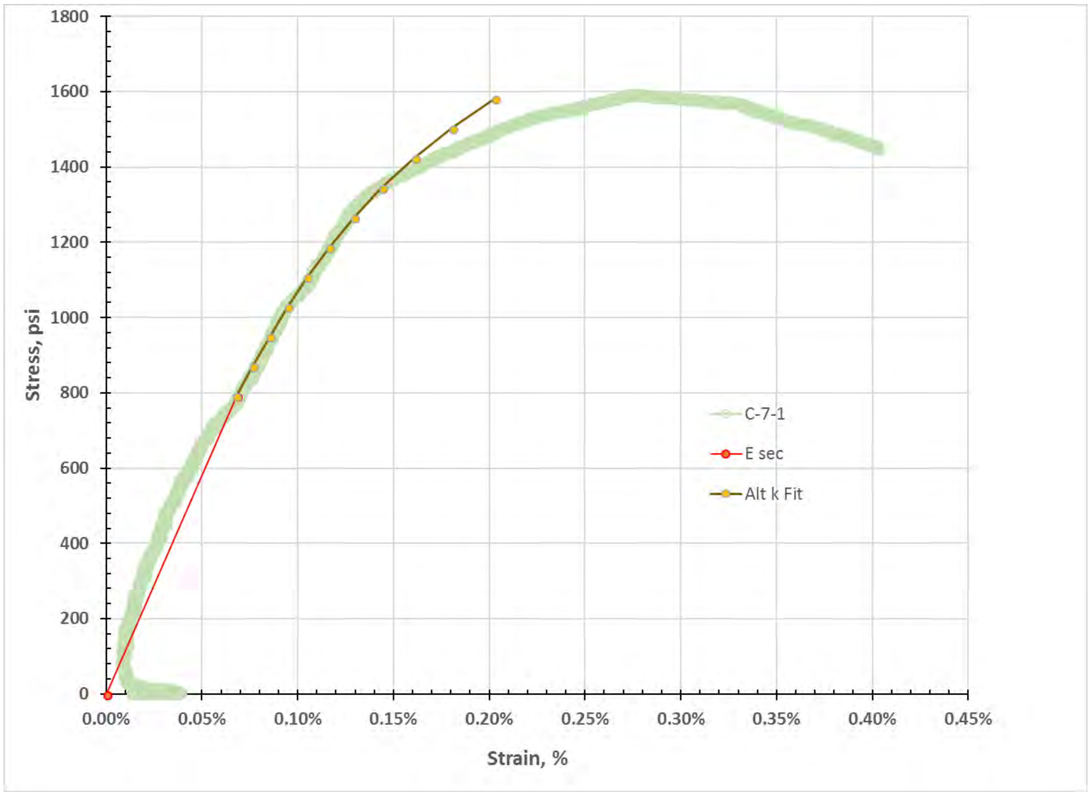

Stress, psi
1800
1600
1400
1200
1000
800
600
400
200
0
0.00%
0.05%
0.10%
0.15%
0.20%
0.25%
0.30%
0.35%
0.40%
0.45%
Strain, %
C-7-1
E sec
Alt k Fit

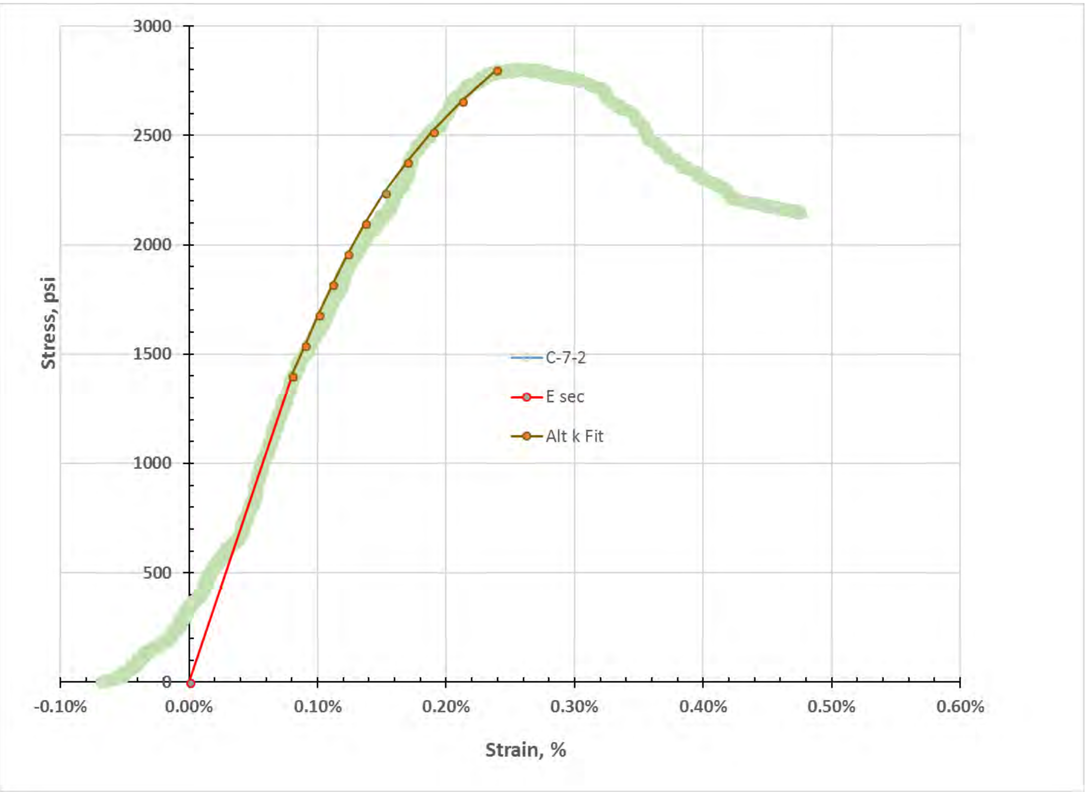

Stress, psi
3000
2500
2000
1500
1000
500
0
-0.10%
0.00%
0.10%
0.20%
0.30%
0.40%
0.50%
0.60%
Strain, %
C-7-2
E sec
Alt k Fit

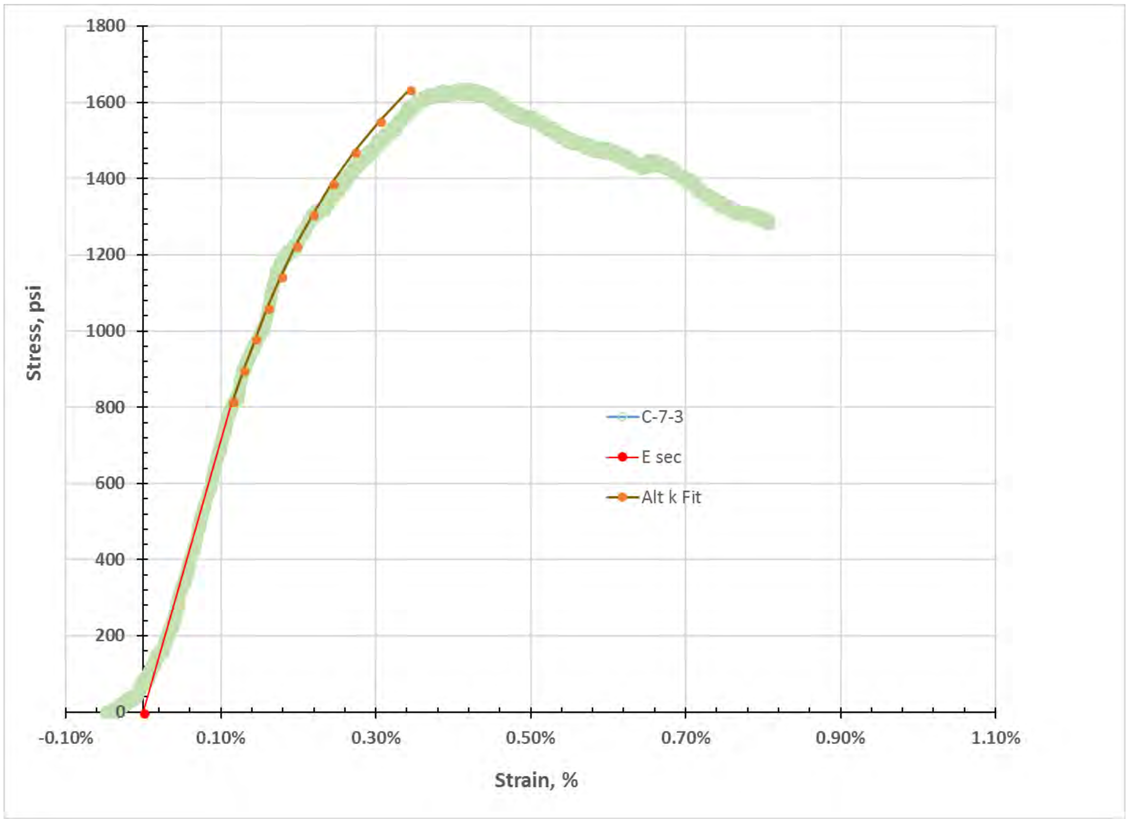
1800
1600
1400
1200
1000
800
600
400
200
0
-0.10%
0.10%
0.30%
0.50%
0.70%
0.90%
1.10%
Stress, psi
Strain, %
C-7-3
E sec
Alt k Fit

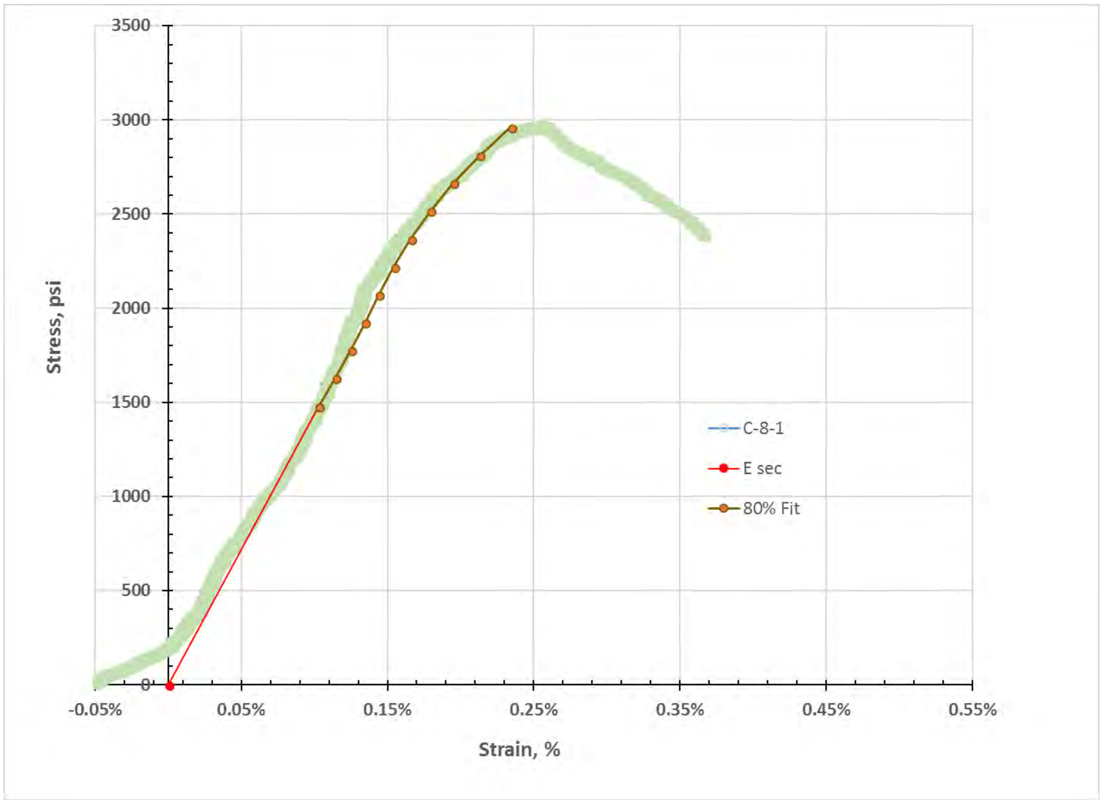
3500
3000
2500
2000
1500
1000
500
0
-0.05%
0.05%
0.15%
0.25%
0.35%
0.45%
0.55%
Stress, psi
Strain, %
C-8-1
E sec
80% Fit

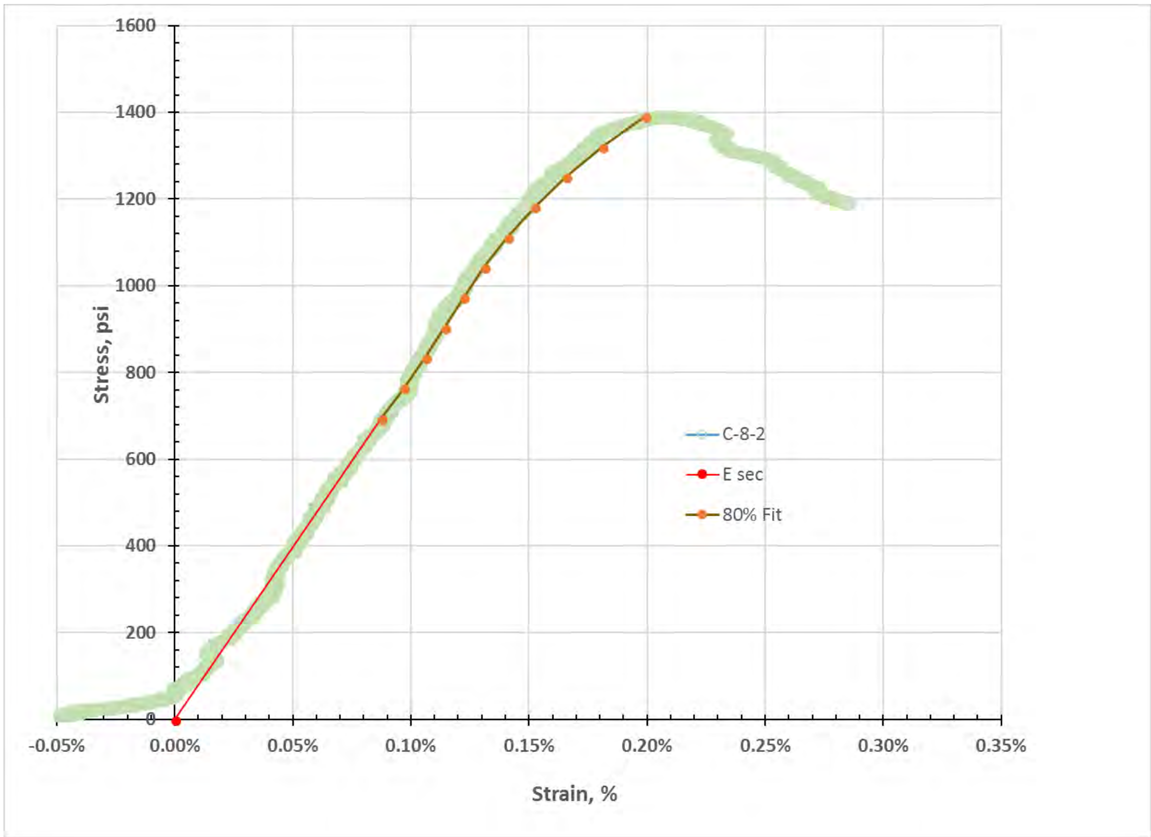
1600
1400
1200
1000
800
600
400
200
0
Stress, psi
-0.05%
0.00%
0.05%
0.10%
0.15%
0.20%
0.25%
0.30%
0.35%
Strain, %
C-8-2
E sec
80% Fit

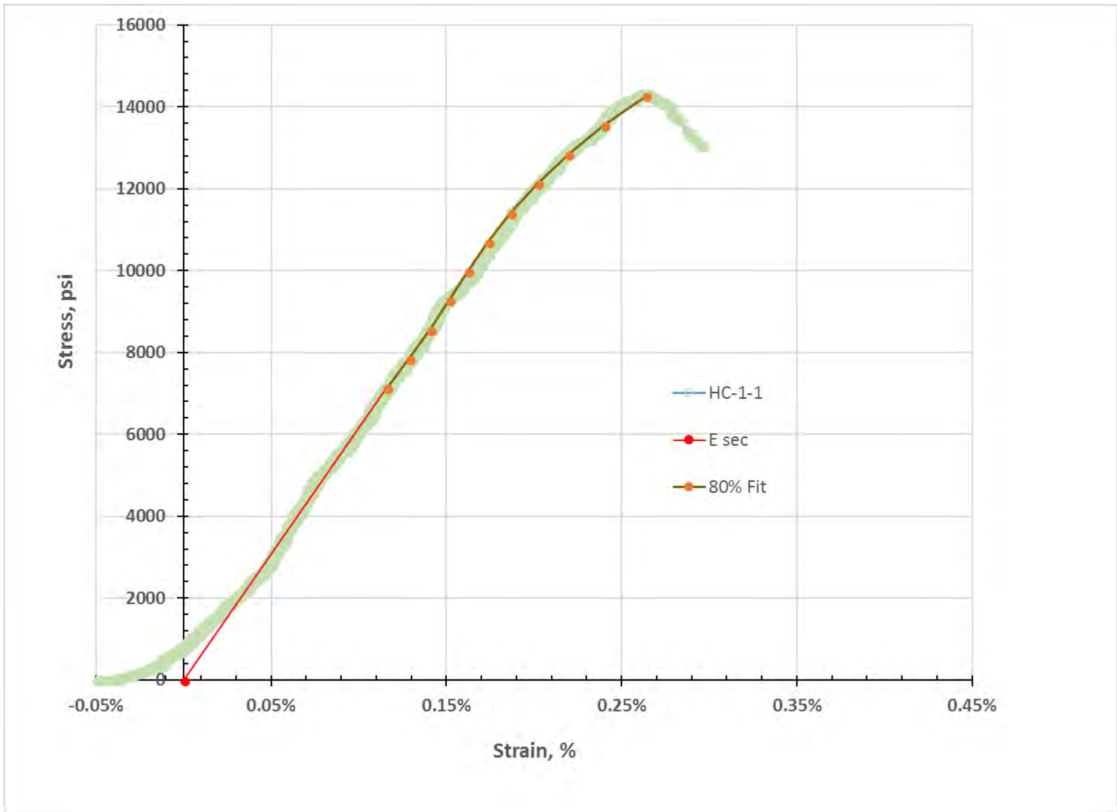
16000
14000
12000
10000
8000
6000
4000
2000
0
Stress, psi
-0.05%
0.05%
0.15%
0.25%
0.35%
0.45%
Strain, %
HC-1-1
E sec
80% Fit

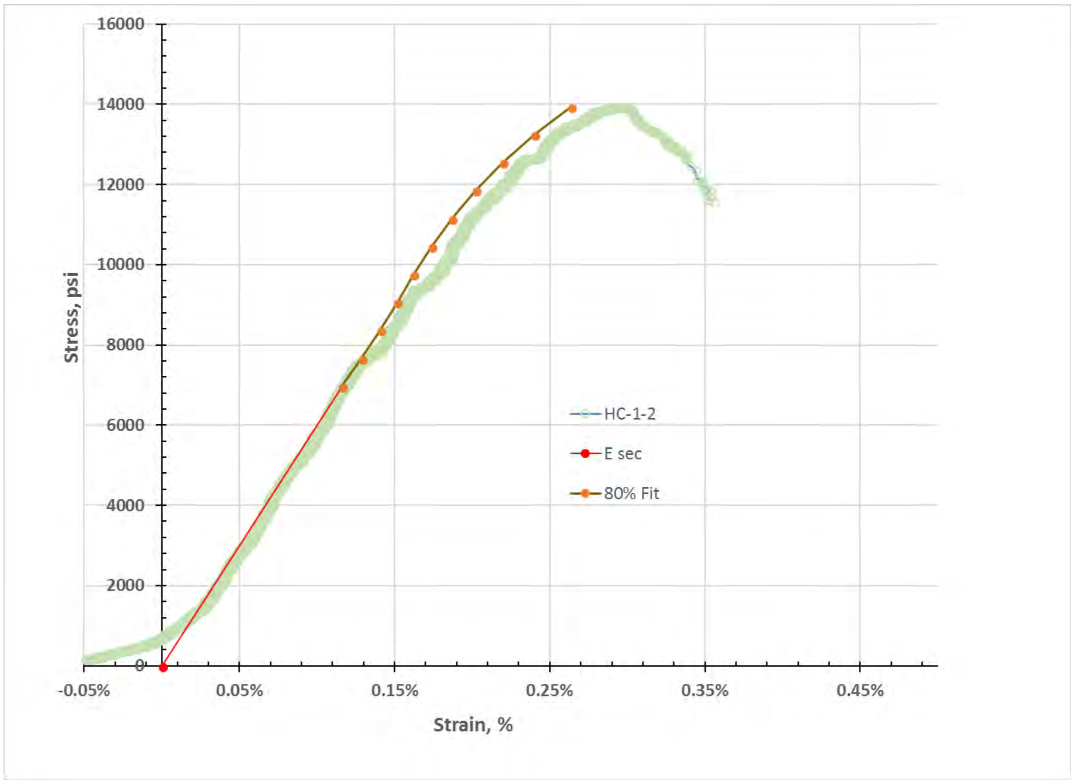
16000
14000
12000
10000
8000
6000
4000
2000
0
Stress, psi
-0.05%
0.05%
0.15%
0.25%
0.35%
0.45%
Strain, %
HC-1-2
E sec
80% Fit

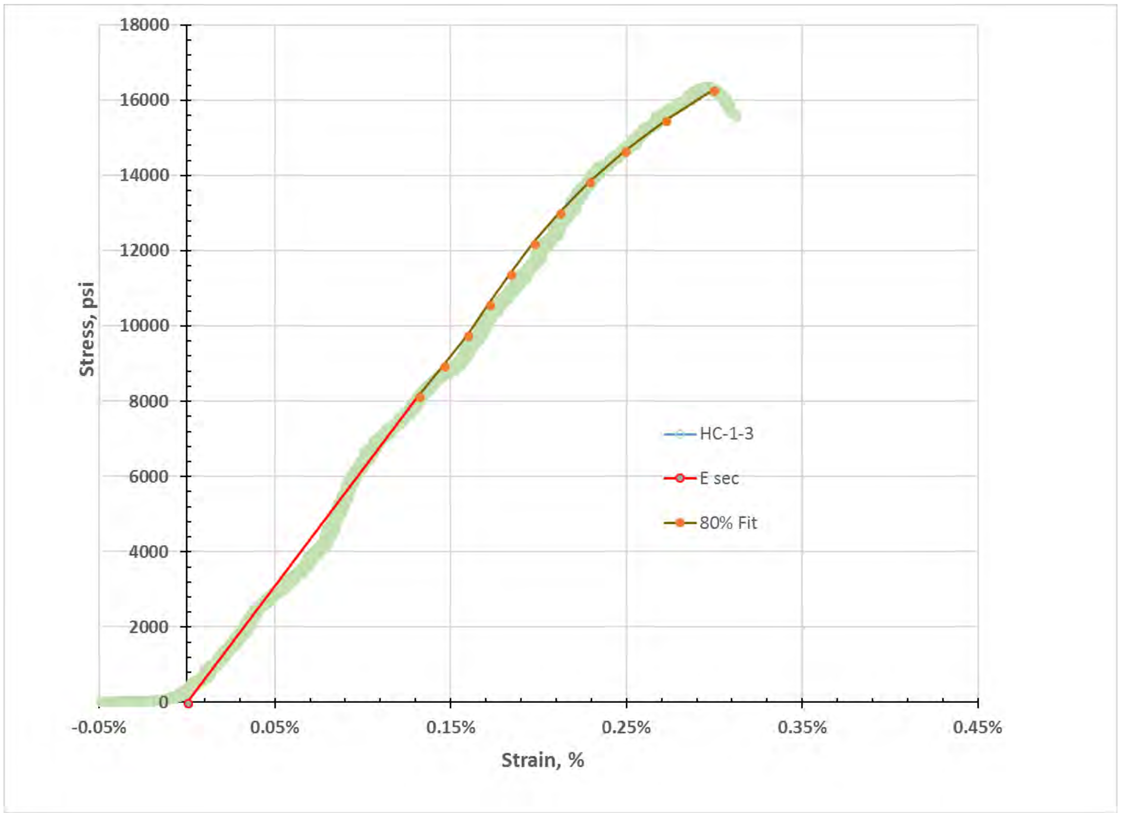
18000
16000
14000
12000
10000
8000
6000
4000
2000
0
Stress, psi
-0.05%
0.05%
0.15%
0.25%
0.35%
0.45%
Strain, %
HC-1-3
E sec
80% Fit

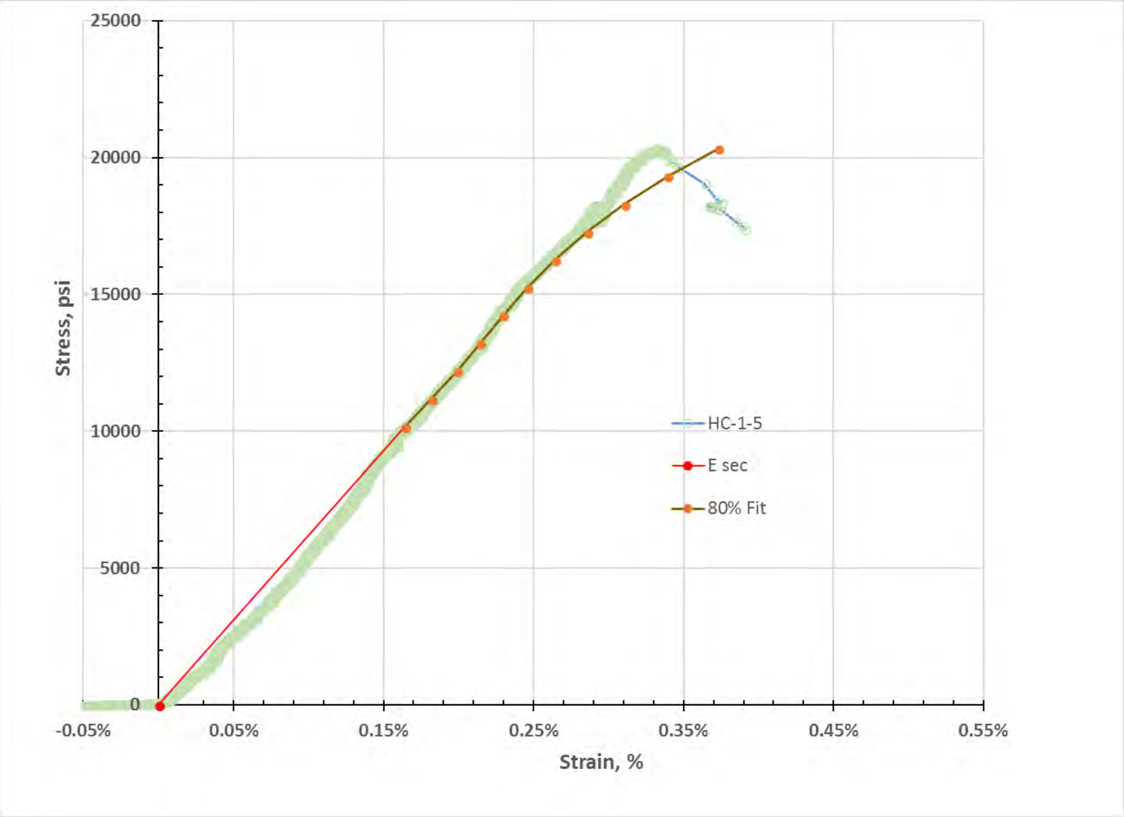

25000
20000
15000
10000
5000
0
Stress, psi
-0.05%
0.05%
0.15%
0.25%
0.35%
0.45%
0.55%
Strain, %
HC-1-5
E sec
80% Fit

Appendix D

Effect of L/D Ratio on Unconfined Compressive Strength

The length to width ratio (L/D) of 2:1 (or greater) specified in ASTM D7012-14 for UCS tests was achieved with only 23 of the 53 samples employing LVDTs for the measurement of axial deformation/strain. This was due to either naturally occurring fracture planes in the material, inherit weaknesses in the moderately cemented soils, or the limited depth of the block from which cores were drilled.

Figure 1 through Figure 3 provide a comparison of UCS test strength (q_u) versus lab shear wave velocity (Vs), elastic modulus (E_{50}) versus shear and P wave velocities, respectively, showing best fit lines to all the data (all L/D tests) and just those with L/D of 2 or greater. As suggested by Tuscay et al (2009), the L/D ratio effect is minor.

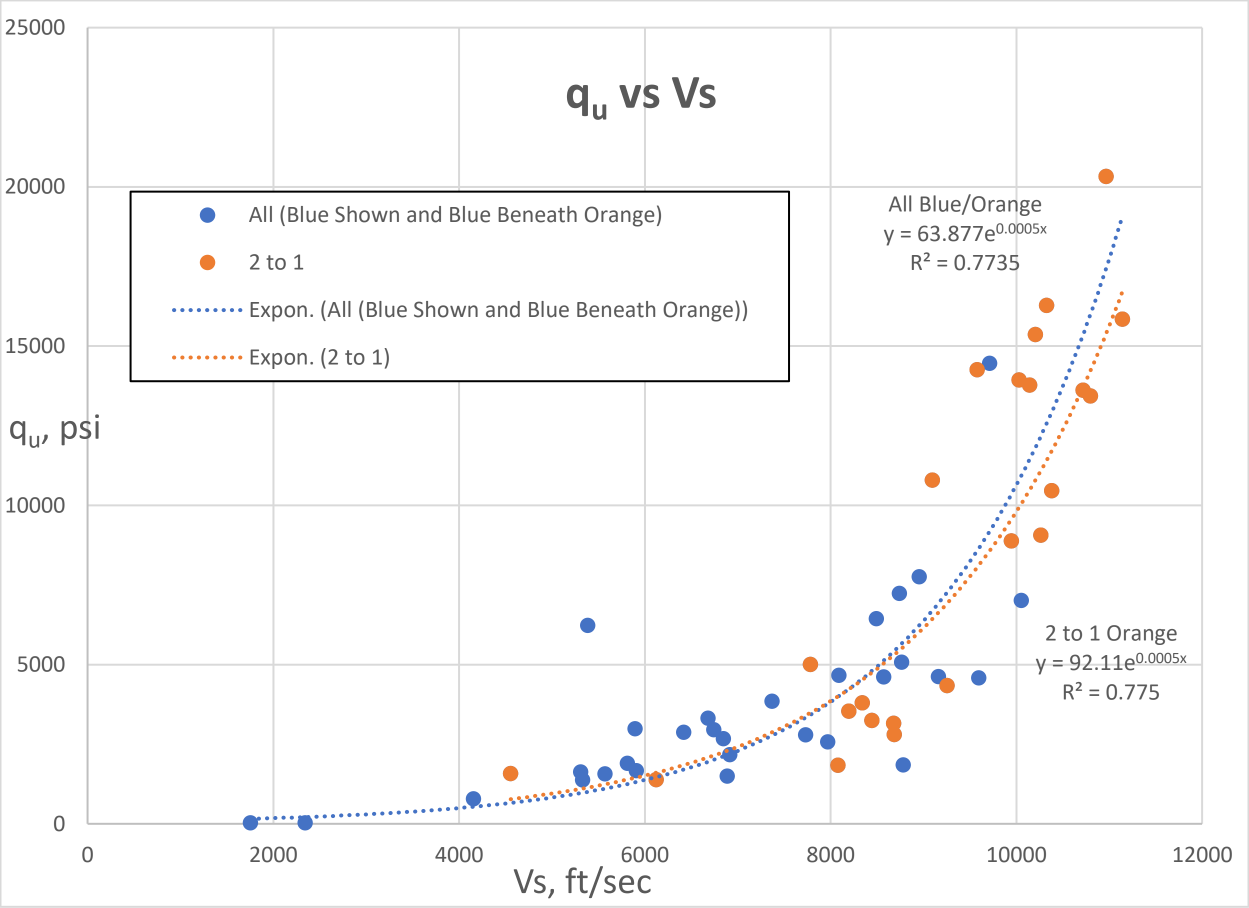

Figure 1: Unconfined compressive strength (q_u) versus shear wave velocity (Vs).

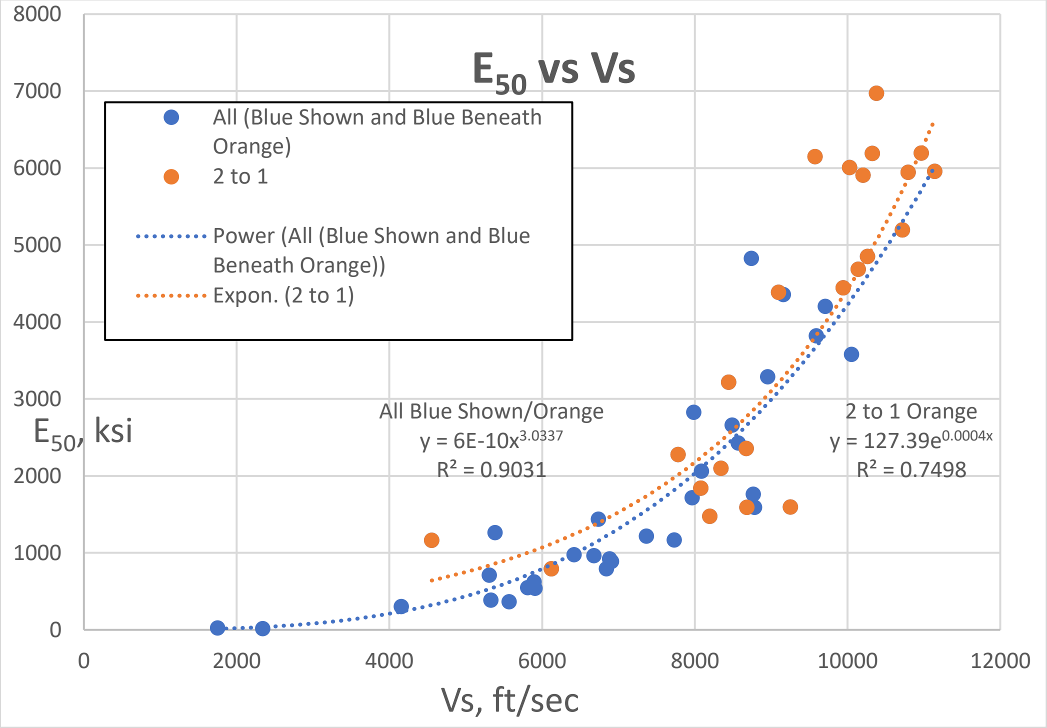

Figure 2: Elastic modulus (E_{50}) versus shear wave velocity (Vs).

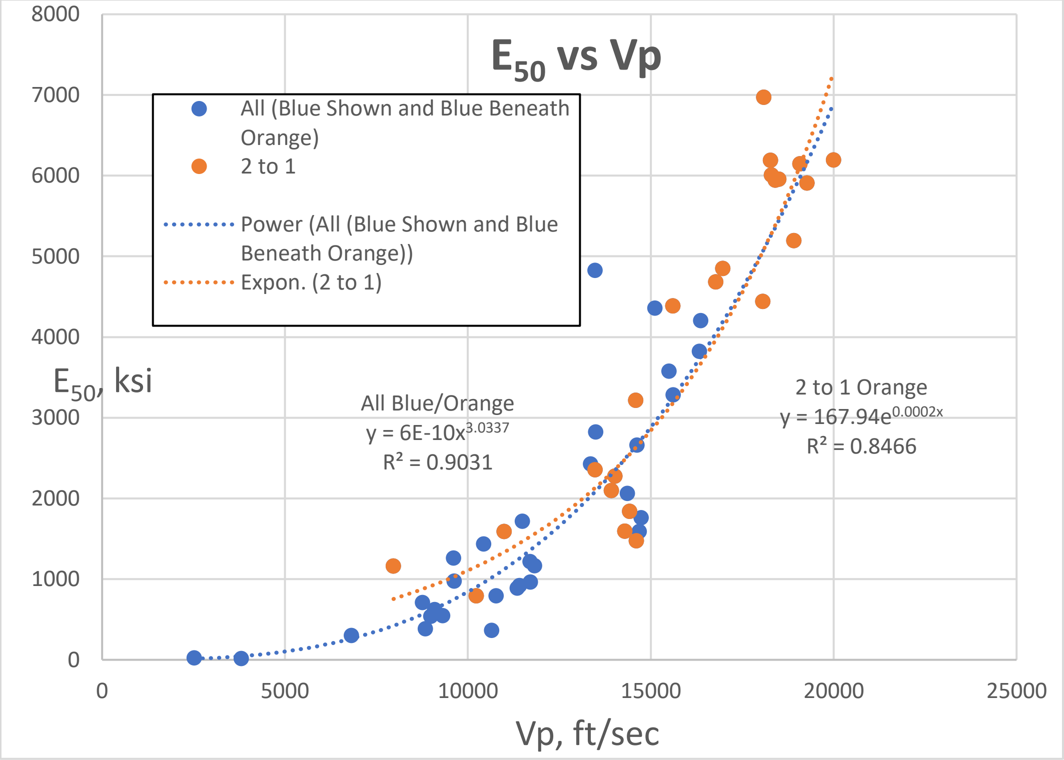

Figure 3: Elastic modulus (E_{50}) versus pressure wave velocity (Vp).

Appendix E

Strain Wedge Model for Laterally Loaded Shafts

Introduction

The strain wedge (SW) model is an approach that has been developed to predict the response of a flexible pile under lateral loading (Norris 1986, Ashour et al. 1996 and Ashour et al. 1998). The main concept associated with the SW model is that traditional one-dimensional Beam on Elastic Foundation (BEF) pile response parameters can be characterized in terms of three-dimensional soil-pile interaction behavior. The SW model was initially established to analyze a free-head pile embedded in one type of uniform soil (sand or clay). However, the SW model has been improved and modified through additional research to accommodate a laterally loaded pile embedded in multiple soil layers (sand and clay). The SW model has been further modified to include the effect of pile head conditions on soil-pile behavior. The main objective behind the development of the SW model is to solve the BEF problem of a laterally loaded pile based on the envisioned soil-pile interaction and its dependence on both soil and pile properties.

The problem of a laterally loaded pile in layered soil has been solved by Reese (1977) as a BEF based on modeling the soil response by p-y curves. However, as mentioned by Reese (1983), the nonlinear p-y curves employed do not account for soil continuity and pile properties such as pile stiffness, pile cross-section shape and pile head conditions.

The SW model was initially developed to assess the response of a laterally loaded long (slender) pile (diameter < 3 ft). As a result, the effect of the vertical side shear (Vv) along the side of a large diameter shaft should be integrated in the SW model analysis to account for such a significant parameter in the analysis of large diameter shafts (Figure 4). In addition, the characterization of the intermediate and short shafts should be incorporated in the SW model analysis to cover broader aspects of the shaft/pile analysis.

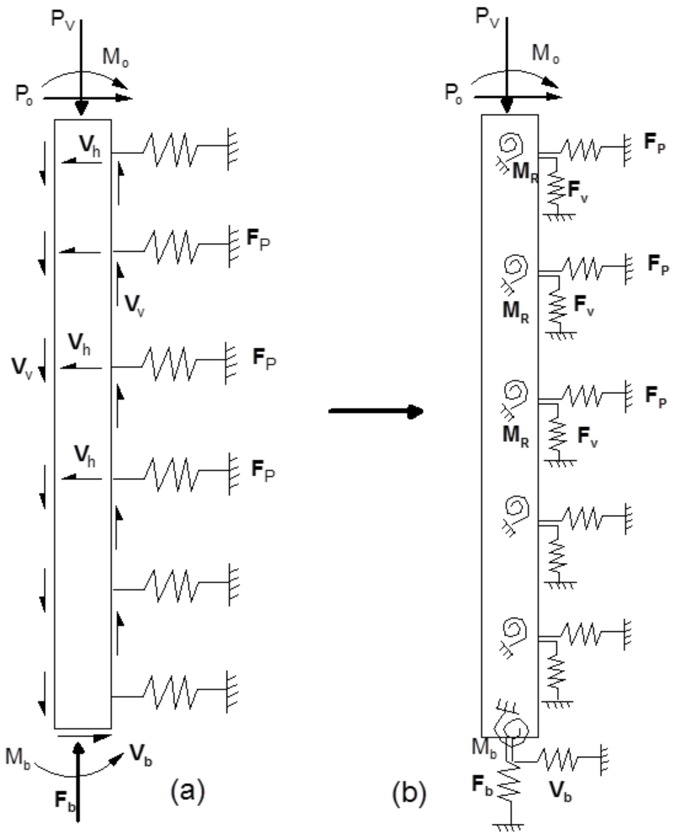

Figure 4: Characterization of Large Diameter Long, Intermediate or Short Shafts In Terms of a) Forces and b) Nonlinear Springs

Theoretical Background of Strain Wedge Model Characterization

The SW model parameters are related to an envisioned three-dimensional passive wedge of soil developing in front of the pile. The basic purpose of the SW model is to relate stress-strain-strength behavior of the soil in the wedge to one-dimensional BEF parameters. The SW model is, therefore, able to provide a theoretical link between the more complex three-dimensional soil-pile interaction and the simpler one-dimensional BEF characterization. The previously noted correlation between the SW model response and BEF characterization reflects the following interdependence:

- the horizontal soil strain (ε) in the developing passive wedge in front of the pile to the deflection pattern (y versus depth, x) of the pile;

- the horizontal soil stress change ($\Delta\sigma_h$) in the developing passive wedge to the soil-pile reaction (p) associated with BEF behavior; and
- the nonlinear variation in the Young's modulus ($E = \Delta\sigma_h/\varepsilon$) of the soil to the nonlinear variation in the modulus of soil subgrade reaction ($E_s = p/y$) associated with BEF characterization.

The analytical relations presented above reflect soil-pile interaction response characterized by the SW model that will be illustrated later. The reason for linking the SW model to BEF analysis is to allow the appropriate selection of BEF parameters to solve the following fourth-order ordinary differential equation to proceed.

$$EI\left(\frac{d^4 y}{d^4 x}\right) + E_s(x)\, y + P_x\left(\frac{d^2 y}{d^2 x}\right) + \left(\frac{d^2 M_R}{d^2 x}\right) = 0 \qquad (1)$$

where M_R is the resisting bending moment per unit length induced along the shaft length (x) due to the vertical side shear (V_V) (Figure 4). The closed form solution of the basic form of the above equation has been obtained by Matlock and Reese (1961) for the case of uniform soil. To appreciate the SW model's enhancement of BEF analysis, one should first consider the governing analytical formulations related to the passive wedge in front of the shaft, the soil's stress-strain and the vertical side shear (t-z curve) formulations, and the related soil-pile interaction.

Soil *Passive Wedge Configuration*

The SW model represents the mobilized passive wedge in front of the pile which is characterized by base angles, φ_m and β_m, the current passive wedge depth h, and the spread of the wedge fan angle, φ_m (the mobilized friction angle of soil). The horizontal stress change at the passive wedge face, $\Delta\sigma_h$, and side shear, τ, act as shown in Figure 5. One of the main assumptions associated with the SW model is that the deflection pattern of the pile is taken to be linear over the controlling depth of the soil near the pile top resulting in a linearized deflection angle, δ, as seen in Figure 6.

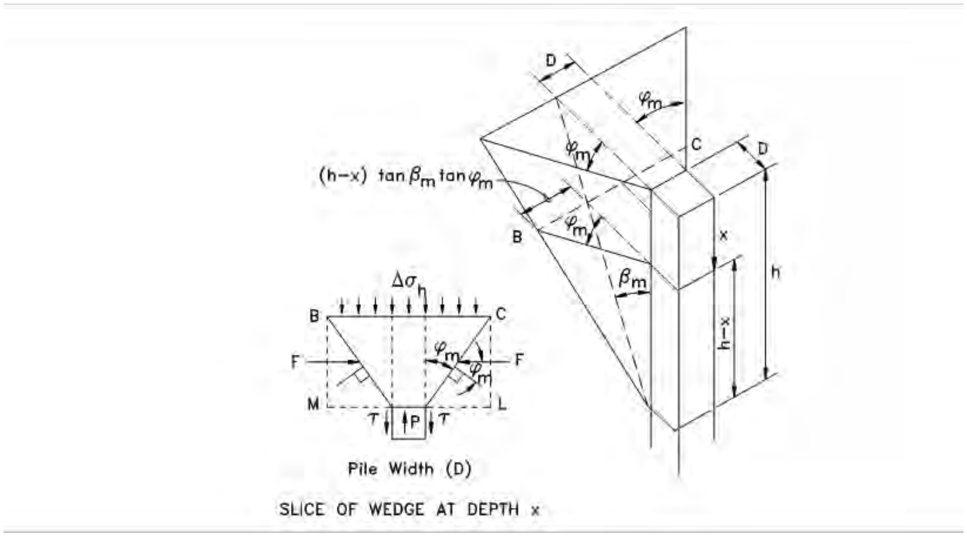
D
φ_m
C
D
φ_m
(h−x) tan β_m tan φ_m
B
φ_m
x
h
β_m
h−x
$\Delta\sigma_h$
B
C
F
φ_m
φ_m
F
M
L
τ
P
τ
Pile Width (D)
SLICE OF WEDGE AT DEPTH x

Figure 5: The basic Strain Wedge in Uniform Soil

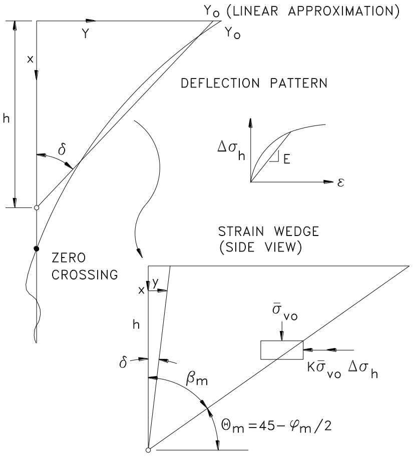
Y₀ (LINEAR APPROXIMATION)
Y
Y₀
x
DEFLECTION PATTERN
h
$\Delta\sigma_h$
E
ε
δ
ZERO CROSSING
STRAIN WEDGE (SIDE VIEW)
x
y
$\bar{\sigma}_{vo}$
h
$K\bar{\sigma}_{vo}$ $\Delta\sigma_h$
δ
β_m
$\Theta_m = 45 - \varphi_m/2$

Figure 6: Deflection Pattern of a Laterally Loaded Long Shaft/Pile and the Associated Strain Wedge

The SW model makes the analysis simpler because forces (F_1) on the opposite sides of the wedge cancel, though the real zone of stress is like the dashed outline shown in Figure 7b.The shear stress (τ) generated on the face of the wedge along incremental distance ds (Figure 7c) can be related to the normal stress ($\Delta\sigma_h$) acting horizontally (across width dx) perpendicular to the direction of pile movement. This relationship is the same as occurs in the conventional triaxial test where $\overline{\sigma}_{vo}$ (i.e. K = 1) is the confining pressure and the horizontal stress change, $\Delta\sigma_h$ (from pile loading), is the deviatoric stresses.

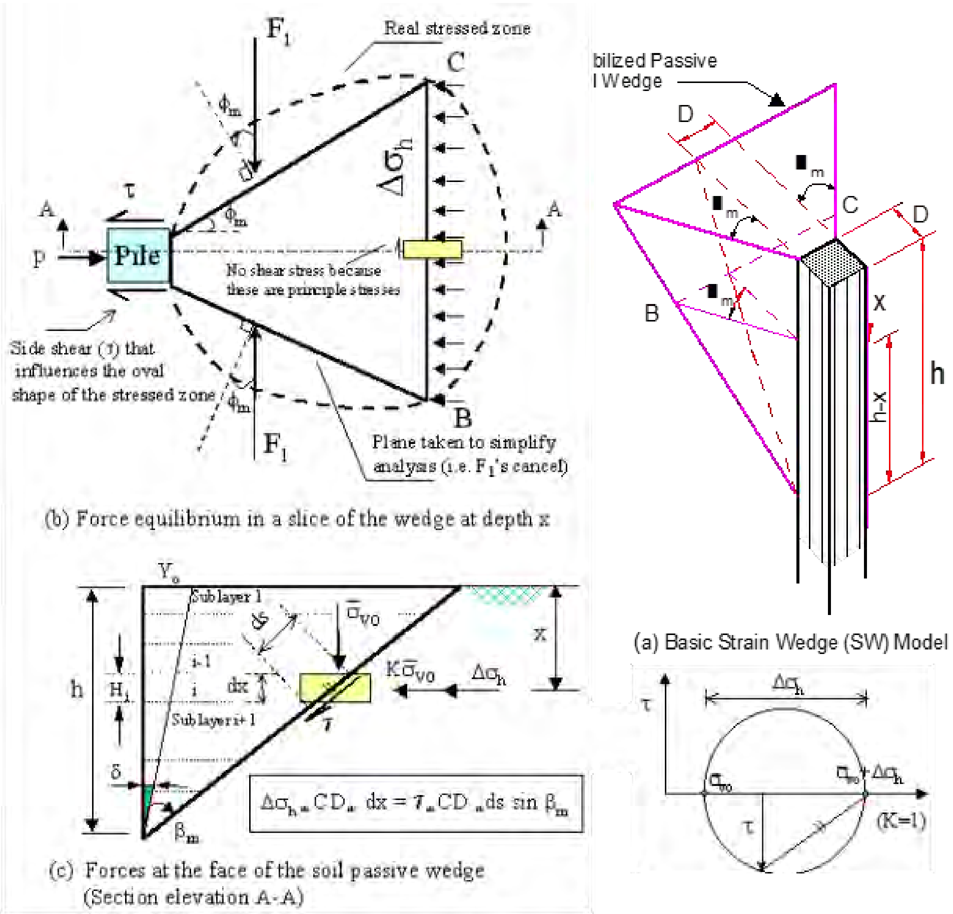
F1
Real stressed zone
C
ϕm
Δσh
A
τ
A
p
Pile
No shear stress because these are principle stresses
Side shear (τ) that influences the oval shape of the stressed zone
F1
B
Plane taken to simplify analysis (i.e. F1's cancel)
(b) Force equilibrium in a slice of the wedge at depth x
bilized Passive
l Wedge
D
C
D
B
x
h
h-x
(a) Basic Strain Wedge (SW) Model
Yo
Sub layer 1
σ̄vo
x
i-1
i
dx
Kσ̄vo
Δσh
h
Hi
Sub layer i+1
τ
δ
βm
Δσh . CD . dx = τ . CD . ds sin βm
(c) Forces at the face of the soil passive wedge
(Section elevation A-A)
τ
Δσh
σvo
σvo+Δσh
(K=1)

Figure 7: Characterization and Equilibrium of the SW Model

The relationship between the actual (closed form solution) and the linearized deflection pattern of long pile/shaft has been established by Norris (1986) as $h/X_o = 0.69$, where h is the current height of the wedge and X_o is the zero crossing. As seen in Figure 8, the relationship (h/X_o) between the actual and linearized deflection for the short shaft is equal to 1 and varies for the intermediate shafts from 0.69 at ($L/T = 4$) to 1 at ($L/T = 2$). L is the total embedded length of the shaft and T is its characteristic stiffness.

It should be noted that the idea of a change in Rowe's (1956) passive wedge (i.e. a developing or mobilized passive wedge at different levels of deflection) employed in the SW model has been shown experimentally by Hughes and Goldsmith (1978).

Changes in the shape and depth of the upper passive wedge, along with changes in the state of loading and shaft/pile deflection, occur with change in the uniform strain (ε) in the developing passive wedge. As seen in Figure 9b, two mobilized (tip to tip) passive wedges are developed in soil in front of the short shaft. Because of the shaft's straight-line deflection pattern of deflection angle δ, the soil strain (ε) will be the same in both (i.e. upper and lower) passive wedges.

As shown in Figure 8 and Figure 9, the deflection pattern is no longer a straight line for the intermediate shaft, and the lower passive wedge has a curved shape that is similar to the shaft's deflection pattern. Accordingly, the soil strain (ε_x) at depth x below the zero crossing will not be uniform and will be evaluated in an iterative method based on the associated deflection at that depth (Figure 9c)

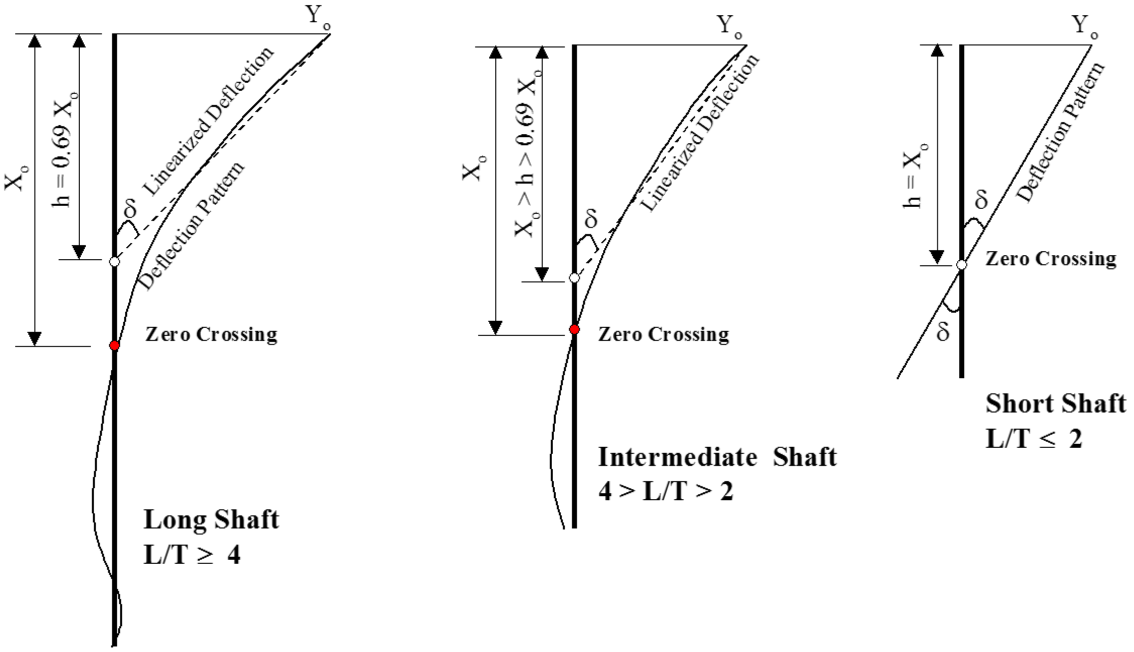
Y_o
X_o
$h = 0.69 X_o$
Linearized Deflection
Deflection Pattern
δ
Zero Crossing
Long Shaft
L/T ≥ 4
Y_o
X_o
$X_o > h > 0.69 X_o$
Linearized Deflection
δ
Zero Crossing
Intermediate Shaft
4 > L/T > 2
Y_o
$h = X_o$
Deflection Pattern
δ
Zero Crossing
δ
Short Shaft
L/T ≤ 2

Figure 8: Deflection patterns of long, intermediate and short shafts.

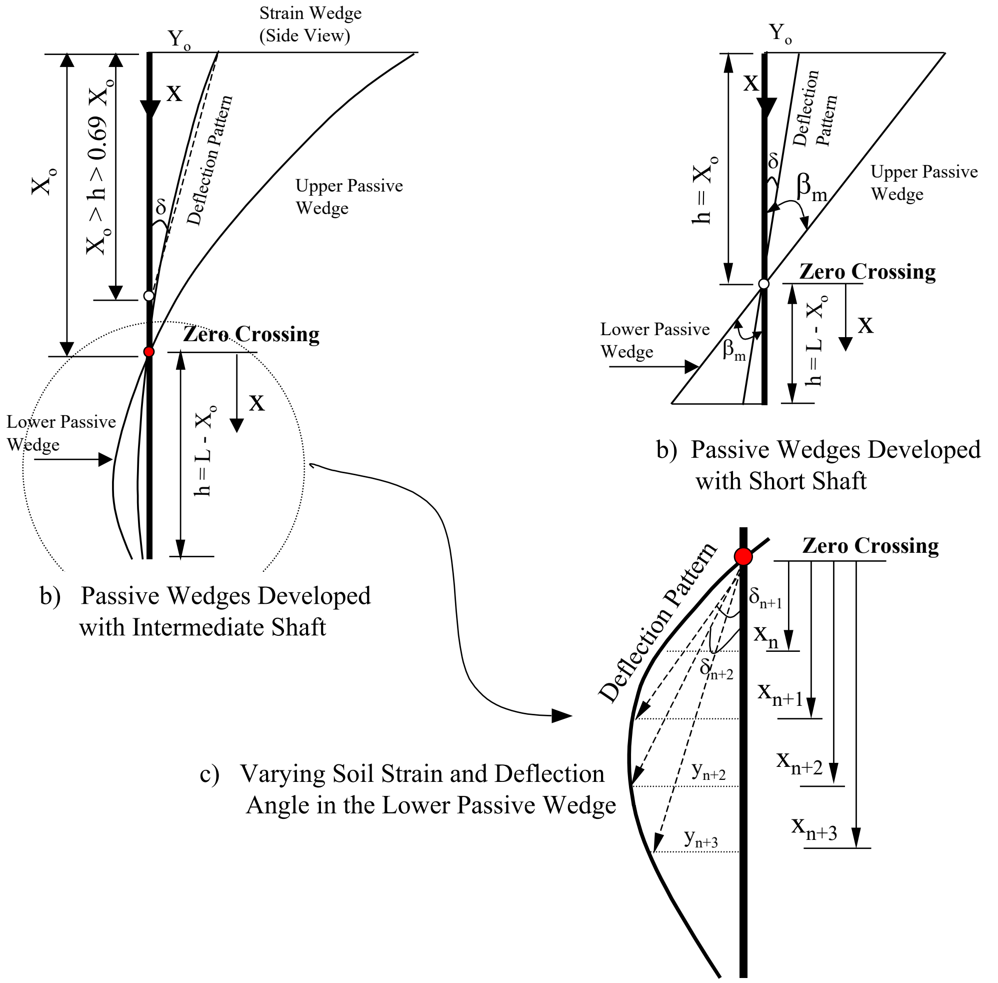
Strain Wedge (Side View)
Y_o
X
X_o
$X_o > h > 0.69\ X_o$
δ
Deflection Pattern
Upper Passive Wedge
Zero Crossing
Lower Passive Wedge
X
$h = L - X_o$
Y_o
X
$h = X_o$
δ
Deflection Pattern
β_m
Upper Passive Wedge
Zero Crossing
Lower Passive Wedge
β_m
$h = L - X_o$
X
Deflection Pattern
Zero Crossing
δ_{n+1}
x_n
δ_{n+2}
x_{n+1}
y_{n+2}
x_{n+2}
y_{n+3}
x_{n+3}

b) Passive Wedges Developed with Intermediate Shaft

b) Passive Wedges Developed with Short Shaft

c) Varying Soil Strain and Deflection Angle in the Lower Passive Wedge

Figure 9: Developed passive wedges with short and intermediate shafts

The lateral response of the short shaft is governed by both (upper and lower) developed passive wedges (Figure 9b). However, with the intermediate shaft, less soil strain (and stress on the soil) develops in the lower passive soil wedge (the inverted wedge below the point of zero crossing) compared to the upper one (Figure 9a). The non-uniform soil strain (ε_x) in the lower passive soil wedge (Figure 9c) becomes much smaller compared to the strain in the upper soil wedge as the intermediate shaft's deflection pattern approaches the deflection pattern of the long shaft. Since the lateral deflection of the long pile/shaft below the zero crossing is always very small, the associated soil strain and developing passive wedge will be very small as well.

Consequently, the developing upper passive soil wedge (and uniform strain therein) dominates the lateral response of the long pile/shaft; hence the adopted name "strain wedge" (SW).

As seen in Figure 6 and Figure 9, the configuration of the wedge at any instant of load and, therefore, base angle, φ_m, mobilized friction angle, φ_m, and wedge depth, h, is given by the following equation:

$$\Theta_m = 45 - \frac{\varphi_m}{2} \tag{2}$$

or its complement

$$\beta_m = 45 + \frac{\varphi_m}{2} \tag{3}$$

The width, $\overline{BC}$, of the wedge face at any depth is

$$\overline{BC} = D + (h - x) 2 \tan \beta_m \tan \varphi_m \tag{4}$$

where x denotes the depth below the top of the studied passive wedge, and D symbolizes the width of the pile cross-section. It should be noted that the SW model is based upon an effective stress analysis of both sand and clay soils. As a result, the mobilized fanning angle, φ_m, is not zero in clay soil as assumed by Reese (1958, 1983).

The above equations are applied to the upper and lower passive wedges in the case of short and intermediate shafts where x for any point on the lower passive wedge (Figure 9c) is measured downward from the zero crossing and replaces the term (h - x) in Eqn. 4. Therefore,

$$\varepsilon_x = \varepsilon \, (y_x / x) / \delta \quad = \quad \varepsilon \left(\frac{\delta_x}{\delta}\right) \tag{5}$$

where ε and δ are the uniform soil strain and linearized shaft deflection angle of the upper passive wedge, respectively. y_x and δ_x are the shaft deflection and secant deflection angle at depth x below the zero crossing (Figure 9c).

Strain Wedge Model in Layered Soil

The SW model can handle the problem of multiple soil layers of different types. The approach employed, which is called the multi-sublayer technique, is based upon dividing the soil profile and the loaded pile into sublayers and segments of constant thickness, respectively, as shown in Figure 10. Each sublayer of soil is considered to behave as a uniform soil and have its own properties according to the sublayer location and soil type. In addition, the multi-sublayer technique depends on the deflection pattern of the embedded pile being continuous regardless of the variation of soil types. However, the depth, h, of the deflected portion of the pile is controlled by the stability analysis of the pile under the conditions of soil-pile interaction. The effects of the soil and pile properties are associated with the soil reaction along the pile by the Young's modulus of the soil, the stress level in the soil, the pile deflection, and the modulus of subgrade reaction between the pile segment and each soil sublayer. To account for the interaction between the soil and the pile, the deflected part of the pile is considered to respond as a continuous beam loaded with different short segments of uniform load and supported by nonlinear elastic supports along soil sublayers, as shown in Figure 11. At the same time, the point of zero deflection (X_o in Figure 8) for a pile in a particular layered soil varies according to the applied load and the soil strain.

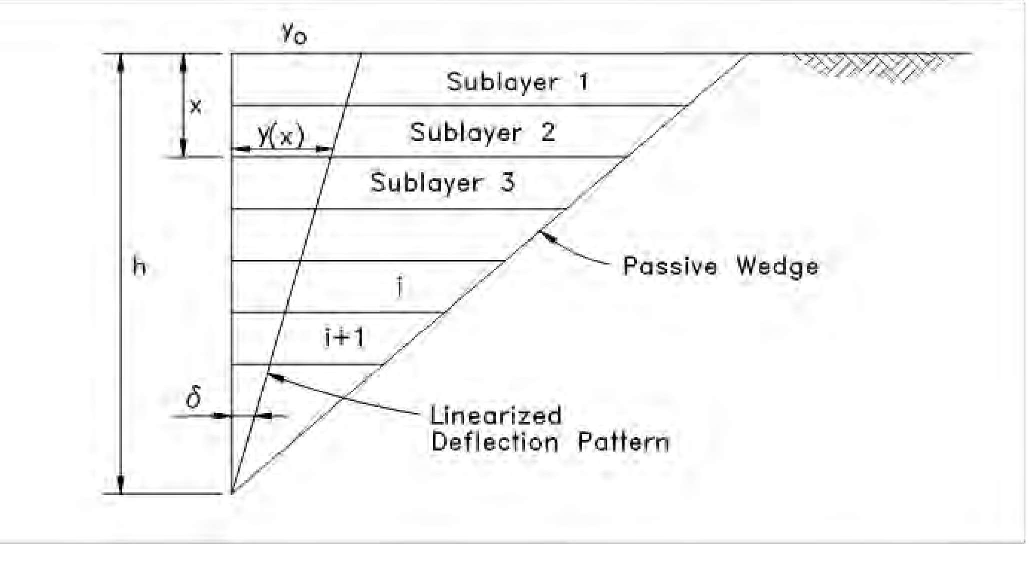

Figure 10: The linearized deflection pattern of a pile/shaft embedded in soil using the multi-sublayer strain wedge model.

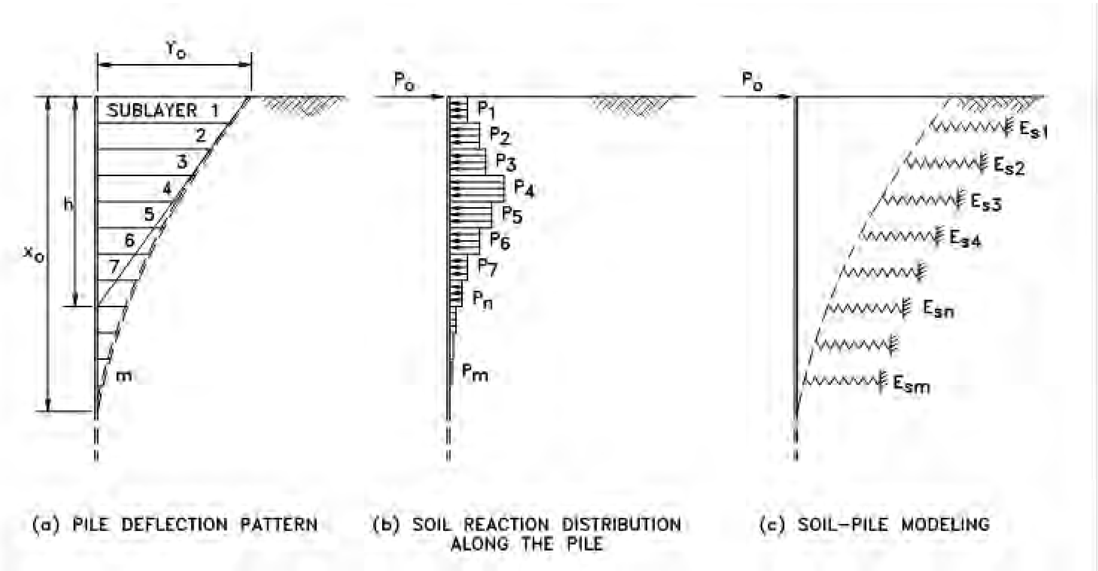
Y₀
SUBLAYER 1
2
3
4
5
6
7
m
h
x₀
P₀
P₁
P₂
P₃
P₄
P₅
P₆
P₇
Pₙ
Pₘ
P₀
Es1
Es2
Es3
Es4
Esn
Esm
(a) PILE DEFLECTION PATTERN
(b) SOIL REACTION DISTRIBUTION ALONG THE PILE
(c) SOIL-PILE MODELING

Figure 11: Soil-pile interaction in the multi-sublayer technique.

The SW model in layered soil provides a means for distinguishing layers of different soil types as well as sublayers within each soil layer where conditions (ε_{50}, SL, φ_m) vary even though the soil and its properties ($\bar{\gamma}$, e or D_r, φ , etc.) remain the same. As shown in Figure 12, there may be different soil layers and a transition in wedge shape from one layer to the next, with all components of the compound wedge having in common the same depth h. In fact, there may be a continuous change over a given sublayer; but the values of stress level (SL) and mobilized friction angle (φ_m) at the middle of each sublayer of height, H_i, are treated as the values for the entire sublayer.

As shown in Figure 12, the geometry of the compound passive wedge depends on the properties and the number of soil types in the soil profile, and the global equilibrium between the soil layers and the loaded pile. An iterative process is performed to satisfy the equilibrium between the mobilized geometry of the passive wedge of the layered soil and the deflection pattern of the pile at each level of loading.

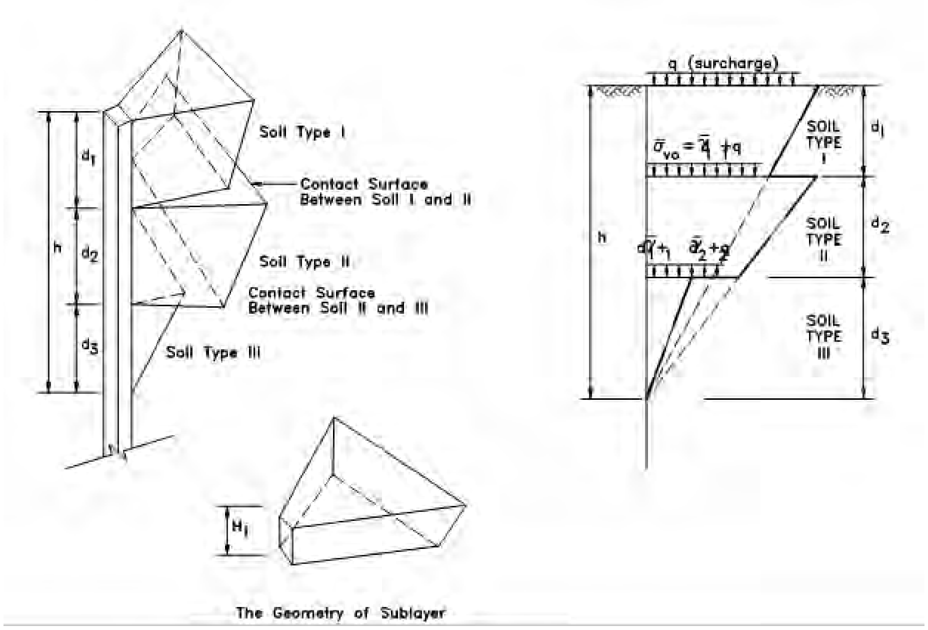
Soil Type I
Contact Surface Between Soil I and II
Soil Type II
Contact Surface Between Soil II and III
Soil Type III
h
d1
d2
d3
Hi
The Geometry of Sublayer
q (surcharge)
σ̄vo = γ̄1 +q
h
SOIL TYPE I
SOIL TYPE II
SOIL TYPE III
d1
d2
d3

Figure 12: The proposed geometry of the compound passive wedge.

While the shape of the wedge in any soil layer depends upon the properties of that layer and, therefore, satisfies the nature of a Winkler foundation of independent "soil" springs in BEF analysis, realize that there is forced interdependence given that all components of the compound wedge have the same depth (h) in common. Therefore, the mobilized depth (h) of the compound wedge at any time is a function of the various soils (and their stress levels), the bending stiffness (EI), and head fixity condition (fixed, free, or other) of the pile. In fact, the developing depth of the compound wedge can be thought of as a retaining wall of changing height, h. Therefore, the resultant "soil" reaction, p, from any soil layer is really a "soil-pile" reaction that depends upon the neighboring soil layers and the pile properties as they, in turn, influence the current depth, h. In other words, the p-y response of a given soil layer is not unique. The governing equations of the mobilized passive wedge shape are applied within each one- or two-foot sublayer i (of a given soil layer I) and can be written as follows:

$$(\Theta_m)_i = 45 - \frac{(\varphi_m)_i}{2} \tag{6}$$

$$(\beta_m)_i = 45 + \frac{(\varphi_m)_i}{2} \tag{7}$$

$$\left(\overline{BC}\right)_i = D + (h - x_i)\, 2\left(\tan\beta_m\right)_i\left(\tan\varphi_m\right)_i \tag{8}$$

Where, h symbolizes the entire depth of the compound passive wedge in front of the pile and x_i represents the depth from the top of the pile or compound passive wedge to the middle of the sublayer under consideration. Equations 6 through 8 are applied at the middle of each sublayer. In the case of short and intermediate shafts, x_i is measured downward from the point of zero crossing and replaces the term $(h - x_i)$ in Eqn.8, as shown in Figure 9, for analysis of the lower wedge.

Soil Stress-Strain Relationship

The horizontal strain (ε) in the soil in the developing/mobilized passive wedge in front of the pile is the predominant parameter in the SW model; hence, the name "strain wedge". Consequently, the horizontal stress change ($\Delta\sigma_h$) is constant across the width of the rectangle BCLM (of face width BC of the passive wedge), as shown in Figure 5. The stress-strain relationship is defined based on the results of the isotropically consolidated drained (sand) or undrained (clay) triaxial test. These properties are summarized as follows:

- The major principle stress change ($\Delta\sigma_h$) in the wedge is in the direction of pile movement, and it is equivalent to the deviatoric stress in the triaxial test as shown in Figure 7 (assuming the horizontal direction in the field is taken as the axial direction in the triaxial test).
- The vertical stress change ($\Delta\sigma_v$) and the perpendicular horizontal stress change ($\Delta\sigma_{ph}$) in the field equal zero, corresponding to the standard triaxial compression test where deviatoric stress is increased while confining pressure remains constant.
- The initial horizontal effective stress is taken as

$$\bar{\sigma}_{ho} = K\,\bar{\sigma}_{vo} = \bar{\sigma}_{vo}$$

where K=1 due to pile installation effects. Therefore, the isotropic confining pressure in the triaxial test is taken as the vertical effective stress ($\bar{\sigma}_{vo}$) at the associated depth.

- The horizontal stress change in the direction of pile movement is related to the current level of horizontal strain (ε) and the associated Young's modulus in the soil, as are the deviatoric stress and the axial strain, to the secant Young's modulus ($E = \Delta\sigma_h/\varepsilon$) in the triaxial test.
- Both the vertical strain (ε_v) and the horizontal strain perpendicular to pile movement (ε_{ph}) are equal and are given as

  $\varepsilon_v = \varepsilon_{ph} = -\nu\varepsilon$

  where ν is the Poisson's ratio of the soil.

It can be demonstrated from a Mohr's circle of soil strain, as shown in Figure 13, that shear strain, γ, is defined as

$$\frac{\gamma}{2} = \frac{1}{2}(\varepsilon - \varepsilon_v)\sin 2\Theta_m = \frac{1}{2}\varepsilon(1+\nu)\sin 2\Theta_m \tag{9}$$

The corresponding stress level (SL) in sand (see Figure 14) is

$$SL = \frac{\Delta\sigma_h}{\Delta\sigma_{hf}} = \frac{\tan^2(45+\varphi_m/2)-1}{\tan^2(45+\varphi/2)-1} \tag{10}$$

where the horizontal stress change at failure (or the deviatoric stress at failure in the triaxial test) is

$$\Delta\sigma_{hf} = \bar{\sigma}_{vo}\left[\tan^2\left(45+\frac{\varphi}{2}\right)-1\right] \tag{11}$$

In clay and cemented soils,

$$SL = \frac{\Delta\sigma_h}{\Delta\sigma_{hf}}\ ; \qquad \Delta\sigma_{hf} = 2S_u \tag{12}$$

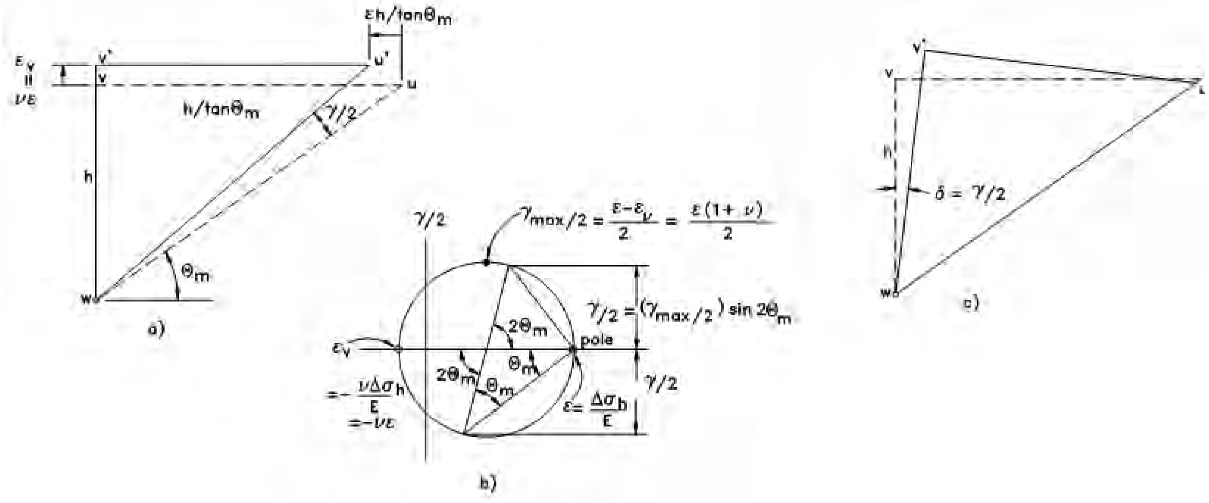
εh/tanθm
εv = νε
v'
v
u'
u
h/tanθm
γ/2
h
θm
w
a)
γ/2
γmax/2 = (ε−εv)/2 = ε(1+ν)/2
γ/2 = (γmax/2) sin 2θm
2θm
θm
pole
εv
= −νΔσh/E = −νε
2θm
θm
ε= Δσh/E
γ/2
b)
v'
v
h
δ = γ/2
w
c)

Figure 13: Distortion of the wedge a), The associated Mohr circle of strain b), and the relationship between pile deflection and wedge distortion c).

Where, S_u represents the undrained shear strength which may vary with depth. Determination of the values of SL and φ_m in clay requires the involvement of an effective stress analysis which is presented later in this appendix.

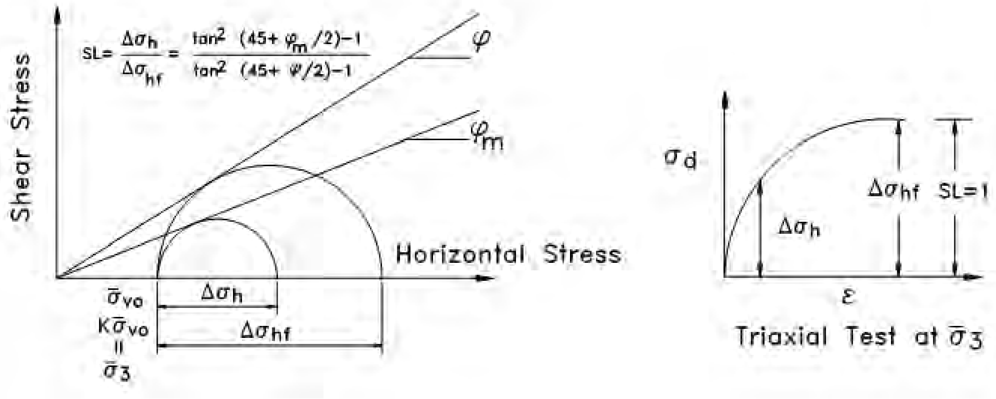
SL= Δσh/Δσhf = (tan² (45+ φm/2)−1)/(tan² (45+ φ/2)−1)
φ
φm
Shear Stress
Horizontal Stress
σ̄vo
Kσ̄vo = σ̄3
Δσh
Δσhf
σd
Δσhf
SL=1
Δσh
ε
Triaxial Test at σ̄3

Figure 14: Relationship between horizontal stress change, stress level, and mobilized friction angle.

The relationships above show clearly that the passive wedge response and configuration change with the change of the mobilized friction angle (φ_m) or stress level (SL) in the soil. Such behavior provides the flexibility and the accuracy for the strain wedge model to accommodate both small and large strain cases. The above equations are applied to each soil sublayer along the shaft to evaluate the varying stress level in the soil and the geometry of the components of the passive wedge (Figure 12).

A power function stress-strain relationship is employed in SW model analysis for both sand and clay soils. It reflects the nonlinear variation in stress level (SL) with axial strain (ε) for the condition of constant confining pressure. To be applicable over the entire range of soil strain, it takes on a form that varies in stages as shown in Figure 15. The advantage of this technique is that it allows the three stages of horizontal stress, described in the next section, to occur simultaneously in different sublayers within the passive wedge.

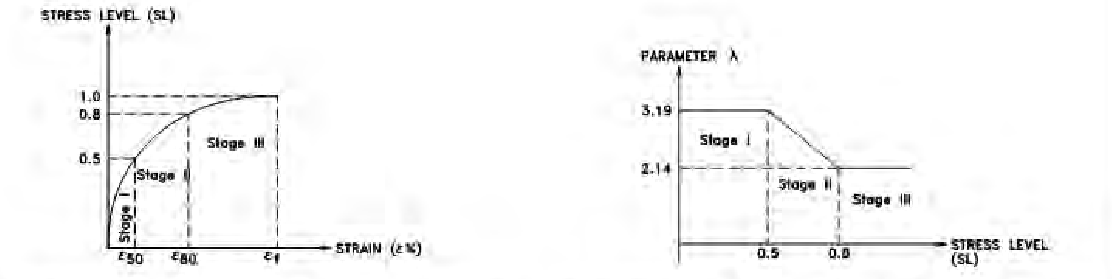

(a) THE DEVELOPED HYPERBOLIC STRESS–STRAIN RELATIONSHIP IN SOIL (b) THE VARIATION OF THE FITTING PARAMETER λ VERSUS STRESS LEVEL (SL)

Figure 15: The Stress-Strain Relationship for Soil.

Horizontal Stress Level (SL) in Sand and Clay

Stage I ($\varepsilon \leq \varepsilon_{50\%}$)

The relationship between strain and stress level at each sublayer (i) in the first stage is assessed using the following equation,

$$\varepsilon = \mathrm{SL}\ e^{(3.707\, SL)}\, \varepsilon_{50} / \lambda \qquad (13)$$

where 3.707 and λ (λ= 3.19) represent the fitting parameters of the power function relationship, and ε_{50} symbolizes the soil strain at 50 percent stress level at the associated confining pressure.

Stage II ($\varepsilon > \varepsilon_{50\,\%}$)

In the second stage of the stress-strain relationship, Eqn. 5.13 is still applicable. However, the value of the fitting parameter λ is taken to vary as given in Eqn. 14.

$$\lambda = -7.121\ SL^2 + 7.0592\ SL + 1.4403 \qquad (14)$$

Equation 14, a second order polynomial is a modification of previously employed SW model stress strain formulation that is both simpler and yields a better match at SL = 0.50 ($\boldsymbol{\varepsilon = \varepsilon_{50}}$) with Stage I variation than before. It will be shown in in the next section that the stress strain formulation for Stage II for cemented soil (e.g. caliche) that a different second order polynomial expression for λ will apply.

As shown in Figure 16, if ε_{50} of the soil is constant with depth (x), then, for a given horizontal strain (ε), SL from Eqns. 13 or 14 will be constant with x. On the other hand, since strength, $\Delta\sigma_{hf}$, varies with depth (e.g., see Eqns. 11 and 12), $\Delta\sigma_h$ (= SL $\Delta\sigma_{hf}$) will vary in a like fashion. However, ε_{50} is affected by confining pressure ($\bar{\sigma}_{vo}$) in sand and S_u in clay. Therefore, SL for a given ε will vary somewhat with depth. The Young's modulus of the soil from both the shear loading phase of the triaxial test and the strain wedge model is

$$E_i = \frac{(\Delta\sigma_h)_i}{\varepsilon} = \frac{SL_i\,(\Delta\sigma_{hf})_i}{\varepsilon} \qquad (15)$$

It can be seen from the previous equations that stress level, strain and Young's modulus in each sublayer (i) depend on each other, which results in the need for an iterative solution technique to satisfy the equilibrium between the three variables.

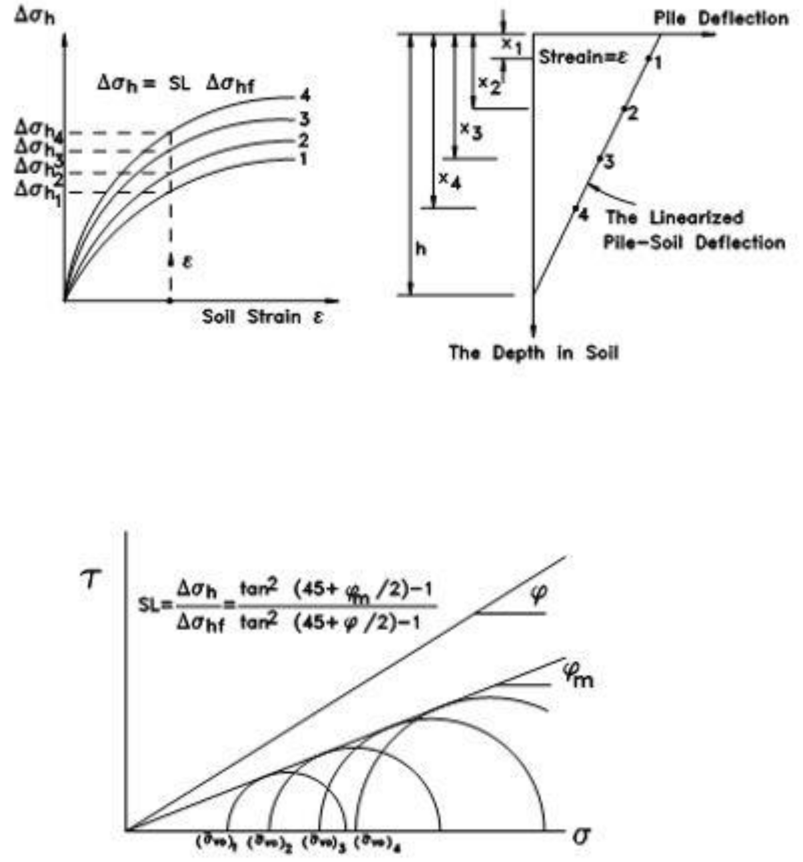
Δσh
Δσh = SL Δσhf
4
3
2
1
Δσh4
Δσh3
Δσh2
Δσh1
ε
Soil Strain ε
Pile Deflection
x1
x2
x3
x4
h
Streain=ε
1
2
3
4
The Linearized Pile-Soil Deflection
The Depth in Soil
τ
SL= Δσh / Δσhf = tan2 (45+ φm /2)-1 / tan2 (45+ φ /2)-1
φ
φm
σ
(σvo)1 (σvo)2 (σvo)3 (σvo)4

Figure 16: The variation of stress ($\Delta\sigma_h$) with depth in soil for constant strain (ε).

Horizontal Stress Level (SL) in caliche Materials

Stage I (SL ≤ 0.55)

Based on experimental data, the relationship between stress level and strain in caliche materials in the first stage is assessed using the following equation,

$$\varepsilon_m = 2SL\varepsilon_{50} \qquad \text{for SL} < 0.55$$

Stage II (SL> 0.55)

In this second stage of loading which extends from 55 percent to 100percent stress level, the following equations apply.

$\varepsilon_m = SL\ e^{(3.707\ SL)}\ \varepsilon_{50}/\lambda$ same as Eqn.13 but for SL>0.55

Where,

$$\lambda = 40.123\ SL^2\ -30.866\ SL + 8.6503 \qquad (14b)$$

Here,

$\Delta\sigma_{hf} = q_u$; q_u is the unconfined compressive strength (UCS)

and the secant Young's modulus is

$$E_i = \frac{SL\ \left(\Delta\sigma_{hf}\right)_i}{\varepsilon_m} \qquad (15b)$$

To take account of possible initial fracture closure, the actual or full strain is given as

$$\varepsilon_{actual} = \varepsilon_m + \Delta\varepsilon \qquad (13b)$$

where the closure strain, Δε, when considered (Δε>0) varies with UCS as given below

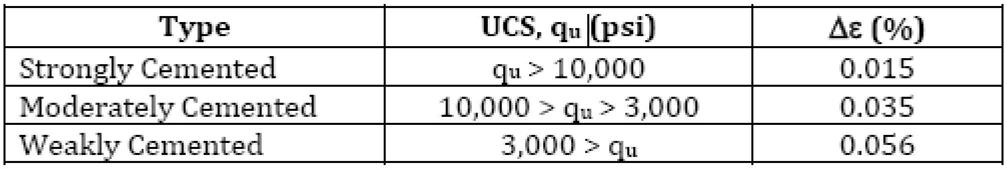

Type	UCS, q_u (psi)	Δε (%)
Strongly Cemented	$q_u > 10{,}000$	0.015
Moderately Cemented	$10{,}000 > q_u > 3{,}000$	0.035
Weakly Cemented	$3{,}000 > q_u$	0.056

Shear Stress along The Pile Sides (SLt)

Shear stress (τ) along the pile sides in the SW model (see Figure 5 and Figure 7) is evaluated according to the soil type (sand or clay).

Pile Side Shear in Sand

In the case of sand, the shear stress along the pile sides depends on the effective stress (σ_{vo}) at the depth in question and the mobilized angle of friction between the sand and the pile (φ_s). The mobilized side shear depends on the stress level and is given by the following equation,

$$\tau_i = (\bar{\sigma}_{vo})_i \tan\left(\varphi_s\right)_i ; \qquad where \qquad \tan\left(\varphi_s\right)_i = 2\tan\left(\varphi_m\right)_i \qquad (16)$$

In Eqn. 16, note that the tangent of the mobilized side shear friction angle, tanφ_s, is taken to develop at twice that of the sand in the wedge (tanφ_m). Of course, φ_s is limited to the fully developed friction angle (φ) of the soil.

Pile Side Shear Stress in Clay and Cemented Soils

The shear stress along the pile sides in clay depends on the clay's undrained shear strength. The stress level for shear along the pile sides (SL_t) differs from that in the wedge in front of the pile. The side shear stress level is function of the shear movement, equal to the pile deflection (y) at depth x from the ground surface. This implies a connection between the stress level (SL) in the wedge and that of the pile sides (SL_t). Using the Coyle-Reese (1966) "t-z" shear stress transfer curves (Figure 17), values for SL_t can be determined as given by Norris (1994). The shear stress transfer curves represent the relationship between the shear stress level experienced by a one-foot diameter pile embedded in clay with a peak undrained strength, S_u, and side resistance, τ_{ult} (equal to ζ times the adhesional strength αS_u), for shear movement, y. The shear stress load transfer curves of Coyle-Reese can be normalized by dividing curve A ($0 < x < 3$ m) by $\zeta = 0.53$, curve B ($3 < x < 6$ m) by $\zeta = 0.85$, and curve C ($x > 6$ m) by $\zeta = 1.0$. These three values of normalization (0.53, 0.85, 1.0) represent the peaks of the curves A, B, and C, respectively, in Figure 18a. Figure 18b shows the resultant normalized curves. Knowing pile deflection (y), one can assess the value of the mobilized pile side shear stress (τ) as

$$\tau_i = (SL_t)_i (\tau_{ult})_i \qquad (17)$$

where

$$(\tau_{ult})_i = \zeta (\alpha S_u)_i \qquad (18)$$

and α indicates the adhesion value after Tomlinson (1957).

The normalized shear stress load transfer curves can be represented by the following equations.

For the normalized curves A ($x < 3$ m) and B ($3 < x < 6$ m),

$$SL_t = 12.9\, y\, D - 40.5\, y^2\, D^2 \qquad (19)$$

For the normalized curve C (x > 6 m)

$$SL_t = 32.3\, y\, D - 255\, y^2\, D^2 \qquad (20)$$

where y is in cm and D in m.

From the discussion above, it is obvious that SL_t varies nonlinearly with the pile deflection, y, at a given soil depth, x (Figure 18). Also, SL_t changes nonlinearly with soil depth for a given value of soil strain and varying displacement (see Figure 17). These concepts are employed in each sublayer of clay.

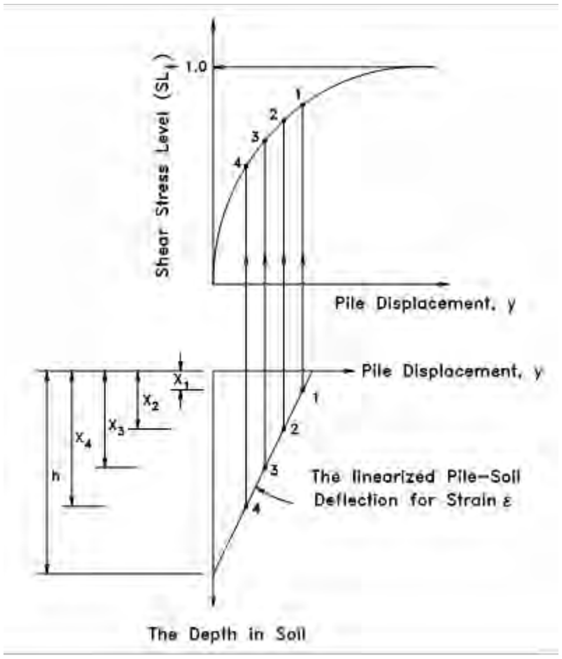
Shear Stress Level (SL_t)
1.0
1
2
3
4
Pile Displacement, y
Pile Displacement, y
X_1
X_2
X_3
X_4
h
1
2
3
4
The linearized Pile–Soil Deflection for Strain ε
The Depth in Soil

Figure 17: The side shear stress-displacement response in clay.

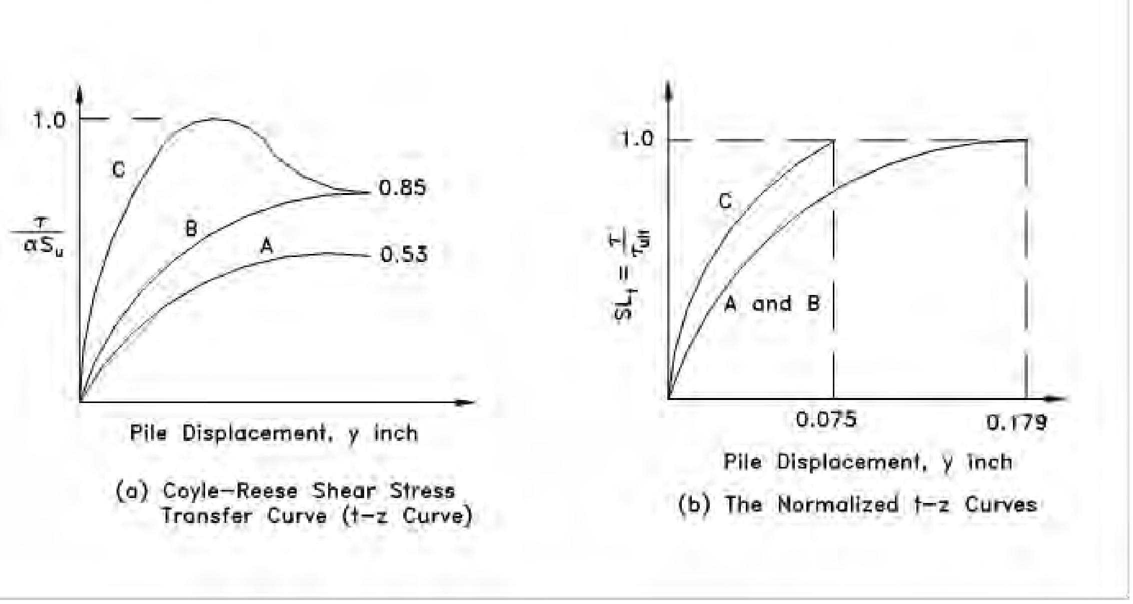

Figure 18: The nonlinear variation of shear stress level (SLt) in clay with depth (Zones A, B and C) after (a) Reese (1996) and (b) as modified/normalized by Norris (1994).

Soil Property Characterization in The Strain Wedge Model

One of the main advantages of the SW model approach is the very basic soil properties needed to analyze the problem of a laterally loaded pile. The properties required represent the most commonly assessed properties of soil, such as the effective unit weight and the angle of internal friction or undrained strength.

The soil profile is divided into one or two foot sublayers, and each sublayer is treated as an independent entity with its own properties (the multi-sublayer approach). In this fashion, the variation in soil properties or response (such as ε_{50} and φ in the case of sand, or S_u and $\bar{\varphi}$ in the case of clay) of each sublayer of soil can be explored. It is obvious that soil properties should not be averaged at the mid-height of the passive wedge in front of the pile for a uniform soil profile (as in the earlier work of Norris 1986), or averaged for all sublayers of a single uniform soil layer of a multiple layer soil profile.

Properties Employed for Sand Soil

- Effective unit weight (total above water table, buoyant below), $\bar{\gamma}$

- Void ratio, e, or relative density, D_r
- Angle of internal friction, φ
- Soil strain at 50% stress level, ε_{50}

While standard subsurface exploration techniques and available correlations may be used to evaluate or estimate $\bar{\gamma}$, e or D_r, and φ, some guidance may be required to assess ε_{50}.

The ε_{50} represents the axial strain (ε_1) at a stress level equal to 50 percent in the ε_1-SL relationship that would result from a standard drained (CD) triaxial test. The confining (consolidation) pressure for such tests should reflect the effective overburden pressure ($\bar{\sigma}_{vo}$) at the depth (x) of interest. ε_{50} changes from one sand to another as well as with density. To obtain ε_{50} for a particular sand, one can use the group of curves shown in Figure 19 (Norris 1986) which show a variation based upon the uniformity coefficient, C_u, and void ratio, e. These curves have been assessed from sand samples tested with "frictionless" ends in CD tests at a confining pressure equal to 42.5 kPa (Norris 1977). Since the confining pressure changes with soil depth, ε_{50}, as obtained from Figure 19, should be modified to match the existing pressure as follows:

$$(\varepsilon_{50})_i = (\varepsilon_{50})_{42.5}\left(\frac{(\bar{\sigma}_{vo})_i}{42.5}\right)^{0.2} \qquad (21)$$

$$(\Delta\sigma_{hf})_i = (\bar{\sigma}_{vo})_i\left[\tan^2\left(45+\frac{\varphi_i}{2}\right)-1\right] \qquad (22)$$

where $\bar{\sigma}_{vo}$ should be in kPa.

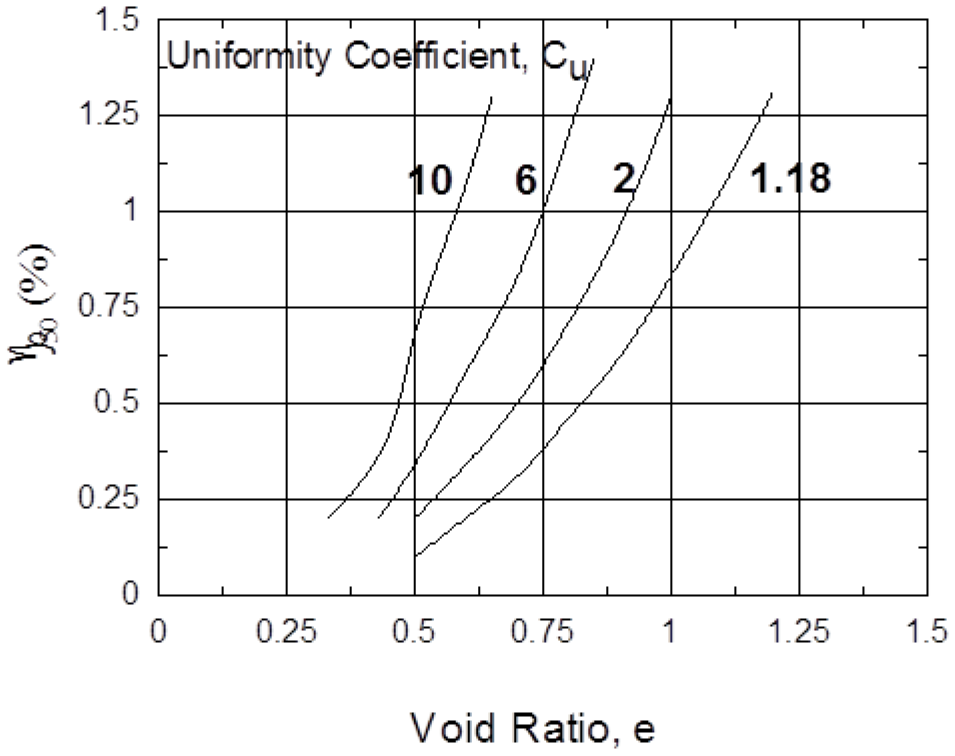

Figure 19: relationship between ε_{50}, uniformity coefficient (C_u) and void ratio (e) after Norris (1986).

The Properties Employed for Clay

- Effective unit weight, $\bar{\gamma}$
- Plasticity index, PI
- Effective angle of friction, $\bar{\varphi}$
- Undrained shear strength, S_u
- Soil strain at 50% stress level, ε_{50}

Plasticity index, PI, and undrained shear strength, S_u, are considered the governing properties while the effective stress angle of internal friction, $\bar{\varphi}$, can be estimated from the PI based on Figure 20. The ε_{50} from an undrained triaxial test (UU at depth x or CU with $\sigma_3 = \bar{\sigma}_{vo}$) can be estimated based on S_u as indicated in Figure 21.

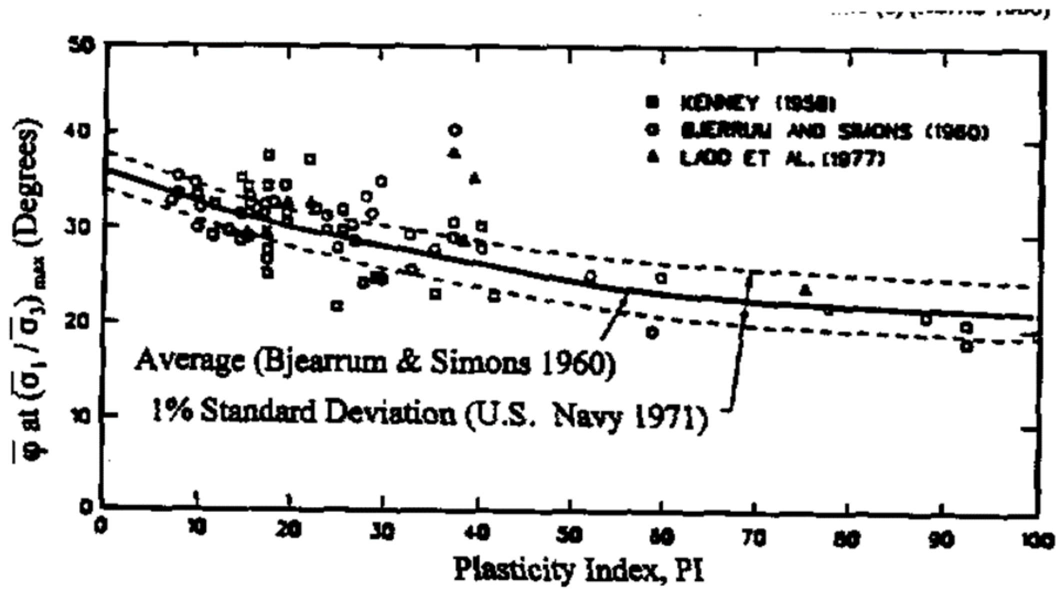

Figure 20: relationship between plasticity index (PI) and effective stress friction angle (φ) after US Army Corps of Engineers (1996).

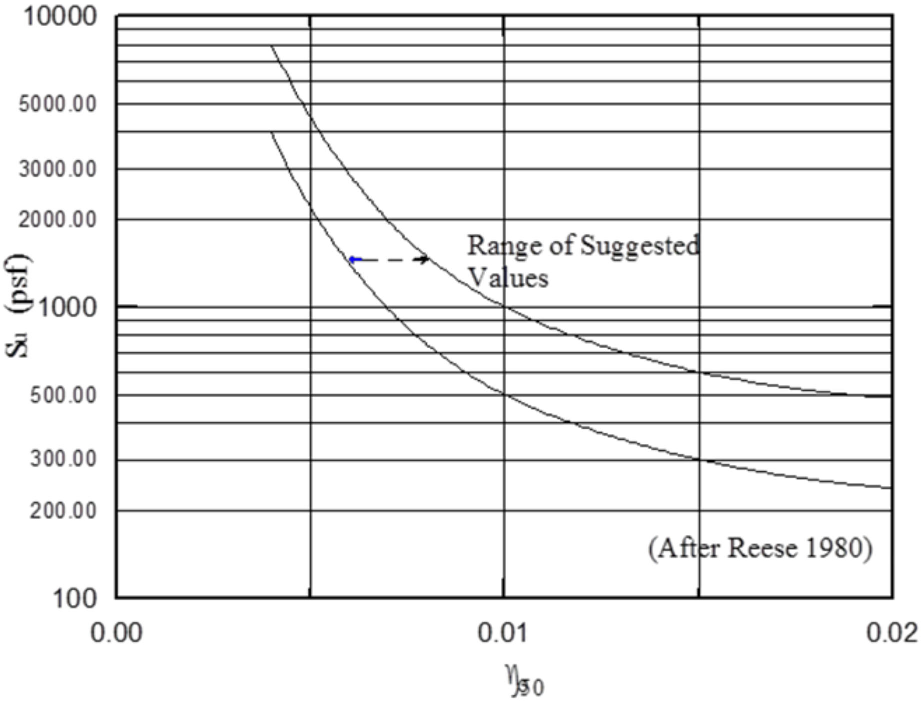

Figure 21: Relationship between ε50 and undrained shear strength, S_u after Reese as given in Evans and Duncan (1982).

An effective stress (ES) analysis is employed with clay soil as well as with sand soil. The reason behind using the ES analysis with clay, which includes the development of excess porewater pressure with undrained loading, is to define the three-dimensional strain wedge geometry based upon the more appropriate effective stress friction angle, $\bar{\varphi}$. The relationship between the normally consolidated clay undrained shear strength, S_u, and $\bar{\sigma}_{vo}$ is taken as

$$S_u = 0.33\,\bar{\sigma}_{vo} \tag{23}$$

assuming that S_u is the equivalent undrained standard triaxial test strength. The effective stress analysis relies upon the evaluation of the developing excess porewater pressure based upon Skempton's equation (1954), i.e.

$$\Delta u = B\left[\Delta\sigma_3 + A_u\left(\Delta\sigma_1 - \Delta\sigma_3\right)\right] \tag{24}$$

where B equals 1 for saturated soil. Accordingly,

$$\Delta u = \Delta\sigma_3 + A_u\left(\Delta\sigma_1 - \Delta\sigma_3\right) \tag{25}$$

Note that $\Delta\sigma_3 = 0$ both in the shear phase of the triaxial test and in the strain wedge. Therefore, the mobilized excess porewater pressure is

$$\Delta u = A_u\,\Delta\sigma_1 \tag{26a}$$

where $\Delta\sigma_1$ represents the deviatoric stress change in the triaxial test and $\Delta\sigma_h$ in the field, i.e.

$$\Delta u = A_u\,\Delta\sigma_h \tag{26b}$$

Therefore, using the previous relationships, the Skempton equation can be rewritten for any sublayer (i) as follows:

$$(\Delta u)_i = (A_u)_i\,SL_i\,(\Delta\sigma_{hf})_i = (A_u)_i\,SL_i\,2\,(S_u)_i \tag{27}$$

The initial value of parameter A_u is 0.333 and occurs at very small strain for elastic soil response. In addition, the value of parameter A_{uf} that occurs at failure in any sublayer (i) is given by the following relationship

$$(A_{uf})_i = \frac{1}{2}\left(1 + \frac{1/(S_u)_i}{(\bar{\sigma}_{vo})_i} - \frac{1}{\sin \bar{\varphi}_i} \right) \tag{28}$$

after Wu (1966) as indicated in Figure 22.

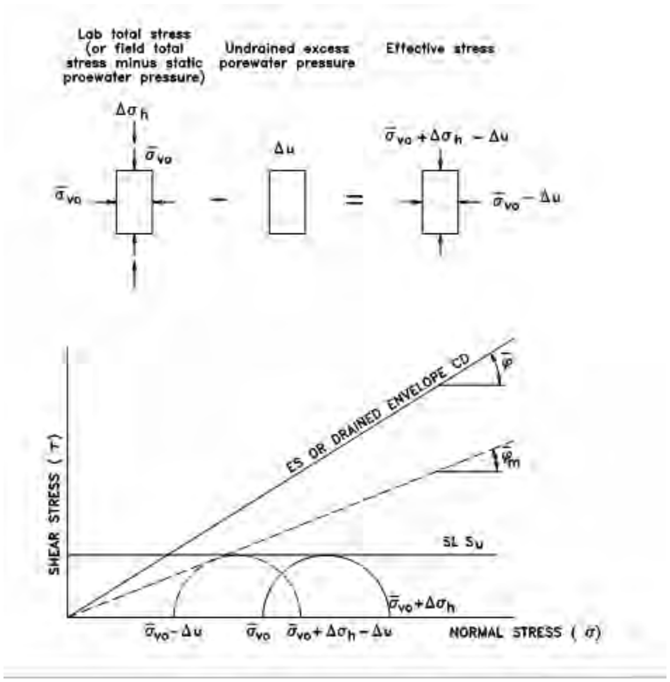
Lab total stress (or field total stress minus static proewater pressure)
Undrained excess porewater pressure
Effective stress
$\Delta\sigma_h$
$\bar{\sigma}_{vo}$
$\bar{\sigma}_{vo}$
Δu
$\bar{\sigma}_{vo} + \Delta\sigma_h - \Delta u$
$\bar{\sigma}_{vo} - \Delta u$
SHEAR STRESS (τ)
ES OR DRAINED ENVELOPE CD
$\bar{\varphi}$
$\bar{\varphi}_m$
SL S_u
$\bar{\sigma}_{vo} + \Delta\sigma_h$
$\bar{\sigma}_{vo} - \Delta u$
$\bar{\sigma}_{vo}$
$\bar{\sigma}_{vo} + \Delta\sigma_h - \Delta u$
NORMAL STRESS (σ)

Figure 22: Relationship between effective stress and total stress conditions.

In Eqn. 29, $\bar{\varphi}$ symbolizes the effective stress angle of internal friction; and, based on Eqn. 23, $S_u/\bar{\sigma}_{vo}$ equals 0.33. However, A_u is taken to change with stress level in a linear fashion as

$$(A_u)_i = 0.333 + SL_i \left[(A_{uf})_i - 0.333 \right] \tag{29}$$

By evaluating the value of A_u, one can effectively calculate the excess porewater pressure, and then can determine the value of the effective horizontal stress, ($\bar{\sigma}_{vo} + \Delta\sigma_h - \Delta u$), and the effective confining pressure, ($\bar{\sigma}_{vo} - \Delta u$) at each sublayer, as shown in Figure 22. Note that the mobilized effective stress friction angle, $\bar{\varphi}_m$, can be obtained from the following relationship.

$$\tan^2\left(45+\frac{(\overline{\varphi}_m)_i}{2}\right)=\frac{\left(\overline{\sigma}_{vo}+\Delta\sigma_h-\Delta u\right)_i}{\left(\overline{\sigma}_{vo}-\Delta u\right)_i} \tag{30}$$

The targeted values of $\overline{\varphi}_{mi}$ and SL_i in a clay sublayer at a particular level of strain (ε) can be obtained by using an iterative solution that includes Eqns.12 through 14, and 27 through 30.

D.7.1 The Properties Employed for Caliche

- Effective unit weight, $\overline{\gamma}$
- Lab shear wave velocity, V_{sl}
- Effective angle of friction, $\overline{\varphi}$
- Undrained shear strength, S_u (=½ unconfined compressive strength, $q_u/2$)
- Caliche strain at 50% stress level, ε_{50}
- Fracture closure strain, $\Delta\varepsilon$

From correlations presented in Chapter 5.

$V_{sl}=0.0878\ \gamma^{2.2842}$;	V_{sl} in ft/sec for ɣ in lb/ft^3	(31)
$q_u=70.074\ e^{0.0005\ V_{sl}}$	q_u in psi for Vs in ft/sec	(32)
$E_{50}=4*10^{-7}V_{sl}^{3.27}$	E_{50} in psi for V_{sl} in ft/sec	(33)

where

$$\varepsilon_{50} = (0.5\ q_u)/E_{50} \tag{34}$$

$$\Delta\sigma_{hf} = 2\ S_u = q_u \tag{35}$$

The mobilized friction angle $\overline{\varphi}_m$ varies with SL as follows,

$$SL = \Delta\sigma_h / \Delta\sigma_{hf} = (\tan \bar{\varphi}_m)/(\tan \bar{\varphi}) \tag{36}$$

Soil-Pile Interaction in The Strain Wedge Model

The strain wedge model relies on calculating the variation in modulus of subgrade reaction, E_s, with depth that reflects the soil-pile interaction at any level of soil strain during pile loading. E_s also represents the secant slope at any point on the p-y curve, i.e.

$$E_s = \frac{p}{y} \tag{37}$$

Note that p represents the force per unit length of the pile or the BEF soil-pile reaction, and y symbolizes the pile deflection at that soil depth. In the SW model, E_s is related to the soil's Young's modulus, E, by two linking parameters, A and ψ_s. It should be mentioned here that the SW model establishes its own E_s from the Young's modulus of the strained soil, and therefore, one can assess the p-y curve using the strain wedge model analysis. Therefore, E_s should first be calculated using the strain wedge model analysis to identify the p and y values.

Corresponding to the horizontal slice (a soil sublayer) of the passive wedge at depth x (see Figure 5 and Figure 7), the horizontal equilibrium of horizontal and shear stresses is expressed as

$$p_i = (\Delta\sigma_h)_i \overline{BC}_i S_1 + 2\tau_i D S_2 \tag{38}$$

where S_1 and S_2 are equal to 0.75 and 0.5, respectively, for a circular pile cross section, and equal to 1.0 each for a square pile (Briaud et al. 1984). Alternatively, one can write the above equation as follows:

$$A_i = \frac{p_i / D}{(\Delta\sigma_h)_i} = \frac{\overline{BC}_i S_1}{D} + \frac{2\tau_i S_2}{(\Delta\sigma_h)_i} \tag{39}$$

where A symbolizes the ratio between the equivalent pile face stress, p/D, and the horizontal stress change, $\Delta\sigma_h$, in the soil. (In essence, it is the multiplier that, when taken times the horizontal stress change, gives the equivalent stress at the face of the pile) From a different perspective, it represents a normalized width (that includes side shear and shape effects) that, when multiplied by $\Delta\sigma_h$ yields p/D. By combining the equations of the passive wedge geometry and the stress level with the above relationship, one finds that

$$A_i = S_1\left(1+\frac{(h-x_i)2(\tan\beta_m\tan\varphi_m)_i}{D}\right)+\frac{2S_2(\bar{\sigma}_{vo})_i(\tan\phi_s)_i}{(\Delta\sigma_h)_i} \qquad in\ sand \qquad (40)$$

$$A_i = S_1\left(1+\frac{(h-x_i)2(\tan\beta_m\tan\bar{\varphi}_m)_i}{D}\right)+\frac{S_2(SL_t)_i}{SL_i} \qquad in\ clay \qquad (41)$$

Here the parameter A is a function of pile and wedge dimensions, applied stresses, and soil properties. However, given that $\Delta\sigma_h = E\varepsilon$ in Eqn. 38,

$$p_i = A_i D(\Delta\sigma_h)_i = A_i D E_i \varepsilon \qquad (42)$$

For the upper passive wedge, ε represents the uniform soil strain and is replaced by ε_x for soil sublayers of the lower passive wedge. The second linking parameter, Ψ_s, relates the soil strain in the SW model to the linearized pile deflection angle, δ. Referring to the normalized pile deflection shape shown in Figure 6 and Figure 8

$$\delta = \frac{\gamma}{2} \qquad (43)$$

$$\frac{\gamma}{2} = \frac{\gamma_{\max}}{2}\sin 2\Theta_m \qquad (44)$$

and

$$\frac{\gamma_{\max}}{2} = \frac{\varepsilon - \varepsilon_v}{2} = \frac{(1+\nu)\varepsilon}{2} \qquad (45)$$

where γ denotes the shear strain in the developing passive wedge. Using Eqns. 44 and 45, Eqn. 43 can be rewritten as

$$\delta = \frac{\varepsilon(1+\nu)\sin 2\Theta_m}{2} \qquad (46)$$

Based on Eqn. 46, the relationship between ε and δ can expressed as

$$\Psi = \frac{\varepsilon}{\delta} \tag{47}$$

or

$$\Psi = \frac{2}{(1+\nu)\sin 2\Theta_m} \tag{48}$$

The parameter ψ varies with the Poisson's ratio of the soil and the soil's mobilized angle of internal friction (φ_m) and the mobilized passive wedge angle (Θ_m).

Poisson's ratio for sand can vary from 0.1 at a very small strain to 0.5 or lager (due to dilatancy) at failure, while the base angle, Θ_m, can vary between 45° (for $\varphi_m = 0$ at $\varepsilon = 0$) and 25° (for, say, $\varphi_m = 40°$ at failure), respectively. For this range in variation for ν and φ_m, the parameter Ψ for sand varies between 1.81 and 1.74 with an average value of 1.77. In clay soil, Poisson's ratio is assumed to be 0.5 (undrained behavior) whereby the value of the passive wedge base angle, Θ_m, varies between 45° (for $\varphi_m = 0$ at $\varepsilon = 0$) and 32.5° (for, say, $\bar{\varphi}_m = 25°$ at failure). Therefore, the value of the parameter ψ will vary from 1.47 to 1.33, with an average value of 1.4.

It is clear from the equations above that employing the multi-sublayer technique greatly influences the values of soil-pile interaction as characterized by the parameter, A_i, which is affected by the changing effective stress and soil strength from one sublayer to another. The final form of the modulus of subgrade reaction can be expressed as

$$(E_s)_i = \frac{p_i}{y_i} = \frac{A_i D \varepsilon E_i}{\delta (h - x_i)} = \frac{A_i}{(h - x_i)} D \Psi E_i \tag{49}$$

It should be mentioned that the SW model develops its own set of non-unique p-y curves which are function of both soil and pile properties, and are affected by soil continuity (layering) as presented by Ashour et al. (1996). For the lower passive wedge, $(h - x_i)$ is be replaced by x_i that is measured downward from the point of zero crossing (Figure 9).

Pile Head Deflection

As mentioned previously, the deflection pattern of the pile in the SW model is continuous and linear. Based on this concept, pile deflection can be assessed using a simplified technique which provides an estimation for the linearized pile deflection, especially y_o at the pile head. By using the multi-sublayer technique, the deflection of the pile can be calculated starting with the base of the mobilized passive wedge and moving upward along the pile, accumulating the deflection values at each sublayer as shown in the following relationships and Figure 23.

$$y_i = H_i \delta_i = H_i \frac{\varepsilon}{\Psi_s} \tag{50}$$

$$y_o = \Sigma y_i \qquad i = 1 \, to \, n \tag{51}$$

where the ψ_s value changes according to the soil type (sand or clay), and H_i indicates the thickness of sublayer i and n symbolizes the current number of sublayers in the mobilized passive wedge.

The main point of interest is the pile head deflection which is a function of not only the soil strain but also of the depth of the compound passive wedge that varies with soil and pile properties and the level of soil strain.

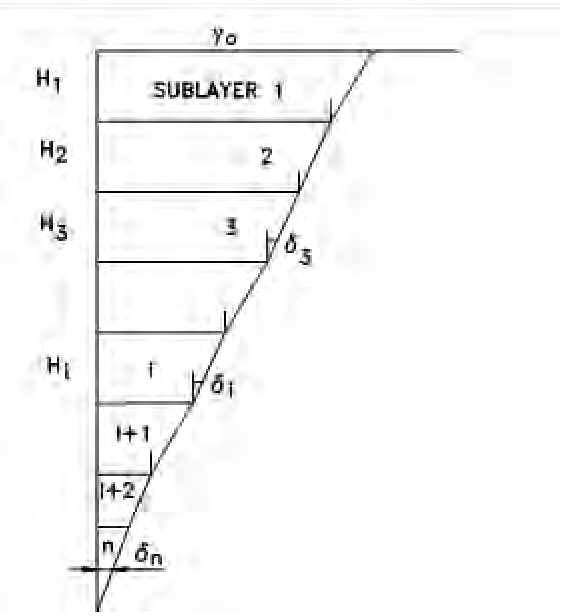

Figure 23: The assembling of pile head deflection using the multi-sublayer technique.

Ultimate Resistance Criteria in Strain Wedge Model

The mobilized passive wedge in front of a laterally loaded pile is limited by certain constraint criteria in the SW model analysis. Those criteria differ from one soil to another and are applied to each sublayer. Ultimate resistance criteria govern the shape and the load capacity of the wedge in any sublayer in SW model analysis. The progressive development of the ultimate resistance with depth is difficult to implement without employing the multi-sublayer technique.

Ultimate Resistance Criterion of Sand Soil

The mobilization of the passive wedge in sand soil depends on the horizontal stress level, SL, and the pile side shear resistance, τ. The side shear stress is a function of the mobilized side shear friction angle, φ_s, as mentioned previously, and reaches its ultimate value ($\varphi_s = \varphi$) earlier than the mobilized friction angle, φ_m, in the wedge (i.e. $SL_t \geq SL$). This causes a decrease in the rate of growth of sand resistance and the fanning of the passive wedge as characterized by the second term in Eqns 38 and 40, respectively.

Once the stress level in the soil of a sublayer of the wedge reaches unity ($SL_i = 1$), the stress change and wedge fan angle in that sublayer cease to grow. However, the width BC of the face of the wedge can continue to increase as long as ε (and, therefore, h in Eqn. 8) increases. Consequently, soil-pile resistance, p, will continue to grow more slowly until a condition of initial soil failure ($SL_i = 1$) develops in that sublayer. At this instance, $p = p_{ult}$ where p_{ult} in sand, given as

$$(p_{ult})_i = (\Delta\sigma_{hf})_i \, \overline{BC}_i \, S_1 + 2\,(\tau_f)_i \, D \, S_2 \qquad (52)$$

p_{ult} is “a temporary” ultimate condition, i.e. the fanning angle of the sublayer is fixed and equal to φ_i, but the depth of the passive wedge and, hence, BC continue to grow. The formulation above reflects that the near-surface “failure” wedge does not stop growing when all such sublayers reach their ultimate resistance at SL = 1 because the value of h at this time is not limited. Additional load applied at the pile head will merely cause the point at zero deflection and, therefore, h to move down the pile. More soil at full strength (SL = 1) will be mobilized to the deepening wedge as BC, therefore, p_{ult} will increase until either flow around failure or a plastic hinge in the pile occurs.

Recognize that flow around failure occurs in any sublayer when it is easier for the sand at that depth to flow around the pile in a local bearing capacity failure than for additional sand to be brought to failure and added to the already developed wedge. However, the value at which flow failure occurs [$A_i = (A_{ult})_i$, $(p_{ult})_i = (\Delta\sigma_{hf})_i (A_{ult})_i D$] in sand is so large that it is not discussed here. Alternatively, a plastic hinge can develop in the pile when the pile material reaches its ultimate resistance at a time when $SL_i \leq 1$ and $A_i < (A_{ult})_i$. In this case, h becomes fixed, and BC_i and $\overline{p}_i$ will be limited when SL_i becomes equal to 1.

Ultimate Resistance Criterion of Clay and Cemented Soils

The situation in clay soil differs from that in sand and is given by Gowda (1991) as a function of the undrained strength $(S_u)_i$ of the clay sublayer.

$$(p_{ult})_i = 10 (S_u)_i D S_1 + 2 (S_u)_i D S_2 \tag{53}$$

Consequently,

$$(A_{ult})_i = \frac{\dfrac{(p_{ult})_i}{D}}{(\Delta\sigma_{hf})_i} = \frac{(p_{ult})_i}{D\, 2 (S_u)_i} = 5 S_1 + S_2 \tag{54}$$

A_{ult} indicates the limited development of the sublayer wedge geometry for eventual development of flow around failure ($SL_i = 1$) and, consequently, the maximum fanning angle in that sublayer becomes fixed, possibly at a value $\varphi_m \leq \overline{\varphi}$. If a plastic hinge develops in the pile at SL_i less than 1, then h will be limited, but BC, and $\overline{p}_i$ will continue to grow until A_i is equal to A_{ult} or p_i is equal to $(p_{ult})_i$.

Vertical Side Shear Resistance

As seen in Figure 24, the vertical side shear stress distribution around the shaft cross section is assumed to follow a cosine function. It is assumed that there is no contact (active pressure) on the backside of the shaft due to the lateral deflection. The peak (q) of side shear stress develops at angle θ = 0 and decreases to zero at angle θ = 90°. The total vertical side shear force (V_v) induced along a unit length of the shaft is expressed as

$$V_v = 2\int_0^{\pi/2} q\,r\,\cos\theta\,d\theta \quad = \quad 2q\,(r\sin\theta)_0^{\pi/2} \quad = \quad D\,q \tag{55}$$

and the induced moment ($M_{x\text{-}x}$) per unit length of the shaft is given as

$$\begin{aligned} M_{x-x} &= 2\int_0^{\pi/2} (q\,r\cos\theta\,d\theta\,)\,(r\cos\theta) \quad = \quad 2q\,r^2\int_0^{\pi/2}\cos^2\theta\,d\theta \\ &= 2q\,r^2\int_0^{\pi/2}\frac{1}{2}\,(\cos 2\theta\;+1)\,d\theta \\ &= q\,r^2\int_0^{\pi/2}(\cos 2\theta\;+1)\,d\theta \\ &= q\,r^2\left(\frac{1}{2}\,(\sin 2\theta\;+\theta\right)_0^{\pi/2} \quad = \frac{q\,D^2\,\pi}{8} \end{aligned} \tag{56}$$

$M_{x\text{-}x}$ represents the term M_R in Eqn. 1.

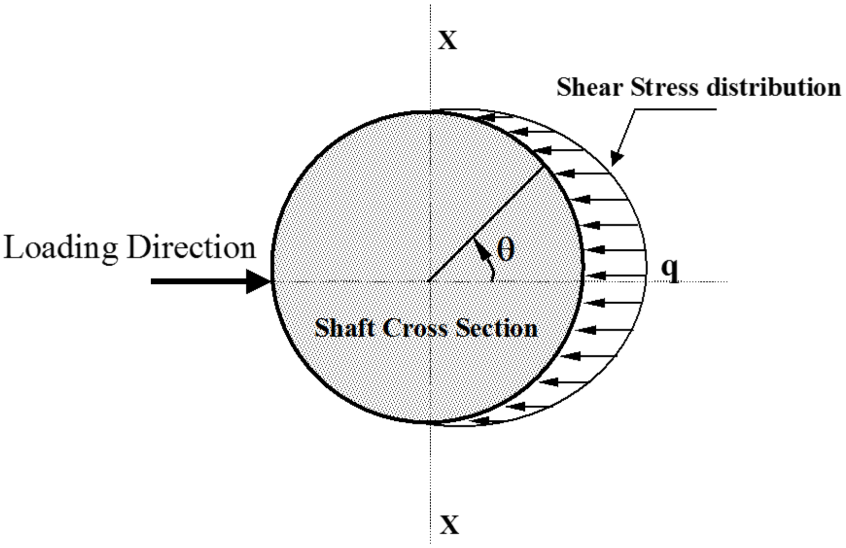

Figure 24: Vertical side shear stress distribution on the shaft cross section.

Vertical Displacement of Shaft Sections Under Lateral Deflection

Figure 25 portrays the change in elevation of a point on the shaft surface (i.e., the cross section) due to shaft rotation and bending deformation. The vertical displacement component (v) of shaft segment i is governed by the rotation of the shaft (i.e., v_d) and the bending deformation (i.e., v_b) of that particular segment. Therefore,

$$v_i = (v_d + v_b)_i \tag{57}$$

In this situation, v is mainly dominated by the shaft vertical displacement component (v_d) that decreases as it approaches the pivot point (i.e., the zero deflection point), as is shown in Figure 25 and expressed as

$$(v_d)_i = y_i \alpha_i \tag{58}$$

where i is the number of the shaft segment and α is the rotation angle of shaft segment i. However, the bending deformation of the shaft segment could add a much smaller value of vertical displacement (v_b) to the total amount of vertical displacement (v) on the passive side of the shaft. In addition, v_b induced by the flexural deformation (i.e., the cross section curvature, η) diminishes approaching the location of the neutral axis of the section (Figure 25).

$$(v_b)_i = L_1 \, \eta \tag{59}$$

It should be mentioned that the term *z* represents the shaft vertical displacement under "axial load" which is directly related to the *t-z* curve. Therefore, the term *v* is used to differentiate between the shaft vertical displacement (*z*) caused by the axial load and the shaft vertical displacement component (*v*) generated by shaft deflection under lateral load. Practically, the shaft surface could be subjected to two components of vertical displacement (*z* and *v*) when axial and lateral loads are applied at the pile/shaft head, which is a common case.

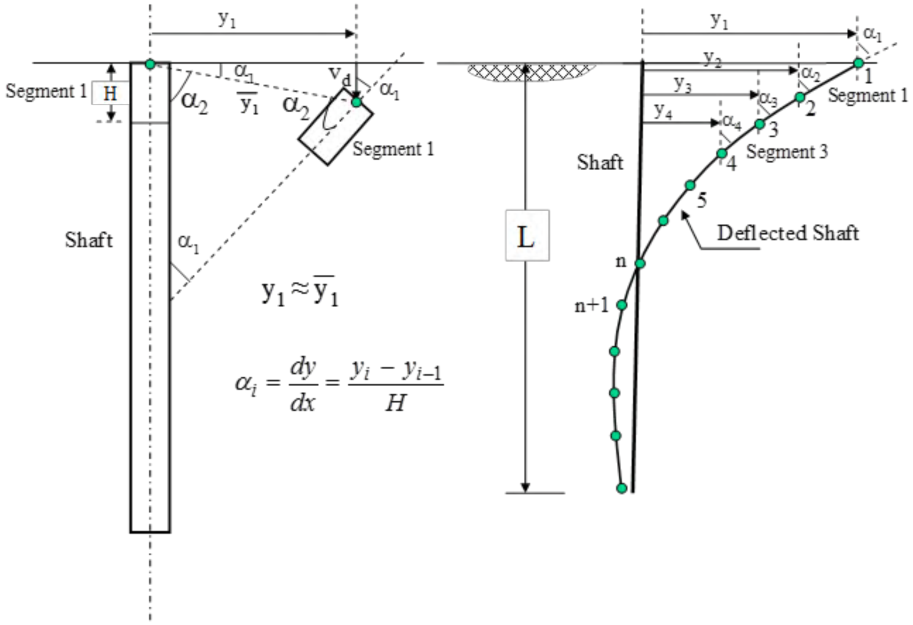
y1
Segment 1
H
α1
α2
ȳ1
α2
vd
α1
Segment 1
Shaft
α1
y1≈ȳ1
αi = dy/dx = (yi − yi−1)/H
y1
α1
y2
α2
1
y3
α3
2
Segment 1
y4
α4
3
Segment 3
4
Shaft
5
L
Deflected Shaft
n
n+1

Figure 25: The development of the vertical shear displacement component (v_d) with shaft deflection.

Vertical Side Shear (τv) in Stiff Clay and Cemented Soils (aka caliche)

The vertical side shear stress (τ_v) develops at the soil-pile interface as a result of the vertical displacement *v*. τ_v is assessed as a function of q_u and ε_{50} of clay, intermediate geo-materials and cemented soils. For a given vertical displacement *v*, the mobilized shear stress (τ_v) at the shaft-soil interface can be expressed as a function of the ultimate shear strength (τ_{ult}) via the shear stress level $SL_t = \dfrac{\tau_v}{\tau_{ult}}$ which is characterized by the Ramberg-Osgood model (Richart 1975), i.e.

$$\frac{v}{v_r} = \frac{\gamma}{\gamma_r} = \frac{\tau_v}{\tau_{ult}} \left[1 + \beta \left(\frac{\tau_v}{\tau_{ult}} \right)^{R-1} \right] = SL_t \; \left[1 + \beta \left(SL_t \right)^{R-1} \right] \tag{60}$$

where *v* is the vertical displacement of the shaft segment. γ and τ_v are the average shear strain and stress in the soil adjacent to the shaft segment generated by the soil-shaft displacement *v*. The reference strain (γ_r) is determined as

$$\gamma_r = \frac{S_u}{G_i} = \frac{\tau_{ult}}{G_i} \qquad (61)$$

G_i is the initial shear modulus at a very low stress/strain, and v_r is the shaft segment movement associated with γ_r (Figure 26).β and *R-1* are the fitting parameters of the Ramberg-Osgood model. At $\tau/\tau_{ult} = SL_t = 1$, β can be expressed as

$$\beta = \frac{\gamma_f}{\gamma_r} - 1 \qquad (62)$$

At $\tau/\tau_{ult} = 0.5$ and $\gamma = \gamma_{50}$, *R-1* is obtained as follows:

$$R-1 = \frac{\log\left(\dfrac{2\dfrac{\gamma_{50}}{\gamma_r}-1}{\beta}\right)}{\log\ (0.5)} = \frac{\log\left(\dfrac{2\dfrac{\gamma_{50}}{\gamma_r}-1}{\dfrac{\gamma_f}{\gamma_r}-1}\right)}{\log\ (0.5)} \qquad (63)$$

To determine β and *R-1*, the normal stress-strain relationship for clay (σ - ε) presented by Ashour et al. (2010), based on ε_{50} and S_u, is employed to find γ_r, γ_{50}, and γ_f of Figure 7.23. For a given shaft, one finds that

$$\frac{v_{50}}{v_f} = \frac{\gamma_{50}}{\gamma_f} \qquad (64)$$

where v_{50} and γ_{50} are the pile/shaft vertical displacement and associated shear strain in soil at $SL_t = 0.5$ (i.e. $\tau_v = 0.5\,\tau_{ult}$), respectively. v_f and γ_f are the shaft displacement and associated shear strain at failure where $SL_t = 1.0$ (i.e. $\tau = \tau_{ult}$). Therefore, the variation in the soil shear strain (γ) occurs in concert with the variation in shaft vertical displacement. The shear strain at failure (γ_f) is determined in terms of the normal strain at failure (ε_f) as given in Eq. 60. ε_f is evaluated at $SL = 1$ or at normal strength, σ_f, where $\sigma_f = q_u = 2\ S_u$. Accordingly,

$$\gamma_f = \frac{\varepsilon_f}{(1+\nu)} = \frac{\varepsilon_f}{1.5} \qquad \text{(at failure)} \qquad (66)$$

At $SL_t = 0.5$

$$\gamma_{50} = \frac{0.5\, S_u}{G_{50}} \tag{67}$$

The initial shear modulus (G_i) at a very low SL_t and the shear modulus at $SL_t = 0.5$ (i.e. G_{50}) can be determined via their direct relationship with the normal stress-strain relationship and Poisson's ratio (ν). While $\nu = 0.5$ for clay under undrained conditions, ν varies linearly with SL, i.e.

$$\nu = 0.1 + 0.4\, SL_t \tag{68}$$

for weak rock and caliche. Hence,

$$\mathrm{G_i} = \frac{E_i}{2\,(1+\nu)} \quad = E_i \,/\, 2.2 \tag{69}$$

and

$$\mathrm{G_{50}} = \frac{E_{50}}{2\,(1+\nu)} \quad = E_{50} \,/\, 2.6 \tag{69}$$

where $\mathrm{E_i}$ and $\mathrm{E_{50}}$ of caliche are equal to $4*10^{-7} V_{sl}^{3.27}$ and $\mathrm{S_u}/\varepsilon_{50}$, respectively. E_i is the initial Young's modulus of clay at a very small value of the normal strain (ε) or SL. Evans and Duncan (1982) provide ε_{50} for clay (Figure 21) after Reese. Ashour and Helal (2014) provide the detailed calculations of the Ramberg–Osgood (*R–O*) model fitting parameters β and $R\text{-}1$ which are equal to 18.14 and 2.92, respectively, for caliche.

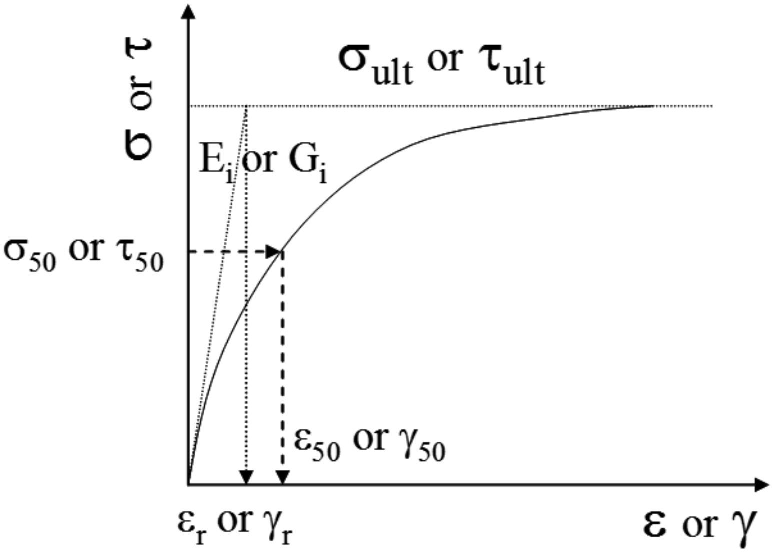

Figure 26: Normal and shear stress–strain relationship (σ-ε and τ-γ).

Stability Analysis in The Strain Wedge Model

The objective of the SW model is to establish the soil response as well as model the soil-pile interaction through the modulus of subgrade reaction, E_s. The shape and the dimensions of the passive wedge in front of the pile basically depend on two types of stability which are the local stability of the soil sublayer and the global stability of the pile and the passive wedge. However, the global stability of the passive wedge depends, in turn, on the local stability of the soil sublayers.

Local Stability of a Soil Sublayer in the Strain Wedge Model

Local stability in strain wedge model requires equilibrium and compatibility of the pile segment deflection, soil strain, and soil resistance for the soil sublayer under consideration. Such analysis allows the correct development of the actual horizontal stress change, $\Delta\sigma_h$, pile side shear stress, τ, and soil-pile reaction, p, associated with that soil sublayer (see Figure 5 and Figure 7). It is fundamental that key parameters for local stability analysis are soil strain, soil properties, and pile properties.

Global Stability in the Strain Wedge Model

Global stability, as analyzed by the strain wedge model, requires the general compatibility among soil reaction, pile deformations, and pile stiffness along the entire depth of the developing passive wedge in front of the pile. Therefore, the depth of the passive wedge depends on the global equilibrium between the loaded pile and the developed passive wedge. This requires a solution for Equation. 1.

Global stability is an iterative beam on elastic foundation (BEF) calculation that determines the correct dimensions of the passive wedge, the corresponding straining actions (deflection, slope, moment, and shear) in the pile, and the external loads on the pile. Satisfying global stability conditions is the purpose for linking the three-dimensional strain wedge model to the BEF approach. The major parameters in the global pile stability problem are pile stiffness, EI, and the modulus of subgrade reaction profile, E_s, as determined from local stability in the strain wedge analysis. Since these parameters are determined for the applied soil strain, the stability problem is no longer a soil interaction problem but a one-dimensional BEF problem. Any available numerical technique, such as the finite element or the finite difference method, can be employed to solve the global stability problem. The modeled problem, shown in Figure 11c, is a BEF and can be solved to identify the depth, X_o, of zero pile deflection.

Summary

The SW model approach presented here provides an effective method for solving the problem of a laterally loaded pile/shaft in layered soil. This approach assesses its own nonlinear variation in modulus of subgrade reaction or p-y curves. The SW model allows the assessment of the nonlinear p-y curve response of a laterally loaded pile based on the envisioned relationship between the three-dimensional response of a flexible pile in the soil to its one-dimensional beam on elastic foundation parameters. In addition, the SW model employs stress-strain-strength behavior of the soil as established from the triaxial test in an effective stress analysis to evaluate mobilized soil behavior.

The SW model accounts for the vertical side shear resistance that develops effectively with large diameter shafts. Such resistance enhances the performance of large diameter shafts and increases with progressive lateral deflection. The evaluation of the vertical side shear resistance is based on the assessed t-z curve and affects the shape of the predicted p-y curve.

Compared to empirically based approaches, which rely upon a limited number of field tests, the SW approach depends on well-known or accepted principles of soil mechanics (the stress-strain-strength relationship) in conjunction with effective stress analysis. Moreover, the required parameters to solve the problem of the laterally loaded pile are a function of basic soil properties that are typically available to the designer.

Appendix F

Material of the Hands-on Training

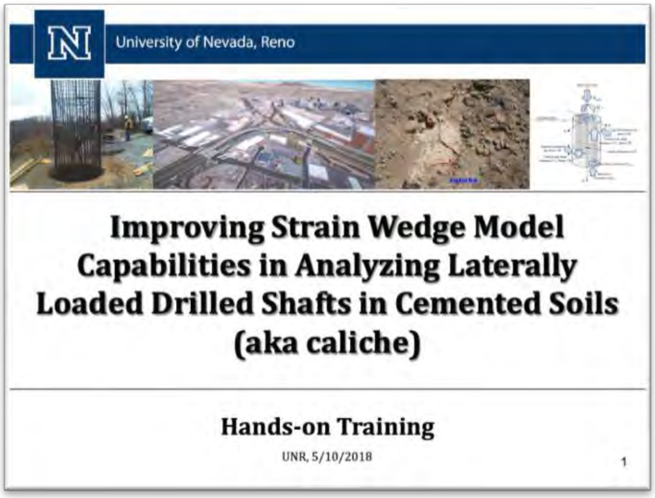

University of Nevada, Reno

Improving Strain Wedge Model Capabilities in Analyzing Laterally Loaded Drilled Shafts in Cemented Soils (aka caliche)

Hands-on Training

UNR, 5/10/2018

Project Team

- Sherif Elfass, PI
- Robert "Bob" Watters, Co-PI
- Mohamed Ashour, Consultant
- Gary Norris, Consultant **
- Evan Saint-Pierre, Graduate Assistant

** Not supported on the project

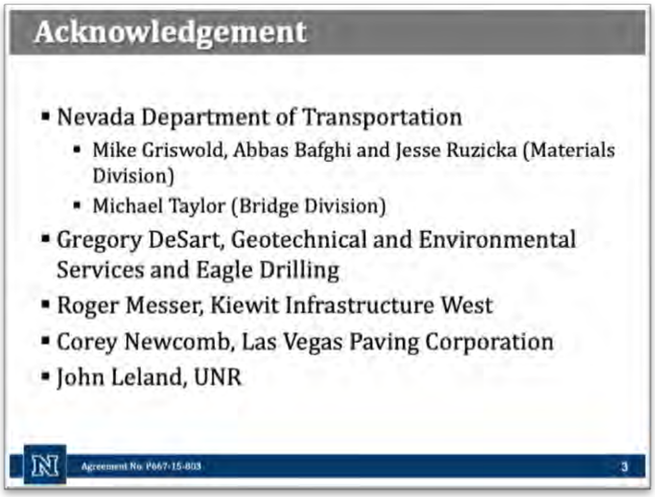

Acknowledgement

- Nevada Department of Transportation
  - Mike Griswold, Abbas Bafghi and Jesse Ruzicka (Materials Division)
  - Michael Taylor (Bridge Division)
- Gregory DeSart, Geotechnical and Environmental Services and Eagle Drilling
- Roger Messer, Kiewit Infrastructure West
- Corey Newcomb, Las Vegas Paving Corporation
- John Leland, UNR

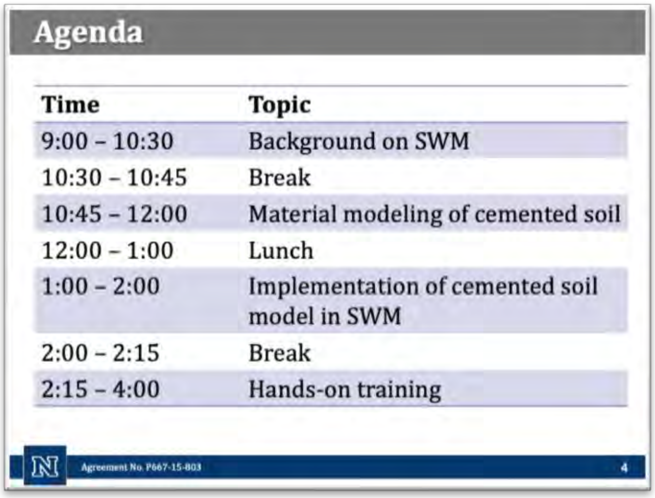

Agenda

Time	Topic
9:00 – 10:30	Background on SWM
10:30 – 10:45	Break
10:45 – 12:00	Material modeling of cemented soil
12:00 – 1:00	Lunch
1:00 – 2:00	Implementation of cemented soil model in SWM
2:00 – 2:15	Break
2:15 – 4:00	Hands-on training

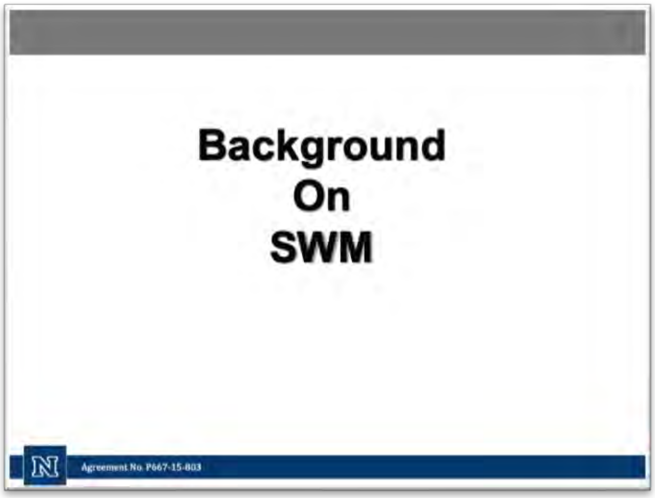

Background
On
SWM

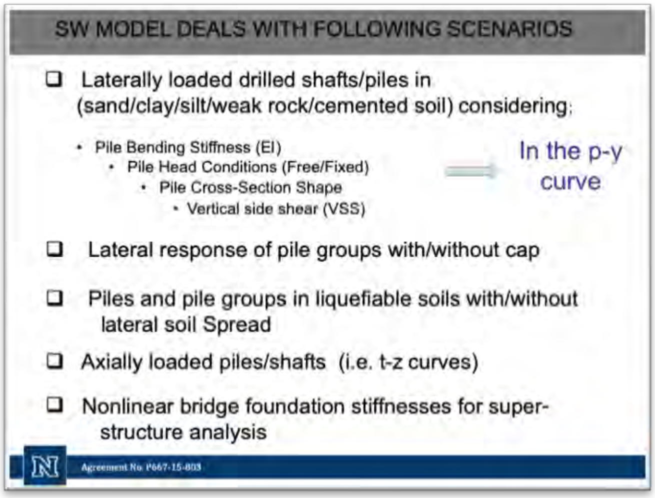

SW MODEL DEALS WITH FOLLOWING SCENARIOS

- ☐ Laterally loaded drilled shafts/piles in (sand/clay/silt/weak rock/cemented soil) considering:
  - Pile Bending Stiffness (EI)
    - Pile Head Conditions (Free/Fixed)
      - Pile Cross-Section Shape
        - Vertical side shear (VSS)

→ In the p-y curve

- ☐ Lateral response of pile groups with/without cap
- ☐ Piles and pile groups in liquefiable soils with/without lateral soil Spread
- ☐ Axially loaded piles/shafts (i.e. t-z curves)
- ☐ Nonlinear bridge foundation stiffnesses for super-structure analysis

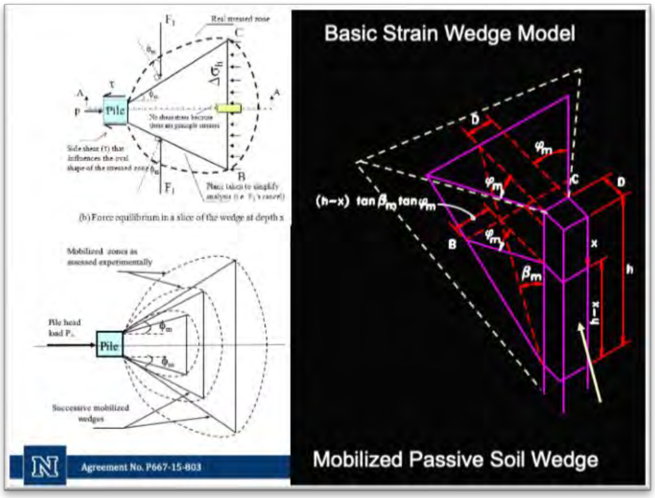

Basic Strain Wedge Model

F1
Real stressed zone
C
φm
Δσh
τ
A
p
Pile
No shear stress because these are principle stresses
A
Side shear (τ) that influences the oval shape of the stressed zone
φm
F1
B
Plane taken to simplify analysis (i.e. F1's cancel)
(b) Force equilibrium in a slice of the wedge at depth x
Mobilized zones as assessed experimentally
Pile head load Po
Pile
φm
φm
Successive mobilized wedges
D
φm
φm
(h−x) tan βm tan φm
C
D
φm
B
x
h
βm
h−x

Mobilized Passive Soil Wedge

Agreement No. P667-15-803

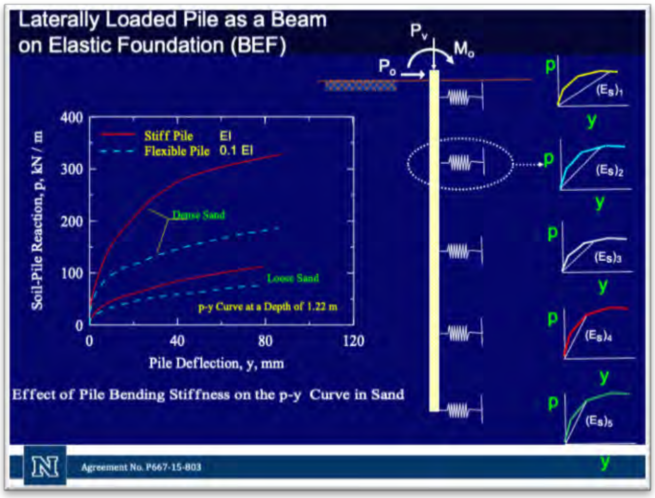

Laterally Loaded Pile as a Beam on Elastic Foundation (BEF)

Effect of Pile Bending Stiffness on the p-y Curve in Sand

Agreement No. P667-15-803

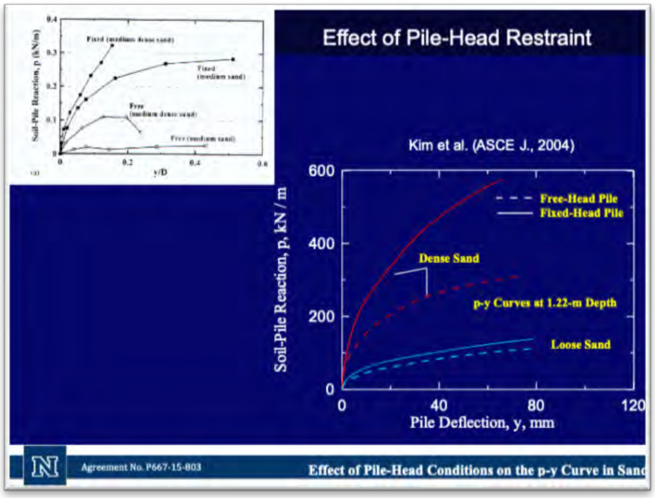

Effect of Pile-Head Restraint

Agreement No. P667-15-803

Effect of Pile-Head Conditions on the p-y Curve in Sand

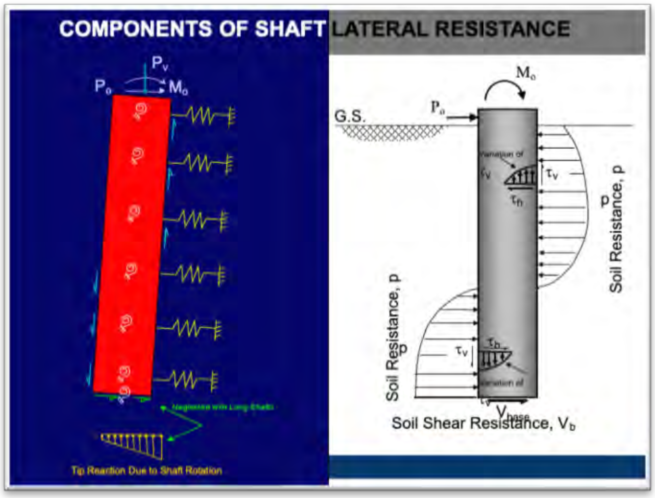

COMPONENTS OF SHAFT LATERAL RESISTANCE

P_v
P_o
M_o
Negligible with Long Shafts
Tip Reaction Due to Shaft Rotation
M_o
G.S.
P_o
Variation of τ_v
τ_v
τ_h
p
Soil Resistance, p
Soil Resistance, p
τ_h
τ_v
Variation of τ_v
V_{base}
Soil Shear Resistance, V_b

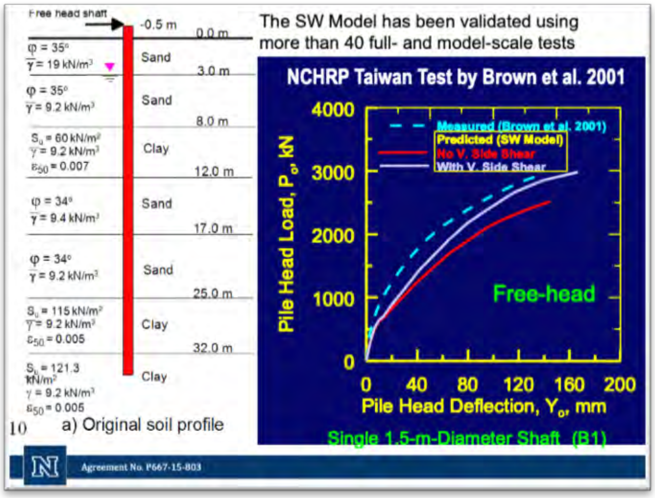

The SW Model has been validated using more than 40 full- and model-scale tests

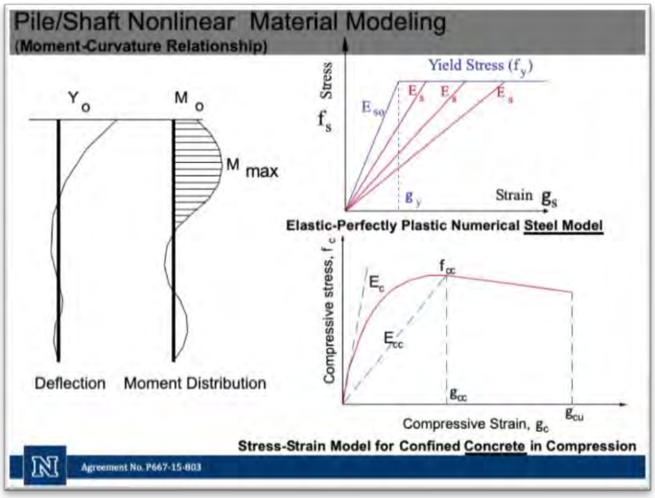

Pile/Shaft Nonlinear Material Modeling

(Moment-Curvature Relationship)

Y_o
M_o
M_{max}
Deflection
Moment Distribution
Stress f_s
Yield Stress (f_y)
E_{so}
E_s
E_s
E_s
ε_y
Strain ε_s
Elastic-Perfectly Plastic Numerical Steel Model
Compressive stress, f_c
f_{cc}
E_c
E_{cc}
ε_{cc}
ε_{cu}
Compressive Strain, ε_c
Stress-Strain Model for Confined Concrete in Compression
Agreement No. P667-15-803

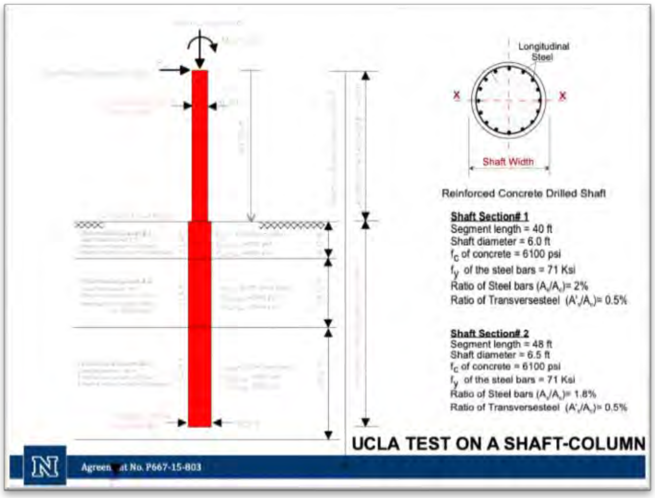

Reinforced Concrete Drilled Shaft

Shaft Section# 1
Segment length = 40 ft
Shaft diameter = 6.0 ft
f_c of concrete = 6100 psi
f_y of the steel bars = 71 Ksi
Ratio of Steel bars (A_s/A_g)= 2%
Ratio of Transversesteel (A'_s/A_g)= 0.5%

Shaft Section# 2
Segment length = 48 ft
Shaft diameter = 6.5 ft
f_c of concrete = 6100 psi
f_y of the steel bars = 71 Ksi
Ratio of Steel bars (A_s/A_g)= 1.8%
Ratio of Transversesteel (A'_s/A_g)= 0.5%

UCLA TEST ON A SHAFT-COLUMN

Agreement No. P667-15-803

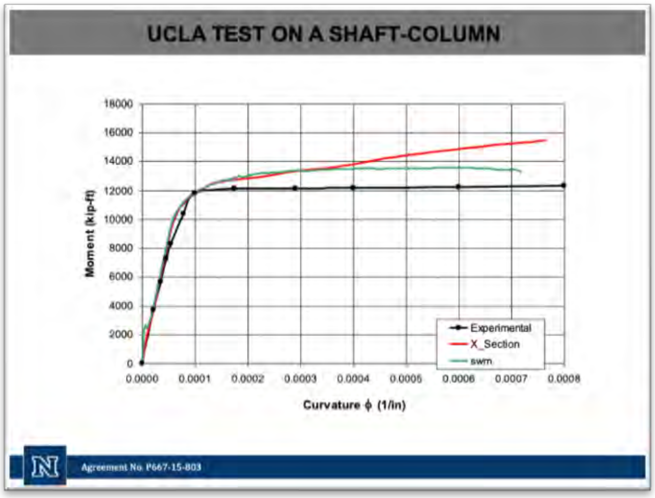

UCLA TEST ON A SHAFT-COLUMN

Agreement No. P667-15-803

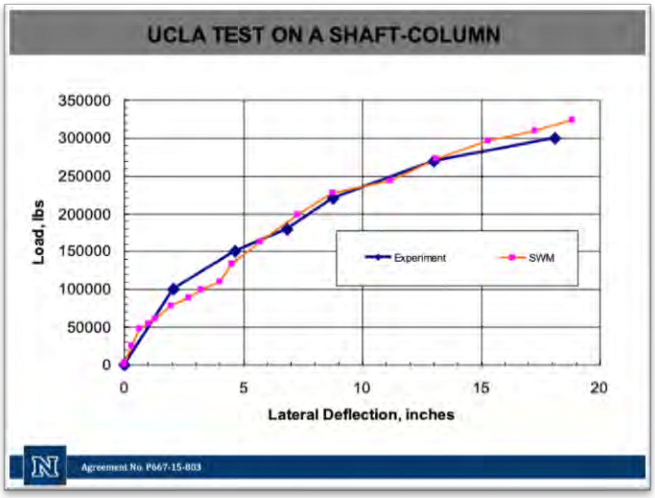

UCLA TEST ON A SHAFT-COLUMN

Agreement No. P667-15-803

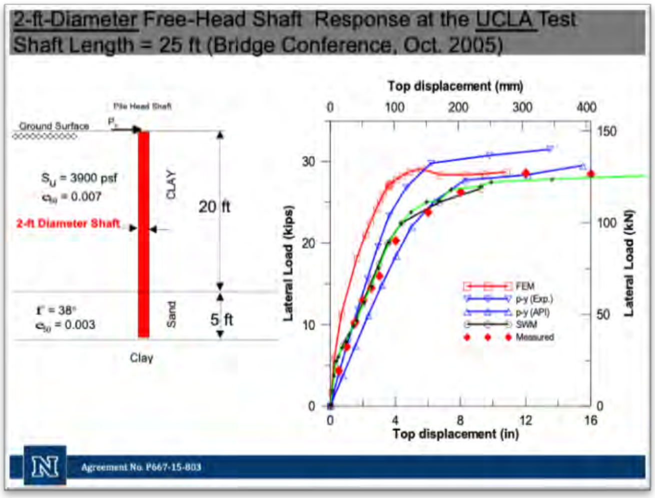

2-ft-Diameter Free-Head Shaft Response at the UCLA Test Shaft Length = 25 ft (Bridge Conference, Oct. 2005)

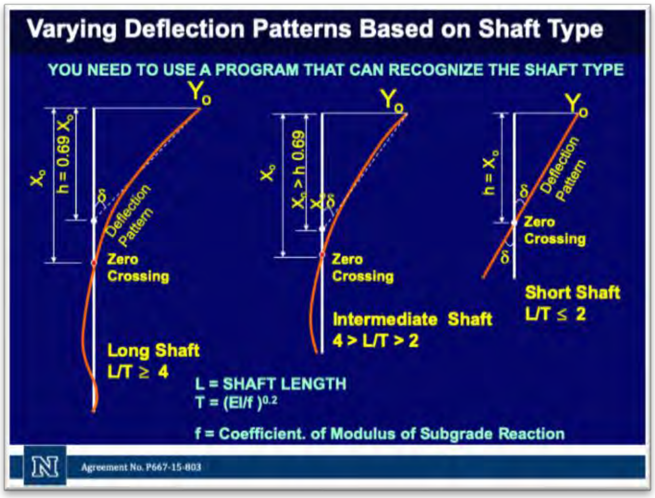

Varying Deflection Patterns Based on Shaft Type

YOU NEED TO USE A PROGRAM THAT CAN RECOGNIZE THE SHAFT TYPE

Y_o
X_o
$h = 0.69\ X_o$
δ
Deflection Pattern
Zero Crossing
Long Shaft
$L/T \geq 4$
Y_o
X_o
$X_o > h\ 0.69\ X_o$
δ
Zero Crossing
Intermediate Shaft
$4 > L/T > 2$
Y_o
$h = X_o$
δ
Deflection Pattern
Zero Crossing
δ
Short Shaft
$L/T \leq 2$
Agreement No. P667-15-803

L = SHAFT LENGTH

$T = (EI/f)^{0.2}$

f = Coefficient. of Modulus of Subgrade Reaction

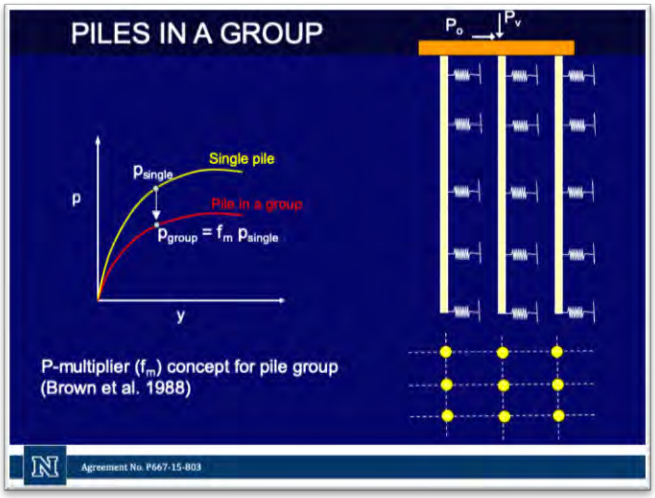

PILES IN A GROUP

P_o
P_v
p
y
p_{single}
Single pile
Pile in a group
$p_{group} = f_m\ p_{single}$
Agreement No. P667-15-803

P-multiplier (f_m) concept for pile group (Brown et al. 1988)

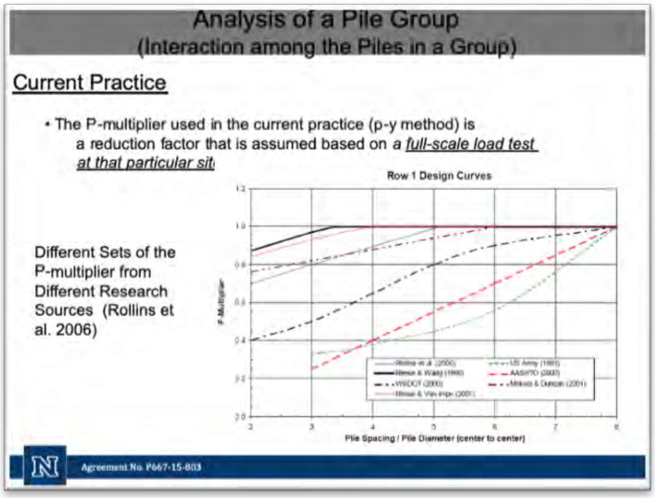

Analysis of a Pile Group
(Interaction among the Piles in a Group)

Current Practice

- The P-multiplier used in the current practice (p-y method) is a reduction factor that is assumed based on *a full-scale load test at that particular sit*

Different Sets of the P-multiplier from Different Research Sources (Rollins et al. 2006)

Agreement No. P667-15-803

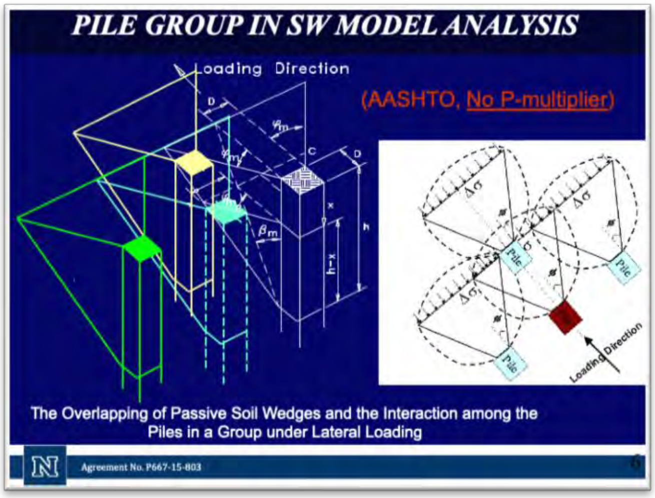

PILE GROUP IN SW MODEL ANALYSIS

(AASHTO, No P-multiplier)

Loading Direction
D
φm
C
D
βm
x
h
h-x
Δσ
Δσ
Δσ
Pile
Pile
Pile
Loading Direction

The Overlapping of Passive Soil Wedges and the Interaction among the Piles in a Group under Lateral Loading

Agreement No. P667-15-803

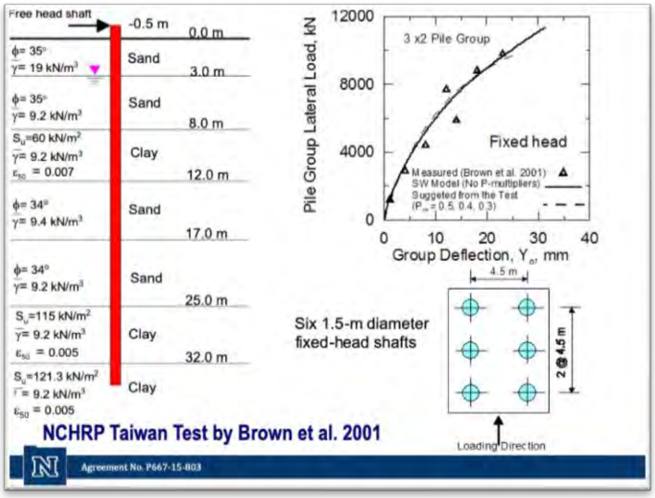

Six 1.5-m diameter fixed-head shafts

NCHRP Taiwan Test by Brown et al. 2001

Agreement No. P667-15-803

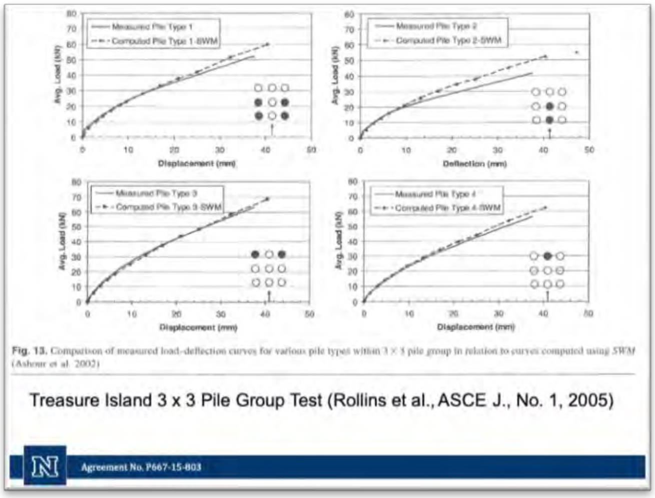

Fig. 13. Comparison of measured load-deflection curves for various pile types within 3 × 3 pile group in relation to curves computed using SWM (Ashour et al. 2002)

Treasure Island 3 x 3 Pile Group Test (Rollins et al., ASCE J., No. 1, 2005)

Agreement No. P667-15-803

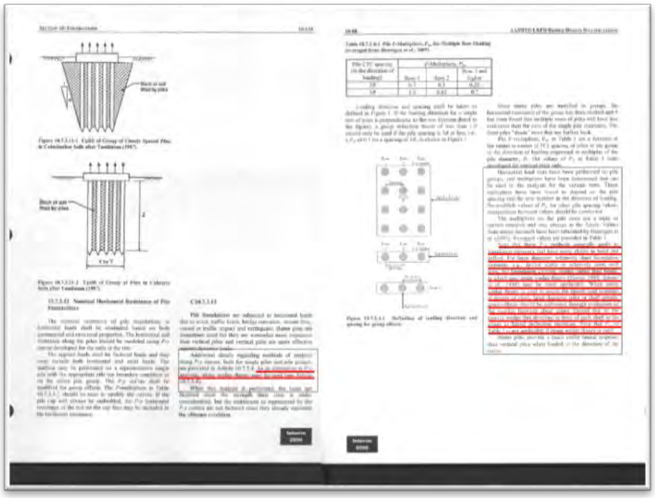

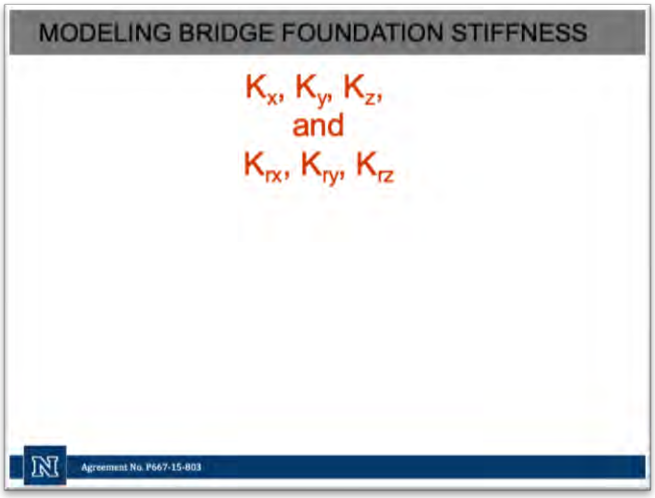

MODELING BRIDGE FOUNDATION STIFFNESS

K_x, K_y, K_z,

and

K_{rx}, K_{ry}, K_{rz}

Agreement No. P667-15-803

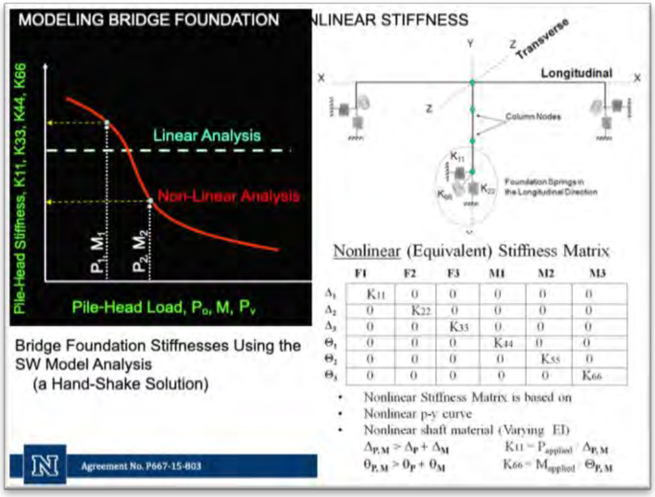

MODELING BRIDGE FOUNDATION NLINEAR STIFFNESS

Pile-Head Stiffness, K11, K33, K44, K66
Linear Analysis
Non-Linear Analysis
P1, M1
P2, M2
Pile-Head Load, Po, M, Pv
Y
Z
Transverse
Longitudinal
X
X
Z
Column Nodes
K11
K66
K22
Foundation Springs in the Longitudinal Direction

Bridge Foundation Stiffnesses Using the SW Model Analysis
(a Hand-Shake Solution)

Nonlinear (Equivalent) Stiffness Matrix

	F1	F2	F3	M1	M2	M3
Δ_1	K11	0	0	0	0	0
Δ_2	0	K22	0	0	0	0
Δ_3	0	0	K33	0	0	0
Θ_1	0	0	0	K44	0	0
Θ_2	0	0	0	0	K55	0
Θ_3	0	0	0	0	0	K66

- Nonlinear Stiffness Matrix is based on
- Nonlinear p-y curve
- Nonlinear shaft material (Varying EI)

$\Delta_{P,M} > \Delta_P + \Delta_M$ $K11 = P_{applied} / \Delta_{P,M}$

$\theta_{P,M} > \theta_P + \theta_M$ $K66 = M_{applied} / \Theta_{P,M}$

Agreement No. P667-15-803

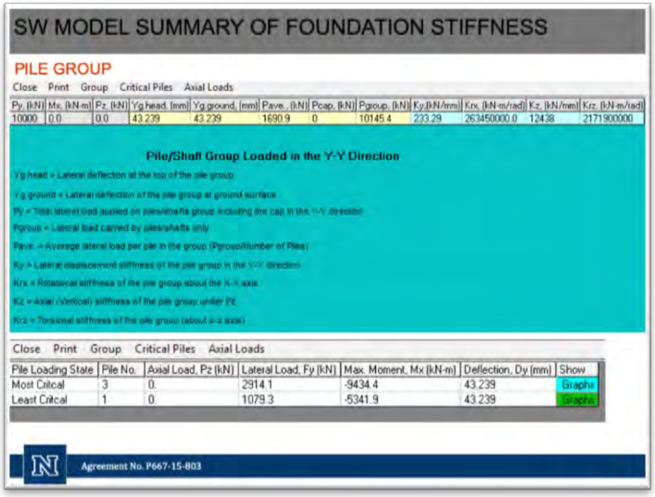

SW MODEL SUMMARY OF FOUNDATION STIFFNESS

PILE GROUP

Close Print Group Critical Piles Axial Loads

Py, (kN)	Mx, (kN-m)	Pz, (kN)	Yg head, (mm)	Yg ground, (mm)	Pave., (kN)	Pcap, (kN)	Pgroup, (kN)	Ky,(kN/mm)	Krx, (kN-m/rad)	Kz, (kN/mm)	Krz, (kN-m/rad)
10000	0.0	0.0	43.239	43.239	1690.9	0	10145.4	233.29	263450000.0	12438	2171900000

Pile/Shaft Group Loaded in the Y-Y Direction

Yg head = Lateral deflection at the top of the pile group

Yg ground = Lateral deflection of the pile group at ground surface

Py = Total lateral load applied on piles/shafts group including the cap in the Y-Y direction

Pgroup = Lateral load carried by piles/shafts only

Pave. = Average lateral load per pile in the group (Pgroup/Number of Piles)

Ky = Lateral displacement stiffness of the pile group in the Y-Y direction

Krx = Rotational stiffness of the pile group about the X-X axis

Kz = Axial (Vertical) stiffness of the pile group under Pz

Krz = Torsional stiffness of the pile group (about z-z axis)

Close Print Group Critical Piles Axial Loads

Pile Loading State	Pile No.	Axial Load, Pz (kN)	Lateral Load, Fy (kN)	Max. Moment, Mx (kN-m)	Deflection, Dy (mm)	Show
Most Critcal	3	0.	2914.1	-9434.4	43.239	Graphs
Least Critcal	1	0.	1079.3	-5341.9	43.239	Graphs

Agreement No. P667-15-803

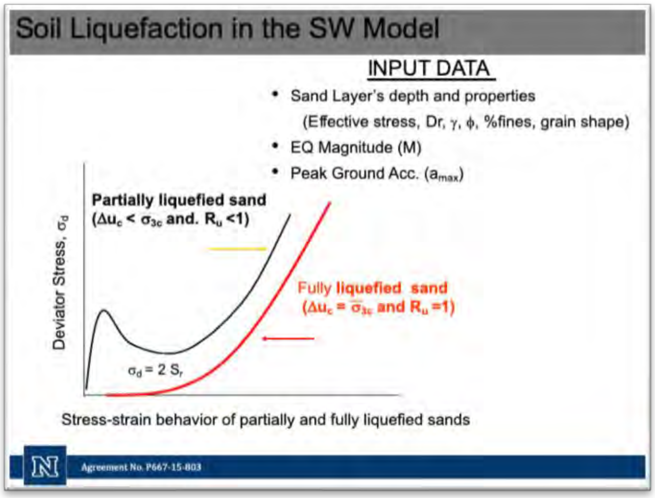

Soil Liquefaction in the SW Model

INPUT DATA

- Sand Layer's depth and properties
  (Effective stress, Dr, γ, ϕ, %fines, grain shape)
- EQ Magnitude (M)
- Peak Ground Acc. (a_{max})

Stress-strain behavior of partially and fully liquefied sands

Agreement No. P667-15-803

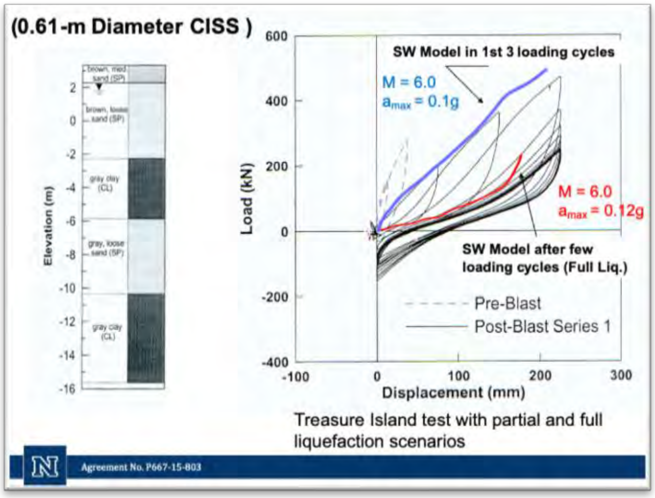

(0.61-m Diameter CISS)

Treasure Island test with partial and full liquefaction scenarios

Agreement No. P667-15-803

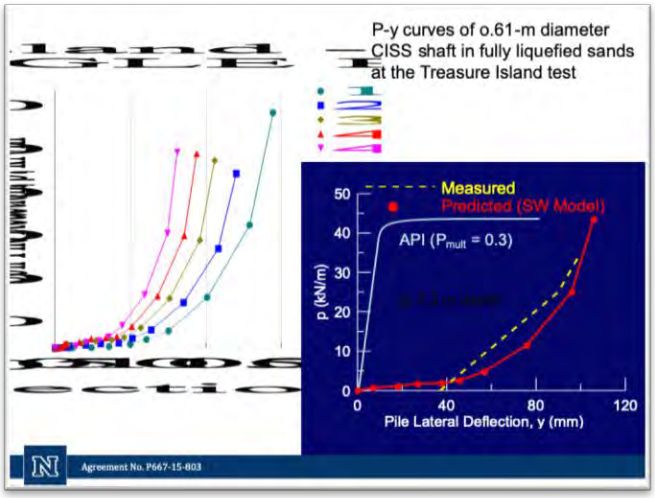

P-y curves of o.61-m diameter CISS shaft in fully liquefied sands at the Treasure Island test

Agreement No. P667-15-803

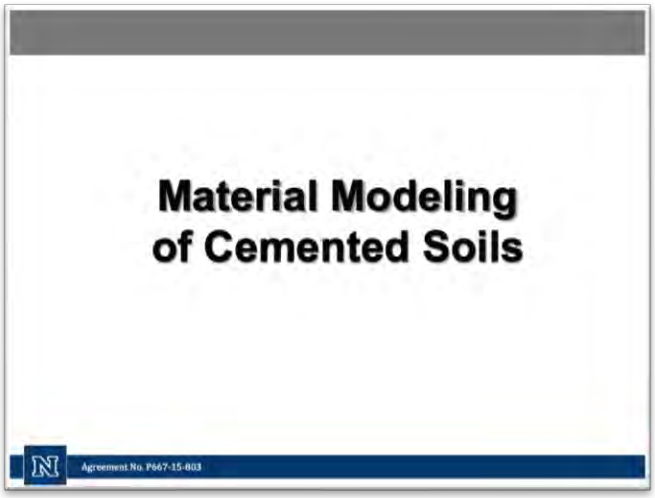

Material Modeling of Cemented Soils

Agreement No. P667-15-803

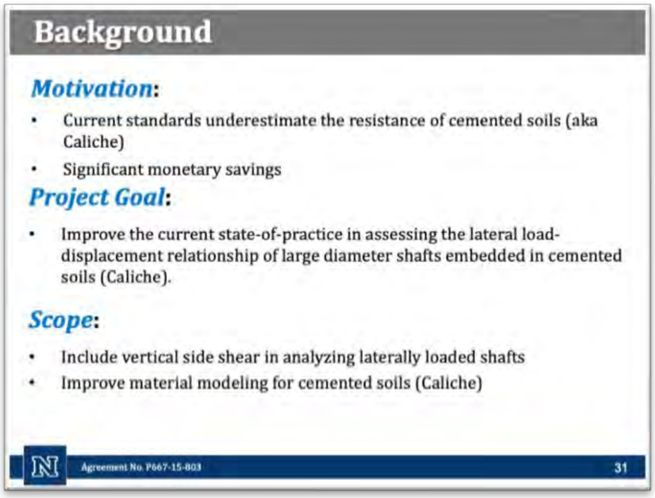

Background

***Motivation*:**

- Current standards underestimate the resistance of cemented soils (aka Caliche)
- Significant monetary savings

***Project Goal*:**

- Improve the current state-of-practice in assessing the lateral load-displacement relationship of large diameter shafts embedded in cemented soils (Caliche).

***Scope*:**

- Include vertical side shear in analyzing laterally loaded shafts
- Improve material modeling for cemented soils (Caliche)

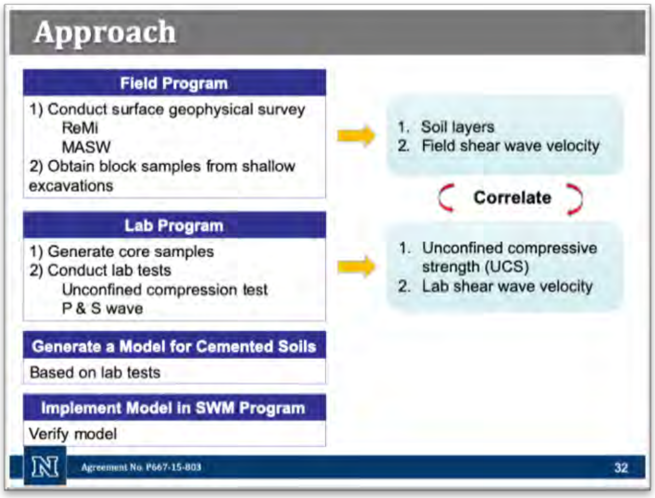

Approach

Field Program

1) Conduct surface geophysical survey
   ReMi
   MASW
2) Obtain block samples from shallow excavations

1. Soil layers
2. Field shear wave velocity

Correlate

Lab Program

1) Generate core samples
2) Conduct lab tests
   Unconfined compression test
   P & S wave

1. Unconfined compressive strength (UCS)
2. Lab shear wave velocity

Generate a Model for Cemented Soils

Based on lab tests

Implement Model in SWM Program

Verify model

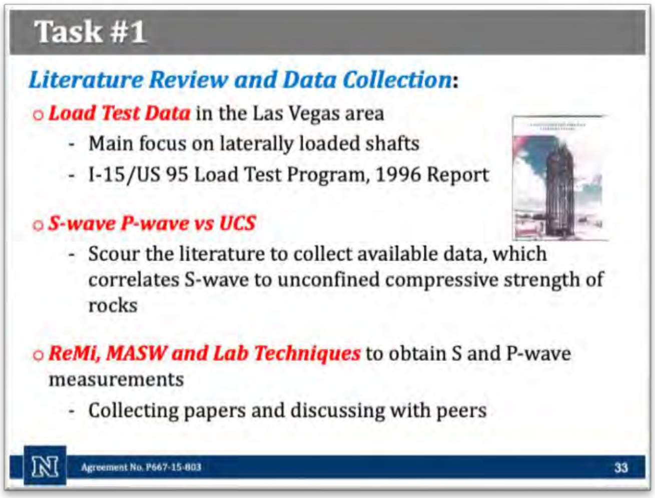

Task #1

***Literature Review and Data Collection*:**

- ***Load Test Data*** in the Las Vegas area
  - Main focus on laterally loaded shafts
  - I-15/US 95 Load Test Program, 1996 Report
- ***S-wave P-wave vs UCS***
  - Scour the literature to collect available data, which correlates S-wave to unconfined compressive strength of rocks
- ***ReMi, MASW and Lab Techniques*** to obtain S and P-wave measurements
  - Collecting papers and discussing with peers

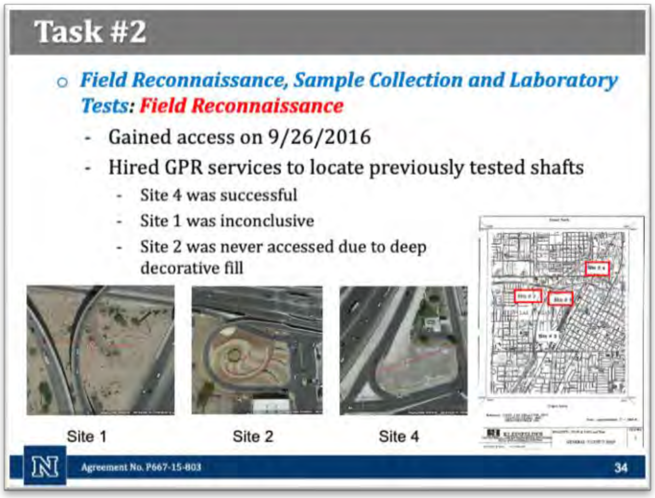

Task #2

- *Field Reconnaissance, Sample Collection and Laboratory Tests*: ***Field Reconnaissance***
  - Gained access on 9/26/2016
  - Hired GPR services to locate previously tested shafts
    - Site 4 was successful
    - Site 1 was inconclusive
    - Site 2 was never accessed due to deep decorative fill

Site 1 Site 2 Site 4

Agreement No. P667-15-803 34

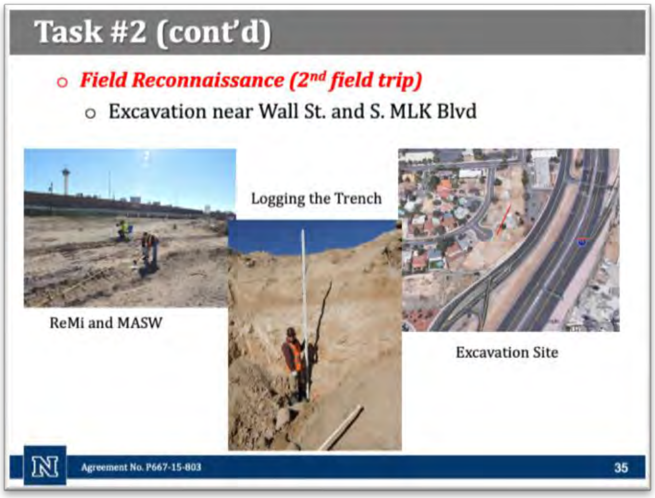

Task #2 (cont'd)

- ***Field Reconnaissance (2nd field trip)***
  - Excavation near Wall St. and S. MLK Blvd

ReMi and MASW

Logging the Trench

Excavation Site

Agreement No. P667-15-803 35

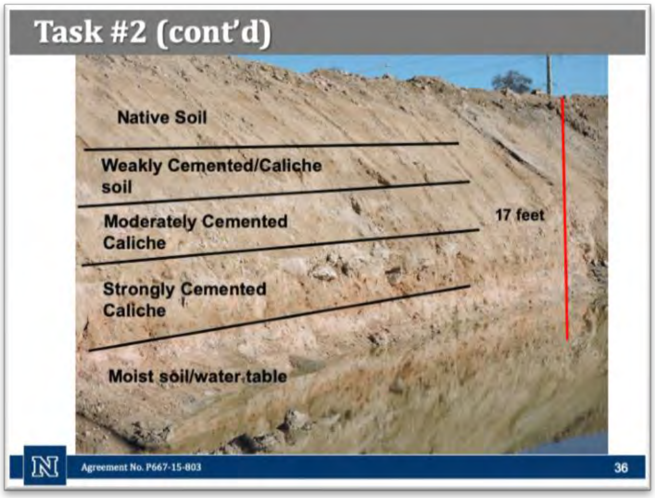

Task #2 (cont'd)

Native Soil
Weakly Cemented/Caliche soil
Moderately Cemented Caliche
17 feet
Strongly Cemented Caliche
Moist soil/water table

Agreement No. P667-15-803 36

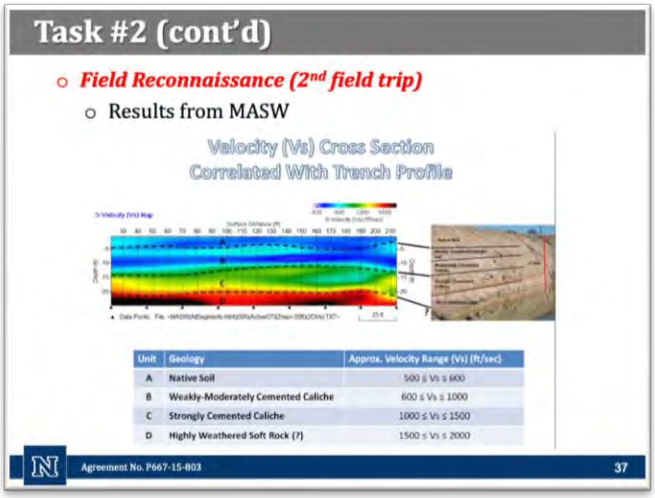

Task #2 (cont'd)

- *Field Reconnaissance (2nd field trip)*
  - Results from MASW

Velocity (Vs) Cross Section
Correlated With Trench Profile

Unit	Geology	Approx. Velocity Range (Vs) (ft/sec)
A	Native Soil	500 ≤ Vs ≤ 600
B	Weakly-Moderately Cemented Caliche	600 ≤ Vs ≤ 1000
C	Strongly Cemented Caliche	1000 ≤ Vs ≤ 1500
D	Highly Weathered Soft Rock (?)	1500 ≤ Vs ≤ 2000

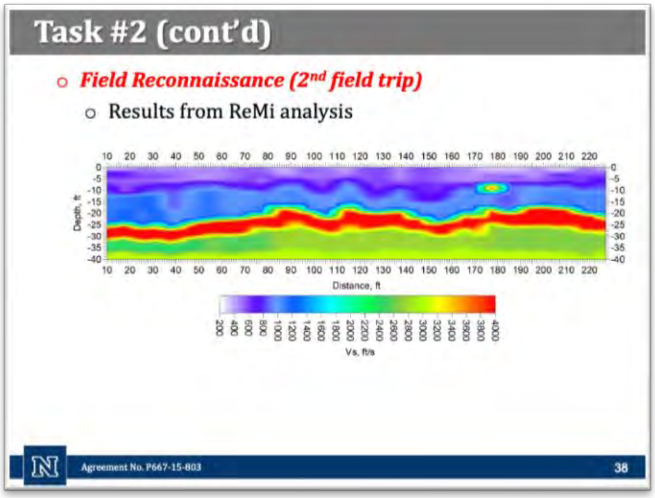

Task #2 (cont'd)

- *Field Reconnaissance (2nd field trip)*
  - Results from ReMi analysis

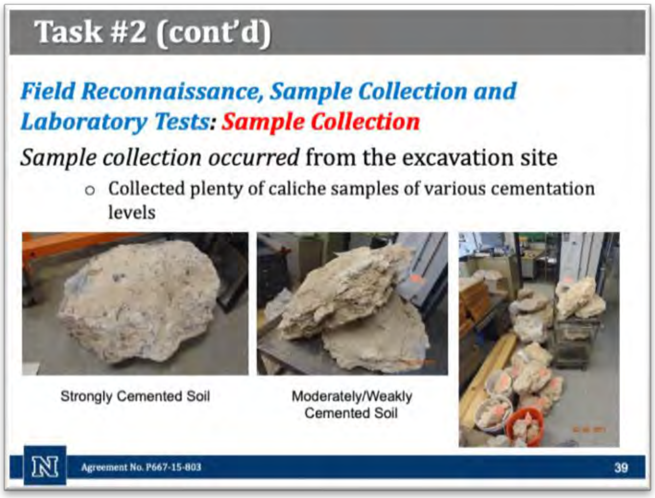

Task #2 (cont'd)

Field Reconnaissance, Sample Collection and Laboratory Tests: Sample Collection

Sample collection occurred from the excavation site

- Collected plenty of caliche samples of various cementation levels

Strongly Cemented Soil

Moderately/Weakly Cemented Soil

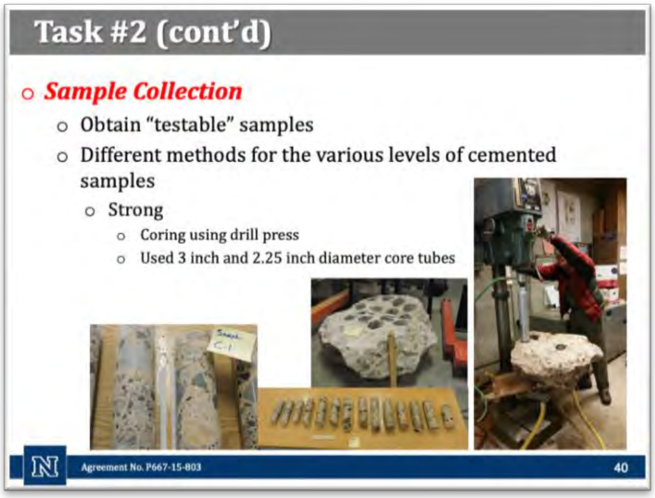

Task #2 (cont'd)

- ***Sample Collection***
  - Obtain "testable" samples
  - Different methods for the various levels of cemented samples
    - Strong
      - Coring using drill press
      - Used 3 inch and 2.25 inch diameter core tubes

Agreement No. P667-15-803 40

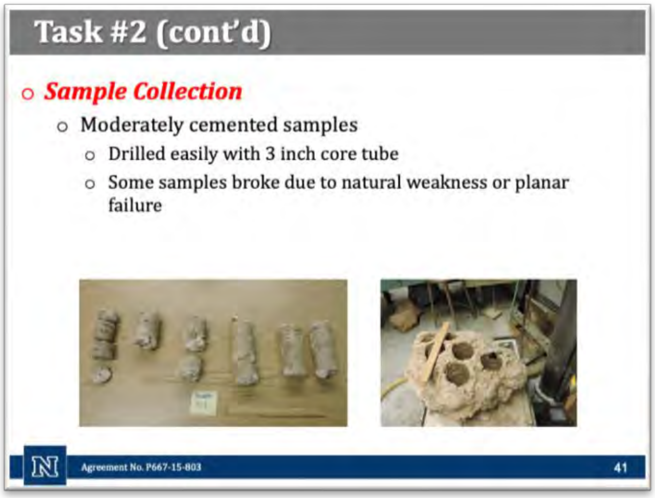

Task #2 (cont'd)

- ***Sample Collection***
  - Moderately cemented samples
    - Drilled easily with 3 inch core tube
    - Some samples broke due to natural weakness or planar failure

Agreement No. P667-15-803 41

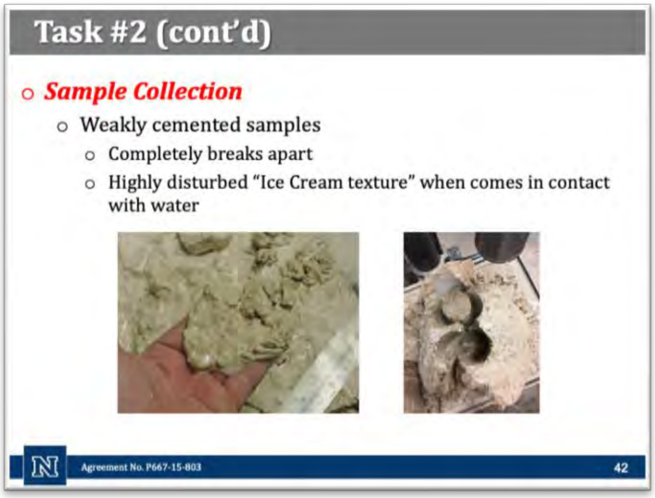

Task #2 (cont'd)

- ***Sample Collection***
  - Weakly cemented samples
    - Completely breaks apart
    - Highly disturbed "Ice Cream texture" when comes in contact with water

Agreement No. P667-15-803 42

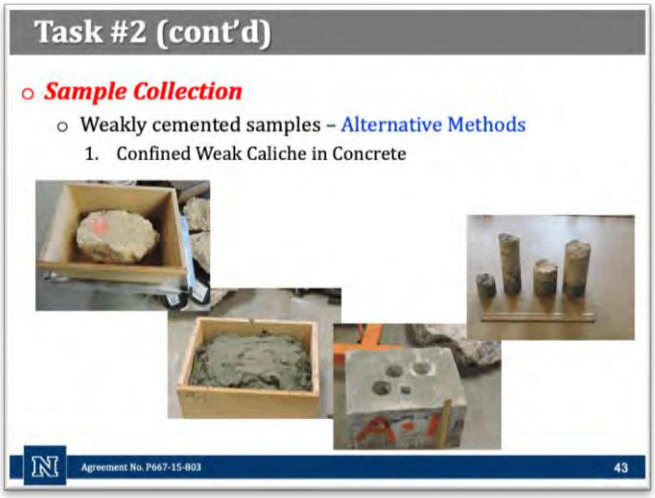

Task #2 (cont'd)

- *Sample Collection*
  - Weakly cemented samples – Alternative Methods
    1. Confined Weak Caliche in Concrete

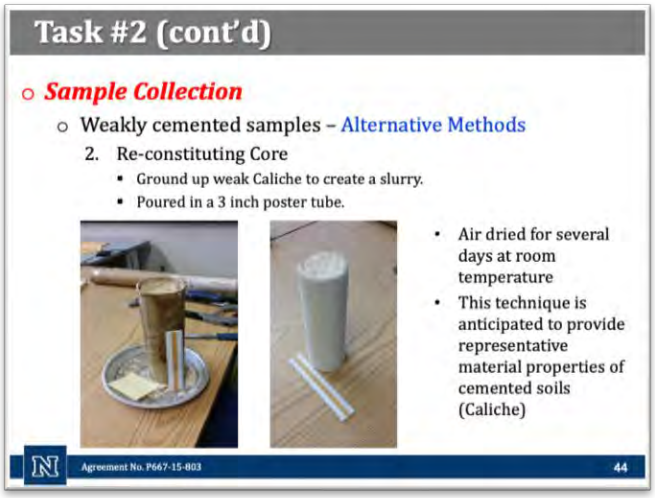

Task #2 (cont'd)

- *Sample Collection*
  - Weakly cemented samples – Alternative Methods
    2. Re-constituting Core
       - Ground up weak Caliche to create a slurry.
       - Poured in a 3 inch poster tube.
- Air dried for several days at room temperature
- This technique is anticipated to provide representative material properties of cemented soils (Caliche)

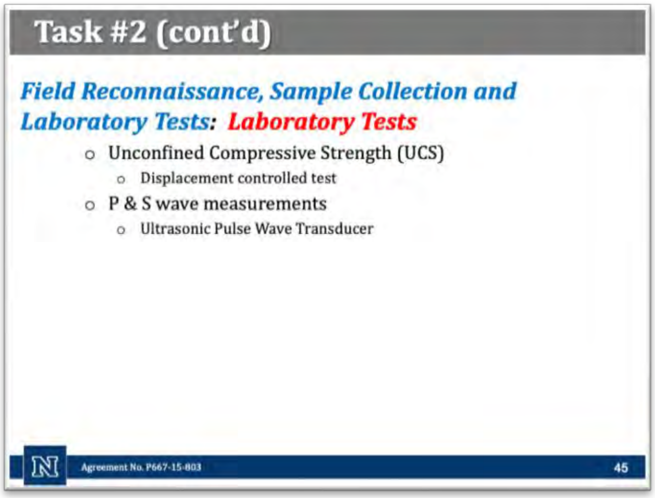

Task #2 (cont'd)

Field Reconnaissance, Sample Collection and Laboratory Tests: Laboratory Tests

- Unconfined Compressive Strength (UCS)
  - Displacement controlled test
- P & S wave measurements
  - Ultrasonic Pulse Wave Transducer

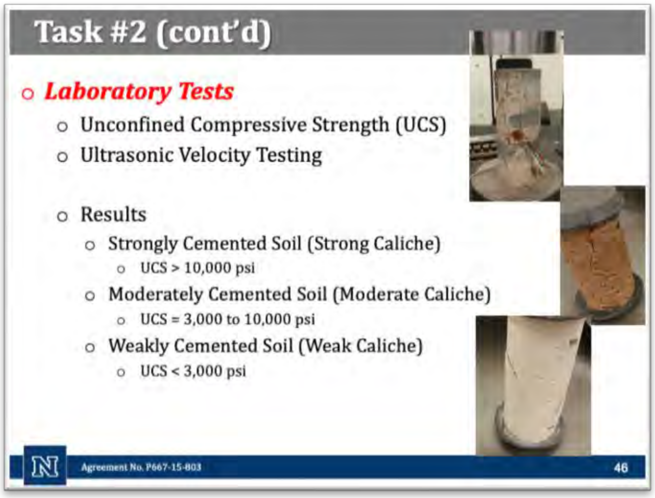

Task #2 (cont'd)

- ***Laboratory Tests***
  - Unconfined Compressive Strength (UCS)
  - Ultrasonic Velocity Testing
  - Results
    - Strongly Cemented Soil (Strong Caliche)
      - UCS > 10,000 psi
    - Moderately Cemented Soil (Moderate Caliche)
      - UCS = 3,000 to 10,000 psi
    - Weakly Cemented Soil (Weak Caliche)
      - UCS < 3,000 psi

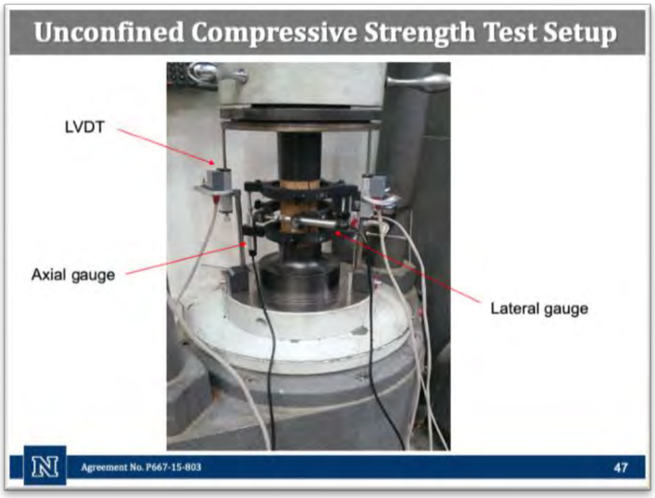

Unconfined Compressive Strength Test Setup

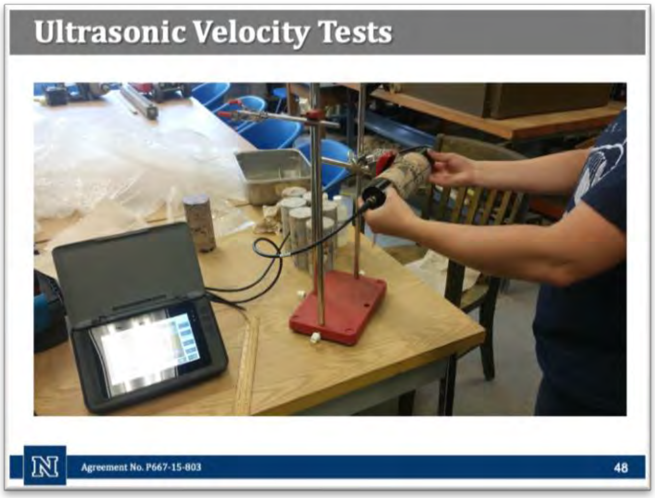

Ultrasonic Velocity Tests

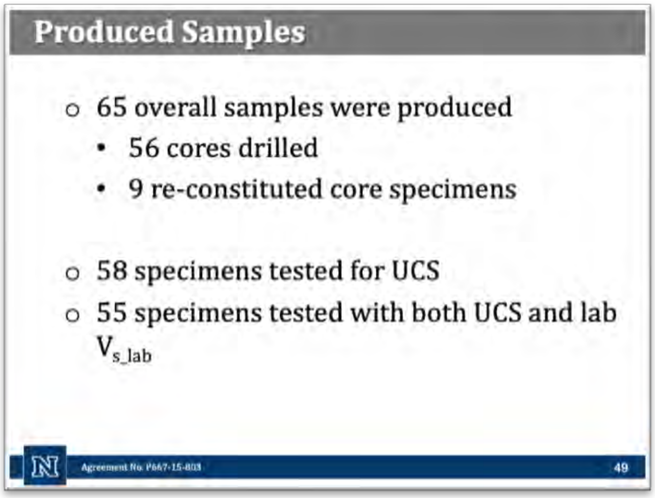

Produced Samples

- 65 overall samples were produced
  - 56 cores drilled
  - 9 re-constituted core specimens

- 58 specimens tested for UCS
- 55 specimens tested with both UCS and lab V_{s_lab}

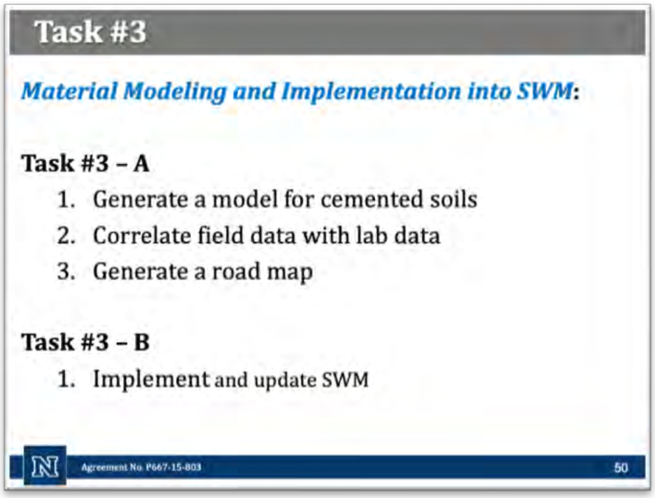

Task #3

***Material Modeling and Implementation into SWM*:**

Task #3 – A

1. Generate a model for cemented soils
2. Correlate field data with lab data
3. Generate a road map

Task #3 – B

1. Implement and update SWM

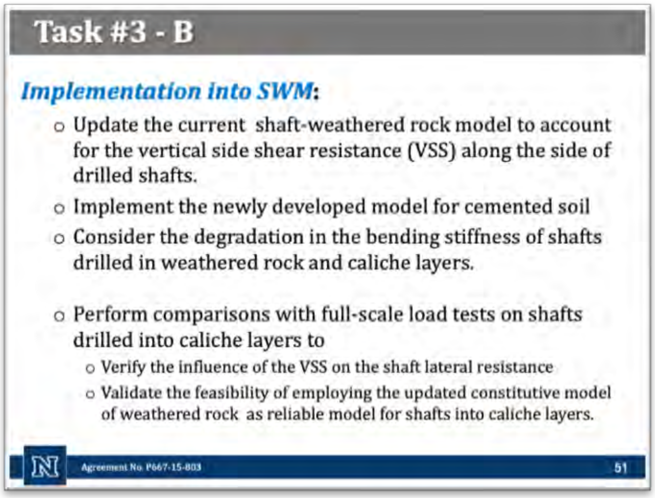

Task #3 - B

***Implementation into SWM*:**

- Update the current shaft-weathered rock model to account for the vertical side shear resistance (VSS) along the side of drilled shafts.
- Implement the newly developed model for cemented soil
- Consider the degradation in the bending stiffness of shafts drilled in weathered rock and caliche layers.

- Perform comparisons with full-scale load tests on shafts drilled into caliche layers to
  - Verify the influence of the VSS on the shaft lateral resistance
  - Validate the feasibility of employing the updated constitutive model of weathered rock as reliable model for shafts into caliche layers.

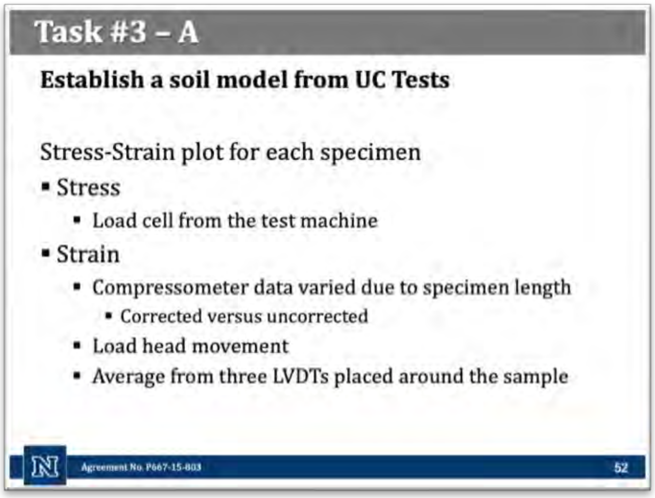

Task #3 – A

Establish a soil model from UC Tests

Stress-Strain plot for each specimen

- Stress
    - Load cell from the test machine
- Strain
    - Compressometer data varied due to specimen length
        - Corrected versus uncorrected
    - Load head movement
    - Average from three LVDTs placed around the sample

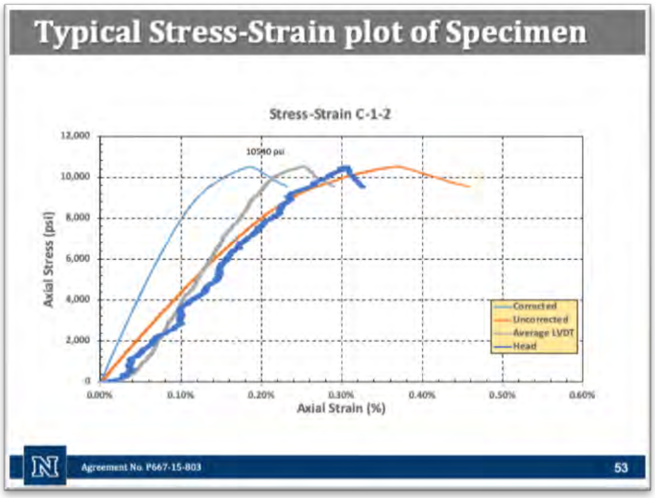

Typical Stress-Strain plot of Specimen

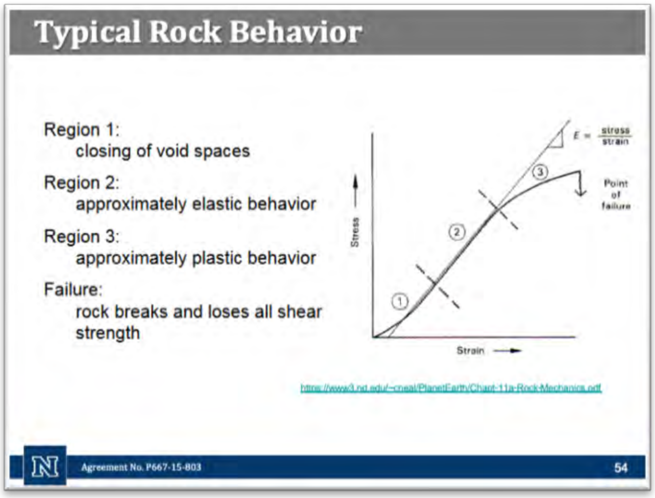

Typical Rock Behavior

Region 1:
closing of void spaces

Region 2:
approximately elastic behavior

Region 3:
approximately plastic behavior

Failure:
rock breaks and loses all shear strength

https://www3.nd.edu/~cneal/PlanetEarth/Chapt-11a-Rock-Mechanics.pdf

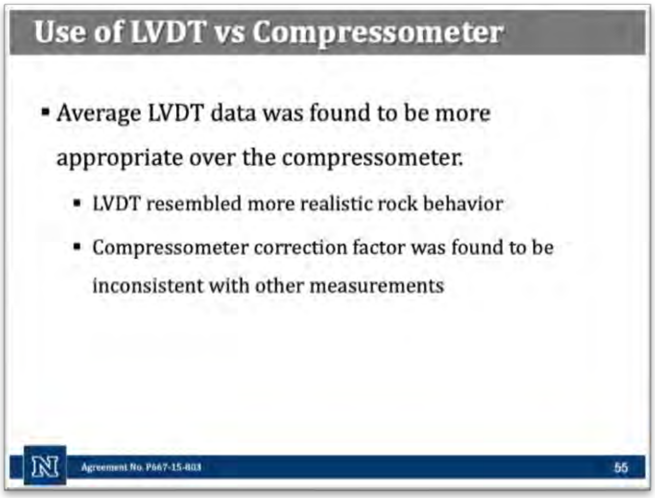

Use of LVDT vs Compressometer

- Average LVDT data was found to be more appropriate over the compressometer.
  - LVDT resembled more realistic rock behavior
  - Compressometer correction factor was found to be inconsistent with other measurements

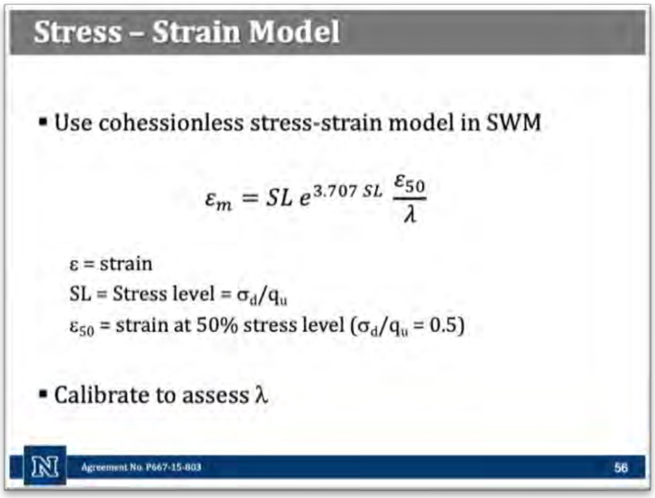

Stress – Strain Model

- Use cohessionless stress-strain model in SWM

$$\varepsilon_m = SL\, e^{3.707\, SL}\, \frac{\varepsilon_{50}}{\lambda}$$

ε = strain
SL = Stress level = σ_d/q_u
ε_{50} = strain at 50% stress level ($\sigma_d/q_u = 0.5$)

- Calibrate to assess λ

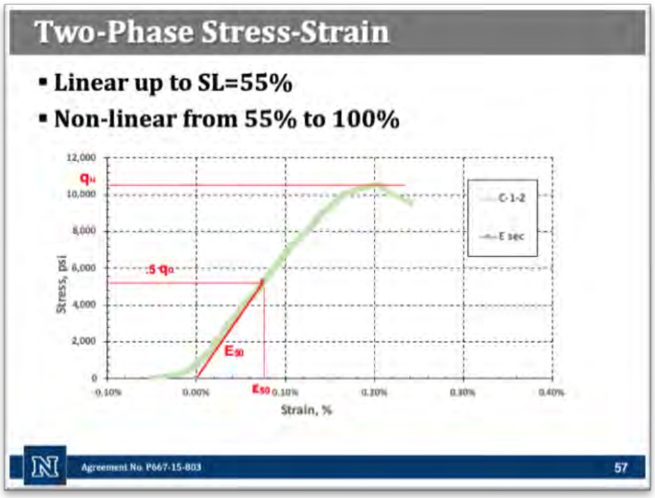

Two-Phase Stress-Strain

- **Linear up to SL=55%**
- **Non-linear from 55% to 100%**

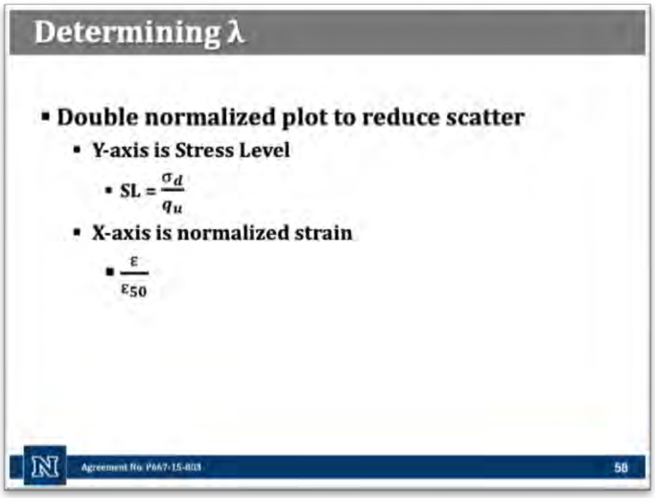

Determining λ

- Double normalized plot to reduce scatter
  - Y-axis is Stress Level
    - $SL = \frac{\sigma_d}{q_u}$
  - X-axis is normalized strain
    - $\frac{\varepsilon}{\varepsilon_{50}}$

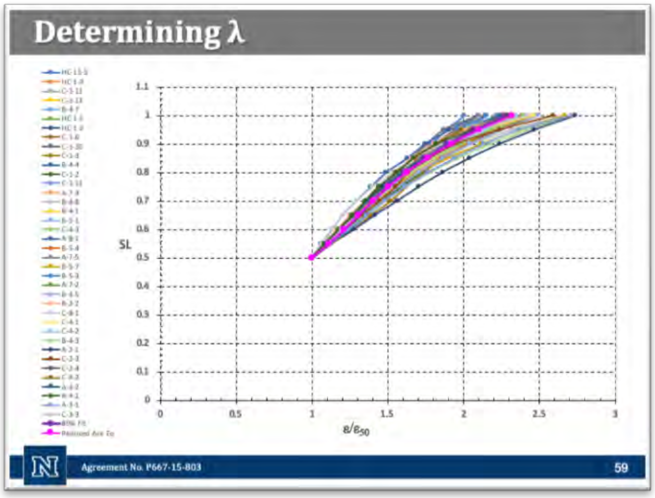

Determining λ

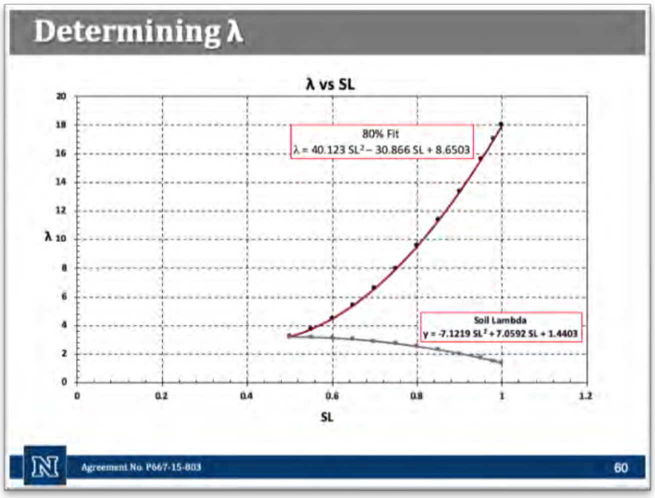

Determining λ

λ vs SL

80% Fit
$\lambda = 40.123\ SL^2 - 30.866\ SL + 8.6503$

Soil Lambda
$y = -7.1219\ SL^2 + 7.0592\ SL + 1.4403$

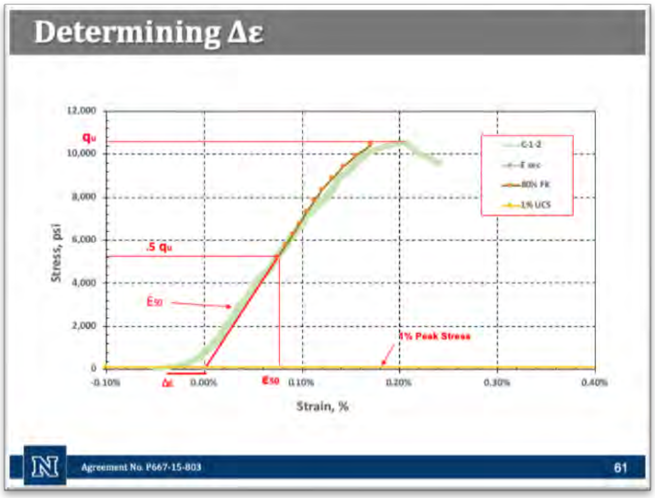

Determining Δε

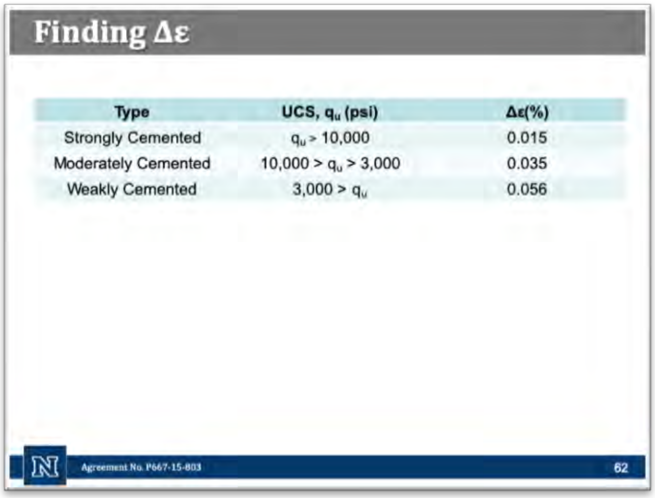

Finding Δε

Type	UCS, q_u (psi)	Δε(%)
Strongly Cemented	$q_u > 10{,}000$	0.015
Moderately Cemented	$10{,}000 > q_u > 3{,}000$	0.035
Weakly Cemented	$3{,}000 > q_u$	0.056

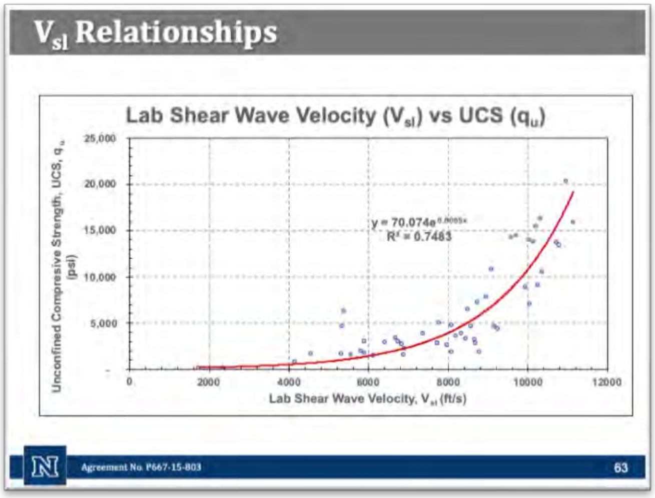

V_{sl} Relationships

Lab Shear Wave Velocity (V_{sl}) vs UCS (q_u)

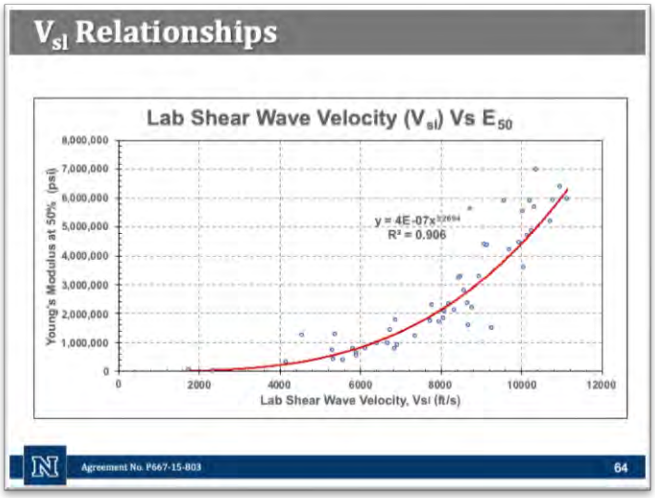

V_{sl} Relationships

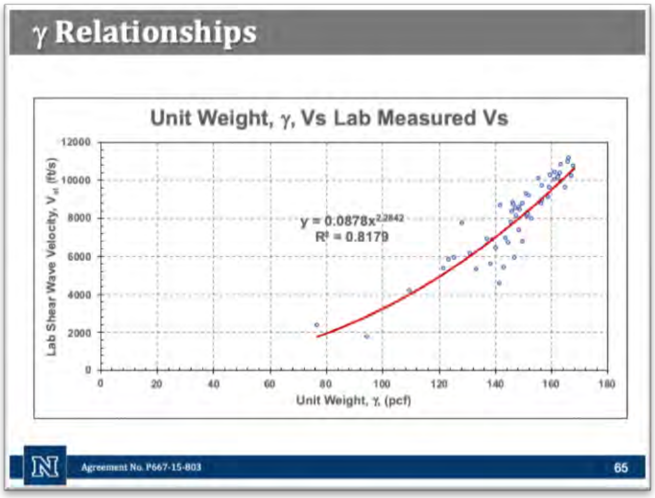

γ Relationships

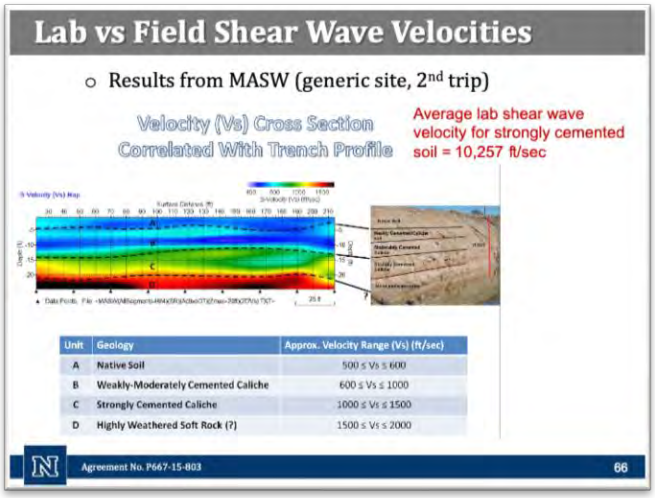

Lab vs Field Shear Wave Velocities

- Results from MASW (generic site, 2nd trip)

Velocity (Vs) Cross Section Correlated With Trench Profile

Average lab shear wave velocity for strongly cemented soil = 10,257 ft/sec

S Velocity (Vs) Map
Surface Distance (ft)
S-Velocity (Vs) (ft/sec)
Depth (ft)
A
B
C
D
25 ft

Unit	Geology	Approx. Velocity Range (Vs) (ft/sec)
A	Native Soil	500 ≤ Vs ≤ 600
B	Weakly-Moderately Cemented Caliche	600 ≤ Vs ≤ 1000
C	Strongly Cemented Caliche	1000 ≤ Vs ≤ 1500
D	Highly Weathered Soft Rock (?)	1500 ≤ Vs ≤ 2000

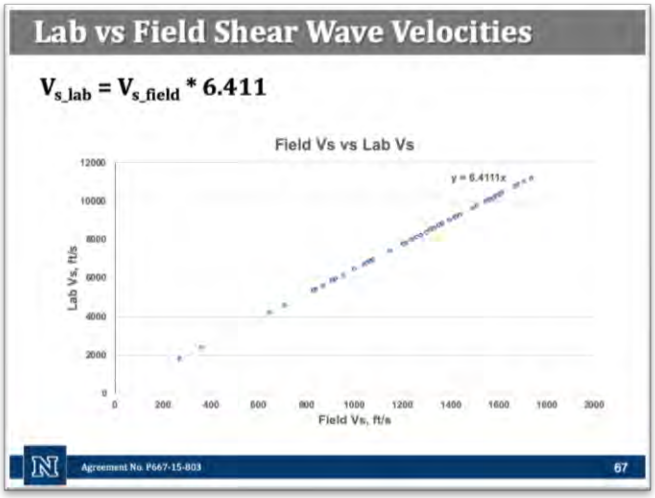

Lab vs Field Shear Wave Velocities

$V_{s\_lab} = V_{s\_field} * 6.411$

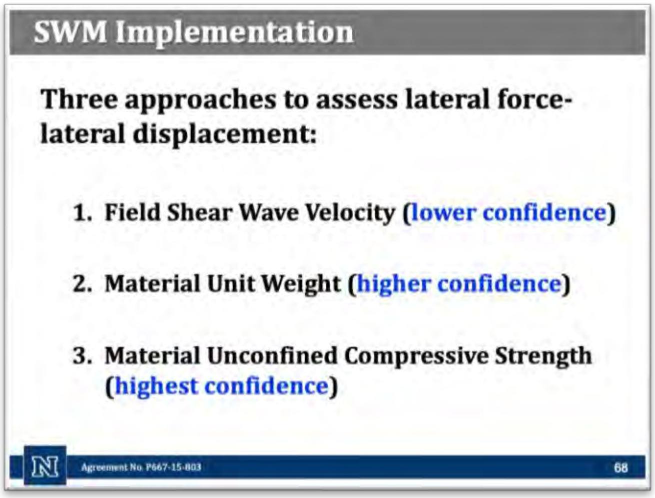

SWM Implementation

Three approaches to assess lateral force-lateral displacement:

1. **Field Shear Wave Velocity (lower confidence)**
2. **Material Unit Weight (higher confidence)**
3. **Material Unconfined Compressive Strength (highest confidence)**

Agreement No. P667-15-803
68

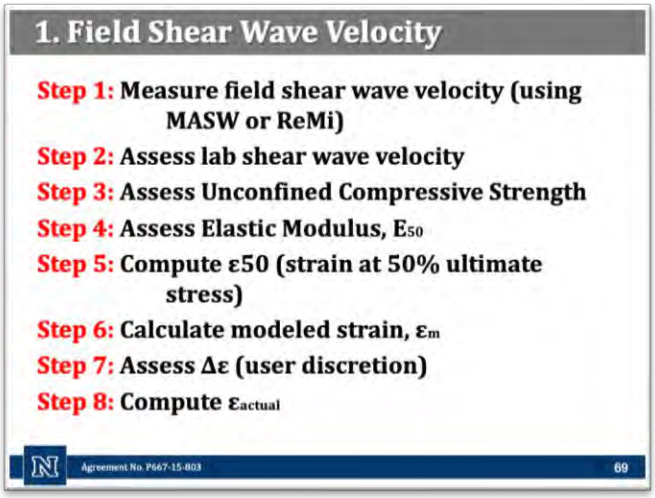

1. Field Shear Wave Velocity

Step 1: Measure field shear wave velocity (using MASW or ReMi)

Step 2: Assess lab shear wave velocity

Step 3: Assess Unconfined Compressive Strength

Step 4: Assess Elastic Modulus, E_{50}

Step 5: Compute ε50 (strain at 50% ultimate stress)

Step 6: Calculate modeled strain, ε_m

Step 7: Assess Δε (user discretion)

Step 8: Compute ε_{actual}

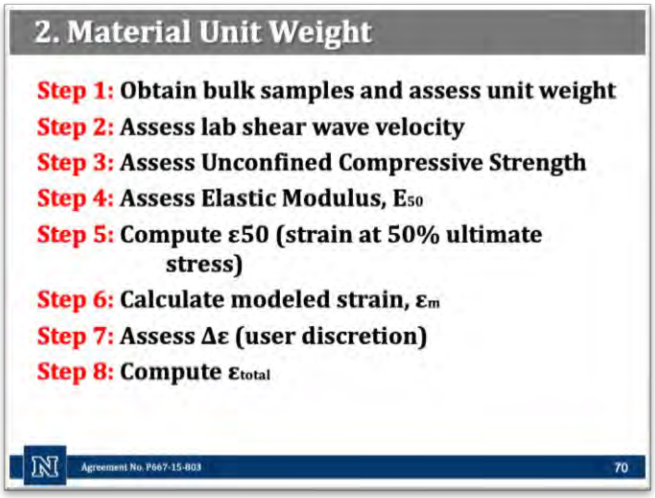

2. Material Unit Weight

Step 1: Obtain bulk samples and assess unit weight
Step 2: Assess lab shear wave velocity
Step 3: Assess Unconfined Compressive Strength
Step 4: Assess Elastic Modulus, E_{50}
Step 5: Compute ε50 (strain at 50% ultimate stress)
Step 6: Calculate modeled strain, ε_m
Step 7: Assess $\Delta\varepsilon$ (user discretion)
Step 8: Compute ε_{total}

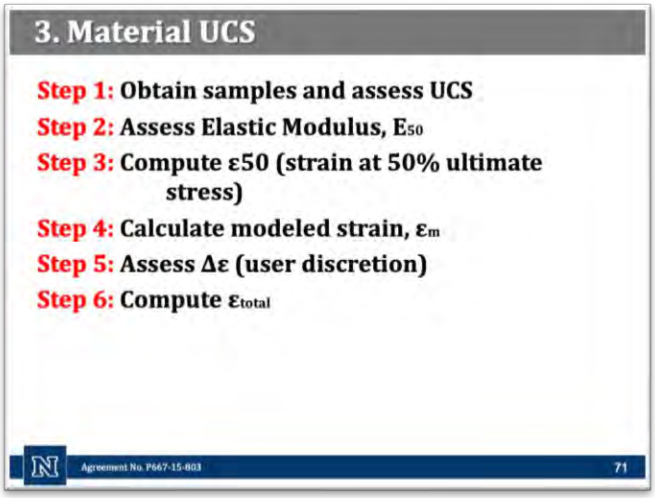

3. Material UCS

Step 1: Obtain samples and assess UCS
Step 2: Assess Elastic Modulus, E_{50}
Step 3: Compute ε50 (strain at 50% ultimate stress)
Step 4: Calculate modeled strain, ε_m
Step 5: Assess $\Delta\varepsilon$ (user discretion)
Step 6: Compute ε_{total}

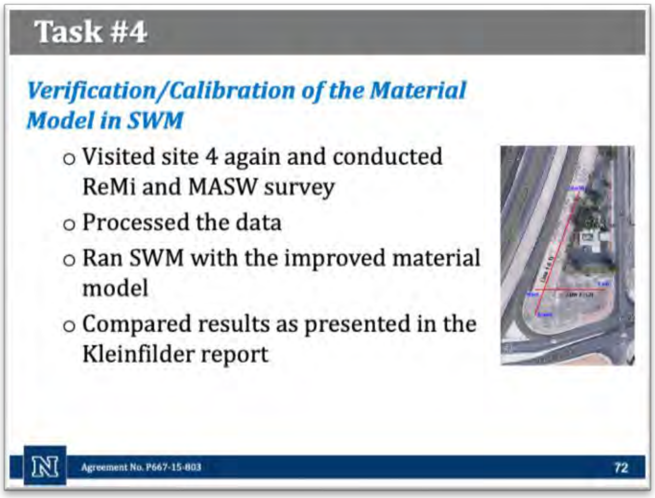

Task #4

Verification/Calibration of the Material Model in SWM

- Visited site 4 again and conducted ReMi and MASW survey
- Processed the data
- Ran SWM with the improved material model
- Compared results as presented in the Kleinfilder report

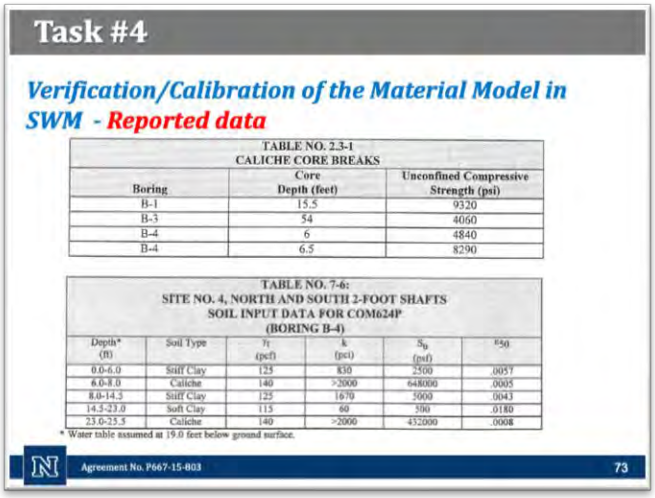

Task #4

Verification/Calibration of the Material Model in SWM - Reported data

TABLE NO. 2.3-1
CALICHE CORE BREAKS

Boring	Core Depth (feet)	Unconfined Compressive Strength (psi)
B-1	15.5	9320
B-3	54	4060
B-4	6	4840
B-4	6.5	8290

TABLE NO. 7-6:
SITE NO. 4, NORTH AND SOUTH 2-FOOT SHAFTS
SOIL INPUT DATA FOR COM624P
(BORING B-4)

Depth* (ft)	Soil Type	γ_t (pcf)	k (pci)	S_u (psf)	ε_{50}
0.0-6.0	Stiff Clay	125	830	2500	.0057
6.0-8.0	Caliche	140	>2000	648000	.0005
8.0-14.5	Stiff Clay	125	1670	5000	.0043
14.5-23.0	Soft Clay	115	60	500	.0180
23.0-25.5	Caliche	140	>2000	432000	.0008

* Water table assumed at 19.0 feet below ground surface.

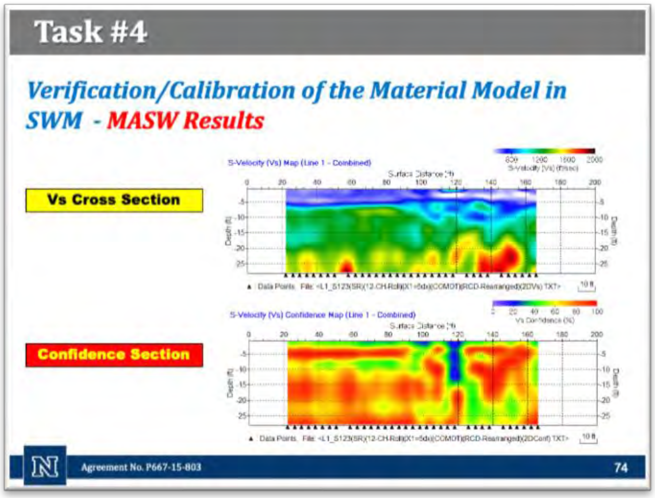

Task #4

Verification/Calibration of the Material Model in SWM - MASW Results

Vs Cross Section

Confidence Section

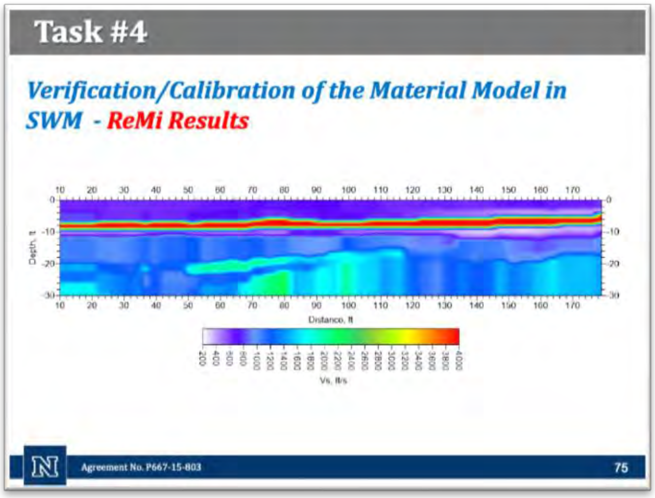

Task #4

Verification/Calibration of the Material Model in SWM - ReMi Results

Conclusions

- It is very challenging to capture the properties of commented soils (aka Caliche)
- The newly proposed material model for cemented soils provides good results
- Incorporating the contribution of vertical side shear to laterally loaded shafts improves SWM capabilities in capturing shaft field response

Implementation of Cemented Soil Model in SWM

LAS VEGAS TEST (2-FT DIAMETER SHAFT, SITE 1)

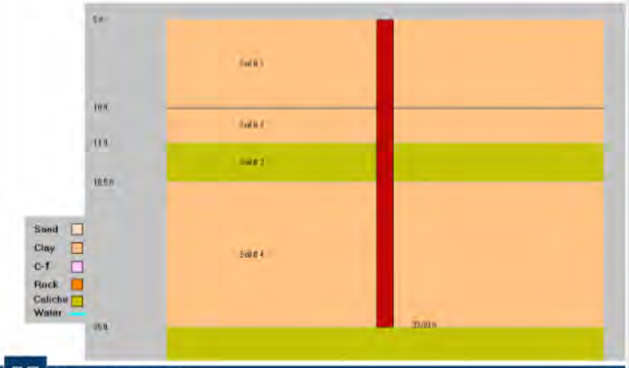

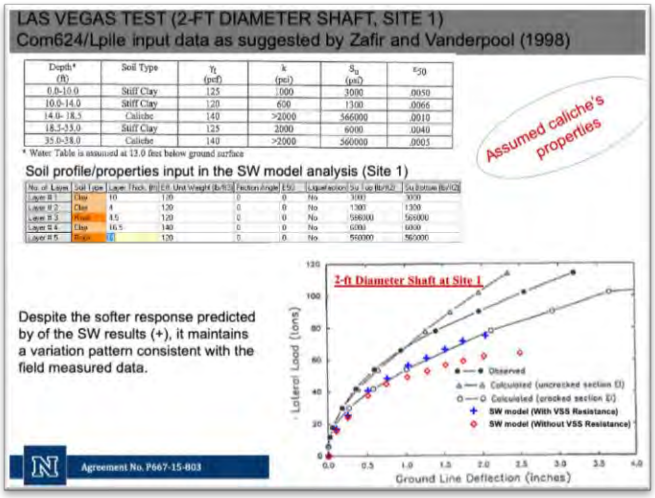

LAS VEGAS TEST (2-FT DIAMETER SHAFT, SITE 1)
Com624/Lpile input data as suggested by Zafir and Vanderpool (1998)

Depth* (ft)	Soil Type	γ_t (pcf)	k (pci)	S_u (psf)	ε_{50}
0.0-10.0	Stiff Clay	125	1000	3000	.0050
10.0-14.0	Stiff Clay	120	600	1300	.0066
14.0- 18.5	Caliche	140	>2000	566000	.0010
18.5-35.0	Stiff Clay	125	2000	6000	.0040
35.0-38.0	Caliche	140	>2000	560000	.0005

* Water Table is assumed at 13.0 feet below ground surface

Soil profile/properties input in the SW model analysis (Site 1)

No. of Layer	Soil Type	Layer Thick. (ft)	Eff. Unit Weight (lb/ft3)	Friction Angle	E50	Liquefaction	Su Top (lb/ft2)	Su Bottom (lb/ft2)
Layer # 1	Clay	10	120	0	0	No	3000	3000
Layer # 2	Clay	4	120	0	0	No	1300	1300
Layer # 3	Rock	4.5	120	0	0	No	566000	566000
Layer # 4	Clay	16.5	140	0	0	No	6000	6000
Layer # 5	Rock	3	120	0	0	No	560000	560000

Despite the softer response predicted by of the SW results (+), it maintains a variation pattern consistent with the field measured data.

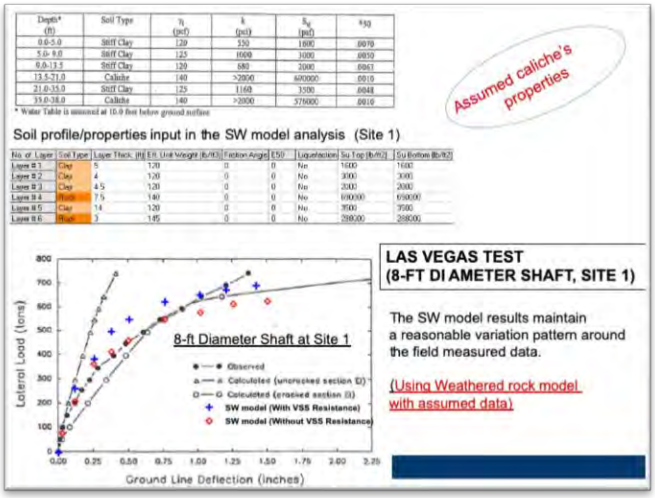

Depth* (ft)	Soil Type	γ_t (pcf)	k (pci)	S_u (psf)	ε_{50}
0.0-5.0	Stiff Clay	120	550	1600	.0070
5.0- 9.0	Stiff Clay	125	1000	3000	.0050
9.0-13.5	Stiff Clay	120	680	2000	.0067
13.5-21.0	Caliche	140	>2000	690000	.0010
21.0-35.0	Stiff Clay	125	1160	3500	.0048
35.0-38.0	Caliche	140	>2000	576000	.0010

* Water Table is assumed at 10.0 feet below ground surface

Soil profile/properties input in the SW model analysis (Site 1)

No. of Layer	Soil Type	Layer Thick. (ft)	Eff. Unit Weight (lb/ft3)	Friction Angle	E50	Liquefaction	Su Top (lb/ft2)	Su Bottom (lb/ft2)
Layer # 1	Clay	5	120	0	0	No	1600	1600
Layer # 2	Clay	4	120	0	0	No	3000	3000
Layer # 3	Clay	4.5	120	0	0	No	2000	2000
Layer # 4	Rock	7.5	140	0	0	No	690000	650000
Layer # 5	Clay	14	120	0	0	No	3500	3500
Layer # 6	Rock	3	145	0	0	No	288000	288000

LAS VEGAS TEST
(8-FT DI AMETER SHAFT, SITE 1)

The SW model results maintain a reasonable variation pattern around the field measured data.

(Using Weathered rock model with assumed data)

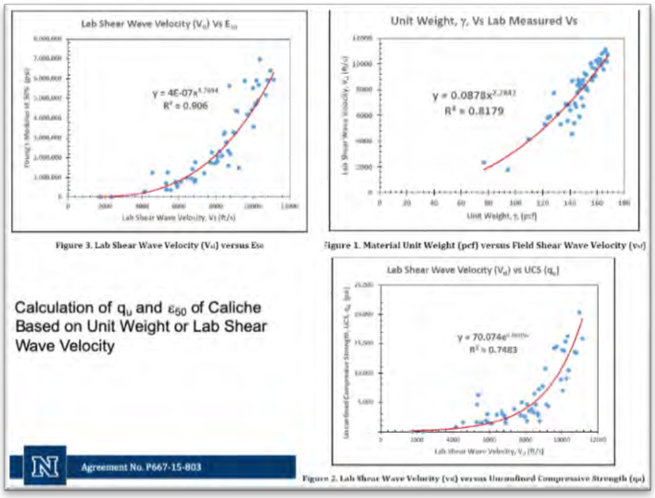

Figure 3. Lab Shear Wave Velocity (V_s) versus E_{50}

igure 1. Material Unit Weight (pcf) versus Field Shear Wave Velocity (v_s)

Calculation of q_u and ε_{60} of Caliche Based on Unit Weight or Lab Shear Wave Velocity

Figure 2. Lab Shear Wave Velocity (v_s) versus Unconfined Compressive Strength (q_u)

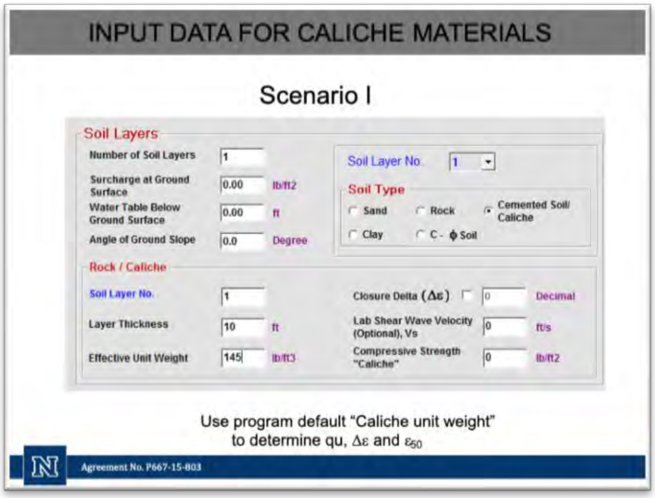

INPUT DATA FOR CALICHE MATERIALS

Scenario I

Soil Layers

Number of Soil Layers: 1
Surcharge at Ground Surface: 0.00 lb/ft2
Water Table Below Ground Surface: 0.00 ft
Angle of Ground Slope: 0.0 Degree

Soil Layer No.: 1

Soil Type

○ Sand ○ Rock ● Cemented Soil/ Caliche
○ Clay ○ C - ϕ Soil

Rock / Caliche

Soil Layer No.: 1
Layer Thickness: 10 ft
Effective Unit Weight: 145 lb/ft3
Closure Delta (Δε) ☐ 0 Decimal
Lab Shear Wave Velocity (Optional), Vs: 0 ft/s
Compressive Strength "Caliche": 0 lb/ft2

Use program default "Caliche unit weight"
to determine qu, Δε and ε_{50}

Agreement No. P667-15-803

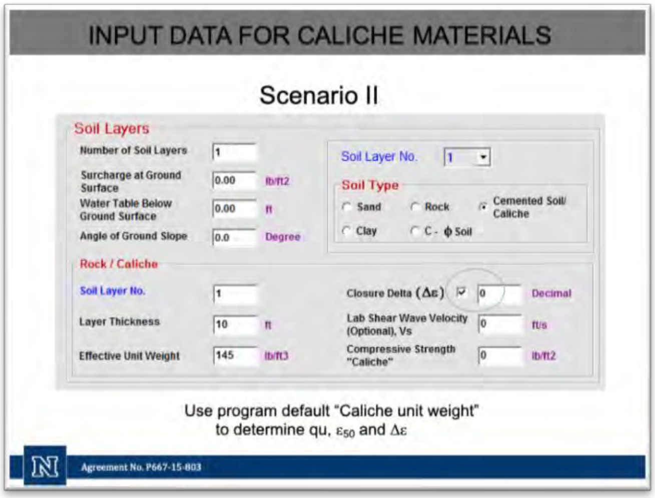

INPUT DATA FOR CALICHE MATERIALS

Scenario II

Soil Layers

Number of Soil Layers: 1
Surcharge at Ground Surface: 0.00 lb/ft2
Water Table Below Ground Surface: 0.00 ft
Angle of Ground Slope: 0.0 Degree

Soil Layer No.: 1

Soil Type

○ Sand ○ Rock ● Cemented Soil/ Caliche
○ Clay ○ C - ϕ Soil

Rock / Caliche

Soil Layer No.: 1
Layer Thickness: 10 ft
Effective Unit Weight: 145 lb/ft3
Closure Delta (Δε) ☑ 0 Decimal
Lab Shear Wave Velocity (Optional), Vs: 0 ft/s
Compressive Strength "Caliche": 0 lb/ft2

Use program default "Caliche unit weight"
to determine qu, ε_{50} and Δε

Agreement No. P667-15-803

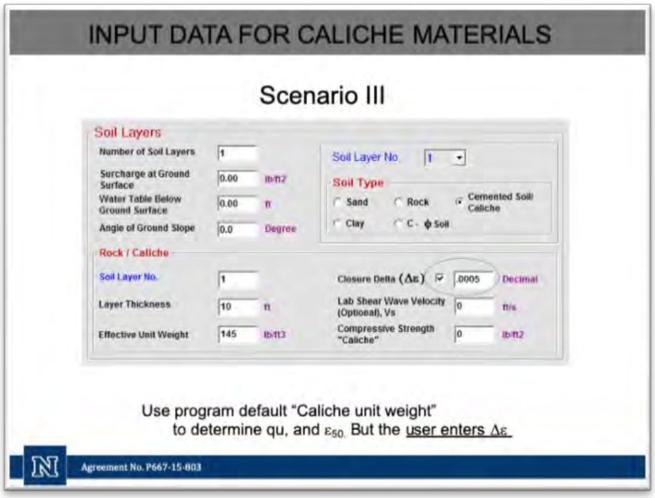

INPUT DATA FOR CALICHE MATERIALS

Scenario III

Soil Layers

Number of Soil Layers: 1
Surcharge at Ground Surface: 0.00 lb/ft2
Water Table Below Ground Surface: 0.00 ft
Angle of Ground Slope: 0.0 Degree

Soil Layer No.: 1

Soil Type

○ Sand ○ Rock ● Cemented Soil/ Caliche
○ Clay ○ C - ϕ Soil

Rock / Caliche

Soil Layer No.: 1
Layer Thickness: 10 ft
Effective Unit Weight: 145 lb/ft3
Closure Delta (Δε) ☑ .0005 Decimal
Lab Shear Wave Velocity (Optional), Vs: 0 ft/s
Compressive Strength "Caliche": 0 lb/ft2

Use program default "Caliche unit weight"
to determine qu, and ε_{50}. But the user enters Δε

Agreement No. P667-15-803

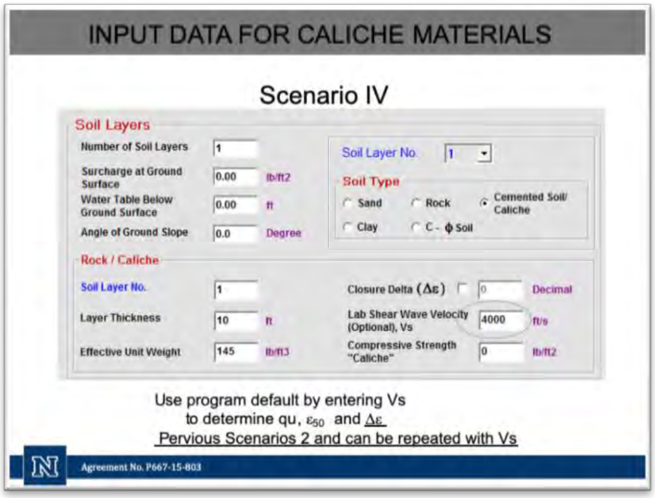

INPUT DATA FOR CALICHE MATERIALS

Scenario IV

Soil Layers

Number of Soil Layers: 1

Surcharge at Ground Surface: 0.00 lb/ft2

Water Table Below Ground Surface: 0.00 ft

Angle of Ground Slope: 0.0 Degree

Soil Layer No.: 1

Soil Type

○ Sand ○ Rock ● Cemented Soil/ Caliche

○ Clay ○ C - ϕ Soil

Rock / Caliche

Soil Layer No.: 1

Layer Thickness: 10 ft

Effective Unit Weight: 145 lb/ft3

Closure Delta ($\Delta\varepsilon$) ☐ 0 Decimal

Lab Shear Wave Velocity (Optional), Vs: 4000 ft/s

Compressive Strength "Caliche": 0 lb/ft2

Use program default by entering Vs to determine qu, ε_{50} and $\Delta\varepsilon$

Pervious Scenarios 2 and can be repeated with Vs

Agreement No. P667-15-803

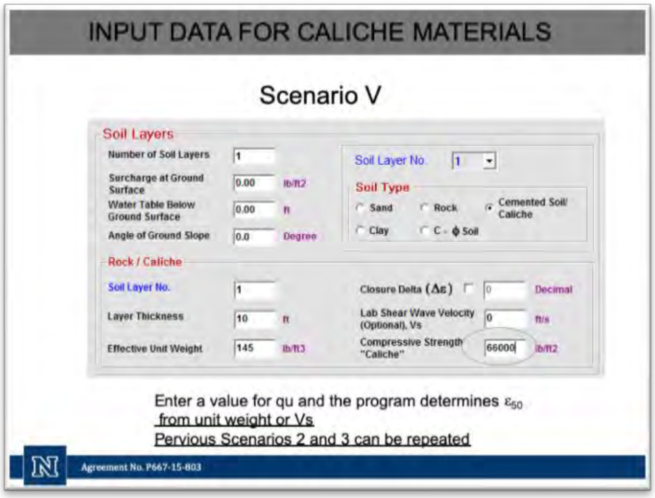

INPUT DATA FOR CALICHE MATERIALS

Scenario V

Soil Layers

Number of Soil Layers: 1

Surcharge at Ground Surface: 0.00 lb/ft2

Water Table Below Ground Surface: 0.00 ft

Angle of Ground Slope: 0.0 Degree

Soil Layer No.: 1

Soil Type

○ Sand ○ Rock ● Cemented Soil/ Caliche

○ Clay ○ C - ϕ Soil

Rock / Caliche

Soil Layer No.: 1

Layer Thickness: 10 ft

Effective Unit Weight: 145 lb/ft3

Closure Delta ($\Delta\varepsilon$) ☐ 0 Decimal

Lab Shear Wave Velocity (Optional), Vs: 0 ft/s

Compressive Strength "Caliche": 66000 lb/ft2

Enter a value for qu and the program determines ε_{50} from unit weight or Vs

Pervious Scenarios 2 and 3 can be repeated

Agreement No. P667-15-803

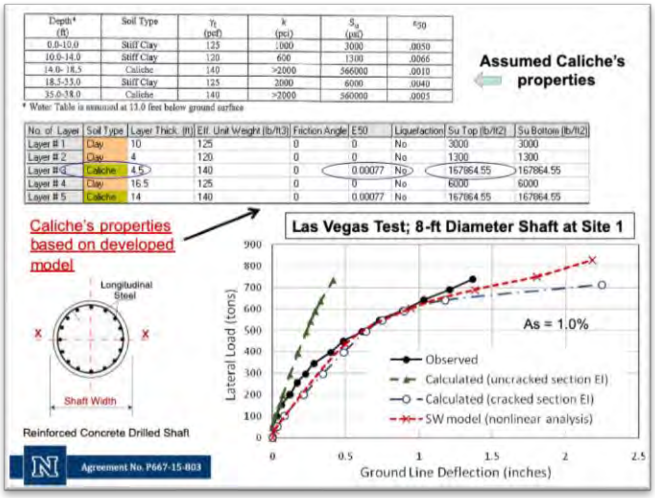

Depth* (ft)	Soil Type	γ_t (pcf)	k (pci)	S_u (psf)	ε_{50}
0.0-10.0	Stiff Clay	125	1000	3000	.0050
10.0-14.0	Stiff Clay	120	600	1300	.0066
14.0- 18.5	Caliche	140	>2000	566000	.0010
18.5-35.0	Stiff Clay	125	2000	6000	.0040
35.0-38.0	Caliche	140	>2000	560000	.0005

* Water Table is assumed at 13.0 feet below ground surface

Assumed Caliche's properties

No. of Layer	Soil Type	Layer Thick. (ft)	Eff. Unit Weight (lb/ft3)	Friction Angle	E50	Liquefaction	Su Top (lb/ft2)	Su Bottom (lb/ft2)
Layer # 1	Clay	10	125	0	0	No	3000	3000
Layer # 2	Clay	4	120	0	0	No	1300	1300
Layer # 3	Caliche	4.5	140	0	0.00077	No	167864.55	167864.55
Layer # 4	Clay	16.5	125	0	0	No	6000	6000
Layer # 5	Caliche	14	140	0	0.00077	No	167864.55	167864.55

Caliche's properties based on developed model

Las Vegas Test; 8-ft Diameter Shaft at Site 1

Longitudinal Steel
x
x
Shaft Width
Reinforced Concrete Drilled Shaft
Lateral Load (tons)
900
800
700
600
500
400
300
200
100
0
0
0.5
1
1.5
2
2.5
Ground Line Deflection (inches)
As = 1.0%
Observed
Calculated (uncracked section EI)
Calculated (cracked section EI)
SW model (nonlinear analysis)

Agreement No. P667-15-803

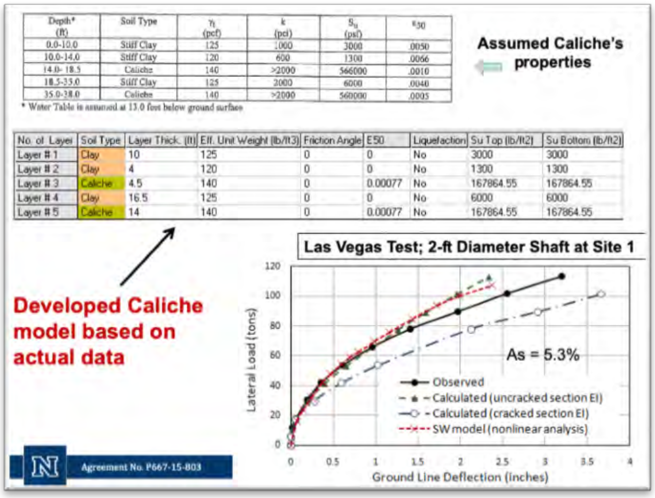

Depth* (ft)	Soil Type	γ_t (pcf)	k (pci)	S_u (psf)	ε_{50}
0.0-10.0	Stiff Clay	125	1000	3000	.0050
10.0-14.0	Stiff Clay	120	600	1300	.0066
14.0- 18.5	Caliche	140	>2000	566000	.0010
18.5-35.0	Stiff Clay	125	2000	6000	.0040
35.0-38.0	Caliche	140	>2000	560000	.0005

* Water Table is assumed at 13.0 feet below ground surface

Assumed Caliche's properties

No. of Layer	Soil Type	Layer Thick. (ft)	Eff. Unit Weight (lb/ft3)	Friction Angle	E50	Liquefaction	Su Top (lb/ft2)	Su Bottom (lb/ft2)
Layer # 1	Clay	10	125	0	0	No	3000	3000
Layer # 2	Clay	4	120	0	0	No	1300	1300
Layer # 3	Caliche	4.5	140	0	0.00077	No	167864.55	167864.55
Layer # 4	Clay	16.5	125	0	0	No	6000	6000
Layer # 5	Caliche	14	140	0	0.00077	No	167864.55	167864.55

Developed Caliche model based on actual data

Las Vegas Test; 2-ft Diameter Shaft at Site 1

Lateral Load (tons)
120
100
80
60
40
20
0
Ground Line Deflection (inches)
0
0.5
1
1.5
2
2.5
3
3.5
4
As = 5.3%
Observed
Calculated (uncracked section EI)
Calculated (cracked section EI)
SW model (nonlinear analysis)

Agreement No. P667-15-803

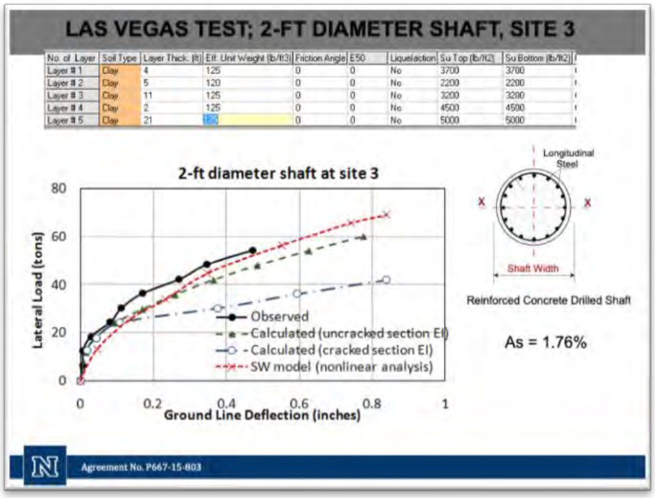

LAS VEGAS TEST; 2-FT DIAMETER SHAFT, SITE 3

No. of Layer	Soil Type	Layer Thick. (ft)	Eff. Unit Weight (lb/ft3)	Friction Angle	E50	Liquefaction	Su Top (lb/ft2)	Su Bottom (lb/ft2)
Layer # 1	Clay	4	125	0	0	No	3700	3700
Layer # 2	Clay	5	120	0	0	No	2200	2200
Layer # 3	Clay	11	125	0	0	No	3200	3200
Layer # 4	Clay	2	125	0	0	No	4500	4500
Layer # 5	Clay	21	125	0	0	No	5000	5000

2-ft diameter shaft at site 3

Reinforced Concrete Drilled Shaft

As = 1.76%

Agreement No. P667-15-803

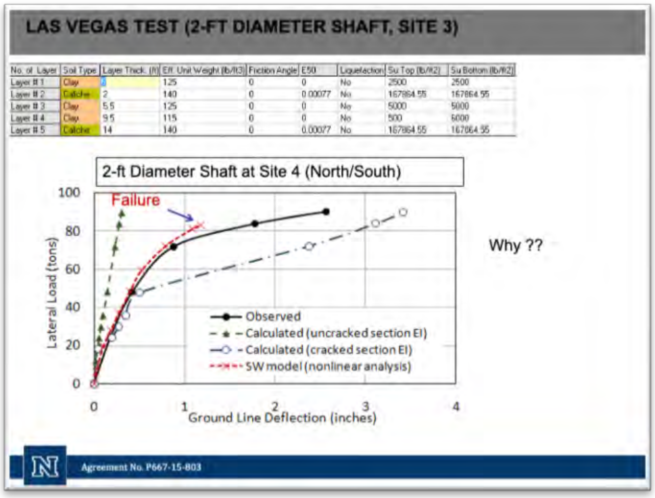

LAS VEGAS TEST (2-FT DIAMETER SHAFT, SITE 3)

No. of Layer	Soil Type	Layer Thick. (ft)	Eff. Unit Weight (lb/ft3)	Friction Angle	E50	Liquefaction	Su Top (lb/ft2)	Su Bottom (lb/ft2)
Layer # 1	Clay	6	125	0	0	No	2500	2500
Layer # 2	Caliche	2	140	0	0.00077	No	167864.55	167864.55
Layer # 3	Clay	5.5	125	0	0	No	5000	5000
Layer # 4	Clay	9.5	115	0	0	No	500	6000
Layer # 5	Caliche	14	140	0	0.00077	No	167864.55	167864.55

2-ft Diameter Shaft at Site 4 (North/South)

Failure
Lateral Load (tons)
100
80
60
40
20
0
Ground Line Deflection (inches)
0
1
2
3
4
Observed
Calculated (uncracked section EI)
Calculated (cracked section EI)
SW model (nonlinear analysis)

Why ??

Agreement No. P667-15-803

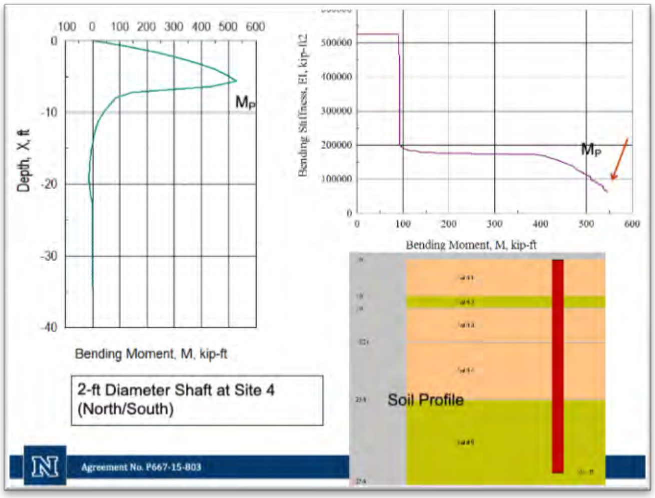

2-ft Diameter Shaft at Site 4
(North/South)

Soil Profile

Agreement No. P667-15-803

PROGRAM DEMONSTRATION
&
TRAINING SESSION

Agreement No. P667-15-803

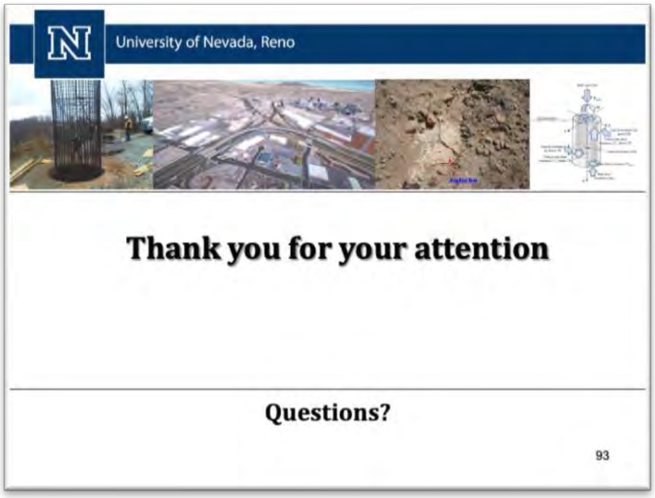

University of Nevada, Reno

Thank you for your attention

Questions?

THE GREAT SEAL OF THE STATE OF
NEVADA
ALL FOR OUR COUNTRY

Nevada Department of Transportation
Kristina L. Swallow, P.E. Director
Ken Chambers, Research Division Chief
(775) 888-7220
kchambers@dot.nv.gov
1263 South Stewart Street
Carson City, Nevada 89712